1998

Microstructure and corrosion of magnetron sputtered sacrificial coatings for sheet steel

Bryan Andrew Shedden
University of Wollongong

MICROSTRUCTURE AND CORROSION OF MAGNETRON SPUTTERED SACRIFICIAL COATINGS FOR SHEET STEEL

A thesis submitted in fulfilment of the requirements for the award of the degree of

DOCTOR OF PHILOSOPHY

from

THE UNIVERSITY OF WOLLONGONG

by

BRYAN ANDREW SHEDDEN

BE (Hons.)

DEPARTMENT OF MATERIALS ENGINEERING

January 1998

In dedication to the memory of my wonderful mother

GAI NITA SHEDDEN

deeply missed

CANDIDATE'S CERTIFICATE

This is to certify that the work presented in this thesis was original and carried out by the candidate in the Department of Materials Engineering at the University of Wollongong and has not been submitted to any other university for a higher degree.

Bryan A. Shedden

ACKNOWLEDGEMENT

The research presented in this thesis was carried out under the supervision of Dr. Masoud Samandi of the University of Wollongong and Dr. Brian Window of CSIRO (retired 1995). Access to facilities in the Department of Materials Engineering at the University of Wollongong, CSIRO Division of Applied Physics, and the Coated Steel Research Laboratories of BHP Research, was gratefully received. Acknowledgement is extended to the affable contribution of T-DYN computer simulations by Dr. Ilia Katardjiev and Dr. Sören Berg from Uppsala University, Sweden.

I would like to thank the University of Wollongong for providing me with an Australian Postgraduate Research Award to support this work. The generosity of BHP Research is appreciated in granting me a leave of absence for the duration of this study, and for providing a modest degree of financial assistance.

My earnest gratitude is extended to Dr. Brian Window for taking me under his wing and ensuring the suitable complexion of my studies. This thesis has benefited greatly from Brian's generosity in sharing the invaluable knowledge gathered through his years of research. The guidance and support of Dr. Masoud Samandi is genuinely appreciated. I thank him for introducing me to a fascinating area of research, and for ensuring the development of my academic career through encouraging me to present my research at international conferences.

The management and staff of both BHP Research and CSIRO are acknowledged for their support of this research. In particular, my sincere thanks are directed to BHP Research staff members, Mr. Alan Richards and Mrs. Janelle Bond for providing me with a home away from home, and Mr. Udo Buecher for enduring the distractions to my full-time employment over the last year. Their co-workers Dr. Peter Mercer, Dr. David Willis, and Dr. Geoff Walter, are thanked for numerous enlightening discussions. Dr. Geoff Harding, Dr. Corinna Horrigan, Dr. Leszek Wielunski, and Dr. Philip Martin of CSIRO were all especially helpful, and their endurance is much appreciated. Some fascinating discussions and correspondence with Mr. Robin Bates and Mr. Peter Kelly of the University of Salford, and Professor Welville Nowak of Northeastern University, were highly beneficial. Many thanks are also due to Mr. Stuart Street, Mr. Andrew Scobie, and Mr. Greg Tillman from the University of Wollongong, for their respective

contributions. Assistance with interpretation of electrochemical data by Professor Glenn Stoner of the University of Virginia was also very helpful.

I would like to thank my good friend Professor Robert Griffin in his adopted role as my mentor. His kind encouragement and motivation was readily embraced. Thanks also to Mr. Lee Falk for his insightful lessons of patience, dedication, and compassion, as told through his newspaper adventure strip, *The Phantom.* With the good grace of my examiners, I will have a companion for my "Doctorate of Phantomology."

Lastly, my most sincere and heartfelt thanks go to my fiancé, Ms. Fiona Kaul, for her limitless love and affection, and for persevering with the disruption to our personal life that this thesis has demanded. Furthermore, Fiona's contribution as a professional colleague is greatly appreciated. Her insightful proof-reading and skills of summation, were paramount in the eventual completion of this dissertation.

SYNOPSIS

Sheet steels intended for atmospheric exposure invariably require a sacrificial corrosion protective coating. Such coatings are commonly applied by either hot-dip galvanising or electrodeposition using large scale continuous processes. Armed with the desire to produce new products with improved performance, there has been considerable industrial interest in the use of physical vapour deposition (PVD) for the coating of sheet steels, and practical experience extends over the last three decades. Only in the last few years, however, have the most attractive aspects of PVD been investigated with some vigour: the preparation of novel alloy and multilayer coatings.

In recognition of this climate, the research presented in this thesis was commenced with the intention of evaluating the microstructures of a range of alloy coatings prepared by magnetron sputtering. The investigation considered the impact of ion assistance on coating composition and microstructure, by using an unbalanced magnetron design and varying the bias voltage of the substrates, while maintaining a substrate temperature of 50°C. The coating compositions targeted for study were based on the Al-Mg-Zn ternary system, with emphasis on the binary alloys. The study was mainly concerned with the investigation of supersaturated solid solubility and other metastable crystalline or amorphous phases. Coating characterisation was achieved by energy dispersive spectrometry (EDS), scanning electron microscopy (SEM), Bragg-Brentano X-ray diffraction (XRD), and the Crystallite Group Method (CGM). This latter technique is particularly effective for evaluation of the residual stress and strain-free lattice parameters for strongly fibre textured coatings. CGM was used for the first time for coatings with a close-packed hexagonal (cph) crystal structure.

Elemental coatings of Zn, Al and Mg all developed strong fibre textures with the close-packed planes oriented parallel to the substrate surface. Ion assistance enhanced the texture of Zn and Al coatings while disrupting the preferred orientation of Mg coatings. Compressive residual stress was developed in ion assisted Al and Mg coatings due to the atomic peening mechanism. Energetic bombardment of Zn coatings resulted in tensile stress despite a dense, columnar structure which typically indicates compressive stress. This was explained by constrained shrinkage of the Zn coatings during dynamic recrystallisation. Zn and Mg coatings were subject to very high proportions of entrapped Ar which was correlated to the residual stress, but was not causative. Al coatings did not retain detectable amounts of Ar.

Binary Al-Zn alloy coatings possessed a dual phase structure with discrete (Al) and (Zn) grains. Supersaturation of the (Al) phase was apparent but there was some indication that it declined by spinodal decomposition or precipitation after ageing at room temperature. The surface appearance of Al-Zn coatings was influenced by the Zn content and substrate temperature, such that smooth reflective coatings with high Zn content (<55 at%) could only be achieved at low temperatures (50°C). Ion assistance resulted in the preferential resputtering of Zn, while favouring textured growth in the (Al) and (Zn) phases. The presence of Zn in (Al) solid solution tended to produce a <111> textured structure at lower substrate bias than was necessary for elemental Al coatings, probably because of a sputter yield amplification effect. The (Zn) phase in the alloy coatings also retained high proportions of Ar.

Coatings of Al-Mg alloys were characterised by single-phase supersaturated (Al) solid solutions with up to about 38 at.%Mg, or a combination of supersaturated (Mg) and an amorphous phase for coatings with between 40 and 90 at.%Mg. The amorphous phase was thought to possess a composition of about 39 at.%Mg. The use of ion assistance resulted in preferential resputtering of Mg from the coatings, due to the differences in surface binding energy. The consequential modification in stoichiometry was sufficient to produce different phases in the coatings, and also caused a sharp reduction in the supersaturation of (Al) and (Mg) solid solutions. Coatings containing the (Mg) phase were susceptible to the entrapment of exceptionally high proportions of Ar (<22 at.%), while those with an (Al) solid solution retained almost no Ar. The high Ar content was thought to contribute to amorphisation of the (Mg) phase, and also heavy oxidation that tended to occur after several months of ageing.

The microstructure of binary Zn-Mg alloy coatings was also dependent on the composition. Coatings with between 15 and 40 at.%Mg were entirely amorphous due to slow growth kinetics of complex intermetallic phases within this composition range. Higher and lower Mg content typically provided coatings with a combination of terminal solid solutions and the amorphous phase. The solid solubility of (Zn) and (Mg) phases was considered to be within the equilibrium limits. Several intermetallic phases were detected in Zn-rich coatings, and some of these phases could not be identified. Ion assistance resulted in the preferential resputtering of Mg from the alloy coatings, which is opposite to the trend anticipated from elemental sputtering yields. This effect was attributed to sputter yield amplification, and was confirmed by Monte Carlo simulation of the ion assisted deposition process using the T-DYN code. All of the Zn-Mg coatings were susceptible to the retention of high proportions of Ar, particularly for the Mg-rich compositions. As for the Al-Mg coatings, the entrapped Ar appeared to favour

amorphisation of the (Mg) phase. Coatings with high Ar content were sensitive to heavy oxidation with ageing.

The ternary Al-Mg-Zn alloy coatings produced were based on Al-rich compositions. Ion assistance had a dramatic effect on the coating stoichiometry and microstructure. Increasing the ion energy resulted in the preferential resputtering of Mg, followed by Zn at higher energy. Coatings deposited with low bias were found to be amorphous, while those with virtually identical composition but prepared with high bias were found to contain (Al) phase with a strong <111> fibre texture. Relatively high proportions of Ar were also present in coatings deposited with elevated bias, but did not interrupt the growth of (Al) phase, suggesting that it was associated with an undetected amorphous phase.

The electrochemical performance of a range of the sputtered coatings was examined using a dilute chloride aqueous solution. The data was interpreted with the aim of pinpointing a coating with an optimum combination of both barrier and sacrificial properties which would ensure long term corrosion protection for a sheet steel substrate. All alloy coatings were found to exhibit passive regions. The results were interpreted to indicate that Al-41 at.%Zn and Al-13at.%Mg-20at.%Zn coatings would provide an ideal combination of good barrier protection and acceptable sacrificial protection of sheet steel. Coatings consisting of Zn-20 at.%Mg offered improvements in sacrificial protection relative to pure Zn coatings, while possibly having greater barrier protection properties.

RELEVANT PUBLICATIONS

Publications by the candidate presented in support of this thesis.

1 B.A.Shedden, M.Samandi, B.Window
Stoichiometry of unbalanced magnetron sputtered Al-Mg alloy coatings
Surface and Coatings Technology, (in press), 1998.
5th Int. Conf. Plasma Surface Engineering, Garmisch-Partenkirchen, Germany, 9-13 Sept 1996.

2 B.A.Shedden, F.N.Kaul, M.Samandi, B.Window
The role of energetic neutrals in reactive magnetron sputtering of nitrogen-doped austenitic stainless steel coatings
Surface and Coatings Technology, (in press), 1998.
5th Int. Conf. Plasma Surface Engineering, Garmisch-Partenkirchen, Germany, 9-13 Sept 1996.

3 B.A.Shedden, F.N.Kaul
Texture and stress analysis of thin films using parallel beam optics on a conventional x-ray diffractometer
Int. Schools and Conf. on X-Ray Analytical Methods, Sydney, Australia, 18-25 January 1996, Australian X-Ray Analytical Assoc., p.C-28 (abstract only), 1996.

4 B.A.Shedden, M.Samandi, G.A.Collins
Surface/interface analysis of a nitrogen implanted austenitic stainless steel
Materials Science Forum, **189-190**, 435-440, 1995.

5 B.A.Shedden, M.Samandi, B.Window
Influence of substrate bias on the microstructure of sputtered Al-Zn alloy coatings
Surface and Coatings Technology, **68/69**, 332-338, 1994.

6 M.Samandi, B.A.Shedden, D.I.Smith, G.A.Collins, R.Hutchings, J.Tendys
Microstructure, corrosion and tribological behaviour of plasma immersion ion-implanted austenitic stainless steel
Surface and Coatings Technology, **59**, 261-266, 1993.

TABLE OF CONTENTS

Chapter 1

Introduction

Sheet steel is widely used in the building, construction, automotive, appliance, and packaging industries, although a more thorough list of applications would probably extend to virtually all industries. The most common type of sheet steel has a low carbon content and only minor alloy additions, consisting almost entirely of ferritic iron. A rough guide to the typical sheet steel compositions is provided in Table 1.1 [1]. Sheet thickness typically ranges from about 0.3 to 2.0 mm. The sheet steel is produced on continuous process lines in coil form with strip widths of up to 2 m, and coil mass of up to about 30 t, such that the total strip length is in the order of 5 km. The vast number of different applications call for a range of mechanical properties and this can be achieved through a combination of judicious alloying, thermomechanical processing, and controlled annealing. Yield strengths of up to 700 MPa are achievable for high strength unrecrystallized products, while tensile elongations of up to 30% with high *r*-values can be attained for fully annealed deep drawing steels.

Table 1.1 Typical chemical composition for sheet steels [1]

Element	Quality		
	Commercial (wt.%)	Bending and Profiling (wt.%)	Drawing and special drawing (wt.%)
C (max.)	0.15	0.10	0.10
Mn (max.)	0.25-0.60	0.50	0.50
P (max.)	0.04	0.04	0.04
S (max.)	0.05	0.05	0.05
Cu (min.)	0.20	0.20	--

Well in excess of half all sheet steel produced goes into the building and construction industries [1]. Thus, sheet steel products are invariably exposed to the atmosphere where they must interact with a range of corrosive species. Steel is thermodynamically unstable and there exists a natural driving force to return iron to an

oxidised form. The oxidised form of iron usually has a characteristic red-orange appearance and the "rusting" of steel products is a common fact of life. This can lead to premature failure of steel products with the burden of continual replacement, or even serious safety concerns. Fortunately, most atmospheric conditions are relatively mild and steel rusting is usually a cosmetic concern, although even this form of corrosion is frequently undesirable.

1.1 Sheet Steel Corrosion Protection

Rusting of sheet steel is certainly avoidable. Stainless steels are perhaps the most familiar solution, whereby Cr and Ni are added to Fe to produce a steel that is resistant to rusting. In an ideal world all sheet steel products could possess such compositions, but economic reality dictates that these products are much more expensive than low carbon steel. A pragmatic approach suitable for most applications is to apply a coating to the steel sheet that provides corrosion protection. In order to understand the reasons for the selection of particular coatings, a basic understanding of corrosion theory is essential. It is not the purpose of this chapter, however, to provide a detailed description of corrosion theory or testing methods, and the reader is directed to reference texts such as [2,3] for further background.

1.1.1 Theoretical Basis of Corrosion

Corrosion of metals invariably involves the transfer of electronic charge in an aqueous solution. Such "electrochemical" reactions can be divided into anodic and cathodic reactions which correspond to the release and the consumption of electrons, respectively. The conversion of metals to their ionic form (ie. corrosion products), requires the release of electrons and is therefore an anodic reaction. For atmospheric exposure the most important cathodic reaction is the reduction of oxygen. Each of these reactions can be summarised by half-cell electrochemical reactions [3]:

$$M \rightarrow M^{n+} + ne^- \quad (1.1)$$

$$O_2 + 2H_2O + 4e^- \rightarrow 4OH^- \quad (1.2)$$

Under equilibrium conditions, the progress of each of these reactions involves a change in free energy which can be represented by an electrochemical potential. It is impossible to measure the absolute value of any half-cell electrode potential. The potential difference between two coupled half-cells can be measured, with one selected as a primary reference. The standard hydrogen electrode (SHE) is often used for this purpose, but

other references such as the saturated calomel electrode (SCE) are more commonly used for electrochemical measurements. The potential difference between any two half-cells is independent of the reference cell selected to measure the potentials.

A selection of standard half-cell electrode potentials, measured with respect to the standard hydrogen electrode (SHE), are listed in Table 1.2. Noble metals such as Au are denoted by positive potentials while active metals such as K have negative potentials. When two half-cells are coupled, a driving force exists for a spontaneous electrochemical reaction if the sum of oxidation and reduction standard potentials is positive (oxidation standard potentials are the opposite sign of reduction potentials). For example, when the Zn half-cell is coupled with the oxygen half-cell (pH=7), oxidation of metallic Zn is thermodynamically favourable since the potential difference is +1.58 V.

Table 1.2 Standard reduction potentials for selected reactions [3]

	Reaction	Standard Potential, e^o (volts vs. SHE)
Noble	$Au^{3+} + 3e^- = Au$	+1.498
	$O_2 + 4H^+ + 4e^- = 2H_2O$ (pH=0)	+1.229
*	$O_2 + 2H_2O + 4e^- = 4OH^-$ (pH=7)	+0.82
	$O_2 + 2H_2O + 4e^- = 4OH^-$ (pH=14)	+0.401
	$Cu^{2+} + 2e^- = Cu$	+0.337
	$2H^+ + 2e^- = H_2$	0.000
	$Pb^{2+} + 2e^- = Pb$	-0.126
	$Sn^{2+} + 2e^- = Sn$	-0.136
	$Ni^{2+} + 2e^- = Ni$	-0.250
	$Co^{2+} + 2e^- = Co$	-0.277
	$Cd^{2+} + 2e^- = Cd$	-0.403
	$Fe^{2+} + 2e^- = Fe$	-0.440
	$Cr^{3+} + 3e^- = Cr$	-0.744
	$Zn^{2+} + 2e^- = Zn$	-0.763
	$2H_2O + 2e^- = H_2 + 2OH^-$	-0.828
	$Al^{3+} + 3e^- = Al$	-1.662
	$Mg^{2+} + 2e^- = Mg$	-2.363
	$Na^+ + e^- = Na$	-2.714
Active	$K^+ + e^- = K$	-2.925

* Not a standard state but included for reference

The standard reduction potentials are useful for predicting the direction of an electrochemical reaction. As a simple rule of thumb, the half-cell reaction with the more

active potential proceeds by oxidation while the more noble half-cell reaction proceeds by reduction. However, care should be taken in accounting for the concentrations of reactants and products, as this affects the electrode potentials via the Nernst relationship. Furthermore, such predictions do not provide any indication of reaction kinetics.

The kinetics of electrochemical reactions are frequently represented in terms of Evans diagrams, conventionally shown by a graph of potential as a function of the logarithm of current density. The current density i ($A.cm^{-2}$) is directly related to corrosion rate r by Faraday's Law, which can be reduced to the following expression [3]:

$$r = \frac{i\,M}{n\,F} \tag{1.3}$$

where M is the atomic mass, n is the number of electrons transferred, and F is Faraday's constant. An example is given in Fig.1.1a which demonstrates via "mixed potential theory" the kinetics of Zn corrosion in an acid solution. The intersection between the line representing Zn oxidation and the line for H^+ reduction indicates the corrosion current density, i_{corr}, and the corrosion potential, E_{corr}. It should be noted that E_{corr} is intermediate between the reversible potentials, e, for the H_2/H^+ and Zn/Zn^{2+} reactions. It should be noted that Zn is polarized to anodic overpotentials such that the Zn corrosion rate in acid solution is increased with respect to the equilibrium corrosion rate i_o in a standard solution containing 1 M Zn^{2+} ions.

Ideal electrochemical reactions are represented by straight lines on Evans diagrams, where the gradient is defined as the Tafel constant. Departure from linearity can occur for several reasons. Firstly, the requirement for migration of reaction species to the metal surface can restrict the increase in current density if the reaction should become diffusion limited. This is demonstrated for the oxygen reduction reaction in Fig.1.1b, where i_L represents the diffusion limited current density. Any means by which the diffusion of reaction species is increased, such as increased solution agitation, temperature or concentration, will raise i_L. Secondly, anodic polarization of some metals can result in an active to passive transition, with a corresponding large reduction in current density. The typical S-shaped anodic polarization curve for an active-passive metal is shown in Fig.1.1c. The passivation of the metal is attributed to the formation of a very stable, thin, resistant, surface film. Such behaviour occurs for stainless steels and aluminium, and the high corrosion resistance of these metals in most environments is attributed to spontaneous passivation.

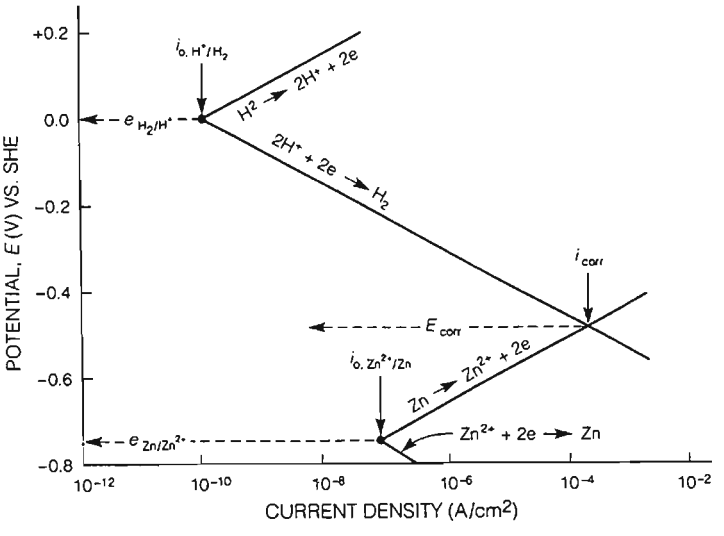

(a)

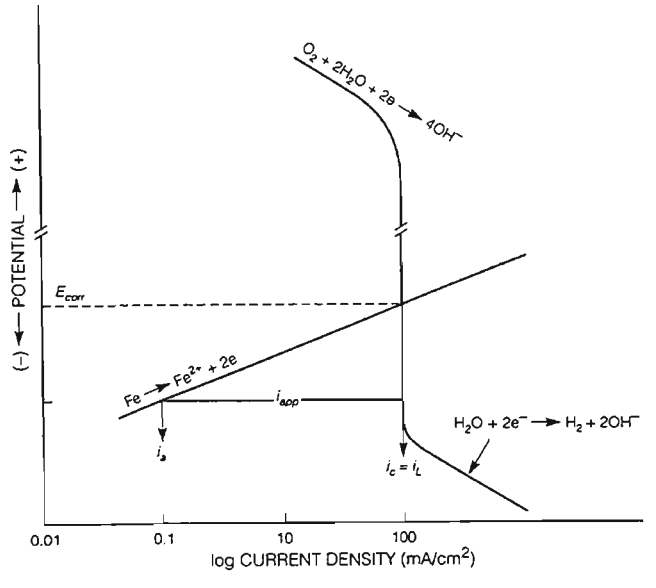

(b)

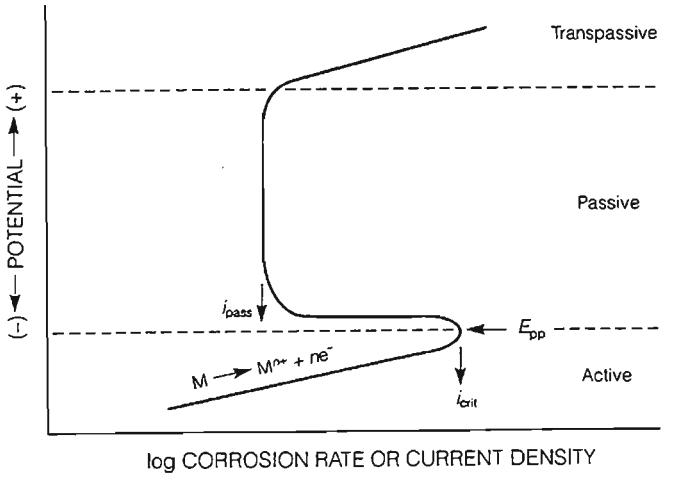

(c)

Fig.1.1 *Evans diagrams illustrating various electrochemical effects* [3] :
(a) Zn corrosion in acidic solution,
(b) diffusion limited oxygen reduction on iron,
(c) characteristic anodic polarization of an active-passive metal

1.1.2 Anatomy of a Corrosion Protective Coating

The corrosion resistance of sheet steel is often addressed by applying various types of coatings. Corrosion protective coatings can be metallic (galvanized), organic (paints and laminates), or inorganic (chromate and phosphate treatments). Metallic coatings are of prime interest for the present study, and the other types of coatings will not be discussed here, except in relation to combined performance with metallic coatings (Sect.1.2). There are two main issues for metallic coatings on sheet steel: barrier protection and galvanic corrosion [3,4]. As it will be demonstrated, each are critical for the long term corrosion protection of sheet steels.

Barrier protection by metallic coatings results from both the inherent corrosion resistance of the coating and also due to its corrosion products. An ideal barrier coating would cover the sheet steel substrate entirely so that no steel is exposed to the external environment. Corrosion of the coated steel is then controlled by the corrosion rate of the metallic coating. The initial barrier protection results from passive surface films or by the inherent nobility of the coating. For example, an Al coating on steel provides excellent barrier protection due to the air-formed passive film on its surface. The surface oxide film on Zn coatings, however, is less effective as a barrier since it is much more soluble in water. Noble metals, such as Cu, Ag, Au, Pt and their alloys, can also be used to provide barrier protection. They are obviously expensive and commercial application is usually restricted to decorative applications.

The corrosion resistance of sheet steel can also be improved by the secondary barrier effect of coating corrosion products. For Zn coatings, the main corrosion products are hydroxides and basic salts, and the type of product depends on the characteristics of the environment. Zinc carbonates are thought to be particularly important as they can provide a barrier to further coating corrosion. This mechanism is particularly relevant for alloy coatings such as Galvalume® (Sect.1.2.3). Atmospheric corrosion of these dual-phase coatings is concentrated at Zn-rich regions, and the corrosion products evolved tend to block the interdendritic regions, minimising further degradation of the coating.

Galvanic corrosion is an inherent issue for sheet steels coated with dissimilar metals. Sheet steel inevitably has sheared edges exposed to the atmosphere, and mechanical damage to the surface can also result in exposure of steel through the coating. Each of these regions are potentially subject to galvanic corrosion due to differences between the corrosion potential of the steel substrate and the coating. This phenomena is used to advantage for sacrificial coatings such as Zn. In this case, the coating is more

active than the steel substrate, and any steel exposed at edges or scratches will be cathodically polarized – hence the description "cathodic protection". This has the effect of substantially reducing the corrosion of the exposed steel at the expense of corrosion of the coating. It follows that the lifetime of sheet steel coated with a sacrificial metal will be largely dependent on the coating thickness.

On the basis of standard potentials (Table 1.2), it might be expected that Al coatings would offer even better sacrificial protection than Zn. However, the ready passivation of Al tends to increase the corrosion potential to a value only slightly less than that of Fe, and hence only minor sacrificial protection is afforded. For this reason, galvanic coupling is more commonly evaluated on the basis of the galvanic series, which lists various metals and alloys in order of their activity in seawater [3]. Noble metal coatings have the opposite effect to Zn coatings since any exposed steel substrate is polarized anodically. This causes the rate of Fe corrosion to increase with respect to uncoated steel. Noble metal coatings are particularly undesirable from the consideration of the relative surface area. Larger cathode area provides more surface for the reduction reaction, and the anodic current must increase to compensate. Hence, corrosion of the steel at small defects through the coating is accelerated substantially by the large cathode area provided by the coating.

It is apparent that a corrosion protective coating for sheet steel should present a compromise between the low corrosion rates of a barrier coating, and the sacrificial properties afforded by galvanic coupling. Such properties would ensure long term corrosion protection during atmospheric exposure. The requirement for sacrificial protection restricts the range of metals available for consideration to those which are more active than steel. The most obvious candidate metals are Zn, Al, Mg, Mn, and their alloys. Health issues are of further concern, which prohibit the use of other active metals such as Cd and Be. Alkali metals are far too reactive to be used for more than minor alloy additions. Alloying of the candidate metals with other elements should not only be judged on a scientific basis, but also in terms of economic viability.

1.2 Commercial Coated Sheet Steel

Sacrificial metal coatings are usually applied to sheet steel by one of two main processes: hot dipping and electrodeposition [1,3,4]. Each of these processes have been used to apply Zn coatings since the early 19th century. Other coating processes such as cladding, spraying, diffusion coating, and vapour deposition are much less widely used for sheet steels. The basis of the hot dipping process, as the name suggests, involves submerging the substrate into a bath of liquid coating metal. The liquid metal alloys with the surface of the substrate and after withdrawl from the bath, adherent liquid solidifies to form a coating. The process obviously involves elevated temperatures, and for coating low carbon sheet steel, the bath temperature can be as high as 700°C. In contrast, electrodeposition is usually conducted at temperatures less than about 65°C. The process involves the conversion of metallic ions into plated metal via the application of an electric current (cathodic polarization). High concentration aqueous solutions of inorganic salts are used, and the pH can be as low as 3 for acidic baths. The disposal of waste solutions produced via electrodeposition poses a significant environmental issue.

Each of these two coating processes are targetted at different regimes of coating thickness [4]. Due to a proportionality between coating thickness and electric power consumption, electrodeposition is usually only economical for coatings of 2 to 8 μm thickness. Hot dipping usually produces much thicker coatings, ranging from 4 to 50 μm for most sheet steel applications. Electrodeposited coatings have other advantages in that they can be applied to one side of the steel strip only, the "spangles" or surface crystals typical of hot dipping are absent, and automotive finishes can be applied to the coated surfaces. However, these advantages are becoming less significant with the development and production of hot dipped coatings that do not produce a spangle ("zero-spangle"), and those suitable for automotive panels via annealing subsequent to hot dipping ("galvannealing").

Hot dipping and electrodeposition are not restricted to the production of only Zn coatings for sheet steels (Sect.1.2.1), although these products probably represent the largest tonnages. Aluminised coatings are produced for niche markets where barrier corrosion protection and heat resistance is important (Sect.1.2.2). The properties of both galvanized and aluminised coatings have been combined to varying extents by the production of Al-Zn alloy coatings (Sect.1.2.3). These new generation coated sheet steels have proven to be very successful and they are widely used in building and construction industries in both bare metallic and prepainted form. The automotive industry has developed a demand for corrosion resistant sheet steels for body panels and structural parts, and this has been met by electrodeposited and galvannealed Zn-Fe alloy

coatings (Sect.1.2.4). Improvements in corrosion resistance have also been obtained with a variety of other alloy coatings, particularly Zn-Ni (Sect.1.2.5).

1.2.1 Zinc Coatings

Zinc coatings are most commonly applied by hot dipping in a process known as galvanizing [4]. Commercial galvanizing of sheet steel is performed by feeding coiled strip continuously through a non-oxidising furnace, followed by dipping in a molten Zn bath. The furnace provides a clean active surface suitable for galvanizing, firstly by cracking any organic contaminants during the heating stage, and secondly by reducing iron oxide on the steel surface during the annealing stage. Recovery and recrystallization of the steel substrate can be controlled, enabling the attainment of different strength and ductility grades. Immediately after the annealing furnace, the steel strip is immersed into a Zn bath, turned around a submerged roll and extracted vertically. Air-wiping jets are used to control coating thickness, and upper air blowers are often used to accelerate cooling.

Galvanizing with a pure Zn bath results in the formation of a thick Fe-Zn intermetallic alloy layer as shown in Fig.1.2a [4]. This alloy layer is highly undesirable for sheet steel since it leads to peeling and cracking during subsequent forming operations. Thus, most galvanizing lines use additions of about 0.2 wt.%Al to inhibit the growth of the alloy layer (Fig.1.2b). Pb or Sb is also added to the bath in amounts of less than 0.2 wt.% in order to promote the formation of large crystalline grains or "spangles", and also to help control bath fluidity. The spangle can be minimised by various methods which increase the nucleation density. Hence, "zero spangle" galvanized product is not truly free of spangles but the spangle density is so high that they cannot be detected with the naked eye. Minimised and zero spangle galvanized steel are in favour for subsequent painting, since they provide a much smoother surface that does not reveal the topographical features of the large spangles. Post-galvanizing temper rolling is also often used to improve surface finish.

A galvanized coating on steel serves as a barrier and provides galvanic protection [3]. Initially atmospheric corrosion causes the formation of non-protective $Zn(OH)_2$, but this compound can react with CO_2 and moisture in the air to produce a protective carbonate layer. The Zn corrosion products are white or colourless, and are less objectionable than the red rust products from steel. Any underlying steel that is exposed at scratches or cut edges is sacrificially protected by galvanic corrosion of Zn. The time before the appearance of red rust on galvanized steel sheet in atmospheric exposure is linearly related to the coating thickness. Environments that are more severe, usually indicated by high chloride or sulphate levels, reduce the lifetime of the coating. For

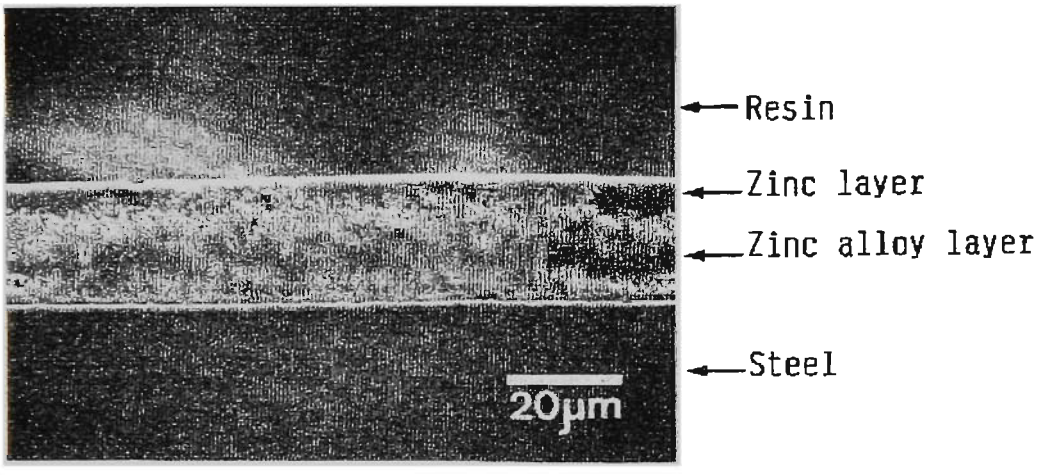

(a) No addition

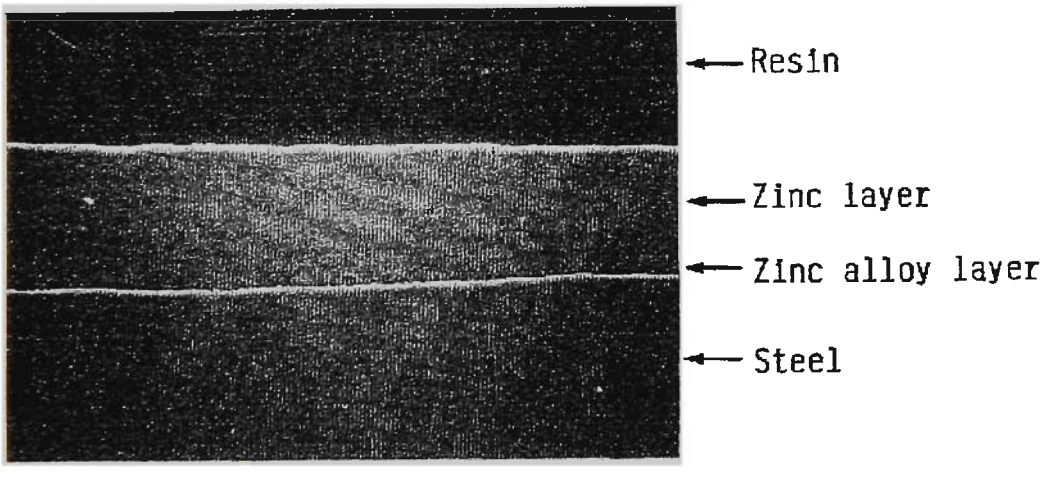

(b) Aluminum addition

Fig.1.2 *Metallographic cross-sections of galvanized steel sheet [4]*
(a) no aluminium addition
(b) with 0.2 wt.% aluminium addition

example, the time to initial red rust for a galvanized steel sheet with 140 $g.m^{-2}$ Zn per side (about 20 μm) would be 2, 4 and 10 years in industrial, marine and rural environments respectively [5]. Thus, greater coating durability is afforded by increasing the coating thickness within both practical and economical limitations.

Pure Zn coatings are also often applied continuously to sheet steel by electrodeposition (electrogalvanizing). Steel cleanliness is particularly critical for good adhesion since surface alloying with the substrate does not occur. Electrogalvanizing lines usually address this issue by incorporating various stages of degreasing, pickling and rinsing prior to the plating stages. The electrodeposition bath is usually acidic and based on either sulphate or chloride salts. The corrosion performance of electrogalvanized coatings are essentially the same as hot dip galvanized coatings of comparable thickness. Hence, the typically thin electrogalvanized coatings are rarely used for bare atmospheric exposure applications, and are more commonly used for painted automotive body panels where the supreme surface finish is most important.

1.2.2 Aluminium Coatings

Pure Al coatings can be applied to sheet steel continuously using a similar process to that of galvanizing [4]. Due to the high melting point of Al (660°C), control of surface oxidation is critical and particular attention must be paid to the control of the non-oxidising furnace. The high bath temperature results in a rapid reaction between the molten Al and steel substrate, such that a very thick alloy layer forms in the aluminized coatings. These intermetallic Fe-Al phases are very hard and brittle and consequently cause the coating to peel and crack when the steel is severely formed. The ductility of the coating can be improved substantially by the addition of 5 to 10 wt.% Si to the bath. The alloy layer formed in these coatings is a ternary Al-Fe-Si phase, and is much thinner than in pure Al coatings. Aluminized coatings with Si additions are referred to as Type I, while those produced with pure Al baths are called Type II. Examples of the microstructure for each type of aluminized steel are shown in Fig.1.3.

Aluminized coatings show much slower corrosion rates than galvanized coatings of equivalent thickness [3]. However, red rust spots at coating defects and cut edges appear fairly rapidly after atmospheric exposure of aluminized steel. This occurs because Al is only slightly more active than the steel substrate in most atmospheric conditions. The aluminized coating acts primarily as a barrier coating with minimal sacrificial protection. It is usually necessary to apply much thicker aluminized coatings to achieve the same resistance to red rusting as is possible with galvanized coatings. Hence

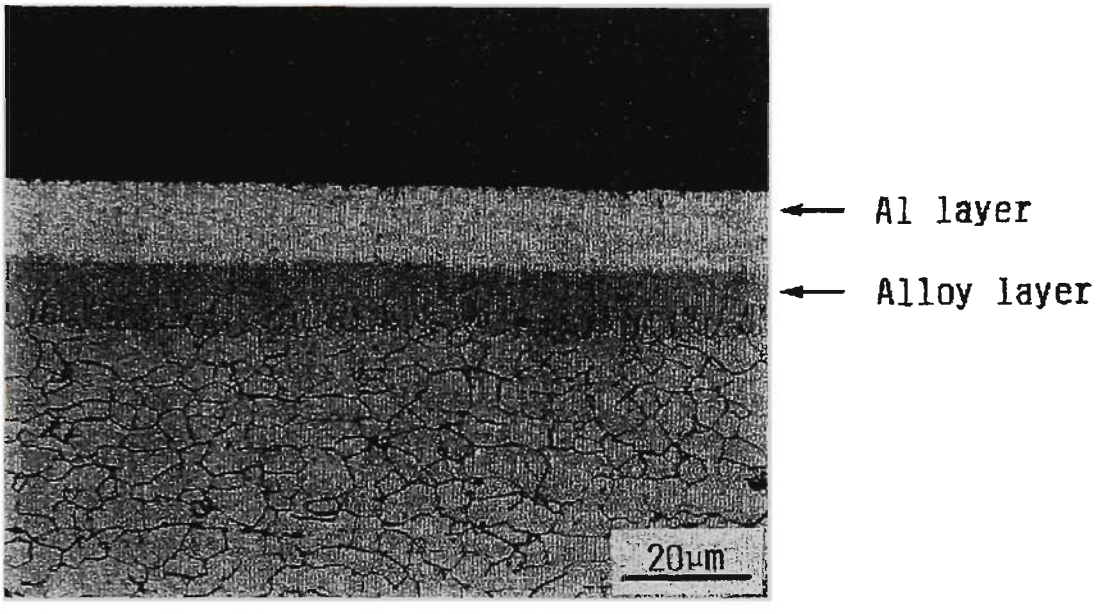

(a) Type II Pure Aluminum coated steel

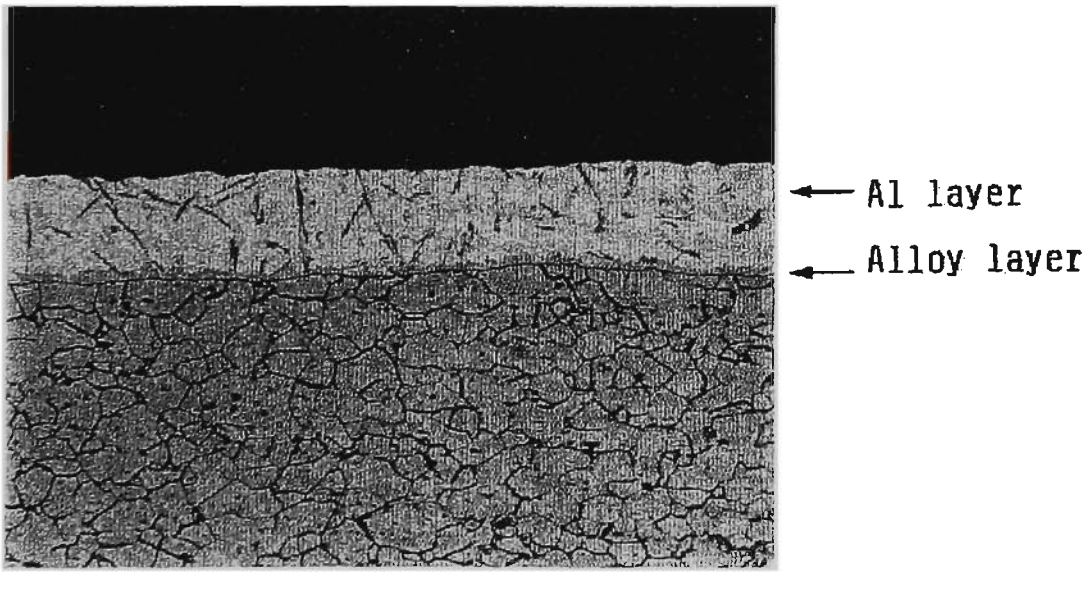

(b) Type I 9% Silicon addition

Fig.1.3 *Metallographic cross-sections of aluminized steel sheet* [4]
(a) without silicon addition (Type II)
(b) with 9 wt.% silicon addition (Type I)

aluminized coatings have found only limited use in applications requiring heat resistance, such as automotive exhaust mufflers.

1.2.3 Aluminium-Zinc Alloy Coatings

The present industrial interest in Al-Zn alloy coatings for sheet steel stems from the work of researchers at Bethlehem Steel commencing in 1962 [6]. The intention of this work was to improve the corrosion resistance of galvanized and aluminized steels by alloying. On the basis of literature concerning Al-10 wt.%Zn sacrificial anodes for ships, they investigated hot-dip Al-Zn alloy coatings with a range of compositions. Problems with a rapid exothermic reaction between the bath and steel substrate were overcome by the addition of small amounts of Si to the bath. This had the effect of stifling the alloy layer growth by slow formation of a quaternary intermetallic layer. A series of pilot line trials covering a range of Al content from 1 to 70 wt.% were conducted in 1964. The Si content was arbitrarily selected as 3 wt.% of the total Al content, in reflection of the required Si content in Type I aluminized coatings.

Atmospheric exposure at a range of test sites after 8 years of testing highlighted the Zn-55 wt.%Al-1.5 wt.%Si (approximately Al-25 at.%Zn) coatings as the optimum composition for providing a balance between barrier and sacrificial protection [6]. Commercial production of this new product, named Galvalume®, was commissioned in 1972 under the protection of a series of patents. In 1974, John Lysaght (Australia), a subsidiary of BHP Steel, negotiated a license and the exclusive rights to produce Zincalume® (JLA's tradename for Galvalume) in Australia. JLA's first Zincalume line was commissioned in 1976, which had been converted from galvanizing. An extensive marketing programme aimed at converting the Australian steel building market to both painted and unpainted Zincalume was highly successful. Galvalume/Zincalume has been widely accepted as a premium hot dip coated product. In other countries the "55%Al-Zn" product is also known by other names such as Alugalva, Aluzink, Aluzinc, Algafort and Zalutite. Patent protection for Galvalume/Zincalume has expired over the last few years, opening the market to unlicensed producers.

The microstructure of Zincalume is shown in Fig.1.4 [4]. The coating consists of four phases: cored Al-rich dendrites, interdendritic Zn-rich precipitates, Si particles, and an Fe-Si-Al-Zn intermetallic phase distributed in the alloy layer and throughout the coating. Rapid cooling of the coating subsequent to hot dipping was found to be essential for good control of the dendrite arm spacing and spangle growth. The excellent corrosion performance of this coating is attributed to the dual phase microstructure [3]. Initial atmospheric corrosion was found to be quite rapid and proceeded via the preferential

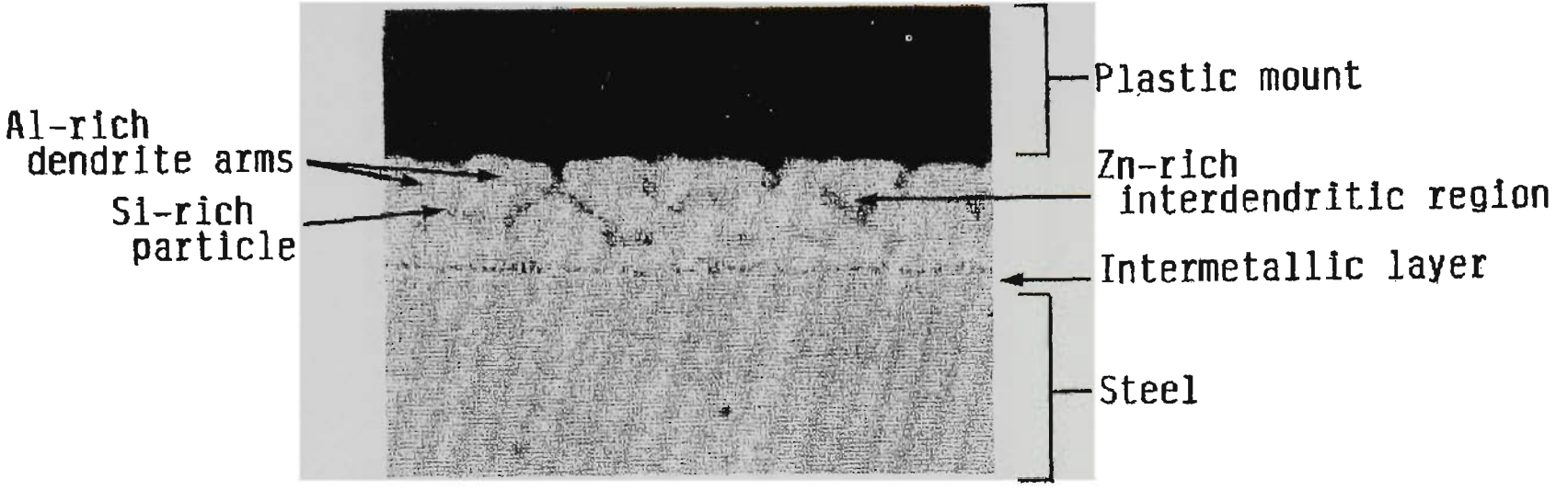

Fig.1.4 Metallographic cross-sections of Galvalume coated steel sheet [4]

attack of Zn-rich regions. However, the formation of insoluble Zn- and Al-based corrosion products fill the corroded regions. Some Zn-rich regions remain to provide further sacrificial protection, but the general corrosion losses of the coating are limited by the resistance of the remaining Al-rich constituent. Furthermore, the quaternary alloy layer offers very good barrier protection once the bulk of the coating has corroded. It should be noted that after 30 years exposure, the original Zn-55 wt.%Al panels from Bethlehem's 1964 pilot line trial are yet to show significant amounts of red rust at moderate marine, rural and industrial sites [6]. This corresponds to an increase in the coating life compared to galvanized of at least 2 to 3 times. Mass loss measurements suggest this factor may be as high as 5 times for some environments.

In response to the invention of Galvalume, the International Lead Zinc Research Organization (ILZRO) sponsored research into alloy coatings with more modest additions of Al [1,4]. It was long recognised that the eutectic Zn-5 wt.%Al (Zn-88.7 at.%Al) composition would offer improved corrosion resistance over galvanized steel. However, problems with the formation of bare spots on the steel sheet prohibited the production of such coatings. Under the sponsorship of ILZRO, Centre de Recherches Metallurgiques (CRM) examined a range of different ternary additions to the Zn-5 wt.%Al alloy aimed at this issue. In 1980, it was found that the addition of 0.1 wt.% mischmetal (a naturally occurring mixture composed predominantly of the rare earth elements La and Ce), to the hot dipping bath provided acceptable quality coatings. The commercial coating produced from such compositions is known as Galfan. A similar product that substitutes Mg for mischmetal was developed in 1985 by researchers from Nippon Steel, and is commercially known as Superzinc. Another slight difference between these two products is that Galfan specifies a hypereutectic bath composition slightly in excess of 5 wt.%Al, whereas hypoeutectic Zn-4.5 wt.%Al is used for Superzinc.

The microstructure of Galfan/Superzinc is typified by a eutectic structure with closely-spaced lamella of Al-rich and Zn-rich phases, as shown in Fig.1.5 [7]. The mischmetal or Mg additions are thought to be associated with the Al-rich phase. Quite often, large globular primary Zn phase is present in the coatings. The alloy layer is extremely thin, if present at all, and probably consists of an Fe-Zn-Al intermetallic phase. Galfan coatings have been shown to increase the lifetime with respect to galvanized coatings, by a factor of between 2 and 4 times. The improvement in coating lifetime is thought to be due to its low corrosion rate at the time of initial exposure.

Comparisons are frequently made between the performance of Galfan and Galvalume, most commonly with a heavy marketing emphasis. Galfan generally does not offer the same extent of product lifetime as can be achieved with Galvalume. This

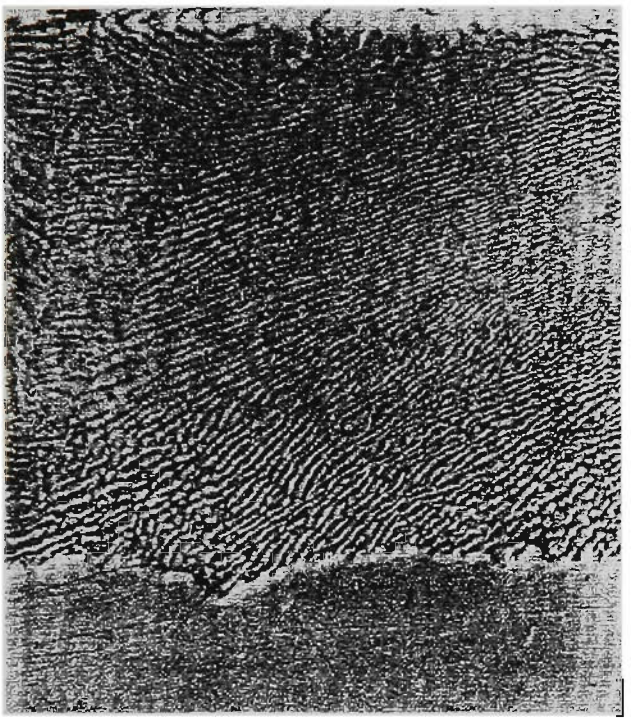

Fig.1.5 Metallographic cross-sections of Galfan coated steel sheet [7]

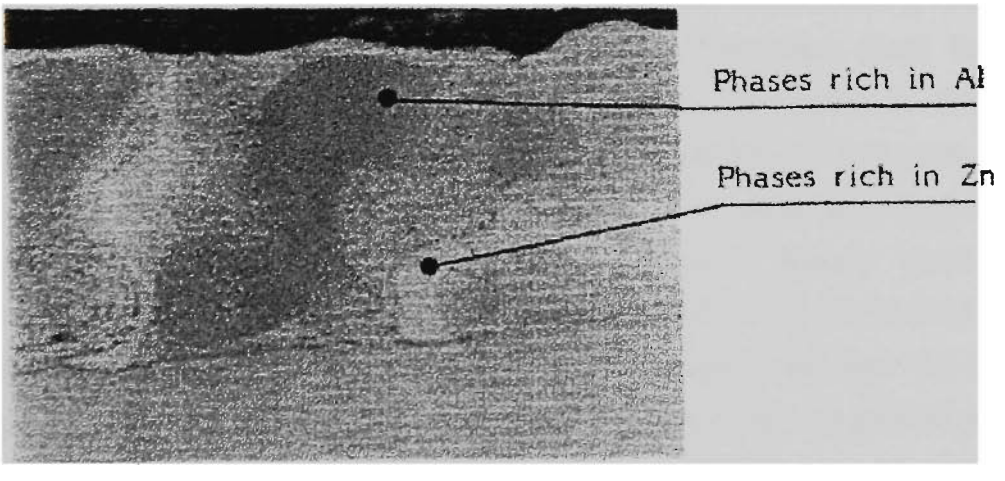

Fig.1.6 Metallographic cross-sections of Lavegal coated steel sheet [8]

position is countered by the claim that sacrificial protection of cut edges and scratches with Galfan coatings is similar to that of galvanized, and much better than for Galvalume. Each of the products also have their own specific problems. For example, Galvalume is susceptible to rapid alkaline attack of the Al-phase which prohibits its use in direct contact with wet concrete; and Galfan is subject to excessive darkening upon atmospheric exposure, which is considered aesthetically undesirable. For prepainted sheet applications, Galvalume is generally recognised as being the superior substrate due to the excellent resistance to surface blistering. However, there are particular environmental conditions for which Galvalume is unsuitable. Some examples are the excessive undercutting of paint films in particular cases, and red rust staining on tension bends in acid rain or agricultural environments. In such applications Galfan and (to a lesser extent) galvanized are more attractive paint substrates.

The only other Al-Zn alloy composition of any commercial significance for sheet steel coatings is Zn-30 wt.%Al (Al-50 at.%Zn). Lavegal is a product developed in Italy during the mid-1980s based on a coating composition of Zn-30 wt.%Al-0.2 wt.%Mg-0.2 wt.%Si [8,9]. The coating microstructure of Lavegal is similar to that of Galvalume although with a greater volume fraction of Zn-rich regions (Fig.1.6). Intended as a compromise between Galvalume and Galfan compositions, Lavegal offers improved sacrificial protection with respect to Galvalume, and better prepainted performance with respect to Galfan with less undercutting than Galvalume. A similar coating composition (without the Mg addition) was actually considered by Bethlehem Steel before the 55%Al-Zn composition was settled upon, with plant trials conducted in 1965. The greatest obstacle to the acceptance of this product is the atmospheric exposure work by Bethlehem [6], which showed that Zn-30 wt.%Al metallic coatings did not perform any better than galvanised coatings, and in some environments actually provided less protection. However, it is possible that the poor performance of Zn-30 wt.%Al coatings in this early study was related to inappropriate cooling conditions, and the corrosion performance might be improved by better microstructural control. At present it appears that the Lavegal product has not received much support.

1.2.4 Zinc-Iron Alloy Coatings

Zinc-iron alloy coatings are primarily used for automotive applications where a moderate degree of sacrificial protection is called for in case of paint scratching [1,4]. Pure Zn coatings are occasionally used for automotive applications but are generally restricted to hidden structural parts which require thicker Zn coatings for adequate corrosion protection and subsequently produce an undesirably rough painted surface. The aesthetic paintability and weldability is substantially improved by adding a moderate

amount of Fe to the coating, while maintaining sufficient corrosion protection. Some studies indicate that the optimum composition corresponds to 7 to 25 wt.%Fe, for which the coating lifetime is 1.5 to 2 times that of a Zn coating. However, the Fe content of the coating is more often determined by the requirement for high resistance to powdering during forming, which can occur when inappropriate Fe-Zn phases are present. Zn-Fe coatings are rarely used in the unpainted condition since atmospheric corrosion of the intermetallic phases results in early formation of red rust staining.

Coatings of Zn-Fe alloys can be produced by either "galvannealing" or electrodeposition. Galvannealing involves the heat treatment of galvanized coatings at above the melting point of Zn (500°C) for a very brief duration by passing the strip through a radiation-type furnace attached to the end of a continuous galvanizing line. The resultant coating consists of a thick layer of intermetallic Fe-Zn phases with a surface ideally suited to chemical pretreatment and painting. The type of Fe-Zn phase formed in the coating is critical to achieving satisfactory formability, with the ζ-$FeZn_{13}$ phase being preferred. The required formation of ζ-phase generally restricts the galvanneal treatment to low coating weights (<100 $g.m^{-2}$). Zn-Fe coatings can also be produced by electrodeposition, with either acidic sulphate or chloride baths. Conventional electrodeposition using low current densities would usually result in Fe-rich coatings, since Fe is more noble than Zn. However, when high current densities are applied on a commercial scale, the formation of $Zn(OH)_2$ near the steel surface inhibits the deposition of Fe, and Zn-rich coatings can be produced by anomalous codeposition. Such coatings are generally only produced at low coating masses since thick coatings are too expensive to electrodeposit.

1.2.5 Other Alloy Coatings

The quest for improved corrosion resistance of automotive panels has also spurned the development of other electrodeposited alloy coatings based on the Zn-Ni, Zn-Co and Zn-Mn binary systems [1,4]. Electrodeposited Zn-Ni coatings are produced primarily in Japan and exclusively for painted automotive body panels. Optimal corrosion resistance has been claimed to occur at a composition of about 12 wt.%Ni, which increased the time to red rust in salt spray testing by a factor of 2 to 5 times relative to Zn coatings. This improvement was mainly attributed to dealloying of the coating by preferential loss of Zn, resulting in a more corrosion resistant Ni-rich surface. Galvanized coatings with such high Ni content are not possible due to the excessively high liquidus temperature. Minor additions of Ni to galvanized coatings (<0.1 wt.%) are occasionally used in commercial batch dipping. However these Ni additions are made in

order to control the Fe/Zn reaction rather than in any consideration of corrosion performance.

The addition of between 0.15 and 1.0 wt.% Co to Zn coatings has been found to significantly improve salt spray life of sheet steel [1,4]. Such coatings are applied by electrodeposition, and it appears that Co additions have not been seriously considered for galvanised coatings. The principle advantage of Co alloying appears to be related to improvement in the receptivity to chromate treatment. Zn-Co alloys are also the subject of continuing research particularly in regard to the ternary addition of Mn and Cr.

Another interesting alloy coating that has been studied is Zn-Mn [4]. Mn is anodic with respect to both Zn and Fe, so this alloy provides excellent sacrificial protection for sheet steel. An added attraction is that Mn is relatively inexpensive and available in abundant supply. Salt spray testing of electrodeposited Zn-Mn coatings revealed that the time to red rust occurrence increased rapidly above a Mn content of 20 wt.%, and was relatively constant above 50 wt.%Mn (1000-2000 hours for 20 $g.m^{-2}$ coating). These coatings consist of a dual phase structure with essentially pure Zn and Mn phases. However, the oxide of Mn has a dark-brown or black appearance which is considered to be aesthetically undesirable. Large additions of Mn to galvanizing baths are not possible due to the corresponding large increase in liquidus temperature. Additions of only a few percent Mn to galvanizing baths have been studied but did not provide any substantial benefit in corrosion performance.

Although of little significance to the present work, mention should also be made of other conventional coatings such as Sn, and Pb-Sn. Electrodeposited Sn coatings, otherwise known as tinplate, are widely used for canning of food products. Under normal atmospheric conditions, Sn is cathodic to steel and would offer no sacrificial protection. However, in the acidic deaerated environment typical of canned food products, the potentials of Sn and steel are reversed, such that the coating provides sacrificial protection. The corrosion products of tin are non-toxic and tasteless which is an essential characteristic for canning. Sacrificial protection is lost after opening the can, due to passivation of the tin. Pb-Sn alloy coatings, commercially known as terneplate, are usually produced by hot-dipping in a bath containing 8-15 wt.%Sn. The coating is noble with respect to steel, and offers only barrier protection. Terneplate is used primarily for fuel tanks of automobiles since it is resistant to sparking.

1.3 Vapour Deposition for Sheet Steels: A Historical Perspective

The development of new metallic corrosion protective coatings that perform better than existing commercial products has long been a core activity of numerous academic and industrial research groups. There are three basic approaches to such development. Firstly, incremental improvements to existing products can aid the marketability of a product. An example of this approach is the slight improvement in Galvalume ductility afforded by trace additions of V and Sr [10]. The key here is to make only small changes to the existing products, such as by minor alloy additions to the hot-dip bath, which simplify the coating process or are perceived by the end customer to be advantageous.

Secondly, radically new alloy compositions can be investigated. This includes markedly different compositions from the Al-Zn alloy system, in addition to novel Mg- and Mn-alloys, etc. The primary restriction on such an approach for hot dipping is the necessity of limiting the metal bath temperature to less than 700°C. Bath temperatures above 700°C create several problems, such as shape distortion and undesirable structural changes in the sheet steel, rapid alloy growth in the coating, oxidation of the bath metal, and the environmental problems associated with excessive Zn vapourisation and dross formation. Consequently, the range of alloy compositions available is restricted. For example, in the Zn-Mn binary system, additions of more than about 1 wt.%Mn raise the liquidus temperature above the 700°C limit. The range of alloys and compositions that can be coated by electrodeposition is also restricted, due to various electrochemical peculiarities.

Thirdly, there is the possibility to develop alternative coating techniques, while maintaining the basis of existing processes; that is, the steel strip directly interacts during the coating process with either liquid metal (hot dipping) or liquid chemicals (electrodeposition). Numerous possibilities have been proposed, such as planar strip casting for rapidly solidified coatings, and magnetic levitation of galvanising baths [11] for greater process versatility. Novel methods of electrodeposition also have been developed for single-sided coating. At the present stage, several organisations are pursuing such systems and the vast majority of this work is protected by commercial secrecy.

Finally, it would be beneficial to investigate alternative coating techniques that completely avoid the use of the liquid phase. The range of techniques under consideration belong to the large family of processes collectively named Physical Vapour Deposition (PVD). With these processes, a coating is produced via the condensation or deposition of

a metal vapour flux at a low pressure. A moderate vacuum is required for optimum efficiency of the process, and this has proven a major psychological barrier to the wider industrial acceptance of PVD. However, well engineered solutions are available to these problems which should not restrict application to continuous coating of sheet steels. PVD is an attractive technique for many reasons. Restrictions placed on the coating composition by the limited bath metal temperature, do not apply to PVD, since virtually any alloy can be deposited by such methods. It is possible to produce amorphous or metastable phases with nanocrystalline grain sizes and extended solid solubility, due to the extremely high quench rates of PVD. Claims are also often made that PVD is an environmentally friendly technique since it does not require the use of hazardous chemicals such as the case for electrodeposition.

The concept of coating steel strip by PVD is by no means a recent development. Considerable interest in vacuum deposited Zn coatings was aroused as early as the mid 1960's. Several pilot Zn vapour deposition lines were commissioned during this period, with the intention of evaluating the important process variables (Sect.1.3.1). A proposal for a commercial Zn vapour deposition line capable of operating at 180 $m.min^{-1}$ with 1520 mm wide strip was considered in 1968 by the Jones and Laughlin Steel Corporation in the USA, but it was never constructed. In East Germany during this same period, shortages of Sn for production of plated packaging steel sheet, saw the development of high speed continuous PVD lines capable of depositing thin Al coatings (Sect.1.3.2). The first such commercial facility was commissioned in 1971, with a second line installed in 1982. Much of the development of the technology for large scale, high speed PVD lines has stemmed from these activities, particularly in respect of high power electron beam guns. During the mid 1980s, several Japanese and Korean steel companies were actively involved in the development of PVD processes, culminating in the construction of a full scale commercial PVD Zn coating facility at the Hanshin Works of Nisshin Steel in 1985 (Sect.1.3.3). Over the last few years, research has concentrated on alloy and multilayer coatings, both in terms of equipment development and coating performance evaluation.

1.3.1 Early American, British and Australian Activities

From the early 1960s and into the 1970s, several companies were involved in the development of vacuum deposited Zn and Al coatings [12-14], with several US and British patents marking the occasion [15-18]. Many preliminary investigations were conducted using small bell jar arrangements [19], and these works prompted the construction of various pilot facilities. Jones and Laughlin Steel Corporation had an air-to-air continuous line for coating 280 mm wide strip [13]. Republic Steel Corporation

had a semi-continuous coating line for 250 mm strip [13,20]. Airco Temescal, was a leading manufacturer of vacuum deposition equipment at the time, and had built a continuous coating line which included electron beam evaporators, capable of coating 610 mm strip with Al [20]. In 1965, the United States Steel Corporation installed a continuous PVD line capable of coating 1220 mm wide steel strip with Al at a linespeed of up to 450 $m.min^{-1}$ [12]. Youngstown Sheet and Tube had a 460 mm width continuous line, but had already abandoned the project by 1970 [13]. Bethlehem Steel and Inland Steel were also known to have investigated vacuum deposited Zn coatings [13]. In Australia, John Lysaght (Aust.) investigated the production of Al, Zn and multilayer Al/Zn coatings using a 1.5m x 1.2m x 0.9m experimental vacuum unit [13,14,21,22].

Al PVD coatings were envisaged as a possible substitute for tinplate with coating thickness of 0.25 to 2.5 μm [12]. It was expected at the time that world-wide shortages of Sn would see a move towards thin Al coatings for packaging products. Such thin coatings were highly suited to PVD processes, and suitable lines were designed which would have been capable of very high linespeeds (400 $m.min^{-1}$). Thicker Al coatings were much more difficult to produce due to the release of latent heat, such that the economics were unfavourable compared with hot-dipping. Zn coatings with thicknesses of between 6 and 25 μm were examined as a possible substitute for hot-dip galvanised coatings.

The only PVD technique that was used in these early studies was evaporation, using either resistance and electron beam heating. The basic concept of the process is that the coating metal is vaporised under vacuum and condensed uniformly onto steel strip passing over the evaporation source. Low operating pressures are essential for practical evaporation rates and uncontaminated coatings. Thermal evaporation is the obvious choice for high speed coating lines since it is capable of the highest deposition rates and highest energy efficiency of all the PVD processes. Operating at such high deposition rates created other difficulties which were the prime focus of early research.

With the simple thermal evaporation processes, it was found at an early stage that absolute cleanliness was essential for good coating adhesion, particularly for Zn coatings [13]. The minor degree of surface oxidation that occurs after conventional in-line precleaning operations was sufficient to cause loss of adhesion. This is not surprising in light of the low energy of the thermalised metal vapour, which means that the adatom mobility is almost negligible under conventional operating conditions. Various forms of precleaning operations were found to encourage adhesion of vacuum deposited coatings, such as mechanical abrasion [13], chemical and electrochemical cleaning [18], and high

voltage glow discharge sputter cleaning [15]. Prior application of a very thin adherent flash coating was also found to enhance coating adhesion, and was widely used in pilot lines [16,17,21].

Preheating of the steel strip was noted to be generally essential for good coating adhesion [13,21]. Moreover, it was necessary to keep the strip temperature below a certain limit to prevent the re-evaporation of deposited metal. This was especially important for Zn coatings due to the high vapour pressure of this metal. Preferred preheat temperatures ranged widely from 50°C to 200°C. The maximum strip temperature was often limited to 230°C. With these operating temperatures, the deposited Zn was not observed to alloy with the substrate. An important consideration in the control of strip temperature was the release of latent heat during the condensation of Zn vapour, which was most noticeable with light gauge strip. For example, the deposition of 150 $g.m^{-2}$ Zn on one side (a typical coating mass for building applications), caused a 70°C temperature rise in 1.0 mm strip, compared with a 170°C rise for 0.5 mm strip [13]. This effect placed limitations on the coating weight that could be deposited in a single pass without interstage cooling. Cooling the steel strip in vacuum was another problem, since radiation is the dominant heat transfer mechanism under such conditions, and consequently cooling was very inefficient. Banks of contact cooling rolls or intermediate line sections operating at higher pressures were suggested as means of reducing the strip temperature to acceptable levels [16,17]. This complicated the engineering of continuous vapour deposition lines, and limited the maximum linespeed.

Other important process issues such as bath spattering, coating uniformity, shielding, and stray deposition control were also investigated. Of particular concern was the excessive maintenance required for vapour deposition lines due to the build-up of stray deposits on shields and chamber walls. This problem continues to plague modern vapour deposition lines, with regular shut-downs necessary for cleaning [23,24].

1.3.2 East German Activities

Concurrent with the American, British and Australian development of vapour deposited coatings, several East German companies were exploring the vapour deposition of Al onto steel strip. Much of the development centred at the Manfred von Ardenne Institute, by Schiller and coworkers [25]. As for the American interest in PVD Al coatings, this work was mainly aimed at the substitution of tinplate. Shortages of Sn were particularly acute in Eastern Bloc countries, and a steep rise in world energy costs made electrolytic deposition less favourable [26]. A small scale commercial PVD line was commissioned in 1971, capable of coating 400 mm wide steel strip with Al at a rate of

20 $\mu m.s^{-1}$, enabling linespeeds of up to 300 $m.min^{-1}$ [25]. Such high deposition rates were achieved via electron beam heating with 600 kW guns [27]. Within the first decade of operation, about 140,000 t of strip steel were coated using this line. In comparison, the estimated world production of tinplate in 1982 was 15 $Mt.year^{-1}$, and thus the output of this line represented a mere 0.1% of world capacity.

Many of the practical engineering lessons learnt from the small scale commercial line were incorporated into a second coating facility commissioned in 1982 [27]. This air-to-air coating line incorporated a series of load locks at the entry and exit end of the vacuum coating chamber. Steel strip up to 800 mm in width was able to be processed at a linespeed of 200 $m.min^{-1}$. The line incorporated four 600 kW electron beam guns; two were used for strip preheating, plus one gun for each of the two evaporation baths. Following this work, a significant volume of knowledge has evolved in Germany concerning the construction of vacuum locks for continuous lines capable of sustaining 1 Pa, and in the use of electron beam guns for heating and evaporation purposes [26,28].

In more recent times, there has been a drive towards the adaptation of Al vapour deposition technology for the deposition of Zn coatings [29]. Conventional electron beam evaporators were considered unsuitably slow, and very high deposition rate jet evaporators were developed. These sources involve evaporation by resistive heating in an enclosed vessel, and ejection of the vapour through a small diaphragm. It was claimed that such a source could produce a 21 $g.m^{-2}$ Zn coating (equivalent to about 3 μm thickness), at a linespeed of 200 $m.min^{-1}$, requiring an electron beam power of 2.6 kW per cm strip width. Thicker coatings could be produced by arranging several sources in line, probably with intercooling stages to avoid strip overheating.

1.3.3 Japanese and Korean Activities

The first industrial Zn vapour deposition line was jointly developed by Mitsubishi Heavy Industries (MHI) and Nisshin Steel. Fundamental research into this project began in 1978, possibly in response to the earlier work by American Steel companies. This was followed by the construction of a pilot plant in 1982, and subsequent testing of the technology and products [30]. The industrial line was installed at the Hanshin Works of Nisshin Steel in 1985, with commercial production commencing in 1987 [31]. Details of the design are available in the open literature [32], and a schematic diagram is shown in Fig.1.7.

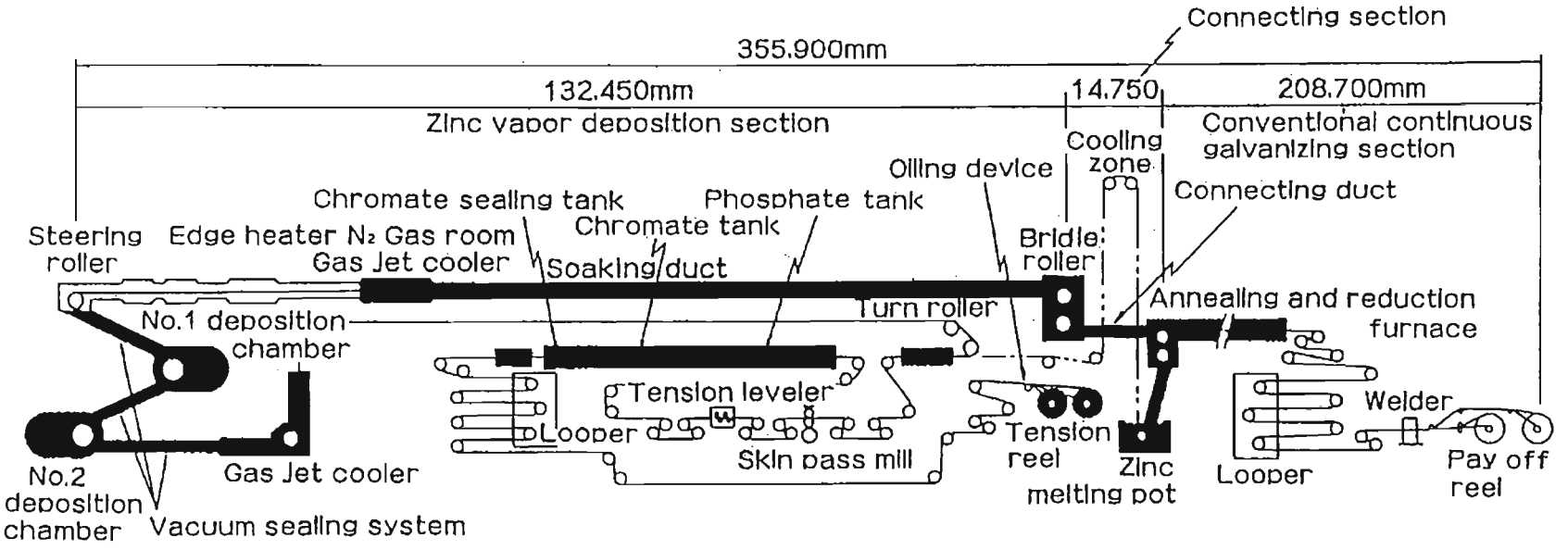

Fig.1.7 Schematic diagram of the continuous zinc vapour deposition line at Nisshin Steel in Japan [31]

The Zn vapour deposition facility was built as an attachment to an existing in-line annealing type hot dip galvanizing line, and it is claimed that this represents a considerable cost saving compared with the construction of an electrodeposition line [32]. The process is virtually identical to hot dip galvanising with the exception of the coating of the strip. A non-oxidising annealing and reduction furnace is used to clean and heat treat the steel surface. The strip passes through a vacuum lock system and each side of the strip is coated in turn by vapour deposition. An exit lock system closes the vacuum chamber, and the strip is then skin-passed and chemically treated before recoiling. The line is claimed to be capable of processing 0.3 to 1.2 mm thickness strip of 760 to 1250 mm width, with linespeed ranging from 20 to 200 $m.min^{-1}$ [31,32]. Coatings ranging from 10 to 150 $g.cm^{-2}$ per side can be applied. The thickest coatings cannot be applied to light gauge steel strip because the release of latent heat results in excessive heating and reevaporation of the coating.

Substantial efforts were made by Nisshin and MHI to design a multistage vacuum sealing system capable of reducing the pressure around the strip from atmospheric pressure to the vapour deposition pressure [30,32]. The employment of multistage differential evacuation minimised the vacuum pump power requirements. Pressure was reduced gradually through several vacuum stages (50 kPa, 16 kPa, 7 kPa, 2 kPa, 300 Pa, 70 Pa, and 1 Pa), with each section divided by a sealing device. The structural design of the sealing rolls is shown in Fig.1.8a. Two coating chambers are used in the Nisshin zinc vapour deposition line, each being used to consecutively coat one side of the strip. The structure of one of the deposition chambers is shown in Fig.1.8b. Pure Zn is melted under atmospheric pressure, in an external resistance heated pot, and fed into the evaporation bath via a snorkel. A series of resistance heaters above the bath are used to evaporate the Zn.

Much of the early coating development work conducted by Nisshin using the vapour deposition line was concentrated on producing pure Zn coatings [30,32-34]. It was established that the corrosion performance of these coatings was very similar to conventional galvanised or electrodeposited coatings. Significant improvements were obtained after chromate conversion treatment [35]. This was thought to be related to the very high retention of chromate by the porous Zn coatings. Some research was conducted on the annealing of vapour deposited Zn coatings, and subsequent formation of Zn-Fe compounds [36]. It was claimed that the press formability of this coating was improved with respect to conventional galvannealed coatings. The product therefore appeared ideal for automotive body panels. More recently, it appears that Nisshin have installed two more coating chambers onto the vapour deposition line, prior to the two chambers shown in Fig.1.7 [24]. Each of these chambers can be used to apply a coating

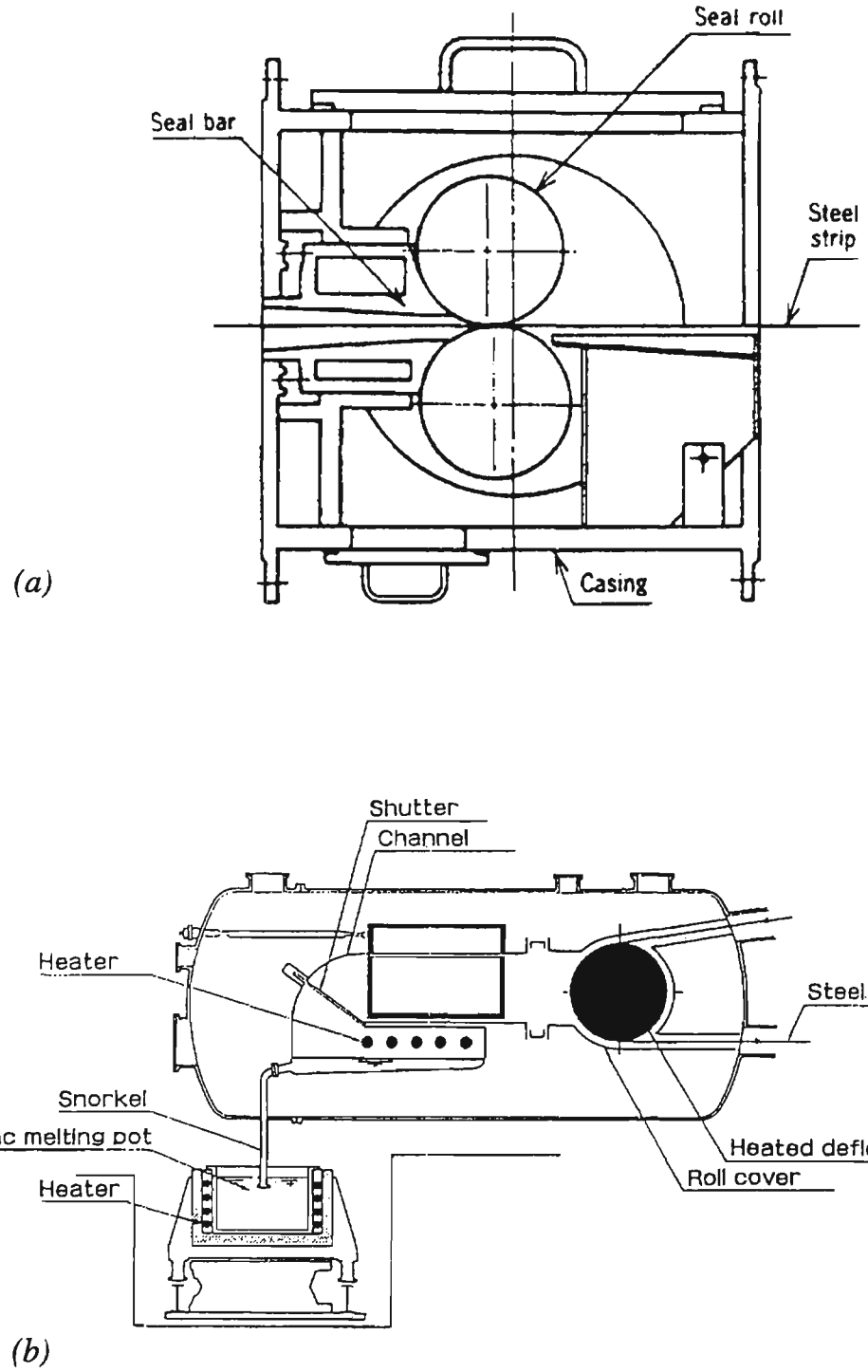

Fig.1.8 Schematic diagrams of some of the components in the Zn vapour deposition line at Nisshin Steel in Japan: (a) vacuum sealing roll housing [32] (b) vapour deposition chamber [31]

simultaneously on both sides of the steel strip by means of dual arc evaporation sources. The operation of all four coating chambers enables the production of trilayer Zn/Mg/Zn coatings (Sect.3.8.3).

The development of vapour deposited alloy coatings for sheet steel has been largely left to other Japanese and Korean steel companies. In 1992, at least six of the major Japanese steel manufacturers were known to have pilot plants for the vapour deposition coating of steel strip [26]. These plants were supplied by German companies, equipped with the expertise of large scale PVD plant and process engineering gained from their earlier work on vapour deposition. Researchers at Kobe Steel have examined a vast range of different alloy and multilayer coatings using a PVD pilot plant [37,38]. This has led to the granting of what can best be described as "saturation" claims in a multitude of Japanese patents. Some of the more realistic claims have been granted US patents [23,39], and these are discussed in Sect.3.6.3. In 1987, Nippon Steel installed a multipurpose PVD facility capable of depositing coatings by ion plating, sputtering and plasma-activated chemical vapour deposition (PA-CVD). They appear to have been principally involved in the deposition of decorative coatings such as TiN, TiC, Cr, Al_xO_y and SiO_2 for stainless steel strip [40-42]. Researchers in Korea have examined a wide range of multilayer coatings, produced by combination of conventional and vapour deposition processes [43-45]. Some of this work is discussed in Sect.3.8.

1.4 Research Objectives

It is apparent that there has been a considerable industrial interest in the use of PVD for the coating of sheet steels on a large commercial basis, with practical experience extending over the last three decades. Only in the last few years, however, have the most attractive aspects of PVD been investigated with some vigour: the preparation of novel alloy and multilayer coatings. In recognition of this climate, the research presented in this thesis was commenced with the intention of evaluating the microstructures of a range of alloy coatings prepared by a PVD method. Emphasis was placed on the investigation of supersaturated solid solutions and other metastable crystalline or amorphous phases. Magnetron sputtering was selected as the most appropriate technique for the preparation of these alloy coatings (Chap.2), and the investigation was extended to consider the impact of ion assisted deposition on coating composition and microstructure. This was particularly relevant in light of the vast range of evidence in support of the use of ion assistance as a process variable for elemental and compound coatings. Finally, the electrochemical performance of a range of the sputtered coatings was examined using a dilute chloride aqueous solution. The data was interpreted with the aim of pinpointing a coating with an optimum combination of both barrier and sacrificial properties which would ensure long term corrosion protection for a sheet steel substrate.

The coating compositions targeted for study were based on the Al-Mg-Zn ternary system, with particular emphasis on the binary alloys. Selection of this alloy system was based on several criteria. Firstly, each of these three metals are more active than Fe. This is an essential requirement for a sacrificial coating on steel substrates (Sect.1.1). Secondly, many commercial coatings are based on this alloy system (Sect.1.2), which provides a useful frame of reference. Thirdly, each of the three metals are available in abundant supply and at an economical price. Not only is this latter factor helpful for the budget of a research project, but more importantly the compositions examined are within the realms of financial viability for large scale commercial application. A detailed review of the previous work on PVD coatings for the Al-Mg-Zn ternary system is presented in Chap.3.

Chapter 2

Sputter Deposition

2.1 Physical Vapour Deposition

Sputter deposition is only one member of a family of coating techniques that are collectively known as physical vapour deposition (PVD). These processes are characterised by the growth of a coating or film using a source material in vapour form. They inherently require the use of low pressures, typically ranging from 100 μPa to 10 Pa (10^{-6} to 10^{-1} torr). The substrate temperature is usually low (less than 500°C) compared with the related technique of chemical vapour deposition (CVD), and this is advantageous for temperature sensitive substrates. The low process temperature necessitates special attention to substrate cleanliness in order to achieve acceptable coating adherence, and many of the cleaning methods used for electrodeposition are suitable.

There are numerous PVD techniques, and they can generally be characterized by the method of vaporization. Thermal evaporation is the simplest method, whereby a source material is heated in vacuum until it vaporizes at a sufficient rate to form a coating. Source heating can be achieved resistively or by means of electron-beam guns. A low pressure is essential so that the vapour pressure of the source material significantly exceeds the background pressure of air and water vapour. Operating with excessively high background pressure results in contamination of the coatings, and poor growth structures. The next method of PVD is sputtering, which requires bombardment of a source material with energetic ions to produce a flux of atoms for subsequent deposition. Sputtering is an inherently energy inefficient process, and is fundamentally slower than thermal evaporation, but offers greater versatility and control. The third method of vaporization is arc evaporation. As the name suggests, this is essentially a variation of thermal evaporation, except that the vapour flux is produced by means of an electric arc on the target source. Arc evaporation usually relies on highly localised flash evaporation which provides a strongly ionized evaporant. Direct ion beam deposition is the fourth and final category of PVD source. With this technique, the source material is entirely ionized and is accelerated to relatively high energy by means of electrostatic acceleration grids.

The four categories of PVD sources can be distinguished in terms of the energy of the species used to deposit coatings. Thermally evaporated atoms typically have an energy of only a few tenths of an electronvolt (eV), sputtered atoms have an average kinetic energy of a few eV, arc evaporated ions develop higher energies due to the multiple charge of metallic ions, and finally ion beam sources can provide up to several hundred keV (more important for ion implantation rather than coating). The energy of the deposition process can also be increased by secondary means. For example, an inert gas plasma can be added to a thermal evaporation source and by electrically biasing the substrate (ion plating), a flux of energetic inert gas ions can be made to bombard the substrate simultaneous with deposition. Alternatively, an ion beam source can be added to the system and energetic ions directed towards the substrate. This approach to increasing the process energy is generically described as "ion assisted deposition", and is almost universally regarded as essential for the deposition of engineering coatings. This is because the energy of the coating process has a strong influence on the coating adhesion, residual stress, stoichiometry, microstructure, and various performance characteristics such as electrical resistivity, abrasion resistance, corrosion resistance, and optical properties [46]. An appropriate balance should be achieved however, since excessive energy can detrimentally affect each of these properties. It can also be justifiably argued that the energy of the PVD process is inversely related to the deposition rate. Thus, the commercial application of PVD for coating of sheet steel would inevitably necessitate the use of thermal evaporation in order to achieve the required process speed.

The present investigation was primarily concerned with the production of alloy coatings for reasons outlined in Chap.1. A perusal of the literature reveals that the vast majority of work with PVD has concentrated on the deposition of elemental or compound coatings. This is perhaps because no PVD method easily deposits alloys while preserving their composition. However, there has been a noticeable movement towards alloys in the last few years, and for a number of reasons, sputtering is widely recognised to be the PVD method of choice for alloy coatings. As such, this investigation adopted the sputtering process for the production of alloy coatings, even though it is fully appreciated that thermal evaporation would be required for commercial sheet steel coating. Moreover, the potential usefulness of ion assistance for alloys was thoroughly evaluated by studying the effects of substrate bias on the composition and microstructure of coatings deposited by unbalanced magnetron sputtering (Sect.2.2.4).

The remainder of this Chapter provides some background to sputtering processes (Sect.2.2), particularly in relation to the use of magnetron sputtering for ion assisted deposition studies. The use of sputtering for the preparation of alloy coatings is reviewed

(Sect.2.3), and the characteristics of sputtered coatings are described (Sect.2.4). For further information on sputtering and other PVD processes, the reader is directed to several excellent review publications [46-53].

2.2 Sputtering Mechanisms and Processes

2.2.1 What is Sputtering?

Sputtering can be defined as the ejection of particles from a condensed matter target due to the bombardment of energetic projectile particles [54]. It is a statistical process that occurs as a result of a series of momentum-exchange collisions between the energetic projectile and the atoms in the surface of the target. Sputtering cannot occur from a single binary collision because conservation of momentum necessitates that the momentum vector of the target atom cannot be altered by more than 90°. Thus, a series of quasi-elastic collisions occur below the surface of the target material, in a process known as a collision cascade. It is possible for the cascade to eventually return back to the surface atoms and if they are provided with sufficient energy, they can be ejected from the target as a sputtered atom. The kinetic energy of the surface atom must exceed the surface binding energy for it to be sputtered, and this value is usually approximated by the heat of sublimation [55]. The collision cascades that lead to sputtering are usually concentrated very close to the surface of the target, typically within the first five atomic layers. If the kinetic energy of the colliding atoms is sufficiently high then the process is well simulated by true elastic collisions. This enables the use of Monte Carlo computer simulations of the sputtering process, such as in the TRIM code [56] which is based on a binary elastic collision model. However, the effects of binding energy become prominent when the kinetic energy is very low, and under these conditions molecular dynamics models are preferred.

The rate of sputtering is quantified in terms of the sputtering yield, defined as the ratio of sputtered atoms per incident particle. The sputter yield is affected mainly by the mass of the incident and target species, plus the kinetic energy and direction of the incident particle. In the vast majority of cases, the energetic bombarding particles are ions since it is relatively easy to control their energy by electrical biasing (as such, the incident particle is hereafter referred to as an ion). The electronic charge of the incident ion is irrelevant to the sputtering mechanism, however, as ions are usually neutralized by Auger electron emission from the target. The sputter yield is measured experimentally, and generally increases almost linearly with the ion energy, with a threshold energy of between 20 and 40 eV. The sputter yield becomes sublinear at very high ion energy.

Sputter deposition processes utilise relatively low energies (< 1 keV) since it is more energy efficient (Sect.2.2.2). The sputter deposition yields of most metals are near unity and within an order of magnitude of each other. This is advantageous for the sputtering of alloy targets (Sect.2.3.1).

2.2.2 The Sputtering Environment

Most sputter deposition processes utilise a glow discharge or plasma as a source of ions for bombardment of the target [47,54]. The plasma can be generated by either dc or rf power depending on the type of target material being used. Sputtering of electrically non-conductive targets requires the use of rf power since a dc current cannot be sustained. Metallic targets can also be operated using rf power, but dc is much easier to set up and control, and is the preferred method with magnetron systems (Sect.2.2.3). The glow discharge requires the use of a gas to provide a source of ions, and this gas supply is flowed continuously through the sputtering chamber such that a fixed low pressure is maintained (0.1 to 15 Pa). Inert gases are the norm since they do not react chemically with the target or sputtered coatings. Ar is the most commonly used sputter gas because it represents an acceptable balance between economical and process suitability. The heavier inert gases, Kr and Xe, are preferred when sputter depositing coatings with high atomic mass metals such as W, and this can be achieved economically by means of a static gas system [57]. Nitrogen, oxygen, and hydrocarbon gases are also used for deposition of reactive coatings, although this is of little relevance to the present work.

When ions from the glow discharge are forced to bombard the target surface, sputtering is not the only subsequent event [47]. The most important target processes are summarised schematically in Fig.2.1. Ions can be reflected from the surface, mostly in neutralized form. Reflected ions can possess a large fraction of their initial kinetic energy, and they are often called "energetic neutrals". These should not be confused with sputtered atoms which are also neutral but derive from the target material and are usually of much lower energy. Energetic neutrals are emitted in the same directions as sputtered atoms and they simultaneously bombard the coating as it deposits. There is considerable evidence to suggest that energetic neutrals can significantly influence the composition and microstructure of sputtered coatings [58,59]. Ion bombardment of the target also results in the emission of secondary electrons which are essential for stabilisation of the glow discharge. Ions can be buried in the target, and this is used to advantage for the ion implantation process whereby controlled amounts of specific impurities are implanted immediately below the surface of a workpiece. Finally, the interaction between the energetic ions and the target atoms can result in radiation damage such as vacancies, interstitials, and compositional modification for alloy or compound targets.

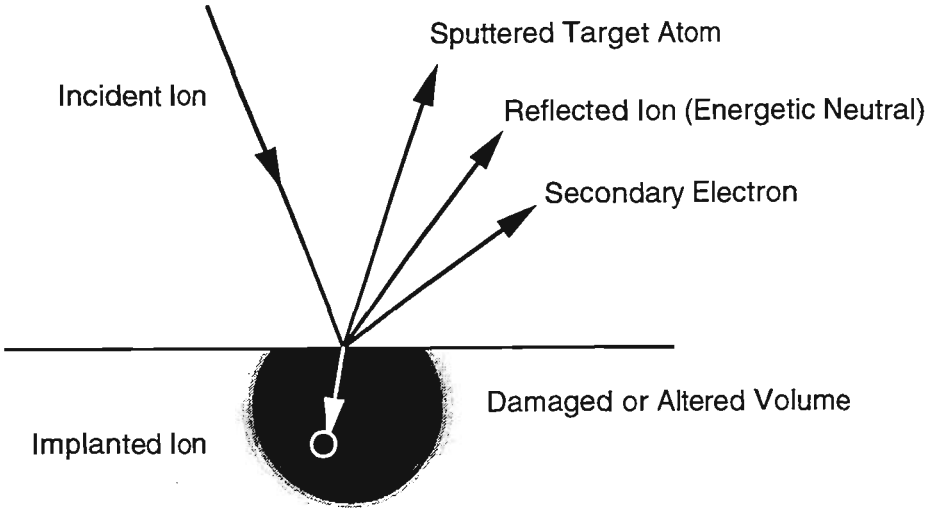

Fig.2.1 Summary of various events that follow from ion bombardment of a target [47]

The energy of sputtered atoms typically ranges from a few eV up to several tens of eV, with a broad-tailed energy distribution curve. The energy of the sputtered atoms represents only a fraction of the energy of the incident ions. When combined with a sputter yield that is usually less than unity, it is apparent that sputtering is an inherently energy inefficient process. This is overcome somewhat by ensuring sputtering systems are operated at voltages that provide optimum sputter yields (several hundred volts). However, most of the input power to the system appears finally as target heating. This heating can be excessive, leading to local temperatures of 400°C if unchecked [47], and hence water-cooling of targets is considered essential.

2.2.3 Diodes, Triodes and Magnetrons

The planar diode shown schematically in Fig.2.2a is the simplest type of sputtering system configuration. A low pressure glow discharge is generated between the cathode (target) and the anode (substrate platform and chamber walls) by means of a dc power supply. Most of the discharge current is carried by positively charged Ar ions passing to the cathode, and electrons passing from the plasma to the anode. Since the ions travel at much slower speeds than the electrons, most of the applied electric potential is concentrated across the "cathode dark space" or sheath region above the surface of the target. This high electric field causes the positive ions to accelerate before impacting with the target. This not only results in sputtering of the target, but also causes emission of "secondary electrons". The electric field causes the secondary electrons to be accelerated back towards the plasma, where they interact with the glow discharge. The secondary energetic electrons accelerated away from the target are often called "primary electrons" (presumably to distinguish them from the secondary electrons produced in the plasma). These "primary electrons" are critical to the maintenance of the glow discharge, since they contribute to ionization by various processes [47].

Planar diode discharges can only be sustained at relatively high pressures (7-13 Pa) and high voltages (~3000 V). High voltages are required to generate secondary electrons at the target, and high pressures ensure sufficient ionization of the gas. The high pressures unfortunately result in gas scattering of sputtered atoms, which reduces their kinetic energy and leads to poor coating microstructures (Sect.2.4). Furthermore, the sputtering rate is limited to a few micrometres per hour since the current density cannot be increased without sacrificing ionization efficiency. These problems can be overcome somewhat by triode sputtering, as shown in Fig.2.2b. With this method a heated electrode is added to the diode arrangement, and thermionic electron emission provides an extra source of electrons for ionization in the discharge. Triode sputtering

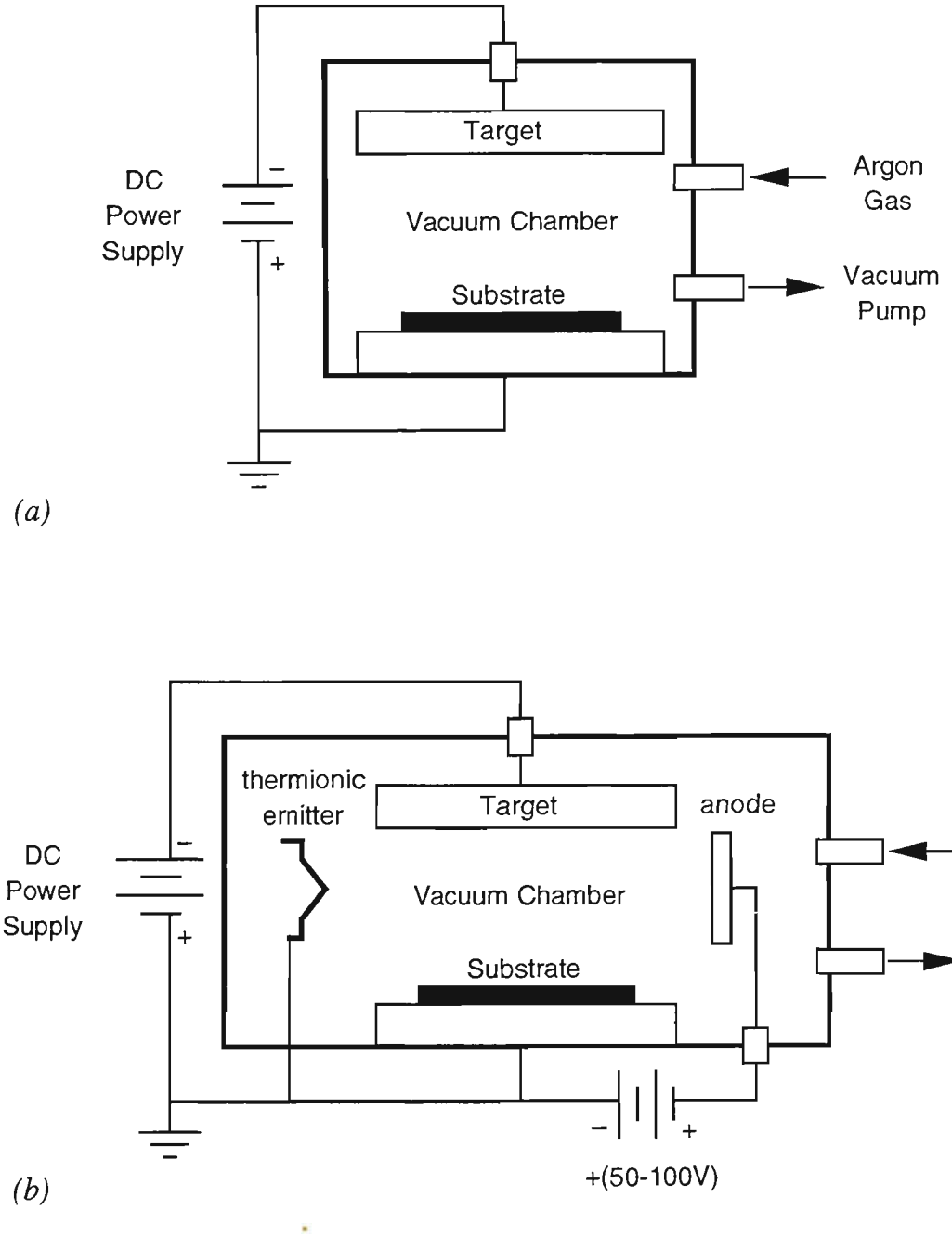

Fig.2.2 Schematic diagrams of simple diode (a) and triode (b) sputtering systems [47]

enables an increase in sputtering rate of up to an order of magnitude, and the operating pressure can be reduced substantially (as low as ~0.1 Pa) [47].

Both diode and triode sputtering systems are difficult to use from the perspective of controlled substrate temperatures. This is because a substantial flux of energetic electrons bombard the substrate during coating deposition, and cause increases in temperature. This issue was addressed with the development of magnetron sputtering in the early 1970s [47]. A schematic diagram of a typical planar magnetron system is shown in Fig.2.3a [60,61]. Either permanent magnets or electromagnetic coils are placed behind the target producing a magnetic field in front of the target. As a result of electromagnetic and electrostatic forces, electrons are forced to follow a helical path along the magnetic field lines, while being repelled from regions of contracted field lines [61]. The net effect is to trap the electrons near the surface of the target so that the loss of primary electrons to the anode walls is virtually eliminated, and the number of ionizing collisions with gas atoms increases substantially. Hence, a very intense volume of plasma concentrates near the surface of the target. Confinement of the plasma substantially reduces the thermal load on the substrates and enables coating of temperature sensitive substrates. The magnets are usually arranged such that they restrict the discharge to a characteristic "racetrack" on the surface of either circular or rectangular planar targets (Fig.2.3b). Such arrangements limit the utilization of the target material, but magnetrons offer other advantages such as very high deposition rates ($> 1\ \mu m.min^{-1}$), and operation at pressures as low as 0.015 Pa [62].

2.2.4 Balanced and Unbalanced Magnetrons

In 1986, Window *et al* [60,63] recognised the potential of magnetron sputtering for ion assisted deposition. They studied the charged particle fluxes from circular planar dc magnetrons with different magnetic field configurations, and reported on the development of a magnetron source capable of providing the unique characteristic of a high deposition rate and concomitant high ion flux. It was shown that with a conventional magnetron, the magnetic field is "balanced" such that the vast majority of field lines from the outer ring of magnets are matched by the opposite magnetic pole in the centre of the magnetron (Fig.2.3a). With the "unbalanced magnetron" design (or UM-gun), the strength of the outer ring of magnets was deliberately increased relative to that of the central magnet, such that a significant proportion of the outer field lines were directed towards the substrate position (Fig.2.4a). Consequently, the modified magnetic field retained the essential electron trapping characteristics of a conventional magnetron, but also caused a beam of plasma to be directed towards the substrate position. Measurements of the ion current at the substrate revealed that the ion flux could be varied

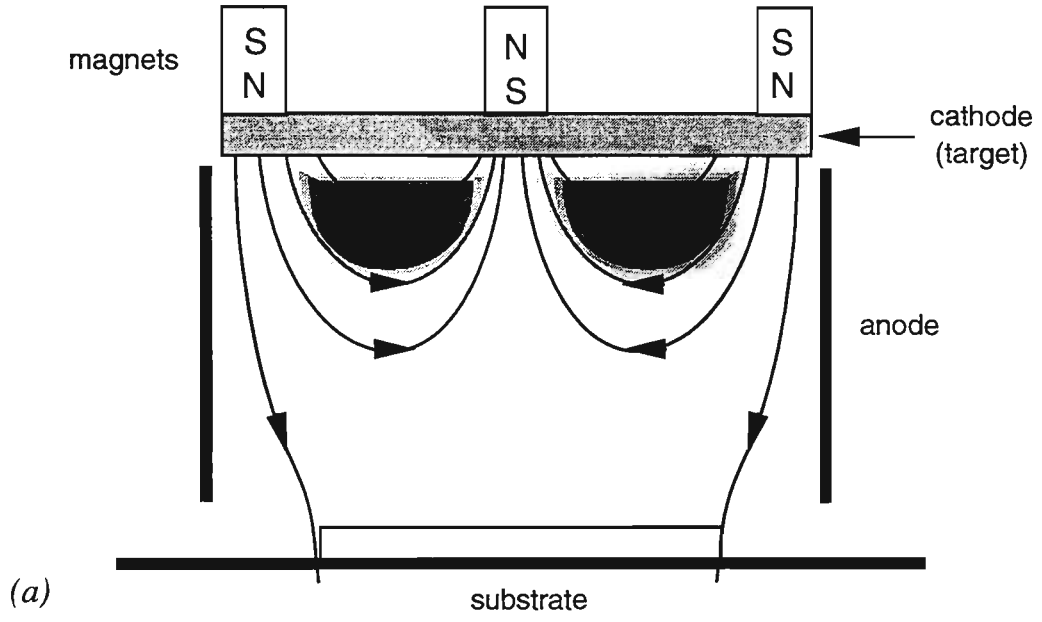

(a)

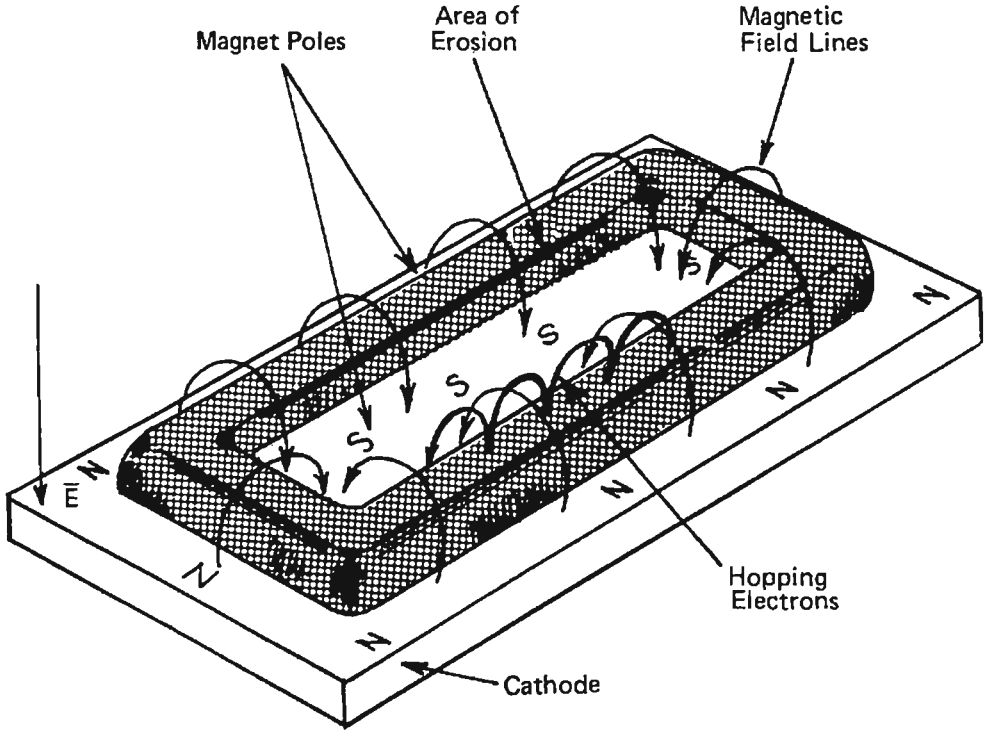

(b)

Fig.2.3 Schematic diagrams of magnetron sputtering configurations: (a) magnetic field produced in front of target showing confinement of glow discharge [61] (b) annular plasma discharge on the surface of a rectangular planar target [47]

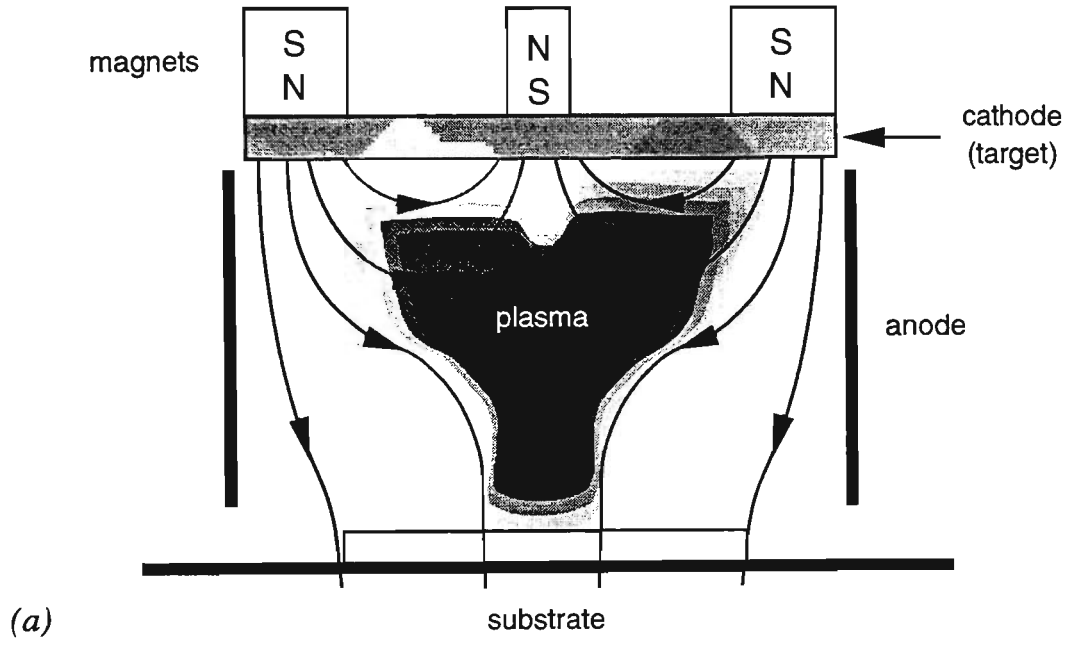

(a)

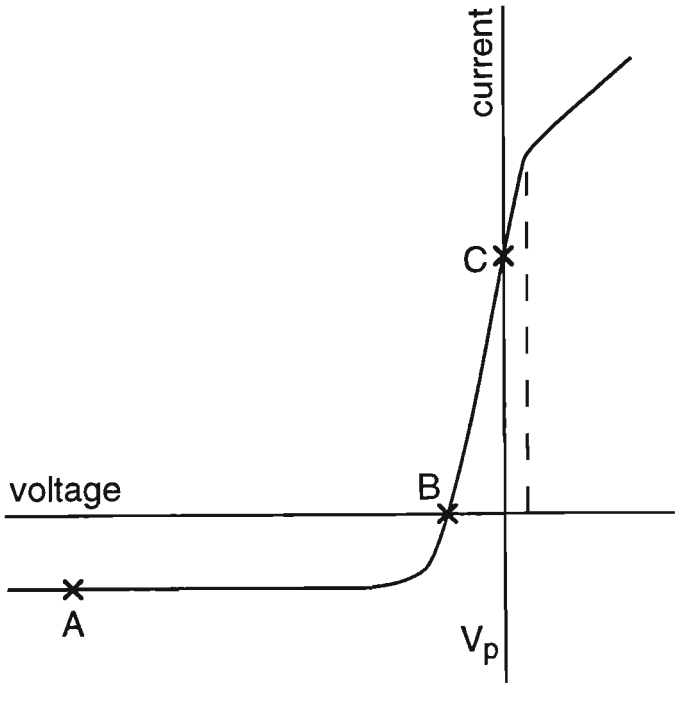

(b)

Fig.2.4 Principles of an unbalanced magnetron sputtering system. (a) schematic diagram illustrating the modification of the magnetic field which directs plasma towards the substrate [61,65] (b) characteristic voltage-current behaviour of an isolated probe at the substrate position [60]

independently of deposition flux by changing the magnetic field configuration [60]. Furthermore, they found that the ion flux was proportional to the discharge current, while being independent of target composition, gas pressure, gas composition, and substrate bias voltage [63]. The characteristics of rf unbalanced magnetrons were also examined and found to have similar characteristics to the dc unbalanced magnetrons except for higher plasma potential and ion flux [64]. The potential application of unbalanced magnetron sputtering for ion assisted deposition was immediately appreciated, and they have subsequently been widely adopted for both research and production [61,65].

The high ion flux of unbalanced magnetrons can be utilised for ion assisted deposition simply by adjusting the voltage bias applied to the substrate [61,65]. This is best demonstrated by means of the voltage-current characteristic of an isolated probe placed in the substrate platform, as shown in Fig.2.4b [60]. The ion current drawn by the probe is approximately constant over the full range shown in this figure and the observed changes in current are mainly due to changes in electron current. With large negative substrate bias (point A), the probe is sufficiently negative to repel almost all electrons, and the current is essentially just the flux of ions that diffuse to the probe from the plasma region. A bias of -100V is usually employed to measure the ion current. As the bias is increased above about -50V, the probe starts to collect electrons and the current increases rapidly. When the probe current is zero (point B), the electron current is equal to the ion current measured at -100V bias. This point is known as the self bias or floating potential, and corresponds to the bias developed on an insulating substrate. When the probe bias is increased to the anode potential (point C), a large current is measured that is dominated by the electron current. However, the substrate is still bombarded with approximately the same number of ions as experienced at -100V bias.

The flux of ions experienced at the substrate can be put to use for ion assisted deposition, since the kinetic energy of the ions will be dependent on the bias voltage. Assuming that the pressure is sufficiently low to avoid gas phase scattering, the kinetic energy of ions that bombard the biased substrate is given by the ion charge (+1 for Ar as a sputter gas) times the voltage difference between the substrate bias and the plasma potential (V_p). For dc magnetrons, the plasma potential is typically within about +2 to +10V of the anode or ground potential [47], but for rf magnetrons values of +20 to +40V are reported [64]. Consequently, coatings deposited with rf magnetrons at earth potentials will have been produced under conditions of intense bombardment. The degree of bombardment is much more readily controlled with dc magnetrons. It must also be recognised that the bombardment associated with unbalanced magnetrons can cause strong heating of the substrates, particularly when they are at earth bias.

The voltage-current characteristic shown in Fig.2.4b applies to all types of magnetrons, not just the unbalanced variety. By simply adjusting the magnetic field configuration, the ion current to the substrate can be varied over at least three orders of magnitude, while retaining an approximately constant deposition rate [64,65]. The greatest degree of process flexibility is achieved when electromagnetic coils are used to supply the magnetic field [62], although permanent rare earth magnets are much simpler to use when a fixed ion flux is called for. It is important to realise that the ion flux in the more strongly unbalanced designs is restricted to a narrow beam with a sharply peaked lateral distribution. For example, with the M3 magnet used throughout this thesis, the full-width at half maximum for the ion flux was about 43 mm [64]. If a high ion flux is required, only the central position of the substrate plane can be utilised, which reduces the coating efficiency.

2.3 Sputter Deposition of Alloy Coatings

Evaporation of alloys is certainly possible but it is commonly expected that the composition of an alloy-evaporated coating will be different from that of the source. This is because the various elements evaporate at widely different rates, owing to the order of magnitude differences in vapour pressure. It is possible to determine an optimum evaporation rate for an alloy such that the coating composition can be maintained the same as that of the source throughout source life [66], although this requires considerable experimentation. Evaporation at rates that depart from this ideal value result in coatings that differ in composition to the source. The common solution is to separate the components of the alloy into individual elemental sources, and control the evaporation rates of each independently [67-72]. This technique is known as coevaporation, and enables the deposition of coatings of a wide range of compositions. The main drawback of coevaporation is that it is very difficult to obtain uniform composition over large area substrates, and careful design would be necessary to implement this technique on a production scale for coating sheet steel. Codeposition of complex multielement coatings is impractical because it is difficult to configure more than three or four evaporation sources while providing uniform coating composition. There are also the generic limitations of evaporation to consider, such as the restriction of source temperatures and therefore the limited range of materials that can be deposited.

Sputtering is widely considered to be the best method of depositing alloy coatings by PVD [73]. The superiority of sputtering over evaporation for deposition of alloy coatings, owes primarily to the fact that sputter yields of various elements do not vary with anywhere near the magnitude experienced for the differences in vapour pressure. It

is usually fairly easy to sputter deposit complex multielement alloy coatings from targets of the same composition (Sect.2.3.1). Binary and ternary alloy coatings can be deposited by cosputtering from two or three elemental sources in a fashion similar to coevaporation, but with several of the same restrictions (Sect.2.3.2). These problems can be overcome somewhat by the use of composite targets (Sect.2.3.3), which are particularly useful for deposition of brittle intermetallic alloy compositions. Finally, the recently developed rotatable cylindrical magnetrons have been shown to be especially useful for coating large substrate areas with uniform alloy coatings (Sect.2.3.4).

2.3.1 Alloy Targets

Sputtering offers the unique ability to deposit coatings from a monolithic alloy target while maintaining this same composition in the coating [74-79]. This is possible because of the characteristics of the sputtering mechanism. When a homogeneous target composed of different elements is bombarded with energetic ions, the sputtered flux will initially be rich in one of the components. This occurs because of the relatively small differences in surface binding energy of different elements (compared with the much larger differences in vapour pressure). However, the preferential removal of one of the components causes a corresponding deficiency in the altered surface layer. Fortunately a steady state is achieved after an incubation period where the surface composition offsets the differences in sputter yield. The steady state surface composition of the target will differ from the bulk composition, being enriched in the lower yield element/s, but conservation of mass ensures that the sputtered flux replicates the bulk composition of the target. This modified layer in the target is typically very thin, but depends on the microstructure. For example, a monophase target would be expected to have a modified layer in the order of 3-10 nm, whereas a multiphase target would be considerably more rough with an affected depth of up to several micrometres [54]. Regardless, a steady state sputtered flux can be achieved after an incubation period that is typically only a few minutes.

Alloy targets can be formed by casting or by hot pressing powders. The preparation of cast alloy targets is relatively easy since it involves simply melting the constituent metals in a furnace, homogenising the melt, and then casting into an appropriately sized mold. Commercially wrought or cast alloys can also be used for sputter targets, and this is beneficial for deposition of engineering alloys such as stainless steels [59,80]. Alloys of machinable materials are the most versatile since they can be immediately turned down to the required dimensions and fitted directly into a magnetron gun. Another common practice for preparation of alloy targets is to arc melt pre-weighed mixtures in a high-purity argon environment [81]. Chemical inhomogeneities in the

casting are minimised by melting several times, preferably with a crushing process between each casting step. Correct selection of a backing plate material can eliminate the need for a tertiary bonding material, since the melt can wet the plate, thus ensuring an alloy bond [81]. Alloys containing refractory metals are difficult to melt due to the high melting points, and the technique is better suited to less refractory metals. Some alloy targets are also difficult to produce due to the formation of brittle intermetallic phases [79].

Target materials prepared by hot pressing powders are occasionally used but present particular problems [54,79,82]. The high porosity of powder targets provides a very large surface area for the adsorption of contaminants [83]. Very long evacuation times are required to overcome the outgassing of the porous target material. Furthermore, this contamination can be present throughout the target and provides a continuous virtual leak as the target is used [54]. The sputter yield of powder targets is often very low since the abovementioned surface modification leads to very rough target surfaces. The higher yield components become shielded by protruding regions of low yield material, such that the overall yield can often drop below that of the low yield constituent.

The sputter deposition of alloy coatings that replicate the target composition is not automatic, but depends on a number of factors. The target must be maintained at a sufficiently low temperature to avoid bulk diffusion which could modify the composition of the target surface. This can be especially problematic for volatile alloy compositions [78]. Chemical effects in the target should also be avoided, such as decomposition of compounds with the loss of one constituent, or contamination with reactive components in the sputter gas. Differences in the gas-transport of the various components can cause non-stoichiometric coatings. This is not usually of concern for magnetron sputtering because the low operating pressures ensure that the mean free path is typically greater than the target-substrate separation. Substrate effects are also important, such as differences in the sticking coefficients of the components [54]. Of much greater concern is the effect of preferential resputtering which results from energetic particle bombardment of the substrate. The stoichiometry of alloy coatings is discussed in more detail in Sect.2.4.4.

2.3.2 Cosputtering

It is not always possible or practical to produce monolithic alloy targets. Some alloy compositions can be exceptionally brittle due to the formation of complex intermetallic phases, and are consequently difficult to produce a target that can withstand mechanical and thermal shock. In such cases, alloy coatings can be sputter deposited from multiple planar magnetron sources, with each source containing an elemental target.

This technique is often called "cosputtering" [84], and it is a common commercial and research practice. Cosputtering of binary alloy coatings is usually done with two circular magnetrons [85,86,87], although rectangular magnetrons have also been used to coat larger areas [84] and multiple substrates [88-92]. The major attraction of cosputtering is that the composition of the alloy coating can be easily controlled by varying the power applied to each target [88-90]. This means that virtually any binary alloy composition can be deposited from two elemental magnetron targets, except perhaps for the very dilute compositions.

Many of the disadvantages of coevaporation also apply to cosputtering. Positioning of the magnetron sources so as to provide uniform compositions over a large area is extremely difficult. This is not a concern when small substrates are to be coated, since they can be located at the optimal position to receive the desired coating composition. It does create problems for the coating of large areas, resulting in non-stoichiometric or graded compositions. The deposition of alloys with more than two or three constituents is generally not practical because of the requirement to power each source individually and also for space reasons. Another problem particular to cosputtering is the potential for redeposition of sputtered material from one target onto another. This causes contamination of the targets and can contribute to extremely long run-in times before a steady-state composition is achieved [93]. Redeposition is especially of concern when the magnetron sources are tilted towards each other such that the sputtered flux has a line-of-sight path between each source [84]. This can actually be advantageous in some circumstances, as discussed in Sect.2.3.4.

It has also been demonstrated that coatings prepared by cosputtering and alloy sputtering can have significantly different deposition environments which can influence coating microstructures [94]. Coatings of $Ni_{67}Si_{21}B_{13}$ were prepared by cosputtering from three elemental targets of Ni, Si and B, and by sputtering from a stoichiometric amorphous alloy target. The average kinetic energies measured for the sputtered atoms from the cosputtered targets were found to be significantly higher than those from the alloy target. This was interpreted to indicate that the surface binding energy of the atoms in the amorphous alloy were reduced in comparison with those in the elemental targets, although it is also feasible that sputter yield amplification effects may have occurred for the amorphous target (Sect.2.4.5). Such differences in the kinetic energy of sputtered atoms were found to influence the coating microstructure.

2.3.3 Composite Targets

Cosputtering with multiple magnetron sources is often an expensive option since it requires a sputtering system fitted with multiple sources each capable of being directed towards the substrate position, and investment in an equal number of power supplies. It is possible to combine the various different target materials into a single composite target, thereby enabling cosputtering from only one magnetron source. This is a relatively common practice and three different generic types of composite target designs have been reported in the literature: overlays, inserts, and sectors (Fig.2.5). Apart from the examples presented below, however, it is rare to find published descriptions of composite target designs.

The simplest means of constructing a composite target is to overlay sheets of one metal over the top of a monolithic target of another metal. This can be achieved by physically bonding small pieces of thin sheet to the surface of a target of another material, using a conductive epoxy resin or solder (Fig.2.5a) [93,95]. Overlays can also be attached by mechanical clamping. Window and Harding [61] prepared an Al-Zn composite target by overlaying a Zn target with an Al sheet which had holes of various sizes machined into it (Fig.2.5b). The Al sheet was physically clamped to the Zn target surface. An earlier design by Harding and Lake [96], was a further simplification in that only sheet material of each metal was clamped to a magnetron body (Fig.2.5c). The main problem with this clamping method is that inefficient cooling causes the overlay sheet to buckle during operation. The composition of the sputtered flux drifts substantially as a result. Furthermore, the operating lifetime of such magnetron targets would be largely limited by the thickness of the overlay sheet material.

The second type of composite target is characterized by the use of inserts of a second material. Holes are drilled at various positions into a single-element target and are filled with inserts of another material (Fig.2.5d) [97-99]. The inserts are usually made from bulk material [97,98], but compacted powders have also been used [99]. Coatings of various compositions can be achieved by drilling holes of various diameters and filling the holes with the different proportions of the inserts. This effectively alters the relative areas of each metal on the target surface. Using this approach, it is also possible to prepare a composite target design which is capable of producing a continuous gradient of compositions simultaneously on a series of substrates placed at different locations. Knoll and McClanahan [97] described one such target for use in a cylindrical-post magnetron, which consisted of a Ni cylinder that contained La metal plugs, press fit into drilled holes. The plugs were distributed symmetrically along the cylindrical coordinate, but asymmetrically along the axial coordinate, as shown in Fig.2.5e. The resulting

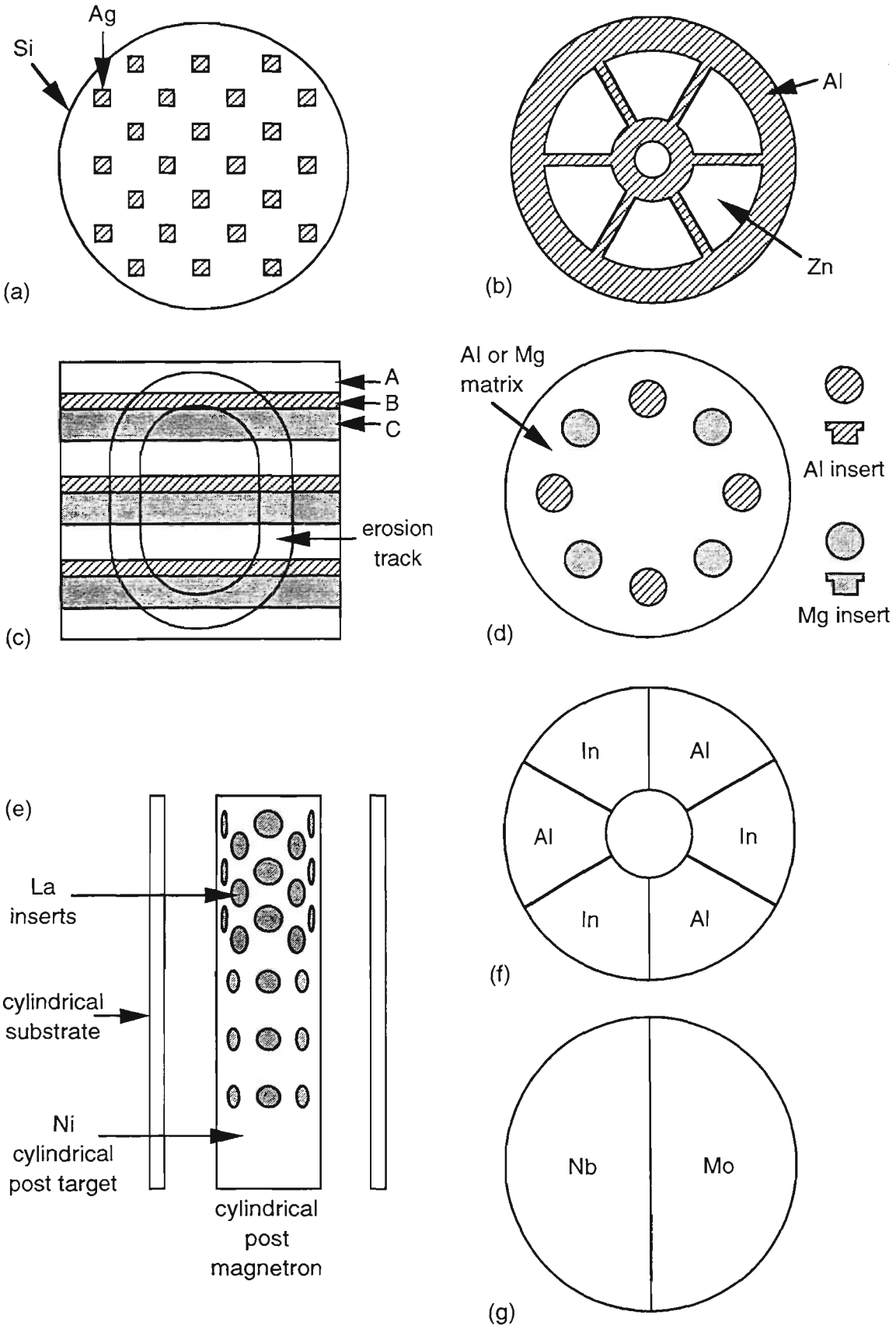

Fig.2.5 Various types of composite target described in the literature: overlay sheet design (a) [93,95], (b) [61], (c) [96]; insert design (d) [98], (e) [97]; and sectored design (f) [100] (g) [101]

composition of the coatings varied continuously from pure Ni at one end to Ni-24 at.%La at the other.

The third design of composite target is constructed from individual pieces or sectors of each metal. Rohde *et al* [100] described a target composed of 60° sectors of two different metals which were arranged alternately in a graphite crucible fitted onto a stainless steel holder (Fig.2.5f). Thermal contact between the crucible and holder was achieved using a thin layer of Ga, which would have been molten during operation, thereby restricting orientation of the magnetron. The method of attaching the target sectors to the crucible was not described. Different coating compositions were achieved using a pinwheel shutter to expose various portions of the target to the ion bombardment from the sputtering discharge. Qadri *et al* [101] described a circular planar target consisting of equal areas of Mo and Nb (Fig.2.5g). Substrates were located in a line below the target such that the composition of the deposited films varied from 20% to 93%Mo depending on their position.

Of the three different generic designs for composite targets, the most versatile would seem to be the sectored design [100]. This design would be the least affected by drifting of the composition of the sputtered flux, which is a major limitation of the sheet overlay design. The sectored design would also permit the use of a range of different magnet assemblies. As the magnetic field configuration and, to a lesser extent, the bias voltage are altered, the radial position of the sputter erosion track can change slightly. This can deleteriously affect the composition of the sputtered flux with the plug insert design. In comparison, the relative area for each component of the composite target is independent of the annular radius of the erosion track. Therefore, the sectored design provides the greatest degree of versatility since it can be used with a wide range of different magnetron configurations.

2.3.4 Rotatable Cylindrical Magnetrons

Rotatable cylindrical magnetrons have been developed in recent years for use in large-area in-line deposition systems [102]. They consist of a cylindrical tube of target material which is rotated about its axis during operation (Fig.2.6). The magnet assembly and cooling system for the magnetron are housed within the tube of target material. The magnets are maintained in a fixed position, and they can be tilted to various angles. Sputter erosion of the cylindrical target is therefore restricted to a specific area on the surface, which is defined by the location of the magnets. The rotation of the target results in constant surface renovation as it moves through the sputter erosion zone. These magnetrons are capable of very high power operation due to the excellent target cooling

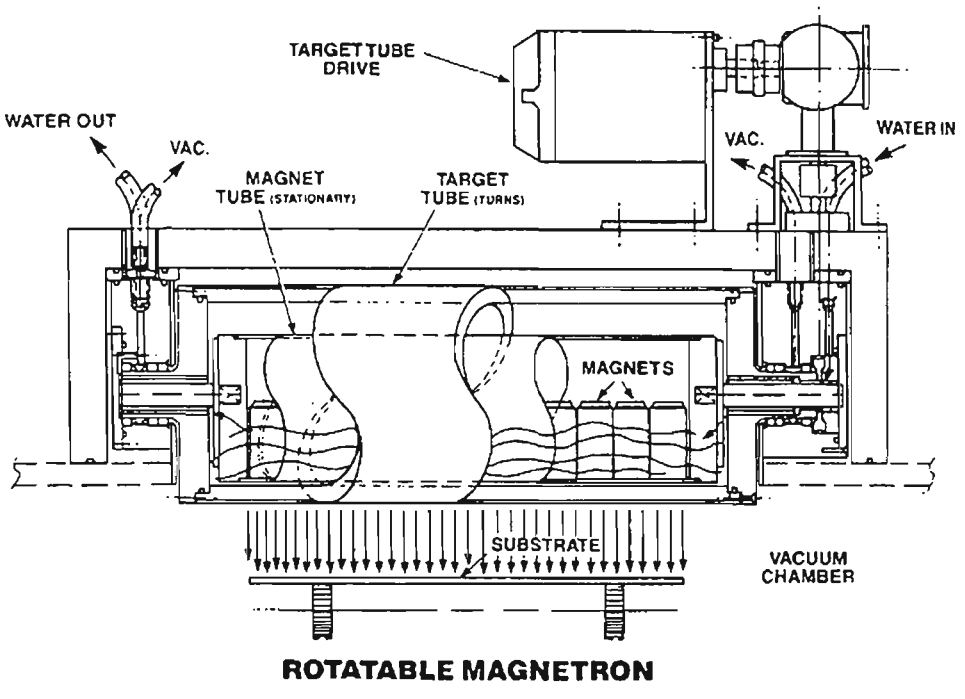

(a)

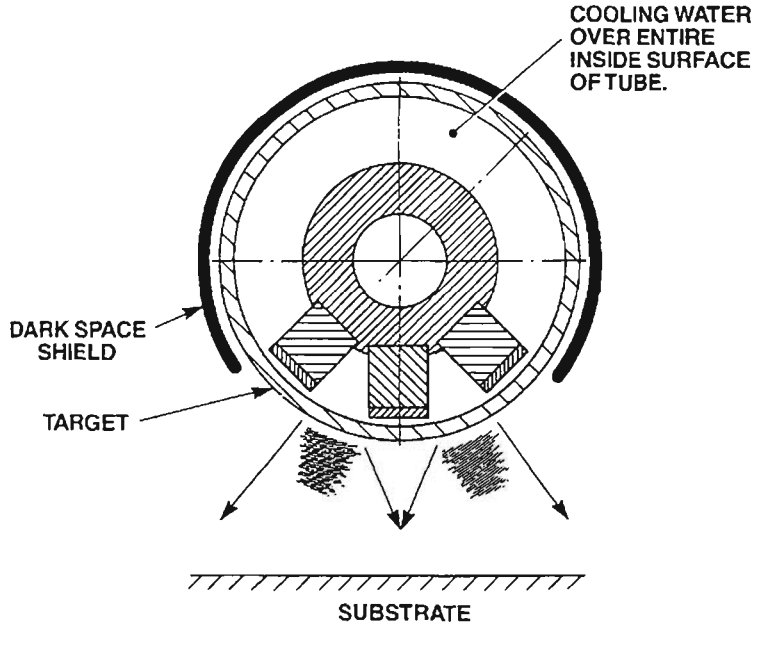

(b)

Fig.2.6 Schematic diagrams of a rotatable cylindrical magnetron: (a) side view, (b) cross-sectional end view [102]

characteristics. Target utilisation is very high since virtually the entire surface is passed through the sputter zone during rotation. Cylindrical rotatable magnetrons have therefore found numerous applications in the glass sheet coating and web coating industries.

Several novel methods of producing binary alloy coatings have been reported that utilise rotatable cylindrical magnetrons [84,103,104]. One method involves cosputtering from a pair of rotatable cylindrical magnetrons. The sputter zones on the two magnetrons are inclined such that the sputtered material from both targets are faced slightly toward each other, and in the direction of the substrate (Fig.2.7a). Cross contamination deliberately occurs and it is possible to empirically determine a set of tilt angles that provide very uniform and stable coating compositions over large substrate areas. A short period of target preconditioning (typically a few minutes), is required to stabilise the cross contamination of the dual cylindrical magnetrons. The coating composition can be controlled by changing the powers applied to each target. Compositional uniformity of ±1% can be attained over reasonably large surfaces, which make this an ideal technique for continuous coating of strip materials with binary alloys.

Serial cosputtering is a method of depositing binary alloy coatings using a combination of cylindrical rotatable magnetrons and a conventional planar magnetron [103,104]. It is specifically designed for alloy systems in which one of the component materials cannot be manufactured into a cylindrical target, and is only available in a conventional planar form. Material from the planar target is continually sputtered onto the back of a rotating cylindrical magnetron composed of the second constituent (Fig.2.7b). As the cylindrical target rotates into the sputter zone, both materials are simultaneously sputtered to form a binary alloy coating. These alloy coatings suffer from some compositional nonuniformity which can be partially overcome by adding a second rotatable cylindrical magnetron (Fig.2.7c). Both cylindrical magnetrons are constructed from the same material, and are rotated in opposite directions. The alloy coatings deposited in this way are roughly homogenous over a large substrate surface, but there are still remnants of the non-uniform distribution. Therefore, the cosputtering method is preferred to serial cosputtering.

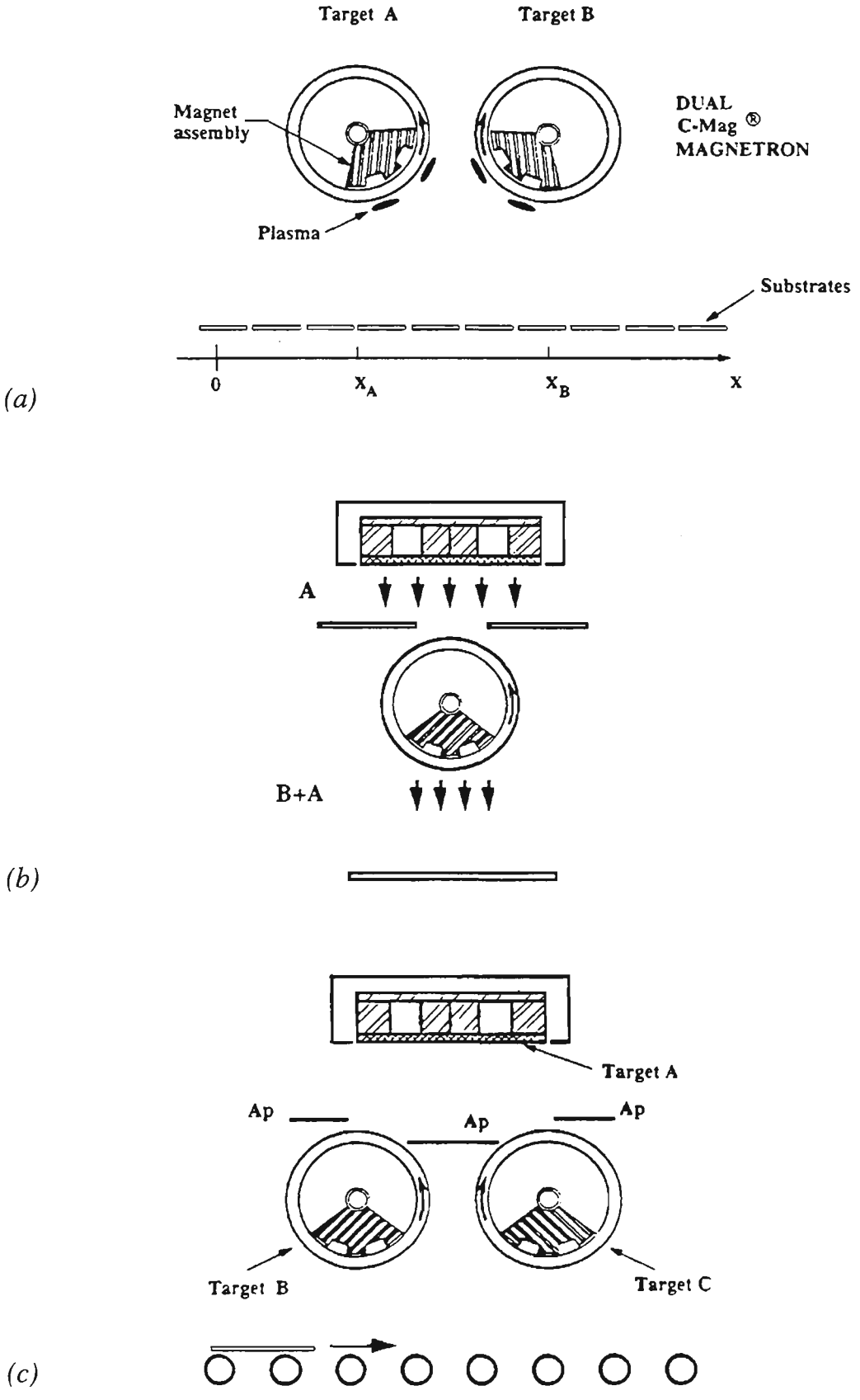

Fig.2.7 Various configurations of rotatable cylindrical magnetrons for the deposition of binary alloy coatings [104] : (a) cosputtering; (b) serial cosputtering with one cylindrical magnetron; and (c) serial cosputtering with two cylindrical magnetrons.

2.4 Characteristics of Sputtered Coatings

2.4.1 Microstructure

The development of microstructure in PVD coatings is an exceptionally complex process which is influenced by a variety of factors. The coating grows in thickness from discrete nuclei, and by grain boundary migration and recrystallisation which may occur concurrently [105]. Thus, the growth process is dependent on the incident coating flux, the coating atom adsorption probabilities, the density of surface sites, the adatom surface mobility, and the relevant grain boundary energies. These parameters depend in turn on the coating atom energy and angle of incidence, the exposed crystallographic surfaces, the presence of foreign atoms, and most important, the substrate temperature. In an attempt to simplify the complexities of the microstructural features, PVD coatings have traditionally been described in terms of structure zone models. These models attempt to correlate the observed microstructural features with various deposition parameters, such as substrate temperature, chamber pressure, deposition rate, particle energy, and film thickness. Although these models were initially developed for evaporated coatings, they have been extended to sputtered coatings, and can be applied to virtually all PVD processes.

Movchan and Demchishin [106] were the first to introduce the concept of a schematic structure zone model, which was used to summarise the apparent dependence of the microstructure of thick (< 2mm) evaporated coatings on the homologous substrate temperature, T/T_m (T = substrate temperature, T_m = melting point of the coating material, both measured in degrees Kelvin). They identified three characteristic structural *zones*, separated by T/T_m boundaries of 0.3 (slightly lower for oxide coatings), and 0.45-0.5. The schematic diagram they developed to summarise the structures is shown in Fig.2.8. Zone 1 was characterised by tapered grains and a domed surface structure. The widths of these tapered crystallites increased with increasing substrate temperature. Beyond T/T_m of about 0.3, the coarse tapered grains abruptly gave way to relatively narrow columnar crystallites in Zone 2. The distinctive feature of this structure was the presence of well defined grain boundaries, which were absent from Zone 1, and a smooth and matt surface appearance. This dense columnar structure coarsened with increasing temperature, up to the second transition temperature. In Zone 3, the surface was "bright" and the structure gradually changed to equiaxed grains with a characteristic polyhedral surface structure.

Thornton [105] adapted the Movchan and Demchishin zone model for the description of magnetron sputtered coatings by introducing the important process variable of Ar pressure. The dependence of microstructural features on T/T_m and inert gas

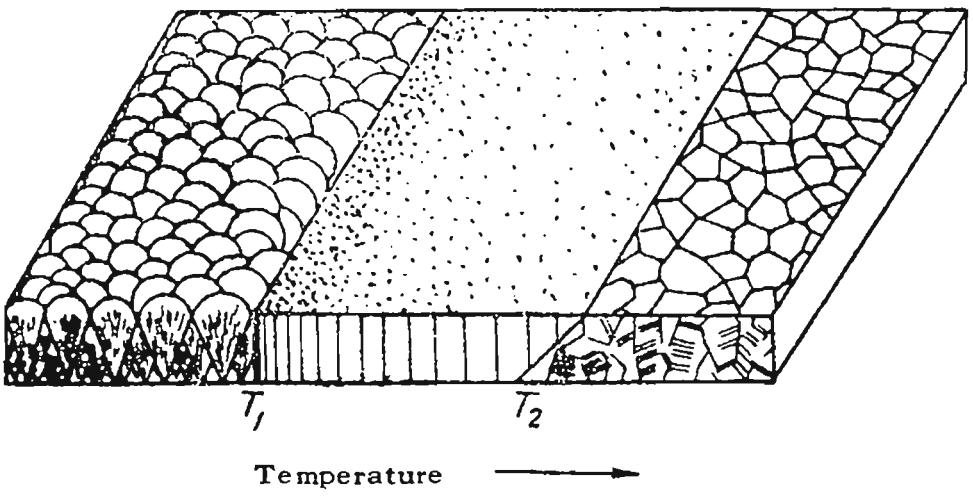

Fig.2.8 Structure zone model for evaporated coatings [106]

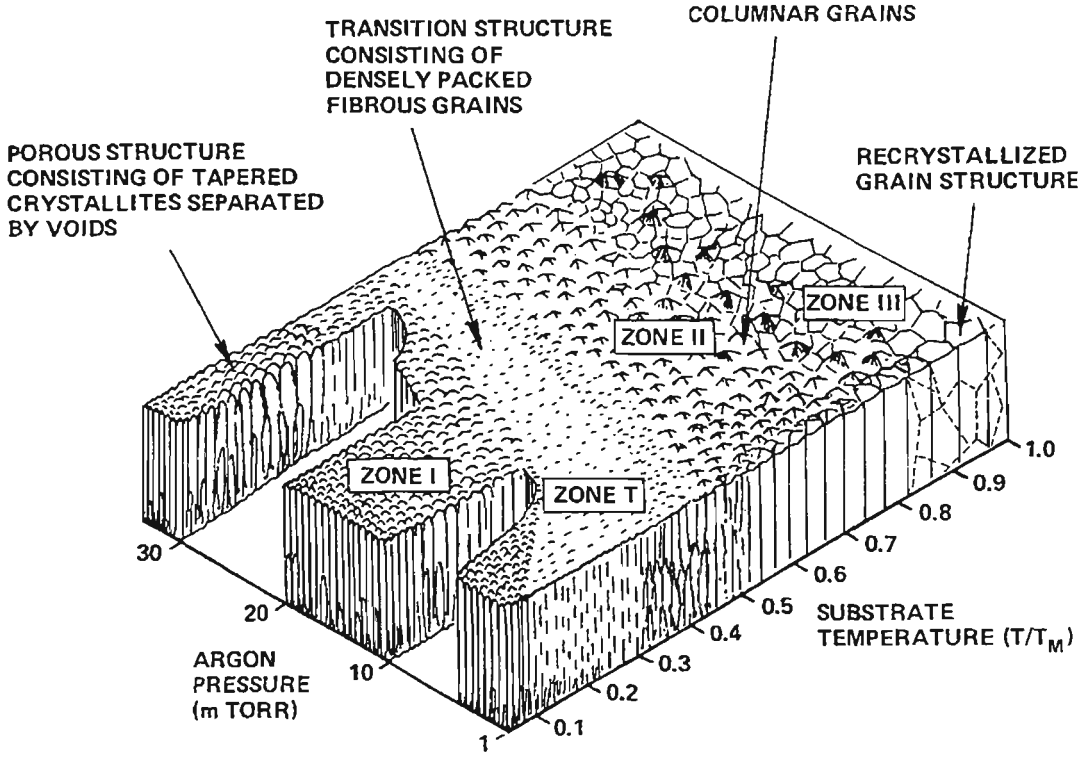

Fig.2.9 Structure zone model for magnetron sputtered coatings [107]

pressure was summarised by a modified structure zone model, as shown in Fig.2.9 [107]. The microstructures were generally consistent with the model for evaporated coatings, with three notable differences: 1) a broad transition zone (Zone T) was noted between the Zone 1 and Zone 2 regions, consisting of "densely packed fibrous grains" which were essentially very fine Zone 1 grains [108]; 2) Zone 2 columnar grains tended to be faceted at elevated temperatures, although facets were often replaced by smooth flat surfaces at higher temperatures; and 3) Zone 3 equiaxed grains were generally not observed at the deposition conditions investigated. The transitions due to temperature increases are thought to be the result of the onset of surface and bulk diffusion. Inert gas pressure is not the fundamental parameter, but rather the pressure affects the microstructure through several indirect mechanisms [108]. At high pressures, the sputtered atoms experience gas scattering which enhances the oblique component of the deposition flux resulting in a more open Zone 1 structure. As the pressure is reduced, the sputtered atoms and energetic neutrals experience much less gas scattering, such that the deposition process becomes more energetic. This can contribute to densification of the coating and the development of a Zone T structure.

Several revisions of the Thornton structure zone model have attempted to provide a more universally applicable model based on the level of energetic bombardment rather than gas pressure [109,110]. In each case the pressure axis was effectively replaced by a term which represented the process energy. Since ion bombardment has the greatest influence on the coatings deposited under conditions of low adatom mobility, the majority of these studies have only been concerned with low T/T_m. Messier *et al* [109] showed that the scale of structure in Zone 1/T sputtered coatings can exist over a vast range of grain sizes. They identified nano-columns which were clumped together to produce micro-columns, and in turn these were grouped to produce macro-columns. This explained the association between the Zone 1 and T structures as they merely represent different fractal-like levels of the same form of evolutionary growth that is experienced with conditions of low adatom mobility [111]. Thus, the structure zone model was extended to include a film thickness axis to indicate the evolutionary nature of coating microstructure as the dominant features moved through different size scales.

It is important to recognise that the structure zone models were primarily intended to provide a simple method of qualitatively characterising observed coating microstructures [108]. Quantitative application to different types of systems is inadvisable because the various diagram boundaries depend on parameters such as the coating and working gas species, the size and shape of the target, the position and orientation of the substrates relative to the target, and the ratio of ion to atom fluxes.

Furthermore, the models generally apply to elemental or single compound coatings, and it appears that no such generalised models for alloy coatings have been attempted.

Texture or preferred orientation is commonly observed in sputtered coatings. The film texture is usually axial if the direction of coating flux is normal to the substrate. Hence, the vast majority of crystallites in such films have their preferred crystallographic plane oriented parallel to the substrate surface, but are randomly oriented around the direction normal to this plane. This type of preferred orientation is often described as "fibre texture". If the coating flux is not normal to the substrate, the axis of the texture usually shifts towards the direction of flow. Similarly, energetic particle bombardment of the coating as it deposits can cause the fibre texture to align in the direction of the energetic flux [59,112-115]. The fibre texture formed is often observed to be the one that has the lowest surface energy. This is not always the case, however, as the texture can be influenced by the introduction of impurities or by ion bombardment. For example, it has been demonstrated that TiN coatings can be deposited with either <100> or <111> fibre textures depending on the particular process variables [112,116]. Recently, numerical models based on the minimisation of surface energy have been proposed [117,118], and it was demonstrated that changes in preferred orientation could be induced during coating growth, provided there was sufficient adatom mobility.

Final mention should be made of recrystallization that can occur subsequent to deposition. This is a factor generally ignored in most studies of sputter deposited coatings. As it is a nucleation and growth process, recrystallization requires thermal activation and tends to occur much more rapidly as temperature is increased. The temperature required for complete recrystallization within one hour is commonly known as the *recrystallization temperature*, and is typically about $0.4T_m$. Low melting point metals such as Sn, Cd, Pb and Zn, have recrystallization temperatures below room temperature [119]. Hence, it can be surmised that these metals are likely to recrystallize concurrently with deposition at ambient temperature. Coatings of metals which have recrystallization temperatures of about 100°C may be expected to undergo changes in the coating microstructure as a function of time after deposition. Indeed, room temperature recrystallization has been observed to occur for sputtered Cu coatings, after a post-deposition period ranging from a few hours to a week [120-122]. The kinetics of recrystallization may be enhanced by the high vacancy defect concentration that is characteristic of PVD coatings.

2.4.2 Residual Stress

PVD coatings usually develop residual stresses as a consequence of the deposition process conditions. Control of these stresses is important because excessive residual stress can result in delamination or cracking, or can influence the performance characteristics. The total residual stress state of a coating is determined by the sum of the intrinsic and extrinsic stresses. The latter form of stress is merely the result of thermal mismatch between the expansion coefficients of the coating and substrate materials. Extrinsic stresses can be controlled by appropriate selection of substrate-coating combinations, or by depositing the coatings at the anticipated operating temperature. The intrinsic stress is the cumulative result of chemical and microstructural defects incorporated into the coating during the deposition process. Of these two types of stresses, only intrinsic stresses can be independently controlled by adjustment of process variables, and in many cases they are much greater than the extrinsic stresses. The following section provides a brief introduction to the origins of residual intrinsic stress in PVD coatings, based on thorough reviews published elsewhere [123-127].

Coatings deposited at low pressures by either triode or magnetron sputtering are usually found to exist in a state of compressive stress, whereas the vast majority of diode sputtered and evaporated coatings are subject to tensile stress. The cause of this effect was investigated in a thorough series of experiments by Thornton and Hoffman, which were recently summarised in a historical review paper [127]. They found that the coating stress was closely related to the sputtering pressure such that as the pressure was reduced over a fairly narrow range, there was an abrupt transition from tensile stress to compressive stress (Fig.2.10a [128]). The "critical pressure" required for the stress transition was found to have a semi-logarithmic dependence on the atomic mass of the target (Fig.2.10b [127]), or more importantly the mass ratio of the target and gas species. Furthermore, the general appearance of the coatings closely matched the stress transition; those with tensile stresses had a dark non-reflective appearance, while those with compressive stress were bright and lustrous. The stress transition was attributed to the effects of energetic neutrals (backscattered ions) that simultaneously bombard coatings deposited at low pressure. The kinetic energy of sputtered atoms was largely overlooked but subsequently recognised as another possible source of bombardment that could induce compressive stress.

Energetic bombardment by ions can also influence the residual stress of PVD coatings. It has been demonstrated that bombarding an evaporated coating during deposition with an ion beam leads to the same sharp transition from tensile to compressive stress as described above [127]. This type of process, were an ion beam is combined

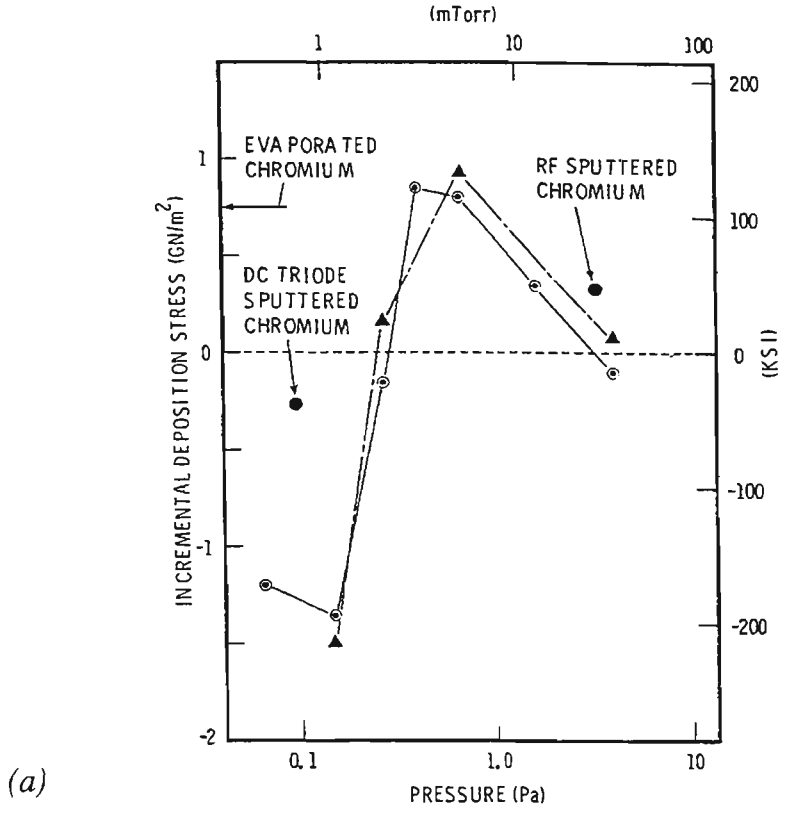

(a)

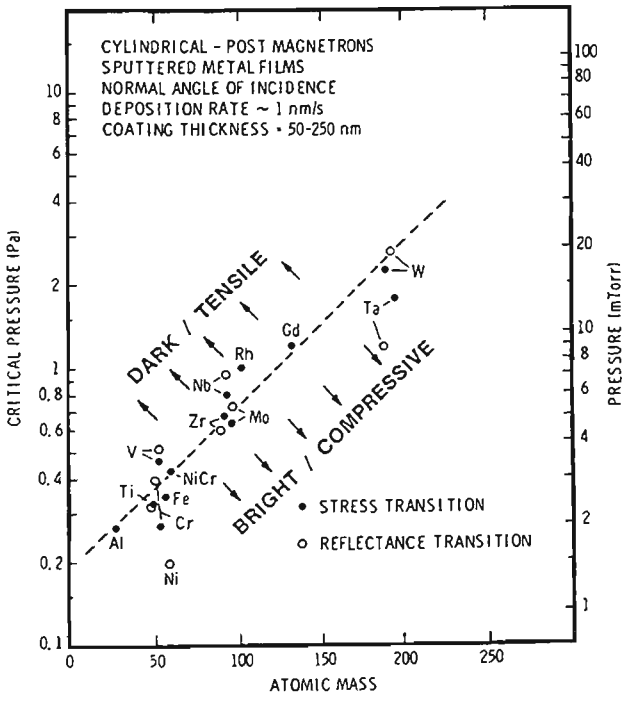

(b)

Fig.2.10 Residual stress in magnetron sputtered coatings: (a) stress as a function of inert gas pressure for Cr coatings [128] ; and (b) critical transition pressure as a function of the coating atomic mass [127]

with thermal evaporation, is known as ion beam assisted deposition (IBAD) [49]. Unbalanced magnetron sputtering has also been widely used for ion assisted deposition, and several studies have examined the influence of ion energy (ie. substrate bias voltage) on the coating stresses [65,123,129,130]. It is therefore apparent that intrinsic stress in coatings is common to all types of PVD processes. The inherent variable that controls the level of stress is energetic particle bombardment, whether it be in the form of sputtered atoms, energetic neutrals, or accelerated ions from a plasma or ion beam.

It is widely accepted that the intrinsic stress is directly related to coating microstructure. Tensile stresses usually correspond to coatings with a loosely-packed, porous structure (Zone 1), whereas compressive stresses are found in densely packed, lustrous coatings (Zone T). Thus, it has been a common practice to use the residual stress as a "litmus test" of the coating microstructure [127]. This begs the question of what are the microstructural effects that cause such stresses. Various models have been proposed which attempt to explain tensile and compressive stresses in PVD coatings [126]. Tensile stress in polycrystalline films is usually explained by the grain boundary relaxation model. The stress derives from the interatomic attractive forces acting across the gaps between contiguous grains in loosely packed Zone 1 structures. Adhesion of the coating to the substrate restrains the grains, such that the intragrain tensile forces are balanced by relaxation at the grain boundaries. Molecular dynamics modeling of the deposition of two-dimensional coatings has confirmed the relationship between porous structures and tensile stress [115].

Compressive stress in PVD coatings can be attributed to either the impurity or atomic peening mechanisms [126]. Impurities in PVD coatings can be either reactive or inert. The presence of oxygen as an impurity can cause oxidation at grain boundaries in the coating, which modifies the surface energy of neighbouring grains such that the grain boundary relaxation distance is reduced. Similar observations for hydrogen and water contamination have also been reported, although the exact mechanism has not been identified. Such reactive impurities are usually not encountered with present day coatings due to improvements in the quality of vacuum systems. Inert gas entrapment in sputtered coatings (Sect.2.4.3) has often been correlated with the level of compressive stress. Most researchers tend to dismiss such correlations as coincidental, preferring to attribute the compressive stress to lattice damage induced by particle bombardment. This latter mechanism is described as "atomic peening" [124] and represents the most widely accepted model for compressive stress in PVD coatings. The physical process that links the lattice damage to generation of compressive stress is poorly defined, but assumes that the disruption caused by bombardment contributes a volumetric distortion, which in turn generates a stress if the distortion is restrained. Quantitative modeling predicts that the

level of compressive stress should have a square-root dependence on particle energy, and this was confirmed by experimental measurements [126]. In spite of such strong support for the atomic peening mechanism, some researchers continue to attribute compressive stresses to inert gas burial [131,132].

Although the atomic peening mechanism adequately accounts for the influence of energetic bombardment on the coating microstructure, it does not explain how the volumetric distortion results in generation of an intrinsic stress. It seems feasible that such stresses may be generated in response to interatomic forces acting between adjacent grains, as is thought to be the case for intrinsic tensile stresses. The interatomic force is schematically illustrated as a function of the separation distance in Fig.2.11 [133]. There are striking similarities between this curve and Fig.2.10a. As the interatomic separation decreases, the interatomic force increases to a maximum attractive force, before dropping sharply towards a repulsive force for very close separation. A model based on the porosity between adjacent grains would therefore seem to apply. It is speculated that the repulsive force region may explain the generation of compressive stresses in coatings deposited at low pressures, where atomic peening results in the exceptionally tight packing of grain boundaries. Such a model would help to explain the relationship between Zone 1 and Zone T microstructures which are considered to be different levels of the same form of growth, but share opposite signs of stress.

In cases of particle bombardment with very high flux, mass and/or energy, it is frequently reported that the compressive stress in coatings begins to reduce [126]. This effect is shown schematically in Fig.2.12, in terms of the bombardment energy [129], which equates to the inverse of gas pressure. The reduction in compressive stress that occurs with heavy bombardment has been attributed to yielding and plastic flow of the highly stressed material in the coating [123,129]. As the compressive stress approaches a maximum, plastic flow initiates in grains oriented such that the resolved stresses exceed the shear stress. Such preferential flow can lead to changes in the preferred orientation. The reduction in compressive stress at still higher bombardment was thought to be due to the annealing effect of thermal spikes produced by bombardment, or possibly by plastic flow in the damaged layer below the surface.

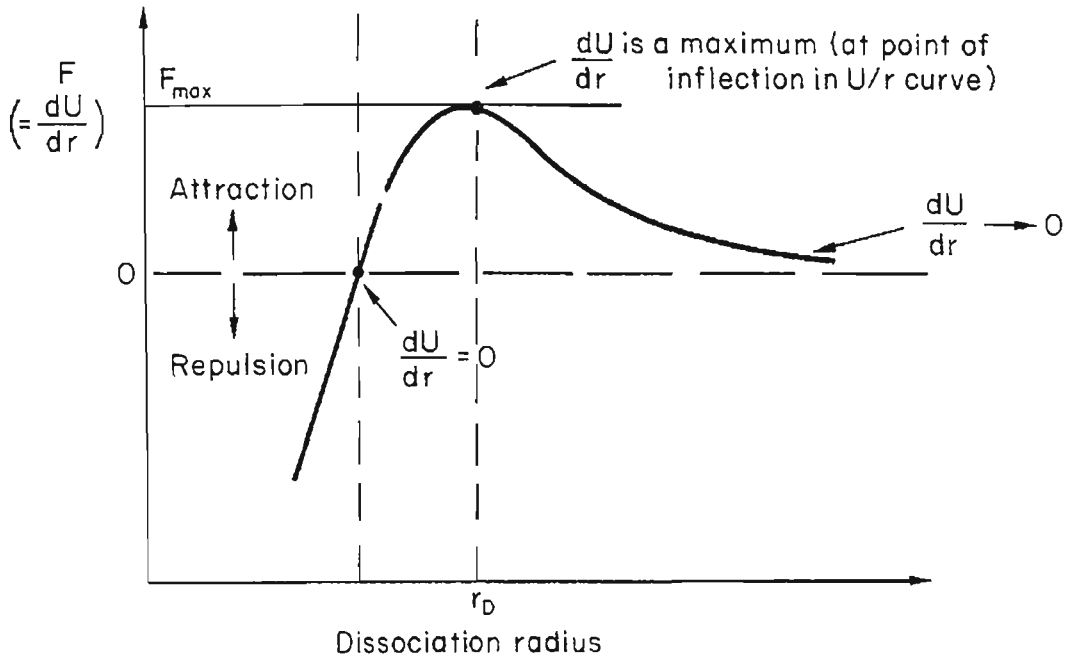

Fig.2.11 Relationship between interatomic force, F, and separation distance, r. Note that U represents the potential energy of the interatomic bonds. [133]

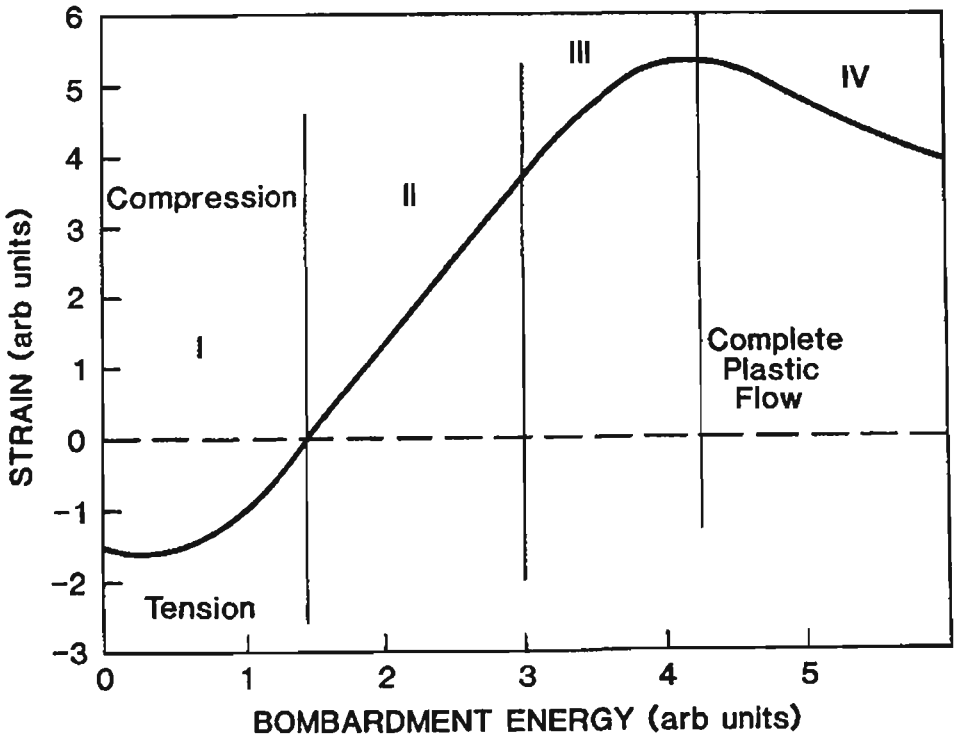

Fig.2.12 Schematic representation of the residual stress in PVD coatings expressed as a function of the energy of bombarding particles [129]

2.4.3 Inert Gas Burial

The burial of inert gas in sputtered coatings has long been recognised as a potential source of contamination [83]. Generally the proportion of inert gas trapped in sputtered coatings is less than about 2 at.% [127], but there are reports of values as high as 5 to 14 at.% [58,97,132,134-137]. The buried inert gas usually remains in the coating for long periods of time when kept at room temperature [58], although elevated temperatures can cause desorption [138].

There are three ways in which inert gas can become trapped in a sputtered coating [77,139]: (a) adsorption of gas atoms, (b) energetic neutral bombardment, and (c) ion bombardment. Inert gases are not readily adsorbed on metallic surfaces, and the first mechanism accounts for only trace amounts of entrapped gas. Energetic neutral bombardment is particular to sputtering and is very noticeable in cases where the ratio of target to gas atomic mass is high. For example, W coatings sputter deposited with Ar contain much greater proportions of inert gas than when Xe is used [57]. This is a direct result of greater kinetic energy of the Ar neutrals causing them to be implanted into the growing coatings. Special sputtering systems have been devised that enable the use of heavy inert gases such as Xe, which provide substantially less energetic neutral bombardment of the coatings [57]. Inert gas is also more likely to be buried in coatings as pressure is reduced because there is less gas scattering of energetic neutrals, plus the neutrals are more energetic due to the coincident increase in discharge voltage [57].

Coatings deposited with ion assistance are usually much more prone to the retention of inert gas. This is because the flux of energetic ions is additional to the inherent flux of energetic neutrals and often dominates. The most studied ion assistance variable is the ion energy, although it is also important to consider the flux of ions relative to the atomic flux (*i/a* ratio). It has been found that at low energy (~50 eV), ion bombardment can actually aid in removing adsorbed inert gas from the coating surface [139]. However, as the ion energy is increased to about 100 eV, inert gas starts to become embedded in the coating. Within this region, it is expected that the inert gas content will increase with the square of ion energy [140], and this has been experimentally confirmed [81,139,140]. Others have found a linear dependence on ion energy [132]. Most researchers have not studied highly energetic ions, but one study of the deposition of W coatings with Ne bombardment revealed a peak in the inert gas burial at about 600 eV, followed by a reduction [58]. Very similar results were obtained for unbalanced magnetron sputtered Zn coatings using Ar as a sputter gas, where a maximum inert gas content of 8 at.% was encountered at about -400V [136,137] (refer Sect.3.1.2).

An increase in the *i/a* flux ratio is expected to cause a linear increase in the proportion of buried inert gas in coatings deposited with ion assistance. This has been confirmed for coatings of Mo and Cr deposited by unbalanced magnetron sputtering with Ar and Xe, respectively [140]. However, the same study found that the inert gas content of Cr coatings sputtered with Ar, decreased as the *i/a* ratio was raised. It was argued that enhanced diffusion due to the high concentration of bombardment-induced vacancies, leads to the escape of inert gas from the coating before it could be buried by the depositing atoms. This same explanation was also used to explain similar results in an earlier study of Ar sputtered Al-5 at.%Cu coatings [134]. Furthermore, it was predicted that there should be a condition where nearly all of the implanted inert gas becomes entrapped. A continued increase in the ion flux will then lower the fraction of inert gas trapped in the coating. This model can be extended to suggest that for both ion energy and *i/a* ratio, the inert gas content should reach a peak at some particular value, and decrease as bombardment becomes more energetic, as a result of diffusional losses.

The role of buried inert gases in terms of their effect on microstructure and properties has been examined to varying degrees. It appears that the concentration of buried inert gas is important in determining the distribution it adopts in the coatings. Those coatings with only minor amounts of entrapped gas tend to retain it in metastable solid solution, probably at substitutional sites. This was found to be the case for Au coatings sputter deposited with Ar gas [57]. Inert gases have very low solubility in all metals and therefore prefer to segregate into bubbles [46]. This is sometimes observed if the buried inert gas concentration is sufficiently high. Some excellent TEM work revealed the presence of bubbles of solid Kr and Xe in Al coatings prepared by ion beam assisted deposition using Kr^+ and Xe^+ ions [113]. Inert gases can apparently also disrupt the coating structure. The entrapment of very large amounts of Ar in Zn coatings was found to be closely correlated with various microstructural effects, leading to the suggestion that the inert gas caused suppression of grain growth [136,137]. Finally, it was found that large proportions of buried Kr gas contributed to amorphization of Ni-La alloy coatings [97].

Since inert gases interfere in various possible ways with the coating microstructure, it is likely that they influence the performance characteristics. One such example is for sputtered W coatings, for which the electrical resistivity was found to increase markedly with the inert gas content [58]. As previously discussed in Sect.2.4.2, inert gases have often been identified as the cause of residual intrinsic stress in sputtered coatings. However, it is more commonly accepted that inert gas burial and intrinsic stress are both the result of energetic bombardment.

2.4.4 Stoichiometry of Alloy Coatings

It was demonstrated in Sect.2.3 that it is relatively easy to obtain a sputtered alloy flux that reflects the bulk composition of the target. Replicating the sputtered flux composition in the deposited coating is not guaranteed and depends on several other factors [83,141]. Firstly, the various constituents of the sputtered flux can have different affinity for the substrate surface. This is referred to as the "sticking coefficient", and in cases where constituents differ in this respect, the coating will not replicate the sputtered flux composition. Secondly, heating of the substrates during deposition can lead to preferential sublimation of volatile species. This is a particular problem for high vapour pressure materials. Thirdly, and probably of greatest significance, any energetic particle bombardment of an alloy coating as it deposits is likely to result in preferential resputtering of one or more constituents. This effect occurs due to differences in partial sputter yield of the elements in the alloy coating. Combination of thermal and resputtering effects can also contribute to unexpected alteration of the coating composition.

The sticking coefficient can be defined as the fraction of a constituent that is absorbed on a surface, relative to the total arrival amount. For metal vapours impinging on a clean metal surface, the sticking coefficient is usually one, whereas most molecular gases have sticking coefficients less than unity [141]. Consequently, for most metallic alloys, differences in sticking coefficient are not an issue. This is not necessarily true if the substrate temperature is relatively high, and therefore substrate cooling is often considered useful. Reactive deposition using gases such as nitrogen and oxygen generally requires much more gas in the system than would be required if the sticking coefficient was unity.

Elevated substrate temperatures can have a profound effect on alloy coating composition. Sources of substrate heating are not necessarily intentional, as bombardment with primary and secondary electrons, energetic neutrals, sputtered atoms, and accelerated ions can all contribute to substrate heating. It has been estimated that between 75 and 90% of the energy of these species will be transferred as heat if they are permitted to strike the substrate [83]. If the substrate temperature is excessively high, it is possible for the more volatile constituents of an alloy coating to be preferentially sublimed. This effect has been found to apply to Cu-Sn alloy coatings which were deficient of Sn when deposited on substrates above room temperature [75].

Most studies of alloy coatings have been concerned with more refractory metals which are not likely to be affected by differences in sticking coefficient or loss of volatile constituents at elevated temperatures. For these alloys, the main issue with obtaining

stoichiometric coatings is preferential resputtering. Bombardment of alloy coatings during deposition causes resputtering of a fraction of the arriving atoms, but the fraction resputtered may differ greatly for different species [142]. In many cases, the preferentially resputtered constituent is that with the highest elemental sputter yield [74,77,81,143]. However, predictions of preferential resputtering in multicomponent coatings on the basis of pure elemental sputtering yields, are often completely erroneous. In some cases, the element with the higher elemental sputtering yield is found to have the lower yield in an alloy or compound material [144]. Two such examples are the preferential resputtering of Al from Al-Cu alloys [134], and La from Ni-La alloys [97].

The partial sputter yields for constituents of an alloy differ from their elemental yields for several reasons. The thermodynamics of alloys can mean that segregation and second-phase formation may be favourable, and under appropriate kinetic conditions, alloys can form a multitude of different microstructural variants [134]. These effects make it very difficult to predict how the constituents in the alloy will be sputtered, since the surface binding energy will be related to the strength of the bonds between atoms. More significantly, the partial sputter yields can differ significantly from the elemental yields purely as a result of the close proximity of different elements in an alloy coating. This is known as the "sputter yield amplification" effect and has been thoroughly investigated by Berg *et al* [103,142,145-147]. The essence of this effect is that the collision cascades that occur with energetic particle bombardment tend to occur much deeper below the surface of a light element than for a heavy element. By alloying a heavy and light element, the cascades are concentrated at an intermediate depth, such that the light element experiences greater near-surface disruption than would be the case for a elemental target. Thus, the partial sputter yield of a light element will be increased relative to the elemental yield when alloyed with a heavier element, and vice versa.

The work by Berg *et al* was primarily based on the application of a Monte Carlo simulation of ion assisted deposition called T-DYN [148]. This program was developed from the TRIM code [56,149], which is still widely used to determine implantation depth and damage profiles, but is limited to a static composition of the target material. T-DYN incorporates ion beam mixing of the different atoms due to collision cascades and recoil implantation. Sputtering of the substrate and deposition of neutral atoms is also treated. The treatment area in the program consists of a 10 nm x 10 nm square which is divided into 0.2 nm wide channels. For each ion that penetrates the target, the program tracks the number of atoms sputtered and the changes in composition, so that the next ion encounters a slightly different target. In addition, T-DYN allows simultaneous codeposition of up to five different non-energetic species, making it possible to simulate ion bombardment during multicomponent coating deposition.

Berg *et al* [147] have examined some peculiar aspects of ion assisted deposition of alloy coatings, by simulating deposition of an atomic flux of Al-20 at.%W simultaneously bombarded with 500 eV Ar^+ ions. They showed that the coating developed a steady state composition of about 30 at.%Al, indicating that there was substantial preferential resputtering of Al due to sputter yield amplification (Fig.2.13a). The composition approached that of the atomic flux only near the extreme surface of the coating. The steady state composition is determined by the deposition rate and/or ion energy, such that a wide range of concentrations can be achieved using the same atomic flux [83,141]. However, care should be taken when coating substrates that have high surface topography, since the composition is also dependent on the incident ion angle [134,142]. The substrate material was also demonstrated to have a profound effect on the coating composition at the coating-substrate interface [147]. Coatings deposited on a heavy Pt substrate quickly developed the steady state alloy composition (Fig.2.13a). However, when a Si substrate was used the sputter yield amplification effect resulted in the development of an interface region enriched with Al (Fig.2.13b). This substrate effect is mainly controlled by the atomic mass of the substrate material relative to the coating material.

The combination of elevated substrate temperatures and preferential resputtering is especially problematic and often unpredictable. Increasing the substrate temperature results in greater mass transfer in the coating via diffusion, such that the coating surface can become enriched with one of the alloy constituents. The extent of preferential resputtering can be substantially increased relative to that predicted from sputter yield amplification effects alone. Such combination of surface segregation and preferential resputtering was used to explain the preferential loss of Si from $TiSi_2$ [142,150], Al from Al-Cu [134,142], and Fe from Ni-Fe [77]. Unfortunately, simulations of ion assisted deposition are not yet mature enough to incorporate the effects of substrate temperature. Therefore, the effects of ion assisted deposition on the stoichiometry of alloy coatings are still best examined by physical experiments.

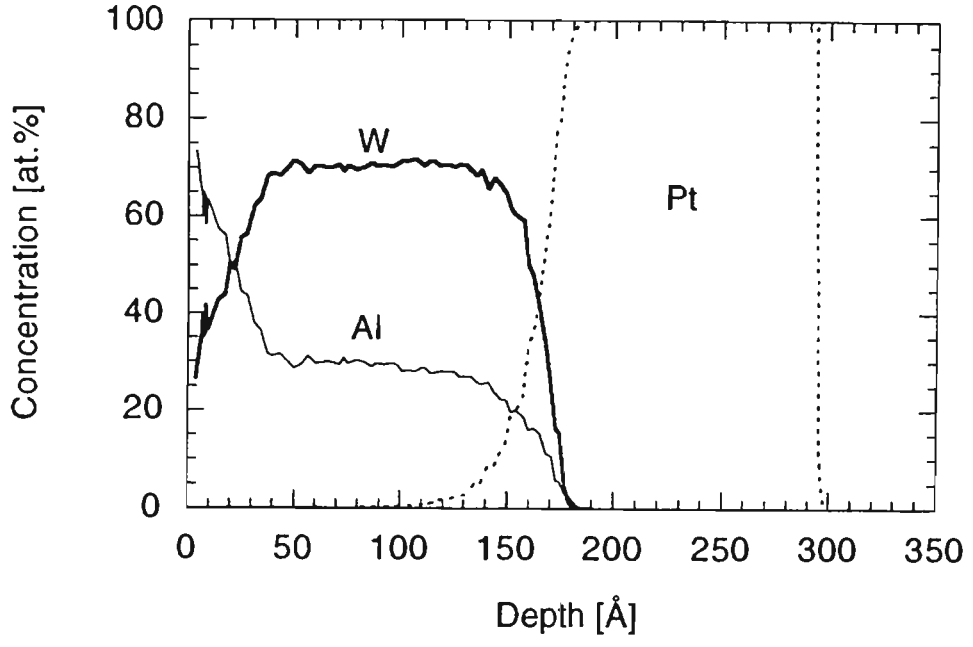

(a)

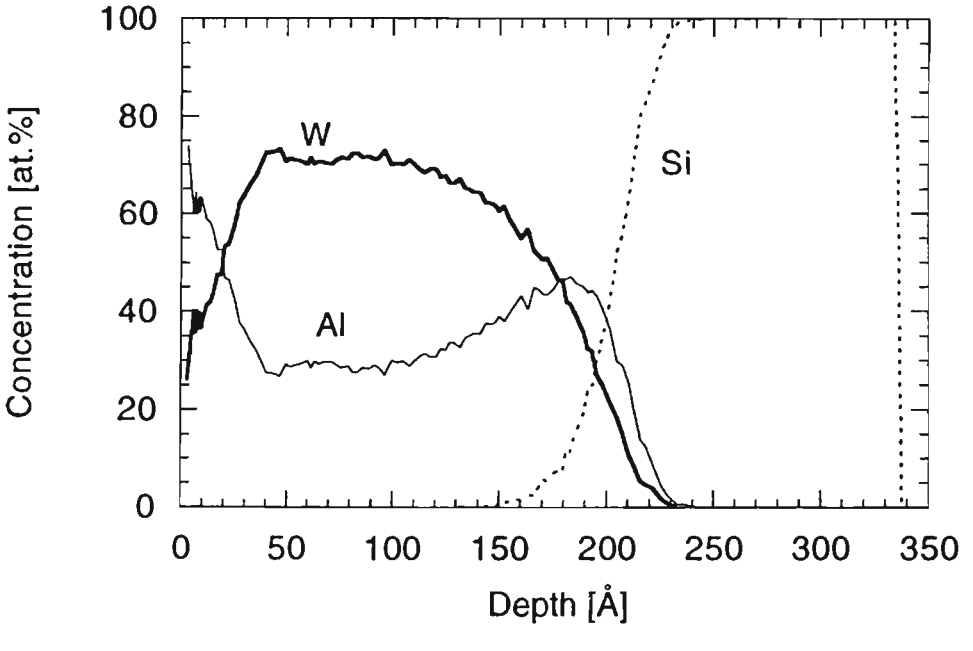

(b)

Fig.2.13 Chemical composition profile of a hypothetical Al-W coating deposited with ion assistance (500eV Ar), obtained by simulation with T-DYN software: (a) Pt substrate; (b) Si substrate. [147]

Chapter 3

Literature Review of PVD Coatings from the Al-Mg-Zn System

A vast number of publications have appeared in the literature, particularly over the last decade, that consider the corrosion protective nature of PVD coatings. In particular, Hashimoto *et al* from Tohoku University in Japan have conducted a thorough electrochemical evaluation of aluminium-based coatings alloyed with various transition metals, such as Ti, Cr, Zr, Nb, Mo, Ta and W [151]. Most of these studies are concerned with the inherent corrosion resistance of the coatings as isolated films. Of greater concern for the corrosion protection of sheet steel is the ability of the coating to sacrificially protect the substrate (Sect.1.1). Cathodic protection of steel has been considered for Al-Ti and Al-Cr binary alloy coatings [82,99,152]. Such alloy coatings were found to possess a corrosion potential sufficiently active to be able to afford good sacrificial protection for galvanically exposed sheet steel [152]. However, Ti and Cr are relatively expensive metals which would be prohibitive to the commercial application of such binary coatings.

The present investigation concentrated on magnetron sputtered coatings of elemental, binary and ternary compositions from the Al-Mg-Zn system. These compositions were evaluated since they represented an extension of established commercial hot-dipped coatings which are based on this system (Sect.1.2). Furthermore, these three elements are commercially available in abundant supply and their market price is not prohibitive to widespread use for sheet steel coatings. In this Chapter, the literature on vapour deposited elemental and alloy coatings from the Al-Mg-Zn system is reviewed in detail. The equilibrium phase diagrams and various intermetallic phases are introduced. Work on rapid solidification of such compositions is discussed in relation to the formation of metastable crystalline and amorphous phases, and their subsequent decomposition. Finally, a brief review of the work on multilayer PVD coatings is presented. Although of little direct relevance to the present study, this last section demonstrates the potential of vapour deposition for the production of novel coating architectures.

3.1 Zinc Coatings

The application of Zn coatings on sheet steels by vapour deposition is by no means a new concept. Indeed, as early as 1970 two American steel companies were well advanced in the development of the process, and plans were in hand to construct a commercial continuous Zn PVD line [13]. Much of this work was discussed in Sect.1.3. The following introductory comments concern the relationships established during these early studies, between PVD process conditions and the characteristics of Zn coatings produced.

The early work on vapour deposited Zn coatings was reviewed in a confidential report by Finlayson of JLA [13]. The processing steps required for Zn vapour deposition were discussed, including schematic diagrams of what a full-scale commercial facility would be envisaged to look like. It was emphasised that there was a need for absolute strip cleanliness and preheating of the steel strip to achieve good adhesion. It was also necessary to keep the strip temperature below about 230°C to prevent excessive re-evaporation of Zn. Descriptions were given for several samples of vapour deposited Zn coated steel obtained from a steel company with a pilot line facility. These materials were either single- or double-sided, and had a range of coating masses. The coatings were observed to have a very uniform non-spangled appearance similar to that of electrodeposited or galvannealed coatings, and before post-treatment were similarly quite susceptible to finger-marking. The structure of the coating was noted to be variable and dependent on the deposition rate and the preheat temperature. They were "dendritic or columnar" at low preheat temperatures (10-100°C), and developed a "more equiaxed" structure at higher temperatures (170-175°C). The dendritic coatings were also observed to have a high degree of porosity. Irrespective of the microstructure of the coating, the PVD Zn surface was found to be an excellent substrate for paint, and this feature was recognised as an outstanding attraction for the product.

The report by Finlayson was conducted in order to determine the most suitable approach for his own development work to be undertaken using a large experimental vacuum deposition system (chamber dimensions 1.5m x 1.2m x 0.9m) [153]. Unfortunately, difficulties were experienced with obtaining consistently adherent Zn coatings [21]. Various cleaning procedures and modifications to evaporator baffle designs were attempted but none proved successful. Reasonable adhesion was achieved by depositing a thin Cu flash coating onto the steel substrate before depositing the Zn. The Cu flash adhered well to the steel and the Zn alloyed with the flash during the deposition process. The corrosion performance of PVD Zn coatings on steel sheet was

reported to be slightly better than that of hot-dipped galvanised coatings of similar coating mass. However, this improvement was only due to the more uniform coating distribution and not because of any inherent difference in corrosion resistance. It was claimed that the presence of the Cu flash did not adversely influence the corrosion performance, despite the anticipated galvanic effects. Helwig and Murray [19] subsequently found that adherent Zn coatings could be produced by application of a thin iron flash coating, provided that the substrates were heated to at least 175°C. Coatings of up to 18 μm thickness could be produced in this fashion without loss of adhesion. Thicker coatings required a post-deposition annealing treatment at 400°C or greater, and immediate quenching such that the total thermal cycle was completed within 25 seconds.

Following this early work, the development of Zn PVD coatings for continuous coating of sheet steels was shelved by American and Australian industries. The emphasis shifted towards evaluation of hot-dipped Al-Zn alloy coatings, which had been recently developed by Bethlehem in the USA (refer Sect.1.2.3). However, academic research into vapour deposited Zn coatings has continued to the present day. Much of this work has been on a laboratory scale, although in recent times there has been a shift back towards examining continuously coated steel strip. Most studies have been concerned with evaporation of Zn by either resistance or electron-beam heating [154-159]. Several studies have concentrated on examining the modification of the porous structure by incorporating some form of ion assistance. In terms of the present investigation, the most important work dealt with the deposition of Zn coatings by magnetron sputtering [136,137,160]. Other ion assisted deposition processes such as ion plating [110,161], ion beam assisted deposition [162], ionised cluster beam deposition [163,164], and anodic arc deposition [165] have been evaluated. Finally, there has also been a limited amount of work on Zn coatings deposited by chemical vapour deposition [166,167], thermal spraying [168], and pulsed air arc deposition [169], although these are of little concern to the present investigation.

3.1.1 Evaporation

The structure of a Zn coating evaporated onto a copper substrate cooled with liquid nitrogen (-196°C) was examined by Robertson and Unvala [154]. Evaporation of the Zn was conducted at a pressure of 1.3 μPa (10^{-8} torr), and the coating was transferred into a TEM without exposure to atmosphere immediately after deposition. Reflection electron diffraction patterns of the coating at liquid nitrogen temperature indicated that it was non-crystalline. In situ warming of the coating revealed that the Zn crystallised at a temperature of -105°C. This transformation temperature was confirmed by measurements of the electrical resistance of Zn coatings deposited onto glass substrates

with identical conditions. A sudden and irreversible change in resistance occurred at the same temperature as that at which the crystalline change was noted. This work suggests that all Zn coatings deposited onto substrates held at temperatures of about -100°C or greater will be crystalline.

Neirynck *et al* [155] studied the influence of substrate temperature on the microstructure of evaporated Zn coatings. The coatings were deposited onto polished steel substrates from a resistance heated iron-boat at a vacuum of 13 mPa (10^{-4} torr). The deposition rate was between 2.4 and 6.0 $\mu m.min^{-1}$, producing coatings of about 10 μm thickness. The substrates were held at three different temperatures during deposition: 50, 150 and 250°C. Substrate temperature was found to have a significant influence on the surface appearance, grain morphology and size, coating porosity, and preferred orientation. At 50°C, the Zn coating was blue-grey and dull in appearance, with small faceted grains (3-5 μm), inter- and intra-granular porosity, and a slight <0001> fibre texture. At 150°C, the coating surface was white and less dull, with larger plate-like grains (8-10 μm), inter-granular porosity, and a strong <0001> fibre texture. At 250°C, the coating was white and specular with well-defined 20-30 μm equiaxed grains, very little porosity, and a strong <0001> fibre texture. Surface micrographs taken with an SEM are shown in Fig.3.1. It was claimed that the microstructure of the 250°C sample indicated that the coating had condensed from the liquid phase. The deposition rate was also varied but no clear trends were determined. However, it was established that increasing the deposition rate caused an increase in the maximum temperature at which re-evaporation could be avoided. The influence of the deposition rate on the substrate temperature was not considered, although it has been clearly established that high deposition rates influence the substrate temperature due to the release of latent heat [13,21,153].

An intensive examination of the morphology of vapour deposited Zn coatings under various conditions was reported by Wang and Harris [156]. The variables studied were substrate temperature, base pressure and the presence of Ar gas in the chamber. Base pressures were 65 Pa and 500 Pa which correspond to medium and rough vacuum, respectively. As such, the pressures used in this work were very poor for vacuum deposition processes, and it seems highly likely that the growth of Zn deposits were influenced by a low mean free path and oxygen contamination. A vast range of Zn crystal morphologies were reported, some of which are reproduced in Fig.3.2. Unfortunately, the inter-relationships between the "controlled" variables made it extremely difficult to determine a clear assessment of any trends in results.

(a)

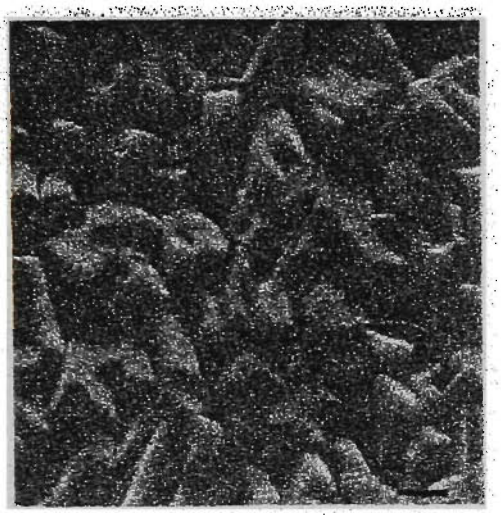

(b)

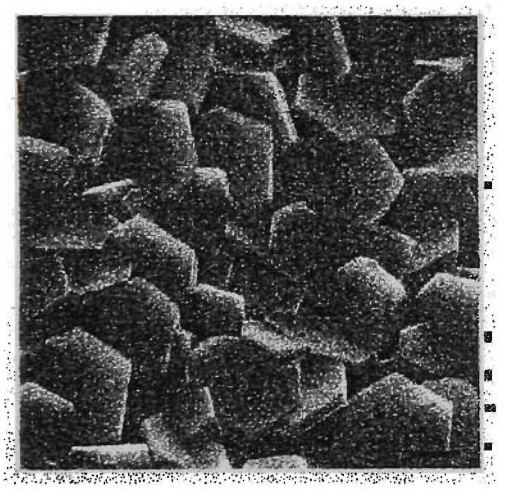

(c)

Fig.3.1 SEM surface micrographs of evaporated zinc coatings at various substrate temperatures; (a) 50°C (b) 150°C (c) 250°C. No scale was reported in the reference. [155]

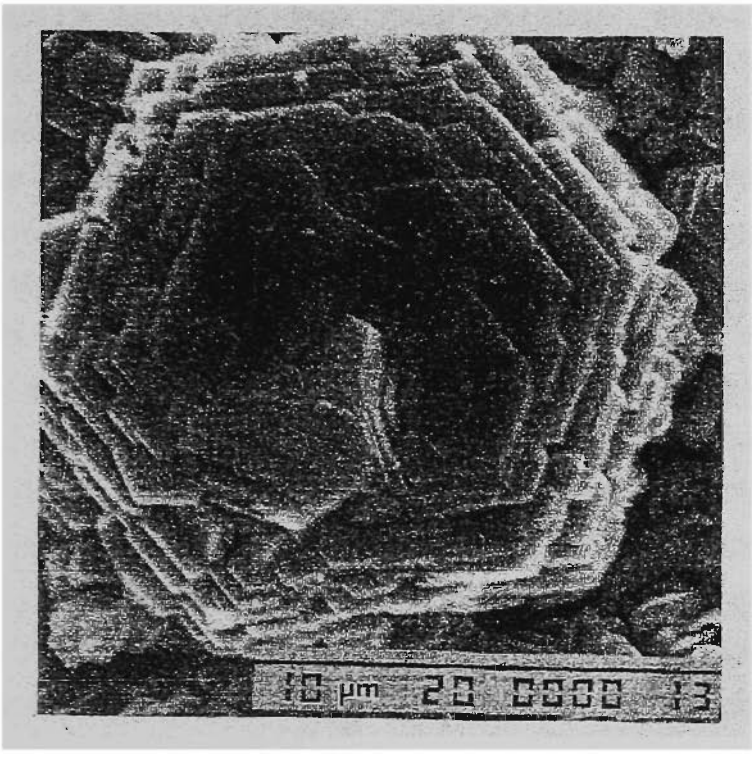

(a)

(b)

Fig.3.2 Some examples of SEM surface micrographs of evaporated Zn coatings obtained at a base pressure of 65 Pa. [156]

An interesting alternative application of Zn coatings is in capacitors for the electronic and electrical applications. Vapour deposited films of Zn are used because of their resistance to capacitance loss during operation. However, the Zn films are susceptible to atmospheric corrosion, resulting in the early failure of such devices. In an attempt to optimise the corrosion resistance of Zn coatings for capacitors, a range of Zn coatings were deposited using various evaporation bath temperatures (650 to 740°C) and substrate temperatures (-25° to -5°C) [159]. The Zn film thickness was about 70 nm, and it was found that the average Zn grain size was reduced by increasing the temperature of the bath, or by decreasing the substrate temperature. This latter result is consistent with the Movchan and Demchishin zone model for evaporated coatings [106], and confirms the general trend for Zn coatings previously reported by Neirynck *et al* [155]. The atmospheric corrosion resistance was highest for the films consisting of the smallest grain size. X-ray diffraction of the coatings indicated that the Zn films were heavily textured with a <0001> preferred orientation. Furthermore, the width of the diffraction peaks, as measured by FWHM, decreased proportionally with the grain size. This result was the opposite of that predicted by the Scherrer formula [170], and it was therefore concluded that the observed relationship between grain size and FWHM was due to the extent of preferred orientation, rather than a domain size effect. The influence of microstress on FWHM was discounted with the argument that coating stress was attributable to thermal expansion mismatch alone. However, this conclusion is unconvincing because thermal stresses result in changes in the residual macrostress and do not affect microstress [171].

Within the last few years, there has been revived interest in examining the feasibility of evaporated Zn coatings for sheet steels. Arezzo *et al* [157,158] used a commercial PVD batch facility to deposit Zn coatings onto relatively large steel sheet samples, with the primary objective of optimising adhesion, thereby replicating much of the work of 25 years earlier [13,19,21,153]. In their batch coating equipment, steel sheet measuring 300mm wide by 1800mm length was strapped to a drum sample holder and rotated above the evaporation source at a rate of 0.2-20 $m.min^{-1}$. Firstly, the substrates were heated to various temperatures at the start of deposition (115-185°C). The substrate temperature also increased during deposition due to the release of latent heat combined with the rapid deposition rate (10-50 $\mu m.s^{-1}$). The surface and cross-sections of these and other coatings are reproduced in Fig.3.3. Adhesion of these coatings was generally very poor. The second approach was to use mechanical brushing of the substrates prior to deposition. Adhesion was significantly improved due to the removal of surface oxide from the substrate, but also caused severe localised damage which was deemed unsatisfactory. The third approach was to use Ar ion etching prior to deposition in order to clean the substrate surface. This had a similar effect on adhesion as did mechanical brushing but did not damage the surface. Deposition at elevated temperatures (120°C)

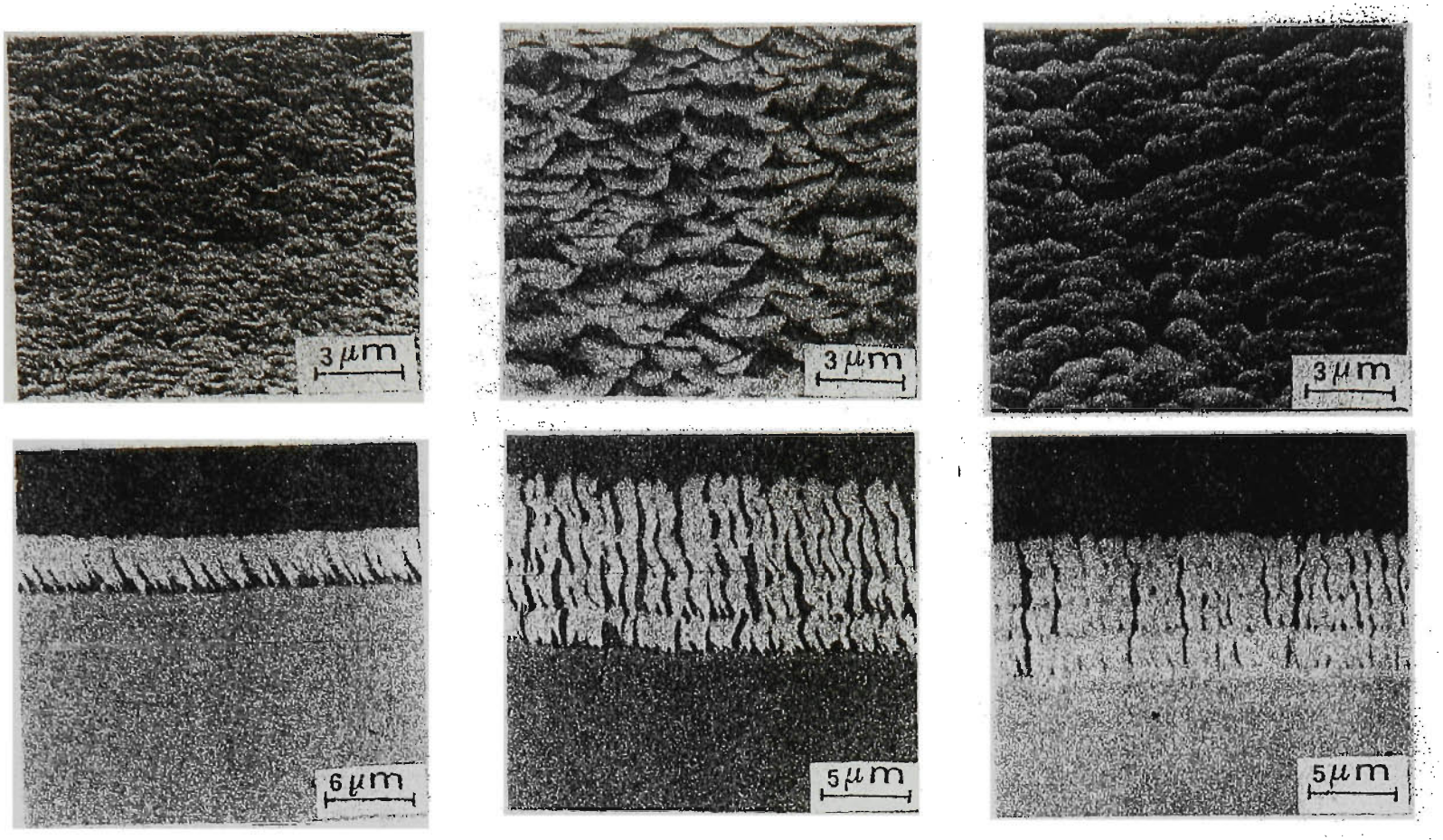

(a) *(b)* *(c)*

Fig.3.3 *Typical surface and cross-sectional SEM micrographs of evaporated Zn coatings [158] :*
(a) typical of coatings produced without surface pretreatment (poor adhesion);
(b) Ar-ion etched and 70°C substrate temperature (moderate adhesion);
(c) Ar-ion etched and 120°C substrate temperature (good adhesion).

was found to be necessary, even when mechanical brushing or Ar etching was used. The microstructures of all Zn coatings were extremely porous, as shown in Fig.3.3. Salt spray testing showed that the Zn coatings survived 6.5 hr per micrometre of coating before the onset of red rust, which was approximately half the lifetime of conventional hot-dipped and electrodeposited coatings. However, this result is not surprising considering that the high porosity would have influenced the thickness of the PVD Zn coating.

3.1.2 Magnetron Sputtering

Only two studies of magnetron sputtered Zn coatings are available in the literature. The first is by Shedden *et al* [160] and represents the preliminary work conducted as part of this thesis. The second study by Musil *et al* [136,137] was published midway through the experimental phase of this thesis, and prompted further work with higher substrate bias voltages by the present author. Owing to the similarity of the deposition conditions to those adopted in this thesis, a thorough review of the research by Musil is presented below and discussed further in Chap.5.

A planar disc unbalanced magnetron with a Zn target of 100 mm diameter was used to deposit the Zn coatings using a range of bias voltages from floating potential to -800 V [136]. The base pressure of the chamber was $5x10^{-4}$ Pa and the argon pressure was typically 0.3 Pa. The magnetron incorporated two electromagnetic coils which were individually powered, and it would appear that a "moderately unbalanced" magnetic field configuration was produced. Measurements of the ion current to the sample were reported and a simple calculation (refer Sect.4.3.1), indicates that the *i/a* ratio was in the order of 0.09. The target to substrate distance was 60 mm, which is roughly equivalent to the mean free path of Ar gas at such pressures [47]. The substrates were polished ferritic stainless steel discs, 18 mm in diameter, which were inserted into the substrate platform so that they were electrically and thermally isolated. This meant that during deposition of the coatings, the substrates increased in temperature from ambient to less than 120°C. The increase in substrate temperature during Zn sputter deposition was consistent with previous work [160]. It was also found that the maximum substrate temperature during a given deposition time increased with bias voltage.

It was demonstrated that smooth specular Zn coatings of up to 2.5 μm thickness could be deposited using the above conditions, provided that the substrate bias was -300 V or greater [136]. Coatings produced at a bias of -200 V or less had a diffusely reflecting surface of matt and milky appearance, similar to that of evaporated Zn coatings [155]. Bias voltages in the range from -200 to -300 V were not evaluated and the

transition to a smooth specular appearance was possibly within this range. The transition is visual appearance was correlated with observations of the surface morphology. Matt coatings tended to have rough surfaces with clumped agglomerated grains that were less than 500 nm in diameter (Fig.3.4a). In the earlier work by Shedden *et al* [160], the agglomerated structure was shown to consist of thin hexagonal plates, typically 20 nm in thickness and 100 nm across. This rough surface structure was thought to be responsible for the light scattering effect for the matt coatings.

The specular Zn coatings produced at high bias voltages had smooth surfaces, free of large agglomerated grains (Fig.3.4b) [136]. Virtually no surface structure could be resolved by SEM examination due to the lack of topographical contrast. Consequently, these coatings were specular because the coating morphology replicated the specular surface of the silicon wafer substrates. The removal of the granular surface structure at high substrate bias voltages was attributed to the effect of energetic ion bombardment of the coatings during growth. It was remarked that the bias required to produce a smooth specular Zn coating was also expected to be a function of the deposition rate. However, no mention was made of the potential effect of the ion current, or more significantly the *i/a* ratio, even though this parameter is recognised as being important in the ion assisted deposition of coatings [172,173].

The principle disadvantage of using such high bias voltages was that considerable amounts of Ar were found to be retained in the sputtered Zn coatings [136]. The Ar content increased rapidly beyond -200 V to a maximum of about 8 at.% at -400 V (Fig.3.5). Further increases in bias voltage saw the Ar content drop to a constant level of about 3 at.% over the range from -600 to -800 V. The burial of inert gas in the coating was tentatively linked as the underlying cause of the smooth coating surface, since it was thought that it might aid in the suppression of grain growth by a pinning mechanism. The influence of resputtering induced by energetic ion bombardment seems to have been overlooked as an alternative mechanism.

The Zn coatings were subjected to a very thorough microstructural evaluation [137], incorporating several different XRD techniques, such as Bragg-Brentano diffraction, texture analysis, rocking curves, and asymmetric diffraction with the crystallite group method (CGM) (refer Sect.4.4). It was found that the maxima in the Ar concentration for its dependence on substrate bias was coincident with maxima in the XRD line broadening, texture, *a* lattice parameter, and unit cell volume. Similarly, a minima in the *c* lattice parameter was coincident with the Ar maxima. From this it was argued that the changes in the Ar content were the main reason for the microstructural

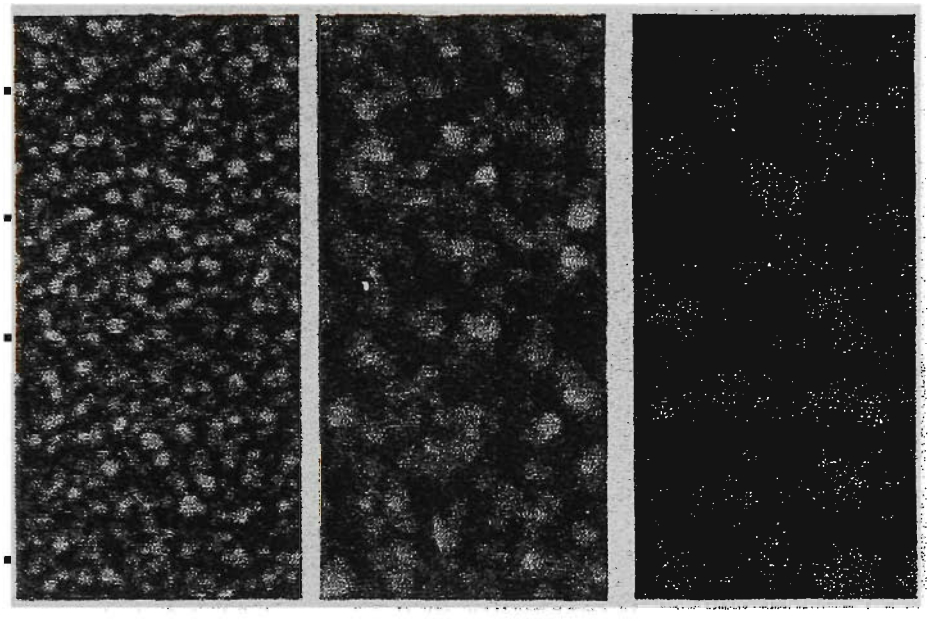

(a) *30s, -34V, 0mA* *120s, -36V, 0mA* *240s, -100V, 2.1mA*

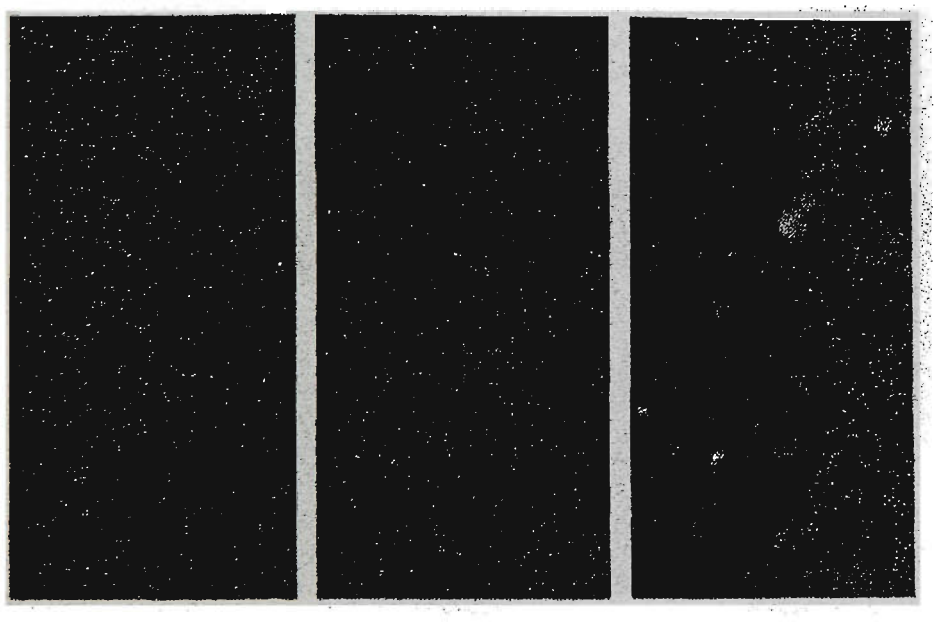

(b) *120s, -300V, 2.1mA* *480s, -300V, 2.1mA* *480s, -400V, 2.1mA*

Fig.3.4 SEM surface micrographs of magnetron sputtered Zn coatings produced with low (a) and high (b) substrate bias voltage. The deposition time, substrate bias, and sample current for each coating is listed below the micrographs. For purpose of scale, each micrograph corresponds to an area of about 3μm x 7μm. [136]

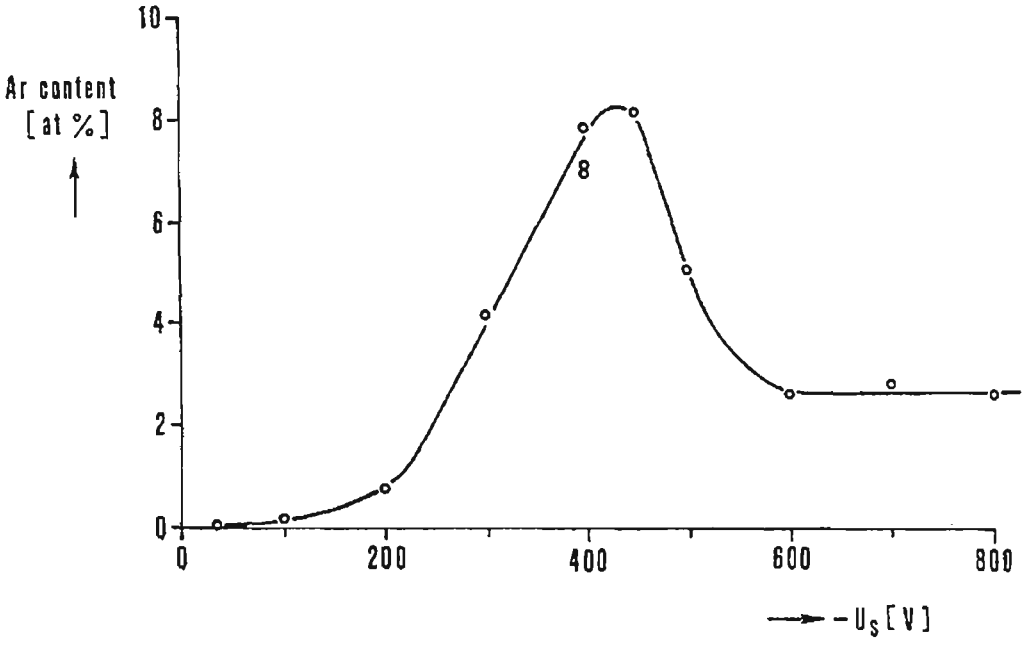

Fig.3.5 Atomic concentration of Ar incorporated into sputtered Zn films as a function of negative substrate bias voltage [136]

effects observed by XRD. Each of these observations are critically discussed in the following paragraphs, and contrasted with the results of the present thesis in Chapter 5.

Preferred Orientation

The Zn coatings possessed a <0001> preferred orientation, that was particularly strong for the coatings that had a specular surface; only the {0002} peak and its higher order reflections were observed for the high bias Zn coatings [136]. Very strong <0001> fibre texture was also reported for the sputtered Zn coatings reported by Shedden *et al* [160]. This was examined further by means of XRD rocking curves of the {0002} peak [137]. The half-widths of the rocking curves were found to exhibit a minima (strongest texture) for the coating corresponding to the maximum in Ar content (Fig.3.6b). A fibre texture was concluded, with the fibre axis being oriented perpendicular to the substrate surface, or slightly tilted from it. For bias voltages above and below about -350V, the strength of the fibre texture decreased, and the random texture component became more prominent.

Residual Microstrain

The Bragg-Brentano XRD line broadening was found to be almost exclusively restricted to the grains oriented with the <0001> direction perpendicular to the substrate surface [137]. Peak broadening was attributed to residual microstrain rather than a crystallite size effect, and was strongly correlated with the Ar content of the coatings (Fig.3.6). As a result of the highly textured nature of the coatings, diffraction of peaks other than the {0002} family were rarely observed. However, in those coatings which had these extra peaks, their peak broadening was insignificant indicating that those particular grains had very little microstrain. Therefore, strong evidence was found that suggested the high microstrain was present only in the <0001> fibre textured grains. The authors believed the microstrain in the fibre textured grains was related to entrapped Ar. Furthermore, the Bragg-Brentano diffraction peaks for {0002} planes were found to be highly asymmetric towards low diffraction angles, which was interpreted to indicate a gradient of Ar content below the coating surface, consistent with the increasing substrate temperature during deposition.

Residual Macrostress

Residual macrostress in the sputtered Zn coatings was examined by the Seeman-Bohlin method [137]. It was concluded that the Zn coatings were essentially free of any residual macrostress irrespective of the substrate bias, although there is some doubt over this interpretation. The Seeman-Bohlin method relies on a random orientation of grains with the stress uniformly distributed throughout all grains. The line broadening data suggested that there were two distinctly different types of grains in the coatings: highly textured grains with large microstrains, and a small randomly oriented component with negligible microstrain. It is reasonable to predict that the distribution of macrostress would be similarly restricted to the highly textured grains. Therefore, the stress measured

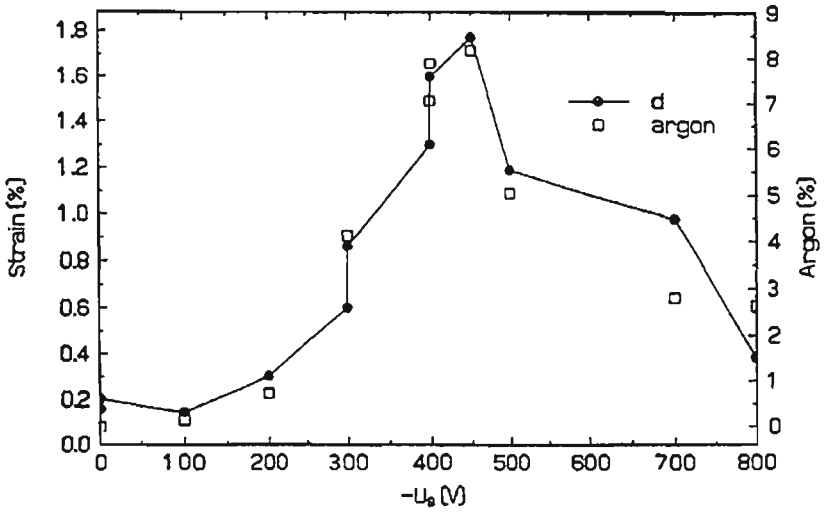

(a)

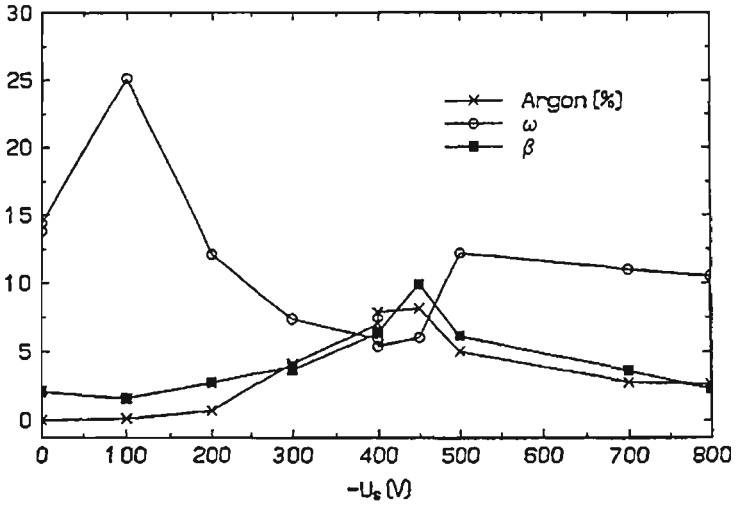

(b)

Fig.3.6 Substrate bias voltage dependence of various coating parameters for magnetron sputtered Zn coatings [137] : (a) residual microstrain and Ar content; (b) halfwidth of ω scans (0.1deg), integral breadth β of 200 peaks (10^{-10} m^{-1}), and Ar content (at.%).

with the Seeman-Bohlin technique corresponded only to the small fraction of randomly oriented grains in the coatings. The macrostress in the {0002} oriented grains, which comprised the majority of the coating volume, was not considered. The *d*-spacing of {0002} planes measured by Bragg-Brentano XRD suggested that the textured coatings may have been subject to large tensile stresses. This possibility was discounted on the basis that smooth specular coatings are usually in compressive stress. However, it is considered that the interpretation of zero macrostress in the Zn coatings was unsubstantiated.

c lattice parameters

Based on the assumption that stress in the coatings was negligible in all cases, it was reported that samples with high argon content had a contraction of the *c* parameter and an expansion of the *a* parameter [137]. Lattice parameters were measured using three different XRD techniques; Bragg-Brentano, Seeman-Bohlin, and CGM. Close examination of the *c* lattice parameter measurements for each of the three different techniques revealed significantly large differences between the lattice parameters determined with each (Fig.3.7a), placing doubt on the author's interpretation. It is feasible that the Zn grains with the strong <0001> preferred orientation, had significantly different lattice parameters compared with the randomly oriented grains, especially considering the observations regarding the peak broadening. In support of this argument, the *c* parameter measured from the {0002} peak in Bragg-Brentano scans shows large variations as a function of the substrate bias, whereas the Seemann-Bohlin data shows no such dependence (Fig.3.7a). This is a consequence of the diffraction conditions whereby the Seemann-Bohlin geometry reveals the randomly oriented grains, while Bragg-Brentano sees the fibre textured grains. Therefore these two diffraction techniques revealed lattice parameter data for two different crystallite groups in the coatings.

a lattice parameters

The method by which the *a* lattice parameters were extracted from the data from the three different XRD techniques was not described in detail [137]. It must be presumed that all the diffraction peaks, when available, were used for determination of *a* from the Bragg-Brentano data. This is supported by the fact that *a* values were only measured from Bragg-Brentano data for low bias samples (Fig.3.7b), for which several non-basal diffraction peaks were detected. Following the above discussion, it is likely that the randomly oriented grains corresponding to these non-basal peaks have a different set of lattice parameters to those of the highly textured grains. Therefore the use of the randomly oriented component in the determination of a single *a* parameter for the entire coating material is unjustified. Similar arguments apply to the use of the Seeman-Bohlin diffraction data, although in this case it is likely that the refined *a* parameters relate only to the random component of the textured coating. This is supported by the observation that the *a* parameter was relatively independent of substrate bias, when measured by Seeman-

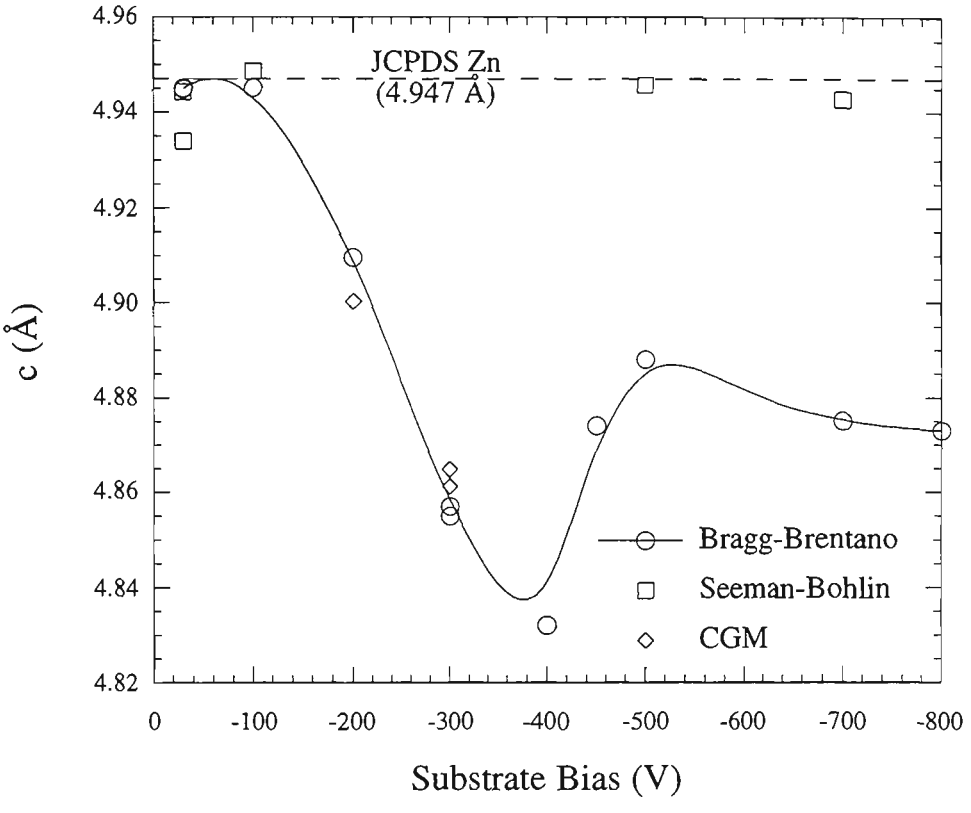

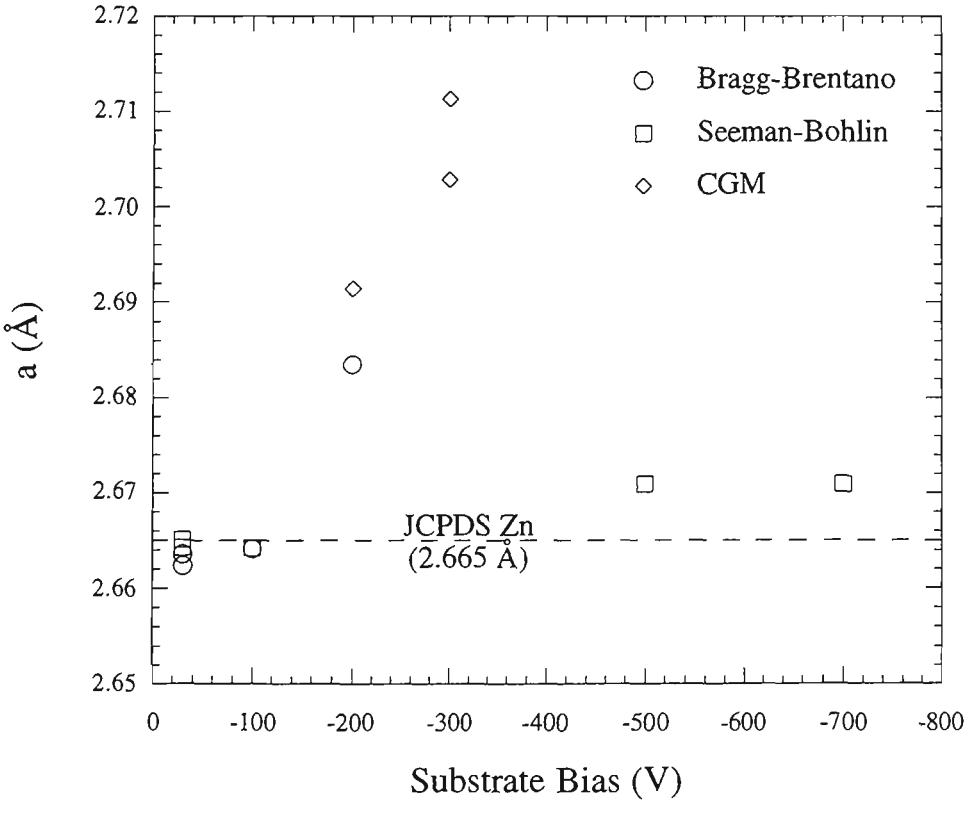

Fig.3.7 Lattice parameters of magnetron sputtered Zn coatings measured by Bragg-Brentano, Seeman-Bohlin, and Crystallite Group Method (CGM, refer Sect.4.4) X-ray diffraction techniques [137]. The lattice parameters of pure, strain-free Zn powder are shown for reference.

Bohlin XRD (Fig.3.7b). The use of CGM data to determine *a* parameters necessitated the assumption that residual stress in the coating was negligible. The *a* parameters could then be determined from favourably oriented planes in the highly textured grains (eg. {10.2} and {10.3}), subsequent to the measurement of *c* from the {0002} and {0004} peaks. This assumption is considered unsatisfactory following the arguments presented above. The effect of residual macrostress on the diffraction peak positions cannot be justifiably ignored.

In summary, significant flaws have been highlighted in the interpretation of XRD results for magnetron sputtered Zn coatings by Musil *et al* [137]. Undoubtably the high amount of Ar buried in the coatings has a significant effect on the various crystallographic parameters (lattice parameters, macrostress, microstrain, texture), but it appears that the arguments presented by these authors are not strictly justified because of oversights made in their assumptions. These problems were primarily caused by the undue elimination of residual stress as a possible cause of XRD peak shifts. Therefore, a model which adequately explains the way in which the entrapped Ar influences the microstructure and residual stress of sputtered Zn coatings remains to be proposed.

3.1.3 Other Ion Assisted Deposition Techniques

Fountzoulas and Nowak [110,161] were the first to investigate the effects of ion assistance on the microstructure of PVD Zn coatings. They deposited coatings of Zn by ion plating onto glass substrates which had been pre-coated with a 10 nm flash coat of Au/Pd. A range of voltages between -900V and -1300V were used for the Ar glow discharge at a pressure of 2.6 Pa. The substrates were held at a range of temperatures during deposition, from the liquid nitrogen boiling point (-196°C) up to 142°C. It should be noted, however, that these temperatures were those of the cathode platform, and not necessarily the substrate temperature. The deposition rate was 0.4 $\mu m.min^{-1}$ and coating thickness was in the order of 1 μm. Micrographs of the Zn coatings produced in this study are shown in Fig.3.8. The microstructure was described as possessing an "agglomerated" type of structure. It was reported that the zone 1 and zone T structures from the Thornton zone model (Sect.2.4.1) were suppressed in these coatings, and only the zone 2 and zone 3 structures were observed. This effect was attributed to the surface heating effect of energetic ion bombardment, which shifted the zone 2 and 3 regions to lower temperatures. Measurements of the cathode temperature using a thermocouple confirmed that a temperature rise of 50-100°C occurred. Some of the Zn coatings were reported to exhibit a combination of zone 1 and T surfaces with zone 2 internal structure. This would seem to imply that the characterization of these Zn coatings by the conventional zone descriptions is inappropriate, particularly in light of the high porosity

(a)

(b)

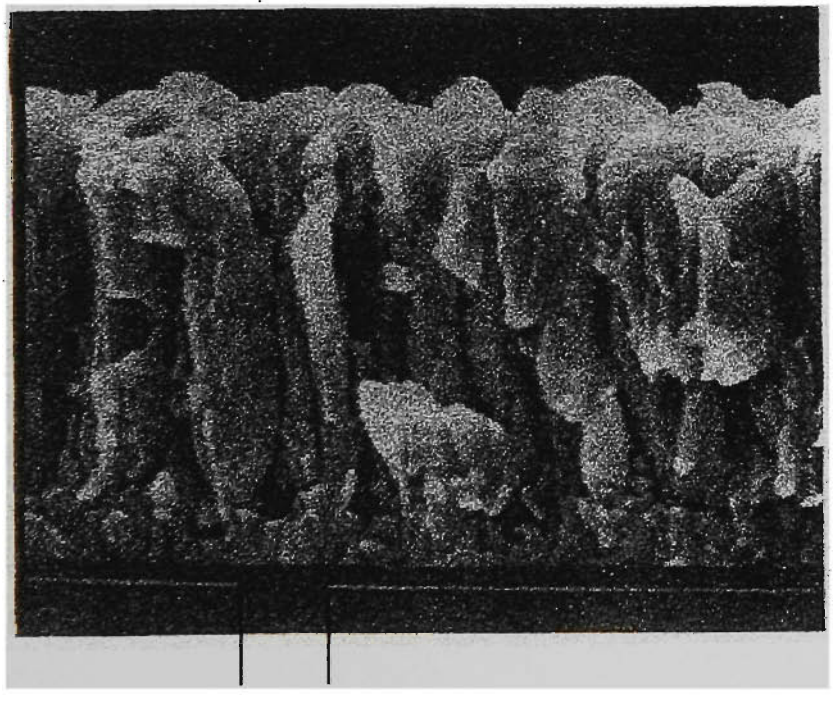

Fig.3.8 SEM micrographs of the surface and fracture cross-section of an ion-plated Zn coating: (a) 160eV Ar ions, T/T_m = 0.33; (b) 250eV Ar ions, T/T_m = 0.16. For purpose of scale, the gap indicated in each micrograph represents 0.5μm. [110]

present in these Zn coatings which are ordinarily absent from zone 2 and 3 structures. Problems were also encountered with obtaining adherent Zn coatings when substrate temperatures of 25°C or higher were used. This effect is probably due to the significant differences in thermal expansion coefficients of the glass substrates and the Zn coating, which would have caused high thermal expansion mismatch stresses (Sect.2.4.2).

The recently developed coating technique known as ionised cluster beam (ICB) deposition has been used to deposit Zn coatings [163,164]. Zn was evaporated from pyrolytic graphite crucibles by electron bombardment at three different temperatures: 1000, 1100, and 1180°C. At these temperatures, the Zn vapour pressure was extremely high (eg. 1130 kPa [11.2 atm] at 1180°C), and a jet of vapour was forced through a carefully designed nozzle which assisted in the formation of clusters of Zn atoms. The background pressure was maintained in the low 10^{-4} Pa range. The evaporated Zn was then passed by an ionising filament, which partially ionised the Zn clusters. The Zn clusters covered a range of sizes and the peak of the size distribution curve moved from 200 atoms/cluster at the lowest crucible temperatures to about 2200 atoms/cluster at the highest temperatures. Approximately 10% of the Zn mass flux was found to be ionised. These partially ionised clusters of Zn were accelerated towards the substrate which was nominally at ambient temperature. The neutral component of the Zn had a typical deposition rate of about 0.26 $\mu m.min^{-1}$. The substrates used for this work were (111) oriented Si wafers. Increasing the crucible temperature resulted in an increase in the size and a decrease in the density of Zn clusters. However, AFM images of the surface of the Zn films indicated that the opposite effect occurred in the deposit, whereby higher temperatures in the crucible favoured the formation of smaller grains that were more densely nucleated. The cluster size and energy had little effect on the film microstructure, suggesting that the island growth mechanism was dominated by the interaction of Zn and the substrate rather than the characteristics of the incident beam. It would therefore seem that ionised cluster beam deposition is unsuitable for the production of dense Zn coatings, at least using the conditions adopted for this work.

Musa *et al* [165] reported on the production of Zn coatings by anodic arc evaporation. This PVD technique is essentially a variation on conventional electron beam evaporation, whereby the electron source is brought into close proximity to the anodic target. Under such conditions, raising the voltage to a critical level results in the ignition of a glow discharge between the two electrodes, that is stable up to currents of about 1 A. The discharge contains ionized source material which can be utilised to produce a coating. Unfortunately, the degree of ionization for Zn was found to be very low and coatings produced by anodic arc evaporation possessed a columnar structure similar to that obtained by thermal evaporation. Furthermore, at the present state of development, this

type of arc is characterized by small sized electrodes, resulting in low evaporation rates. It is feasible that greater success may be possible with the related technique of cathodic arc evaporation, although it appears that there is no published research on Zn coatings prepared by this method.

3.2 Aluminium Coatings

Numerous commercial applications exist for Al coatings deposited by PVD techniques, such as web-coating of polymeric films and compact disc metallisation. However, metallurgical uses for vapour deposited Al coatings are comparatively limited, and primarily aimed at improving the corrosion performance of various substrates via a barrier protection mechanism (Sect.3.2.1). Possibly the most widespread use of PVD Al coatings is for integrated circuits (Sect.3.2.2). A vast amount of research has been directed towards understanding the relationships between ion assisted deposition process conditions, coating microstructure, and the performance of Al coatings in such applications. These process-microstructure relationships are meaningful in relation to the present investigation, in spite of the differences in the intended application.

3.2.1 Metallurgical Applications

The Ivadizing process [174] is used by McDonnell Douglass for applying an Al coating on steel and titanium alloy fasteners used in air-frame construction. The Al coating provides barrier protection for the fasteners that would ordinarily cause galvanic corrosion due to coupling with the aluminium alloy in the air-frame. Ivadizing is an ion plating process [175], and involves deposition of Al evaporated from a resistance-heated source in a partial pressure of about 1 Pa argon gas. The parts to be coated are either hung on racks if they are large, or small parts such as fasteners are tumbled in a barrel. A voltage bias of -2kV generates a glow discharge with the parts acting as the cathode. Energetic ion bombardment from the discharge aids in reducing coating porosity, thereby improving the barrier protection properties of the coatings. Typically the Al coating is about 1 μm in thickness.

The continuous PVD lines used for coating steel strip (Sect.1.3), also represent an industrial-scale metallurgical use of Al coatings. Such products were intended as a potential replacement for Sn-plated steel sheet used in packaging products. A considerable amount of research was conducted during the late 1960s and early 1970s into vapour deposited Al coatings for this application [12,14,153]. This work was aimed at establishing the feasiblity of large scale continuous PVD lines, and therefore addressed

the issues of high deposition rates and coating adhesion. It was recognised that the maximum thickness of vapor deposited Al coatings was inherently limited when high deposition rates were employed. Some degree of substrate heating was required prior to deposition in order to achieve sufficient adhesion, and the temperature of the steel strip increased further because of the release of latent heat during the coating process. Therefore, the strip temperature could eventually reach the level at which the deposited coating was re-evaporated, and this placed limitations on the maximum coating thickness. Much of the interest in vapour deposition for steel strip declined following the commercial success of Zincalume/Galvalume hot-dipped alloy coatings. However, industrial interest in the deposition of thin Al coatings on continuous PVD lines appears to have survived to the present day with the operation of several coating lines in East Germany.

The inherent problems with vapour deposited Al coatings for corrosion protection were highlighted by Egert and Scott [176]. These authors studied ion plated Al coatings for the corrosion protection for uranium. The significance of uranium substrates is discussed at length in Sect.3.4.5. Suffice to say at this stage that the galvanic corrosion of Al coatings coupled with U is probably similar to that of the same coatings coupled with steel. Coatings deposited at high rates and low bias voltages possessed a columnar structure with voids between columns (Fig.3.9a). These coatings provided very little barrier protection for the U substrates. Ion plating at low deposition rates and high bias voltages was shown to produce a dense, non-columnar microstructure (Fig.3.9b) that offered improved barrier protection for the U substrates. However, this dense non-columnar coatings did not completely prevent corrosion of U, but simply delayed it somewhat. It was explained that this was caused by isolated defects in the coating that offered a path for access of water vapour to attack the substrate. Such defects are difficult to avoid with PVD coatings. The poor sacrificial protection properties of the Al coatings consequently led to early cosmetic "failure" of the coated product. Improving the sacrificial protection properties is the primary motivation for making alloy additions to Al coatings.

3.2.2 Integrated Circuits

A vast deal of attention has been directed towards the use of PVD Al coatings for integrated circuits [113,135,177-180]. Such coatings are typically only a few hundred nanometres in thickness, and their main functional requirement is low electrical resistivity. The performance of the coatings is affected by their microstructure, residual stress, and inert gas burial. Another particular problem that has been highlighted is electromigration. This involves the diffusion of Al atoms from one location on a circuit to another, due to the application of a high electrical current density. It often results in the development of

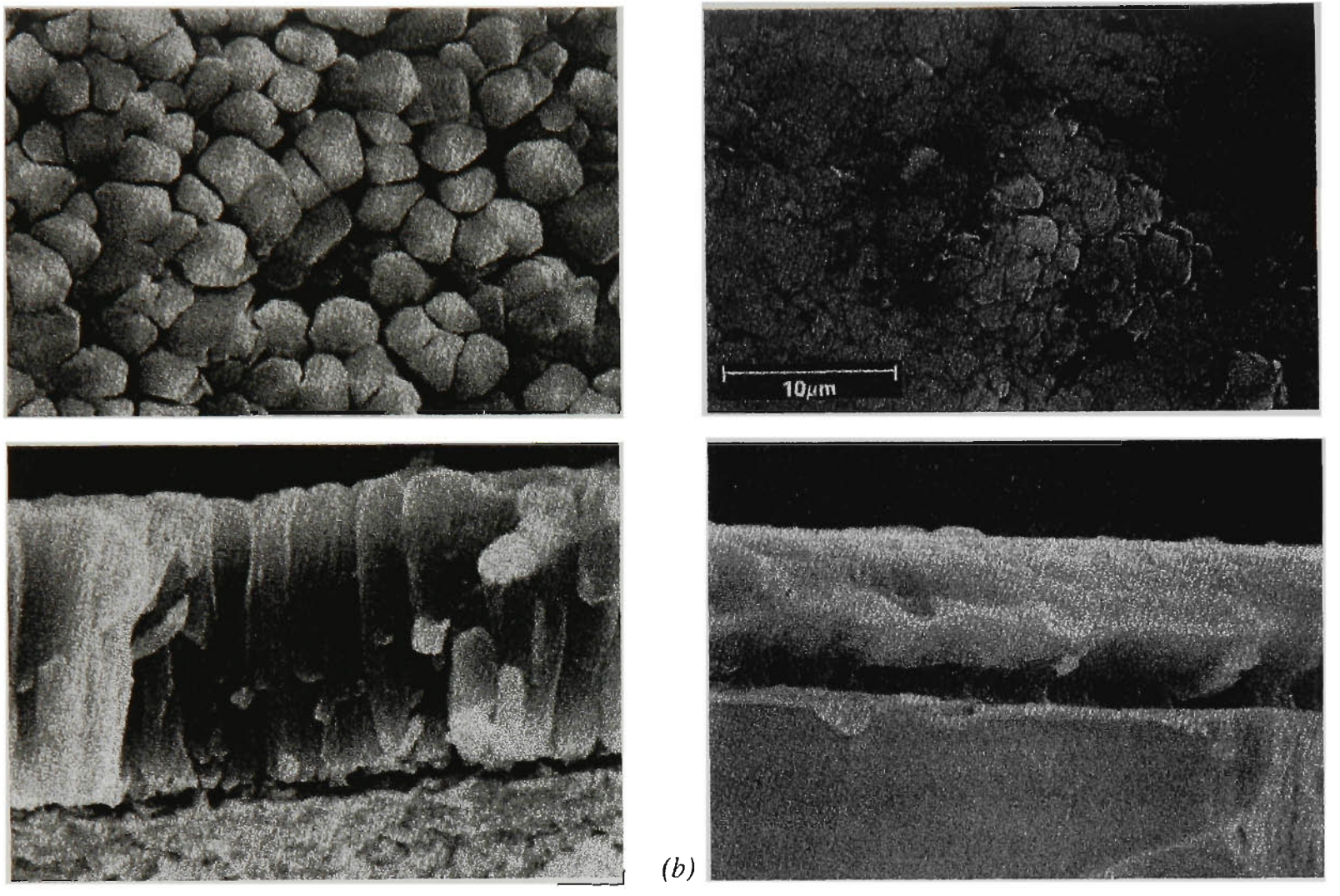

Fig.3.9 Surface and fracture section SEM micrographs of ion plated Al coatings: (a) voided columnar structure produced at high deposition rate and low bias voltage; and (b) dense non-columnar structure produced at low deposition rate and high bias voltage. [176]

voids and hillocks at opposite ends of an interconnect. Electromigration eventually leads to the failure of integrated circuits, and therefore considerable effort has gone into developing solutions to this problem. This is not surprising in light of the enormous financial rewards for computer development.

A number of process variables can be manipulated during the deposition of Al coatings. The most commonly examined variables are substrate temperature and deposition rate. Adding some form of ion bombardment during the deposition process introduces several other variables such as ion to atom ratio (*i/a*), ion energy, and ion species. Some of the findings of researchers in the field of interconnects are of relevance to the present investigation and a brief review of the more important aspects are presented.

Chang and Vook [179] studied the effects of deposition rate and substrate temperature on the surface morphology and grain size of evaporated Al films. The coatings were about 0.3 μm in thickness, deposited onto oxidised silicon wafers. Deposition rate ranged from 0.01 to 0.54 $\mu m.min^{-1}$, and substrate temperature was varied between 24° and 250°C. Hillocks were found to develop on the surface of coatings deposited at low temperatures and low rates. The high deposition rate coatings were smooth and completely free of hillocks. It was surmised that the hillocks formed subsequent to deposition of the coating as a means of stress relaxation. The transverse grain size of the coatings was found to be highly dependent on the substrate temperature with a dramatic increase in grain size occurring between 150°C and 250°C. The average grain size at a deposition temperature of 24°C was 0.1-0.2 μm, compared with 0.4-0.5 μm at 250°C. Deposition rate had a much smaller effect, causing a slight increase in grain size with increasing rate. The coatings were also found to develop a <111> fibre texture at elevated substrate temperatures.

Residual macrostress plays in important role in the adhesion of coatings for integrated circuits. The deposition parameters thus need to be optimised in order to ensure sufficient adhesion. Korhonen and Paskiet [177] applied the Crystallite Group Method (CGM) to determine the residual macrostress and strain-free lattice parameter of several evaporated Al coatings on oxidised silicon wafer substrates (refer Sect.4.4). All of the coatings possessed a very strong <111> fibre texture, with the fibre axis perpendicular to the substrate. This microstructure enabled the application of CGM. The residual stress measured in the coatings after an ageing period of 130 days was subsequently found to be compressive at 26±2 MPa. This stress was relatively independent of coating thickness over a range between 0.25 and 1.05 μm. After annealing the coatings at a temperature of 450°C for one hour, the stress at room temperature was found to be tensile and increased to 120-140 MPa. This change in

residual stress of the coating was due to thermal expansion mismatch with the substrate material. CGM also provided a lattice parameter value almost identical to that of a stress-free Al powder. Determination of the optimum residual stress was not the intention of these authors. They were primarily concerned with presenting CGM as a useful technique for evaluating residual stress in coatings with a strong fibre texture.

The effects of low energy (<1.5 keV) ion bombardment with Kr^+ and Xe^+ ions during UHV electron beam evaporation of Al coatings was examined by Dietz *et al* [113]. The deposition conditions corresponded to normalized energies (E_n) in the range 0-200 eV.(Al atom)$^{-1}$. Coatings of about 5 μm thickness were deposited onto oxidized Si wafers at 250°C. The Al coatings deposited with E_n=0 were found to have a very strong <111> fibre texture. Increasing E_n first caused a tilting of the fibre axis, and at very high E_n (≥80 eV) a single crystal orientation was favoured. Residual stress in the coatings was tensile due to the elevated deposition temperature, and about 45 MPa for the E_n=0 coatings. Increasing the ion energy caused the stress to increase to a maximum of about 100 MPa at E_n=5 eV, decrease back to about 50 MPa at E_n=20 eV, and then increase to about 200 MPa at E_n=200 eV. This oscillation in the residual stress was attributed to an inverse variation in grain size, in a fashion similar to the well-known Hall-Petch relationship. Burial of inert gas in the Al coatings was found to increase with E_n before reaching a saturation level beyond E_n=10 eV. Kr was more efficiently retained at a saturation level of 3 at.%, compared with 1 at.% for Xe. The inert gas was found to precipitate as inter- and transgranular bubbles.

The influence of ion assistance on the grain size of Al coatings on Si wafers, prepared by ion beam assisted deposition (IBAD), was studied by Terrasi *et al* [135]. The Al coatings were about 0.1 μm in thickness, and substrate temperature was ambient. A range of IBAD conditions were used, with argon ion energies ranging from 300 to 650 eV and *i/a* ratios between 0.04 and 0.20. It was found that the transverse grain size of the crystalline Al grains decreased with increasing *i/a* or decreasing ion energy. This was explained in terms of modification of kinetics of growth induced by IBAD. Counter to the findings of other researchers [113,178], the normalised ion energy (eV per ion per Al atom) was not unique for each particular film microstructure. Residual amounts of Ar were found to be trapped in the coatings, at levels ranging from 2 to 6 at.%, although the authors did not relate the Ar content to the ion energy or *i/a* ratio. The resputtering yield of Al from the coatings was found to be in the order of 5, which was about double that of the post-deposition sputtering yield. This sputter yield amplification was attributed to the fine grain size of the coatings. Indeed, resputtering yield was shown to be inversely proportional to the Al grain size.

Preferred orientation of Al coatings for interconnects is considered to be an extremely important parameter. This is because texture plays the dominant role in determining the susceptibility to electromigration. Thus, controlling the film texture has been the main objective for much of the research into Al films. Masaki *et al* [178] examined the effects of *i/a* and ion energy on the preferred orientation of Al coatings formed by ion beam assisted deposition. The Al was evaporated from an electron beam source at a rate of about 0.12 $\mu m.min^{-1}$ onto glass substrates, producing coatings of 0.5 to 1.0 μm thickness. The Ar^+ ion source impinged on the substrate at an angle of 5° from the surface normal. Ion energy was varied between 50 and 200 eV, while the *i/a* was controlled between 0.002 and 0.1. Preferred orientation was determined from Bragg-Brentano XRD scans, by calculating the ratio of intensities for the {111} and {200} peaks, I_{111}/I_{200}. In all cases, a <111> fibre texture was detected in addition to some residual randomly oriented grains. Increased ion energy tended to favour a stronger <111> preferred orientation. For a constant ion energy, a maximum in I_{111}/I_{200} was achieved at a specific *i/a* ratio. The *i/a* required to achieve this maximum I_{111}/I_{200} tended to be inversely related to the ion energy. For this reason, an optimum normalised ion energy of 1.2 eV per Al atom corresponded with the peak in preferred orientation. This value was noted to be coincident with the activation energy for the self-diffusion of Al in the bulk crystalline material. Therefore the optimum growth of <111> texture was attributed to a balance between the rearrangement of Al atoms on the surface of the coating, and the opposite effect of increased nucleation density.

The development of <111> fibre texture in Al coatings was also studied by Kim *et al* [180]. They prepared 0.3 μm Al coatings on oxidised silicon wafers at 65°C from highly ionised beams provided by an ultrahigh-vacuum primary-ion deposition source. The energy and proportion of Al^+ ions was independently varied from 10 to 120 eV and from 0% to 68% respectively, where the remainder of the flux was neutral Al. All of the Al coatings exhibited very strong <111> fibre texture which increased with increasing ion energy and ion fraction. TEM examination of the coatings revealed that the grain size decreased with increasing ion energy. Thermally evaporated Al coatings had a columnar grain diameter of 370 nm compared with 90 nm for the highest ion energy (120 eV). Residual intracolumnar defects were detected in the primary-ion deposited coatings, and the defect density increased slightly with increasing ion energy. It was shown by varying the deposition conditions midway though the coating run, that the initial stages of film deposition play a dominant role in determining the film texture evolution. TEM examination of the coatings formed in this way confirmed that the initially formed texture was transmitted even after switching from primary-ion deposition to evaporation. However, the transgranular defects induced by ion bombardment were not transmitted to the overlayer. It was concluded that highly textured thick Al layers, essentially free of

defects, can be deposited by thermal evaporation through the use of a primary-ion deposited buffer layer. Similar results could possibly be achieved with sputter deposition by first applying a thin buffer layer with ion assisted conditions, and then reducing the bias voltage to floating or earth bias.

3.3 Magnesium Coatings

Magnesium is the most active metal used in engineering applications. With a standard reduction potential of -2.363 V vs SHE (-2.122 V vs SCE) [3], it is more active than both Zn and Al, and does not usually benefit from a highly protective passive film. Mg and its alloys are relatively susceptible to corrosion, and their use in bulk form is usually restricted to mild atmospheric exposures. Despite these restrictions, Mg alloys find numerous important structural component applications in the aerospace and automotive industries because of their superior strength to weight, and stiffness to weight ratios [181]. In its pure form, Mg has found widespread use as sacrificial anodes for sub-soil steel pipelines. The very active corrosion potential of Mg is sufficient to overcome the large soil resistivities that are often present, thereby providing cathodic protection to the steel pipes [3]. The corrosion rate of the sacrificial anodes is not excessive because the high soil resistivity limits the galvanic current that can flow between the Mg anode and steel cathode. Mg anodes are unsuitable for use in sea water because the low solution resistivity ensures that the anodes are consumed rapidly.

Owing to the poor corrosion resistance of pure magnesium, there are very few practical applications for Mg coatings, and it is not surprising that very little work can be found in the literature on such coatings formed by PVD techniques. The majority of the published research is aimed at producing free-standing films [182,183], or as a means of studying PVD process fundamentals [184,185]. Some studies of PVD Mg alloy coatings have also included pure Mg coatings as a point of reference [186-190]. The most relevant findings of these investigations are briefly summarised. Before discussing this work, however, the electrochemical behaviour of bulk Mg is explained in a little more detail.

3.3.1 Electrochemical Behaviour of Bulk Magnesium

Mg can be dissolved in aqueous environments by electrochemical reaction with water to produce $Mg(OH)_2$ and H_2 gas [191]. Oxygen reduction generally is not important to the corrosion of Mg. The $Mg(OH)_2$ film is thermodynamically stable above about pH 11, and below this pH the kinetics of dissolution are mainly controlled by diffusion of reactants or products through the surface film. However, the surface film

does not usually offer extensive protective capacity since it is less stable than the true passive layer formed on metals such as Al. The corrosion potential of Mg in a neutral aqueous solution is generally less than -1.5 V (SHE). Consequently, Mg can dissolve rapidly by evolving H_2 gas unless the pH at its surface is kept above about 11.

The electrochemical behaviour of magnesium is peculiar in that it displays poor coulombic efficiency when galvanically coupled with a more noble metal [191,192]. The more noble cathode supplies a current to the Mg, and it is possible to calculate the expected increase in Mg mass loss, by means of Faradays Law. However, the mass loss of the Mg anode is usually much greater than predicted. Furthermore, the rate of evolution of hydrogen from the Mg anode increases at anodic overpotentials, where a reduction in hydrogen evolution would be expected from mixed potential theory. This behaviour is described as a "negative difference" effect since the uncoupled H_2 evolution rate is greater than that of the anodically polarized anode.

Several possible explanations for the negative difference effect have been proposed [191], although most models are unable to explain the complete anodic and cathodic polarization behaviour of Mg. Very recently, Song *et al* [192] firmly established that a partially protective film was a principal factor controlling corrosion of Mg, and that the film coverage decreased with increasing applied anodic overpotential. They demonstrated that the breakdown of the partially protective film occurs at potentials slightly cathodic to the rest potential of Mg, and was marked by a sharp change in the Mg dissolution and H_2 evolution rates. Predictions from their model were able to qualitatively replicate the observed trends in Mg dissolution rate and H_2 evolution, at both anodic and cathodic overpotentials.

The general consensus on Mg corrosion is that the partially protective film does not offer any significant passive protection during anodic polarization. The anodic behaviour of Mg is entirely active with no passive region [192]. It follows that during atmospheric exposure of a steel substrate coated with Mg, the coating would corrode very rapidly at any exposed edges or scratches in the coating. As such, pure Mg coatings for sheet steel are not attractive since they would be unable to provide long term protection. However, alloying can improve the corrosion performance of Mg coatings [191], and work in this respect is dicussed in Sects.3.5, 3.6 and 3.7. It follows that much of the research on Mg coatings prepared by PVD techniques has not been focused on cathodic protection applications.

3.3.2 Microstructure of PVD Magnesium Coatings

Nieh and Wadsworth [182,183] investigated thick (50 μm) free-standing foils of Mg alloys. The vapour deposited coatings were prepared by either electron-beam or resistance heating an AZ61 Mg alloy source, in a vacuum chamber at a base pressure of 1 mPa. This Mg alloy designation contains 5.8-7.2 wt.%Al, 0.4-1.5 wt.%Zn, 0.15 wt.%Mn and trace amounts of Fe and Cu, but the deposited coatings consisted of essentially pure Mg due to the large differences in vapour pressure of the various constituents. The Mg coatings were fully dense with a columnar structure when deposited on substrates held at 200°C, but were porous, defective and brittle when the substrates were at room temperature.

Nieh and Wadsworth [182,183] also produced Mg films by dc magnetron sputtering from a 150 mm diameter AZ31 Mg alloy target. This alloy designation contains 2.5-3.5 wt.%Al, 0.6-1.4 wt.%Zn, 0.2 wt.%Mn, trace amounts of Fe and Cu, and the balance with Mg. The base pressure was 0.5 mPa, and the target was sputtered with Ar gas at a pressure of 0.7 Pa, onto substrates located 100 mm from the target. The deposition rate was about 0.8 $\mu m.min^{-1}$, such that the production of 50 μm films required about 1 hr operation. The chemical composition of the sputtered coatings was very similar to the target composition. Films sputtered onto room temperature substrates contained extremely fine tapered crystalline grains with numerous pores located at the grain boundary regions. The film density was improved to near bulk by increasing the substrate temperature to 200°C. The grain size of these films was about 5 μm, which contributed to a dull appearance of the film surface. X-ray diffraction indicated that the film formed at 200°C was very strongly textured with the basal plane oriented parallel to the surface.

Arnell and Bates [98] found that fully dense Mg coatings could be obtained by unbalanced magnetron sputtering, without increasing the substrate temperature. Their Mg coatings were deposited using a magnetron source located 100-150 mm from the substrates, in a 0.65 Pa Ar atmosphere and -200V substrate bias. X-ray diffraction indicated that the Mg coatings were very strongly textured such that only the (0002) diffraction peak was detected. The microstructure was found to be "fully dense" and free of any columnar grain structure.

A handful of researchers [184,185] have prepared Mg coatings by cluster beam deposition, as a means of studying the process itself, rather than for any specific application of the coatings. Tochitsky *et al* [184] deposited the Mg onto single crystal NaCl substrates held at room temperature, with a deposition rate of about 0.5 $\mu m.min^{-1}$.

Conventional vapour deposited coatings were found to have a slight preferred orientation with $(01\bar{1}\ 0)_{Mg}//(001)_{NaCl}$. Partially ionizing the vapour flux and applying a -5 kV substrate bias resulted in the formation of smaller grains of a more even size distribution and an enhancement of the preferred orientation with increasing ion energy. Epitaxial films were obtained for cluster beam deposition, provided that the cluster size was in the range from 100 to 1000 atoms/cluster. Partial ionization of the cluster beam, degraded the epitaxial growth such that fibre textured coatings were produced. Similarly, epitaxial growth was disturbed when the cluster size was much greater than 1000 atoms/cluster. The epitaxial growth of the cluster beam deposited Mg coatings was attributed to the enhancement in average energy per atom delivered with this technique in comparison with vapour deposition. This enabled the Mg atoms on the substrate to reorient themselves and occupy epitaxial sites. It was recognised that an optimum cluster size and/or ion energy exists for epitaxial growth. Clusters which are too large are less mobile and have a low probability of reorientation. Delivering too much energy to the surface has the effect of resputtering coating atoms and introducing defects which disrupt the epitaxial growth.

Hagena *et al* [185] prepared coatings of Mg by cluster beam deposition onto glass and Si (111) wafer substrates held at room temperature. Deposition rates of up to 5 $\mu m.min^{-1}$ were achieved for Ar/Mg mixtures, and 11 $\mu m.min^{-1}$ for pure Mg vapour. Films of about 1 μm thickness were examined by XRD. Atomic beams tended to form coatings which had a randomly oriented structure, whereas those from cluster beams had a strong preferred orientation of {0002} planes aligned parallel to the substrate. XRD rocking curves indicated that this fibre texture was restricted to within ±10° of the surface normal. The development of preferred orientation was found to be independent of the substrate used or the presence of an inert gas carrier. The surface morphology of the Mg coatings was examined by scanning tunneling microscopy (STM). The grain size was found to be strongly dependent on the deposition rate, although it was not known whether this was an effect of the cluster size or the rate increase. Furthermore, all coatings were found to oxidise during ambient air exposure for several months, such that they changed from a highly specular silver colour to a golden-yellow colour. The only exception was for the coating which had the largest grains.

3.3.3 Corrosion of Magnesium Coatings

The corrosion performance of PVD Mg coatings has been examined by several researchers [186-190]. These studies appear to have been only cursory and several of the findings are inconsistent. Nowak and Seyyedi [186] prepared a pure Mg coating by ion plating with an argon glow discharge at 1.5 kV and 3.3 Pa. Potentiodynamic measurements in aerated, neutral 3.5 wt.% NaCl solutions indicated that the Mg coating

had a rest potential of -1685 mV (SCE), pitting potential of -1670 mV (SCE), and a passive current density of 14 $\mu A.cm^{-2}$. The passive range was therefore very narrow (15 mV), and the electrochemical behaviour of the coating was almost completely active. As such, the corrosion behaviour of the ion plated Mg coating was very similar to that of bulk magnesium. Comparable results were obtained by Baldwin *et al* [190] for evaporated Mg films, although they reported a more active corrosion potential of -1920 mV (SCE).

In contrast to these results, Chang *et al* [187-189] found that an ion plated Mg coating on a depleted U-alloy substrate displayed a significant passive region when tested under the same conditions. The following parameters were measured: rest potential -1450 mV (SCE), pitting potential -750 mV (SCE), passive current density $4x10^{2}$ $\mu A.cm^{-2}$. This "passive" current density is very high, and represents a dissolution rate of about 1 $\mu m.hr^{-1}$. Therefore, the corrosion of the Mg coating in this test solution was not "passive" in the traditional sense whereby the corrosion rate is very low. Prior to corrosion testing, the coating was noted to consist of agglomerations of droplets and layering, with irregular islands of agglomerates with a smooth surface. Deeper layers of agglomerates were seen between the islands. It was also noted that the coating broke and flaked off when polarized above the pitting potential. This would suggest that galvanic coupling between the substrate and coating probably occurred throughout testing, and may have influenced the polarization behaviour.

3.4 Aluminium-Zinc Binary Alloys

3.4.1 Equilibrium Phase Diagram

The microstructure of all except highly dilute Al-Zn alloys are characterised by the eutectoid decomposition into terminal solid solutions of (Al) and (Zn). No intermetallic phases are stable at room temperature, and the degree of solid solubility is very limited under equilibrium conditions. The phase diagram presented in Fig.3.10a is the most commonly accepted form for the Al-Zn system [193-195]. It should be noted that there is continued controversy regarding the existence of a peritectic intermetallic compound in the Al-Zn system (Sect.3.4.2), and its expected position is shown in Fig.3.10b.

The (Al) or α phase is capable of retaining very high proportions of Zn in solid solution, but only at elevated temperature. The maximum solubility is 67.0 at.%Zn at the (Al) + (Zn) eutectic temperature of 381°C [194]. The (Al) phase containing 59 at.%Zn (α') decomposes by a eutectoid (monotectoid) reaction at 277°C into less concentrated (Al), and (Zn). This transformation can be suppressed by quenching for alloys containing less than about 33 at.%Zn [196]. A miscibility gap exists in the (Al) phase field which has a critical point at 39.5 at.%Zn and 351.5°C [194]. The solid solubility of Zn in (Al) decreases with decreasing temperature and contains only 1.7 at.%Zn at a temperature of 100°C. In comparison with the (Al) phase, the (Zn) or β phase is not capable of retaining large proportions of solute in solid solution. The maximum Al solid solubility is 2.8 at.% at 381°C [194,195], but this decreases to 0.07 at.%Zn at room temperature [194].

The presence of alloy additions in solid solution has a significant effect on its lattice parameter. This is best demonstrated for the (Al) solid solution which has a face-centred cubic (fcc) structure ($Fm\bar{3}\,m$) [197]. Variation in the lattice parameter of the (Al) phase with Zn content has been reported in [196,198-203]. Data from these references are reproduced in Fig.3.11a, which shows the change in lattice parameter of (Al) with additions of Zn, at a temperature of 25°C. These findings indicate that the addition of Zn solute results in a linear decrease in the lattice parameter a of (Al), according to the following equation:

$$a\ (\text{nm}) = 0.40494 - 8.3306\text{x}10^{-5}\ \text{Zn (at.\%)} \quad (< 35\ \text{at.\%Zn}) \qquad (3.1)$$

This equation provides a ready means of predicting the amount of solute in Al-Zn solid solution given a known lattice parameter, or vice versa. Similar compilations of lattice parameter data have been reported elsewhere [194,203].

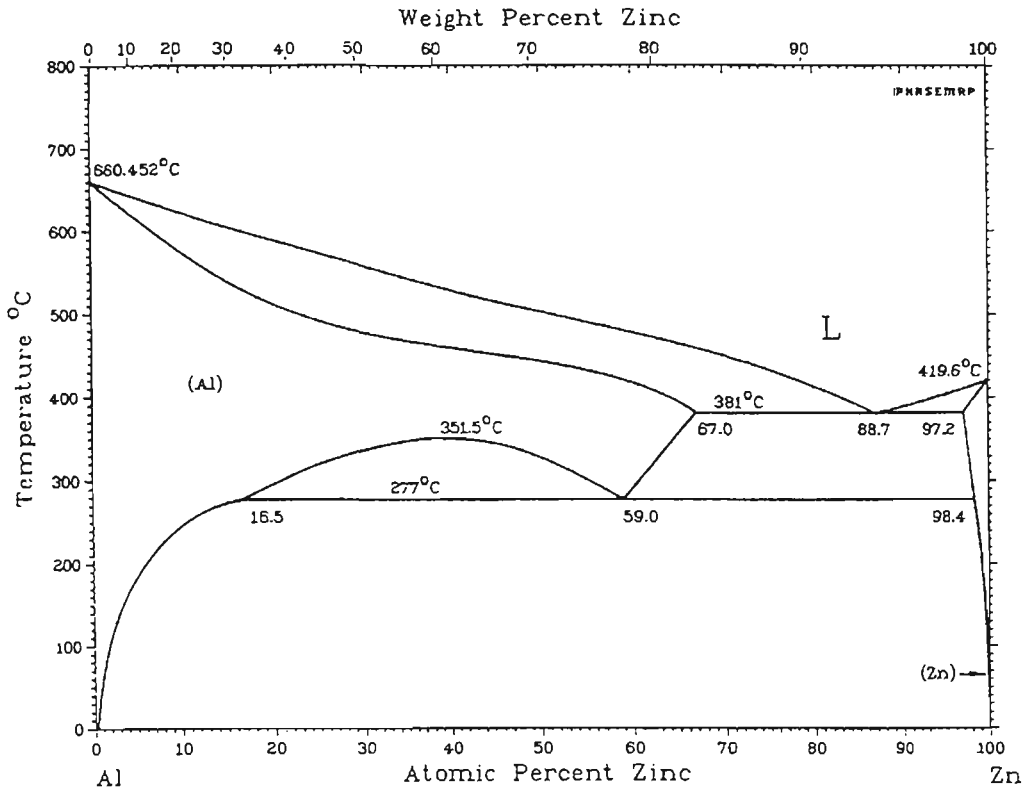

(a)

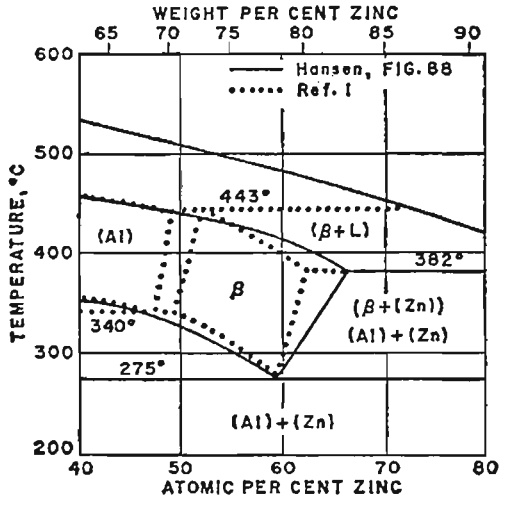

(b)

Fig.3.10. Al-Zn binary phase diagrams (a) the conventional diagram [194] (b) a section showing the controversial peritectic intermetallic phase [207] . Note that the intermetallic is identified as β whereas it is designated as γ in the text.

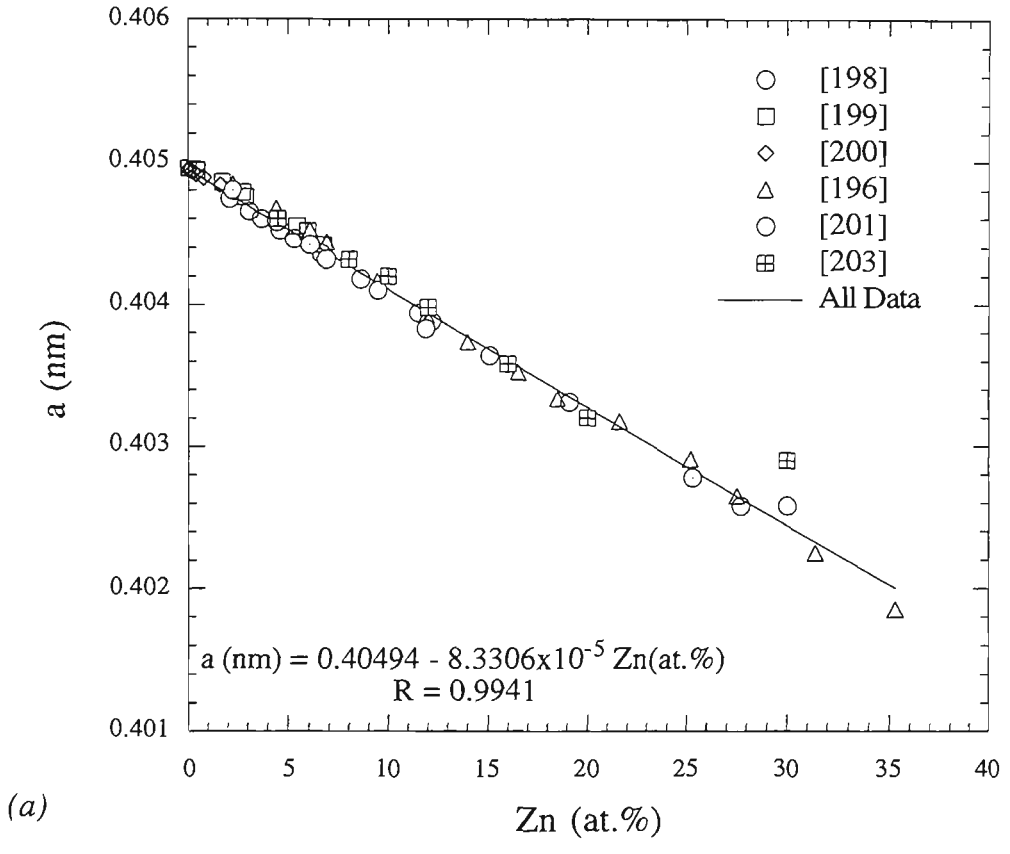

(a)

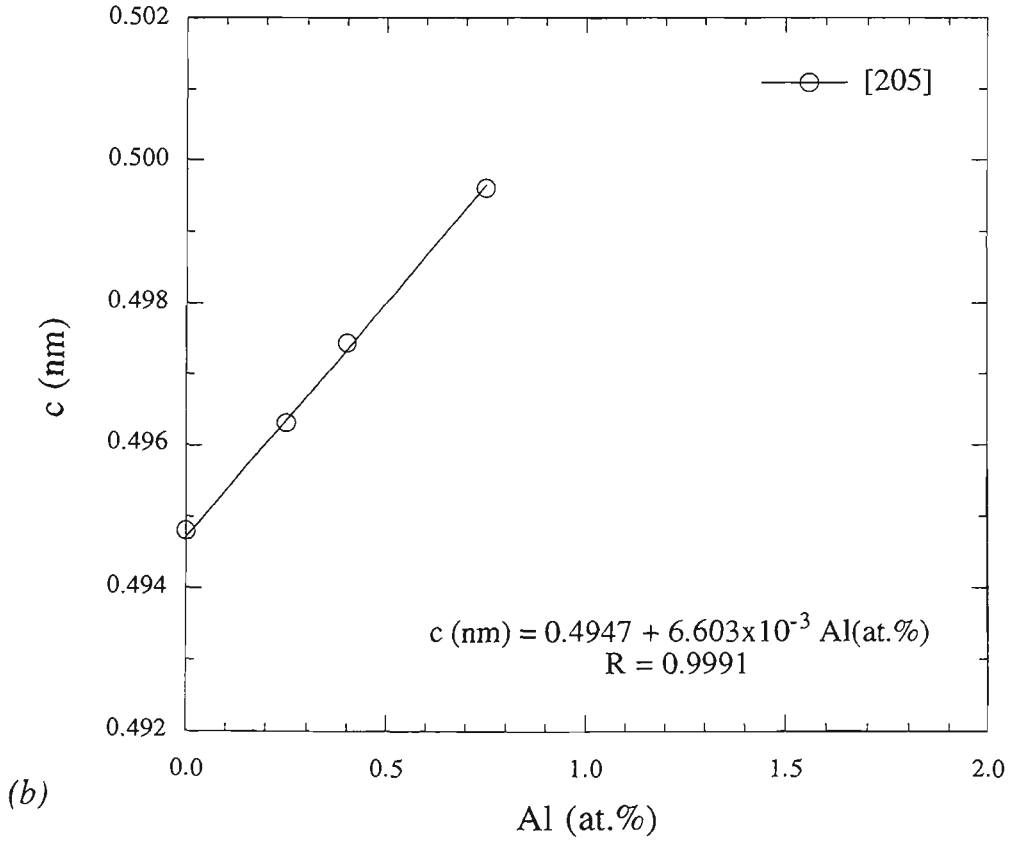

(b)

Fig.3.11 Lattice parameters at room temperature for Al-Zn solid solutions as a function of solute content: (a) a-parameter of (Al) phase with Zn additions; (b) c-parameter of (Zn) phase with Al additions.

The change in lattice parameter for the (Al) phase with addition of Zn is roughly proportional to the size of the solute atom alone. This effect is shown in Fig.3.12 in which the data from Fig.3.11a is reproduced in terms of the average atomic radii. Linear extrapolation of the Goldschmidt atomic radii for pure Al (0.14317 nm) and Zn (0.13945 nm), is very similar to the experimental data. This suggests that Vegard's Law [204] is approximately correct for the Al-Zn system: "The lattice spacing/composition curve for a solvent and solute of the same crystal structure is a straight line joining the values for the two pure metals, and a similar relation with a correction for effects of co-ordination number exists for the atomic diameter values when the two metals have different structures." Following this definition it should be noted that a correction for coordination number is not necessary in the case of Al-Zn solid solutions since both (Al) and (Zn) phases have close-packed structures.

The effect of Al additions on the room temperature lattice parameters of close-packed hexagonal ($P6_3/mmc$) (Zn) solid solution have received very little attention. Only one brief study could be found in the literature [205]. This work indicated that the c lattice parameter for (Zn) was increased by the addition of Al (Fig.3.11b), consistent with the expected trend from the atomic radii (Fig.3.12). The Al solute content and the c lattice parameter of (Zn) were found to be related by the following equation:

$$c\ (\text{nm}) = 0.4947 + 6.603\text{x}10^{-3}\ \text{Al}\ (\text{at.}\%) \quad (< 2.8\ \text{at.}\%\text{Al}) \qquad (3.2)$$

Insufficient data was available to evaluate the effects of Al additions on the a lattice parameter and c/a ratio of (Zn) solid solution. It is thought that the solubility of Al in (Zn) can be extended by rapid solidification, and thermodynamic considerations predict that a maximum of 16 at.%Al in (Zn) solid solution can be achieved [194]. However, a search of the literature failed to reveal any specific work dealing with rapid solidification of Al-Zn alloys in this composition range.

3.4.2 The Peritectic Intermetallic Compound

There has been considerable controversy over the years regarding the possible existence of a peritectic intermetallic compound in the Al-Zn phase diagram. The unusual shape of the solidus of the (Al) phase, with the inflection point at about 45 at.%Zn (Fig.3.10a), has prompted some authors to speculate that the phase diagram is not as simple as is commonly accepted [193].

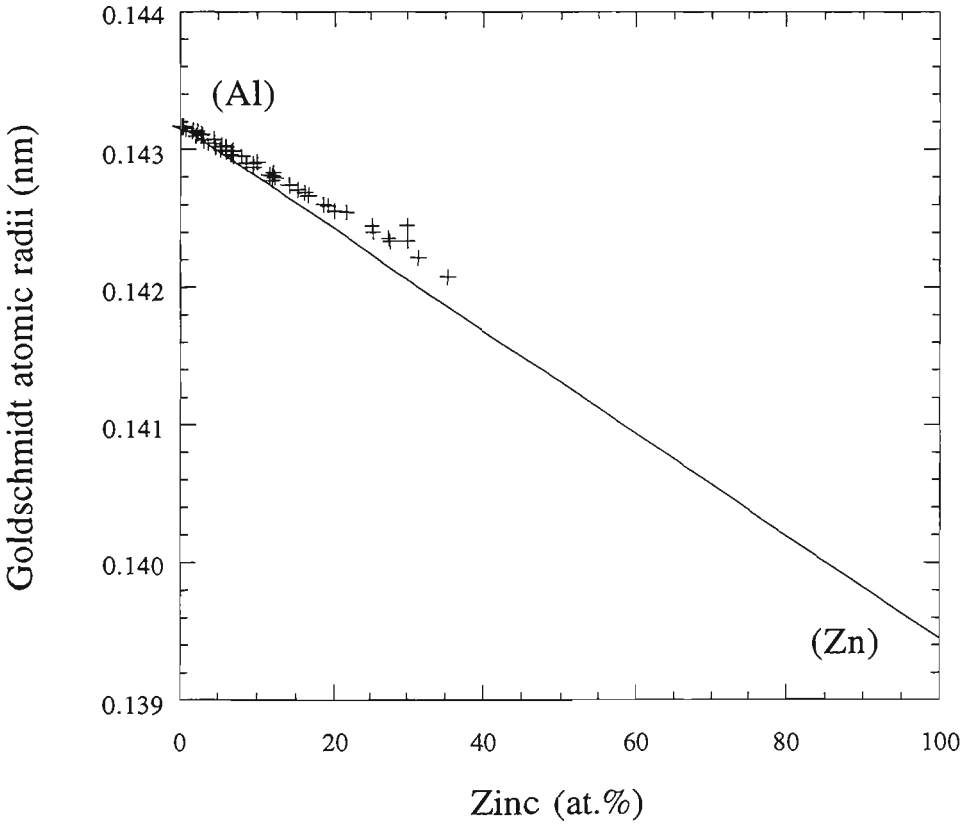

Fig.3.12 Goldschmidt atomic radii for (Al) solid solution in Al-Zn alloys. The line between (Al) and (Zn) phases represents an extrapolation according to Vegard's Law.

Careful high-temperature X-ray diffraction experiments by Presnyakov *et al* [206], indicated that a peritectic reaction L + α-(Al) = γ was likely to be present in the Al-Zn system. The γ phase (also called β in some publications [207]) was reported to be cubic with a lattice parameter of 0.40445 nm at 360°C, which is only slightly different to the lattice parameter of the α-(Al) phase extrapolated to the same Zn concentration and temperature. It was therefore surmised that the γ phase was some form of ordered structure based on (Al). A section of the modified equilibrium phase diagram which takes into account this peritectic reaction is shown in Fig.3.10b. A eutectoid reaction at 340°C was also required for this diagram to be consistent. The presence of the peritectic reaction was used to explain the previous observations of the inflection in the (Al) solidus curve. The peritectic phase could not be distinguished from the (Al) phase by metallographic observation, and this was explained in terms of their structural similarity. The high-temperature XRD studies of Presnyakov *et al*, where confirmed in a similar investigation by Goldak and Parr [202]. Their lattice parameter measurements provided direct evidence for the existence of a eutectoid reaction α' = α + γ at 340°C. A binary α' + γ field was found to exist, about 1 at.% in width, that extended from a eutectoid point at 48.5 at.%Zn to a peritectic horizontal at 443°C. Each of these observations provided strong support for the existence of the γ phase.

In spite of this compelling XRD evidence, recent revisions of the Al-Zn phase diagram have discounted the γ phase [194,195,208]. In a comprehensive review of the Al-Zn system, Murray [194] did not accept the existence of the peritectic γ phase on the grounds of thermodynamic implausibility, because the α (α') and γ phases are isostructural (fcc) with only slight differences in lattice parameter, and are only marginally different in composition. The anomalies in the lattice parameter values reported by Presnyakov *et al* [206] and Goldak and Parr [202], were regarded by Murray as being within experimental error for an (Al) solid solution, and were possibly caused by segregation effects. An Mey *et al* [208] also reported that the inclusion of the γ phase in their thermodynamic calculations did not significantly improve the fit with phase diagram data. However, the experimental observations of Presnyakov *et al* and Goldak and Parr have not been conclusively explained by Murray or An Mey *et al*, and it would seem premature to completely reject the existence of the peritectic γ phase in the Al-Zn system. This conclusion is especially valid in light of the suggestion that the γ phase may have an ordered structure [206,202], which would then be thermodynamically and crystallographically distinct from the (Al) phase. Given such confusion, it is not surprising that Al-Zn phase diagrams which include the γ phase, continue to appear in recent publications [1].

3.4.3 Rapid Solidification

The decomposition of supersaturated (Al) solid solutions in the Al-Zn system has been the target of a significant amount of research because of the complexities of the precipitation process and also because of its importance in developing high strength light alloys [203]. In an attempt to examine the earliest stages of decomposition, rapid solidification was pursued as a means of minimising the solute clustering which occurs during quenching from the solid phase [209]. Work in this area provides some information about the types of structures formed at high quench rates, which may be extended to PVD coatings. However, such research invariably indicated that the rapidly solidified structures were extremely short-lived and had often transformed within the short time required to transfer the samples into the testing equipment.

Agarwal and Herman [209] prepared an Al-22 at.%Zn alloy by liquid quenching from 150°C above the liquidus temperature using the gun technique. Films about 100μm in thickness were produced, with some electron-transparent areas which enabled observation in a TEM immediately after the film production. A modulated structure was always observed, even after a delay of only 15 minutes that was required to transfer the film into the TEM. The spacing for this modulation was measured to be about 4 nm, representing clusters with a diameter in the order of only 10 atoms.

Boswell and Chadwick [210] produced Zn-40.6 at.%Al alloys by splat-quenching from the liquid state onto ambient and liquid nitrogen cooled substrates. This alloy was almost exactly equivalent to the eutectoid composition. They found a large proportion (> 70 vol.%) of a lamellar structure, which had formed from decomposition of the quenched peritectic γ phase within only a few minutes ageing at room temperature (< 20 min.). This lamellar structure was typically extremely fine with an interlamellar spacing of 10-20 nm, and it decomposed rapidly at room temperature to a granular structure consisting of roughly equiaxed grains of (Al) and (Zn) phases. They also reported that the films contained a tiny proportion (< 1 vol.%) of the peritectic γ phase.

3.4.4 Decomposition of Supersaturated Aluminium Solid Solutions

Decomposition of supersaturated (Al) solid solutions results in the formation of a series of metastable structures: spherical and ellipsoidal Guinier-Preston (GP) zones, platelets of coherent fcc precipitates that undergo a rhombohedral distortion, and incoherent $(\alpha'\text{-Al})_R$ [194,197]. It has been argued [203], that the metastable equilibria for Al-Zn are governed by two metastable miscibility gaps, such that the GP zones and the rhombohedrally distorted platelets were considered as two distinctly different phases.

However, this argument has been refuted [194], and it is now accepted that the metastable phase is thermodynamically a single phase, the fcc Zn-rich solid solution, α'-(Al).

The first structure to form at low temperatures in supersaturated (Al) is the spherical GP zone [194]. These zones are typically less than 5 nm in diameter, and beyond this limit, the particles are distorted to oblate ellipsoids. Coherency is maintained with the matrix on the {111} planes, and the distortion consists of a compression of close-packed planes in the <111> direction. Coherency is gradually lost on the other planes as the particle grows rapidly to sizes of 70-200 nm, thereby forming platelets. These platelets are referred to in the literature as "partially incoherent rhombohedral transition phase R" [203]. However, the R phase is still "fully coherent" in terms of thermodynamics, and the difference between R and ellipsoidal GP zones is one of size only [194]. Eventually the coherency on the {111} planes is lost, and this marks the coherent-to-incoherent transition. At temperatures above 150°C, the coherent precipitate grows quickly, to become a coherent plate with a rhombohedral crystal structure.

3.4.5 Aluminium-Zinc PVD Coatings

Aluminium-zinc alloy coatings prepared by PVD techniques have been studied by several researchers. The most comprehensive evaluation was conducted by Nowak and co-workers from the Department of Mechanical Engineering, Northeastern University, Boston, MA, USA [143,211,212]. The major reported findings of this research group are outlined and discussed below. The work on Al-Zn PVD coatings by several other authors is also outlined, although most of this is based on non-ferrous substrate materials. Generally, the Al-Zn coatings are intended for improving the corrosion protection of a bulk material. However, some researchers have considered Al-Zn coatings for examining the fundamentals of resistivity in alloys [213].

Corrosion Protection of Ferrous Substrates

Nowak *et al* have studied Al-Zn alloy coatings prepared by both ion plating [211] and unbalanced magnetron sputtering [143,212]. The latter of these investigations is particularly relevant to the present work since it was concerned with the effects of substrate bias on the microstructure and composition, in addition to the corrosion performance of the sputtered coatings. Five different alloy targets were used for deposition of the sputtered coatings (3, 15, 25, 32, 62, 89 at.%Zn), and the film thickness ranged from 1.6 to 4 μm. The substrate biases were as high as -780 V, although -185 V was used for most targets. This suggests that the ion bombardment of the coatings during deposition was highly energetic, although the authors gave no indication of the *i/a* ratio at the substrate position. The substrate temperature was claimed

to be less than 90°C, although higher temperatures appear to have been possible owing to poor substrate clamping.

The microstructure of the sputtered Al-Zn coatings was found to be dependent on their Zn content and the bias voltage [143,212]. Coatings with a high Zn content (>30 at.%Zn) had a rough surface with a fine grained, clumped, porous structure (Fig.3.13a). Conversely, coatings rich in Al (<12 at.%Zn), tended to have smooth surfaces with columnar grains typically about 0.3 μm in diameter (Fig.3.13b). Some extremely thin coatings (40-70nm) deposited from a Al-32at.%Zn at three different bias voltages were examined by TEM. All coatings were found to be polycrystalline and randomly oriented, as indicated by smooth electron diffraction rings. The grain size of the coating was reduced by increasing bias voltage. The reason for this effect is unclear, as the microstructure of alloy coatings is expected to be influenced by both composition and energetic bombardment (Sect.2.4). The authors also claimed that the coating deposited with -185V bias formed the metastable phase, α'_R, while the coatings at lower and higher bias consisted of (Al) and (Al)+(Zn) respectively. The indexing of the α'_R phase may also be explained by a supersaturated (Al) phase and/or residual tensile macrostress, since only the fcc reflections were reported. This general trend in the types of phases formed in the bias sputtered coatings is consistent with their Zn content.

Nowak *et al* [143,212] also prepared coatings from the Al-25 at.%Zn target using a wide range of bias voltages. Figure 3.14 reproduces the composition of the sputtered Al-Zn alloy coatings as a function of substrate bias voltage [143]. The rapid reduction of Zn content with increasing bias was interpreted as being due to the combined effects of preferential resputtering and re-evaporation. This result also adds credence to the above suggestion that the actual substrate temperature was probably higher than reported, because of the thermal load from energetic particle bombardment. Attempts were made to correlate the effect of bias voltage with the change in microstructure, as per the Messier Zone Model [109]. However, this interpretation is unwarranted due to the complication of compositional modification caused by resputtering. From the work presented by these authors, it is not possible to specify whether or not the microstructure of an Al-Zn alloy coating of one particular composition at one bias voltage, will be different to that of another produced with a different target composition and bias voltage but resulting in a coating of the same composition. There remains the question of whether or not the bias voltage will influence the microstructure of the alloy coatings, independent of the influence on composition.

(a)

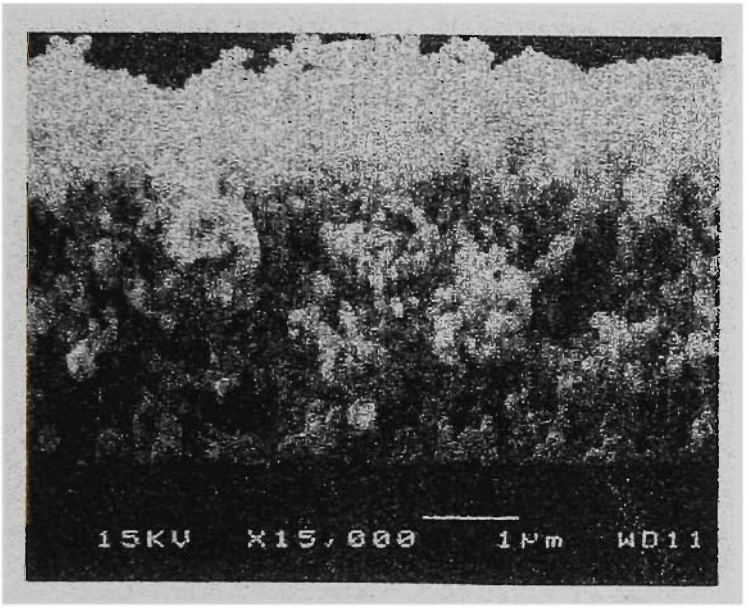

(b)

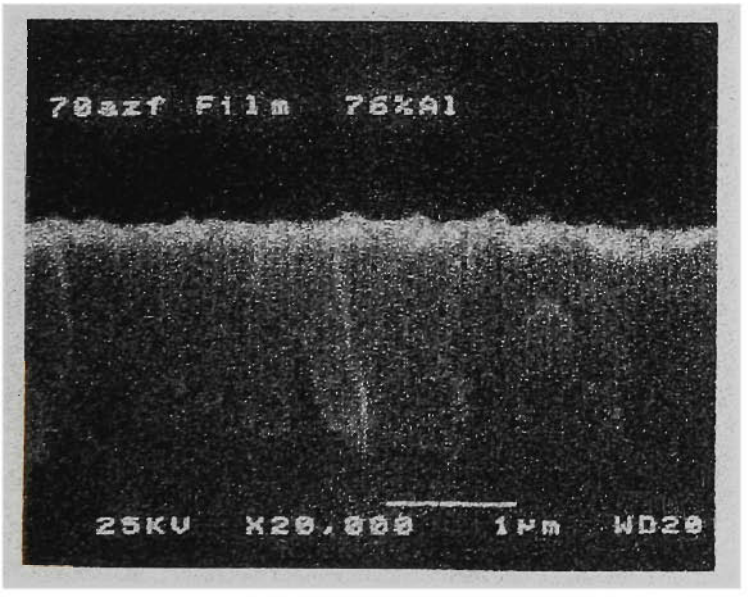

Fig.3.13 ***Cross-section*** *morphologies of sputtered Al-Zn coatings on glass substrates [143] : (a) Al-61at.%Zn coating (Al-62at.%Zn target, -185V bias); and (b) Al-**11at.%Zn coating** (Al-15at.%Zn target, -185V bias)*

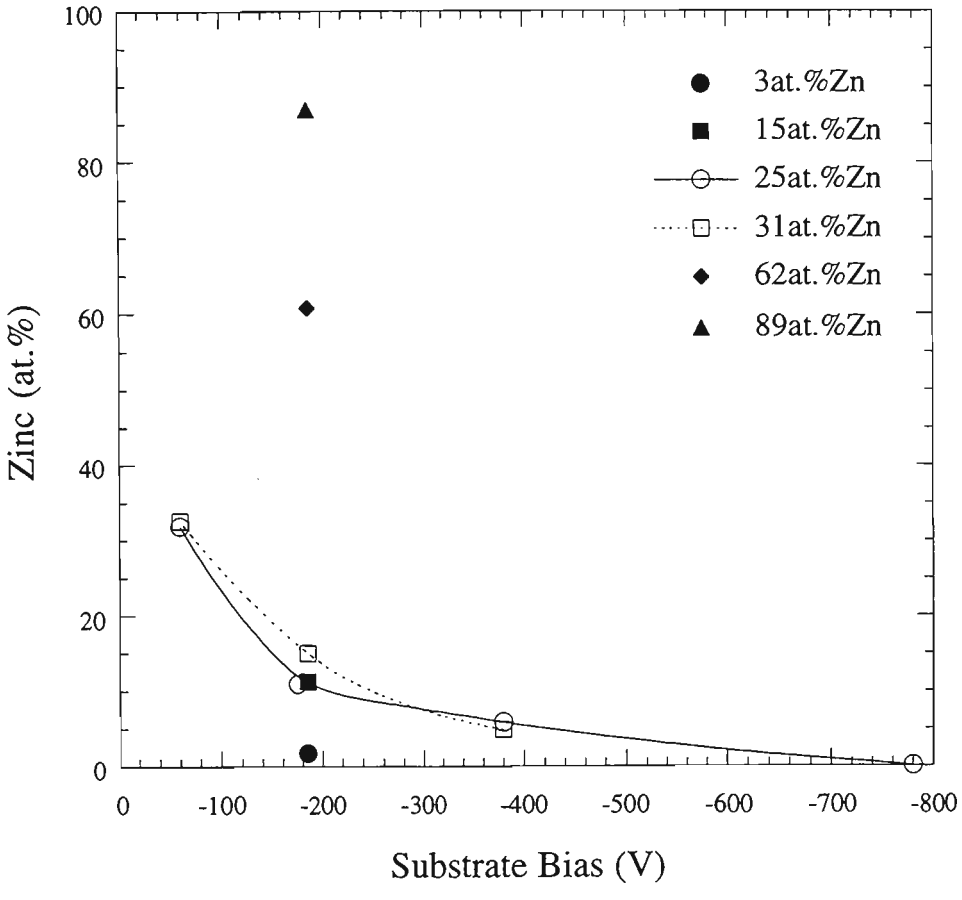

Fig.3.14 Zinc content of magnetron sputtered Al-Zn coatings as a function of substrate bias. Data was extracted from tables in [143].

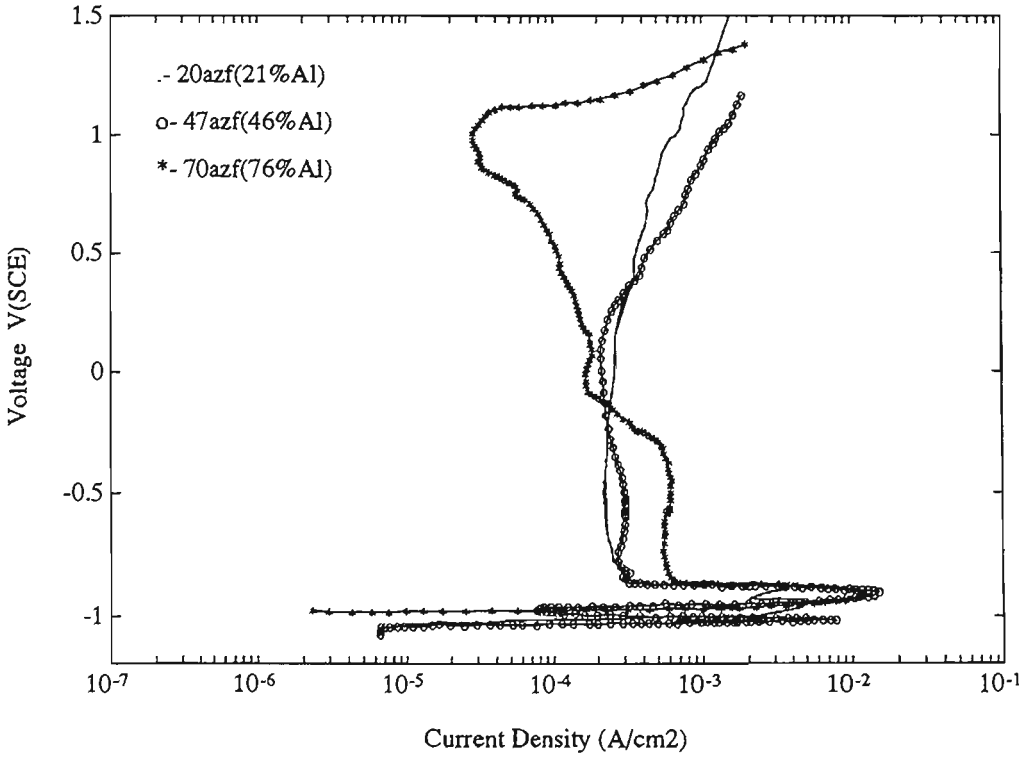

Fig.3.15 Anodic polarization scans of sputtered Al-Zn coatings on stainless steel. The compositions shown in parentheses are in wt.%: 21wt.%Al = 11at.%Zn, 46wt.%Al = 33at.%Zn, 76wt.%Al = 61at.%Zn. [143]

A preliminary study by Shedden *et al* [160] confirmed several of the microstructural observations by Nowak *et al* [143,212]. Alloy coatings were prepared by unbalanced magnetron sputtering at a range of bias voltages, using Al-20at.%Zn and Al-50at.%Zn alloy targets. For self bias conditions, the composition of the sputtered coatings was found to be very similar to that of the target material. Application of negative substrate bias caused a very dramatic decrease in the Zn content of the coatings at a critical bias voltage. This critical bias was about -50V for the Al-20at.%Zn target and -120V for the Al-50at.%Zn target. At higher bias, the coatings were almost completely free of Zn. This effect was partially attributed to preferential resputtering of Zn from the coating. However, coatings deposited on earthed substrates were also deficient of Zn. It was surmised that the severe electron bombardment experienced with earthed substrates probably caused an increase in their temperature, resulting in reevaporation of the Zn. Subsequent measurements [214] indicated that after a deposition run of 8 minutes, the substrates temperature increased to 120-130°C at bias voltages between self and -200V, compared with 180°C when earthed. Hence the reevaporation of Zn was expected to be significant for biased substrates, but not to the extent encountered with earthed bias. The problem of excessive substrate heating was avoided in the present investigation by effective clamping (Sect.4.1).

The electrochemical behaviour of both ion plated [211] and bias sputtered [143,212] Al-Zn coatings was also examined by Nowak *et al.* In each study alloy coatings of various compositions were deposited onto polished ferritic stainless steel substrates. In the case of ion plating, a vast number of different compositions were obtained by evaporating from separate Al and Zn sources. Potentiodynamic anodic polarization scans were conducted starting at the rest potential, in aerated near-neutral 3.5 wt.% NaCl aqueous solution at room temperature. Typical polarization curves for three different alloy coatings produced by bias sputtering [143,212] are reproduced in Fig.3.15. It was claimed that all the alloy coatings had a passive protection range of about 2.2V (corrosion potential to transpassive potential), independent of their composition. Unfortunately, this good result actually represents the electrochemical behaviour of the stainless steel covered with a completely oxidised coating. The coatings were generally entirely corroded within the first few hundred millivolts. The measured passive current density of the oxidised coating on the substrate was found to be 10 to 100 times that of the uncoated substrate [212], possibly as a result of pitting at discontinuities in the coating. It is unclear why stainless steel substrates were used for this work considering that they are inherently corrosion resistant and do not require sacrificial protection.

Not all of the electrochemical work by Nowak *et al* [143,211,212] was affected by this problem. Measurements of the polarization resistance for the sputtered Al-Zn alloy coatings were also conducted, presumably before commencing the polarization scans. Alloy coatings were found to have a higher polarization resistance (lower corrosion rate) than bulk alloy of the same composition. From this observation it was concluded that fine-structured Al-Zn coatings provide better corrosion prevention than conventional hot-dipped Al-Zn coatings, based on their low corrosion rate and good galvanic protection.

Relatively dilute Al-Zn alloy coatings have been examined by Teer and Abu Zeid [215] and Arezzo *et al* [157,158]. Only dilute alloy coatings were prepared in each case. Teer and Abu Zeid [215] deposited Al-1 at.%Zn and Al-2 at.% Zn coatings onto low-carbon steel substrates, by ion plating from a resistance heated crucible. The net compositions of the resultant coatings were approximately the same as those of the alloy feed material, but it was expected that there would be periodic variations in composition. An SEM micrograph of the Al-1 at.%Zn coating indicated that it had an open columnar structure which was claimed to be typical for the coating parameters. Cyclic immersion corrosion tests were conducted using a bath of synthetic sea water (10 minutes immersion over a one hour cycle). Uncoated steel samples developed first signs of red rust within 3 hours, whereas the development of red rust on the Al-Zn alloy coated samples was a function of the coating thickness. Coatings of 1 μm thickness showed red rust after 10 days, whereas those with thicknesses of 8 μm or greater showed no signs of red rust after 6 months of testing. These tests were conducted with all edges masked from the corrosive media, and hence were a test of the barrier protection of the coatings. It was also found that the sacrificial protection of pure Al coatings could be improved significantly by the addition of only 2 at.%Zn.

Arezzo *et al* [157,158] prepared coatings of Zn-5 at.%Al alloy deposited onto steel sheet by electron-beam evaporation in a commercial PVD batch coating facility (refer Sect.3.1.1). The Al and Zn were evaporated from separate sources and deposited onto the steel strip, which was heated to various temperatures at the start of deposition (115-185°C). The substrate temperature increased during deposition due to the release of latent heat. The coatings did not flake or peel after bending the substrate 180° at zero thickness bend radius. Salt spray testing gave a result of 28.9 $hr.\mu m^{-1}$ coating to the first sign of red rust, which was similar to the result for a commercial Galfan product. The vapour deposited coating was essentially the same composition as the Galfan product and therefore it appears that the vapour deposited microstructure did not significantly influence the salt spray lifetime.

Corrosion Protection of Non-Ferrous Substrates

Various types of coatings deposited by PVD techniques, including Al-Zn alloys, have been investigated by Chang *et al* [187-189,216] as a means of providing corrosion protection for a depleted U-alloy (DU-0.75 wt.%Ti). These authors are affiliated with the US Army Materials Technology Laboratory in Watertown, MA, and their interest in U-alloy derives from its superior armour piercing capabilities. However, this material is susceptible to corrosion when exposed to high humidity and salt laden environments, and therefore sacrificial coatings have been investigated as a means of alleviating these problems. Although this work might sound rather exotic, it is of significant importance to the present investigation since the corrosion potential of U-alloy in aqueous chloride electrolytes (-820 mV SCE), is similar to that of low carbon steel (-650 mV SCE). It might be expected that the performance of Al-Zn coatings on U-alloy substrates could be similar to identical coatings on sheet steel substrates. Therefore, a brief review of this work is warranted. Other authors have also reported the vapour deposition of Al-Zn coatings onto Al-alloy substrates and, although of less significance to the case of sheet steel substrates, this work is also reviewed.

Chang *et al* prepared Al-Zn alloy coatings by cathodic arc evaporation using either separate elemental targets [187-189], or an alloy target [216]. The coatings prepared from separate elemental targets had a composition of Zn-14 at.%Al, which is similar in composition to the Galfan coating. The surface morphology of the Zn-Al coating consisted of a "*spongy structure with holes of diameter 1 μm and smaller.*" No macroparticles were observed on the coating surface. Electrochemical polarization scans in aerated 3.5 wt.% NaCl aqueous solution at pH 5.5 were conducted. Large passive protection ranges were claimed, but examination of the polarization curves presented in Fig.2 of [187], suggests that a passive region was not present for the Zn-Al alloy coating. Immersion tests of U-alloy substrates with various coatings were also conducted. The samples had a 1.6 mm diameter hole drilled into them, in order to evaluate the sacrificial protection ability of the coating. The test solution was again 3.5 wt.% NaCl at ambient temperature. The Zn-Al coating was found to give the best performance of all coatings examined after 120 days immersion. Some white corrosion product was noticed and there was no corrosion of U around the drilled hole. In comparison, Zn coatings exhibited significantly more corrosion of both the coating and substrate, and it was suggested the presence of Al reduced the rate at which the sacrificial coating corroded.

The composition of the alloy target used for arc deposition by Chang *et al* [216] was Al-25 at.%Zn, and provided coatings with 53 at.%Zn. The enrichment of the coating with Zn was thought to be caused by the higher rate of evaporation for Zn relative to Al, and is a problem commonly encountered with arc evaporation of alloy targets. The

coating thickness was measured to be about 8 μm, and the surface morphology consisted of spheroidal or flattened particles of a wide size distribution between about 1 and 35 μm. Such a morphology is typical of the macroparticle dominated flux produced by an unfiltered cathodic arc source. Numerous defects such as pits and micropores were observed in the coatings, and it would be expected that the substrate was still accessible to corrosive solution through the coating. The electrochemical tests in 0.5 N NaCl solution indicated that the Al-Zn coatings were active with no passive region. However, it is anticipated that the pits and micropores in the coating would have had a significant impact on this test. A galvanic corrosion test confirmed that the coating provided adequate sacrificial protection to an equal area of U-alloy after full immersion for 4.5 days.

Al-Zn alloy coatings have also been considered for corrosion protection of Al-alloys. Koch and Meyer [217] deposited Al-Zn coatings by magnetron sputtering onto aluminium alloy substrate materials. The corrosion performance was evaluated by immersion tests and electrochemical measurements. It was found that the adhesion of the coating to the substrates was the main phenomena influencing corrosion. Fernandes and Ferreira [218] applied coatings of Al-1 at.%Zn and Al-3 at.%Zn to aluminium alloy substrates by vapour deposition. Potentiodynamic polarization scans of these coatings in 3.5 wt.%NaCl aqueous solution indicated that the corrosion potential was dependent on the Zn content of the alloy: -818 mV (SCE) for Al-1%Zn and -907mV (SCE) for Al-3%Zn. The Al-3%Zn coatings were found to retain a higher polarization resistance than Al-1%Zn, which indicated that this coating had a lower corrosion rate. Thus, it was concluded that the Al-3%Zn coating was an effective corrosion protective coating for aluminium alloys because of its low corrosion rate and simultaneous low corrosion potential that would provide sacrificial protection for the substrate.

3.5 Aluminium-Magnesium Binary Alloys

3.5.1 Equilibrium Phase Diagram

The Al-Mg equilibrium phase diagram as shown in Fig.3.16 is characterised by five stable phases: α-(Al), β-Al_3Mg_2, R-Al~42 at.%Mg, γ-$Al_{12}Mg_{17}$ and δ-(Mg) [219]. The Al-rich α phase has a maximum Mg solubility of 18.6 at.% at a temperature of 450°C [195], but this value decreases to 2.1 at.% at 100°C [193]. The α-(Al) terminal solid solution has a face-centred cubic structure ($Fm\bar{3}\ m$) [197]. The variation in the lattice parameter of the α phase with Mg content has been reported in [220-222]. These findings indicated that the addition of Mg solute results in a linear increase in the lattice parameter of α. The Mg-rich δ phase has a maximum Al solubility of 11.8 at.% at a temperature of 437°C [195], but this value decreases to 1.3 at.% at 100°C [193]. The δ-(Mg) terminal solid solution has a close-packed hexagonal structure ($P6_3/mmc$) [197]. Accurate lattice parameter measurements for the Mg-rich solid solution are reported in [223-225]. These studies indicated that both the *a* and *c* lattice parameters for δ-(Mg) are decreased by the addition of Al, but the *c/a* ratio increases slightly. The effect of solute content on the lattice parameters of the α and δ phases is discussed further in Sect.3.5.2.

The three intermetallic phases in the Al-Mg system generally have low melting points and very complex crystal structures. The β phase has a narrow composition range from 38.5 to 40.3 at.% Mg [195], and has a congruent melting point of 451°C [219]. The crystal structure of β is complex cubic and isotypic to α-Mn ($Fd\bar{3}\ m$), with a lattice parameter of 2.8239 nm, and about 1170 atoms in each unit cell [219]. The R phase, which is also known as ε, is a line compound with a composition of about 42 at%. It is thought to be formed by peritectoid reaction at 370°C but it soon decomposes by eutectoid reaction at 320°C [219]. This phase is hexagonal ($R\bar{3}$) with a=1.283 nm and c=2.175 nm [226]. The γ phase ranges in composition from 45 to 60.5 at.% Mg at 450°C and narrows to 52 to 60 at.% Mg at 300°C [219]. It has a congruent melting point of 455°C [219]. The crystal structure of γ is body-centred cubic ($I\bar{4}\ 3m$) [197] with 58 atoms per unit cell. The lattice parameter of γ varies linearly from 1.0469 nm at 51.6 at.%Mg to 1.0591 nm at 61.5 at.%Mg [193].

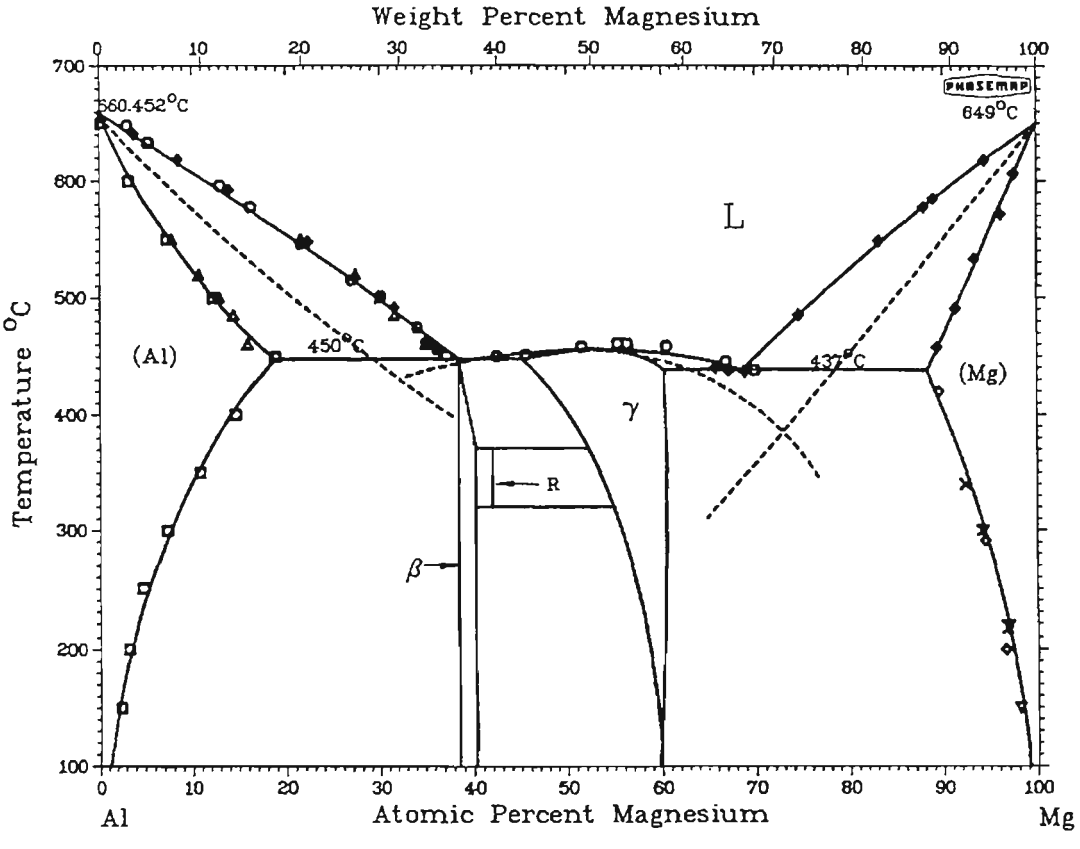

Fig.3.16 Al-Mg binary phase diagram [219]

3.5.2 Rapid Solidification

Supersaturated solid solutions

Rapid cooling of alloys from the liquid state is well known to provide solid solutions beyond the equilibrium concentrations, provided that the compositions are miscible in the liquid state. This has long been known to be valid for rapid solidification of Al-Mg alloys [227]. The solid solubility of Mg in α-(Al) can be extended up to 38.4 at.% by rapid solidification [227-230]. Analysis of the equilibrium data [199,220-222] combined with the rapid cooling data [227,228] shown in Fig.3.17, indicates that the lattice parameter of the α phase increases linearly with Mg additions according to the following equation:

$$a\ (\text{nm}) = 0.40494 + 4.3387\text{x}10^{-4}\ \text{Mg (at.\%)} \quad (< 38.4\ \text{at.\%Mg}) \qquad (3.3)$$

Similarly, the solid solubility of Al in the δ-(Mg) phase can also be greatly extended by rapid solidification. However, the maximum supersaturation of Al in δ-(Mg) has not been determined with the same precision attained for the α-(Al) solid solution. Consideration of the experimental data reported in the literature would seem to indicate that the limit is between 23 and 28 at.%Al [227,231]. Thermodynamic calculations [230] suggest that a maximum solubility of about 27 at.%Al can be expected. Analysis of the published rapid cooling data [227,231] combined with the equilibrium data [223-225] as shown in Fig.3.18, indicates that the lattice parameters of the δ-(Mg) phase decrease linearly with Al additions according to the following equations:

$$a\ (\text{nm}) = 0.320936 - 3.95175\text{x}10^{-4}\ \text{Al (at.\%)} \quad (< \sim 27\ \text{at.\%Al}) \qquad (3.4)$$

$$c\ (\text{nm}) = 0.52112 - 5.2216\text{x}10^{-4}\ \text{Al (at.\%)} \qquad (3.5)$$

$$c/a = 1.6238 + 3.7518\text{x}10^{-4}\ \text{Al (at.\%)} \qquad (3.6)$$

The relationships between the lattice parameters of the solid solutions and the solute content are proportional to the size of the solute atom alone. This effect is shown in Fig.3.19 in which the data from Figs.3.17 and 3.18a are reproduced in terms of the average atomic radii. Linear extrapolation of the Goldschmidt atomic radii for pure Al (0.14317 nm) and Mg (0.16017 nm), is very similar to the experimental data, with only a slightly negative deviation. This suggests that Vegard's Law [204] is approximately correct for the Al-Mg system. Hence, equations 3.4 and 3.5 provide a ready means of predicting the amount of solute in Al-Mg solid solution given a known lattice parameter, or vice versa.

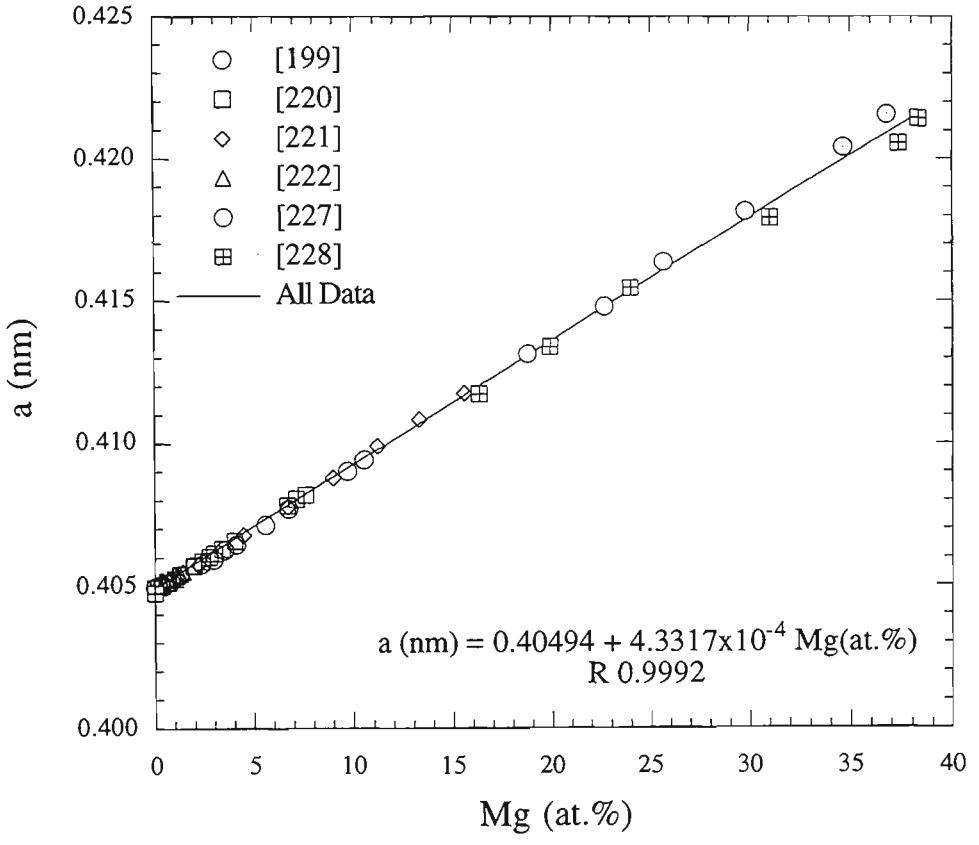

Fig.3.17 *Lattice parameter at room temperature of (Al) solid solution in Al-Mg alloys as a function of solute content.*

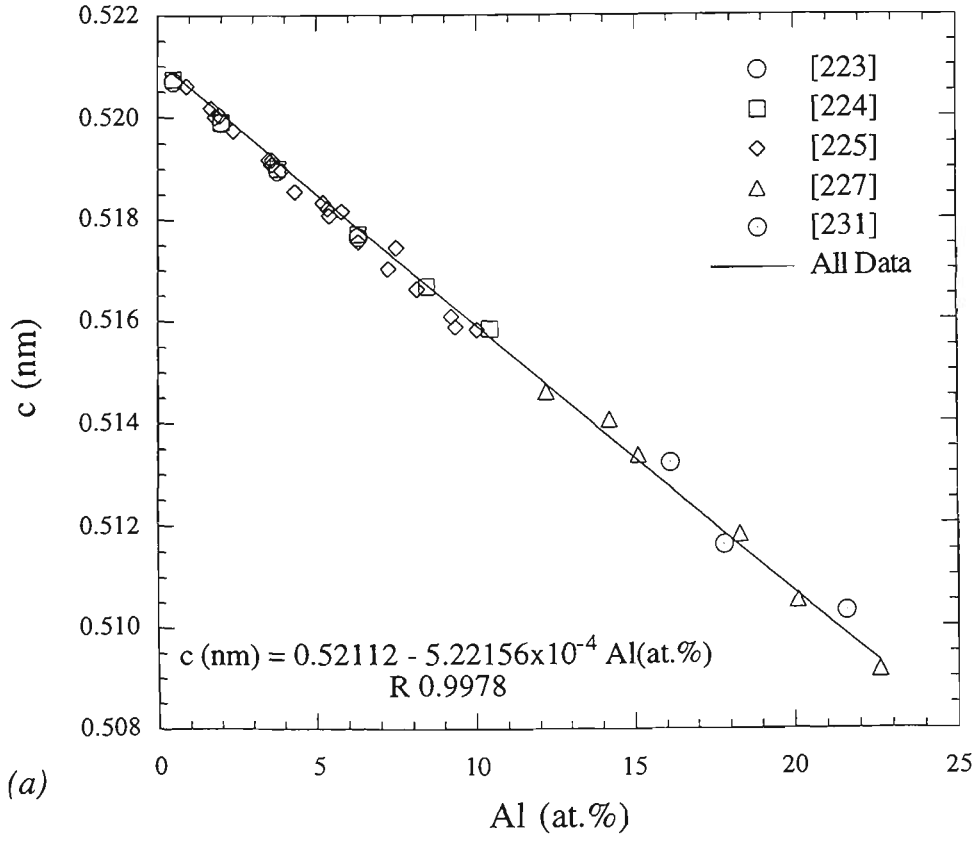

(a)

Fig.3.18 *Lattice parameters at room temperature of (Mg) solid solution in Al-Mg alloys as a function of solute content; (a) c-parameter, (b) a-parameter, (c) c/a ratio.* *(see next page)*

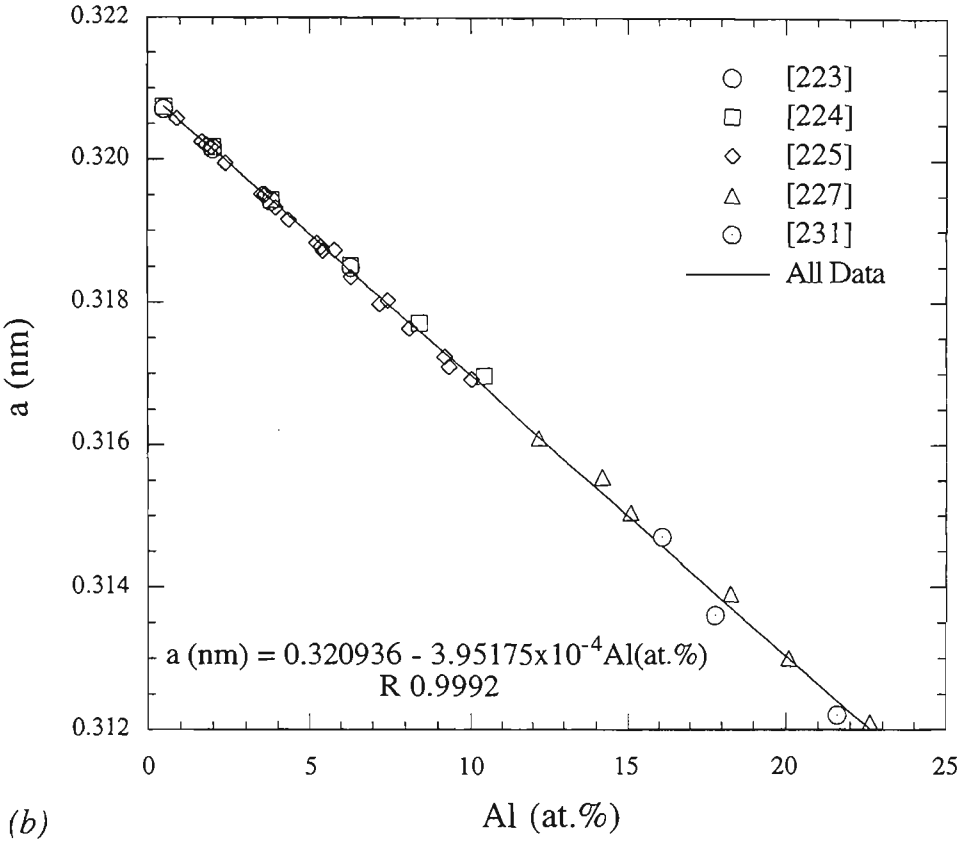
0.322
0.320
0.318
0.316
0.314
0.312
a (nm)
0
5
10
15
20
25
Al (at.%)
[223]
[224]
[225]
[227]
[231]
All Data
a (nm) = 0.320936 - 3.95175x10-4Al(at.%)
R 0.9992

(b)

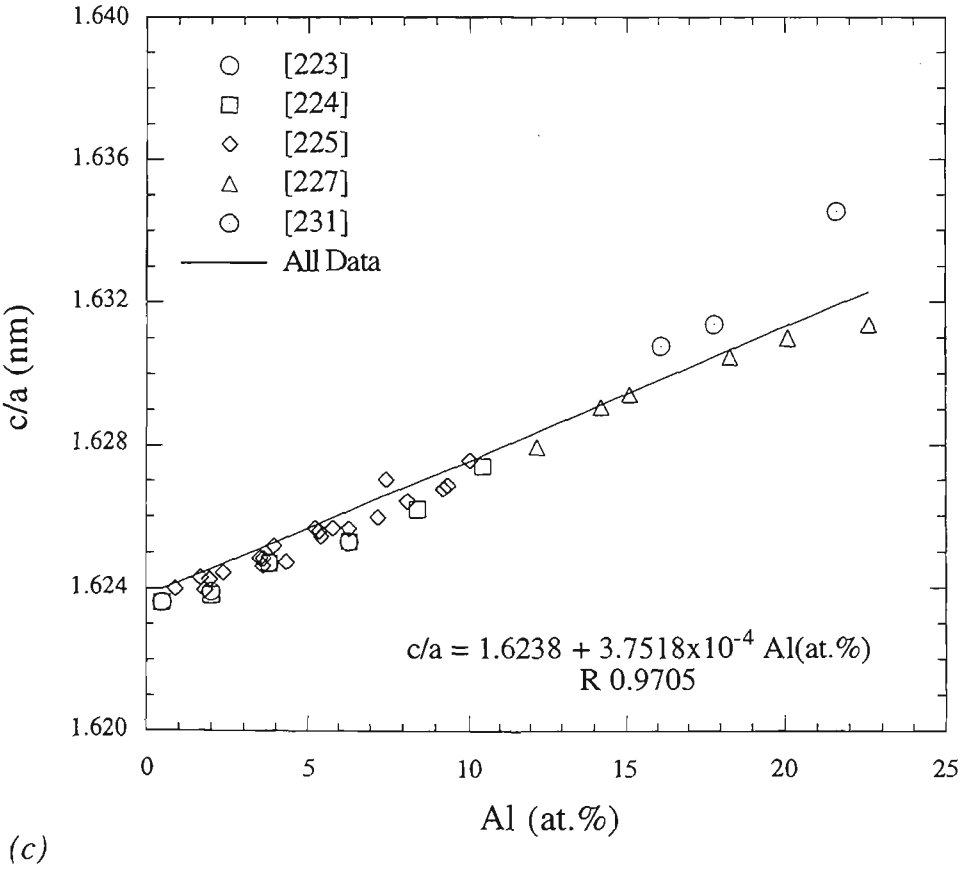
1.640
1.636
1.632
1.628
1.624
1.620
c/a (nm)
0
5
10
15
20
25
Al (at.%)
[223]
[224]
[225]
[227]
[231]
All Data
c/a = 1.6238 + 3.7518x10-4 Al(at.%)
R 0.9705

(c)

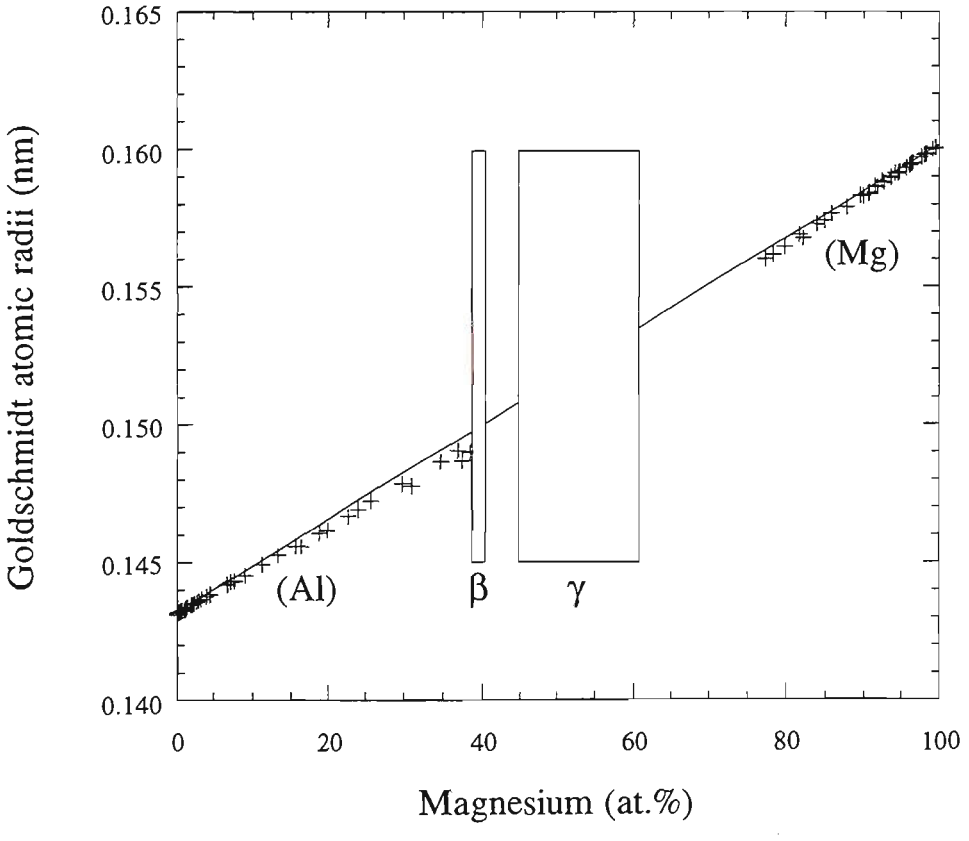

Fig.3.19 Goldschmidt atomic radii for (Al) and (Mg) solid solutions in Al-Mg alloys. The line between (Al) and (Mg) phases represents an extrapolation according to Vegard's Law. The positions of intermetallic phases are indicated for reference.

The supersaturated solid solutions formed in rapidly solidified Al-Mg alloys are generally not stable in the long term. Supersaturated α-(Al) alloys form Guinier-Preston (GP) zones after only a few days of ageing at room temperature [232]. Heating the alloy above 60-90°C results in dissolution of the GP zones. Ageing the supersaturated alloy at a temperature of 130°C for several weeks, causes the precipitation of β' at the grain boundaries initially, and eventually in the bulk. The β' phase is a semi-coherent intermediate phase with a hexagonal unit cell, and lattice parameters of a=1.002 nm and c=1.636 nm. Supersaturated δ-(Mg) alloys containing more than 17.6 at.%Al are subject to rapid transformation at room temperature [231]. The supersaturated δ-(Mg) alloys decompose by precipitation of a new metastable phase γ' at cell boundaries. These metastable phases are discussed further in the next section.

Metastable intermetallic phases

It is well established that Al-Mg alloys with < 38 at.%Mg or > 73 at.%Mg can form supersaturated solid solutions if they are rapidly cooled. In the composition range between these limits, rapid cooling usually results in the formation of one of several different metastable phases. There is considerable controversy over the crystal structures and compositions of these phases [230]. A brief review of the various metastable intermetallic phases in the Al-Mg binary system follows.

Luo *et al* [227] prepared a vast range of rapidly solidified Al-Mg alloys and their results for supersaturated solid solutions have been discussed above. However, they also prepared rapidly solidified alloys with 40, 50 and 70 at%Mg. They interpreted the Debye-Scherrer diffraction pattern for the Al-40 at.%Mg alloy as being attributable to the β phase. The 50 at.%Mg alloy was identified as γ, although the diffraction pattern was diffuse. The 70 at.%Mg had weak lines from δ-(Mg) and a diffuse γ pattern. Although the diffraction patterns were similar to the equilibrium phases, their diffuse nature seems to hint at the possibility of structural differentiation.

Predel and Hülse [228] observed that rapidly solidified alloys in the composition range from 51.5 to 63 at.%Mg consisted of only the γ phase. Alloys of 38.4 to 44.5 at.%Mg produced a tetragonally distorted form of the γ phase, which was called γ'. The amount of distortion decreased with increasing magnesium content. These findings are consistent with those of Luo *et al* [227], and seem to indicate that the diffuse γ pattern observed at 70 at.%Mg by those authors may indeed be due to a distorted metastable form of γ.

Suryanarayana *et al* [233] reported on a new metastable phase Al_2Mg which was detected in an Al-30at.%Mg liquisol-quenched alloy. The XRD pattern was indexed to a

tetragonal unit cell ($I4_1/amd$) with lattice parameters of a=0.4132 nm and c=2.6602 nm. It was inferred that each unit cell contained 24 atoms. This phase coexisted in the rapidly cooled alloy with supersaturated α-(Al). The findings of these authors are at variance with those of Luo *et al* [227] and Predel and Hülse [228], who found rapidly solidified alloys contain exclusively the α-(Al) solid solution up to 35.4 at.%Mg. It is possible that this metastable Al_2Mg phase formed by the partial decomposition of the supersaturated α-(Al) phase after room temperature ageing.

Rajasekharan *et al* [226,234] presented another new metastable phase which they detected in a rapidly solidified Al-40 at.%Mg alloy. This alloy composition corresponds to that of the β phase, although the equilibrium phase was not formed during rapid cooling. The XRD pattern of the metastable phase was indexed to a hexagonal unit cell ($R\bar{3}$) with lattice parameters of a=0.573 nm and c=0.954 nm. These lattice parameters are about half those of the metastable β' phase which forms during decomposition of supersaturated α-(Al) [232]. The new metastable phase transformed to the equilibrium β phase upon thermal treatment [226], as did the β' phase [232]. Therefore, it is probable that these two metastable phases are crystallographically related. The formation of a metastable phase at this composition is opposed by the findings of Luo *et al* [227], who reported the presence of the β phase. However, this variance is not surprising since the diffraction patterns of the metastable phase and equilibrium β phase are quite similar in appearance [226].

Kobayashi *et al* [229,235] investigated rapidly solidified Al-(10-60 at.%)Mg alloys and found that as-quenched ribbons with up to 35 at.%Mg contained a supersaturated α-(Al) solid solution. Ribbons with 20-35 at.%Mg also contained a new metastable phase which they called X. The ribbons with 42 at.%Mg were entirely composed of this new X phase, while those with 60 at.%Mg consisted of single phase γ-$Al_{12}Mg_{17}$. The new metastable phase was not characterized, although electron diffraction patterns were very similar to those of β. Therefore, it is possible that the X phase is simply a distorted form of the β phase, and is therefore equivalent to the metastable Al_2Mg phase reported by Suryanarayana *et al* [233].

Hehmann [231] prepared some rapidly solidified Mg-Al alloys with 16 to 28 at.%Al. A supersaturated δ-(Mg) phase was found in ribbons with 16 to 22 at.%Al. The Mg-28 at.%Al ribbons were partially amorphous with diffuse and very weak reflections of the γ phase. However room temperature ageing of all of the ribbons led to the precipitation of a yet to be characterized phase γ' at the cell boundaries. The γ' phase was ordered and coherent with the matrix. The electron diffraction pattern for the γ'

phase was very complicated indicating a large unit cell, although it could not be determined in this work.

The metastable phase at Al-40 at.%Mg reported by Rajasekharan *et al* [226,234] has been studied more recently by Kulkarni *et al* [236]. It was found that selected area diffraction patterns for this phase were deceptively similar in appearance to those of an icosahedral phase. Twofold, threefold and approximately fivefold patterns from this phase were observed. However, significant differences between the patterns indicated that the phase was "pseudo-icosahedral". The diffraction patterns for the $Mg_{32}Al_{49}$ phase (Al-40at.%Mg) closely resembled those of icosahedral $Mg_{32}(Al,Zn)_{49}$ (refer Sect.3.7.2). Indeed, the structure for the equilibrium phase β which forms at this composition, is characterized by the presence of 672 icosahedral subunits in the unit cell [235]. Therefore, it was concluded that the pseudo-icosahedral phase in rapidly solidified Al-40 at.%Mg was a quasiperiodic low symmetry derivative of the icosahedral phase in the $Mg_{32}(Al,Zn)_{49}$ system, with a $\bar{3}$ *m* point symmetry [236,237]. X-ray diffraction of this phase [238] proved to be identical to the pattern observed by Rajasekharan *et al* [226,234].

To summarise the various investigations into rapidly solidified Al-Mg alloys, it can be said that the supersaturated solid solutions formed in alloys with up to 38.4 at.%Mg or less than ~23 at.%Al, is susceptible to room temperature ageing and subsequent precipitation of metastable phases such as Al_2Mg in α-(Al), and γ' in δ-(Mg). Such precipitation tends to occur at grain boundaries, where diffusion rates are higher owing to the greater vacancy concentration [232]. Rapid solidification of Al-40 at.%Mg results in the formation of a metastable pseudo-icosahedral phase $Mg_{32}Al_{49}$ [236]. The γ phase is formed in alloys with 51 to 63 at.%Mg, and a distorted form of γ is apparently stable between 40 and 51 at.%. It is not clear what phases are formed in the region from 63 to 73 at.%Mg, although there is some indication that an amorphous phase may be formed [231].

3.5.3 Aluminium-Magnesium PVD Coatings

Al-Mg alloy coatings prepared by PVD techniques have been studied by several researchers. The most comprehensive evaluation was conducted by Arnell and Bates at the University of Salford, UK [87-91,98,239]. These authors used unbalanced magnetron sputtering to prepare the coatings and their major reported findings are outlined and discussed below. Other authors have examined Al-Mg alloy coatings prepared by ion plating [186,240], cathodic arc evaporation [187-189], and ion beam assisted deposition [241,242], and this work is also reviewed.

Research at the University of Salford

Arnell and Bates *et al* [87-91,98,239] have been most active in examination of magnetron sputtered Al-Mg coatings. They prepared Al-Mg alloy coatings by sputtering from composite targets [98], and by cosputtering from two separate Al and Mg targets [87-91,239]. Coatings deposited using a single composite target used a magnetron source located 100-150 mm from the substrates, in a 0.65 Pa argon atmosphere and -200V substrate bias [98]. Some degree of energetic Ar ion bombardment of the depositing coatings would therefore have been experienced, although the ion energy distribution would have been broadened due to gas scattering [243]. They examined the relationship between the chemical composition of the coating and the microstructure as revealed by XRD, TEM and SEM [98]. A glassy phase was found to exist in coatings containing approximately 20-70 at.%Mg, and was the only phase present in the range 45-50 at.%Mg. An SEM fracture section of the Al-47 at.%Mg coating is shown in Fig.3.20. None of the equilibrium or metastable intermetallic Al-Mg phases were detected in the coatings, as shown by the schematic XRD patterns in Fig.3.21. It was also claimed that the α-(Al) and δ-(Mg) phases were highly supersaturated with up to 20 at.%Mg and 30 at.%Al respectively [98]. Evidence for this claim came from the lattice parameters measured for the α-(Al) and δ-(Mg) phases in the coatings (Fig.3.22).

More recent publications by Arnell and Bates [87,91], reported that the solubility of Al in δ-(Mg) in cosputtered coatings was limited to 10 at.%. They also found evidence for the γ-$Al_{12}Mg_{17}$ phase in coatings with 60 at.%Mg. Between 60 and 90 at.%Mg, the coatings were a mixture of γ and δ-(Mg) phases, and similarly, the α-(Al) and glassy phases coexisted in the range 20 to 45 at.%Mg. The intermetallic γ phase was thought to be formed by precipitation which occurred after ageing of the coatings [244]. Furthermore, no Ar was detected in any of the coatings, which is probably due to the moderately high substrate temperatures (about 100°C), which would be expected from the high amount of ion bombardment. Such high substrate temperatures would have permitted the implanted Ar to diffuse out during deposition, rather than trapping it in the coating. It may also have accounted for nucleation of the γ phase in these coatings.

Very recently, the results of a thorough study of the corrosion performance of Al-Mg alloy coatings, were reported [239]. Salt spray testing of 8 μm thick alloy coatings on mild steel substrates, indicated an optimum Mg content of 22 at.% (Fig.3.23c). The coatings with less than 32 at.%Mg were found to be susceptible to pitting corrosion, while those with a greater proportion of Mg corroded uniformly. Electrochemical studies of the Al-Mg coatings were also conducted. The corrosion potential E_{corr} of 25 μm thick coatings in 3.5 wt.% $NaCl_{(aq)}$ was monitored over a

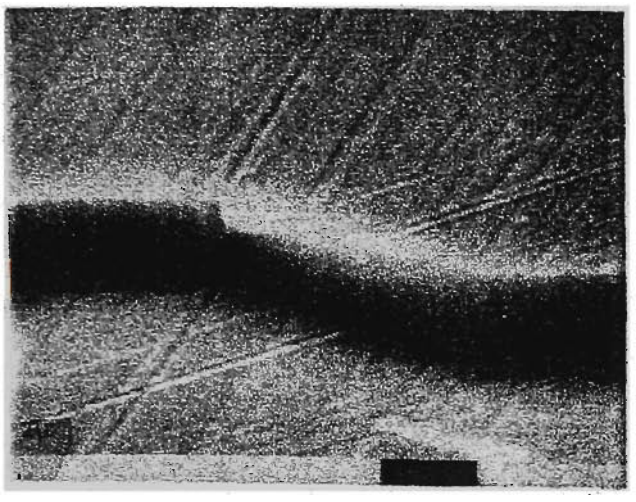

Fig.3.20 ***SEM micrograph*** *of the "glassy" structure of a magnetron sputtered Al-47%Mg coating [88]*

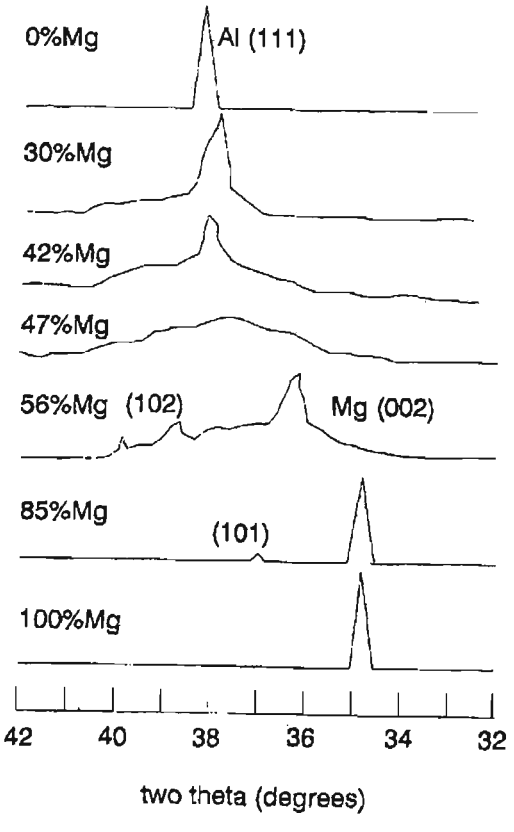

Fig.3.21 ***XRD spectra*** *obtained for various magnetron sputtered Al-Mg coatings [88]*

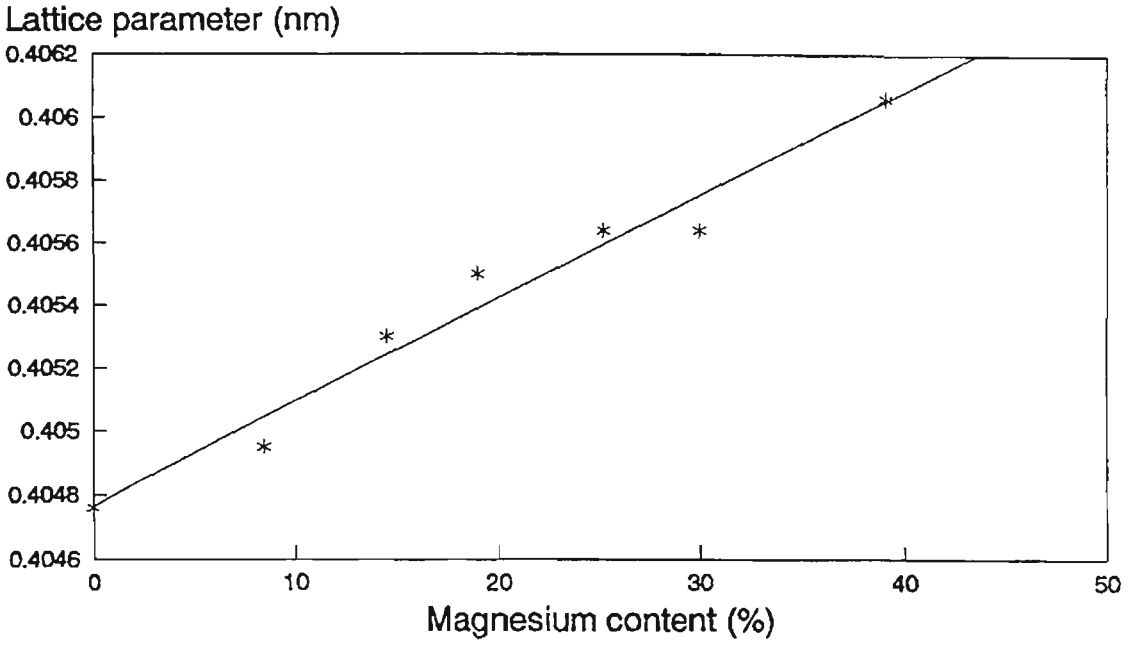

(a)

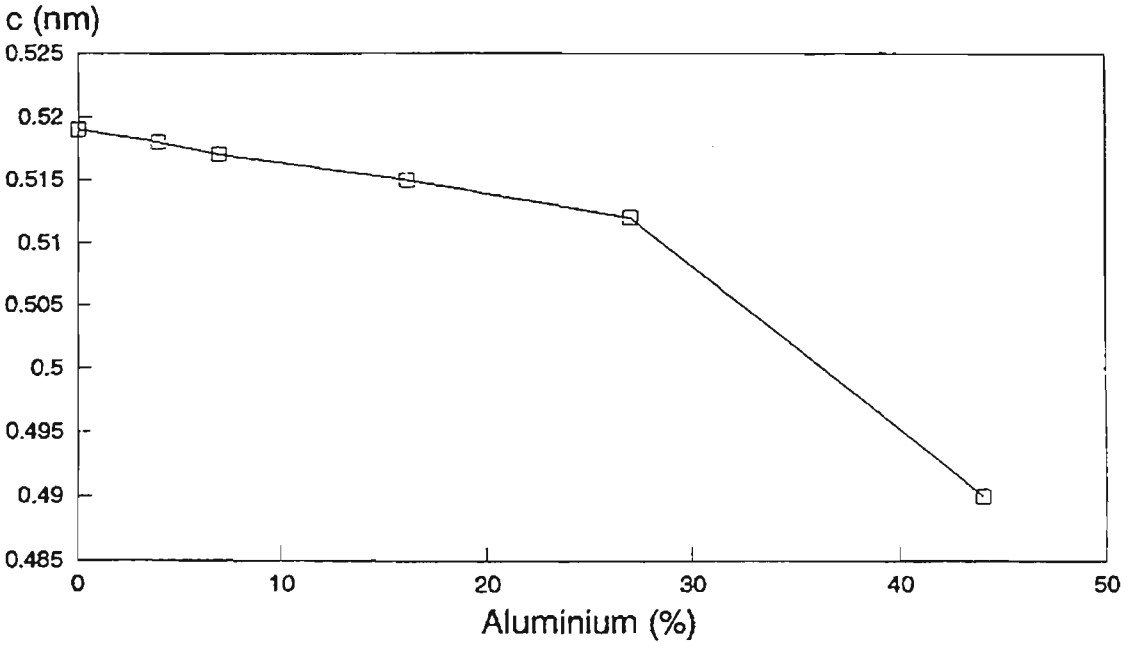

(b)

Fig.3.22 Lattice parameter measurements for various sputtered Al-Mg coatings [98] : (a) a lattice parameter for α-(Al) as a function of Mg content (at.%); and (b) c lattice parameter for δ-(Mg) as a function of Al content (at.%)

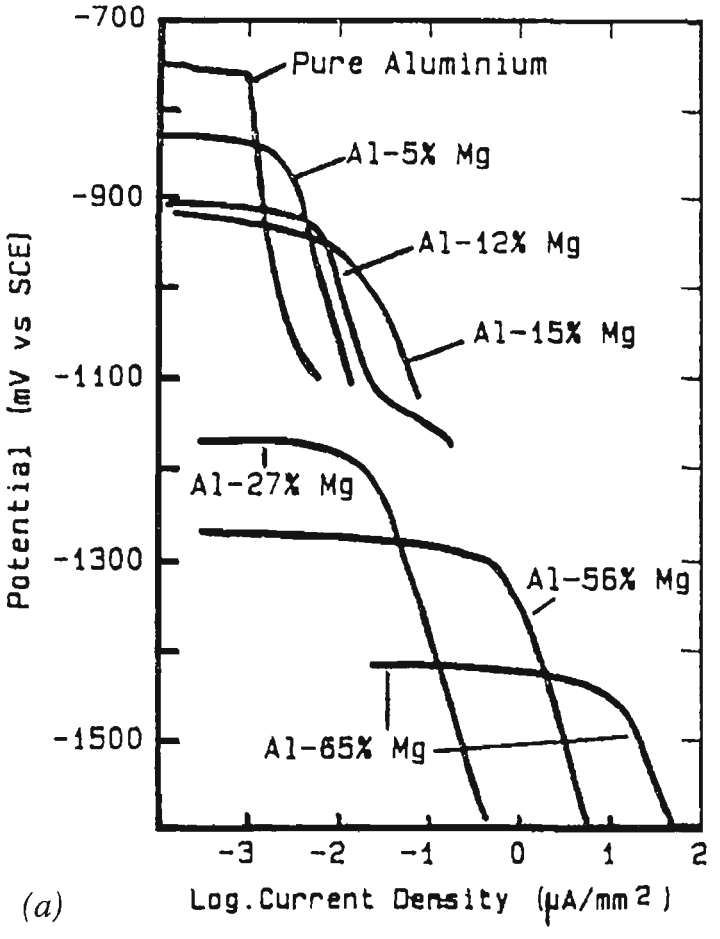

(a)

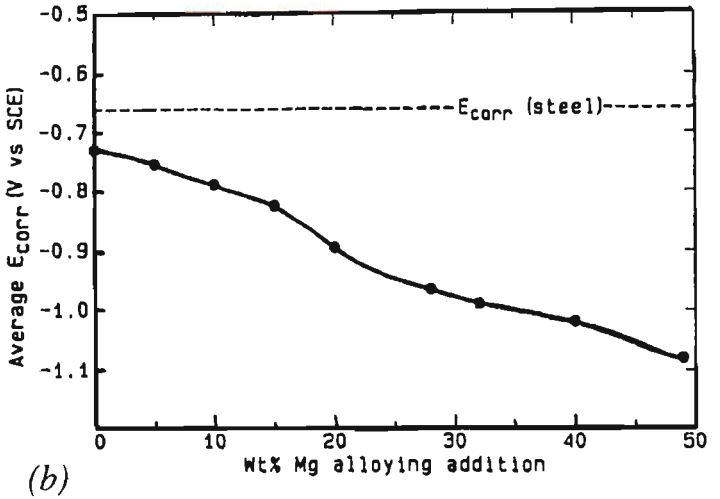

(b)

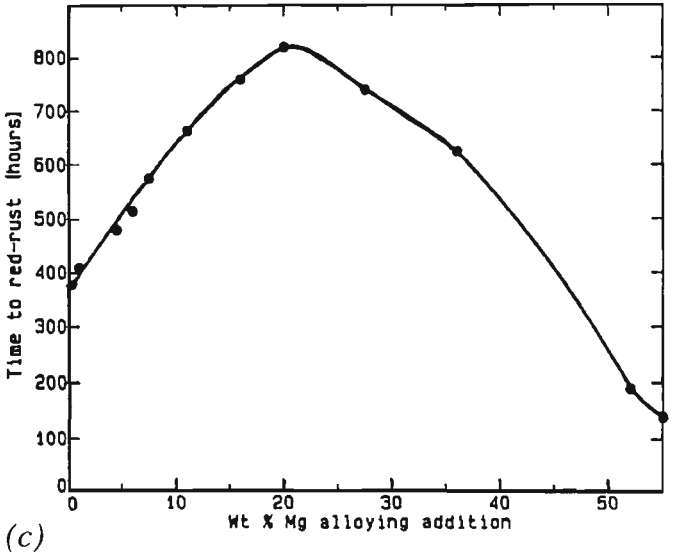

(c)

Fig.3.23 Corrosion behaviour of sputtered Al-Mg coatings [239]
(a) cathodic polarization scans in 3.5 wt.% $NaCl_{(aq)}$;
(b) average corrosion potential in 3.5 wt.% $NaCl_{(aq)}$;
(c) time to red rust after exposure to neutral salt fog.

period of eight days. The average E_{corr} was found to decrease with increasing Mg content of the coatings (Fig.3.23b), and this was interpreted to indicate that the sacrificial protection ability of the coatings was similarly improved. Potentiodynamic cathodic polarization scans revealed that the corrosion of the coatings was under diffusion limited cathodic control (Fig.3.23a). The limiting current density seemed to increase with Mg content of the coatings. This was interpreted to indicate that the barrier protection properties of the coatings were diminished with increasing Mg content. Therefore, the peak in salt spray performance was considered to represent an optimum balance between the barrier and sacrificial properties of the Al-Mg coatings.

Other Research

Nowak and Seyyedi [186] studied ion plated Al-Mg alloy coatings with Mg contents ranging from 0 to 50 at.%. Ion plating was performed with an Ar glow discharge at 1.5 kV and 3.3 Pa, with a source to substrate distance of 130 mm. Considerable Ar^+ ion bombardment of the substrate during deposition would therefore have been experienced. Potentiodynamic measurements in aerated, neutral 3.5% NaCl solutions indicated that all of the Al-Mg alloy coatings exhibited extensive passive regions. A typical scan for an Al-55 at.%Mg coating in comparison with pure Al and Mg coatings is reproduced in Fig.3.24. The 32 at.%Mg composition was considered to be the most resistant to anodic corrosion since it possessed the lowest passive current density. The total length of the passive region was typically about 400 mV and was approximately independent of the Mg content to about 55 at.%. The principal effect of the Mg was to shift the rest potential, although no continuous trends were observed. Reflection electron diffraction seemed to indicate the presence of a spinel oxide on passivated Al-55 at.%Mg alloy films, but this phase did not affect passivation.

Chang *et al* [187-189] considered Al-25 at.%Mg as a coating for the sacrificial corrosion protection of depleted U-alloys. The relevance of this substrate material was discussed in Sect.3.4.5. The coatings were deposited from elemental metallic targets by cathodic arc evaporation. The surface morphology of the coating was typified by a porous structure and numerous macroparticles which are usually encountered with arc deposition. Anodic polarization in aerated 3.5 wt.% NaCl solution indicated that the coatings were anodic to the U substrate. However galvanic coupling between the substrate and coating due to the porous and uneven nature of the coating, meant that complete passivation was not observed.

Lee *et al* [240] performed a similar study to Arnell and Bates [98], except that the Al-Mg coatings were prepared by ion plating with electron-beam evaporation. The substrate temperature was 130-170°C, which was much higher than in [98]. The high

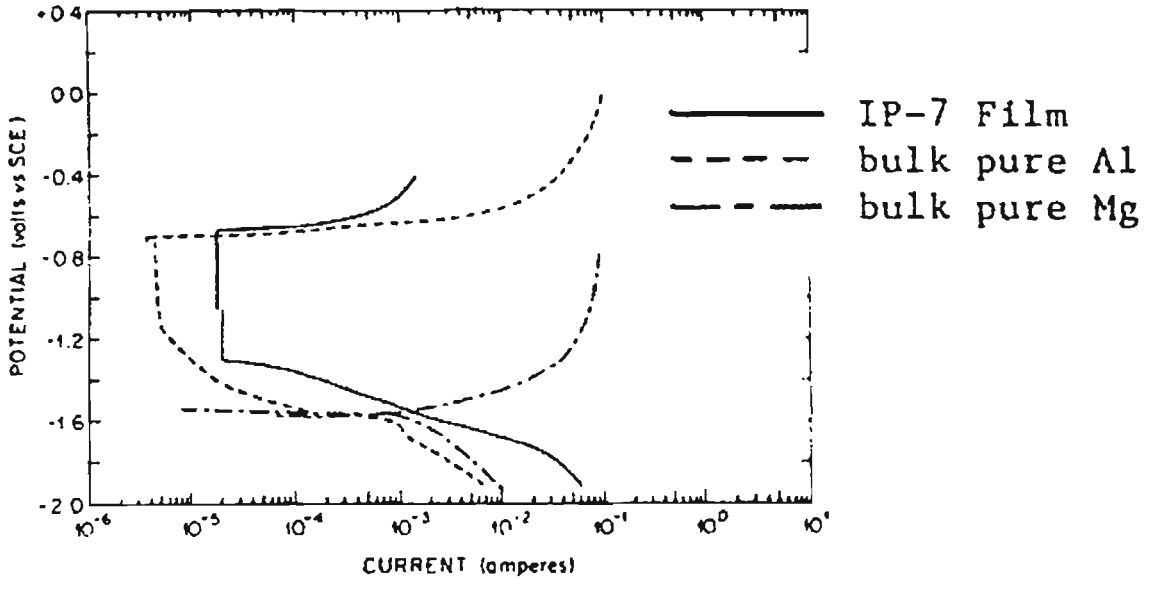

Fig.3.24 Potentiodynamic polarization curves in aerated, neutral 3.5% $NaCl_{(aq)}$ for ion plated coatings. Note that "IP-7" indicates an Al-55at.%Mg coating, and the exposed sample area was 1cm². [186]

temperature was caused by ion bombardment of the substrate due to the application of a 500V Ar discharge. This may have contributed to the observation of some intermetallic phases (Al_2Mg, γ-$Al_{12}Mg_{17}$), in coatings with 12-54 at.%Mg, consistent with work by Arnell and Bates [87,91]. Diffraction peaks for α-(Al) were only detected in the pure Al coating, and it was thought that this phase became amorphous with addition of Mg. The possibility for the burial of Ar ions in the coating was apparently not considered. Shifts in the XRD peak position of the δ-(Mg) phase were attributed to supersaturation. It is difficult to critically assess these microstructural findings since no XRD patterns or *d*-spacing data were presented by the authors. Electrochemical tests of the coatings in 3 wt.% $NaCl_{(aq)}$ seemed to indicate that Mg-3.5 at.%Al coatings had the highest resistance to pitting corrosion, and that increasing the Mg content of the coatings caused the passive current density to decrease. Neither of these results are consistent with other electrochemical studies [186,239].

Enders *et al* [241,242] studied the effect of Ar^+ ion energy on the microstructure of Al-Mg alloy coatings formed by ion beam assisted deposition (IBAD). Al and Mg were evaporated from two separate baths, and the deposited coatings were simultaneously bombarded with an Ar^+ ion beam with an *i/a* ratio of 0.015 and energy ranging from 0 to 20 keV. This equated to a maximum energy per arriving atom of about 300 eV. It was claimed that increasing the energy of ion bombardment increased the solubility of Mg in the Al-rich phase, while decreasing the amount of Mg in a coexisting amorphous phase. However, the potential effect of preferential resputtering seems to have been ignored in making such conclusions, as the actual compositions of the coatings were not measured. The interpretation was based solely on glancing angle XRD measurements, in which shifts in peak position were assumed to be caused only by solid solutions effects, while ignoring residual stress and preferred orientation effects. The metastable Al_2Mg phase was claimed to be present in an Al-60 at.%Mg coating, but this was based on matching of only one diffraction peak, and is therefore unsubstantiated.

As a general statement, it appears that all of the investigations of Al-Mg alloy PVD coatings have automatically incorporated ion assistance. The reason for this is not immediately obvious, although it probably relates to the common experience that ion assistance is required for the production of dense Al coatings [174]. However, very little attention seems to have been paid to the effect of ion assistance on the composition of the resultant coatings. This is despite the fact that it is very well established that energetic particle bombardment during the deposition of multi-component alloy coatings invariably results in modification of the coating stoichiometry due to preferential resputtering [83,141]. Furthermore, the possibility for the burial of implanted ions has also been ignored in all studies of Al-Mg coatings. The influence of buried carrier gas (eg. Ar) in

the coatings would be expected to have some influence on their microstructure. Finally, studies of the corrosion performance of these coatings have concentrated on 3.5 wt.% $NaCl_{(aq)}$ solution which, although being representative of seawater exposure, does not represent typical atmospheric exposure conditions.

3.6 Zinc-Magnesium Binary Alloys

3.6.1 Equilibrium Phase Diagram

The equilibrium phase diagram for the Mg-Zn binary system is shown in Fig.3.25 [245]. This diagram has been revised in recent years [246], but the most current form was only available in terms of weight percent. Hence, the atomic percent diagram of [245] is reproduced here. In addition to the terminal solid solutions (Mg) and (Zn), the Mg-Zn system is characterised by at least five stable intermetallic phases: $Mg_{51}Zn_{20}$ ("Mg_7Zn_3"), MgZn, Mg_2Zn_3, $MgZn_2$ and Mg_2Zn_{11} [246].

The terminal solid solutions in the Mg-Zn system have very little solid solubility at room temperature. The (Mg) phase can contain a maximum of 2.4 at.%Zn in solid solution at the 340°C, but this decreases to about 0.6 at.%Zn at room temperature [246]. Others have reported slightly higher solid solubility limits for (Mg), with up to 3 at.%Zn [225,247]. The published results for various studies on the lattice parameters of (Mg) in the Mg-Zn system are shown in Fig.3.26 [225,247-249]. This data also includes some results for melt-spun dilute Mg-Zn alloys [249]. The lattice parameters of the (Mg) phase decrease linearly with Zn additions according to the following equations:

$$c \text{ (nm)} = 0.52112 - 8.145\text{x}10^{-4} \text{ Zn (at.\%)} \quad (< \sim 2.8 \text{ at.\%Zn}) \tag{3.7}$$

$$a \text{ (nm)} = 0.32094 - 4.817\text{x}10^{-4} \text{ Zn (at.\%)} \tag{3.8}$$

$$c/a = 1.6238 - 2.808\text{x}10^{-4} \text{ Zn (at.\%)} \tag{3.9}$$

The (Zn) phase has a maximum solid solubility of 0.3 at.%Mg at 364°C [246], and contains less than 0.0007 at.%Mg at room temperature [193]. Reliable lattice parameter data for (Zn) solid solutions in the Mg-Zn system could not be found in the literature. However, on the basis of the Goldschmidt radii [250], it is likely that the presence of Mg in (Zn) solid solution would cause an increase in the lattice parameters. Both (Mg) and (Zn) solid solutions possess a close-packed hexagonal structure ($P6_3/mmc$).

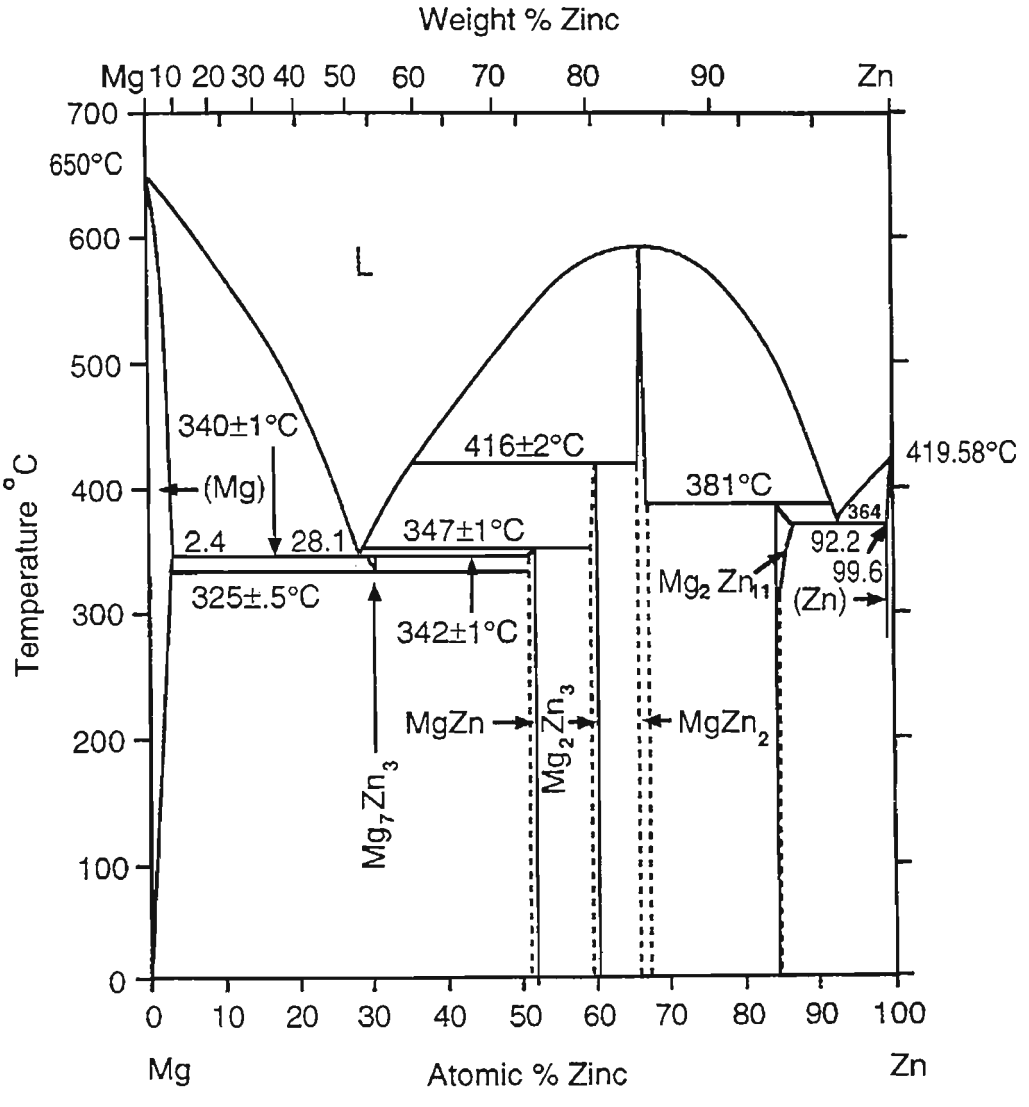

Fig.3.25 Mg-Zn binary phase diagram [245]

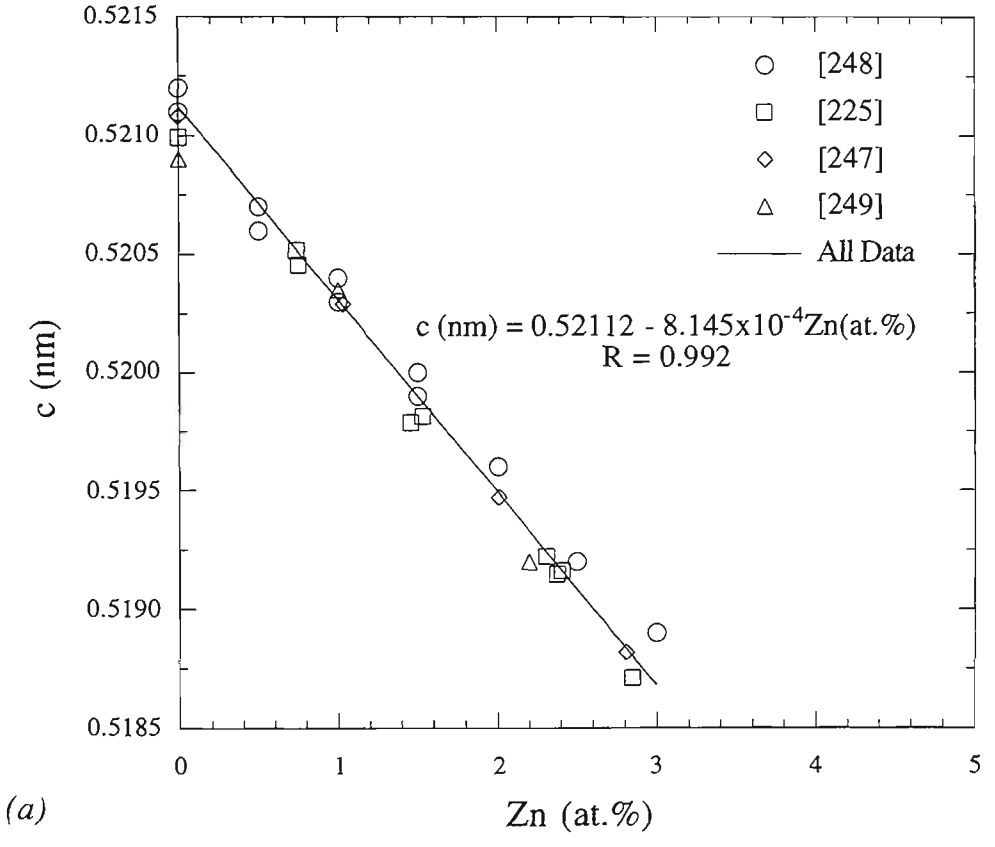

(a)

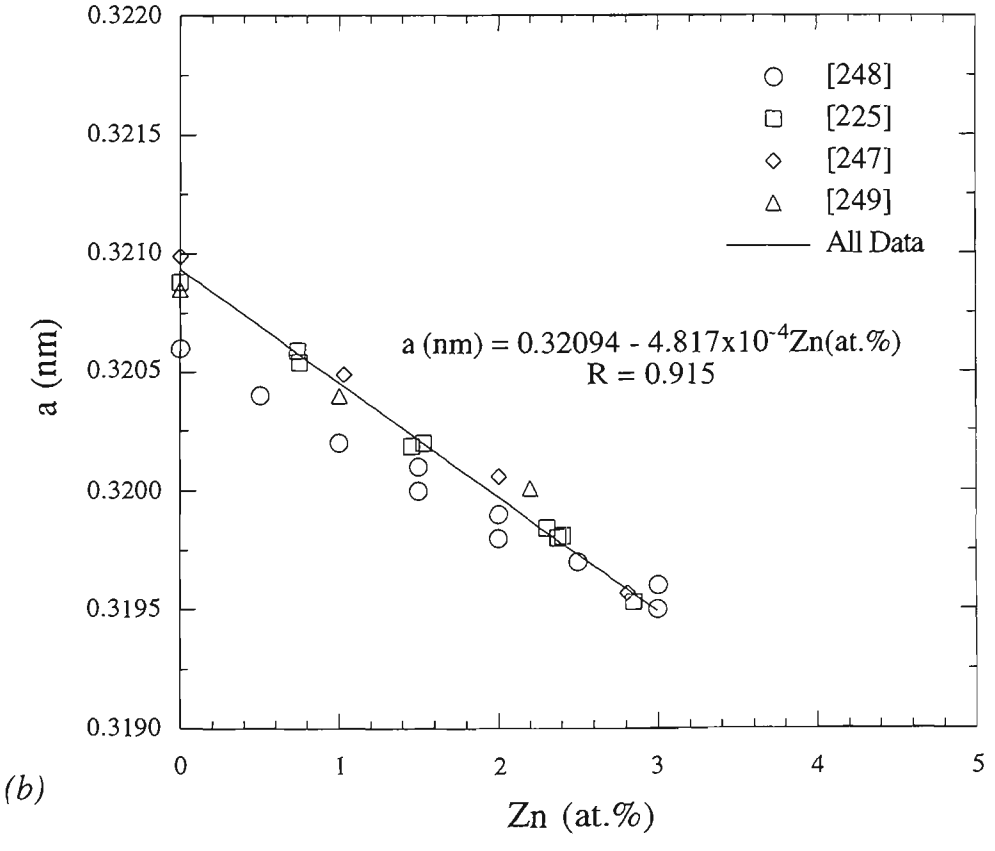

(b)

Fig.3.26 Lattice parameters at room temperature of (Mg) solid solution in Mg-Zn alloys as a function of solute content; (a) c-parameter, (b) a-parameter, (c) c/a ratio. *(see next page)*

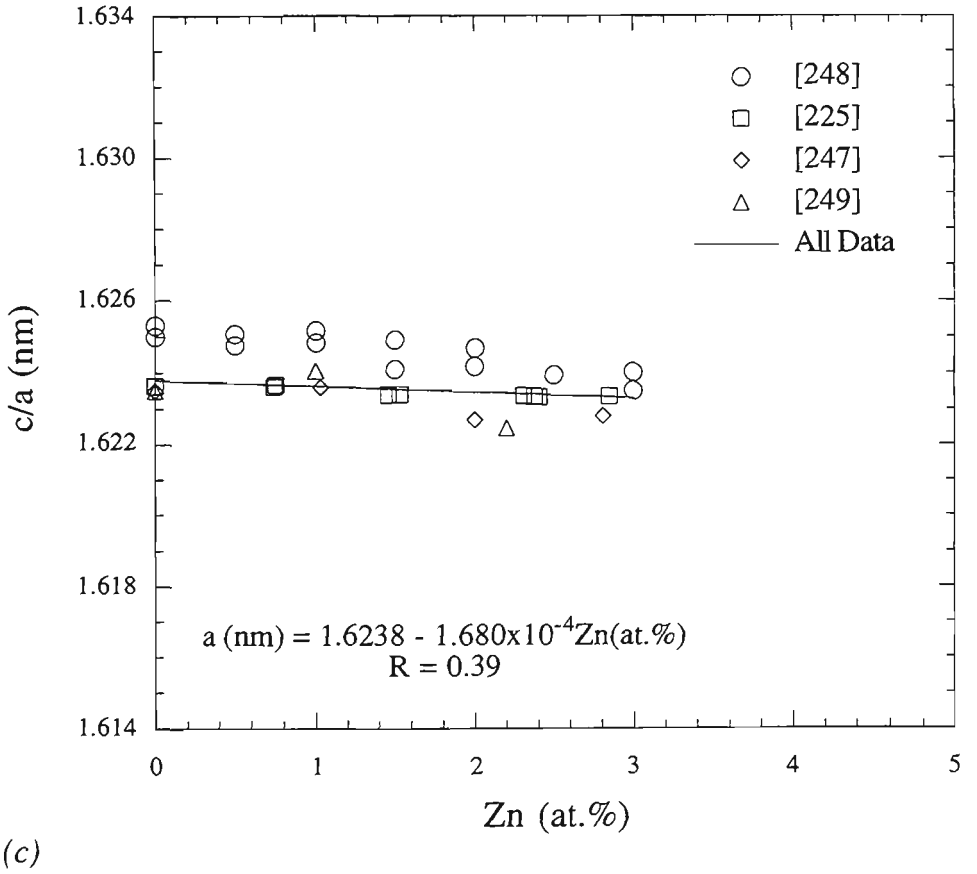
1.634
1.630
1.626
1.622
1.618
1.614
c/a (nm)
0
1
2
3
4
5
Zn (at.%)
[248]
[225]
[247]
[249]
All Data
a (nm) = 1.6238 - 1.680x10-4Zn(at.%)
R = 0.39

(c)

Under equilibrium conditions, the phase "Mg_7Zn_3" is only stable at a narrow temperature and composition range [246]. It forms during cooling by peritectic reaction between MgZn and the liquid phase at 342°C, and decomposes by eutectoid reaction at 325°C, but can be easily retained at room temperature because its decomposition is very sluggish. This phase is also one of the products of the eutectic reaction that occurs at 28.1 at.%Zn and 340°C. Recently this phase has been renamed $Mg_{51}Zn_{20}$ (28.2 at.%Zn) after a thorough identification of the crystal structure of an annealed and quenched alloy [251]. It was established that $Mg_{51}Zn_{20}$ has an orthorhombic unit cell (*Immm*) with the following lattice parameters: a=1.4083 nm, b=1.4486 nm, c=1.4025 nm. The crystal structure was described as an arrangement of distorted icosahedral coordination polyhedra, to which all except one of the atomic sites belong. The individual atom site arrangements are described in detail in [251]. The composition of the $Mg_{51}Zn_{20}$ chemical unit differs slightly from "Mg_7Zn_3", and is within 0.1 at.% of the eutectic composition.

A metastable phase has been reported for Mg-Zn alloys containing 30 at.%Zn [252]. The phase was produced by solution treating the alloy at 330-340°C, followed by slow cooling at a rate of 20 $K.hr^{-1}$. The crystal structure was found to be tetragonal with a=2.027 nm and c=1.064 nm. Mechanical shock to the alloy, such as grinding or hammering, resulted in transformation to $Mg_{51}Zn_{20}$.

The MgZn phase was originally thought to contain 50 at.%Zn, but has since been found to be based on Mg-51.4 at.%Zn [246]. It forms during cooling by peritectic reaction between Mg_2Zn_3 and the liquid phase at a temperature of 347°C. The phase is stable at room temperature and has a rhombohedral (hex.) unit cell with lattice parameters of a=2.5578 nm and c=1.8147 nm [197,252].

Mg_2Zn_3 has a composition of 60 at.%Zn as suggested by the formula name [246]. It forms during cooling by peritectic reaction between $MgZn_2$ and the liquid phase at a temperature of 416°C. The phase is stable at room temperature and has a triclinic unit cell (*C2/m*) with the following lattice parameters: a=1.724 nm, b=1.445 nm, c=0.52 nm, α=96°, β=89°, γ=138° [197].

$MgZn_2$ is a Laves phase which has a composition of 66.7 at.%Zn, although it can range from 66.1 to 67.1 at.%Zn [246]. It melts congruently at a temperature of 590°C, and has a hexagonal unit cell ($P6_3/mmc$) with lattice parameters a=0.52225 nm and c=0.85684 nm [197]. The arrangement of atoms in this type of Laves phase has been thoroughly characterized and the reader is directed towards standard metallic structure texts such as [253] for further information.

The phase Mg_2Zn_{11} has a composition of 84.7 at.%Zn [246]. It forms during cooling by peritectic reaction between $MgZn_2$ and the liquid phase at a temperature of 381°C. The phase is stable at room temperature and has a cubic structure ($Pm\bar{3}$) with 39 atoms per unit cell, and a=0.8552 nm [197]. This phase is also one of the products of a eutectic reaction at 92.2 at.%Zn and 364°C.

Another intermetallic phase for the Mg-Zn system is reported in the JCPDS files but not in the phase diagrams; Mg_4Zn_7 (63.6 at.%Zn) which has a monoclinic unit cell ($C\bar{2}/m$) with the following lattice parameters: a=2.596 nm, b=0.524 nm, c=1.428 nm, β=102.5° [197]. Such a composition would fall between the Mg_2Zn_3 and $MgZn_2$ phases. It is not known if this phase has been experimentally observed under equilibrium conditions or if it is a metastable variation of an equilibrium phase.

3.6.2 Rapid Solidification

The terminal solid solutions in Zn-Mg alloys have only received limited attention in rapid solidification studies [249,254,255]. Most research has been directed towards the amorphous phase which can be formed in alloys near compositions of Mg-28 at.%Zn [252,256-260]. However, it has been established that the solid solubility of Zn in (Mg) can be extended by rapidly quenching the alloys from the liquid phase, although the level of supersaturation is much less than for Al-Mg alloys (Sect.3.5.2).

The solid solubility of Mg in (Zn) that can be attained by rapid solidification was examined by Liu *et al* [254]. Five Zn-based alloys were prepared containing from 1.3 to 7.2 at.%Mg. All of the melt spun ribbons consisted of (Zn) solid solution with various proportions of Mg_2Zn_{11} at grain boundaries, and $MgZn_2$ dispersed through the (Zn) grains. The solid solubility of Mg in (Zn) was extended to 7.2 at.% at the chill surface of the ribbons; this composition is close to the eutectic composition of 7.8 at.%Mg. However heat treatment at temperatures above 200°C resulted in the rapid decomposition of the supersaturated solid solution by precipitation of Mg_2Zn_{11}. The $MgZn_2$ in the as-quenched alloys also dissolved during heat treatment.

The microstructure and mechanical properties of rapidly solidified Zn-Mg alloys were examined by Themines *et al* [249,255]. Single phase (Mg) solid solution supersaturated with up to 2.2 at.%Zn, was possible by rapid quenching. Alloys with 13 and 14 at.%Zn consisted of a two phase mixture of saturated (Mg) and Mg_2Zn_3. The (Mg) phase in these two alloys was found to have a Zn solubility approximately equal to the equilibrium limit of about 2.4 at.%. Alloys with Zn concentrations between 2.2 and

13 at.%Zn were not examined however, so the precise limit of single phase (Mg) supersaturation is not known. Early research on quenched Zn-Mg alloys [225,247,248] suggested that the solubility limit was slightly higher at about 2.8 at.%Zn (Sect.3.6.1). Hence it would appear that rapid solidification cannot extend the Zn solubility in (Mg) phase beyond the equilibrium limit.

The Zn-Mg alloy system has received a great deal of attention from those researchers involved in studying the amorphous metallic structure. This is because it has been found that an amorphous phase can be formed in Zn-Mg alloys by rapid solidification, particularly with compositions near the deep eutectic at Mg-28%Zn [256]. The range of compositions over which the amorphous phase can be formed extends from 22.5 to 35 at.%Zn [257]. The combination of low liquidus temperature and the difference in size between Mg and Zn atoms, is believed to contribute to the formation of the amorphous phase [256]. Decomposition of the amorphous phase in the Zn-Mg system, however, has been the focus of greatest attention. This is because of the relatively low crystallization temperature (~80°C), which makes the Zn-Mg system ideal for studies of crystallization processes [252], and for examination of the room temperature stability of the amorphous phase [259].

The amorphous state in Mg-30 at.%Zn alloys was reported by Ito *et al* [258] to consist of a random aggregate of chemical and structural units which have polyhedral configurations, which are similar to those in crystalline $Mg_{51}Zn_{20}$. During annealing, these units first change their shape and size to enhance coherency with their neighbouring units, until they eventually establish the long range order of the crystalline $Mg_{51}Zn_{20}$. Therefore, the structure of the $Mg_{51}Zn_{20}$ phase was regarded as an important key to understanding the structure of the liquid state just above the eutectic temperature and that of the rapidly quenched amorphous state.

Andonov and Chieux studied the structure of a eutectic Mg-28 at.%Zn alloy in the liquid and amorphous states [261], and the crystallization processes in the amorphous, liquid and undercooled states [260]. The amorphous phase was found to have similar chemical short range order to crystalline $Mg_{51}Zn_{20}$, except for some small differences due to a preference for Zn-Zn atomic pairs. The liquid phase was more disordered than the amorphous phase, but similar preferences in short range order were observed. It was concluded [260] that the structural differences between the disordered states in the liquid and amorphous states, were due to differing sizes of small well organized aggregates. These randomly distributed aggregates were considered to be partially structured but not crystalline. This work seems to confirm the earlier studies of Ito *et al* [258].

Furthermore, the crystallized state was found to be independent of the initial disordered state, such that the $Mg_{51}Zn_{20}$ was always the final atomic arrangement [260].

The room temperature stability of amorphous Zn-Mg alloys in the composition range from 25 to 35 at.%Zn was evaluated by Calka [259]. The ribbons of amorphous Zn-Mg were evaluated before and after six years of room temperature ageing in evacuated silica containers. After the six years of storage, the fully amorphous structure was only observed for the composition Mg-35 at.%Zn. Some amorphous phase was still present in the other alloys, but decomposition was evident in them. The Mg-23 at.%Zn alloy was mostly amorphous but had some Mg precipitated on the ribbon surface. Ribbons with 25, 28 and 30 at.%Zn had a mixture of Mg, $Mg_{51}Zn_{20}$ and MgZn. Thermal analysis of the aged ribbons indicated that different mechanisms of crystallization might exist on each side of the peritectic composition for $Mg_{51}Zn_{20}$. Calka also suggested that dissolved inert gases used in the preparation of master alloys and ribbons, might act as a third alloying element, and affect the stability of the amorphous phase.

The crystallization behaviour of amorphous and liquid Mg-30 at.%Zn was investigated by Khan [252] using dynamic temperature XRD. It was found that the sequence of phases which crystallized from the amorphous state as temperature was increased, was the same as that of the phases which formed from the liquid state as it was cooled. The first crystalline phase to form in the amorphous alloy was always $Mg_{51}Zn_{20}$. This phase began to crystallize at a temperature of about 70°C, using a heating rate of 20 $K.hr^{-1}$. Continued heating of the alloy resulted in decomposition of the $Mg_{51}Zn_{20}$ into MgZn and (Mg) at a temperature of about 180°C. These authors were also responsible for the identification of the crystal structure of the MgZn phase [197,252].

3.6.3 Zinc-Magnesium PVD Coatings

It has been firmly established that rapid solidification of Zn-Mg melts can produce amorphous alloys. The range of compositions that provide single-phase amorphous ribbons is restricted to 22.5 to 35 at.%Zn [262]. However, it is known that amorphous Zn-Mg can also be produced by vapour deposition, and the composition range extended considerably with limits of 10 to 90 at.%Zn [263].

Hauser and Tauc [263] prepared a wide range of Zn-Mg alloy coatings by sputtering alloy taregts onto sapphire substrates which were cooled with liquid nitrogen. Ar was used as the sputter gas, at a pressure of 4 Pa. The thickness of the coatings ranged from 0.4 to 3.5 μm. The alloy sputter targets were prepared by inductively melting the elemental constituents under an Ar atmosphere. Large density differences

between Mg and Zn required the use of an Mg-5 at.%Zn master alloy, which was remelted with additional Zn to obtain the required target compositions. The compositions of the deposited coatings were evaluated by XRF of the sputter target surfaces, and it was assumed that the target composition was replicated in the coatings. XRD of the coatings were performed at liquid nitrogen temperature (-196°C) without exposing the coatings to ambient temperature. The coatings were found to be amorphous over a very wide composition range, from 10 to 90 at.%Mg. It was suggested that the stability of the amorphous phase may have been partially attributed to the incorporation of about 1 at.% Ar during deposition. Only the coatings prepared from pure Mg and Zn targets, and from Mg-5 at.%Zn, were found to contain crystalline phases. The XRD results for the Mg-5 at.%Zn coating were perplexing, however, since they indicated the presence of (Zn) phase with a strong <10.1> fibre texture. In comparison, melt-spun alloys of this composition were found to consist of supersaturated (Mg) at the fastest quench rates [254]. The cause of this apparent discrepancy is not known.

Thèye *et al* [262] deposited several amorphous Zn-Mg alloy films by coevaporation under ultra-high vacuum on sapphire substrates held at liquid nitrogen temperature. Coatings were prepared with compositions ranging from 26 to 35 at.%Zn. Microstructural studies incorporating TEM were attempted but rapid oxidation of the thin films at ambient atmosphere resulted in electron diffraction patterns which were considered too difficult to analyze, and no structural study was made. However, the presence of broad asymmetric rings in the diffraction patterns indicated that these films were amorphous. The coatings were also found to crystallize at about 80-90°C, by the formation of the $Mg_{51}Zn_{20}$ phase. Measurements of electrical resistivity seemed to indicate that the coatings had high "defect" densities, with the level of defects being dependent on deposition conditions.

Of greater interest for the corrosion protection of sheet steels is the work on Zn-rich compositions of Zn-Mg alloy coatings prepared by PVD. In recent years there has been considerable interest in such coatings by large Japanese steel companies such as Kobe [23,37-39,264-266], and Nisshin [24]. It appears that some Korean steel companies are also pursuing this technology [45]. The majority of this work is considered "commercial in confidence" and many of the details are unfortunately not available for public scrutiny. However, some published papers and US patents provide an indication of the work that has been conducted. The work by Nisshin is discussed in Sect.3.8 as it relates to multilayer rather than alloy coatings.

The Zn-Mg alloy coatings studied by Kobe were prepared using a pilot line facility capable of coating steel strip which was passed continuously above the evaporation

sources; the strip width was 150 mm, strip thickness was 0.7 mm, strip length was 400 m, and the linespeed ranged from 1 to 20 m.min^{-1} [37,38]. Zn and Mg were evaporated from separate crucibles by electron beam bombardment [265]. Some Zn-Mg coatings were also produced by evaporation of an alloy source, in which case the coatings were found to be deficient of Mg. A range of steel strip temperatures were used for various experiments, but typically it was at least 200°C. Coatings that have been reported in the literature consist of Zn-33 at.%Mg with a Zn overlayer [265], or a uniform Zn-23 at.%Mg coating [37,38,265,266]. The US patents assigned to Kobe Steel [23,39] provide a much greater insight into the range of coatings examined. Schematic X-ray diffraction patterns were presented for Zn-Mg alloy coatings with compositions ranging from 13 to 85 at.%Mg. All coatings were found to be crystalline and contained various intermetallic phases (Table 3.1). This is probably because of the high deposition temperature, such that significant diffusion occurred in the coating after deposition. However, the phases detected differed considerably from those expected on the basis of the equilibrium phase diagram. Unfortunately the XRD patterns presented by these authors were only schematic, and could not be critically assessed. Amorphous coatings were not reported, counter to the findings of previous authors [262,263] who used lower substrate temperatures.

Table 3.1 Summary of phases present in evaporated Zn-Mg coatings deposited on substrates held at a temperature of between 150 and 250°C [23].

Mg (at.%)	Phases present in coatings				
	(Zn)	Mg_2Zn_{11}	$MgZn_2$	MgZn	(Mg)
13.1	•	•	•		
26.1			•	•	
40.3			•	•	
42.4			•	•	•
59.4			•	•	•
85.3				•	•

Numerous Zn-Mg coating compositions between 1 and 65 at.%Mg were prepared and tested for their corrosion performance [23,39]. Excellent corrosion resistance was claimed, provided that the (Mg) phase was not present in the coatings, and the (Zn) phase was also avoided. Hence the optimal Mg content was claimed to be from 12 to 47 at.% [23]. Salt spray testing indicated that Zn-Mg coated steel sheets were more corrosion resistant than electrogalvanised steel and other PVD coated steels [266]. This was due to the more active corrosion potential for Zn-Mg (about -1100 mV vs. SCE), which provided the substrate with galvanic protection. Also the corrosion product layer was

found to consist of a very dense protective film of $ZnCl_2.4Zn(OH)_2$ which covered the coating surface, rather than the more common ZnO. It was thought that the formation of the chloride corrosion product was assisted by the dissolution of Mg from the coating [265]. There was no preferential corrosion of Mg provided that the (Mg) phase was absent [37,38].

Jun *et al* [45] examined a wide range of alloy and layered coatings prepared by PVD. Several different Zn-Mg alloy coatings were vapour deposited onto sheet steel substrates by means of resistance evaporation using two separate baths. The coating weight was typically 20 to 30 $g.m^{-2}$, and the optimum substrate preheating temperature was 150 to 250°C. Coatings with up to 54 at.%Mg were prepared, and the adhesion of all coatings were poor. X-ray diffraction of the coatings was claimed to have indicated the presence of Zn, $MgZn_2$ and Mg_2Zn_{11}, although the diffraction scans were not presented for evaluation. Salt spray testing indicated that the optimum composition was 19 to 27 at.%Mg, which showed a time to red rust of about 1200 hours for a ~1.5 μm thick coating (20-30 $g.m^{-2}$).

3.7 Aluminium-Magnesium-Zinc Ternary Alloys

3.7.1 Equilibrium Phase Diagram

The Al-Mg-Zn ternary system has been reviewed several times [195,267], and the most recent set of phase diagrams is reproduced in Fig.3.27 [195]. These diagrams are shown in weight percent, with the liquidus projection plus isothermal sections at 335°C and 20°C. The latter diagram has not been altered since it was reviewed in 1936 [268], and therefore does not include the Mg_2Zn_3 phase which was incorporated into the Mg-Zn binary system in more recent times [207]. The isothermal section at 20°C is reproduced in Fig.3.28 in terms of atomic percent, and the Mg_2Zn_3 phase has been added in the expected location.

There seem to be at least three ternary phases in the Al-Mg-Zn alloy system [197]. Only the *T*-$Mg_{32}(Al,Zn)_{49}$ phase (also known as $Al_2Mg_3Zn_3$) is stable at ambient temperature [195]. This ternary phase melts by decomposition, and the liquidus temperature at such compositions ranges from about 480 to 540°C (Fig.3.27a). The *T* phase has a complex cubic crystal structure (*Im3*) with *a* of 1.422 nm, and 162 atoms per unit cell [197,267]. The ideal formula contains 39.5 at.%Mg, but the actual content is variable, generally being around 38 at.%. As suggested by the formula name, the Al and Zn are relatively interchangeable in the *T* phase, such that the Zn content can range from

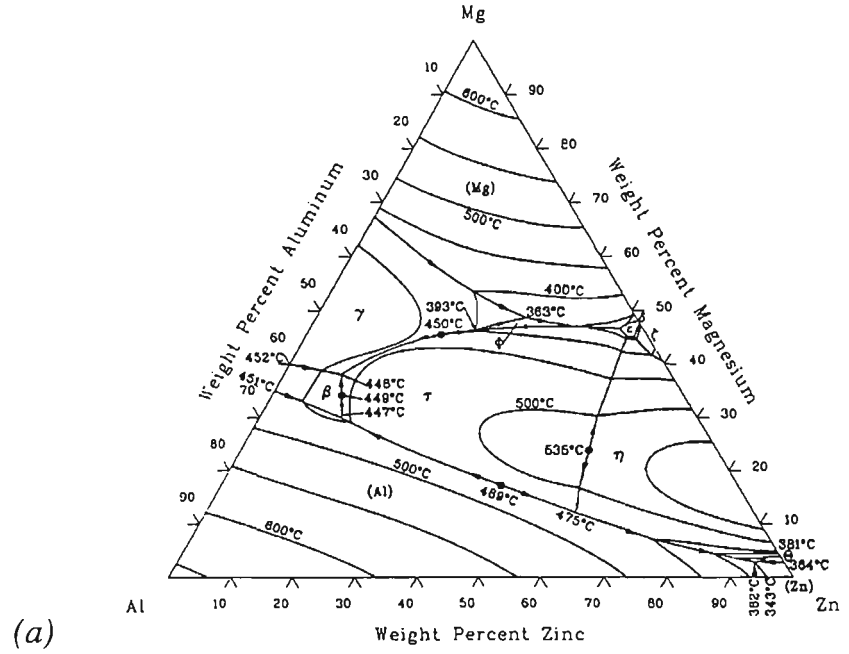

(a)

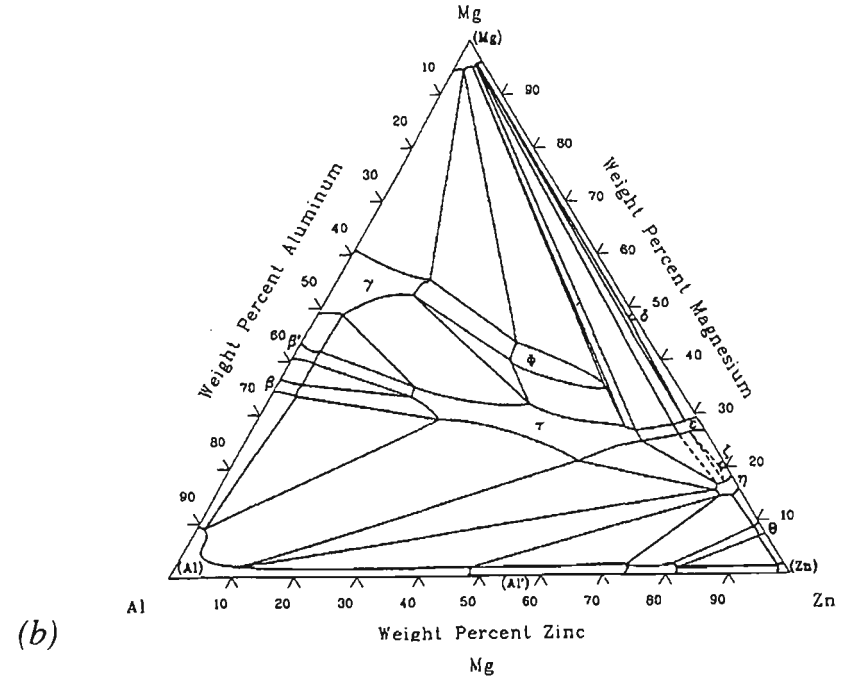

(b)

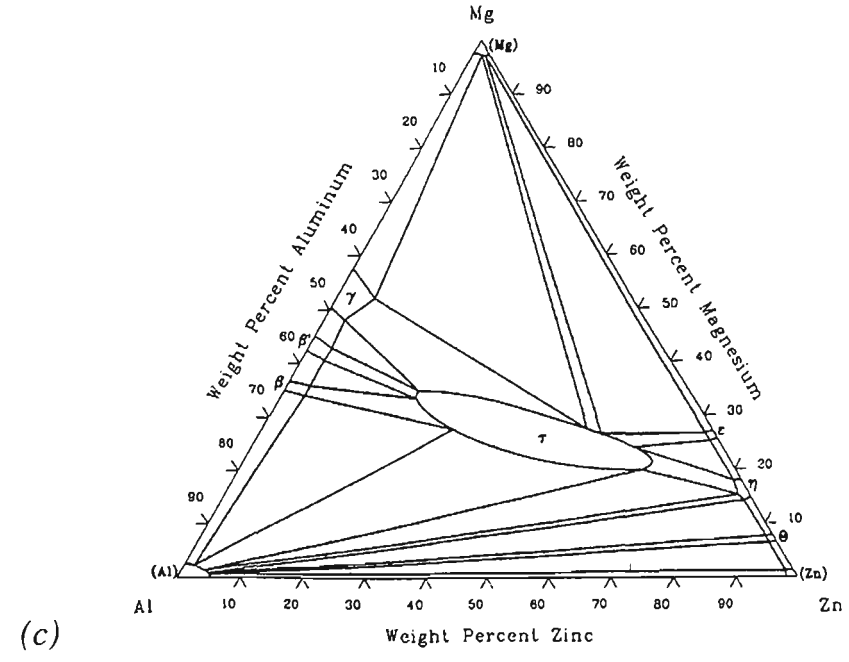

(c)

Fig.3.27 Ternary phase diagrams for the Al-Mg-Zn system (wt.%): (a) liquidus projection; (b) isothermal section at 335°C; (c) isothermal section at 20°C. [195]

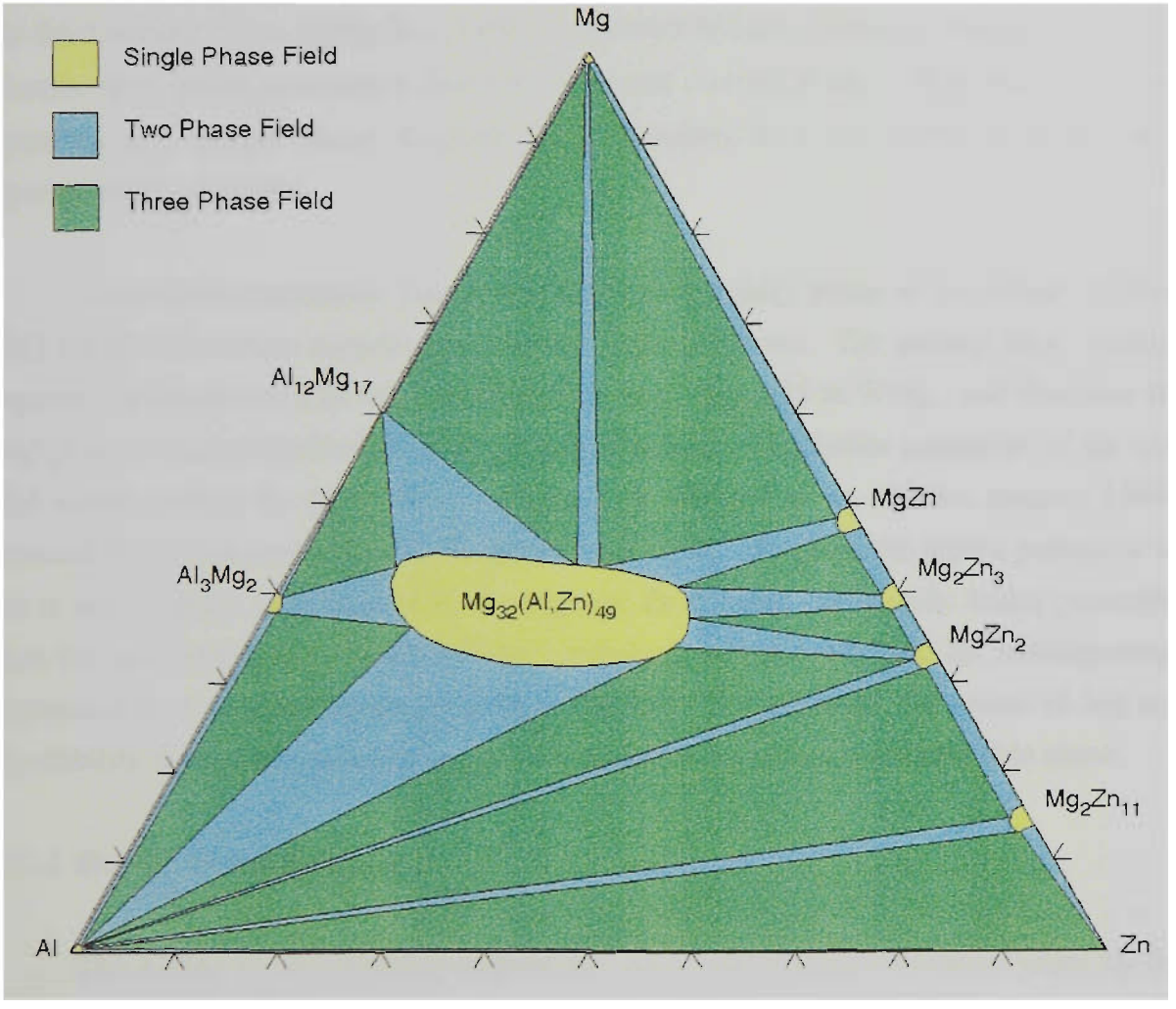

Fig.3.28 Isothermal section at 20°C for the Al-Mg-Zn ternary system represented in terms of atomic percent, from [195,268]

about 10 to 40 at.%, with a reciprocal range of Al content from about 50 to 20 at.% (Fig.3.28).

A second ternary phase ϕ-$AlMg_2Zn$ is stable at elevated temperatures, as shown in Fig.3.27b. The crystal structure of this phase has not been determined but *d*-spacing data is available in standard tables [197]. The ϕ phase is not stable at ambient temperature. The third ternary phase $AlMg_4Zn_{11}$ [197] is reported to have a complex hexagonal crystal structure with lattice parameters a=0.4960 nm and c=1.4020 nm. This phase does not appear on any ternary phase diagrams, and therefore it is not certain if it has been experimentally observed.

Some lattice parameter data is available for the (Mg) phase in the ternary system [225] but this was of no concern to the present investigation. The ternary alloy coatings prepared for this thesis (Ch.11), contained less than about 35 at.%Mg, and therefore the (Mg) phase was not expected to occur in these coatings. The lattice parameter of the (Al) solid solution along the (Al)/(Al)+*T* boundary is affected in an additive manner [269], presumably in close accordance to Vegard's Law [204]. However the lattice parameter of (Al) is not invariant with respect to the Mg and Zn content. A specific lattice parameter value for (Al) corresponds to an infinite number of different Mg and Zn combinations, represented by a straight line on the ternary diagram. Consequently, the extent of Mg and Zn solubility in the (Al) phase cannot be determined from lattice parameter data alone.

3.7.2 Rapid Solidification

The Al-Mg-Zn ternary alloy system has been made famous in recent years by the discovery of a quasi-crystalline icosahedral phase in rapidly solidified alloys that would ordinarily produce *T* phase by conventional casting [234]. Quasi-crystals are a new class of materials that show five-fold rotational symmetry and no translational symmetry. Such symmetry is forbidden in conventional crystallography since long range order with such a unit cell is not possible without the introduction of frustration [270]. However, it has been shown that the quasi-crystalline structure can be represented by a novel form of lattice based on Penrose tiling in three dimensions [271]. Details on the crystallographic and metallographic structures of the quasi-crystalline phase in rapidly solidified Al-Mg-Zn alloys are available in [234,237,238,270-272]. Interestingly, the tendency for the formation of quasi-crystals in $Mg_{32}(Al,Zn)_{49}$ alloys has been attributed to a high proportion (about 61%) of icosahedrally coordinated atoms in the *T* phase crystal structure [272].

The stability of the quasi-crystals in rapidly solidified $Mg_{32}(Al,Zn)_{49}$ alloys have been examined by Chandra and Suryanarayana [272], by annealing at various temperatures for 1 hour. They found that the quasi-crystals were stable at 150°C, and were partially decomposed into *T* phase at 200°C. The quasi-crystalline structure was completely transformed on annealing at 250°C. Transformation to the crystalline structure resulted in the development of fine pores and planar defects due to the lower density of the quasi-crystalline state.

3.7.3 Aluminium-Magnesium-Zinc PVD Coatings

It appears that only very dilute ternary Al-Mg-Zn coatings have been previously deposited by PVD techniques. Nieh and Wadsworth [182,183] studied some magnetron sputtered coatings deposited from an AZ31 Mg alloy target. This alloy designation specifies a composition of 2.5-3.5 wt.%Al, 0.6-1.4 wt.%Zn, 0.2 wt.%Mn, trace amounts of Fe and Cu, and the balance with Mg. Thus it can be considered to be a very dilute Mg alloy from the ternary Al-Mg-Zn system. Since the alloy content was very low, these coatings were discussed in Sect.3.3 as essentially pure Mg coatings. Some researchers have deposited 6000 series aluminium alloy coatings, which are age-hardenable Al-Mg-Si alloys [273]. Although no published examples could be found, it is highly likely that some Al-Mg-Zn coatings from the 7000 series designation, have also been prepared by sputtering.

No previous researchers seem to have examined PVD coatings from the Al-Mg-Zn alloy system with compositions away from the apexes of the ternary diagram. This is somewhat surprising since vapour deposited structures might be expected to provide similar phases to those obtained by rapid solidification, due to the fast quench rates in both cases. It has been demonstrated that quasi-crystalline and amorphous phases can be formed in Al-Mn coatings deposited by PVD [274,275], which provides some justification for this suggestion.

3.8 Multilayer Coatings

The unique ability of PVD techniques to deposit multilayered coatings without restriction has been touted as a strong advantage for its application in sheet steel coating processes. Several papers from the literature [13,22,43-45,157,158,276-279], provide scant reports of some work on bilayer coatings of various combinations. However, these investigations generally have been perfunctory and lacking in diligent evaluation. The principle conclusion which can be drawn from this research is that it is still unknown whether or not a layered coating would indeed provide any distinct advantage over monolayer coatings. This is a question which will require further research. It appears that multilayer coatings with more than three individual layers have not been examined for the corrosion protection of sheet steel, although such a study may possibly be incorporated into the PhD research of a recent candidate [280].

3.8.1 Al/Zn Bilayer Coatings

It is commonly recognised that the ideal sacrificial coating for sheet steel needs to provide sufficient cathodic protection of the steel at exposed edges and scratches, while maintaining a relatively slow general corrosion rate and therefore offering good barrier protection (Sect.1.1). It follows that one solution would be to somehow combine the barrier protection characteristics of aluminised steel with the cathodic protection characteristics of galvanised steels. This has prompted a desire to produce bilayer Al/Zn coatings, usually with the Al layer on the exposed surface. A confidential review paper [13] indicated that vapour deposited bilayer Al/Zn coatings have attracted the interest of industrial researchers since the late 1960s. This was largely because of the excellent performance these coatings exhibited in salt spray corrosion testing. A 2.5 μm Al layer over a 10 μm Zn coating improved the salt spray life of sheet steel by a factor or four times compared to zinc coatings of similar thickness [22]. Unfortunately, it seems that outdoor exposure of these materials did not replicate such improvement, as the Zn layer tended to be subject to undercutting corrosion [281]. Consequently, much of the early interest in Al/Zn layered coatings subsided thereafter.

Despite the discouraging results from early work in bilayered Al/Zn coatings, there has been a revival of industrial interest in layered PVD coatings in more recent times, especially since the commissioning of the Zn vapour deposition line by Nisshin Steel in the late 1980s [30,32]. In an attempt to improve the corrosion performance of conventional hot-dipped and electrodeposited steel sheet, Shin *et al* [43] applied thin overlayers of Al by electron-beam evaporation. The coating mass of the Al layer was between 2 and 6 $g.m^{-2}$, which is equivalent to between 0.7 and 2.2 μm (assuming 100%

density). Adhesion of the Al coating to the substrate was found to be highly dependent on the substrate temperature; at the start of deposition the substrate was required to be more than 170°C and less than 250°C throughout. Improvement of the corrosion performance in salt spray testing was noted in all cases, but to varying degrees. In general, the commercial coatings that possessed the roughest surface morphology prior to Al deposition gave the best salt spray performance. For example, a 6 $g.m^{-2}$ Al coated galvannealed (35 $g.m^{-2}$) sample survived for 2600 hours before showing red rust, and a similar Al coating on an electrodeposited Zn-Ni (30 $g.m^{-2}$) sample showed no red rust after 3000 hours in salt spray. In comparison, similar Al coatings over very smooth electrodeposited Zn-Fe (20 $g.m^{-2}$) coatings, resulted in salt spray failure within 200 hours.

A confusing part of the research by Shin *et al* is whether or not the samples were edge protected during salt spray testing. This has a significant effect on the performance of the product; for example Zincalume coatings corrode to 5% red rust in salt spray after approximately 2800 hr for edge protected, and 1500 hr for edge unprotected [282]. Although it was not specified, it would seem likely that these samples were edge protected considering the inherent single-sided nature of PVD coatings. Therefore, the performance of some of the bilayer coatings were similar to that of hot-dipped Zincalume coatings which have more than double the coating thickness. The corrosion performance of layered coatings with exposed sheared edges remains uncertain, however. Furthermore, metallographic cross-sections were not presented in this paper and it is unknown whether or not there had been a significant amount of interdiffusion between the commercially applied coating and the Al overlayer.

Goldschmied *et al* [277,278] produced some Al/Zn bilayer coatings in a large PVD coating facility which was specifically developed to conduct research into the continuous and batch coating of strip steel [279]. This system is capable of coating a steel strip 300 mm wide by 1800 mm in length in a batch process, or 100 mm wide strip fed at a speed of 10 $m.min^{-1}$ in a semi-continuous process (steel coil is loaded into the vacuum chamber). In the batch process, the strip is wrapped around a drum and rotated above an electron-beam heated evaporation bath at a typical speed of 15 $m.min^{-1}$. The Al/Zn bilayer coatings produced by these researchers consisted of nominally 2 μm of Zn followed by 2 μm of Al, or vice versa. Adhesion of the coatings to the steel strip substrate was initially poor, but was improved with the aid of an undisclosed heat treatment. Salt spray testing of the materials was carried out for a period of 300 hours, after which time no signs of red rust were observable on either the Al/Zn or Zn/Al bilayer samples. The salt spray performance was improved slightly by heat treatment, however the samples were not tested until failure and it is impossible to determine the expected life

of these materials from the results presented. No metallographic examinations were reported, and the overall evaluation of the samples was cursory and insubstantial.

The large PVD coating facility described above is apparently being commercially marketed, and it would seem that Arezzo *et al* [157,158] obtained a system for their own research. They have continued the work on Al/Zn bilayer coatings by preparing various samples consisting of Zn with a thin Al overlayer deposited onto steel sheet by electron-beam evaporation. A typical micrograph of the bilayer coating is shown in Fig.3.29. A discrete Al layer was not achieved, presumably as a result of the elevated temperature during deposition. Instead, a graded layer was produced with the surface concentration of Al ranged from 3.8 to 7.0 at.% (1.6 to 3.0 wt.%), down to a depth of about 0.6 μm, as indicated by XPS depth profiling. However, this interpretation is suspect because the XPS technique provides only a surface average composition and the depth resolution is rather poor, particularly for rough surfaces. The Al overlayer was found to assist in closing some of the deep pores in the Zn vapour deposited coating. Salt spray testing indicated that the corrosion performance was significantly improved over that of the porous Zn PVD coatings, from 6.5 to 24.1 hr per micrometre of coating for the first appearance of red rust. This salt spray performance was similar to that of commercial Galfan tested at the same time. No indication was given, however, of whether or not the salt spray tests were conducted with the edges protected or not. In either case, the corrosion resistance of this bilayer coating was significantly worse than commercial Zincalume.

3.8.2 Other Bilayer Coatings

Bilayer coatings with a cathodic surface and anodic interlayer were examined by Mukherjee *et al* [276]. The coatings consisted of a 1.2 to 5.7 $g.m^{-2}$ layer of Zn deposited onto mild steel and high strength low-alloy (HSLA) steel, followed by a 0.6 to 2.1 $g.m^{-2}$ surface layer of Sn. Such coating masses are typical of light electrodeposited coatings. The total coating thickness was typically between 4 and 9 μm, which suggests that the Zn layer was probably very porous; no metallographic examination was reported, however. As would be expected from the presence of a Sn surface layer, an electrochemical examination in quiescent 3wt.% NaCl aqueous solution indicated that the surface was cathodic with respect to the steel substrate. Measurements of the corrosion mass loss as a function of time revealed that the coatings corroded such that the entire Zn coating mass was lost within less than 24 hours of immersion. The corrosion potential varied between about -50mV and -450mV (SCE) over 17 days immersion, and was therefore always cathodic with respect to the steel substrate. Hence, continued mass loss after the first 24 hours is consistent with the corrosion of the steel substrate due to the large cathodic area

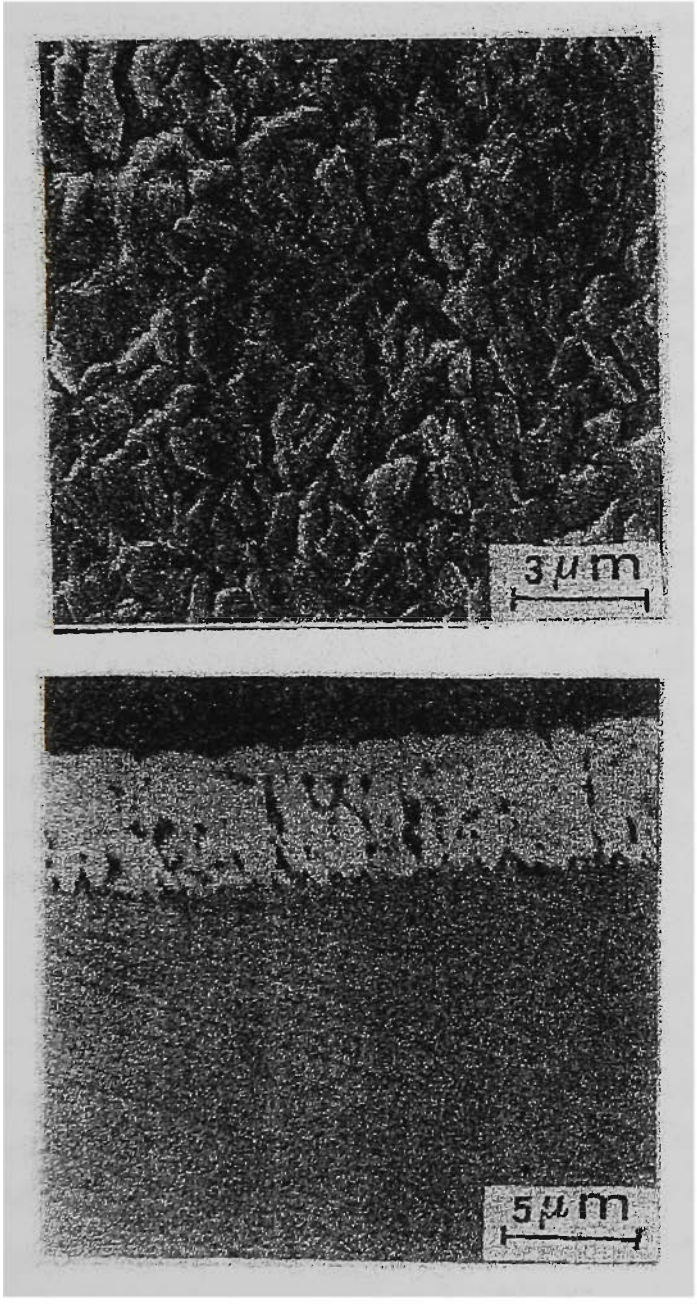

Fig.3.29 ***Typical SEM*** *morphology of a Zn/Al double layer coating produced by evaporation* *[158]*

provided by the Sn-rich surface. The corrosion performance of the Zn/Sn coatings was improved slightly by heat treatment after deposition. However, the trends in corrosion potential with time were relatively unchanged, and the corrosion mass loss rate was quite similar to samples before heat treatment. It was claimed that the slight improvement in performance was due to the formation of Zn-Sn intermetallics in the coating, although no metallographic examination was performed which would confirm this.

Jun *et al* [44] investigated the potential of using thin surface layers of vapour deposited Si as a means of colouring galvanised steel sheet, and also as a means of providing improved corrosion resistance. Thin surface layers of Si (<1 $g.m^{-2}$) were deposited by electron beam evaporation in vacuum onto steel sheet which had been previously coated with Zn by hot-dipping, electrodeposition or PVD. Various colours were achieved depending on the coating thickness, ranging from yellow for the thinnest coatings, through to violet for the thickest. Examination by AES and XPS indicated that a significant proportion of SiO_2 was present throughout the Si layer, presumably due to oxidation during deposition. Salt spray testing of the samples showed that the corrosion resistance of the galvanised steel could be improved by a surface layer of Si, and the lifetime improvement was approximately proportional to the Si thickness. Optimal substrate temperatures during deposition were also indicated, and this was attributed to the uniform coverage of the Zn surface under such conditions. It was also found that the application of a clear polymeric coating to the Si/Zn coating was necessary in order to prevent fingerprint marking of the surface.

In a continuation of their work on layered coatings, Jun *et al* (1994) [45] prepared and evaluated three other bilayer coating combinations. Mn, Mg and Sn were vapour deposited onto 20 $g.m^{-2}$ Zn electrodeposited steel sheet. In each case, the coating mass of the top layer was less than 35 $g.m^{-2}$, and generally in the order of 5 $g.m^{-2}$. The adhesion of the PVD layer was generally good, except for the Mg layer which peeled off during tape testing of a 180° bend. Salt spray testing of the bilayer coated steel samples resulted in the development of red rust after about 1000 hours in all cases. The Mn/Zn bilayer formed a red-brown coloured γ-Mn_2O_3 corrosion product on the surface, which might be expected to be undesirable from a customer's viewpoint.

3.8.3 Trilayer Coatings

Very recently researchers at Nisshin Steel were assigned a US patent for the invention of trilayered Zn-Mg coatings [24]. These coatings were produced on their commercial scale continuous PVD facility (Sect.1.3.3), by fitting two additional evaporation chambers in advance of the existing chambers for Zn deposition. This

enabled the deposition of consecutive Zn, Mg and Zn layers continuously onto both sides of the steel strip. The substrate temperature was typically greater than 180°C prior to coating, and in excess of 270°C at the completion of the coating process. This caused interdiffusion of the three coating layers, such that the optimum coating consisted of a gradient in Mg content from 1 at.% near the substrate, up to 17 at.% or more in the centre of the coating and back to 1 at.% at the surface. The formation of (Mg) phase was necessarily avoided by using such high temperatures, which enabled interdiffusion between the layers. Hence the middle layer consisted of a mixture of $MgZn_2$ and (Zn) phases. The total coating thickness was typically about 4 or 5 μm. The corrosion performance of these trilayered Zn-Mg coatings were significantly improved with respect to PVD Zn coatings, in terms of both static and cyclic salt spray exposure tests. It was also claimed that the low Mg content on the surface of the tri-layered coatings had the advantage of improved spot weldability in comparison with alloy Zn-Mg coatings.

Chapter 4

Experimental Techniques

The selection of a PVD coating process for use in this investigation was largely restricted by the availability of equipment. As discussed in Ch.2, sputtering is the most widely used technique for PVD alloy coatings due to the ease with which alloys can be deposited. Monolithic alloy targets can be used to deposit coatings with the composition of the target being replicated in the coating. Therefore, sputtering was targeted as the best choice of coating process for this work, and fortunately a system was available for use (Sect.4.1). However, this sputtering system was not designed for the production of large area coatings. Cosputtering with two magnetrons would have been possible but the composition of the coatings would have been extremely variable over the substrate surface owing to the large separation of the magnetron sources. Furthermore, it was intended that the effects of ion assisted deposition on the microstructure and composition of alloy coatings would be examined, and this necessitated the use of a single unbalanced magnetron source. Monolithic alloy targets were the obvious choice, and they were used for the work presented in this thesis whenever possible (Sect.4.2.1). Difficulties were encountered preparing monolithic targets for several alloy compositions, and hence a composite target design was developed and constructed (Sect.4.2.2). The composition of the sputtered flux from these composite targets were predicted from simple equations (Sect.4.2.3). The composite targets were found to operate without difficulty in most cases, although the differential etch rates of adjoining metals resulted in a gradual drift in the composition of the sputtered flux (Sect.4.2.4). The substrate materials and cleaning procedures are described in Sect.4.2.5.

The main thrust of this investigation was the microstructural characterization of sputtered coatings prepared with a range of different alloy compositions within the ternary Al-Mg-Zn system. The study primarily concentrated on the binary systems and elemental metals, although two different ternary compositions were examined. A range of substrate bias voltages were employed as a second variable with the aim of investigating ion assisted deposition effects. In a limited number of cases the *i/a* flux ratio was also varied. The characterization techniques that formed the core of study were ion probe

measurements (Sect.4.3.1), coating mass determination (Sect.4.3.2), macroscopic examination and scanning electron microscopy (Sect.4.3.3), chemical analysis by energy dispersive spectroscopy (Sect.4.3.4), and extensive X-ray diffraction experiments (Sect.4.4). Some of the peculiar trends in the composition of the alloy coatings were examined further by simulating the ion assisted deposition process using T-DYN software (Sect.4.3.5). Finally, the corrosion behaviour of the sputtered coatings was evaluated by some simple electrochemical tests (Sect.4.5).

4.1 Magnetron Sputtering System

All coatings for this research were prepared using a magnetron sputtering system at CSIRO Division of Applied Physics. Photographs of the sputtering system are shown in Fig.4.1. This system was built in the late 1980's and an early incarnation was used in the landmark research into charged particle fluxes from planar magnetron sources by Window *et al* in 1986 [60,63]. This sputtering system has been developed over the years to incorporate a magnetron design with various magnet assemblies that can be interchanged while the chamber is evacuated. The simple design eliminates much of the complex configuration required with the use of electromagnets, while maintaining the versatility of being able to select different ion fluxes by exchanging the magnets behind the target. A brief review is given below describing the system and the most pertinent design features that have an impact on the quality of the coatings. The basic procedures for operation of the system are also described.

The vacuum chamber of the sputtering system measures 300 mm in diameter and is 300 mm high, constructed from 3 mm thick austenitic stainless steel. The coating area of the chamber consists of four heater blocks on which an annular Cu platform is attached. A schematic diagram of the substrate platform is shown in Fig.4.2. The outside diameter of the platform is 250 mm and the inside diameter is 125 mm. The platform is located 60 mm below the target surface, and is attached to a rotary feed-through. It has positions for up to 12 samples around its perimeter, which can be coated in one pump-out by sequential rotation under the magnetron. The rotation of the substrate platform can also be driven by a computer-controlled stepper motor [283], although it was not used for this work. One of the sample positions on the platform is usually occupied by an electrically isolated probe of diameter 8.3 mm. This probe is used to measure the ion current density at the substrate position (Sect.4.3.1).

The substrates were positioned on the Cu platform and an Al sheet cover was placed over them and clamped to the platform. The placement of the cover ensured good

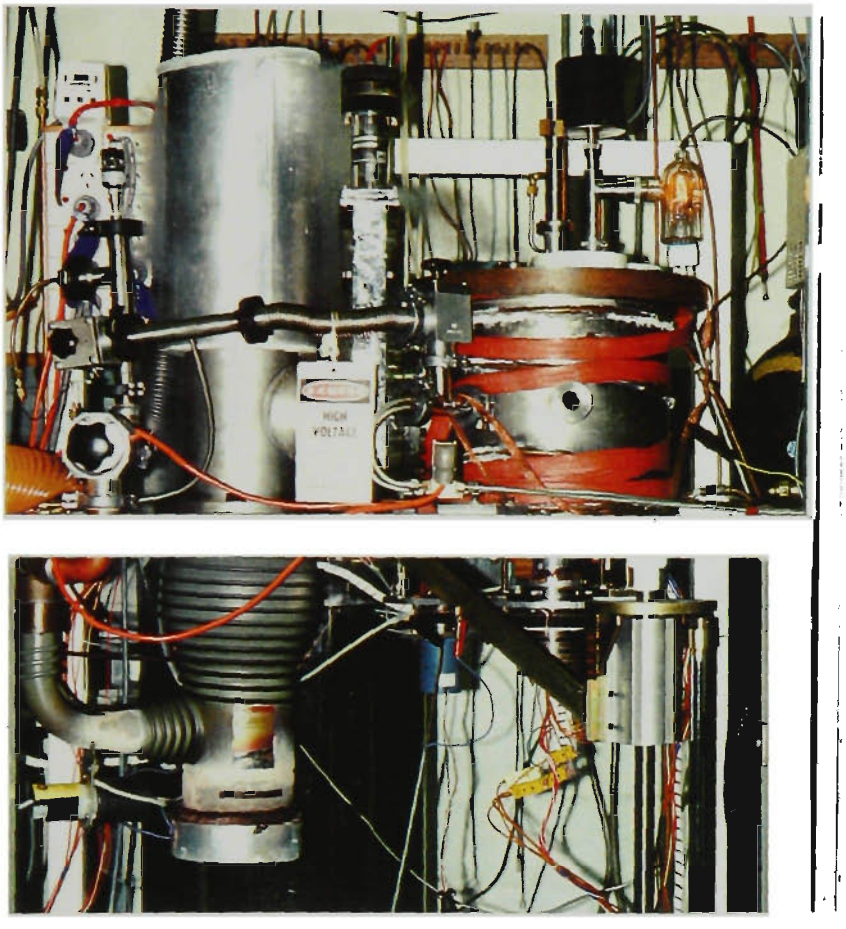

Fig.4.1 *Photographs of the magnetron sputtering system used throughout this work.*

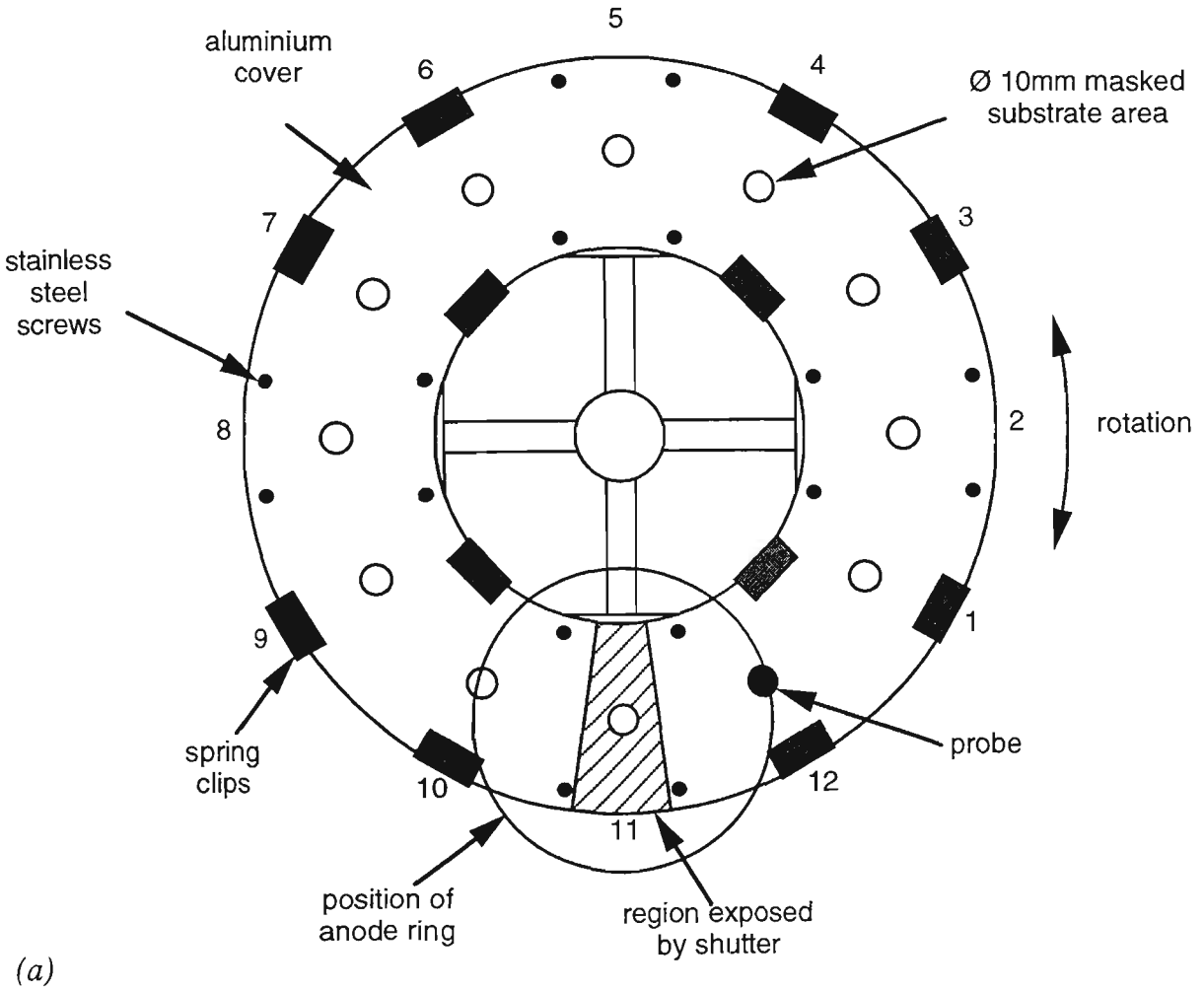

(a)

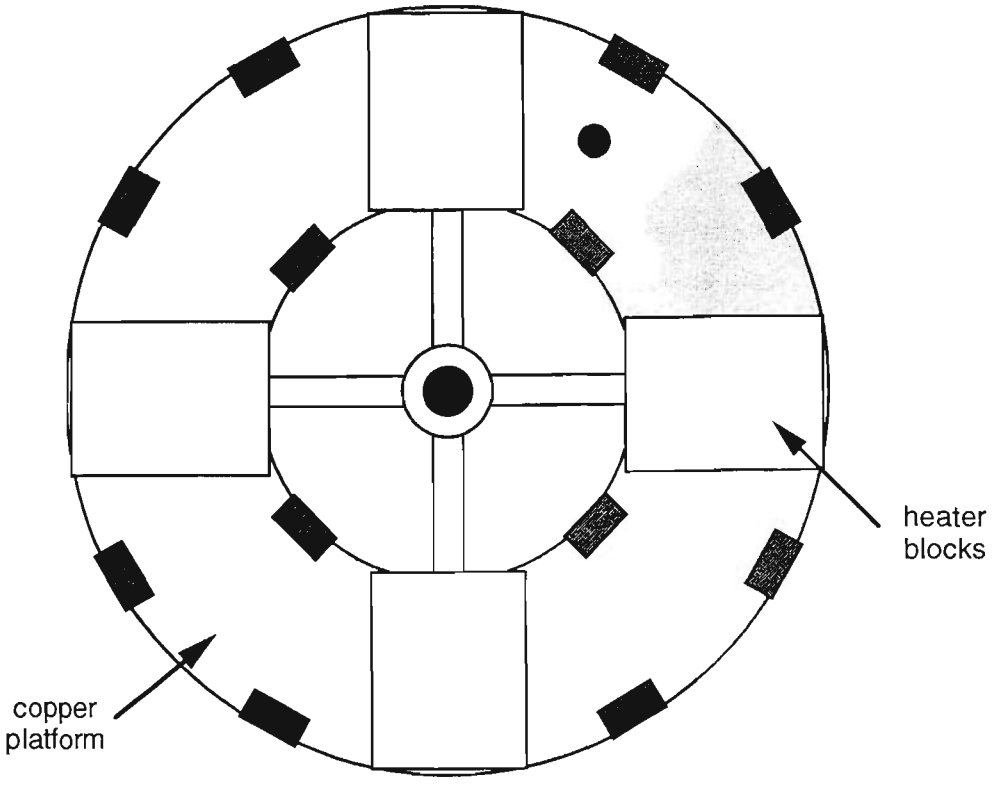

(b)

Fig.4.2 Schematic diagram of substrate platform used in the magnetron sputtering chamber: (a) top view, and (b) bottom view. Sample positions are numbered 1 to 11. Position 12 was used for the ion current probe.

thermal contact between the substrates and the platform, and also provided exposure of a fixed area of each substrate to the coating flux via an aperture (10 or 18 mm diameter). A K-type thermocouple was attached to the platform and in each of the heater blocks to allow measurement of the substrate temperature. All coatings described in this thesis were deposited with a maximum substrate temperature of 50°C. In most cases the temperature was controlled at 50°C throughout the coating run by setting the heater blocks to this value. A shutter was placed immediately in front of the magnetron source and prevented sputtered material from depositing on substrates located to the side of the nominal coating position (refer Fig.4.2). This shutter contained a wedge aperture that was 25 mm wide under the axis of the source, and was originally designed for depositing multilayer coatings using two magnetron sources [283].

The vacuum chamber was evacuated firstly by a backing pump and then by an oil diffusion pump with a liquid nitrogen cold-trap. The chamber pressure was measured using two different devices depending on the level of vacuum: an MKS Baratron gauge for pressures from 140 to 0.1 Pa, and a Varian 880 ionization gauge for pressures from 0.1 Pa to 0.01 mPa. Ultimate base pressures of about 0.04 mPa are achievable after a long pump-out and by heating the chamber to increase the out-gassing rate. However, for all the work conducted in this thesis, the evacuation time was generally about 3-4 hours, and base pressures of less than 0.13 mPa were achieved within this time. Ultra high purity (UHP) Ar was always used as the sputter gas, and it was flowed continuously into the vacuum chamber at a typical rate of about 20 sccm (standard cubic centimetres per minute), such that a constant sputtering pressure of 0.20 Pa was achieved. The cleanliness of the vacuum was improved further during deposition of the coatings by the simultaneous operation of a Ti magnetron sputter gun, which acted as a getter pump [57]. The Ti magnetron was shielded from the substrate platform during deposition runs, and was run at a power of 30 W. The base pressure at the end of each coating run was therefore often slightly better than at the start of the run.

The power supplies used to operate the magnetrons were Advanced Energy MDX 1.5 kW units. Two different supplies were used, each capable of delivering a different maximum voltage: one had a maximum voltage output of 800 V while the other had an output of 1200 V. The high voltage supply was found to control the power setting more efficiently than the low voltage supply, and was subsequently employed for most of the coatings. The substrate platform and rotary feed-through were electrically isolated from the chamber and earth. Therefore, the platform could be permitted to self bias during deposition, or it could be shorted to earth by a simple wire connection between the platform and ground. More significantly, an in-house constructed power supply was used to apply a dc bias to the substrate platform when required. The deposition time was

generally selected so as to provide a coating of about 1 μm thickness, assuming bulk density.

The magnet assemblies used in this thesis have been described previously in the literature [61,64,65], and a schematic diagram in Fig.4.3a shows their placement in relation to the magnetron body. They are designated as M1 to M4 in order of increasing unbalance of the magnetic field (Fig.4.3b). Each magnet assembly has an annular ring of NdFeB permanent magnets bonded to a ferritic stainless steel ring. This ring is then placed onto a ferritic stainless steel backing plate. The width of the outer ring of magnets increases from M1 to M2 (same as M3) and then to M4, corresponding to a similar increase in the strength of the outer magnetic field. The central pole consists of a $SmCo_5$ permanent magnet (M1 and M2), ferritic stainless steel (M3), or simply the backing plate itself (M4). The M3 magnet assembly was used for the preparation of the vast majority of coatings, while the M2 was used for the Ti magnetron pump. For some of the coatings prepared (Zn Series 1-3, Al Series 1, Al-24%Zn, Al-50%Zn), the M3 was found to be slightly demagnetised due to prior overheating. Unless noted otherwise, it should be assumed that the magnets were all fully magnetised.

A photograph of a typical magnetron body with a target fitted onto it is shown in Fig.4.4. These magnetrons were constructed from machined Cu using a CSIRO design, and the magnet assemblies could be easily fitted into the back of the body while the sputtering chamber was under vacuum. The exposed area of the target was about 80 mm in diameter. The assembled magnetrons fitted in the top of the vacuum chamber with the water-cooling hoses attached are shown in Fig.4.1b.

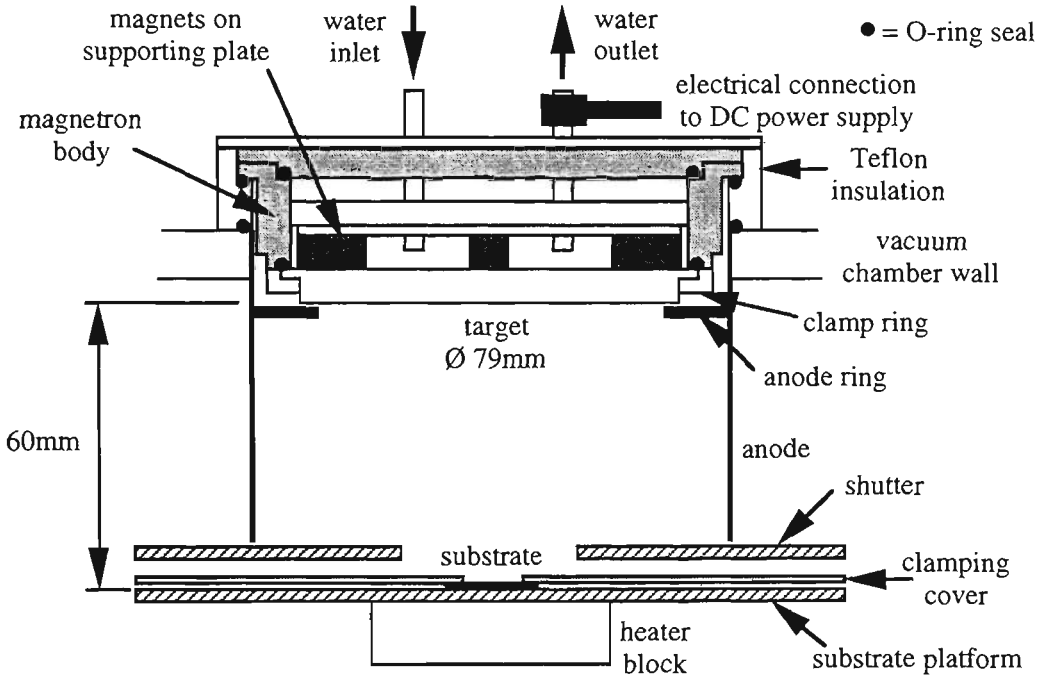

(a)

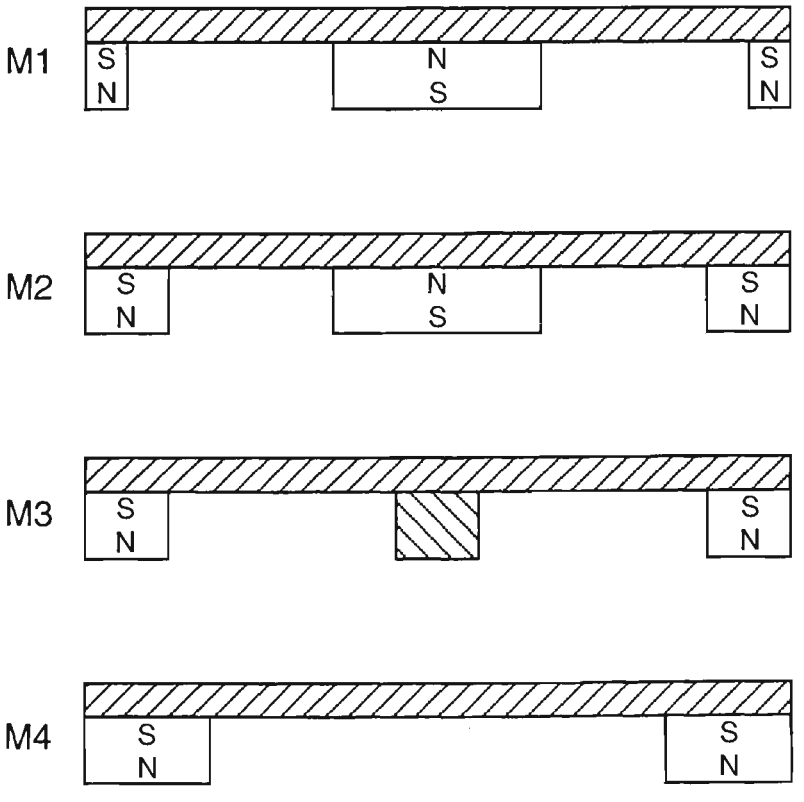

(b)

Fig.4.3 Cross sectional views of (a) the magnetron body and (b) the circular magnet assemblies[64].

Fig.4.4 *Photograph of magnetron body with target fixed in place.*

4.2 Coating Preparation

Melting and casting of Al-Zn alloys was a simple matter and several monolithic alloy targets were prepared for deposition of these coatings. Monolithic targets were also used for the deposition of single element coatings of Al, Mg and Zn. Early attempts to produce alloy castings of Al-Mg alloys proved extremely difficult, however. The highly reactive nature of Mg metal meant that it tended to burn immediately upon melting, unless it was protected by an inert or reducing atmosphere. Similar behaviour was experienced when attempting to remelt a master alloy of Al-50 at.% Mg. Overcoming this problem would have required the use of specialized furnace equipment with a controlled atmosphere; equipment that was not immediately available. Furthermore, the Al-50 at.%Mg master alloy was extremely brittle and prone to fracture at the slightest shock. Therefore, it was decided that monolithic alloy targets would be unsuitable for the preparation of alloy coatings containing Mg. Composite targets consisting of sectors of each constituent metal were constructed for the purpose. The design and manufacture of the monolithic and composite targets are described in the following two sections.

4.2.1 Monolithic Targets

The monolithic sputter targets for this work were prepared by conventional melting and casting techniques. A small resistance-heated pot furnace was used to melt the material for the Al (99.999 wt.%) and Zn (99.99 wt.%) targets, and several of the Al-Zn alloys. Some of the Al-Zn alloys were melted using an rf induction-heated pot furnace (Heraeus). The use of two different furnaces was purely for reasons of convenience and it is not expected to have caused any differences in the consistency of the castings.

A mild steel mould was used to cast the molten metal for the monolithic targets, and it is shown schematically in Fig.4.5. The dimensions shown in this figure are approximated and are not critical. These dimensions were selected so that subsequent machining would remove the chemical inhomogeneities at the surfaces of the casting. This ensured a uniform chemical distribution throughout the target. The castings were removed from the mould and then machined to the required dimensions for use in the magnetron. Figure 4.6 shows a schematic diagram of the machined targets indicating the relevant dimensions; the tolerances were +0/-0.5 mm for the diameters and ±0.2 mm for the thicknesses. The composition of each target was checked prior to use by energy dispersive spectroscopy (EDS) in several locations over the machined surface.

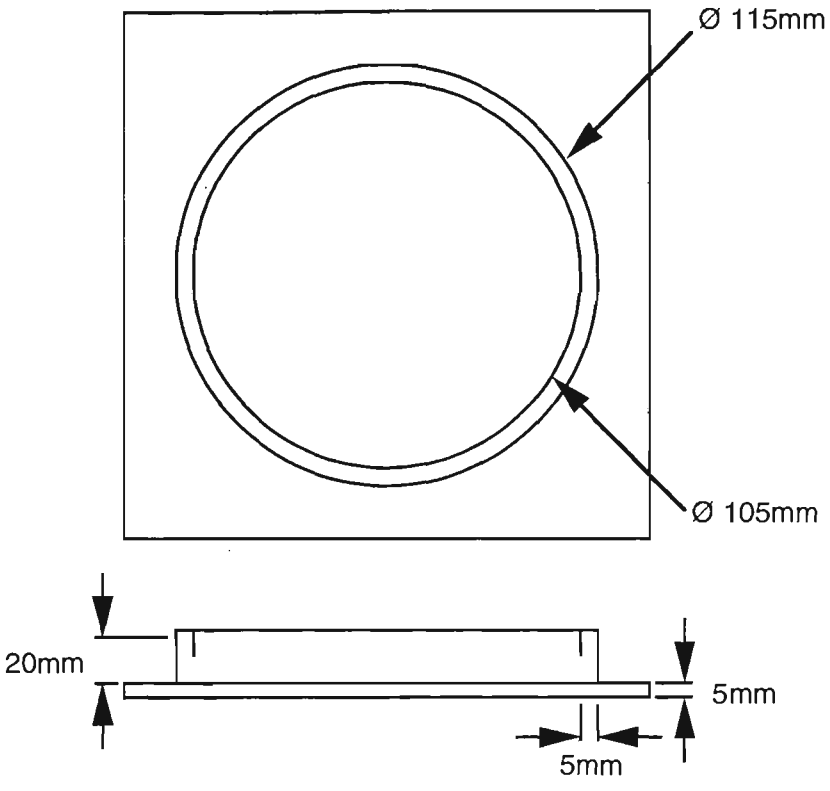

Fig.4.5 Mild steel mould used to cast molten metal for subsequent machining to monolithic targets. The ring and base-plate were joined by a TIG weld.

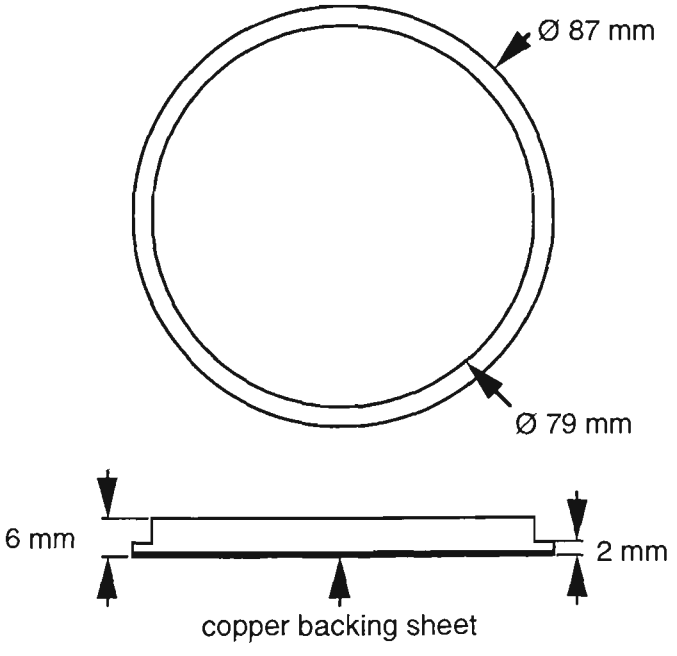

Fig.4.6 Dimensions of machined monolithic targets. The copper backing sheet is shown attached to the rear side of the target, and was approximately 1mm in thickness. The outer 10mm of the copper sheet were given a high quality finish to provide a good O-ring seal.

Six different Al-Zn alloy compositions were melted from high purity Al and Zn ingots. The selected compositions of the alloy melts were achieved by gravimetric means. Immediately before casting, the melts were stirred thoroughly to ensure a homogeneous mixture. The final composition of the targets was measured by EDS analysis on the face of each target surface. The average of between four and six analyses on different regions of each target are listed in Table 4.1. No other impurity elements were detected in this analysis, although it must be emphasised that EDS is not suited to the detection of trace impurities.

Table 4.1 Composition of Al-Zn alloy targets measured by EDS. The estimated error of measurement is ±1.0 at.%.

Target	Composition (at.%)	
	Al	Zn
1	88.5	11.5
2	75.8	24.2
3	60.6	39.4
4	50.5	49.5
5	26.6	73.4
6	10.5	89.5

The relatively high corrosion rates of the Al, Zn and Al-Zn target materials meant that it was not advisable to use direct water cooling. This would have resulted in rapid corrosion of the target material and potentially catastrophic failure of the magnetron assembly. Indirect cooling of the target was attempted initially, but resulted in excessively long pump-out times to achieve an adequate base pressure in the vacuum chamber. This was caused by slow outgassing from the contacting surfaces of the target and the Cu diaphragm of the magnetron body. Therefore an alternative design for cooling the targets was essential. This was achieved by bonding a piece of 1 mm thick Cu sheet to the back of each target. A commercial epoxy resin adhesive (Ciba-Geigy Super Strength Araldite®) was used for this purpose. The epoxy was set with the target placed on a hotplate at a temperature of about 80°C, and a heavy weight placed on top. This ensured that the epoxy resin set very rapidly (within 15 minutes), and minimized the thickness of the adhesive layer between the Cu sheet and target. The Cu backing sheet bonded to each target was subsequently machined to achieve a planar surface with the required outer diameter. Furthermore, the outer 10 mm surface of the copper backing sheet was machined to a high quality finish to ensure an adequate O-ring seal with the magnetron body. The finished copper sheet at the back of the target is shown in the schematic diagram in Fig.4.6.

Bonding sputter targets to backing plates with epoxy resin is a common practice [96]. However, previous workers have commonly used epoxy resins impregnated with silver powder. This was thought to be necessary to achieve the required electrical conductivity. Unfortunately, the incorporation of the silver powder tends to cause the epoxy joint to be excessively thick, which limits heat conduction through the bond. The use of epoxy resins without silver powder results in a much thinner bond which is also in more intimate contact with the target and backing plate. The bond is therefore expected to be stronger and have much higher thermal conductivity. The thickness of the epoxy layer is further minimised by setting it at an elevated temperature, which reduces the viscosity of the resin. Contact between numerous small asperities on the copper sheet and the target ensured good electrical and thermal conductivity across the joint. Therefore the use of silver powder in the resin was found unnecessary. This development should be of some interest to researchers of magnetron sputtering since it means that common epoxy resins can be used in preference to the much more expensive "conductive" resins.

In addition to the sputtering targets which were manufactured in-house, an Mg (99.98 wt.%) target was purchased from Target Materials Inc. [284]. This target was 79 mm in diameter and 6 mm in thickness. In order to fit the target onto the magnetron body it was necessary to bond it to a Cu backing plate. This procedure is described in the following section.

4.2.2 Composite Targets

As previously mentioned, the preparation of monolithic targets of alloys containing Mg proved to be very difficult and impractical. Faced with this problem, a design was developed for composite targets consisting of individual sectors of the required constituent metals. A schematic diagram of a typical composite target for deposition of binary alloys is shown in Fig.4.7. These composite targets were used for the deposition of all the ternary alloy coatings, and all binary alloy coatings which included Mg as one of the alloy constituents (ie. Al-Mg and Zn-Mg binary systems). Each composite target contained three sectors of each constituent metal. The sectors were arranged alternately on the surface of a Cu backing plate. This plate provided mechanical support for the sectors and a means of attachment onto the magnetron body. A thin epoxy resin adhesive layer bonded the sectors to each other and to the Cu backing plate. The backing plates were machined from 10 mm thick Cu plate, and the relevant dimensions are shown in Fig.4.7. The inner 80 mm diameter of the front surface of each backing plate was recessed by about 0.5 mm, to help locate the sectors in the centre of the plate.

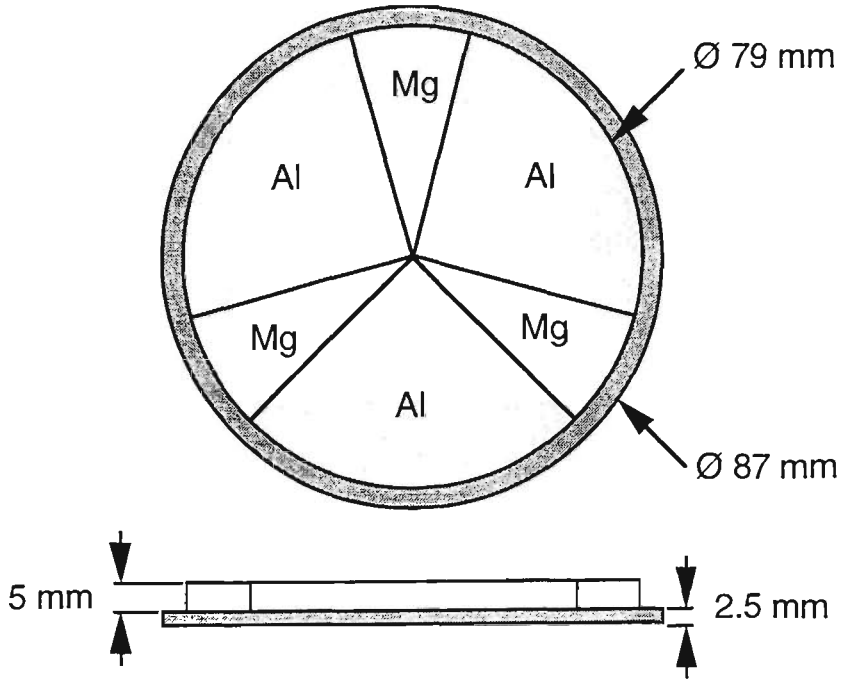

Fig.4.7 Schematic diagram of a typical composite target for deposition of binary alloy coatings. The backing material was copper plate, and the target sectors were attached with epoxy resin adhesive. The target shown consisted of 90° sectors of Al and 30° sectors of Mg.

The outer 10 mm of the back surface of each copper plate was given a very smooth finish, so as to ensure an adequate o-ring seal with the magnetron body.

The individual sectors of the composite targets were prepared in several stages. Firstly, a series of Al (99.997 wt.%) and Zn (99.99 wt.%) ingots were cast using either the steel mould shown in Fig.4.5, or a sand mould. The sand mould consisted of a fired mixture of sand and sodium silicate, into which a cylindrical hole about 100 mm in diameter and about 200 mm deep was prepared. A Mg (99.98 wt.%) ingot was used in as-supplied form in order to avoid difficulties with oxidation during melting and casting. All of the castings were turned down to 80 mm diameter, and cut-off into individual discs of thickness 6 mm. The Al, Mg and Zn discs were marked into the required sector sizes using a precision protractor set. The discs were cut into sectors using an Accutom-5 rotary cut-off wheel, fitted with a 100 mm diameter SiC wheel (457CA). Various feed speeds between 0.050 and 0.200 $mm.s^{-1}$ were required, and a cutting speed of 3000 rpm proved adequate. This equipment was essential for the task because it provided an extremely narrow cut (less than 1 mm width), which was straight and smooth; only a light abrasion with 600 grit SiC paper was required to remove a slight burr from the cut edges. The narrow cut also meant that very little material was lost and the utilisation of the machined discs could be maximised. Sectors as small as 5° were produced without great difficulty.

Upon completion of the manufacture of all the sectors for the composite targets, the sectors were assembled with the Cu backing plates. All the components of the target were first cleaned thoroughly with detergent solution then ethanol, and hot-air dried. The sectors were bonded to the backing plate using a commercial epoxy resin adhesive (Ciba-Geigy Super Strength Araldite®), following the same procedure described in the previous section for monolithic targets. The recessed area on the surface of the copper backing plate prevented the sectors from sliding off while the adhesive was setting. After cooling to ambient temperature, the target was machined to remove the built-up adhesive and provide a clean finish on the target surface.

The sector dimensions for the 12 composite targets prepared for this work are listed in Table 4.2. The predicted and measured compositions of the deposited coatings obtained with self biased substrates are also listed. The method of predicting the composition of the sputtered flux is described in the following section.

Table 4.2 Details of composite sputter targets. Three sectors of each metal were used in each target. Also shown are the film compositions predicted from calculations and the actual measured compositions for coatings deposited onto self biased substrates (about -25V).

Description	Sector Size (°)			Predicted Composition (at.%)			Measured Composition (at.%)		
	Al	Mg	Zn	Al	Mg	Zn	Al	Mg	Zn
Binary Al-Mg Targets									
Al115/Mg5	115	5	---	87	13	---	88	12	---
Al105/Mg15	105	15	---	67	33	---	68	32	---
Al90/Mg30	90	30	---	47	53	---	51	49	---
Al60/Mg60	60	60	---	34	66	---	26	74	---
Al30/Mg90	30	90	---	9	91	---	10	90	---
Binary Zn-Mg Targets									
Zn90/Mg30	---	30	90	---	15	85	---	4	96
Zn60/Mg60	---	60	60	---	34	66	---	24	76
Zn40/Mg80	---	80	40	---	51	49	---	46	54
Zn20/Mg100	---	100	20	---	72	28	---	64	36
Zn10/Mg110	---	110	10	---	85	15	---	81	19
Ternary Al-Mg-Zn Targets									
Al85/Mg25/Zn10	85	25	10	36	36	28	39	32	29
Al105/Mg10/Zn5	105	10	5	61	20	19	65	14	21

4.2.3 Prediction of Sputtered Flux Composition

The symmetry of the composite target design meant that it was a simple matter to estimate the composition of the sputtered flux for each target, given the angular dimensions of the sectors and the deposition rate for the elemental metal targets, ie. Al, Mg and Zn targets. The present design of the composite targets therefore has advantages over other designs previously reported in the literature [93-99]. The molar deposition rates for the elemental targets, Z (mol.mm^{-2}.W^{-1}.min^{-1}), were calculated using the following equation:

$$Z = \frac{4m}{\pi\, d_c^2\, P\, t\, M} \tag{4.1}$$

where m (g) is the coating mass deposited within time t (min), P is the power applied to the magnetron target, M (g.mol^{-1}) is the atomic mass, and d_c (mm) is the diameter of the

circular coated area exposed by the mask cover. The deposition rates at self bias calculated for each of the three elemental targets were:

Al	0.57×10^{-10} mol.mm^{-2}.W^{-1}.min^{-1}
Mg	1.94×10^{-10} mol.mm^{-2}.W^{-1}.min^{-1}
Zn	3.68×10^{-10} mol.mm^{-2}.W^{-1}.min^{-1}

The atomic fraction of each constituent in the sputtered flux from the composite target could then be predicted for any given target geometry, from the radial fraction of each constituent, using the following equations:

$$\text{Binary Targets } a \text{ (at.\%)} = \frac{f_a Z_a}{f_a Z_a + f_b Z_b} \tag{4.2}$$

$$\text{Ternary Targets} \qquad a \text{ (at.\%)} = \frac{f_a Z_a}{f_a Z_a + f_b Z_b + f_c Z_c} \tag{4.3}$$

where *a, b* and *c* represent the constituent metals in the composite target, f is the radial fraction of each metal in the target, and Z is the molar deposition rate of each metal. These equations required the conversion of the angular sizes of the sectors to radial fractions. For example, on a composite target consisting of 90° sectors of Al and 30° sectors of Mg, the radial fractions f_{Al} and f_{Mg} are 3x90°/360° = 0.75, and 3x30°/360° = 0.25, respectively. Such a target would therefore be expected to produce a sputtered flux of Al-53 at.%Mg, from application of equation 4.2. Similarly, equation 4.3 can be used to determine the sputtered flux composition for ternary composite targets. For example, on a composite target consisting of 85° sectors of Al, 25° sectors of Mg, and 10° sectors of Zn, the radial fractions f_{Al}, f_{Mg} and f_{Zn} were 0.708, 0.208, and 0.083, respectively. The predicted sputtered flux for this ternary target is Al-36 at.%Mg-28 at%Zn.

The calculated compositions for the sputtered flux from each of the composite targets are reported in Table 4.2, and compared with the measured coating compositions at self bias voltage in Fig.4.8. These results show that equations 4.2 and 4.3 are capable of predicting the composition of coatings from the composite targets with a reasonable degree of accuracy. The predicted composition is within ±10 at.% of the actual measured composition for all compositions; Zn content was slightly under-estimated, whereas the Mg content was slightly over-estimated. It is expected that the accuracy of the calculation could be improved by more careful measurement of the molar deposition rates for each component. Other potential sources for error are the change in composition with time due to differential volumetric erosion of the target sectors (refer Sect.4.2.4), and sputter yield amplification effects due to redeposition on the target surface. The accuracy of the

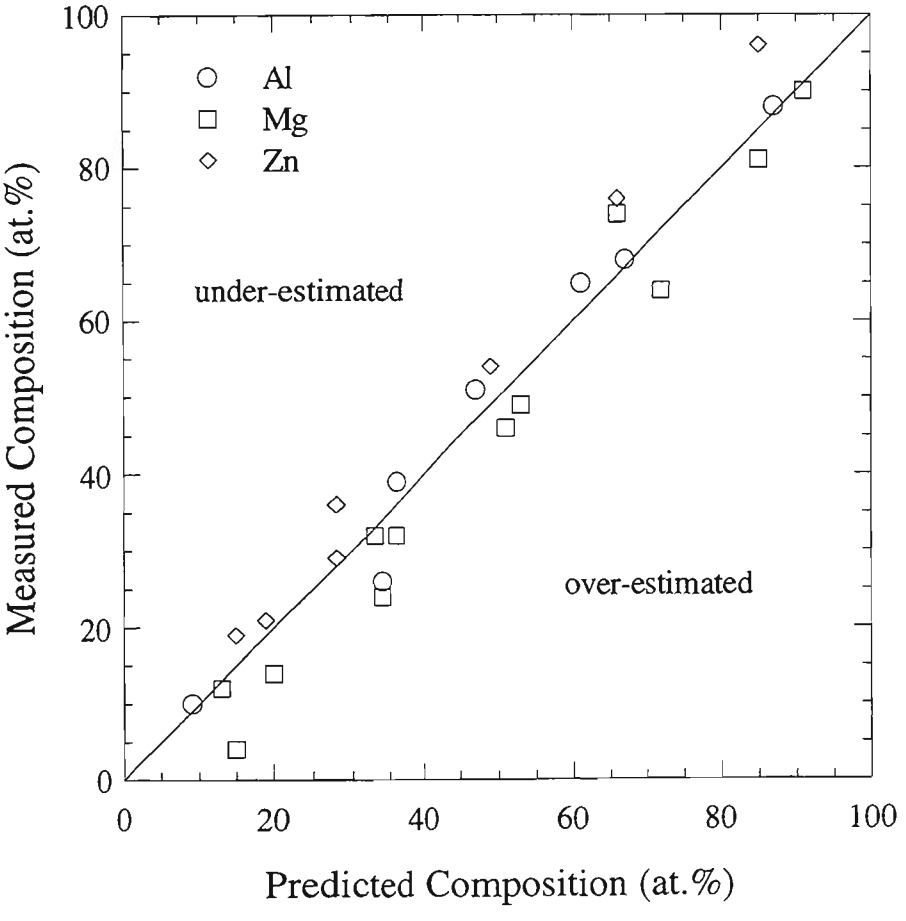

Fig.4.8 Comparison of measured and predicted chemical composition of coatings sputtered from composite targets onto self biased substrates.

predicted compositions were considered to be sufficient for the purposes of this investigation.

Some variation in the composition of the sputtered coatings was expected to occur over large coated areas, reflecting the non-uniform composition of the composite target surface. This problem was minimised by locating the substrates directly under the centre of the composite target. It was a relatively easy task to achieve accurate alignment since this position corresponded to the maximum in ion current measured with the probe. The area of each sample exposed to the sputtered flux was also relatively small (10 or 18 mm diameter). The combination of these conditions ensured that compositional variations over the coated area were negligible.

4.2.4 Operational Behaviour of Composite Targets

It was generally very easy to obtain a stable dc sputtering discharge with the composite targets, regardless of the exposure of the electrically insulating epoxy resin in the joints between the sectors. When operating with constant power, the operating voltage was usually intermediate between those obtained for the constituent elemental metal targets, and was reasonably stable throughout the deposition runs. The magnetron voltage within and between deposition runs typically varied by no more than ±10 V. However, one exception was noted for each of the Al-Mg and Zn-Mg target sets. Both the Al60/Mg60 and Zn20/Mg100 targets were comparatively difficult to operate, and required slow ramping up of the magnetron power in order to prevent the discharge from extinguishing via arcs. This problem was reduced by the use of an arc suppression unit (Advanced Energy MDX Sparc-le 20). This unit operates by detecting arcs and then rapidly switching the applied voltage slightly positive for 5 μs at 20 kHz frequency. However, the arcing problem was not entirely eliminated, and careful running-in was still found necessary before stable magnetron operation could be achieved. Examination of the surface of these targets after operation revealed the presence of several arc burns near the epoxy joint on the outer diameter, which was under the anode cover ring during operation. Furthermore, during the running-in period for both targets, it was often observed that the colour of the glow discharge abruptly changed, and this change was concurrent with a rapid change in the magnetron voltage.

The observations for the operation of the various composite targets seem to suggest that for any combination of two metals, there is a particular combination of sector sizes for which operation is troublesome. The sputtering discharge for such targets tends

to be schizophrenic*, and can abruptly or slowly shift between two different conditions. This is perhaps related to redeposition of sputtered material on the composite target surface [93]. The observed changes in the colour of the discharge are obviously caused by an alteration of the type of excited species in the plasma. The identity of these excited species were not examined in this study, and would require the installation of an optical emission spectrometer. Fortunately, the schizophrenic behaviour of the discharge did not seem to markedly affect the composition of the sputtered flux, and therefore was not considered further. It is certainly a phenomena of interest, however, and warrants further study in the future.

The design of the composite targets with individual sectors of different metals had a significant effect on the development of the annular sputter erosion track. The metals with the higher sputtering rates tended to erode much faster than the lower yield metals. Hence, the Zn sectors were eroded slightly faster than the Mg sectors, and both of these metals were consumed much faster than the Al sectors. The result of this effect was that physical steps were developed in the eroded composite target surface. Figure 4.9 shows the erosion profile of the Al90/Mg30 composite target after approximately 9 hours of operation at a dc magnetron power of 100W. It can be seen from this graph that the Mg sectors developed a much deeper erosion track than the Al sectors. This effect was less noticeable in Zn-Mg composite targets, since the higher sputter yield of Zn was partially off-set by the greater density of Zn in comparison with Mg.

The development of a stepped erosion track on the composite targets resulted in a gradual drift in the composition of deposited coatings, as a function of sputtering time. For example, Fig.4.10 shows the composition of coatings deposited from the various Al-Mg composite targets, over a period of up to 11 hours of target operation. There was a significant reduction in the Mg content of these coatings as the target became more eroded. This effect was less noticeable with the Zn-Mg composite targets, because the stepped erosion profile was not as prominent as for the Al-Mg targets. This gradual drift in coating composition was accounted for in the experimental preparation of the coatings, and in the interpretation of the results.

The construction of the composite targets using epoxy resin as an adhesive material invariably resulted in the entrapment of some adhesive between the individual sectors. Subsequent to machining of the target, a small fraction of the surface area

* The term "schizophrenic" is used here in accordance with the popular misconception that it is related to dual-personalities. In truth, the mental disorder known as schizophrenia is a much more complex and commonly occurring social disease, and only a small fraction of its victims suffer from dual-personality symptoms.

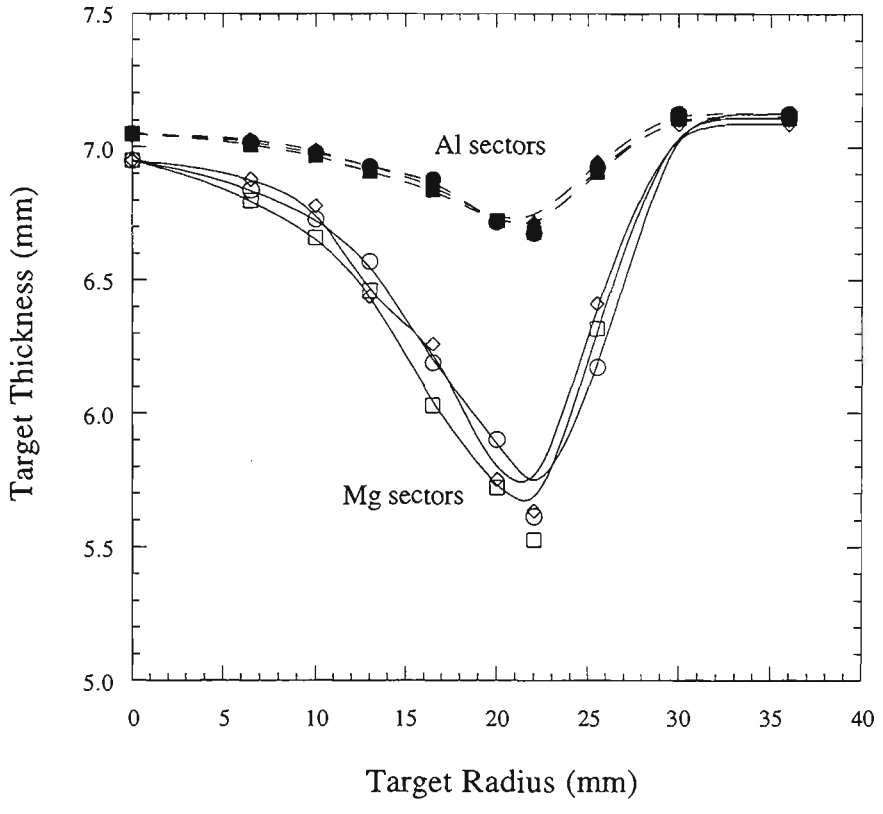

Fig.4.9 Erosion profile of the Al90/Mg30 composite target after approximately 9 hours of operation at 100 W dc power. Results for each of the three sectors are shown for Al and Mg.

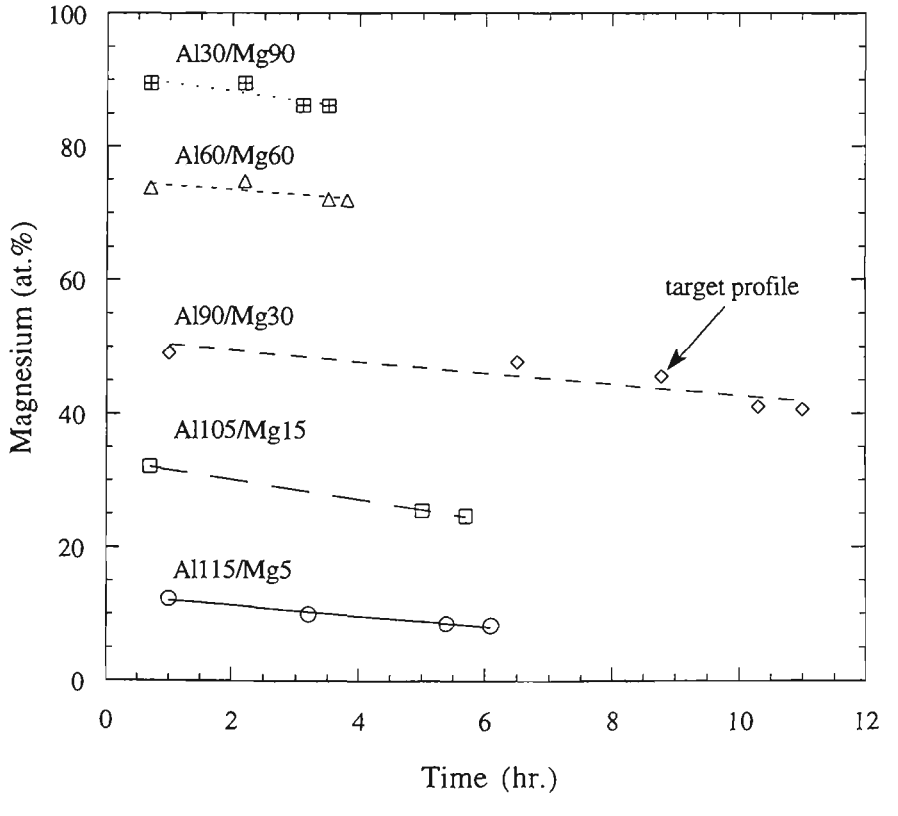

Fig.4.10 Chemical composition of coatings sputtered from Al/Mg composite targets as a function of operating time at 100 W dc power.

consisted of epoxy resin adhesive; the radial fraction of resin exposed is estimated to be less than 0.01. However, it was observed that after sputter erosion of the composite targets, the epoxy resin exposed in these interfaces was left protruding slightly from the target surface. This implied that the resin sputtered at a slower rate than the metallic sectors, and therefore contamination of the deposited coatings with this material, was potentially less than initially expected. Chemical characterization of all coatings by EDS, failed to reveal significant proportions of contaminants from the resin (carbon, nitrogen and oxygen). Unfortunately, the EDS detection limits for these elements are high, so that amounts of only a few percent would be undetectable. Despite this, it is assumed that contamination of the deposited coatings was negligible, given the minimal exposed surface area for the resin and the slower sputtering rate observed for it. Out-gassing of the chamber walls is considered to be a more significant contributor to any contamination, and this latter source of contamination was minimised by ensuring good base pressures.

The principal disadvantage of the composite target design was that the range of coating compositions available was strictly limited by the number of targets that were constructed. Each target would be used to deposit coatings of a single composition, since there was no means of varying the radial fractions of each sector. Furthermore, the composition of the sputtered flux could not be changed once each composite target was constructed. Such restrictions were hoped to be alleviated by the use of moderate amounts of ion assistance to alter the coating composition in a controlled manner [141]. Energetic ion bombardment would result in preferential resputtering of one or more of the components, and by adjusting the substrate bias voltage, the composition of the coatings could be altered.

4.2.5 Substrate Materials and Cleaning Procedures

The procedures for the preparation of all coatings for this work was standardised. Two different materials were used as substrates for the coatings. The first substrate materials were [100] single crystal silicon wafers. The wafers were fractured into small squares measuring approximately 15 mm x 15 mm. The substrates were cleaned with detergent and alcohol prior to being loaded onto the substrate platform in the coating chamber. Eleven of these samples could be coated in each run with an exposed area of 10 mm diameter. These silicon wafer substrates were used for the majority of the coatings deposited for microstructural characterization. This was for reasons of both convenience and design. Firstly, the wafers provided a highly polished surface that simplified the identification of surface morphology of the coating. Secondly, the wafers were ideal substrates for the XRD experiments for reasons highlighted in Sect.4.4.1. Thirdly, it was very easy to fracture the coated wafers in order to enable observation of

the coating cross-section. It is unlikely that these substrates would have influenced the coating microstructure, since an extremely thin amorphous native oxide layer exists on the surface of single crystal silicon wafers. This was tested by depositing Zn coatings on both Si and steel substrates using identical process conditions, and comparing the coating microstructrues obtained (refer Ch.5).

The second type of substrate material was low carbon CA4T-G steel of 0.8 mm thickness supplied by BHP Coated Steel Australia. This is a cold-rolled, aluminium-killed, deep-drawing steel grade. Steel substrates were used for all corrosion testing samples (Sect.4.5.1). Discs having a diameter of 22 mm were punched from the sheet. Burrs on the disc edges were removed by grinding on a rotary abrasive belt. The surfaces of the discs were given a light abrasion with Scotchbrite, and then an ultrasonic clean in a bath of ethanol. The samples were then washed with detergent solution to remove residual rolling oils, and given another ultrasonic bath in fresh ethanol. The discs were given a final rinse with ethanol before being dried with a compressed air stream. They were then immediately loaded into the coating chamber in order to minimise the possibility for surface oxidation. The steel discs were bowed slightly by the punching process, and were placed on the substrate platform with the concave side facing upwards, as shown in Fig.4.11. An Al cover mask was placed over the top of the samples to ensure that they were firmly clamped to the platform, and to expose a fixed area of each substrate to the coating flux.

The cleaning procedures described above are not in any way optimised. The adhesion of the sputtered coatings was sufficient for the crystallographic and chemical characterization, and the corrosion testing conducted in this study. However, this work did not necessarily provide high coating adhesion, as only cursory attempts to maximise the adhesion were made. It is fully anticipated that should these types of coatings be required for sheet steel which is to be formed or rolled in any way, the coating adhesion would be a much more critical parameter. No such forming operations were applied to the samples in this study.

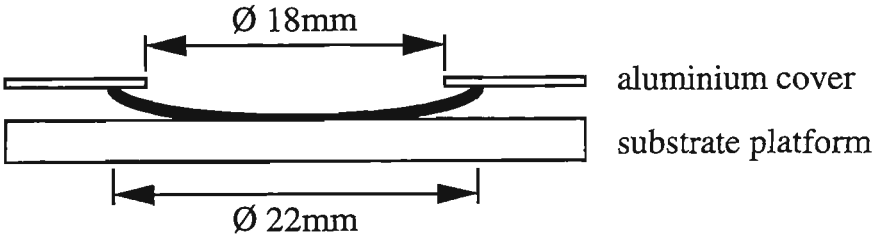

Fig.4.11 Schematic showing the curvature of steel disc substrates (exaggerated), and clamping with the aluminium cover mask.

4.3 Coating Characterization Techniques

4.3.1 Ion Probe Measurements

In all ion assisted deposition processes, one of the most important parameters is the flux of ions relative to the flux of atoms arriving at the substrate, known as the *i/a* ratio. The calculation of *i/a* requires the measurement of ion current density, combined with the measurement of the atomic arrival rate. The latter was estimated from the mass deposition rate measured for self biased substrates (Sect.4.3.2). The *i/a* ratio was calculated from the following equation:

$$i/a = \frac{1}{e\ N_A} \cdot \frac{I_p\ M\ t\ d_c^2}{n\ m\ d_p^2} \tag{4.4}$$

where e is the fundamental charge constant, N_A is the Avogadro constant, I_p (mA) is the probe current, M (g.mol^{-1}) is the atomic mass of the coating, t (s) is the deposition time, d_c (mm) is the diameter of the coated area, n is the valence of the bombarding ions, m (g) is the coating mass, and d_p (mm) is the probe diameter.

For the measurement of ion current, a probe was fitted into the substrate platform at the position shown in Fig.4.2. A cross-sectional schematic of the probe is presented in Fig.4.12. The probe consisted of an 8.3 mm diameter Cu disc soldered to a small bolt. It was inserted through a recessed hole in the substrate platform and was electrically isolated by means of mica spacers. An insulated wire was then attached between the probe and an electrical feed-through in the sputtering chamber. During operation of the magnetron, a multimeter was used to measure the current to the isolated probe. Regular cleaning of the probe to remove built-up deposits was found to be essential for accurate measurement of the current.

The characteristic voltage-current behaviour of the probe located on the substrate platform is shown in Fig.4.13. These results were obtained for a Zn target, operated at 80 W with an M3 magnet, and replicate the general trends reported elsewhere [60], except that the current sign is reversed. It was found that the probe current reached a plateau beyond a bias of about -60 V, indicating predominance of the ion current. A bias voltage of -100 V was used to measure ion current since further increases in bias voltage did not significantly affect the probe current (Sect.2.2.4).

4.3.2 Mass Deposition Rate

The mass deposition rates for the various targets were determined by measuring the coating mass of all of the samples deposited onto Si wafers. A differential mass balance was used for this purpose. This required the measurement of the relative difference in mass between each sample and a standard . All of the substrates were weighed prior to coating, and were selected such that their mass was within ±10 mg of the standard weight (usually ±5 mg). After determining the relative mass for each Si substrate to the nearest μg, they were loaded into the sputtering system for coating. The coated samples were subsequently reweighed to determine their relative mass. The coating mass was obtained simply by the difference between the relative masses of the coated and uncoated substrates. The precision of the coating mass measurement is estimated to be ±10 μg for most samples. With this method, the absolute mass of each substrate was unimportant, and the absolute coating mass could be determined with very high precision. Sufficient care was necessary, however, to avoid fracture of the wafer substrates, particularly when clamping down the cover on the substrate platform.

Following from equation 4.1, the mass deposition rate Z_m ($g.mm^{-2}.W^{-1}.min^{-1}$) was calculated from the coating mass using the following equation:

$$Z_m = \frac{4m}{\pi\, d_c^2 P\, t} \tag{4.5}$$

where m (g) is the coating mass deposited within time t (min), P is the power applied to the magnetron target, and d_c (mm) is the diameter of the coated area.

4.3.3 Visual and SEM Examination

The simplest form of characterization of the coatings was a qualitative description of their macroscopic surface appearance. This was conducted with normal daylight conditions, and the coatings were described in terms of their lustre and colour. Any non-uniform variations in the these qualities were also described. In some cases, the surface appearance varied with the angle of viewing. Quantitative characterization of the colour and reflectivity of the coatings was considered to be unnecessary for the present investigation.

In several cases, the surface of the coatings was examined by scanning electron microscopy (SEM). Initially a JEOL 840 SEM was used for this purpose, but the resolution of this instrument proved to be inadequate for the clear observation of features

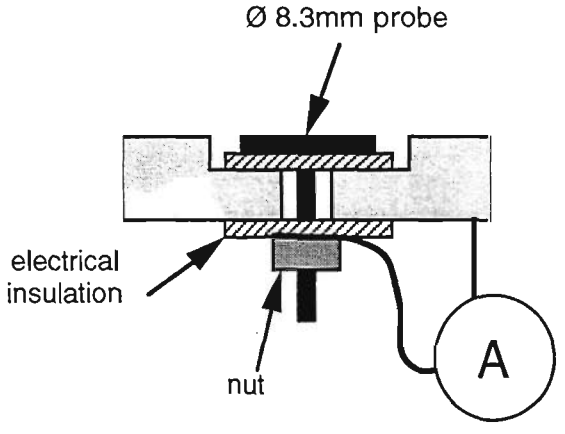

Fig.4.12 Cross-sectional schematic diagram of ion probe in substrate platform

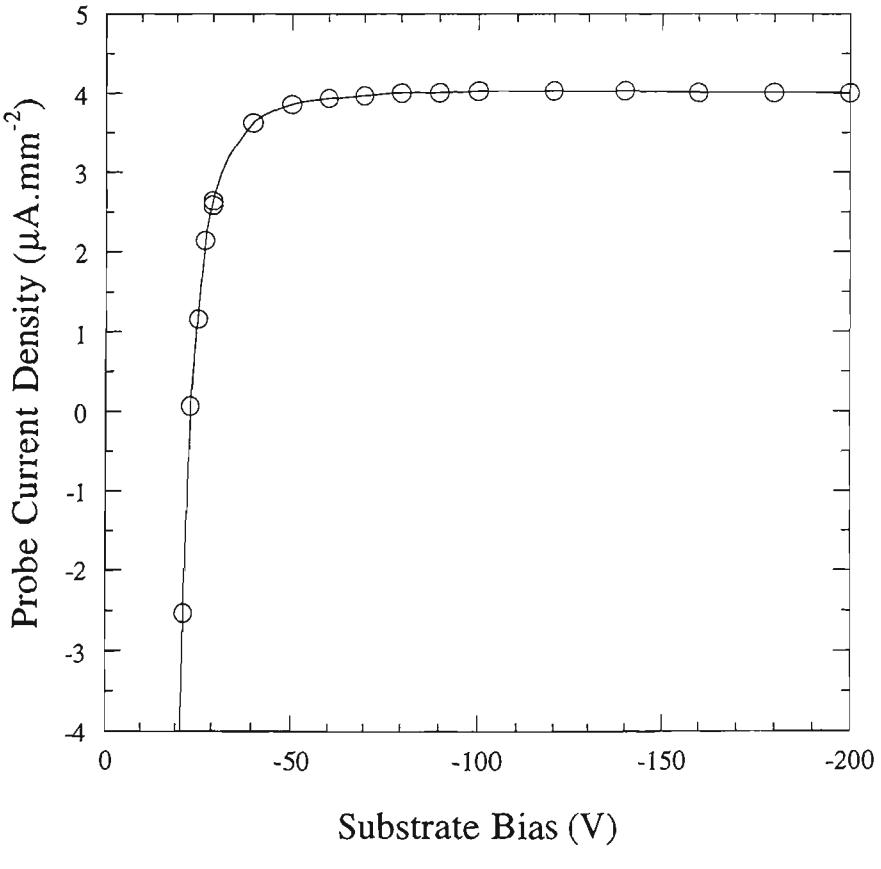

Fig.4.13 Characteristic voltage-current behaviour of the probe located in the substrate platform. These results were obtained with the following operating conditions: Zn target, 80W dc power, M3 magnet, 0.2Pa Ar pressure, 60mm target-substrate distance.

in the very fine structured coatings. A limited number of samples were observed using a JEOL 6300F field emission SEM. The extremely small electron beam spot size produced with this instrument ensures that it is capable of very high resolution. However, very little topographical contrast was present in the majority of coatings, such that even the field emission SEM was unable to reveal sufficient microstructural information. This was somewhat caused by the author's inexperience with operating the field emission SEM, but was also due to the inherently fine microstructure of the sputtered coatings. Consequently, relatively few coatings were examined by field emission SEM.

4.3.4 Chemical Composition

The chemical composition of the sputtered coatings was considered to be one of the most important aspects of this work. However, the large number of samples requiring compositional evaluation (about 300), combined with the desire for a non-destructive test, meant that a simple, rapid and inexpensive chemical analysis was required. For these reasons, the chemical composition of the coatings and sputter targets was evaluated by standardless semi-quantitative energy dispersive X-ray spectrometry (EDS). This analysis was performed using the above mentioned JEOL 840 SEM, with a Kevex Quantum light element EDS detector and Moran Scientific software. At least three analyses were made for each coating and alloy target, and the average result reported. EDS is strictly semi-quantitative and does not require standards. The reported compositions are therefore not expected to be highly accurate, although the precision attainable is quite acceptable. It is estimated that the typical absolute error of the EDS compositional measurements is about ±1 at.%. Unless noted otherwise, all compositions reported in this thesis are in terms of atomic percentages.

EDS analysis involves evaluating the energy and intensity of X-rays emitted from the surface of each coating, as a result of electron beam bombardment. These X-rays are generated in a tear-shaped volume of material below the coating surface [285]. Typically the majority of compositional information comes from a depth of about 1 μm below the surface. This thickness is similar to the total thickness of the sputtered coatings. Therefore, in the vast majority of cases the EDS spectra for the coatings included a signal from the Si wafer substrate in addition to the elements in the coating. Similarly, the coating on the steel substrates had a significant Fe signal in the EDS spectra. The signal from the substrate was not included in the semi-quantitative analysis.

EDS was also used for elemental mapping of the surfaces of some coatings. This was particularly useful for visualising the macroscopic distribution of various elements on the surfaces of several coatings. However, it was not possible to map the extremely fine-

scale distribution of elements expected to occur in dual-phase coatings. This was again due to the relatively large "sampling volume" encountered with EDS analysis, which was orders of magnitude larger than the individual grain sizes.

Peculiarities of the EDS measurement caused some difficulties with the semi-quantitative measurement of certain elements. In coatings that contained large amounts of Al, it was difficult to determine whether or not any residual Ar was present in them. This is because of overlap between the Ar K_α emission line and the "sum" peak from Al K_α emission. Sum peaks occur when two photons of identical energy collide simultaneously with the detector, resulting in a pulse signal with double the energy of the individual photons. They are most commonly detected when the specimen examined contains large amounts of one element, since the intensity of sum peaks are usually a very small fraction of the characteristic peaks. The sum peaks for Al K_α lie within 0.02 keV of the Ar K_α line, and this difference cannot be resolved by the detector which has a channel width of 0.01 keV, and peak half-widths of about 0.05 keV. It was possible to distinguish these two peaks in cases were the Ar K_β line was present, but this generally required several atomic percent Ar before it was detectable. Therefore, the accurate measurement of relatively small amounts of Ar in Al-based coatings was not possible.

4.3.5 Ion Assisted Deposition Simulations

A limited number of T-DYN [148] simulations of the ion assisted deposition process (Sect.2.4.4), were conducted via collaboration with Dr. Ilia Katardjiev from the Department of Solid State Electronics at Uppsala University, Sweden. These simulations were primarily aimed at confirming the observed trends in preferential resputtering for the Zn-Mg alloy coatings. The deposition of an atomic flux of Zn-46 at.%Mg simultaneously bombarded with Ar^+ ions was simulated. The *i/a* flux ratio was varied between 0.25 and 1.33, while the ion energy ranged from 50 eV to 200 eV. Large amounts of buried Ar were found to be present in the experimentally prepared coatings. This was incorporated into the simulations by arbitrarily setting the maximum Ar concentration in the coatings to that observed experimentally at similar ion energies. The excess Ar implanted into the coating during the simulation was "diffused" around to regions with lower concentrations or out of the coating.

The T-DYN simulations were designed to be directly compared with the experimental results obtained for the Zn40/Mg80 target. However, it was anticipated that the comparison would not be accurate on a quantitative basis, for several reasons. Firstly, the simulations are based on a purely elastic binary collision model. With the low ion energies typically used for ion assisted deposition, this approach is not strictly

accurate since bonding energies can play an important role in the resputtering process. Secondly, it was necessary to assume a weighted average surface binding energy, and this does not necessarily reflect the actual conditions experienced on the coating surface. Finally, the simulation does not account for thermal effects that may have been prominent in the sputtered Zn-Mg coatings, due to their moderately low liquidus temperature (~550°C from Fig.3.25). Therefore, the comparison between experimental and simulated results was on the basis of qualitative trends rather than absolute values.

4.4 X-Ray Diffraction Techniques for PVD Coatings

Beyond characterizing the sputter deposition process conditions (*i/a* ratio, mass deposition rate), coating appearance and morphology, and the chemical composition, it is important to determine the phases that are present in the sputtered coatings. The simplest way of achieving this is by X-ray diffraction (XRD). However, PVD coatings present some challenging obstacles which must be overcome before the results of XRD are meaningful. This is because coatings prepared by PVD techniques are invariably found to contain metastable phases with either extended solid solubility or an amorphous structure, strong preferred orientation, and large amounts of residual macrostress. These effects are difficult to resolve using conventional XRD methods (4.4.1). Fortunately, the very strong texture of many of the coatings presented the ideal opportunity to apply the Crystallite Group Method to determine the strain-free lattice parameter and residual macrostress (4.4.2).

4.4.1 Conventional Bragg-Brentano XRD

All of the XRD work presented in this thesis was conducted with a Siemans D5000 X-ray diffractometer. A Kristalloflex 710 long-fine focus copper tube was employed and a post-specimen monochromator calibrated to select only the K_α wavelengths of the diffracted beam. The tube was operated at a voltage of 45 kV and current of 40 mA. The coated Si wafer substrates were mounted on a standard sample holder using a small piece of "Blu-Tack®" to fix them in place. The first stage of characterizing the phases in the coatings required the use of a conventional parafocussing Bragg-Brentano geometry. These scans were conducted with a step size of 0.010° or 0.025° and a step time of 10 s. The 2θ range was generally restricted to 30°-50° in order to process the large number of samples within an acceptable time frame. In a limited number of cases the 2θ range was extended to 20°-100°, although generally this was found to be unnecessary.

Bragg-Brentano is the most commonly used geometry on X-ray diffractometers and involves rotating the detector circle at twice the speed of the sample circle, in order to maintain the parafocussing conditions. The Bragg angle 2θ is defined as the angle between the incident X-ray beam and the detector position. Each 2θ angle can be converted to an equivalent *d*-spacing by means of the Bragg equation:

$$\lambda = 2d \sin\theta \tag{4.6}$$

where λ is the wavelength of the X-rays (Cu $K_{\alpha 1}$ = 0.15406 nm). The expected error for *d*-spacing measurement was estimated from several Bragg-Brentano scans of a quartz external standard. The *d*-spacings measured between 30° and 90° 2θ were found to be displaced from their correct position by -0.02% with an error range of ±0.06% (three standard deviations). Given that the displacement of the *d*-spacing was less than the range in variability, none of the raw *d*-spacing measurements were corrected for instrumental displacement.

The relationship between the Bragg angle, the incident angle α, and the angle ψ between the diffracting planes and the surface of the sample, is given by:

$$\theta = \alpha + \psi \tag{4.7}$$

Obviously, when the incident angle is equal to half the Bragg angle, then ψ is equal to zero. This means that with the Bragg-Brentano geometry the planes in the sample that contribute to diffraction are all aligned parallel to the sample surface. Thus for coatings that have a growth direction perpendicular to the sample surface, the Bragg-Brentano scan will be useful for determining any preferred orientation. In the present work, this was achieved by comparing the relative intensities of the various diffraction peaks for each phase with those from the JCPDS cards [197] which are for randomly oriented material.

The coupled nature of the Bragg-Brentano geometry requires that the incident angle of the X-ray beam, α, increases continuously throughout a θ-2θ scan. This variation in incident angle affects both the size of the illuminated area on the sample surface, and the penetration depth of the X-rays that contribute to diffraction. A simple geometric consideration reveals that the length of the illuminated region on the sample, *L*, is given by the following equation:

$$L = 2R \frac{\sin(\beta/2)}{\sin(\alpha+\beta/2)} \tag{4.8}$$

where β is the divergence angle of the incident X-ray beam, and R is the distance from the X-ray source to the sample (R=200mm for Siemans D5000). For example, with a 1 mm (0.5°) divergence slit, the illuminated length is 9.8 mm for α=10° compared with 2.3 mm for α=50°. This means that the divergence and anti-scatter slits and the 2θ scan range should be tailored to suit the size of the sample. For all Bragg-Brentano scans the divergence and anti-scatter slits were 1 mm. The width of the X-ray beam illumination on the sample was controlled by a set of axial divergence soller slits placed in the path of the incident beam. These soller slits limited the width of the beam to about 20 mm.

Estimation of the penetration depth of an incident X-ray beam is less specific than the calculation of illuminated area. This is because the penetration depth of X-rays into a surface is given by a probability function [286]:

$$x = \frac{\ln(1-G_x)}{-\mu\left(\frac{1}{\sin\alpha} + \frac{1}{\sin(2\theta - \alpha)}\right)} \tag{4.9}$$

where G_x represents the fraction of the total diffracted intensity that derives from the surface to a depth x, and μ is the linear absorption coefficient of the sample. For example, at 2θ=30° in a Bragg-Brentano scan of a bulk Zn sample (μ = 400 cm^{-1} [250]), 50% of the diffracted intensity derives from a depth of up to 5.6 μm whereas 90% derives from up to 18.7 μm. It is common, however, that a penetration depth is stated which corresponds to G_x = (1-1/e) = 63.2%. In the above example this is equal to 8.1 μm. Furthermore, the linear absorption coefficients of Al and Mg are both much less than for Zn. It follows that the majority of the incident X-rays for Bragg-Brentano scans of the coatings examined in this thesis would have penetrated through the coating thickness (typically about 1 μm). Hence the XRD scans represent an average of the total coating thickness.

The penetration of the incident X-ray beam through the thickness of the coatings enabled the use of the Si wafer substrate as an internal standard. After mounting each sample in the substrate holder, a rapid Bragg-Brentano scan was conducted on the 2θ region between 68.9° and 69.5° (step size = 0.005°, step time = 0.2s). A very sharp and extremely intense diffraction peak at 2θ = 69.130° ± 0.005° was obtained from the (400) plane in the single crystal substrate only if it was perfectly aligned and parallel with the surface of the sample holder. No diffraction peak was obtained if the sample was slightly tilted since the Bragg condition of the single crystal substrate was not met. In such cases, the sample was removed from the holder, reapplied and tested until the sharp diffraction peak was obtained. Slight displacement of the sample in the vertical direction

was revealed by a small shift in the 2θ position of the sharp diffraction peak. This could be corrected by pressing the sample and holder against a very flat surface to ensure they were parallel. Following this procedure guaranteed that the surface of all samples were perfectly aligned on the imaginary focusing circle of the Bragg-Brentano diffractometer, thereby minimising errors in *d*-spacing.

A broad background with some sharp peaks were usually also observed in the 2θ range from 32.6° to 37.6°. The *d*-spacing of these peaks corresponded to the expected position of {200} diffraction from the Si wafer. However, {200} is a forbidden plane in the diamond cubic structure of Si and should not have been present. This peak is often detected when Si wafer substrates are used [129], and is thought to be caused by X-ray wavelengths of $\lambda/2$ passing the monochromator. Similarly, other higher and lower order reflections of the {400} planes can be detected at appropriate 2θ ranges, although the {200} reflections were of prime concern in the present case.

The receiving and detector slits selected for the Bragg-Brentano scans were 0.2 mm (0.1°). These slits provided a reasonable compromise between maximising the diffraction peak intensity (large slits), and minimising the peak broadening (small slits). Broadening of the diffracted peaks was measured using the Seimans DIFFRAC-AT software, in terms of a full width at half maximum (FWHM). The FWHM results for the coatings were not corrected for instrument broadening. The instrument broadening is estimated to be about 0.06° based on the FWHM of the (400) peak from the silicon wafer substrate. The FWHM of the coatings was typically much greater than this value.

4.4.2 Brief Review of Stress Measurement by XRD

The conventional method of determining residual biaxial macrostress by X-ray diffraction involves the measurement of *d*-spacing for a single diffraction peak at large 2θ, over a range of ψ angles, where ψ represents the angle between the sample surface and the diffracting plane [171,286,287]. A high 2θ peak is required so as to minimise errors in peak position caused by sample displacement. It can be shown that the strain in the ψ direction, ε_ψ, is related to the biaxial stress, σ, by the following equation:

$$\varepsilon_\psi = \left(\frac{1+\nu}{E}\right)\sigma \sin^2\psi - \frac{2\nu}{E}\sigma \qquad (4.10)$$

where E is the bulk elastic modulus and ν is the bulk Poisson ratio. The strain ε_ψ is equivalent to $(d_\psi - d_o)/d_o$, where d_o is the "strain-free" lattice parameter, and d_ψ is the *d*-spacing in the ψ direction. Therefore a plot of d_ψ as a function of $\sin^2\psi$ should yield a

straight line with the slope being directly proportional to the biaxial stress. Implicit in this calculation are the assumptions that the material is elastically isotropic and that it is randomly distributed with the stress acting on all grains.

The conventional $\sin^2\psi$ approach to stress determination has been used widely for several decades. However attempts to apply this technique to the study of PVD coatings has proven troublesome. Numerous examples can be found in the literature of cases where this analysis results in non-linear d_ψ vs. $\sin^2\psi$ plots [171,286,287]. Furthermore, most coatings examined are typically very thin and therefore many researchers have used the Seeman-Bohlin [288-290] or parallel beam [291-294] geometries for glancing angle X-ray diffraction (GAXRD), in order to maximise diffraction from the coating. In both of these geometries, the X-ray incidence angle is fixed at a small value (typically 1°), and the detector is scanned through a range of 2θ. It follows from equation 4.7 that as 2θ increases, so does the value of ψ. Thus, a plot of lattice parameter as a function of $\sin^2\psi$ can be obtained from a single GAXRD scan, and the residual biaxial stress can be calculated using equation 4.10. This method can also be utilised to evaluate the distribution of biaxial stress through the thickness of the coating [291,293,295]. However, problems have been reported with unusual oscillations in the $\sin^2\psi$ plots which are thought to be related to anisotropic elastic behaviour [296,297].

The linearity of the diffraction data obtained by the glancing angle method can be improved somewhat by accounting for the anisotropic nature of elastic properties [171,297,289,290,298]. This method uses the single crystal elastic constants (XECs) to modify the ψ value of each diffraction peak according to its crystallographic direction. It is assumed in this analysis that the stress is homogeneous throughout the coating, and consequently the strain is different in each grain because of differences in crystallite orientation. This stress-strain behaviour is often described as the Reuss model [171,298]. The Reuss model has found some success in explaining the stress behaviour of several coatings [289,290,299,300].

The Reuss model is often insufficient to deal with anisotropy, especially in cases when plastic flow has occurred, or when strong textures are present. In such cases, several researchers have successfully used a technique known as the Crystallite Group Method (CGM) [59,177,296,301-308]. The technique was originally developed by Willemse *et al* [309,310], and was popularised by Hauk *et al* [311] for the measurement of residual stress in cold rolled sheet [312]. Variations of CGM appear to have been independently developed by other researchers [177,305,306], and the technique has also been called the "fixed crystal orientation" $\sin^2\psi$ method [306]. CGM requires the reduction of the texture to a set of ideal orientations or crystallite groups. In the case of a

strongly fibre textured PVD coating, this method is particularly useful since it enables the stress to be directly measured in the textured component of the coating. This can often be the only way in which the stress can be measured by X-ray methods, since it is not uncommon that only one group of fibre textured grains can be detected in the coatings (Sect.2.4.1).

The stress in the fibre textured crystallite group of PVD coatings is examined by measuring the lattice strain as a function of ψ in those crystallites. This can be achieved in one of two ways. The first approach is to measure the d-spacing of several different planes within the same family of planes [303]. For example, in a <111> fibre textured fcc coating, the (331), (33$\bar{1}$) and (3$\bar{3}$ 1) planes are inclined to the surface of the coating at angles of 22.00°, 48.53°, and 82.39° respectively. The errors associated with misalignment of the diffractometer can be minimised by using a single family of reflections. However, the accuracy of this measurement can be affected by the fact that usually only two or three different reflections are available for any one plane family. The second and most common approach is to examine the d-spacing of several planes from different plane families but within the same crystallite family [59,296,304-308]. For example, in a <111> fibre textured fcc coating, the (222), (311), (331), and (420) planes are inclined at ψ angles of 0°, 29.50°, 22.00°, and 39.23° respectively. This method provides a greater number of data points for stress analysis, but sacrifices the accuracy because of possible instrumental errors that can vary with 2θ. The best compromise is obviously to blend the two approaches [177], but this can lead to excessively long XRD analysis times.

On this basis, CGM appears to be the best method for examining the stress in strongly fibre textured PVD coatings. Consequently, CGM was used throughout the present investigation. The instrumental methods used for CGM are described in Sect.4.4.3, and the mathematical methods by which the residual stress is extracted from the data are described in Sect.4.4.4. It will also be shown that it is possible to determine a strain-free lattice parameter in addition to the residual stress [177,303,305,306].

4.4.3 Asymmetric X-ray Diffraction

The analysis of stress by CGM requires the use of asymmetric X-ray diffraction. In this geometry, the sample is tilted by a fixed amount from the normal Bragg-Brentano arrangement. This can be achieved either around the goniometer axis (Ω-goniometer), or around the axis perpendicular to it and lying in the plane of the sample (ψ-goniometer). The latter case is achieved with four-circle stress/texture goniometers, and enables the measurement of diffraction peaks over a wide range of ψ angles [177,296,303-305]. The

former case can be conducted on a conventional powder goniometer by offsetting the sample position from the usual parafocussing arrangement, while maintaining the coupled scan [59,306,307,308]. Since a four-circle goniometer was unavailable for the present investigation, it was decided to pursue the Ω-goniometer approach to determine stress in the sputtered coatings.

A Siemans D5000 X-ray diffractometer was used for the CGM scans of various sputtered coatings. An asymmetric geometry results in degradation of the parafocussing optics obtained with a conventional diffractometer arrangement, causing the diffraction peaks to be broadened considerably. This is because for ψ angles not equal to zero, the focusing position of the diffracted beam is not coincident with the position of the parafocussing receiving slit [308]. This problem was corrected by replacing the conventional Bragg-Brentano parafocussing attachment with a "grazing incidence" post-specimen attachment [313]. This commercially manufactured attachment [314] consists of a long array of closely spaced copper slits (0.15° divergence angle), which effectively enforce parallel beam optics. This type of attachment is normally used for detector scans with a low fixed-incidence angle (0.1°-3°) for the analysis of thin randomly-oriented films. It was also found that a divergence slit size of 0.2 mm (0.1°) or less was essential in order to avoid instrumental peak broadening effects. Thus, the problems of peak broadening were overcome by using the grazing incidence attachment, and a series of asymmetric scans could be conducted at a range of different ψ angles.

Asymmetric scans on a conventional powder goniometer are restricted by the inherent geometry of the system. It is not possible to obtain diffraction from planes that require the use of incident angles of less than 0° or more than 2θ. The D5000 diffractometer was also fitted with an end stop at 2θ of 127.5° in order to prevent the detector from colliding with the X-ray tube. This placed further limitations on the available scan range.

CGM was applied to the (Al), (Mg) and (Zn) phases found to exist in many of the coatings produced in this investigation. In all cases, the strong fibre texture was oriented with the close-packed planes parallel to the coating surface; <111> for fcc phases and <0001> for cph phases. The angle ψ between the close-packed planes and any other plane in the crystal system can be calculated from standard crystallographic relationships in [253] or similar reference texts. The d-spacings for all planes in the (Al), (Mg) and (Zn) phases were calculated using the lattice parameters for pure strain-free powder [197]. Based on these d-spacings, the corresponding 2θ values were determined from equation 4.6, for Cu K_α radiation. The incident angle α was determined from 2θ and ψ via equation 4.7. This information was finally filtered by the requirements $0° < \alpha < 2\theta$

and $2\theta < 127.5°$ to obtain the possible asymmetric diffraction conditions for CGM analysis, as listed in Table 4.3. Diffraction conditions corresponding to negative ψ values are not shown because they required very large α angles which are not suited to the grazing incidence attachment. The (21.3) reflection for the (Mg) phase was not pursued because the necessary incidence angle was below the angle of total reflection.

Table 4.3 Asymmetric diffraction conditions required for CGM analysis of fibre textured coatings, using Cu K_α radiation.

Phase	Fibre Texture	Plane	ψ(°)	2θ (°)	α(°)
(Al)	<111>	(311)	29.50	78.23	9.62
		(222)	0.00	82.44	41.22
		(331)	22.00	112.03	34.01
		$(33\bar{1})$	48.53	112.03	7.49
		(420)	39.23	116.58	19.06
(Mg)	<0001>	(0004)	0.00	72.49	36.25
		(10.4)	25.11	81.54	15.65
		(11.4)	39.07	99.21	10.53
		(10.5)	20.56	104.25	31.57
		(20.4)	43.15	108.28	10.99
		(21.3)	58.84	117.95	0.14
(Zn)	<0001>	(0004)	0.00	77.05	38.52
		(10.4)	28.19	89.92	16.78
		(10.5)	23.20	115.79	34.69
		(11.4)	42.87	116.37	15.32

The calculated 2θ, ψ and α angles in Table 4.3 were used as a guide for asymmetric diffraction scans, and usually required some modification of 2θ and α in order to account for peak shifts. High 2θ peaks were measured whenever possible in order to minimise errors in peak position. This requirement was less critical than in conventional stress measurement because specimen displacement has little influence on peak position when parallel beam optics are employed [286]. Typically the asymmetric diffraction intensity for each peak was in the order of only 10 cps, and therefore very long count times were required to achieve acceptable count statistics. When combined with a step size of 0.05°, step times of between 60s and 400s were often required for each diffraction peak. Hence all of the scan programmes for asymmetric diffraction required about 24 hr per sample. A typical asymmetric scan programme for the (Al) phase is shown in Table 4.4. In all cases, diffraction peaks were detected in the vicinity of the expected locations.

Table 4.4 A typical asymmetric scan programme for the <111> fibre textured family of grains in (Al) phase. Total scan time for this programme was 24hr 8min.

Plane	2θ range (°)	α range (°)	ψ(°)	Step time (s)	Scan time
(311)	76.0-81.0	8.5-11.0	29.5	80	2 hr 15min
(222)	80.0-85.0	40.0-42.5	0.0	80	2 hr 15min
(331)	109.5-114.5	32.75-35.25	22.0	400	11hr 13min
(420)	114.0-119.0	17.8-20.3	39.2	300	8hr 25min

It should be noted that the asymmetric scans were performed without any sample rotation. Hence, the diffraction data obtained relates to only one azimuthal orientation. It is assumed that there was no azimuthal orientation present in the sputtered coatings. This is a reasonable assumption considering that many previous researchers have shown that azimuthal orientations usually only develop in the case of non-normal atomic and/or ionic fluxes [113,296]. Such conditions were not encountered in this investigation.

4.4.4 Calculation of Stress and Lattice Parameter

Upon the completion of the asymmetric XRD scan, the *d*-spacing of each peak was determined by curve fitting with the Siemans DIFFRAC-AT software. For cubic crystal structures, the *d*-spacings were converted to lattice parameter a_ψ using the following equation:

$$a_\psi = d_{hkl}\sqrt{h^2 + k^2 + l^2} \tag{4.11}$$

For the cph crystal structure, it was necessary to assume that *c/a* was constant and unaffected by any solid solution effects. This enabled the conversion of *d*-spacing to a single lattice parameter c_ψ using the following equation:

$$c_\psi = d_{hkil}\sqrt{\frac{4}{3}(c/a)^2\,(h^2+hk+k^2) + l^2} \tag{4.12}$$

where *c/a* = 1.8563 for Zn, or 1.6238 for Mg [197]

The lattice parameter corresponding to each plane in the crystallite group was then plotted as a function of $\sin^2\psi$. In most cases, very good linear correlations were obtained between the lattice parameter and $\sin^2\psi$. These graphs formed the basis for determination of the residual stress and strain-free lattice parameter.

Relationships exist in the literature for cubic-structured coatings which link the biaxial residual stress, strain-free lattice parameter, and $\sin^2\psi$ for specific fibre textures [177,296,303,305,306,311]. Formal derivations of these relationships are given in [303,315]. The relationships corresponding to two different fibre textures in cubic materials are as follows [303]:

$$\varepsilon_\psi = \frac{a_\psi - a_o}{a_o} = \sigma\left(\frac{2s_{11} + 4s_{12} - s_{44}}{3} + \frac{s_{44}}{2}\sin^2\psi\right) \qquad \text{<111> fibre texture} \qquad (4.13)$$

$$= \sigma\,(\,2s_{12} + (s_{11} - s_{12})\sin^2\psi\,) \qquad \text{<100> fibre texture} \qquad (4.14)$$

where s_{ij} represents the single crystal elastic compliances, and a_o is the strain-free lattice parameter. Each of these expressions can be expanded and rewritten in terms of a_ψ. The <111> fibre texture was relevant for the present investigation, and the corresponding expansion of equation 4.13 is as follows:

$$a_\psi = \left[\frac{\sigma a_o}{3}(2s_{11} + 4s_{12} - s_{44}) + a_o\right] + \frac{\sigma a_o s_{44}}{2}\sin^2\psi \qquad (4.15)$$

This expression is of the form y=A+Bx and therefore the linear regression coefficients of the $\sin^2\psi$ plot can be equated with the coefficients in equation 4.15. This enables calculation of the biaxial residual macrostress and the strain-free lattice parameter, by solving two simultaneous equations, using only the principal elastic compliances [177,303,305,306]. In the present work, the principal elastic constants of the fcc (Al) phase in the sputtered coatings were assumed to be the same as those of pure bulk Al: s_{11}=16.0 TPa^{-1}, s_{12}=35.3 TPa^{-1}, and s_{44}= -5.8 TPa^{-1} [250].

Similar relationships for hexagonal-structured coatings were not available in the literature. It was therefore necessary to derive appropriate relationships based on generalized expressions for the elastic constants. Thokala and Chauduri [316] recently derived a generalized expression for elastic constants ν and $E/(1-\nu)$ for the close packed hexagonal (cph) structure (where ν is the Poisson ratio and E is Young's modulus). In addition, the specific expressions for E, ν, and $E/(1-\nu)$ were given for directions within the two most important planes in the cph structure. These expressions are summarised in Table 4.5 in terms of the principal elastic compliances s_{ij}. It is apparent that the elastic constants are invariant within the basal planes {0001} but not within the $\{11\bar{2}\,0\}$ planes.

Table 4.5 Variations of E, ν, and $E/(1-\nu)$ for directions within the important crystallographic planes {0001} and {11$\bar{2}$ 0} in the cph structure [316].

Plane	Direction of Longitudinal Stress & Strain	Direction of Transverse Strain	E	ν	$\frac{E}{1-\nu}$
{0001}	<11$\bar{2}$ 0>	<1$\bar{1}$ 00>	$\frac{1}{s_{11}}$	$\frac{-s_{12}}{s_{11}}$	$\frac{1}{s_{11}+s_{12}}$
{0001}	<10$\bar{1}$ 0>	<01$\bar{1}$ 0>	$\frac{1}{s_{11}}$	$\frac{-s_{12}}{s_{11}}$	$\frac{1}{s_{11}+s_{12}}$
{11$\bar{2}$ 0}	<0001>	<1$\bar{1}$ 00>	$\frac{1}{s_{33}}$	0	$\frac{1}{s_{33}}$
{11$\bar{2}$ 0}	<1$\bar{1}$ 00>	<0001>	$\frac{1}{s_{11}}$	$\frac{-s_{13}}{s_{11}}$	$\frac{1}{s_{11}+s_{13}}$

In order to apply the elastic constants in Table 4.5 to calculate stress for sputtered cph coatings, one must first consider the nature of the stress. In a coating with a strong fibre texture, the stress state in the plane of the coating can be assumed to be biaxial with no through-thickness stress. This was also true for the expressions derived for the cubic-structured coatings. The most common fibre texture in cph coatings is <0001>, as confirmed in the present work. For a <0001> fibre textured cph coating, the appropriate elastic constants are those for an applied stress in a direction perpendicular to <0001>, resulting in a transverse strain in the <0001> direction. This corresponds to the fourth set of equations in Table 4.5. The direction of the stress in the plane of the film is irrelevant because of the invariant nature of the elastic constants in the {0001} plane. By a similar argument, it can be shown that the elastic constants for a <10$\bar{1}$ 0> fibre textured cph coating are represented by the first three sets of equations in Table 4.5. If required, relationships for <10$\bar{1}$ 1> fibre textured cph coatings can be derived from the generalized expressions in [316].

The elastic constants specific to the <0001> fibre textured coating can then be combined with the equation 4.10, and expanded to give the following expression:

$$c_\psi = c_o\,(1 + 2\sigma\, s_{13}) + \sigma\, c_o\,(s_{11} - s_{13})\,\sin^2\psi \qquad (4.16)$$

where c_o is the strain-free lattice parameter. This expression is once again of the form y=A+Bx, and thus the linear regression parameters from the $\sin^2\psi$ plot can be used to calculate the biaxial residual macrostress and the strain-free lattice parameter c_o. The a_o lattice parameter can also be determined by dividing the c_o parameter by the constant c/a

ratio. To the best knowledge of the author, this method of analysing CGM data has not previously been attempted for strong fibre textured coatings with a cph structure.

The principal elastic compliances used for the analysis of the cph coatings were extracted from a standard reference text [250]. These are summarised for Zn and Mg in Table 4.6, along with derived elastic constants for <0001> fibre textured coatings. It is worth noting that the elastic constants for a textured Mg coating are very similar to those of bulk Mg (E=44.7 GPa, ν=0.291), indicating that the elastic properties of Mg are relatively isotropic. However, the textured elastic constants for a Zn coating are much greater than those of bulk Zn (E=104.5 GPa, ν=0.249), indicating the anisotropic nature of this metal. The importance of using texture-specific elastic constants for the calculation of residual stress can be understood in light of such anisotropic behaviour.

Table 4.6 Principal elastic compliances for pure cph metals [250], and derived elastic constants corresponding to <0001> fibre textured coatings. The units of the compliances are TPa^{-1}.

Material	s_{11}	s_{33}	s_{44}	s_{12}	s_{13}	E (GPa)	ν
Zn	8.22	27.7	25.3	-0.60	-7.0	122	0.852
Mg	22.0	19.7	60.9	-7.8	-5.0	45.5	0.227

4.5 Electrochemical Evaluation

The range of tests available for evaluating the corrosion performance of metals is diverse, and a large number have been reviewed in the literature [2,3]. Each technique is generally specific to certain environments. Knowledge of the anodic dissolution behaviour of a metal can be used to qualitatively determine its ease of passivation and consequently its ultimate corrosion resistance. Consequently, potentiodynamic anodic polarization tests were used to characterise the electrochemical behaviour of the sputtered coatings. The work presented here was intended to provide some indication of the expected corrosion behaviour of the sputtered coatings.

The procedure adopted for anodic polarization testing was based on the ASTM standard designated G5-87 [317]. Some modification of this procedure was necessary for a number of reasons. Firstly, a test cell of the type specified in the standard was not available. An alternative simple cell design was used for this work, which had been previously demonstrated to operate effectively [318]. Secondly, the sample preparation methods had to be modified since the type used in the standard is designed for bulk materials, and this was considered inappropriate for evaluating the performance of coatings. Thirdly, the standard specifies the use of 1.0 M sulphuric acid for the electrolyte, and this was certainly much too aggressive for evaluation of the sputtered coatings. An electrolyte consisting of neutral 100 $mg.L^{-1}$ Cl^- [NaCl] was used in place of the sulphuric acid. This test solution is often used for laboratory tests aimed at simulating the typical chloride levels of coastal atmospheric conditions [319]. Tests with 3.5 wt.% NaCl aqueous solutions are often reported [143,186,211,239,240], but this was considered excessively aggressive since it represents the typical chloride level of sea-water.

4.5.1 Sample Preparation

Previous experience had been gained with the use of epoxy resin masking for the preparation of corrosion test samples [307,318,320]. However, this was a tedious and time-consuming procedure. With this in mind, a very simple design was developed, which enabled the preparation of a sample for testing within about 15 minutes. A schematic diagram showing the construction of the test samples is shown in Fig.4.14. Mechanical support for the coated steel samples was provided by a short length of stainless steel wire, welded to an alligator clip. The wire was then clipped onto the steel substrate, thereby affording a good electrical connection. The sample and clip was covered with an overlayer of clear adhesive film (Contact®), on each side of the sample. Prior to application of the film on the coating side of the sample, a 10 mm diameter hole

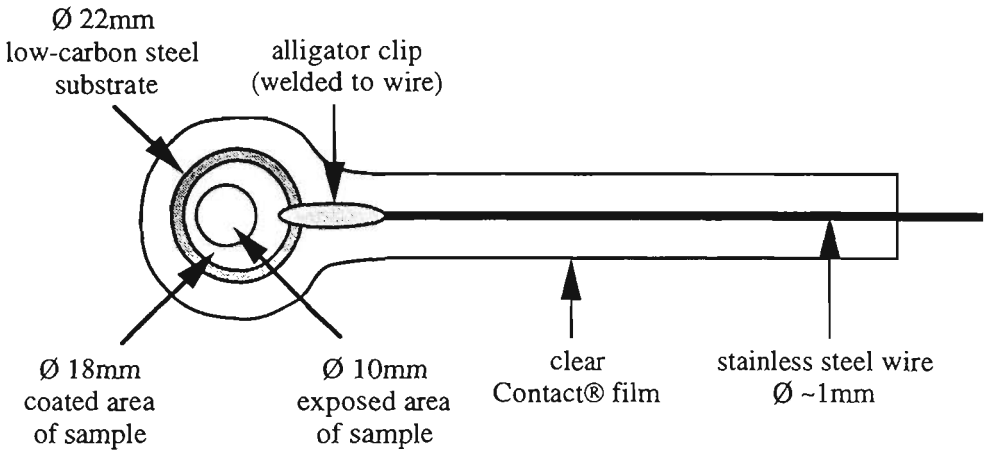

Fig.4.14 Sample design for electrochemical testing.

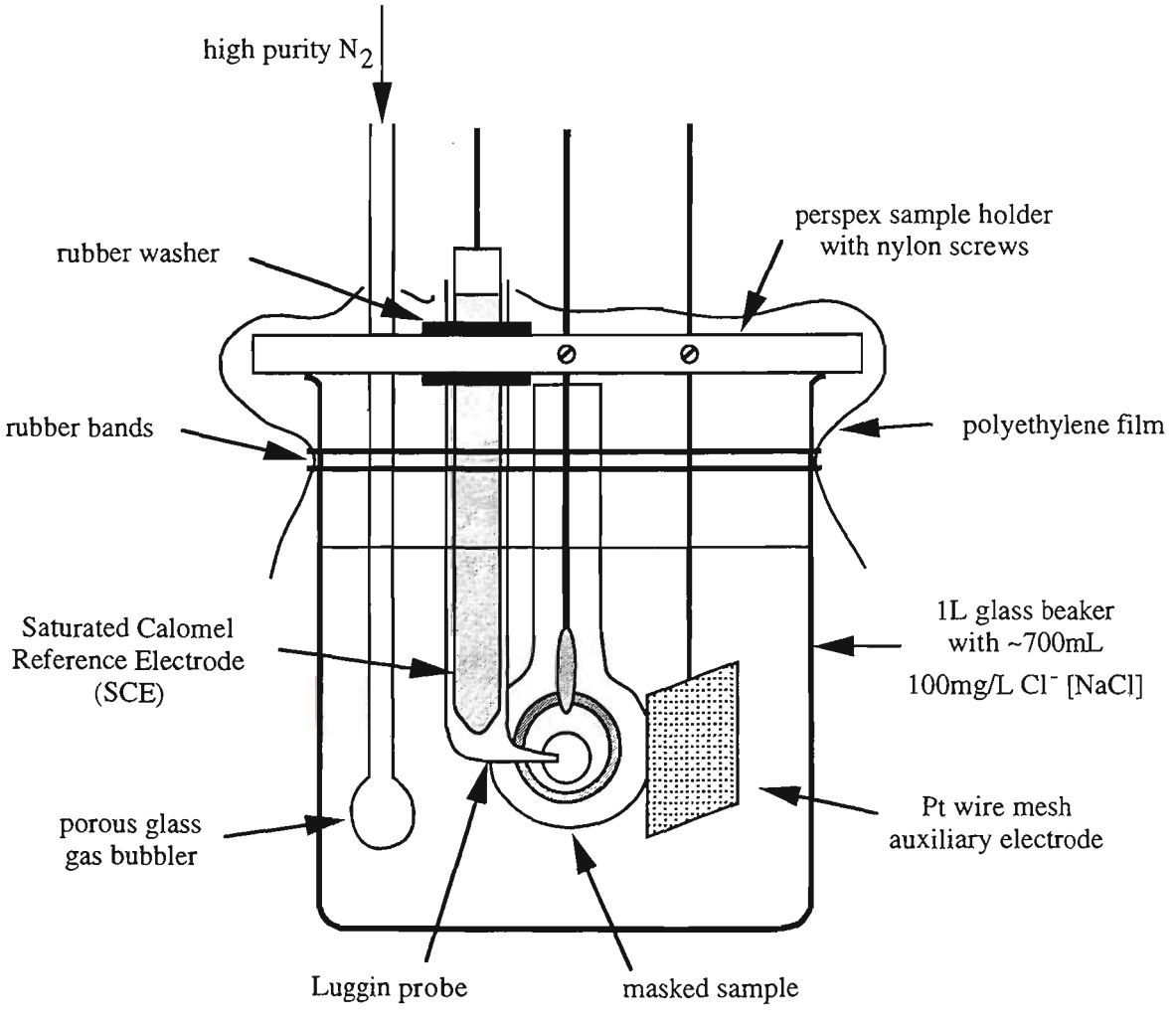

Fig.4.15 Electrochemical test cell configuration.

was punched in the film, in order to provide a constant exposed area of 0.79 cm^2 (the use of cm units is consistent with ASTM standard G3-89 [321]). The adhesive film was rubbed onto the surface of the sample in order to give a water-tight bond, particularly around the edge of the exposed area. The excess film around the sample was trimmed away, leaving the sample ready for testing as shown in Fig.4.14.

The samples were not cleaned once the film had been applied, as it was feared that the adhesive might contaminate the exposed surface of the coating. Cleaning of the samples was conducted before the application of the film, and involved a simple rinse in ethanol and warm air dry. Following completion of the tests, the Contact® around the sample was trimmed away, and the clip removed for re-use with the next sample.

4.5.2 Test Cell Design

The test cell used for anodic polarization testing is shown in Fig.4.15. The cell consisted of a perspex sample holder placed on top of a 1L glass beaker, which was filled with about 700 mL of test solution. A set of nylon screws in the holder were used to fix the sample and platinum wire mesh auxiliary electrode in place. The Luggin probe was held in place by a pair of rubber washers that rested on either side of the perspex sample holder. The Luggin probe acted as a receptacle for the reference electrode. The gap between the probe tip and the sample surface was set at about 2 mm, in order to minimise IR-drop errors. The entire cell was then covered with a double layer of polyethylene film (Glad Wrap®), which was held in place by rubber bands.

The testing solution was 100 $mg.L^{-1}$ Cl^- prepared from distilled water and laboratory grade NaCl. The chloride content of the bulk test solutions was confirmed by chemical analysis, and was always within ±10% of the target concentration. The pH of the solution was nominally neutral and the temperature during testing was typically 21±1°C. Deaeration of the solution was conducted to reduce the cathodic currents so that as much of the anodic curve as possible was experimentally visible [322]. This was achieved by inserting a porous glass frit into the solution and bubbling high purity nitrogen for one hour prior to commencing the polarization test. A gas outlet in the test cell was available through small holes in the polyethylene film where the porous glass frit and Luggin probe entered the cell. The gas flow rate was not monitored, but was simply adjusted so as to minimise the amount of splashing in the cell, while maintaining a regular flow of bubbles.

Testing the polarization behaviour under deaerated conditions was also beneficial from a fundamental viewpoint. Many of the corrosion failure problems of the

Zincalume/Galvalume product are related to conditions in which the oxygen supply is limited, such as in the case of wet stack storage staining and paint film edge undercutting. Under these conditions, the Al in the Zincalume coating does not readily passivate, and this leads to accelerated corrosion of the coating. It would therefore be of interest to examine the ease with which these experimental sputtered coatings can passivate under deaerated conditions.

A saturated calomel electrode (SCE) was used as the reference electrode in all corrosion tests. The potential of the reference electrode was checked daily with respect to a standard Activon SCE which was filled with a gel-electrolyte. The SCE was considered acceptable for use in testing if its potential was within ±25 mV of the standard SCE. Failure to meet this criteria was remedied by cleaning out the old electrolyte in the SCE and replacing it with fresh saturated $KCl_{(aq)}$. The SCE was then rested for at least an hour before re-checking its potential against the standard electrode. Generally, the SCE was not used in corrosion testing for at least another 24 hours, in order to ensure that the electrode had stabilised. A small amount of KCl crystals were always maintained in the bottom of the SCE, to ensure that the electrolyte in the electrode was saturated. The SCE was regularly shaken so that the crystals did not block the porous frit in the tip. This maintenance procedure for the SCE was considered essential in order to minimise instrumental errors.

4.5.3 Test Procedure

All of the measurements of corrosion potential and the polarization scans were conducted using an EG&G Princeton Applied Research (PAR) Model 283 potentiostat. This instrument is capable of automatically changing between nine magnitudes of current sensitivity from 1 nA to 100 mA during the course of a potentiodynamic polarization scan. This ensures accurate measurement of the current density over the entire potential scan range. Unfortunately, instrumental problems were encountered during testing with one of the ranges. This became apparent in the results as regions of unstable current density fluctuations. The problem was intermittent and did not appear to influence the overall outcome of the results. Most of the irregular noise associated with this problem was removed from the polarization scans.

The immersion of each sample was preceded by about five minutes of bubbling nitrogen through the test solution. During this period, the sample was affixed in the perspex holder, with the auxiliary electrode and Luggin probe in place, and the polyethylene film loosely placed over the holder. After removing the gas bubbler, the perspex holder was inserted into the solution. With a minimum of delay, the film was

wrapped down around the beaker and retained with a rubber band. The gas bubbler was inserted through the film and used to back fill the volume above the solution with nitrogen gas. The bubbler was subsequently immersed in the solution and the flow adjusted to a suitable level. The electrical connections to the potentiostat were then attached to the respective electrodes in the test cell. The delay between inserting the sample in the test solution and commencing recording the corrosion potential was typically in the order of five minutes. This was taken into account in the reporting of time-variation in the corrosion potential.

The samples were deaerated by nitrogen bubbling for one hour before commencing the polarization scan. Throughout the deaeration period, the corrosion potential of the sample immersed in the test solution was monitored. This was initially done manually by recording the potential reading on the potentiostat every five minutes or more, although for most samples, the corrosion potential was recorded automatically every 15 s. This gave an excellent indication of the variability and trends in the corrosion potential during the deaeration period. It should be noted that this "static" corrosion potential and that measured dynamically during the polarization scan were generally different due to the differences in solution agitation and activity of the surface.

Immediately before commencing the polarization test, the porous gas bubbler was raised above the level of the solution and the gas flow was increased. This ensured that there was a positive pressure of nitrogen above the solution which prevented oxygen reaching it during testing. It is anticipated that the solution was not completely void of oxygen, but the oxygen solubility would have been reduced considerably relative to a fully aerated solution. Therefore, oxygen reduction would still have been the most likely cathodic reaction, albeit with a lower diffusion-limited current density. In order to minimise the cathodic currents, the potentiodynamic polarization scans were then conducted with quiescent conditions [322]. Typically the starting potential was between -1200 and -1400 mV. This value was selected so that it was one or two hundred millivolts lower than the corrosion potential measured after one hour immersion. The intention was to ensure that the coating was fully activated at the start of the scan [322]. The polarization scan proceeded using an automatic current range selection, scan rate of 1 $mV.s^{-1}$, and scan step size of 2 mV. The scan was continued to about -500 mV, or until the anodic current density reached a level in excess of about 10^{-3} $A.cm^{-2}$. By this stage of the test, the coatings tended to show obvious signs of degradation in the form of gas bubbling or blackening around the outer diameter of the exposed area. The polarization curves are reported in their standard format with potential (SCE) as the ordinate and current density as the abscissa [321]. The current density is given in units of $A.cm^{-2}$ rather than the SI units of $A.m^{-2}$, in accordance with common usage [2,3].

4.5.4 Evaluation of Polarization Curves

Values for E_{corr}, i_p, and E_{pit} were extracted from each polarization curve following the standards specified in Sect.1.1. Most of the polarization curves determined in this study consisted of step-changes between the active, passive and transpassive regions. Hence the above-mentioned three parameters were sufficient to characterise the polarization behaviour. Generally the passive regions of the polarization curves for the coatings examined did not have a distinct critical current density, and therefore E_{pp} and i_{cc} were not determined. An exception was for the Zn-Mg coatings, for which the passive region extended over a large range of current densities. In this case, a maximum and minimum i_p was recorded for each coating.

The polarization curves and derived parameters were useful for predicting the performance of the coatings when galvanically coupled with a steel cathode. It was also possible to evaluate the corrosion rate of the coating in the absence of galvanic coupling, by measurement of either i_{corr} or polarization resistance R_p. It can be shown both theoretically and empirically that R_p is inversely proportional to i_{corr} [3]. Therefore, the measurement of only one of these parameters is required to determine corrosion rates. It was decided that R_p would be measured since it was easier to determine from the data available. The calculation of R_p from the polarization data involved replotting each set of results on a linear scale. The cathodic portion of the results were converted to negative current density, and a linear regression was fitted to the results for overpotentials of less than ±20 mV (typically ±15 mV). The slope of the regression line was a direct measure of R_p.

The use of full polarization curves for the measurement of R_p was not ideal. The scan rate of 1 $mV.s^{-1}$ was considerably more rapid than is usually used for R_p measurement by potentiodynamic methods. The sample was also submitted to relatively large cathodic overpotentials before reaching the corrosion potential, which may have influenced the local environment near the sample surface. However, R_p was measured from scans performed with identical conditions for all samples. It is then reasonable to assume that the interpretation of general trends in R_p for various samples is valid, even if the absolute values are not necessarily accurate. The R_p measurements therefore provided a useful indication of the trends in corrosion rate for the coatings without the need to conduct extra tests. It must also be recognised that the measured R_p values relate only to the specific test conditions used, after an immersion time of about one hour. It is expected that longer immersion periods and/or different test conditions would influence the corrosion rate.

Chapter 5

Zinc Coatings

5.1 Deposition Parameters

Four series of Zn coatings were prepared for microstructural evaluation during the course of this investigation. The important parameters for each series are given in Tables 5.1 to 5.4. The substrate materials were Si wafers except were noted. Series 1 and 2 were essentially identical coating runs and the objective was to establish the reproducibility of the microstructural parameters for nominally identical process conditions. Series 3 employed both Si wafer and low-carbon steel sheet substrate materials, with the intention of ascertaining the influence of substrate material on the coating microstructure. Series 4 was prepared at a late stage of this study, subsequent to the appearance in the literature of the work by Musil *et al* [136,137] on magnetron sputtered Zn coatings. This last series was designed to confirm the observations made by these authors for Zn coatings prepared at comparatively high bias voltages. The findings of Musil *et al* were critically reviewed in Sect.3.1, and are compared at length with the Series 4 Zn coatings in Sect.5.3.1. Furthermore, the Series 4 coatings were deposited using a higher *i/a* ratio than the Series 1-3 coatings, even though all coatings were prepared with the same set of M3 magnets. This enabled a comparison of the effects of different *i/a* ratios on the coatings.

The first three series of Zn coatings were completed using a low voltage power supply which was not capable of accurately controlling the power. The actual magnetron power for these coatings was about 80 W, despite the 100 W set-point. Series 4 was prepared using a high voltage power supply which was able to control the power much more accurately. Operation at the very high bias voltages in Series 4 (-400 and -450V) proved to be slightly unstable with occasional drops in the applied voltage and corresponding large increases in the current to the substrate platform. This effect was thought to indicate that arcing was occurring between the substrate platform and the anode, as a result of their small separation (<5 mm). It was a relatively infrequent event however, and the majority of the deposition time was free of substrate arcing.

Table 5.1 Deposition parameters for Series 1 Zn coatings. Other process variables: base pressure 80 μPa; magnetron power ~80 W; probe current 0.23 mA; deposition time 1.5 minutes per sample.

Magnetron Conditions		Substrate	Coating Mass
Voltage (V)	Current (A)	Bias (V)	(μg)
530	0.14	self (-22)	220
530	0.14	-40	221
529	0.14	-60	219
529	0.14	-80	204
529	0.14	-100	163 *
528	0.14	-120	155 *
528	0.14	-140	144 *
528	0.14	-160	162
528	0.14	-180	161
528	0.14	-200	158
527	0.14	earth	210

* coating mass in error due to substrate breakage

Table 5.2 Deposition parameters for Series 2 Zn coatings. Other process variables: base pressure 130 μPa; magnetron power ~80 W; probe current 0.22 mA; deposition time 1.5 minutes per sample.

Magnetron Conditions		Substrate	Coating Mass
Voltage (V)	Current (A)	Bias (V)	(μg)
528	0.15	self (-22)	214
527	0.15	-40	214
527	0.15	-60	204
526	0.15	-80	192
526	0.15	-100	183
526	0.15	-120	172
526	0.15	-140	164
526	0.15	-160	156
526	0.15	-180	152
526	0.15	-200	128 *
524	0.15	earth	211

* coating mass in error due to substrate breakage

Table 5.3 Deposition parameters for Series 3 Zn coatings Other process variables: base pressure 130 μPa; magnetron power ~80 W; probe current 0.21 mA; deposition time 1.5 minutes per sample.

Magnetron Conditions		Substrate	Substrate	Coating Mass
Voltage (V)	Current (A)	Material	Bias (V)	(μg)
534	0.14	Steel	self (-22)	*
534	0.14		-50	*
533	0.14		-100	*
532	0.14		-150	*
533	0.14		-200	*
535	0.14	Silicon	self (-22)	211
533	0.14		-50	209
532	0.14		-100	178
532	0.14		-150	169
532	0.14		-200	154

* coating mass not measured for coatings on steel substrates

Table 5.4 Deposition parameters for Series 4 Zn coatings. Other process variables: base pressure 90 μPa; magnetron power 100 W; probe current 0.55 mA; deposition time 5 minutes per sample.

Magnetron Conditions		Substrate	Coating Mass
Voltage (V)	Current (A)	Bias (V)	(μg)
467	0.21	self (-25)	937
463	0.21	-50	887
462	0.21	-100	744
461	0.21	-150	606
460	0.21	-200	529
460	0.21	-250	459
459	0.21	-300	387
458	0.21	-350	327
458	0.21	-400	290
457	0.21	-450	228

5.2 Results and Discussion

5.2.1 Mass Deposition Rate

The calculated *i/a* ratios and the deposition rates at self bias for the four sets of Zn coatings are shown in Table 5.5. From these results, it is immediately obvious that the mass deposition rate in the absence of any applied bias is relatively constant for all four coating runs (within ±3.5%). However, the *i/a* ratio for Series 4 was about double that of the first three series. This indicates that the magnetron for Series 4 was much more "unbalanced" than for Series 1-3, even though the same set of magnets was used in all cases. The reason for this effect is that the outer ring of NdFeB magnets in the M3 magnet assembly were slightly demagnetised for the first three series of coatings, probably due to having been accidentally overheated in a previous coating run. This was corrected for the Series 4 coatings by remagnetising the M3 assembly. Consistent magnetisation is a particular problem with the use of permanent magnets, and care must be taken to ensure that they are not heated above their Curie temperature. The degree of magnetron "balance" does not significantly influence the sputtering rate [60,65], and therefore the commonality of the deposition rate at self bias for all four series (Table 5.5) is not surprising.

Table 5.5 Characteristic deposition conditions for Zn coatings at self bias

Series	*i/a* ratio	Substrate Temperature	Deposition Rate ($g.mm^{-2}.W^{-1}.min^{-1}$)
1	0.093	< 50°C	$2.33x10^{-8}$
2	0.091	< 50°C	$2.27x10^{-8}$
3	0.088	< 50°C	$2.24x10^{-8}$
4	0.173	50°C	$2.39x10^{-8}$

The mass deposition rate for all Zn coatings is shown as a function of the substrate bias voltage in Fig.5.1. The most immediate trend in this figure, is that increasing the substrate bias above the floating potential (-22 to -25 V) caused an exponential reduction in the deposition rate due to ion bombardment-induced resputtering. Indeed, the coating mass at a bias voltage of -450V was only about 25% of that deposited at self bias, corresponding to about 75% resputtering (Table 5.5). The deposition rate for the Series 4 coatings was affected by substrate bias to a greater extent than the Series 1-3 coatings. This is consistent with the differences in *i/a* ratios, since a higher proportion of ion flux relative to the atomic flux can be expected to result in a greater amount of resputtering of the deposited coating.

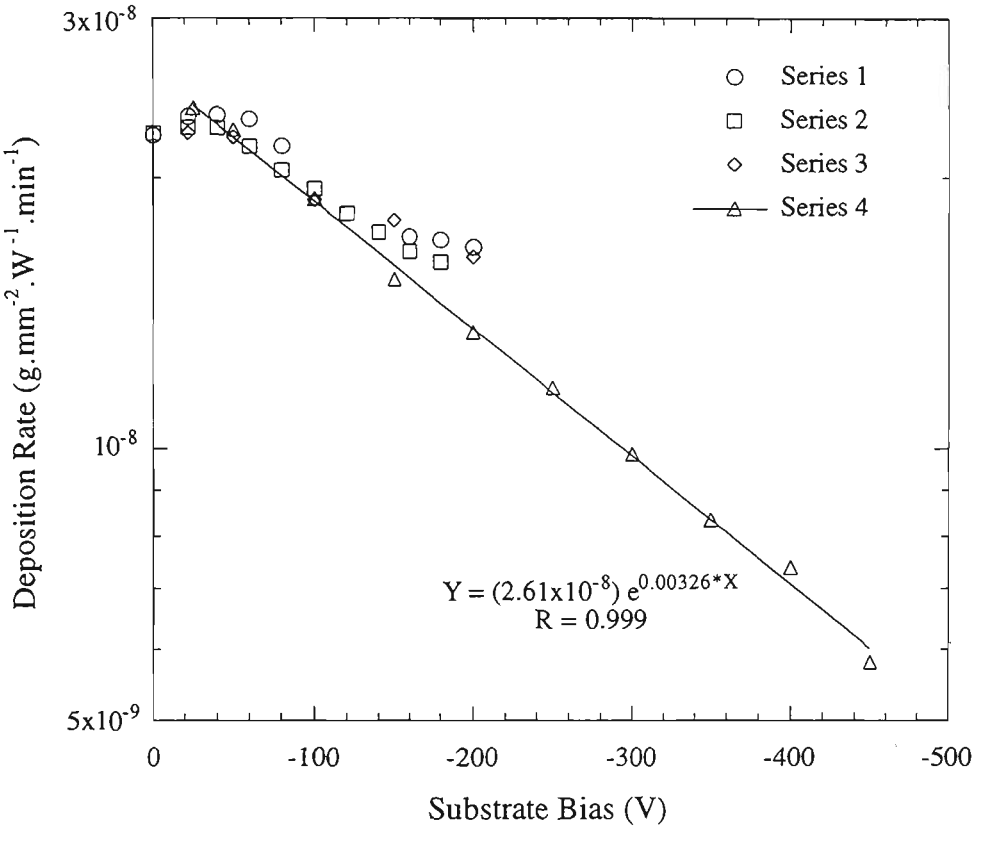

Fig.5.1 *Mass deposition rate for sputtered Zn coatings. Note the ordinate axis is semi-logarithmic.*

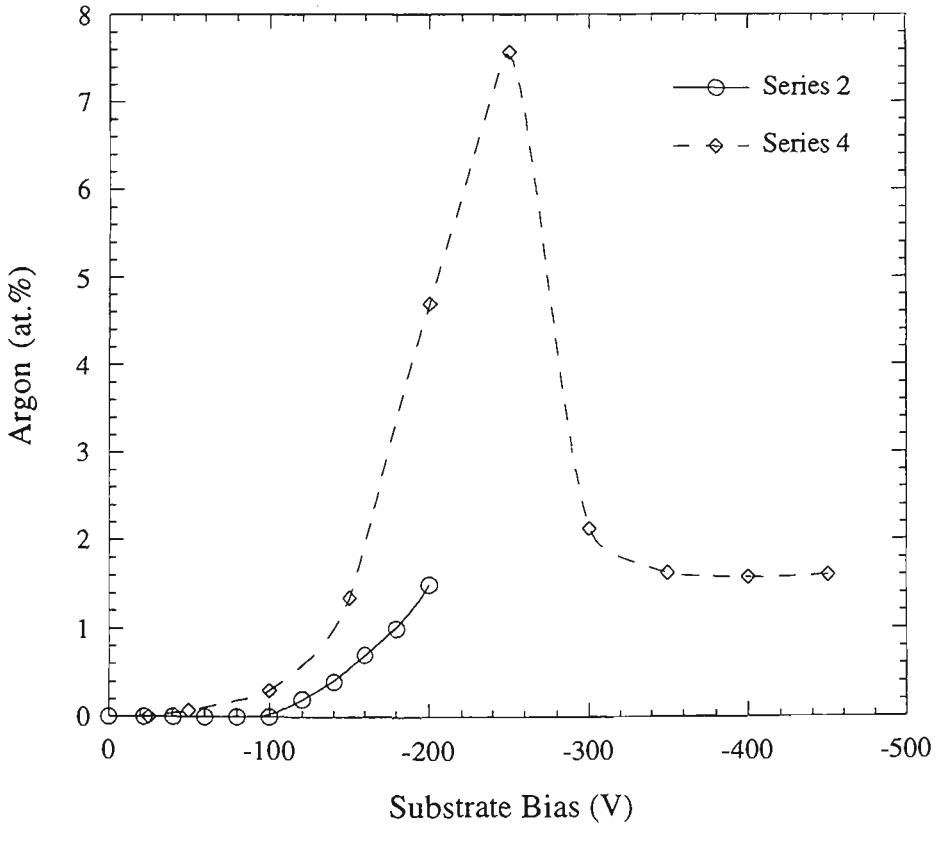

Fig.5.2 *Ar content of sputtered Zn coatings.*

5.2.2 Chemical Composition

Chemical analysis indicated that a very large proportion of Ar gas was trapped in some of the Zn coatings. Figure 5.2 shows the Ar content of each coating from Series 2 and Series 4 as a function of the substrate bias voltage. The compositions of Series 1 and Series 3 coatings were not evaluated. Increasing the bias initially caused a parabolic increase in residual Ar content. There is a suggestion in Fig.5.2 that the *i/a* ratio had an influence on Ar burial, as the data for Series 2 coatings (*i/a* = 0.091) was shifted towards higher bias than that of Series 4 (*i/a* = 0.173). Thus a bias voltage of -200V resulted in a much greater amount of retained Ar in the coatings for the higher *i/a* conditions. This result highlights the inter-relationship between substrate bias (ie. ion energy) and *i/a* ratio in determining the effects of ion assistance on coating formation.

Another significant feature of the chemical composition for the Series 4 coatings was that the Ar content reached a maximum value of 7.5 at.% at -250 V, followed by a dramatic reduction with further increase in bias. Beyond bias voltages of -350V, the Ar content stabilised at about 1.6 at.%. A peak in Ar content was not observed for Series 2 coatings because the bias voltage was not increased to a sufficiently high level. The composition results for the Series 4 coatings suggest that the burial of inert gas in the growing coating is not merely controlled by implantation. It would appear that there is a competing mechanism at high bias voltages that caused a reduction in the amount of entrapped inert gas. This concept is pursued in Section 5.3.3.

5.2.3 Visual and SEM Examination

Coatings prepared with a bias voltage of between earth and about -80V had a non-reflective blue-grey appearance. This is typical of most PVD Zn coatings and has been well documented [13,136,153,155]. With increasing bias, there was a tendency for the coating surface to become more specular and develop a white appearance. For bias voltages of -160V or more, the coatings were quite shiny with only a trace of the original non-reflective appearance visible at certain viewing angles. The transition from a completely non-reflective coating to a shiny coating was gradual and could not be defined at a specific bias condition. For the Series 3 coatings deposited on steel substrates, the specular appearance at high bias was not so obvious, since these substrates were not polished. However, the blue-grey colour observed for coatings prepared at low bias was absent at high bias. The Series 4 coatings tended to follow the same trends in surface appearance as the Series 1-3 coatings. Increasing the bias voltage beyond -200V caused

the development of a slight milky-white appearance in the coatings, while retaining much of the high reflectivity.

Three of the Zn coatings from Series 1 were examined on a field emission SEM. The self bias, -100V and -200V samples were selected for examination. Typical micrographs of the surface and fracture cross-sections of these Zn coatings are shown in Figs.5.3-5.5. Obtaining good quality images proved to be extremely troublesome due to the inherent lack of large scale morphological contrast in the samples, combined with operator inexperience. As such, it was difficult to accurately evaluate the microstructure of the Zn coatings in terms of the conventional Thornton Zone Model descriptions, and hence only the features which could be resolved are described.

All three coatings examined tended to consist of fine-structured grains that were planar with the substrate surface, and a collection of bright protruding grains on the surface that were larger in size. The fine-structured grains could be resolved on the surface of the coatings between the large bright grains. Measurements by the line-intercept method indicated that the grain size of this fine structure was in the order of 70 nm when viewed from the surface, which is consistent with the cross-section shown in Fig.5.5b. It was not possible to determine whether the substrate bias had any significant influence on the size of these grains, but it was obvious that there were no gross changes in grain size. The fracture-section microstructure at self bias can best be described as consisting of a clumped columnar structure. There was a tendency for these fine columnar grains to become more clearly defined at higher bias. It should be noted that the slightly transparent appearance of the coating morphology, particularly in Fig.5.5b, is due to the high accelerating voltage used for the SEM (25 kV).

The effect of a substrate bias was most noticeable for the large protruding grains on the coating surface. On the self bias coating surface, the protruding grains had a population density of about 14 μm^{-2}. Each of these grains were about 140±40 nm in diameter, and extended about 100 nm from the smooth fine-grained coating surface. At -100V bias, these grains increased in size to about 250±80 nm but were much less frequent on the surface, with a population density of about 7 μm^{-2}. At -200V bias, the size of the grains decreased to about 170±60 nm, and the population density decreased to 3 μm^{-2}. From these results, it would seem that increasing the bias voltage tended to cause the large protruding grains to coalesce and to be preferentially resputtered, such that they were almost completely removed at -200V bias. The Series 4 coatings were not examined by SEM, and so the surface appearance at bias voltages in excess of -200V cannot be described.

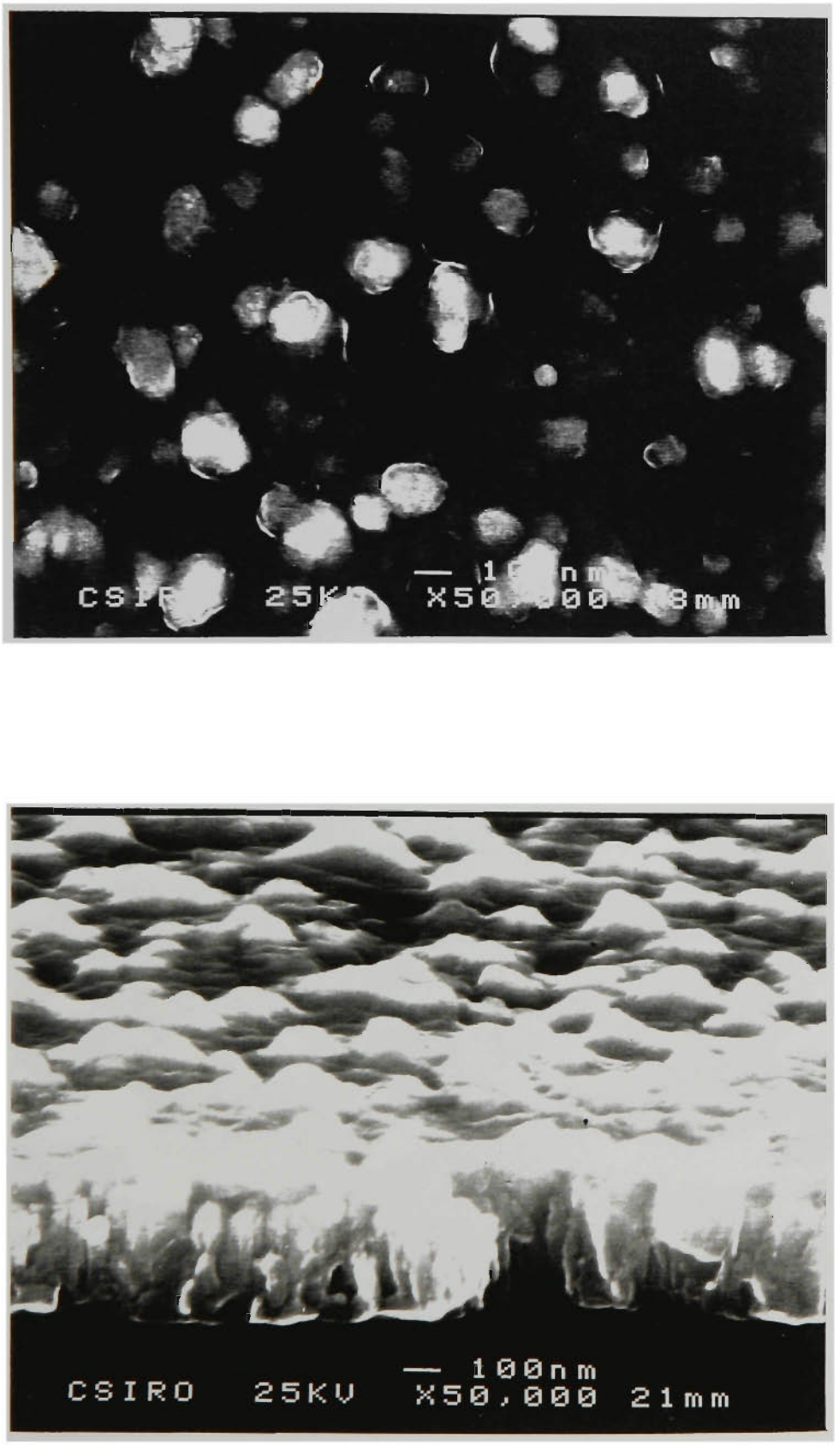

Fig.5.3 Surface and fracture-section SEM micrographs of the Series 1, self bias Zn coating.

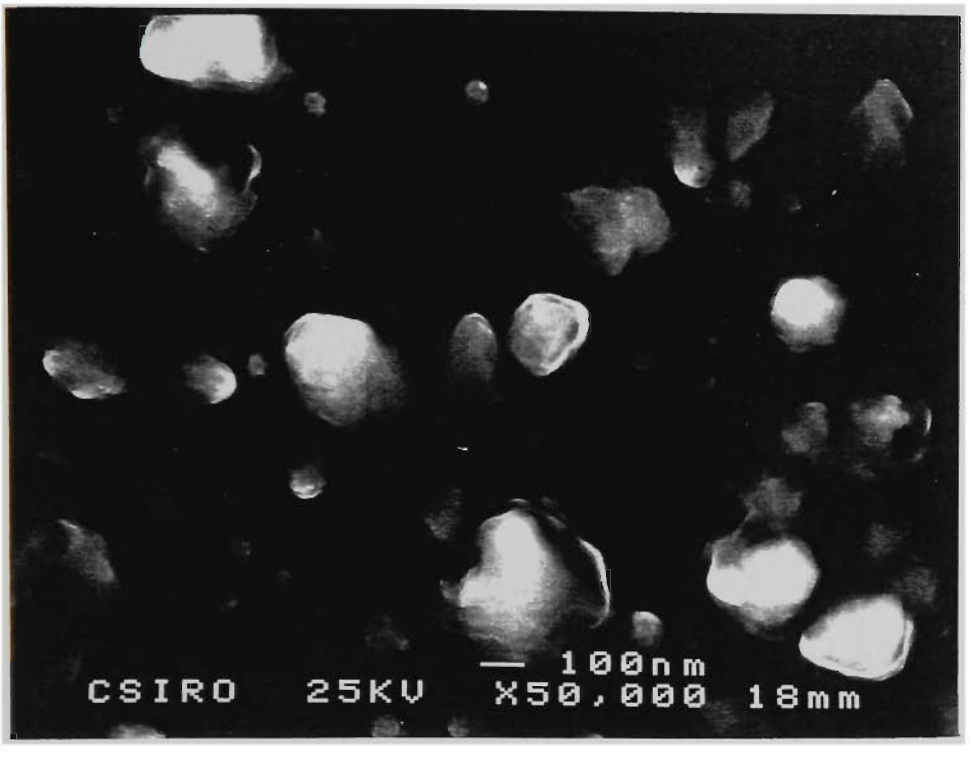

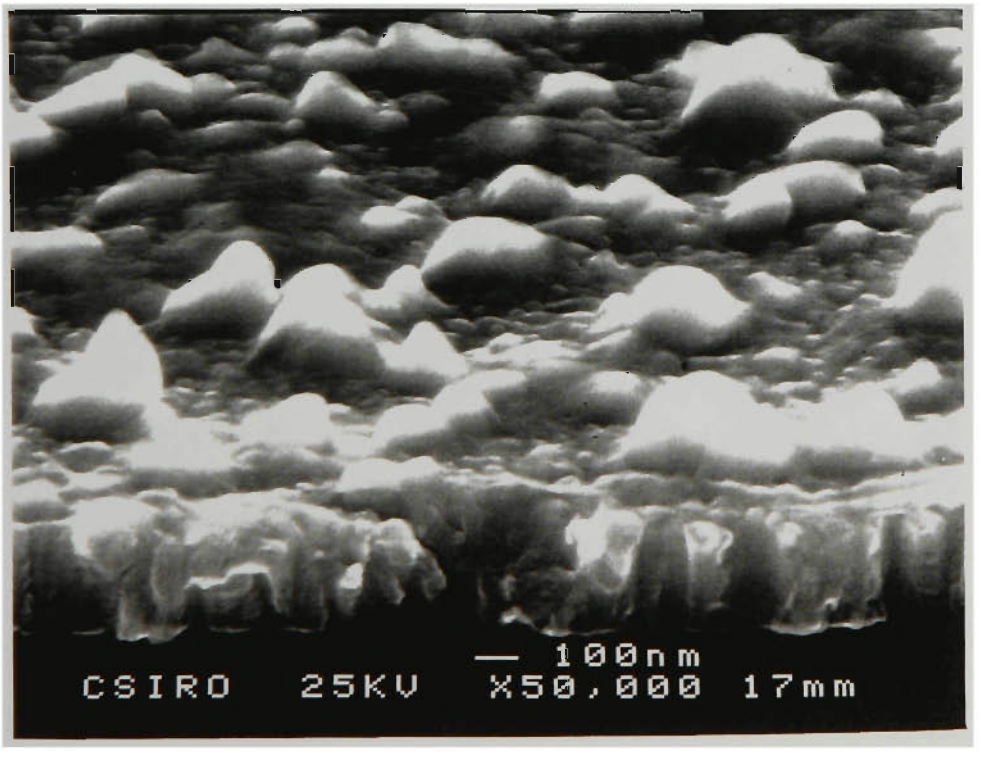

Fig.5.4 Surface and fracture-section SEM micrographs of the Series 1, -100V bias Zn coating.

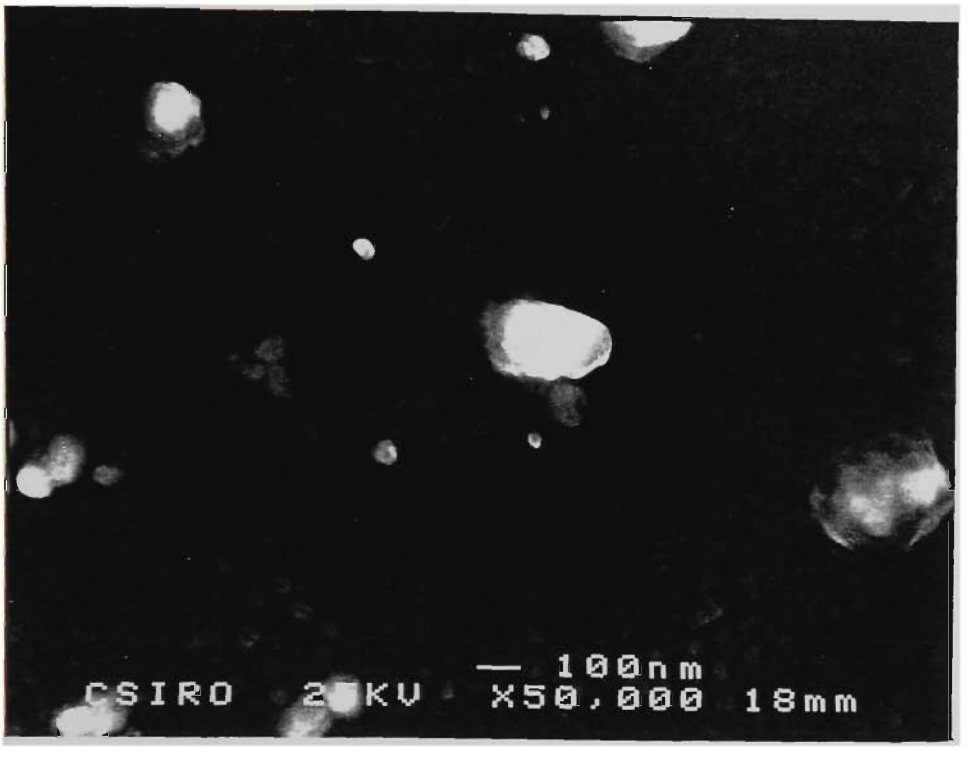

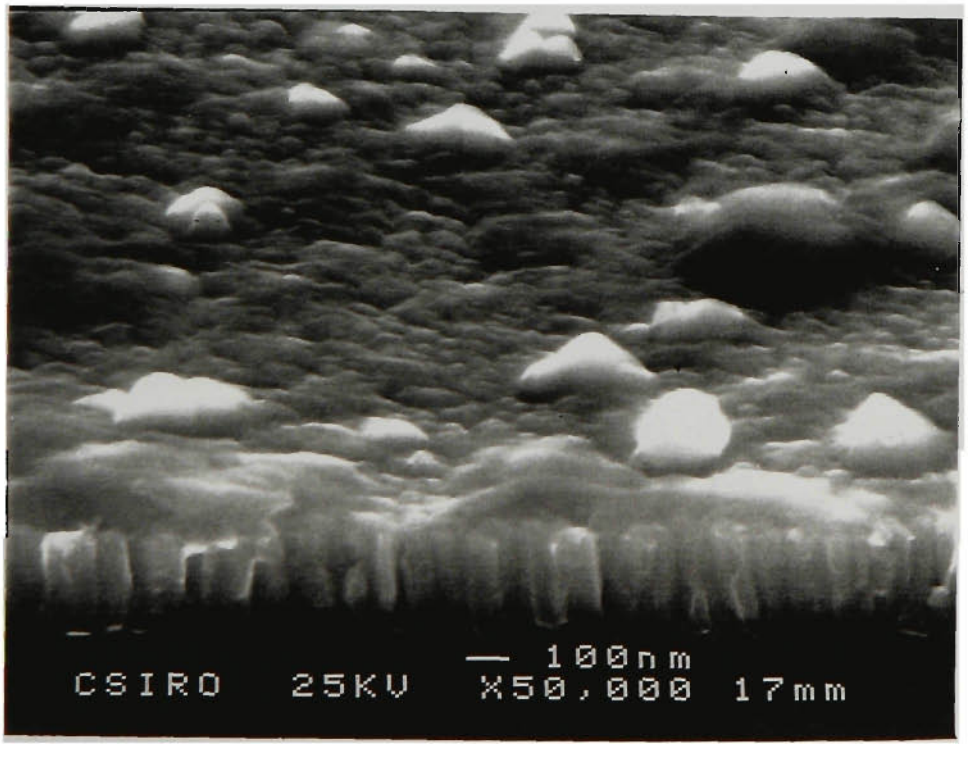

Fig.5.5 *Surface and fracture-section SEM micrographs of the Series 1, -200V bias Zn coating.*

Measurement of the coating thickness was also challenging for reasons which are obvious from examination of the micrographs in Figs.5.3-5.5. The irregular protruding grains on the surfaces of all of the Zn coatings made it difficult to determine the exact position of the surface in fracture cross-sections. Therefore, a range of thicknesses for each of the three coatings were determined, and are shown in Table 5.6. Also listed in this table are the thicknesses predicted from the coating mass, assuming that the density was equal to the theoretical density of pure bulk Zn (7.134 $g.mm^{-2}$). These SEM thickness measurements tend to confirm the observations made for the deposition rate measurements: increasing the bias voltage resulted in less Zn being deposited, and hence thinner coatings.

Table 5.6 Thickness of Series 1 Zn coatings as measured by SEM of fracture sections and from coating mass measurements (assuming 100% density).

Substrate Bias (V)	SEM Measurement (nm)	Predicted from Coating Mass (nm)
-22 (self bias)	400-500	390
-100	300-500	330
-200	200-500	280

5.2.4 Bragg-Brentano X-Ray Diffraction

The sputtered Zn coatings produced a wide range of different XRD spectra, depending on the substrate bias. Very broad peaks, shifted considerably from the expected position for pure Zn were observed, as shown in Fig.5.6 for the Series 4 coatings. The results of Bragg-Brentano XRD scans for all four series of the Zn coatings are summarised in Figs.5.7-5.9. The relative positions of the {0002}, {10.0} and {10.1} diffraction peaks for the (Zn) phase are represented in terms of $\Delta d/d_0$. These values were calculated from the measured d-spacings and the tabulated values for randomly oriented, defect-free Zn powder: {0002} = 0.2473 nm, {10.0} = 0.2308 nm, {10.1} = 0.2091 nm [197]. The d-spacings are therefore plotted in terms of strain in a direction normal to the sample surface. It should be noted that the d-spacings for Series 4 coatings at bias voltages of -300 to -400V were not determined with high precision due to the extremely broad diffraction peak profiles (Fig.5.6). The diffraction peak intensity and full-width-at-half-maximum (FWHM) are also shown in each figure.

Before discussing these XRD results in terms of bias voltage effects, it is worth examining the reproducibility and substrate effects. Series 1 and Series 2 coatings are directly compared in Fig.5.7. These two sets of coatings were prepared under nominally

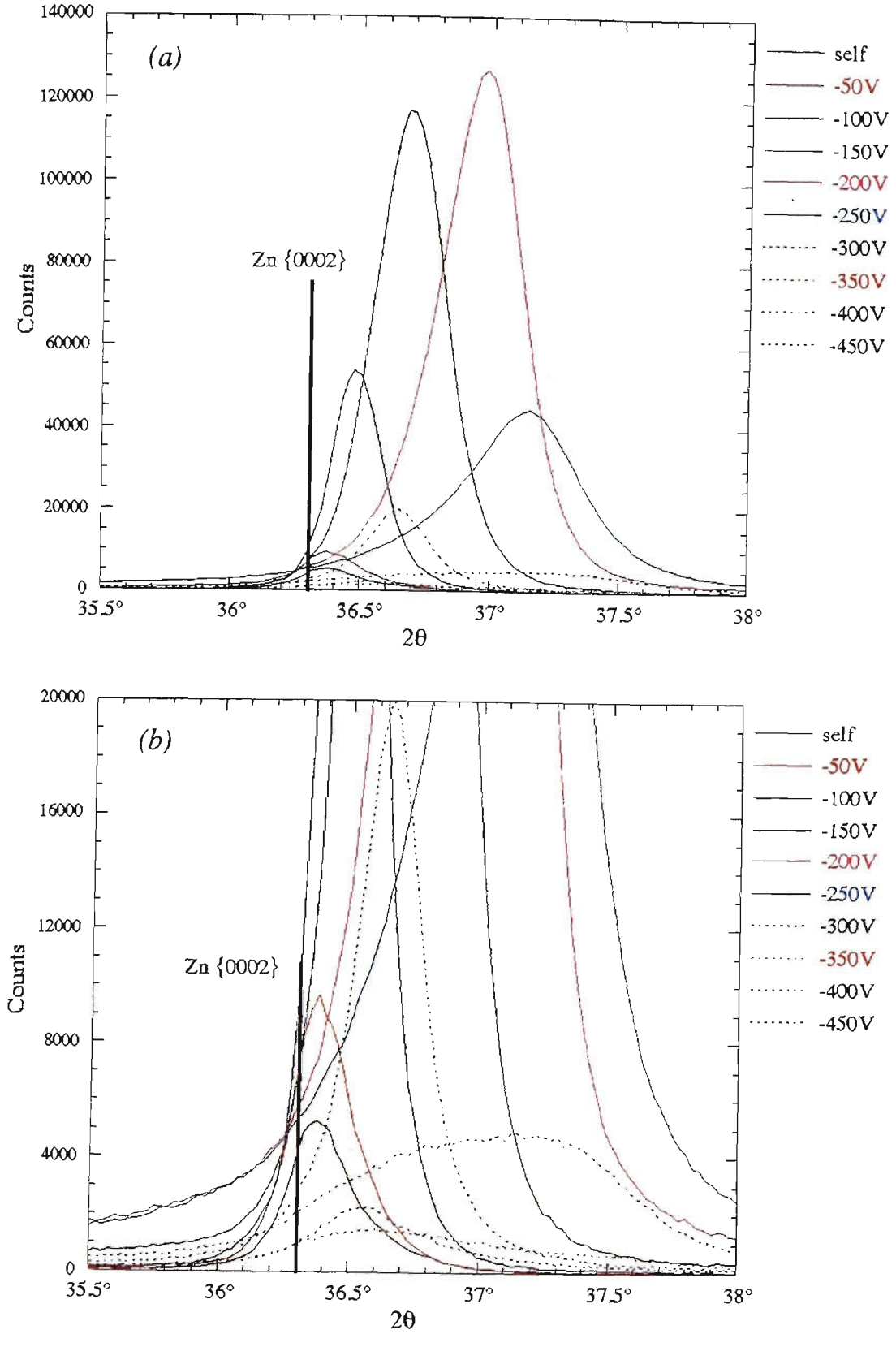

Fig.5.6 *Bragg-Brentano X-ray diffraction spectra for Zn Series 4 coatings*
(a) overview of Zn {0002} diffraction peak
(b) magnified view of low intensity Zn {0002} diffraction peaks

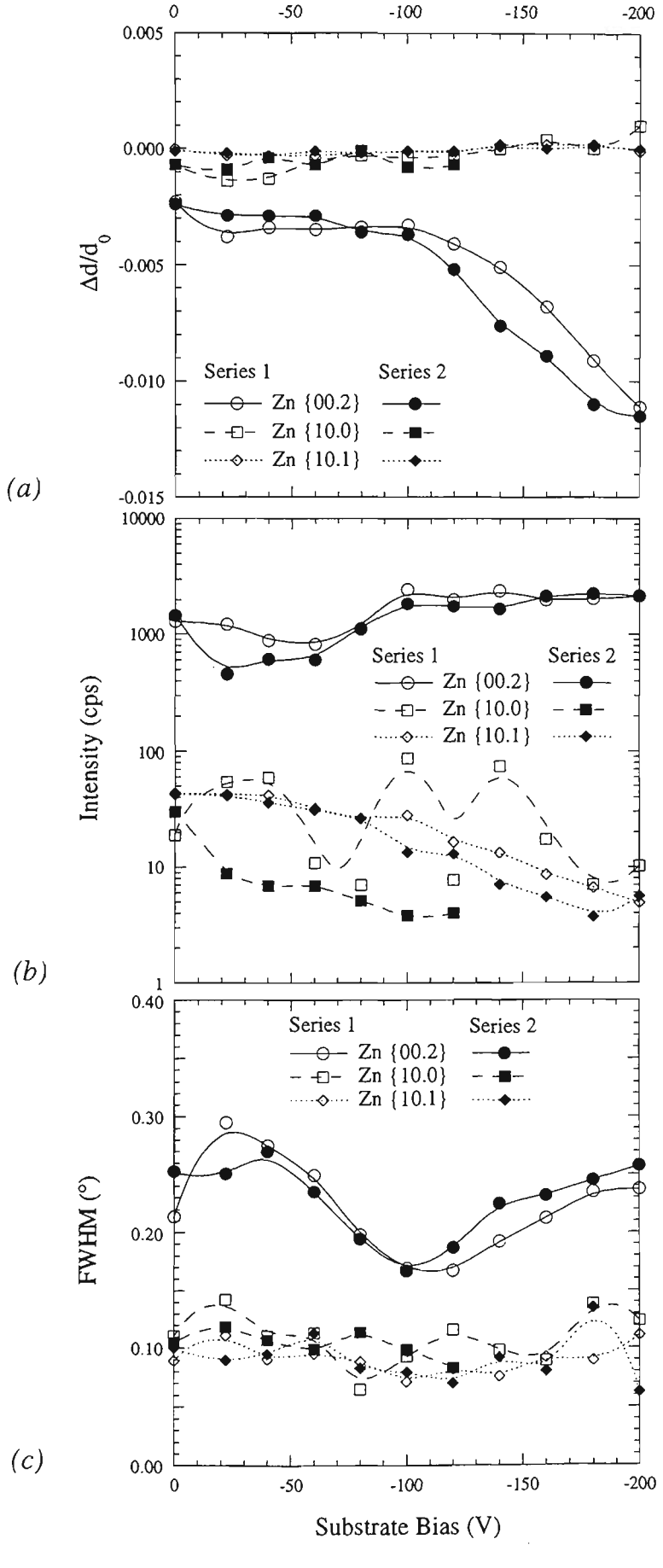

Fig.5.7 Comparison of XRD results for Series 1 and Series 2 Zn coatings: (a) d-spacing expressed as a strain parameter, (b) peak intensity, and (c) FWHM of diffraction peaks.

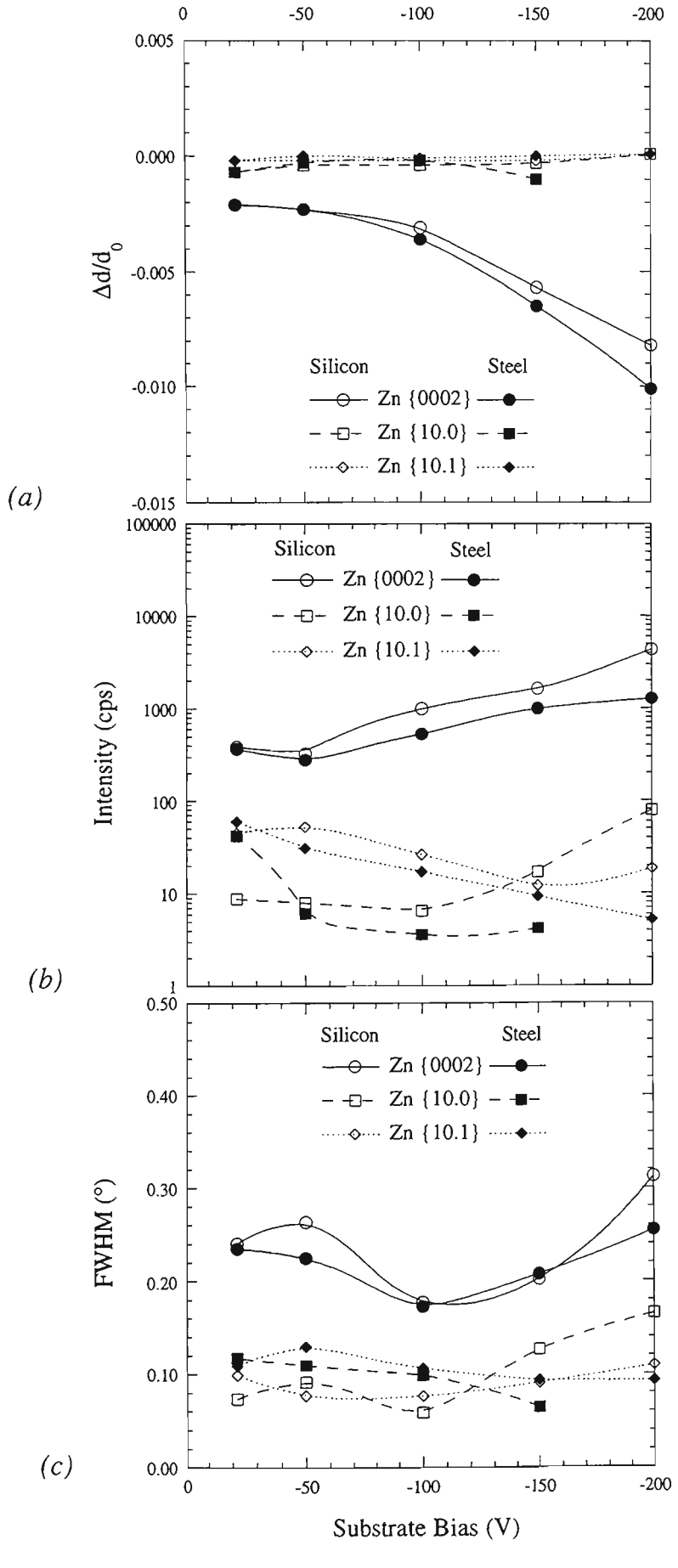

Fig.5.8 Comparison of XRD results for Series 3 Zn coatings deposited on silicon wafer and sheet steel substrates: (a) d-spacing expressed as a strain parameter, (b) peak intensity, and (c) FWHM of diffraction peaks.

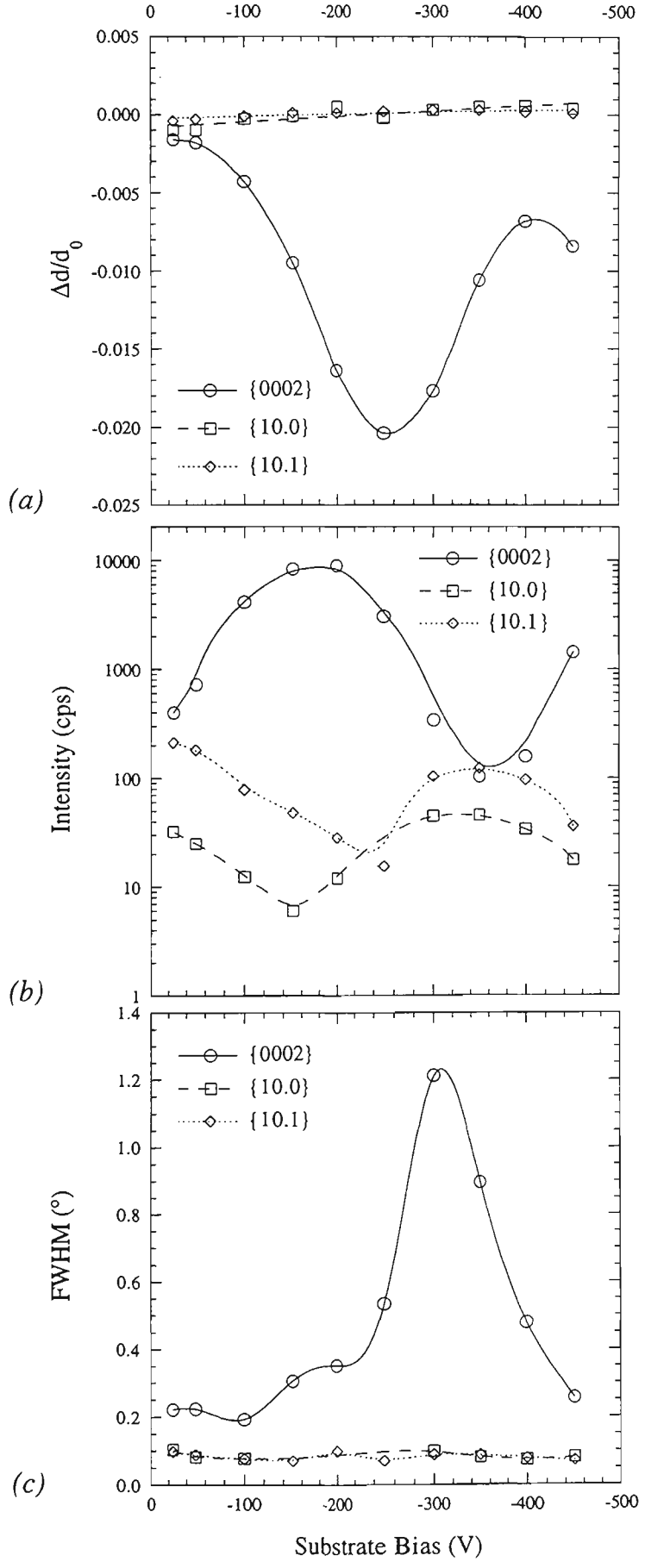

Fig.5.9 XRD results for Series 4 Zn coatings: (a) d-spacing expressed as a strain parameter, (b) peak intensity, and (c) FWHM of diffraction peaks.

identical conditions. The XRD results for each set of coatings were very similar in terms of general trends and magnitude, indicating that the coating process was highly reproducible. The only exception was for the {10.0} peak intensity which showed an apparently random variation in Series 2. The origin of this variation is not known, but is perhaps related to small differences in the efficiency of substrate clamping to the platform during the coating process, and hence the substrate temperature.

The influence of different substrate materials on the coating microstructure is demonstrated for the Series 3 coatings in Fig.5.8. The results for coatings on both Si wafer and steel sheet substrates were very similar in general trends and magnitude. This is an expected result considering that the deposition temperature was only slightly higher than ambient, and therefore thermal expansion mismatch stresses were insignificant. The single crystal nature of the Si wafer did not appear to favour epitaxial growth in the coating. Epitaxy is unlikely at such high deposition rates and low substrate temperatures. Furthermore, the surface of each wafer would actually have been covered by a thin and amorphous native oxide layer [113,177,179], and the Zn coating would not have been in direct contact with the single crystal. These results justify the use of Si wafers as substrate materials, provided that thermal expansion mismatch stresses are avoided or accounted for.

The general trends in XRD results for Series 4 coatings (Fig.5.9) were comparable with those of Series 1-3 (Figs.5.7 and 5.8). The differences in *i/a* ratio for the various coating series had only a small effect on the XRD parameters, whereas bias voltage had a dramatic influence. Therefore, the remainder of this chapter concentrates on the Series 4 coatings with only occasional reference to Series 1-3 in order to highlight effects at low bias voltages.

All of the Zn coatings had a tendency towards preferred orientation of {0002} planes parallel to the substrate surface. This is evidenced by the intensities for {0002}, {10.0} and {10.1} diffraction peaks (Fig.5.9b). For a randomly-oriented Zn powder, these peaks have relative intensities of 53:40:100 [197], whereas those of the Zn coatings at self bias (weakest preferred orientation) were in the order of 100:40:8. The {0002} preferred orientation became stronger as the bias voltage was increased, reaching a maximum at -200V bias. It has been previously demonstrated [137] that this type of preferred orientation corresponds to a <0001> fibre texture, with the fibre axis aligned perpendicular to the substrate surface. As the bias voltage was increased beyond -200V, the {0002} preferred orientation decreased rapidly until at -350V, the intensity of the {0002} peak was similar to that of the {10.1} peak. A bias voltage of -450V resulted in a return to the strong <0001> fibre texture. In addition to the intense {0002} diffraction

peaks, most samples still had some residual diffraction from non-basal peaks. It is thought that this diffraction corresponds to a population of randomly oriented grains in the coatings, which coexisted with the strong <0001> fibre texture. The similarity in trends for {10.0} and {10.1} peaks supports for this model.

The {10.0} and {10.1} *d*-spacings tended to be unaffected by the bias voltage, and were very close to those of a randomly-oriented strain-free Zn powder (Fig.5.9a). In comparison, the {0002} *d*-spacing was highly dependent on the bias voltage. At low bias voltage, they were relatively constant and shifted to slightly lower *d*-spacing than for a pure strain-free Zn powder. However, as the bias was increased beyond about -100V, the {0002} *d*-spacing decreased dramatically. This trend continued up to a bias voltage of -250V, beyond which, the {0002} *d*-spacing returned towards values indicative of pure Zn powder. Such shifts in the *d*-spacing can be caused by the presence of residual macrostress and/or solid solution effects. Based on the Bragg-Brentano XRD results alone, it is impossible to determine which of these two effects are the most dominant in the case of the sputtered Zn coatings, since it is feasible that the buried Ar could contribute to lattice parameter variation should it be retained in solid solution. For this reason, CGM was used to estimate the strain-free lattice parameters and the residual macrostress for Series 4 coatings (Sect.5.2.5).

The broadening of the diffraction peaks also seemed to be very different for the {0002} peaks compared with the non-basal {10.0} and {10.1} peaks (Fig.5.9c). The non-basal peaks tended to be sharply defined with a low FWHM which was independent of bias voltage. It must be noted that the FWHM of the {10.0} and {10.1} peaks was often difficult to measure owing to their very low peak intensity, which accounts for the variability in those results (Figs.5.7c and 5.8c). In comparison, the basal peak was much broader and tended to show a slight minima in FWHM at -100V bias. Between bias voltages of -100V and -200V, the {0002} FWHM increased by about a factor of two. Above -200V bias, it increased very sharply and reached a maximum at -300V bias. Bias voltages of more than -300V caused the FWHM to follow an equally rapid decrease.

Peak broadening is caused by either a fine crystallite size or residual macrostrain, and an analysis of the broadening of several different diffraction peaks can be used to measure the relative impact of each effect [296]. The very dramatic differences between the behaviour of the {0002} peaks compared with {10.0} and {10.1} preclude such treatment, since it would appear that the factors affecting peak broadening in each of these particular grain families are distinctly different. Based on these measurements alone, it is therefore not possible to determine whether microstrain or crystallite size was the dominant effect. However, Musil *et al* [137] performed an analysis using the higher

order basal peaks ({0004}, {0006} etc.), and showed that the peak broadening in sputtered Zn coatings was due primarily to microstrain effects rather than crystallite size. Furthermore, they found strong evidence in support of the idea that the microstrain (broadening) was higher only in the <0001> fibre textured grains. It is anticipated that similar conclusions could be made for the present coatings.

It is interesting to note that the bias voltage at which the FWHM of {0002} peaks began to increase (-100V) corresponded with the condition at which the *d*-spacing began to decrease abruptly, and also with the rapid increase in buried Ar content (Fig.5.2). Almost identical trends were obtained in earlier investigations by Shedden *et al* [160] and Musil *et al* [137], except for differences in the bias voltage at which it occurred (-60V and about -200V respectively). These differences were probably related to the *i/a* ratio used in each case. The bias voltage at which the peak in the Ar content was found, is also very similar to that obtained for the peak in FWHM. These observations for peak broadening, combined with the *d*-spacing and peak intensity data, give a very strong indication that the Ar content of the coatings was associated solely with the <0001> fibre textured grains. Randomly oriented grains tended to be unaffected by the Ar content, except in terms of their peak intensity, and hence their abundance.

5.2.5 Crystallite Group Method

The *d*-spacings of several different planes in the <0001> fibre textured crystallite family were measured via CGM (refer Sect.4.4). Unfortunately, the {0002} preferred orientation in coatings with -300V, -350V and -400V bias was not of sufficient intensity to permit such analysis. The c_{hkil} lattice parameters measured for each plane were graphed as a function of $\sin^2\psi$ (Fig.5.10), and provided very good linear correlations between for all samples. The steep gradient for some of these Zn coatings gave an indication that a considerable degree of residual stress was present in the fibre textured grains. Residual macrostress and strain-free lattice parameter values were extracted from the linear regression equations for each coating using equation 4.16.

The strain-free lattice parameter c_0 and the residual biaxial macrostress σ for each of the Zn coatings examined via CGM are shown in Fig.5.11. The {0002} *d*-spacing measured by Bragg-Brentano XRD and the {0004} *d*-spacing measured from the CGM scans are also shown in Fig.5.11a in terms of a "strain-affected" *c* lattice parameter. The similarity of these two sets of data confirm the reproducibility of the two different XRD techniques. The strain-free *c*-parameter of the Zn coatings was found to be slightly larger than that of a pure Zn powder, and essentially constant for all bias conditions examined. According to the assumption that the *c/a* ratio was constant, it is presumed that the

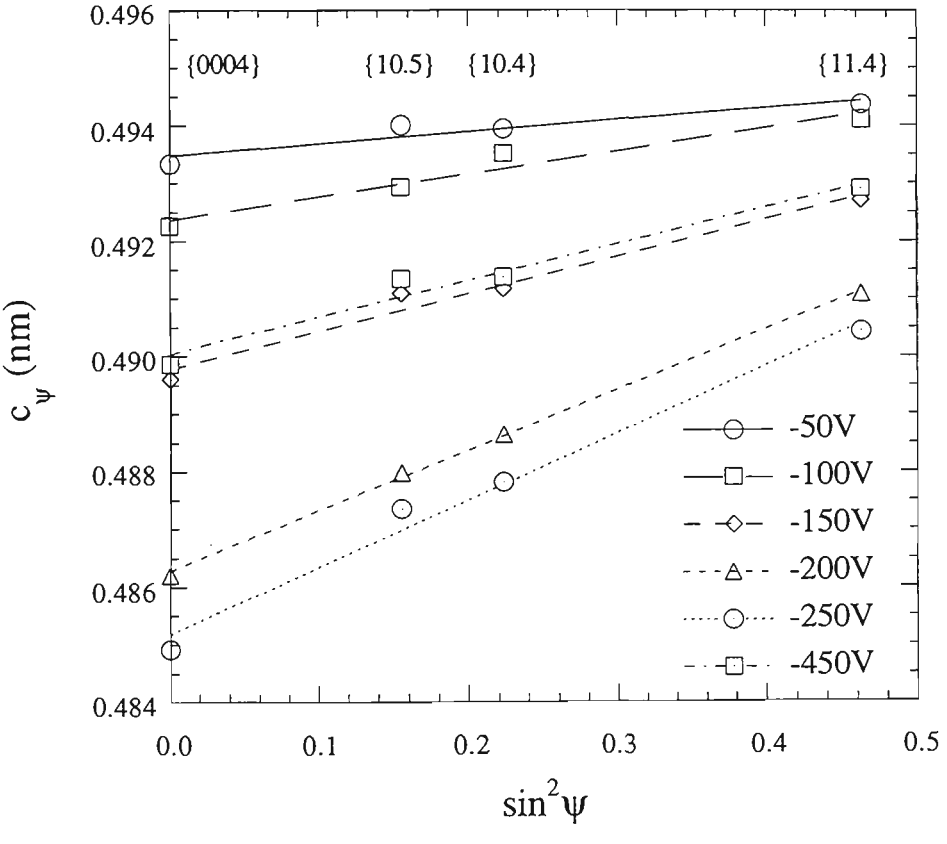

Fig.5.10 *$Sin^2\psi$ plots of CGM data for Series 4 Zn coatings.*

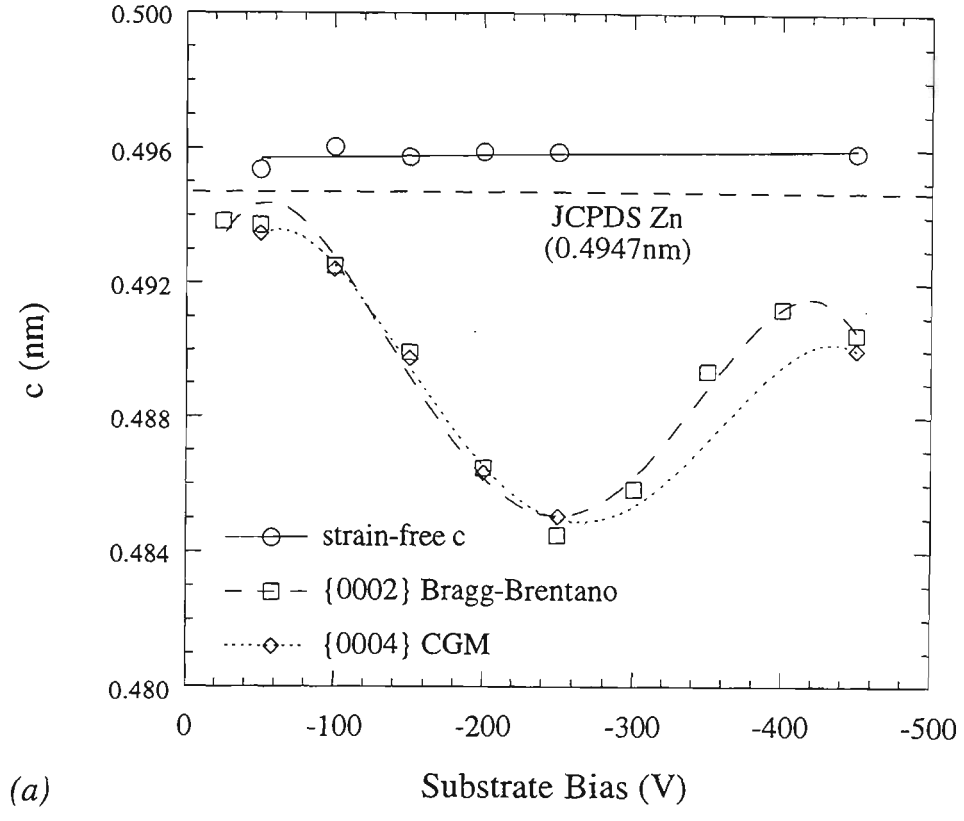

(a)

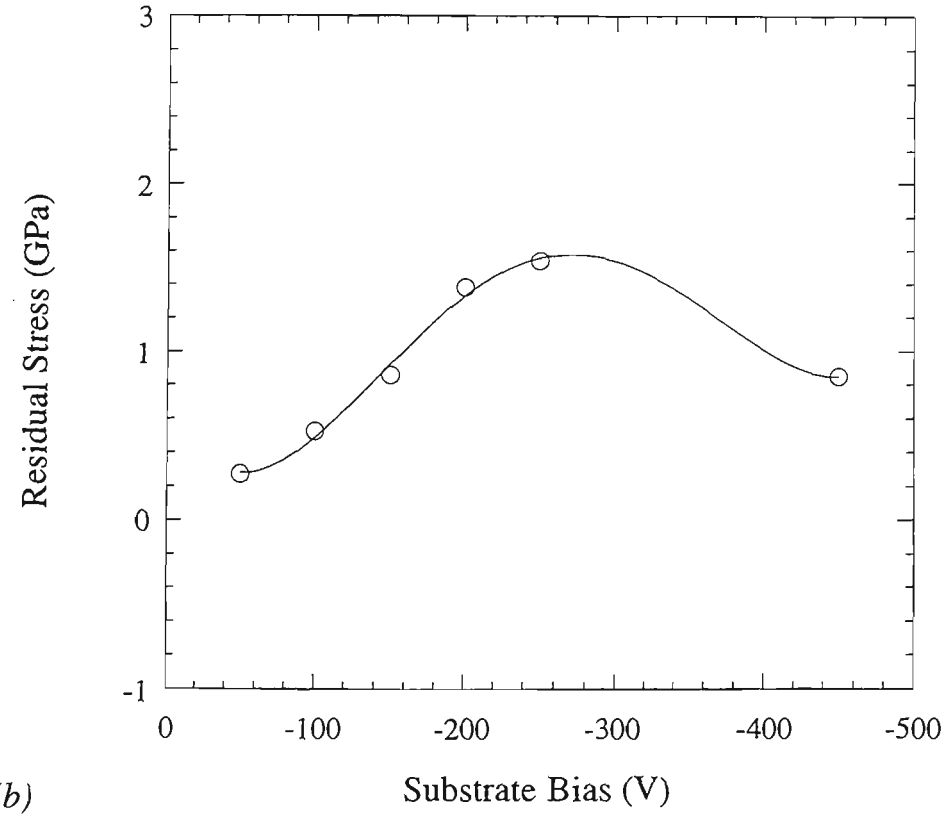

(b)

Fig.5.11 Strain-free c lattice parameter (a) and residual macrostress (b) of the <0001> fibre textured grains in Series 4 Zn coatings.

a-parameter behaved in a similar fashion. This result indicates that little or none of the buried Ar present in the coatings was retained in solid solution.

The corollary of the above finding is that the trends in {0002} *d*-spacing noted to occur with increasing bias (Fig.5.9a) were due almost entirely to residual tensile macrostress. The tensile stress was negligible at bias voltages of -50V or less, and increased to a maximum of about 1.5 GPa at -250V (Fig.5.11b). The lower stress measured at -450V combined with the trends in {0002} *d*-spacing (Fig.11a), suggest that the tensile stress decreased between -250V and -450V. This is perhaps related to the stress relieving effects of plastic flow reported to occur at high bias conditions [123,129]. However, this phenomena is invariably associated with large compressive stresses, and tensile stresses are rarely (if ever) encountered in the type of smooth, dense coatings produced here. It would therefore appear that the stress state of sputtered Zn coatings is atypical, and is perhaps related to the large amounts of Ar trapped in the coatings. This concept is pursued in Sect.5.3.3.

5.3 General Discussion

5.3.1 Comparison with Previous Work

The results of composition analysis and Bragg-Brentano XRD for the magnetron sputtered Zn coatings described in Section 5.2, replicate very closely the findings of Musil *et al* [136,137] for coatings prepared by the same method but with slightly different process conditions (refer Sect.3.1.2). A direct comparison between these two sets of experiments suggests that the main variations are due to differences in the *i/a* ratio afforded by the magnetron arrangement in each case. However, the interpretation of some results by Musil *et al* are found to be erroneous in light of the new evidence gathered from CGM analysis.

Musil *et al* [136,137] determined that the Ar content of their sputtered Zn coatings peaked at about 8 at.% for a substrate bias voltage of -400V (Fig.3.5). Their *i/a* ratio was very similar to those of Series 1-3 in the present investigation, but the substrate temperature was higher (up to 120°C). A comparison of the Ar content for Series 2 coatings (Fig.5.2) with the Musil *et al* results, suggests that higher substrate temperature tended to slightly reduce the Ar content at a given bias voltage. However, changes to the *i/a* ratio appeared to have had a much stronger influence on Ar content (Sect.5.2.2). Thus, the large difference in bias voltage corresponding to the peak of Ar content for Series 4 coatings (-250V) compared to those of Musil *et al* (-400V), was probably related to the factor of two difference in *i/a* ratio (0.17 compared with 0.09), rather than the substrate temperature.

The trends in Ar content reported by Musil *et al* [136,137] were found to correlate very closely with the trends in width of the {0002} XRD peak (Fig.3.6), and were inversely related to the {0002} *d*-spacing (Fig.3.7a). The same form of relationships were established for the present work (Fig.5.9). The trends in *d*-spacing were interpreted by Musil *et al* as being caused only by lattice contraction effects induced by substitutional dissolution of Ar in the Zn matrix. They disregarded the possibility of residual macrostress affecting the *d*-spacing on the basis of stress measurements via the Seeman-Bohlin method. However, it was argued in Sect.3.1.2 that this analysis did not apply to the stress in the <0001> fibre textured Zn grains which comprise the bulk of the coating. This was proven in the present investigation by CGM measurement of residual stress in <0001> fibre textured grains. It was firmly established that, not only were the coatings subject to very large tensile macrostresses, but the strain-free Zn lattice parameters were unaffected by the presence of Ar in the coatings (Fig.5.11). The bias-related trends in

{0002} *d*-spacing measured from Bragg-Brentano XRD scans were therefore indicative of the residual macrostress in the coatings, and not lattice parameter variation.

Musil *et al* [136] reported on a transition from a milky to shiny surface appearance with increasing bias voltage for the sputtered Zn coatings. In the present coatings, this milky appearance was less pronounced, but was very prominent in other Zn coatings deposited with elevated substrate temperature [160]. In each case, it is believed that the non-reflective milky appearance is due to the light-scattering effect of a population of relatively large protruding grains on the coating surface. The transition to a shiny appearance was confirmed by the present study (Sect.5.2.3), and occured at a bias voltage corresponding to the sharp increase in Ar content. However, the transition was much more gradual than was suggested by Musil *et al*, and it has been demonstrated to be related to the reduction in population density of comparatively large protruding grains on the Zn coatings (Figs.5.3-5.5). Such differences are thought to be due to the substrate temperature, since the present coatings were noted to have far fewer protruding grains than were observed on the coatings of Musil *et al* (compare Fig.3.4b with Fig.5.3a). The importance of substrate temperature in defining the microstructure of Zn coatings has been highlighted previously [110,161], but the "transition temperature" (5°C with 200eV ion bombardment), was inconsistent with the present work.

5.3.2 Model of Zn Coating Microstructure

It is apparent from SEM observation of the surfaces of some of the Zn coatings that there were two distinctly different populations of grains in the coating. The majority of the coating thickness consisted of a layer of very fine grains that probably possessed a columnar morphology. Superimposed on top of this fine-grained layer was a collection of larger protuding grains, randomly distributed over the surface. Increasing the bias voltage tended to cause these protruding grains to coalesce and decrease in population density, probably due to resputtering. The decreasing population density of large protruding grains on the surface of the Zn coatings, was concurrent with a decrease in diffraction intensity for the {10.0} and {10.1} peaks (Figs.5.7-5.9). Musil *et al* [137] determined that the Zn grains contributing to the non-basal peak diffraction were relatively large in size and had a minimal amount of microstrain. The very small FWHM measured for all {10.0} and {10.1} peaks supports this interpretation. The grains contributing to {10.0} and {10.1} diffraction were almost completely free of residual macrostress, as indicated by the constant nature of *d*-spacing with bias voltage. This was also supported by the absence of residual macrostress in randomly oriented grains, as determined by Seeman-Bohlin XRD. This suggests that the randomly oriented grains were not directly incorporated into the bulk of the coating where they would be subject to the residual

tensile macrostress found to exist in these coatings. The combination of all of the above observations point to the conclusion that the large protruding grains on the surface of the coatings correlate directly with the randomly oriented component of the Zn coatings.

It follows from this argument, that the fine columnar grains observed to occupy the majority of the coating thickness correspond to the strong <0001> fibre textured component of the coatings. There is further evidence which supports this suggestion. The columnar microstructure is consistent with the observed fibre texture, whereby the texture axis is parallel to the columnar grain growth direction. Residual macrostress in the coating could only be supported by a continuous coating microstructure, and this is the case for the fine columnar layer. Matching the <0001> fibre textured grains with the fine columnar structure, implies that this part of the coating is also the recipient of the vast majority of the buried Ar. Hence, a link can be drawn between the proportion of buried Ar and its effect on the residual macrostress and microstrain of those grains. The corollary of this idea is that very little buried Ar appears to be associated with the large protruding grains on the coating surface.

5.3.3 Argon Burial and Residual Stress

There is a strong suggestion from the arguments presented above that the buried Ar content of the coatings was directly related to the residual tensile macrostress that existed in the <0001> fibre textured grains. This was examined further by plotting the {0002} *d*-spacing as a function of Ar content (Fig.5.12), for Series 2 and Series 4 coatings in addition to the data from [137]. Results for coatings deposited at -300V to -400V bias for Series 4, and -450V to -500V bias for [137] were not included in this plot because the peaks were too broad and weak to provide accurate *d*-spacings. In Fig.5.12, a negative shift in *d*-spacing can be interpreted as an increase in residual tensile macrostress, since it was firmly established that the strain-free lattice parameter of the Zn coatings was not subject to entrapment of Ar in solid solution (Fig.5.11). The non-linear curve fit to this data suggests that the tensile macrostress increased with the square of Ar content. It is apparent that all three sets of data fall along the same general trend, within a reasonable margin of error. It would therefore appear that the relationship between Ar content and residual macrostress was independent of the deposition parameters.

Inert gas entrapment has often been attributed as the cause of compressive stress in sputtered coatings [131,175]. However, it is generally believed that it is not the incorporation of inert gas that causes the stress, but the bombardment of the film by energetic particles that induces lattice damage by direct and recoil atomic displacements [124,127,273]. This ill-defined "atomic-peening" mechanism attributes the high

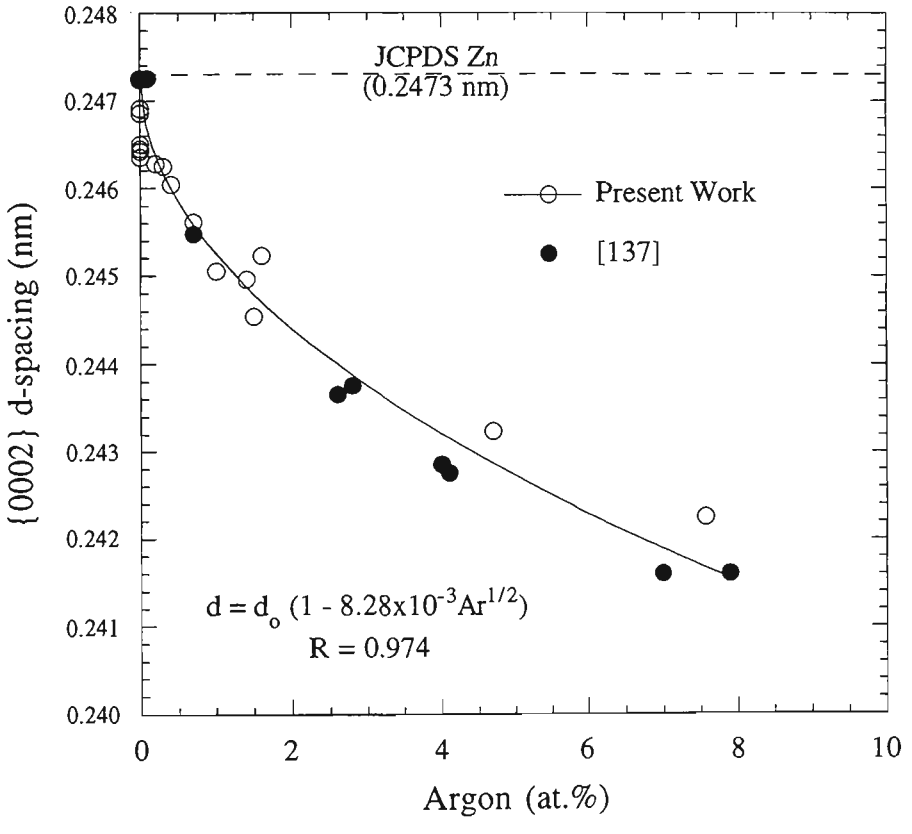

Fig.5.12 *Relationship between {0002} d-spacing of Zn coatings and the buried Ar content.*

concentration of vacancies and other crystallographic defects to the development of compressive biaxial stress in the plane of the coating [323]. It seems that inert gas entrapment is a concurrent event but not the causative factor responsible for the generation of compressive stress. Similarly, inert gas burial is not usually associated with tensile stresses in sputtered coatings. The most commonly accepted cause of tensile stress is the grain boundary relaxation model (Sect.2.4.2) [126]. The model is based on the argument that interatomic forces acting across the gaps between contiguous grains cause an elastic relaxation of the grain walls. Tensile stresses are therefore common in coatings which exhibit a porous zone 1 type of structure [127]. However, in the case of sputtered Zn coatings, it has been established that the smooth and compact coatings produced at elevated bias voltages are subject to large biaxial tensile stresses (Fig.5.11b). It would therefore seem that the Zn coatings are in a category of their own, where none of the accepted models of stress development apply.

5.3.4 Constrained Shrinkage Model

A phenomenological model has been developed in an attempt to explain the observed relationship between tensile stress and buried Ar content of the sputtered Zn coatings. The model is based on constrained shrinkage associated with the dynamic annealing of a high density of defects buried under the surface of the coating as it deposits. This is similar in many ways to the model proposed by Klockholm and Berry [324,325] for explaining the stress in evaporated metal coatings. Their model was based on the crystallization of an amorphous layer below the coating surface, resulting in the generation of biaxial tensile stress . However, this model is rarely encountered as the grain boundary relaxation model is usually preferred.

Increasing the substrate bias raises the kinetic energy of ions bombarding the growing coating. As a result, vacancies and other crystallographic defects are formed in the Zn grains several atomic layers below the surface. The depth to which Ar^+ ions penetrate into Zn increases from about one close-packed plane at 100 eV, up to about three close-packed planes at 450 eV [326]. The amount of radiation damage trapped below the surface of the coating as it grows is thus expected to increase in a similar fashion [327]. The Ar^+ ions implanted into the coating become trapped at these defect sites and are momentarily forced into solid solution. Ar atoms are much larger than Zn atoms according to the Goldschmidt atomic radii [250]. Therefore the strain fields associated with forced substitutional solid solution would be immense, likely to cause plastic flow and the generation of high dislocation densities. The forced Ar solid solubility is also thermodynamically unstable and there is a strong driving force for segregation.

At this stage it must be reminded that the melting point of Zn (419.5°C) is much lower than for conventional materials used in sputtered coatings. A deposition temperature of 50°C corresponds to a homologous temperature of 0.47 for a Zn coating. It would therefore appear likely that recrystallization processes can occur in Zn coatings even at such low substrate temperatures. Recrystallization would be enhanced by the defective structures formed at high bias voltages, due to the concommitent acceleration of volumetric diffusion. A large fraction of the lattice defects would be annihilated by recrystallization of the Zn coating. Ar atoms trapped in solid solution would also be able to diffuse and form bubbles [113], which is a thermodynamically favourable condition. The transition from a highly defective structure to one with a much lower fraction of defects would necessitate a reduction in volume. However, this recrystallization process occurs several atom layers below the Zn coating surface, and the tightly packed columnar grains would be restrained in their axial movement. This results in the development of biaxial tensile stresses in the recrystallized grains. It may also account for the development of a strong <0001> fibre texture, which represents the orientation of lowest surface energy [117,118], and least elastic strain (Sect.2.4.1).

It seems unlikely that the Ar present in the coatings actually caused the residual tensile stress, in agreement with current thought on compressive stress mechanisms [124,127,273]. Conversely, the buried Ar content of sputtered Zn coatings is considered to be a strong indicator of the extent of deformation present in the coating immediately after it is deposited. In this respect, the Zn coatings seem to be particularly effective in their efficiency of trapping implanted Ar. The Ar content consequently scales very closely with the residual tensile stress, independent of the substrate temperature and ion assisted deposition conditions. This is because the defect density, as indicated by Ar content, seems to be the controlling factor in the development of tensile stress in sputtered Zn coatings. The relationship between Ar content and residual tensile stress might be expected to break down at high substrate temperatures, since it may be possible for the implanted Ar to diffuse out of the coating during deposition. This aspect cannot currently be tested theoretically because of an absence of any published data on the diffusion of Ar in Zn. However, the decline in both Ar content and tensile stress at bias voltages in excess of -250V suggests that enhanced diffusion of Ar was possible at such conditions, perhaps because of localised thermal spikes.

A note must finally be made concerning the possible effects of Ar bubbles in the Zn coatings. The broadening of the {0002} XRD peaks (Fig.5.9c) was found to follow a trend similar to that of the Ar content (Fig.5.2), with respect to increasing substrate bias. Musil *et al* [137] explained this correlation in terms of residual microstrain caused by the

presence of Ar atoms in solid solution. Although it has been established that virtually no Ar was present in solid solution, it still remains probable that the presence of bubbles of Ar would induce a similar microstrain effect. This is especially feasible in light of previous work on sputtered Al coatings which established that inert gas bubbles are retained at such high pressure that they can be in solid form [113].

It is anticipated that the constrained shrinkage model for the development of tensile stress in ion assisted sputtered coatings would only be applicable to metals with low melting points and high self-diffusivity. Candidate metals that could be investigated to confirm the universality of the model are Cd, In and Tl. Each of these metals have lower melting points and higher diffusivity than Zn [250]. It is possible that Sn and Pb may also serve this purpose, although they have lower diffusivity than Zn. Other low melting point metals such as Al (660°C) and Mg (649°C) possess only slightly higher melting points, but their self-diffusivities at 50°C are approximately six orders of magnitude slower than for Zn [250]. It is therefore unlikely that they will display the same behaviour, and this was confirmed in Chap.6 and Chap.7.

5.4 Summary

The Zn coatings had a non-reflective blue-grey appearance when deposited with low energy ion assistance conditions. Increasing the substrate bias modified the coatings such that they developed a specular appearance. The visual appearance was related to the size and population density of rough protruding grains on the coating surface.

Two distinct families of Zn crystallites were detected: <0001> fibre textured and randomly oriented grains. Fibre textured grains corresponded to densely packed, fine columnar grains, whereas the randomly oriented grains consisted of larger protruding grains on the coating surface. Fibre textured grains were associated with large proportions of entrapped Ar (up to 7.5%), and the inert gas was not retained in solid solution. Entrapped Ar was correlated with residual microstrain in the fibre textured grains. The randomly oriented grains were preferentially resputtered as bias was increased, leaving an almost entirely <0001> fibre textured coating.

Residual tensile macrostress in the fibre textured grains increased continuously with energy of ion bombardment (above about -100V bias). This is highly unusual for coatings with a very dense columnar structure. The tensile stress was related to the buried Ar content, but the latter was considered not to be the causative factor. Tensile stress development was attributed to a constrained shrinkage model, that involved recrystallization of the bombardment-damaged coating.

Chapter 6

Aluminium Coatings

6.1 Deposition Parameters

Two series of Al coatings were deposited on Si wafer substrates for microstructural evaluation. The important parameters for each series are listed in Tables 6.1 and 6.2. Series 1 coatings were completed using a low voltage rated power supply which was not capable of accurately controlling the power. Therefore, the actual magnetron power for these coatings was about 335 W, despite the 400 W set-point. The coatings in Series 2 were prepared using a high voltage rated power supply which was able to control the power much more accurately. The same M3 magnet was used for both sets of coatings, but for Series 1 it was slightly demagnetised (refer Sect.5.2.1). Thus a comparison of Series 1 and 2 would enable examination of the influence of *i/a* ratio on the coatings produced.

6.2 Results and Discussion

6.2.1 Mass Deposition Rate

The calculated *i/a* ratios and the deposition rates at self bias for the 2 sets of Al coatings are shown in Table 6.3. The normalised mass deposition rate in the absence of any applied bias (ie. at self bias) was relatively constant for the two coating runs. This was equivalent to an actual thickness deposition rate of about 0.21 and 0.12 $\mu m.min^{-1}$ for Series 1 and 2, respectively. The *i/a* ratio for Series 2 was about double that of Series 1, which indicates that the extent of magnetron "unbalance" was different for the two coating runs. This is consistent with the slightly demagnetised outer ring of magnets for Series 1. It should be noted that differences in the *i/a* ratio did not significantly influence the normalised mass deposition rate at self bias. This confirms that the extent of magnetron unbalance is relatively independent of the target sputtering rate.

Table 6.1 Deposition parameters for Series 1 Al coatings Other process variables: base pressure 200 μPa; magnetron power 400 W nominal; probe current 1.11 mA; deposition time 5 minutes per sample.

Magnetron Conditions		Substrate	Coating Mass
Voltage (V)	Current (A)	Bias (V)	(μg)
551	0.61	self (-18)	223
547	0.61	-40	219
544	0.61	-60	213
541	0.62	-80	215
538	0.62	-100	143 *
535	0.62	-120	192
533	0.63	-140	159 *
531	0.63	-160	183
528	0.63	-180	172
526	0.64	-200	176
525	0.64	earth	91 *

* coating mass in error due to substrate breakage

Table 6.2 Deposition parameters for Series 2 Al coatings Other process variables: base pressure 47 μPa; magnetron power 200 W nominal; probe current 1.024 mA at start, 1.068 mA at end; deposition time 8 minutes per sample.

Magnetron Conditions		Substrate	Coating Mass
Voltage (V)	Current (A)	Bias (V)	(μg)
413	0.48	self (-25)	194
410	0.49	-40	194
409	0.49	-60	188
408	0.49	-80	161
407	0.49	-100	160
407	0.49	-120	152
406	0.49	-140	145
406	0.49	-160	131
405	0.49	-180	111 *
405	0.49	-200	121
405	0.49	earth	188

* coating mass in error due to substrate breakage

Table 6.3 Characteristic deposition conditions for Al coatings at self bias

Series	*i/a* ratio	Substrate Temperature	Deposition Rate ($g.mm^{-2}.W^{-1}.min^{-1}$)
1	0.606	< 50°C	$1.69x10^{-9}$
2	1.051	< 50°C	$1.56x10^{-9}$

The mass deposition rate for all Al coatings is shown as a function of the substrate bias voltage in Fig.6.1. A moderate amount of variability in the deposition rate measurements was encountered. This variability was due to the very small deposited mass, which increased the relative error of the deposition rate measurement. For example, assuming 100% bulk density, a 1 μm pure Al coating over a 10 mm diameter area would be expected to have a coating mass of only 212 μg. The error in coating mass measurements is conservatively estimated to be ±10μg, which equates to a relative error of ±5% for the deposition rates plotted in Fig.6.1.

Increasing the substrate bias caused an exponential reduction in the mass deposition rate, obviously as a result of ion bombardment leading to resputtering. The Series 2 coatings were affected by the bias voltage to a greater extent than the Series 1 coatings. This difference in behavior between the coating series was apparently caused by the higher *i/a* ratio for the Series 2 coatings. Earthing the substrate platform had very little effect on the mass deposition rate, as it was very similar to that obtained at self bias.

6.2.2 Chemical Composition

The Ar content of all coatings are shown as a function of the bias voltage in Fig.6.2. All Al coatings appeared to include about 1.2 at.% Ar, regardless of the bias voltage. Unfortunately, this measurement was an artefact of the EDS analysis and did not represent the actual Ar content. The Ar K_α signal measured by EDS was actually due to the Al K_α sum peak (Sect.4.3.4), and did not represent the true Ar content of the coatings. The constant nature of the measured Ar signal in Fig.6.2 suggests that very little Ar was actually present in all of the Al coatings. Some preliminary unreported Rutherford backscattering spectrometry (RBS) analysis of the Series 1 coatings [214], suggested that there may have been about 0.2 at.%Ar present in coatings deposited with -100V and -200V bias. However, RBS characterization was not pursued due to a lack of resources.

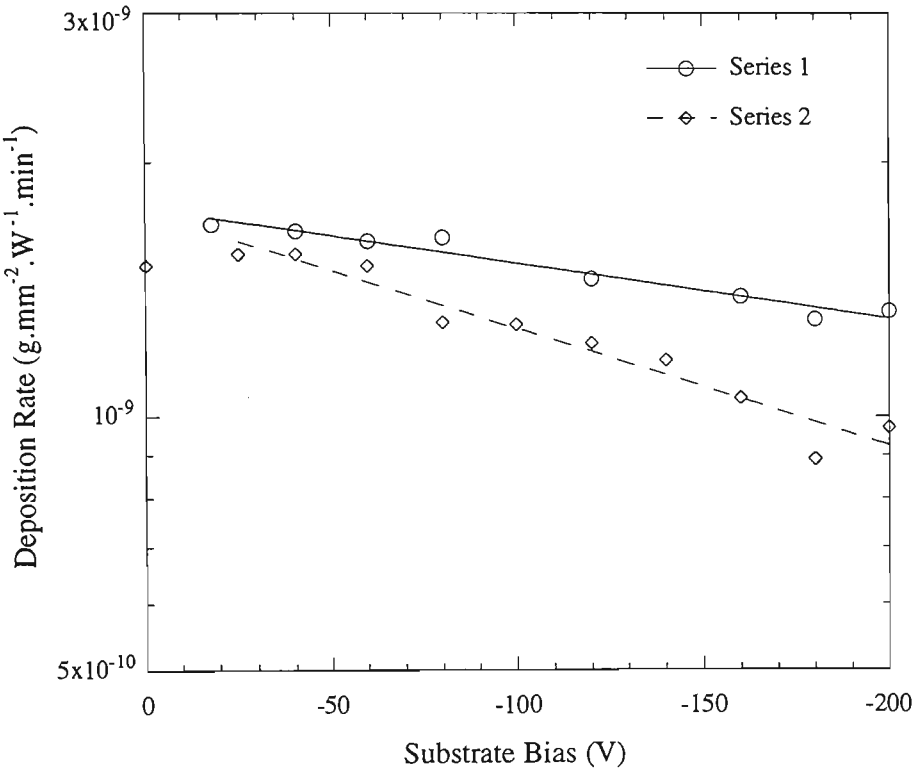

Fig.6.1 Mass deposition rate for sputtered Al coatings. Note the ordinate axis is semi-logarithmic.

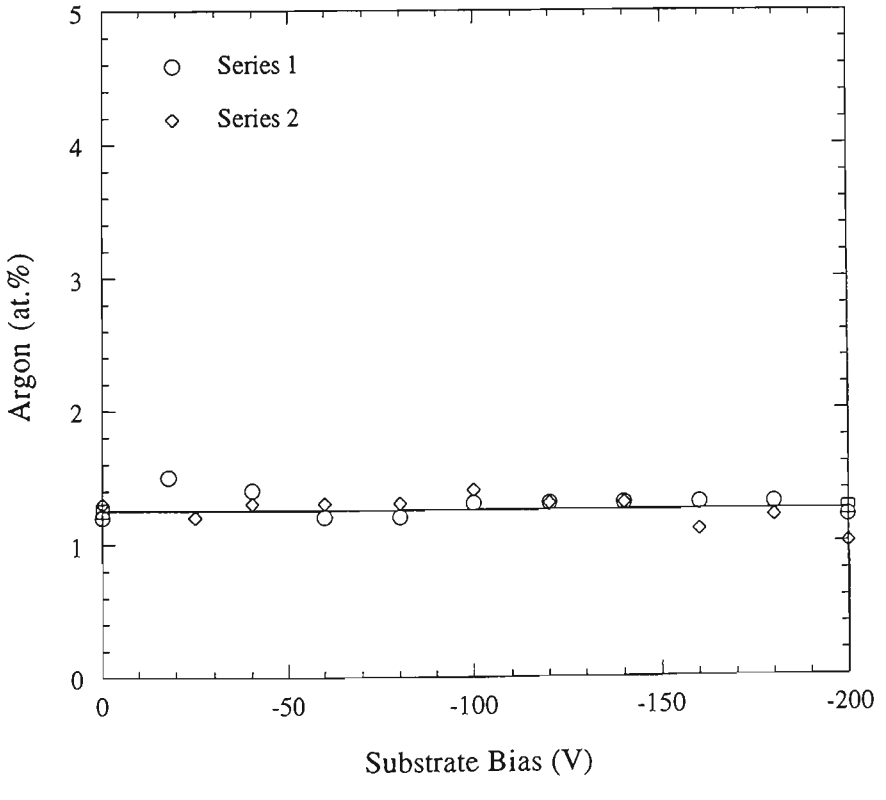

Fig.6.2 Measured Ar content of sputtered Al coatings.

6.2.3 Visual Examination

A visual examination of the Al coatings found them all to be highly lustrous, with a surface finish that closely replicated the polished Si wafer substrate. The coatings all appeared to be slightly bluish-white in colour, typical of bulk Al. There was no change in the macroscopic surface appearance as the bias voltage was altered, nor were there any differences between Series 1 and Series 2 coatings. High resolution field emission SEM examination of these coatings was not attempted.

6.2.4 Bragg-Brentano X-Ray Diffraction

The results of Bragg-Brentano XRD scans for all of the Al coatings are shown in Fig.6.3. The of the {111} and {200} *d*-spacings are plotted in terms of strain in a direction normal to the sample surface, calculated from the measured *d*-spacings and the tabulated values for randomly oriented, defect-free Al powder: {111} = 0.2338 nm, {200} = 0.2024 nm [197].. The diffraction peak intensity and FWHM are also shown in Fig.6.3. The FWHM results for {200} peaks are not shown because of their low diffraction intensity.

All of the Al coatings had a tendency towards preferred orientation of {111} planes parallel to the substrate surface. This is indicated by the intensities for {111} diffraction peaks relative to those of {200} (Fig.6.4b). For a randomly-oriented Al powder, these peaks have relative intensities of 100:47 [197], whereas those of the Al coatings at self bias (weakest preferred orientation) were in the order of 100:10. This type of preferred orientation is common in PVD Al coatings and corresponds to a <111> fibre texture [178,180]. The fibre texture became stronger as the bias voltage was increased, as revealed by the increase in {111} intensity and decrease in {200} intensity. Beyond a bias voltage of -80V, the {200} diffraction peak was undetected which indicated that the coatings were almost entirely <111> fibre textured. The reduction in coating mass with increasing bias voltage was reflected by the slight decrease in {111} peak intensity at bias voltages above about -80V.

The {111} *d*-spacing for both sets of coatings generally increased with bias voltage (Fig.6.4a). The {200} peaks observed at low bias voltages seemed to replicate the behaviour of the more intense {111} peaks. In addition to this trend, the {111} *d*-spacing for both sets of coatings appeared to show a double-maxima with increasing bias voltage. For the Series 1 coatings, the maxima occurred at -60V and -140V bias, compared with -25V (self bias) and -140V bias for the Series 2 coatings. It is interesting to note that the positions of the first of these maxima are identical for both sets of coatings

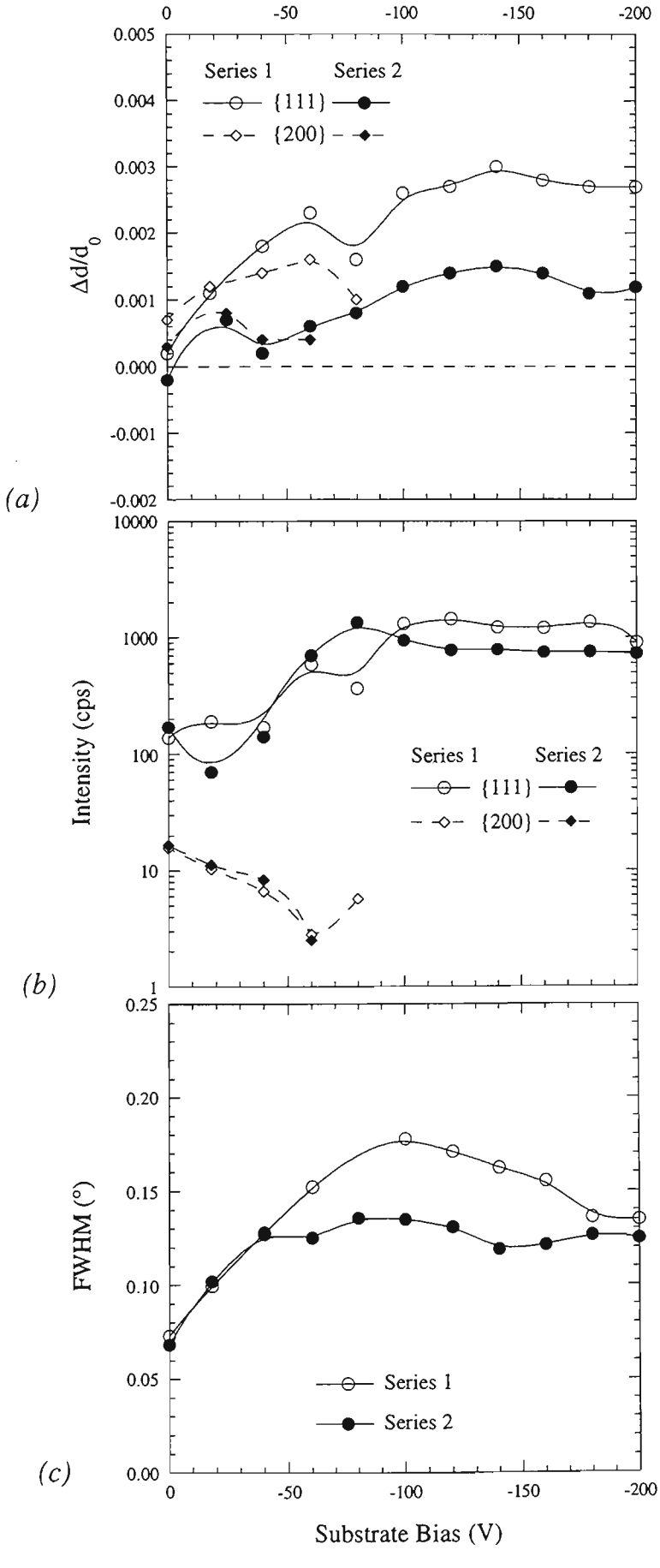

Fig.6.3 Comparison of XRD results for Series 1 and Series 2 Al coatings: (a) d-spacing expressed as a strain parameter, (b) peak intensity, and (c) FWHM of diffraction peaks.

when normalised by the *i/a* ratio; a normalised bias of -36 V/atom is common. The physical cause of this effect is not known, but it would appear that the normalised ion energy is the controlling parameter. In contrast, the second maxima observed at -140V bias for both series of coatings does not seem to have been controlled in this manner. It should be noted however that the observed variations in *d*-spacing at these maxima are within the expected error of measurement and may not be real effects.

Considering that the amount of buried Ar in all Al coatings was found to be negligible, it is likely that the *d*-spacing trends represent an increase in the amount of compressive residual macrostress. Differences between the {111} *d*-spacings for Series 1 and Series 2 coatings were apparent but could not be explained by the instrumental errors, as indicated by the error bars. The *d*-spacing measurements therefore suggest that the Series 1 coatings were subject to a somewhat higher compressive stress than the Series 2 coatings. This is a puzzling result in light of the observation that the *i/a* ratio was highest for Series 2, from which it might be expected that these coatings would develop a greater degree of compressive stress. A possible explanation is that plastic flow or *in situ* annealing of bombardment damage occurred for the higher ion flux conditions. Such effects have been demonstrated to impact on the maximum residual compressive stress [123,129].

The diffraction peaks for the Al coatings all tended to be sharp in comparison with the Zn coatings described in Chap.5. This is indicated by the FWHM which was less than 0.18° for all bias voltage conditions (Fig.6.3c). With increasing bias voltage, the {111} FWHM tended to increase to a maximum and then slowly decrease. The position of this maximum was at slightly lower bias voltage for the Series 2 coatings than for Series 1. The physical explanation for the peak broadening trends is not certain, and could be due to either crystallite size or microstrain effects, although the latter is considered most likely. Hence the lower *i/a* deposition conditions (Series 1) resulted in a more defective and/or finer structure than those produced at higher *i/a*. This is consistent with the observed differences between the two sets of coatings in terms of their {111} *d*-spacing.

6.2.5 Crystallite Group Method

CGM was applied to the <111> fibre textured crystallite group of several Series 2 Al coatings in an effort to verify that the observed peak shifts in Bragg-Brentano diffraction (Fig.6.3a), were indeed caused by residual macrostress and not lattice parameter changes. Only one of the Series 1 coatings was examined by CGM (-120V bias). Data obtained from asymmetric diffraction scans are plotted in terms of the *a* lattice

parameter as a function of $\sin^2\psi$ in Fig.6.4, indicating a linear relationship within an acceptable range of error. Linear regression equations were fitted to the data, and the coefficients used to calculate the strain free lattice parameter a_o and the residual macrostress σ, using equation 4.15. The results of these calculations are graphed as a function of the bias voltage in Fig.6.5

The strain-free lattice parameter was essentially constant for all bias conditions examined (Fig.6.5a). The value of the lattice parameter for all coatings was equal to that of pure bulk Al within ±0.05%, which is less than the expected range of error. Any trace amounts of inert gas that may have been present in these coatings must therefore have been distributed as bubbles [113]. It would appear that the trends in {111} *d*-spacing shown in Fig.6.3a were indeed caused entirely by the effects of residual compressive macrostress. Except for an anomalous result for the -80V bias coating, a small compressive stress of between 40 and 90 MPa was found to be present in the Series 2 coatings (Fig.6.5b). A much larger compressive stress of about 140 MPa was determined for the only Series 1 coating examined, providing some confirmation of the *d*-spacing trends. The residual macrostress in the coatings at low bias voltages could not be examined by CGM due to insufficient {111} diffraction intensity. Comparison between the *d*-spacing trends and the residual stress results suggests that coatings deposited on earthed substrates were subject to virtually no residual macrostress, and increasing the bias resulted in the development of compressive macrostress.

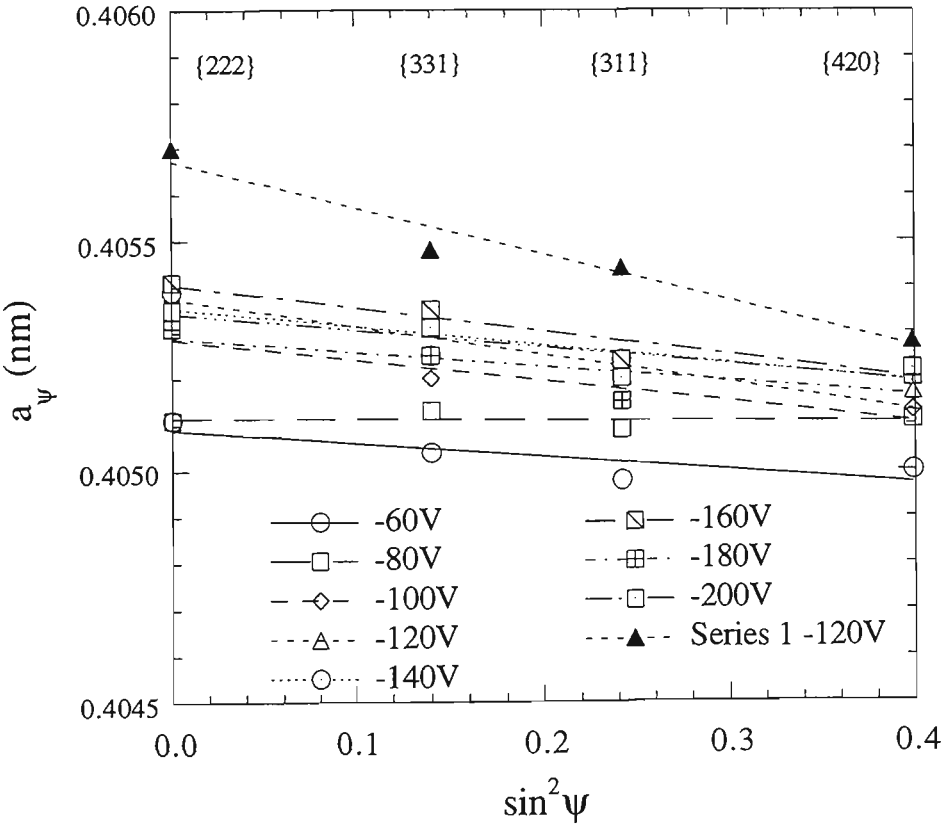

Fig.6.4 *$Sin^2\psi$ plots of CGM data for Al coatings.*

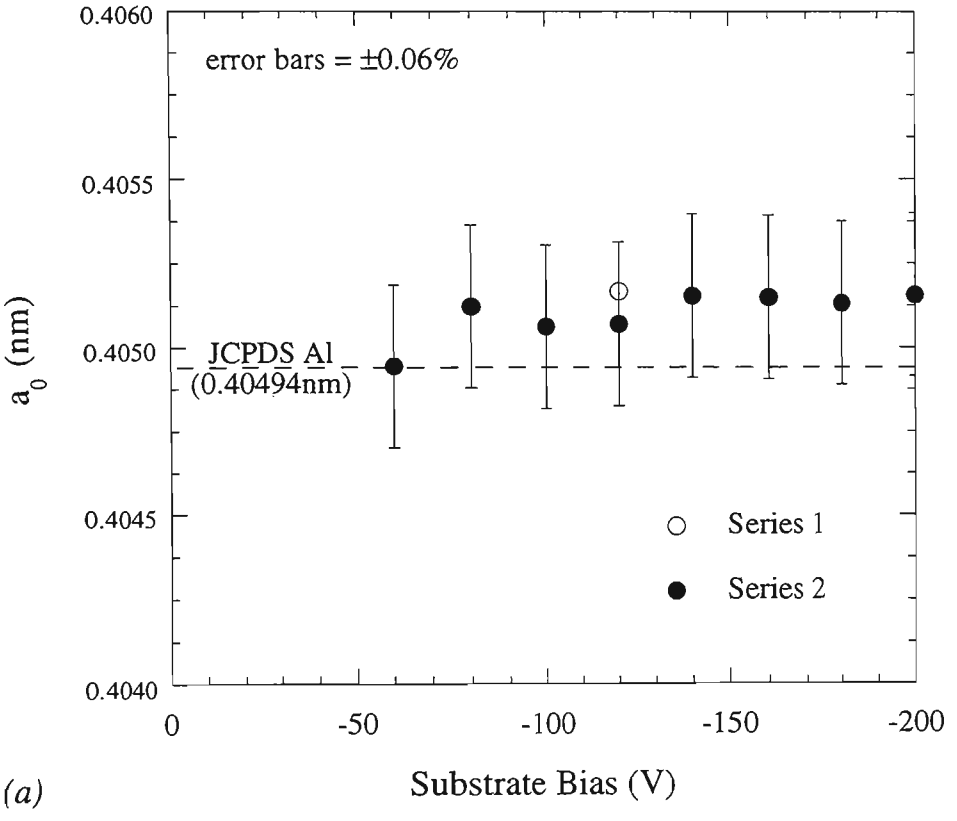

(a)

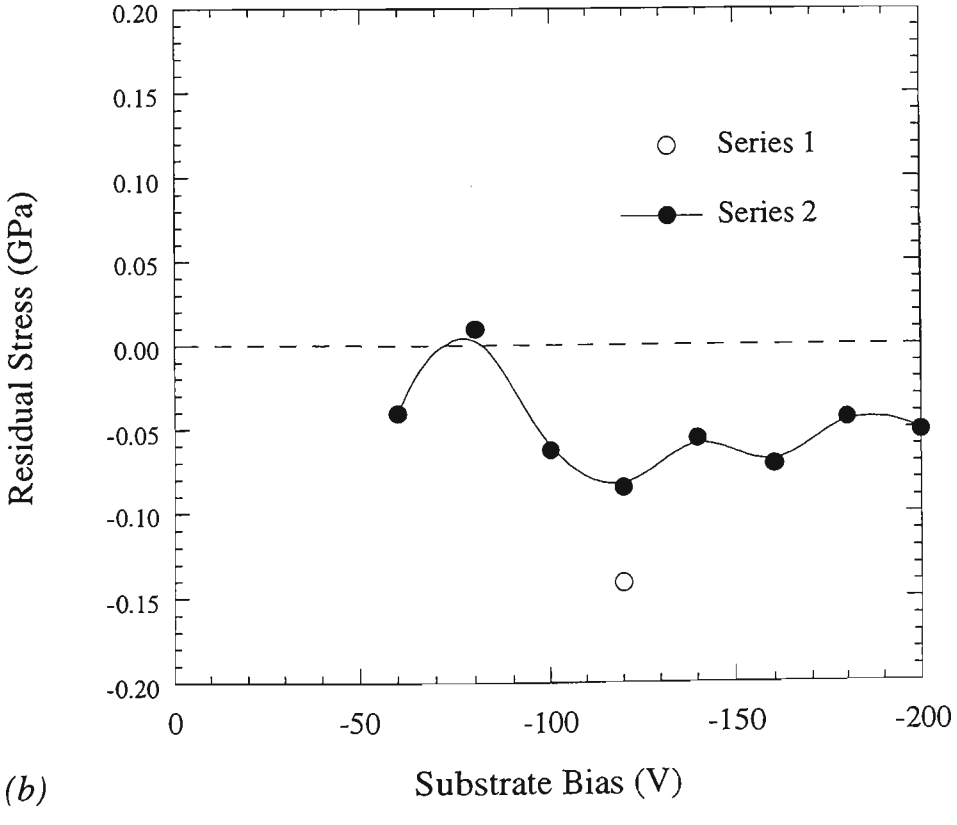

(b)

Fig.6.5 Strain-free lattice parameter (a) and residual macrostress (b) of the <111> fibre textured grains in Al coatings.

6.3 General Discussion

The most dramatic effects of ion assistance with the Al coatings were the enhancement of a strong <111> fibre texture, and an increase in the amount of residual compressive macrostress in this crystallite group. Similar enhancement of the <111> fibre texture has been reported by other researchers [178,180]. However, none of this previous work appears to have replicated the same conditions experienced in the present study. The most similar study was by Masaki *et al* [178] who prepared evaporated Al coatings at a deposition rate equivalent to the Series 1 coatings, with Ar^+ ion beam bombardment at a comparable energy range (50 to 200 eV). However, these authors employed much lower *i/a* ratios (0.002 to 0.1). They found the same type of {111} preferred orientation, although in all cases the intensity of the {200} peak was significant. Other authors have shown that the complete elimination of {200} peaks in favour of a very strong <111> fibre texture, occurs at much higher ion energy or *i/a* ratios [180]. Therefore, the differences in the strength of the <111> fibre texture observed by Masaki *et al* and in the present investigation were probably due to the effect of *i/a* ratio.

The development of a <111> fibre texture in Al coatings has been attributed to the minimisation of surface energy [180]. In the fcc crystal structure, the {111} planes have the lowest surface energy. Process conditions that improve the surface mobility of deposited atoms would therefore be expected to result in the favoured growth of grains oriented with the {111} planes parallel to the coating surface. Increasing the surface mobility can be achieved by raising the substrate temperature, or by reducing the deposition rate substantially [179]. Ion bombardment is another way that the deposited atoms can be redistributed, enabling them to find energetically favourable sites [180]. Hence, increasing the energy or flux of ions bombarding an Al coating as it deposits can enhance the development of a <111> fibre texture (Fig.6.3b).

Ion assisted deposition of Al coatings unfortunately resulted in the generation of relatively large residual compressive stress, particularly at high bias voltages (Figs.6.3a and 6.5b). Granted the calculated stresses of up to 140 MPa were small in comparison with the stresses often obtained with refractory metal coatings [125,126], they were consistent with previous work on Al coatings [177,273]. This is due to the low yield strength of pure Al, which limits the maximum elastic stress that can be retained by the coating. It has been suggested that the residual stress in Al coatings is limited by the grain size, in a fashion similar to the well-known Hall-Petch relationship [113]. Following this concept, the differences between Series 1 and 2 Al coatings in terms of the magnitude of residual stress might have been due to a grain size effect. The comparatively large XRD peak broadening for the Series 1 coatings provides some support for this explanation.

However, without a thorough TEM investigation of the coatings, this conclusion is purely speculative.

It remains to be explained, however, why the Al coatings deposited with a low *i/a* ratio (Series 1) were more severely affected by ion bombardment than coatings produced with high *i/a* ratio (Series 2). It is suspected that this may have been related to excessive adatom mobility resulting from the high *i/a* condition. The defective structure induced by ion bombardment is generally thought to be responsible for the generation of compressive stress (Sect.2.4.2). It seems feasible that as the degree of ion bombardment becomes "excessive", the collision cascades in the surface of the coating may lead to enhanced recovery of the defective structure through diffusional processes. This would be expected to contribute to a reduction in the residual macrostress since the stress-inducing bombardment effects would be self-healed (Figs.6.3a and 6.5b). Alternatively, the observed trends could be explained by plastic flow induced by heavy bombardment [123,129]. According to this mechanism, the residual stress induced in the heavily bombarded coatings would have been initially greater than in coatings produced at lower *i/a*. This stress could feasibly exceed the low yield stress of Al, resulting in plastic flow and consequently a relaxation of the residual coating stress. Each of these mechanisms can account for the low stress observed with high *i/a* ratio ion assisted deposition, but it is not apparent which is the dominant effect.

6.4 Summary

Sputtered Al coatings deposited with minimal ion assistance tended to be randomly oriented with only a trace of preferred orientation. Increasing the substrate bias slightly led to the development of a very strong <111> fibre texture. This was considered to be the result of enhanced adatom mobility, enabling deposited atoms to achieve more energetically favourable sites. Coatings deposited with ion assistance were subject to an increase in the amount of residual compressive macrostress in the <111> fibre textured grains, as a result of the atomic peening mechanism. Excessive ion assistance resulted in a reduction in the residual stress due to either plastic flow, or recovery of lattice defects through enhanced vacancy diffusion. Burial of Ar in Al coatings was not an issue, in spite of the relatively high *i/a* ratio. This may possibly relate to the slow deposition rate for Al in comparison with Zn.

Chapter 7

Magnesium Coatings

7.1 Deposition Parameters

Two series of Mg coatings were deposited onto Si wafers for microstructural evaluation during the course of this investigation. The important parameters for each series are listed in Tables 7.1 and 7.2. Series 1 Mg coatings were completed using the M3 magnet assembly, while Series 2 coatings were prepared with the M2 assembly. All other parameters for the two coating runs were identical. Hence the effect of *i/a* ratio on the coatings could be evaluated by direct comparison of these two series. Ideally, the coating thickness should have been nominally 1 μm in order to maintain consistency with all other coatings. An Mg coating of this thickness and with bulk density would only have a mass of 135 μg, resulting in large errors in measurement of the coating mass. Consequently, the deposition time was selected to provide much thicker Mg coatings. The deposition rate at self bias was about 0.54 $\mu m.min^{-1}$ for both sets of coatings, assuming bulk density.

On the basis of established knowledge of the corrosion behaviour of bulk Mg (Sect.3.3), it is expected that pure Mg coatings would be highly unsuitable as a sacrificial coating for sheet steel. Although Mg coatings should provide very good sacrificial protection to steel, the high corrosion rate of pure Mg would severely restrict the lifetime of the coating. Hence, the Mg coatings described in this section were only prepared with the intention of their being a source of reference for the Mg-alloy coatings (Chap.9 and Chap.10).

Table 7.1 Deposition parameters for Series 1 Mg coatings. Other process variables: base pressure 185 μPa; magnetron power 200 W; M3 magnet assembly; probe current 1.17 mA; deposition time 8 minutes per sample.

Magnetron Conditions		Substrate	Coating Mass
Voltage (V)	Current (A)	Bias (V)	(μg)
380	0.52	self (-23)	592
376	0.53	-40	568
373	0.53	-60	546
371	0.53	-80	507
370	0.53	-100	471
368	0.53	-120	454
368	0.53	-140	425
367	0.54	-160	401
366	0.54	-180	377
364	0.54	-200	365
362	0.55	earth	586

Table 7.2 Deposition parameters for Series 2 Mg coatings. Other process variables: base pressure 92 μPa; magnetron power 200 W; M2 magnet assembly; probe current 0.116 mA at start, 0.124 mA at end; deposition time 8 minutes per sample.

Magnetron Conditions		Substrate	Coating Mass
Voltage (V)	Current (A)	Bias (V)	(μg)
309	0.64	self (-17)	585
307	0.64	-40	594
307	0.64	-60	593
306	0.64	-80	592
305	0.64	-100	589
304	0.65	-120	575
304	0.65	-140	571
304	0.65	-160	571
303	0.65	-180	572
303	0.65	-200	569
302	0.65	earth	587

7.2 Results and Discussion

7.2.1 Mass Deposition Rate

The calculated *i/a* ratios and the deposition rates at self bias for the two sets of Mg coatings are shown in Table 7.3. Changing the magnet assembly from M3 to M2 resulted in an order of magnitude decrease in the *i/a* ratio, while having little influence on the mass deposition rate at self bias. This same observation was made during the first experiments on unbalanced magnetrons [60,63,65], and is recognised as one of the strong advantages of unbalanced magnetron sputtering for ion assisted deposition studies.

Table 7.3 Characteristic deposition conditions for Mg coatings at self bias

Series	*i/a* ratio	Substrate Temperature	Deposition Rate ($g.mm^{-2}.W^{-1}.min^{-1}$)
1	0.347	< 60°C	$4.75x10^{-9}$
2	0.035	< 60°C	$4.73x10^{-9}$

The mass deposition rate for all Mg coatings is shown as a function of the substrate bias voltage in Fig.7.1. Increasing the substrate bias voltage caused an exponential reduction in the mass deposition rate, obviously as a result of resputtering due to ion bombardment. The Series 1 coatings, with their high *i/a* ratio, were affected by the bias voltage to a much greater extent than the Series 2 coatings. This is to be expected since a higher flux of ions would result in a greater proportion of resputtering.

7.2.2 Chemical Composition

The Ar content of the Mg coatings, measured by EDS, is shown in Fig.7.2. The highest Ar content was actually found to exist in the Series 2 coatings, which had a much lower *i/a* ratio than Series 1. This is a strange result since it is anticipated that the Ar content should be in proportion to the fraction of energetic Ar^+ ions available for implantation and entrapment in the coating. The initial rate of increase in Ar content at low bias voltages was consistent with expectations being slightly higher for the Series 1 coatings. However, for bias voltages of more than about -80V, the Ar content of Series 1 coatings was relatively constant, and actually decreased slightly at the higher bias. In comparison, the Ar content of Series 2 coatings increased continuously up to a maximum of about 2.5 at.% at -200V. These results suggest that the high ion flux experienced with Series 1 aided in removing much of the Ar that was implanted into the growing

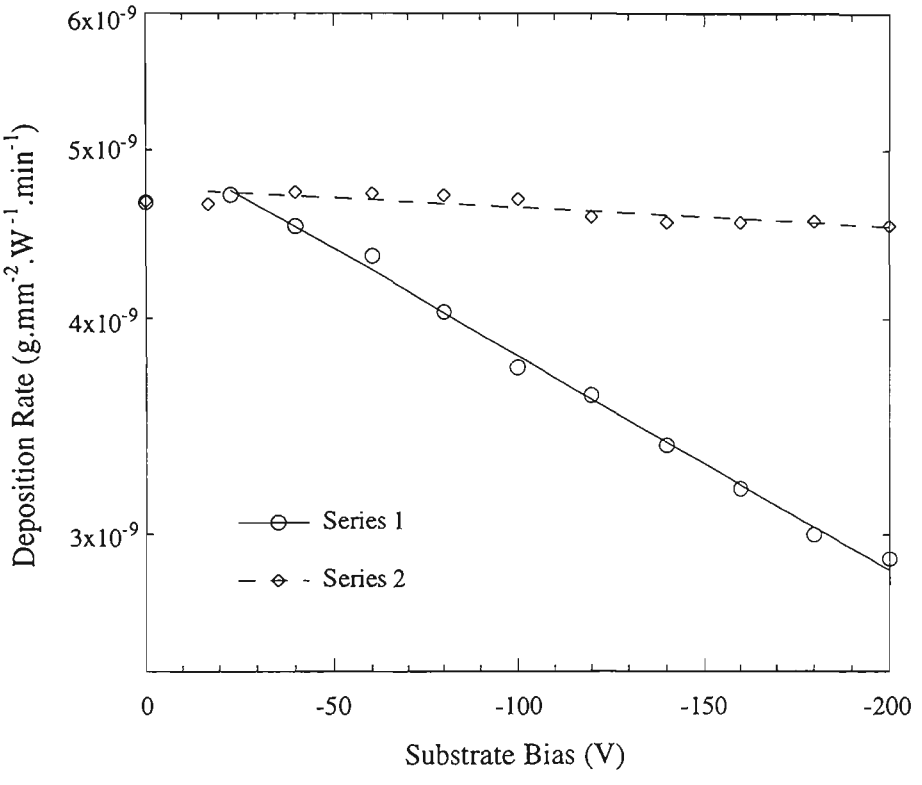

Fig.7.1 Mass deposition rate for sputtered Mg coatings. Note the ordinate axis is semi-logarithmic.

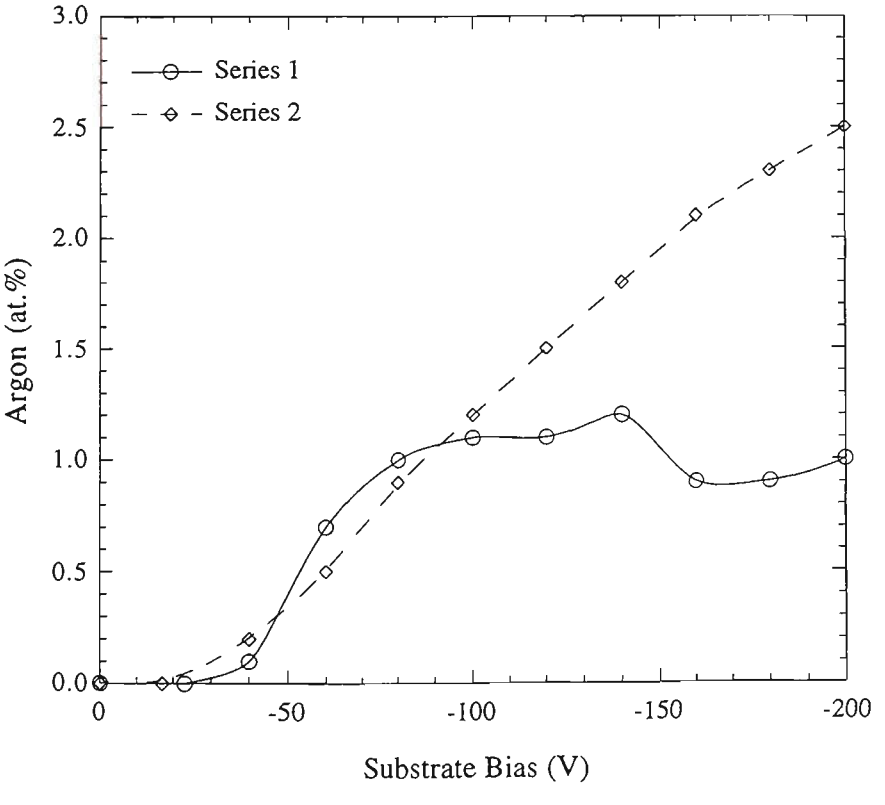

Fig.7.2 Ar content of sputtered Mg coatings.

coating. It is not apparent whether this effect was caused by resputtering or enhanced diffusion due to ion bombardment damage, as both effects would be expected to reduce the Ar content.

7.2.3 Visual Examination

The Mg coatings all had a highly lustrous visual appearance, with a surface finish that closely replicated the Si wafer substrate. Most of the Series 1 coatings also had a central circular region with a "milky" appearance, particularly those prepared at a bias of -100V or higher. This milky region tended to become larger and more prominent at the higher bias voltages. This appearance was not present on the Series 2 coatings, and is therefore thought to be related to the greater amount of ion bombardment experienced with Series 1. Unfortunately, all of the Mg coatings tended to lightly oxidise and stain within a few days of storage in polyethylene bags, and it was difficult to decide whether or not small features observed by SEM on the surfaces were related to oxide growth or inherent to the coating. The rapid discolouration of Mg coatings is consistent with reported results of previous researchers [185]. SEM micrographs are not presented for these coatings since they either lacked sufficient topographical contrast, or the surface features were thought to be related to subsequent oxidation.

7.2.4 Bragg-Brentano X-Ray Diffraction

The results of Bragg-Brentano XRD scans for all of the Mg coatings are shown in Fig.7.3. The relative positions of the {0002} Mg diffraction peaks are represented in terms of the strain parameter $\Delta d/d_o$, calculated from the measured d-spacings and the tabulated values for randomly oriented, defect-free Mg powder: {0002} = 0.2605 nm [197]. The diffraction peak intensity and FWHM are also shown in Fig.7.3. The FWHM and d-spacing results for non-basal planes are not shown in these graphs due to their low peak intensity.

All of the Mg coatings had a tendency towards preferred orientation of {0002} planes parallel to the substrate surface, consistent with a <0001> fibre texture. This is indicated by the very high intensity for {0002} (Fig.7.3b), in comparison with a randomly-oriented Mg powder where the {10.0}, {0002} and {10.1} peaks have relative intensities of 25:36:100 [197]. The trends in preferred orientation were different for each of the two coating series. For Series 1 the {0002} preferred orientation was strongest at -40V, and rapidly decreased with further increase in bias voltage. At -200V the {10.0} peak intensity increased markedly, suggesting that at higher bias, a <10.0> preferred orientation may have replaced the <0001> fibre texture. In comparison, the Series 1

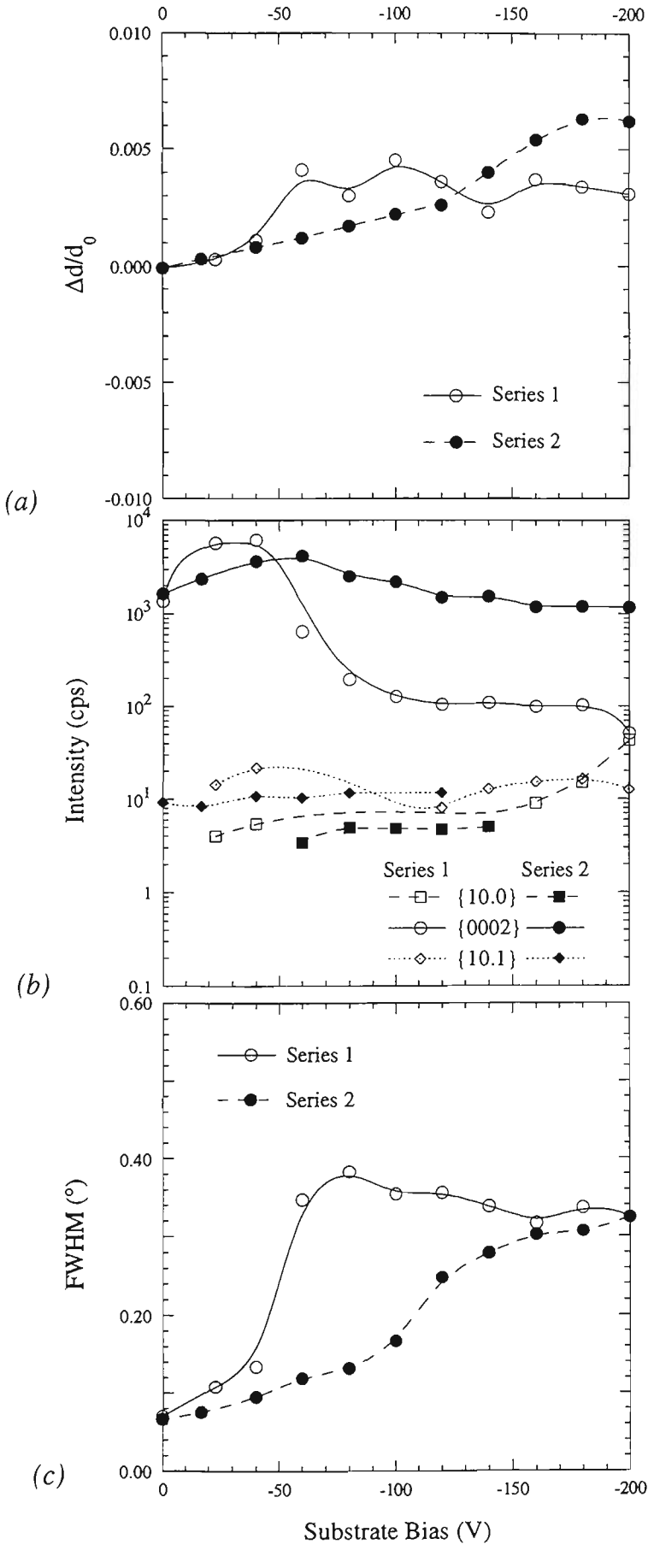

Fig.7.3 Comparison of XRD results for Series 1 and Series 2 Mg coatings: (a) d-spacing expressed as a strain parameter, (b) peak intensity, and (c) FWHM of diffraction peaks.

coatings had a very strong <0001> fibre texture for all bias voltages, the maximum {0002} intensity being attained at -60V. It therefore appears that the majority of the Mg coatings were characterised by a very strong <0001> fibre texture with the fibre axis aligned perpendicular to the coating surface.

The measurement of *d*-spacing for {0002} peaks in Series 1 coatings proved to be difficult due to their high FWHM and sometimes low intensity. This accounts for much of the spread in the data shown in Fig.7.3a. Despite these problems, it can be said that the {0002} *d*-spacing for Series 1 increased very rapidly with only small increases in bias voltage. A plateau of about $\Delta d/d_o = 0.035$ was reached at -60V and maintained with further increase in bias. In comparison, the *d*-spacing of {0002} peaks in the Series 2 coatings increased continuously with increases in the bias voltage. The maximum *d*-spacing attained for Series 2 was higher than that of Series 1. The trend in *d*-spacing of {0002} was also very similar to that observed for the Ar content of the coatings (Fig.7.2), which suggests that there may be a connection between the Ar content and the lattice parameter of the coating. Trends in the {10.0} and {10.1} peaks were difficult to ascertain because of their low intensity. In all cases the non-basal peaks appeared to follow a similar trend in *d*-spacing to that of the {0002} peaks.

It is reasonable to assume that the cause of the *d*-spacing trends was not due to variation in the strain-free lattice parameter. This follows from the results for Zn and Al coatings (Chap.5 and Chap.6), which demonstrated that the strain-free lattice parameter was identical to that of the corresponding pure defect-free powders. It seems unlikely that the Mg coatings would prove an exception to this behaviour. Therefore, the *d*-spacing measurements indicate that the Mg coatings were subject to negligible residual macrostress at low bias voltages, and that a compressive biaxial macrostress developed with increasing bias. The residual macrostress was subsequently measured by CGM for some the coatings with strong fibre texture (Sect.7.2.5).

The FWHM of {0002} Mg peaks (Fig.7.3c) indicate that changes in bias voltage significantly influenced the peak broadening. The trends in FWHM were similar to those experienced for the {0002} *d*-spacing. For Series 1 coatings, FWHM increased rapidly up to a maximum of 0.38° at -80V, and beyond this bias, the peak broadening decreased slightly but remained above 0.3°. Series 2 coatings followed a similar trend which was shifted to higher bias voltages. For these coatings, the FWHM of {0002} peaks increased continuously with bias voltage, reaching a maximum of 0.32° at -200V. It is thought that the broadening of the diffraction peaks is due to microstrain within the coatings, rather than a crystallite size effect. However, it was not possible to unequivocally distinguish these effects with the available data.

7.2.5 Crystallite Group Method

Two of the Series 2 coatings were evaluated by CGM in order to confirm that the trends in {0002} *d*-spacing were caused by residual macrostress and not solid solution effects due to dissolution of trapped Ar. The c_{hkil} lattice parameters measured for each plane were found to be linearly correlated with $\sin^2\psi$ for both samples (Fig.7.4). Residual macrostress and strain-free lattice parameter values were extracted from the linear regression equations for each coating using equation 4.16.

Table 7.4 Strain-free lattice parameter and residual macrostress for <0001> fibre textured crystallite group in Series 2 Mg coatings

Substrate Bias (V)	strain-free *c* lattice parameter (nm)	residual macrostress (GPa)
-180	0.5213	-0.15
-200	0.5214	-0.14

The strain-free lattice parameter c_o and the residual biaxial macrostress σ for the two Mg coatings are shown in Table 7.4. The strain-free *c* parameter of the <0001> fibre textured crystallite group in the Mg coatings was slightly larger than that of a pure Mg powder (c=0.52112 nm [197]), although this difference was within the instrumental error of ±0.06%. According to the assumption that the *c/a* ratio was constant, it is presumed that the *a*-parameter behaved in a similar fashion. This result confirms that little or none of the buried Ar present in the coatings was retained in solid solution. Hence, the trends in {0002} *d*-spacing noted to occur with increasing bias (Fig.7.3a), were due almost entirely to residual compressive macrostress. The compressive stress would therefore have been negligible at earth and self bias for both sets of coatings. The trends in *d*-spacing suggested that the maximum compressive stress occurred at a bias of -180V with the Series 2 coatings. The magnitude of the compressive stress in this coating was about 150 MPa (Table 7.4). It would appear that the compressive stress in the Series 1 coatings was generally less than about 100 MPa.

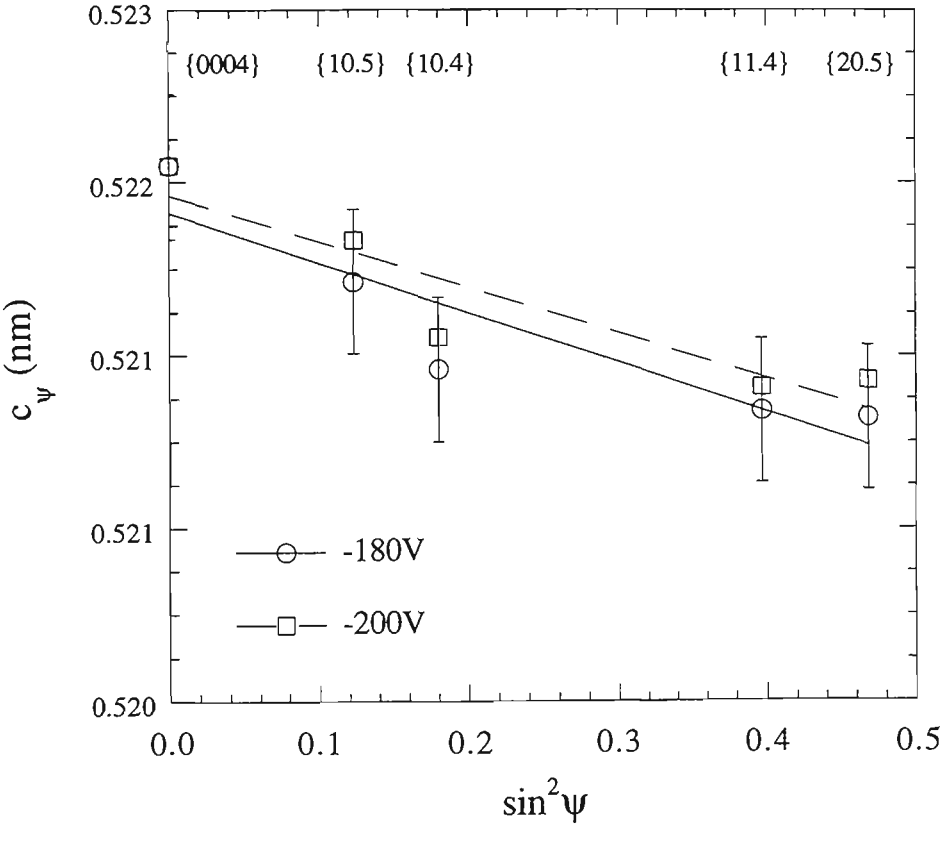

Fig.7.4 *$Sin^2\psi$ plots of CGM data for Mg coatings.*

7.3 General Discussion

7.3.1 Comparison with Previous Work

Most previous studies of Mg coatings prepared by PVD have reported that <0001> fibre texture is the favoured growth orientation [98,182,183,185]. However, one author has reported that <10.0> fibre textures were produced by ionised cluster beam deposition [184]. This result could perhaps have been influenced by epitaxial effects with the NaCl single crystal substrates that were used. However, these strong textures were mainly produced when very high substrate bias was applied (-5 kV). The development of a <10.0> fibre texture in Mg coatings would therefore appear to be favoured under conditions of very intense energetic particle bombardment.

The present investigation confirmed that <0001> fibre textures were produced in most Mg coatings prepared by unbalanced magnetron sputtering. This texture was strongest at low bias voltages (-40V for Series 1 and -60V for Series 2) and tended to decrease as the intensity of ion bombardment was increased (Fig.7.3b). The reduction in preferred orientation was particularly pronounced for the Series 1 coatings and eventually resulted in a change from <0001> to <10.0> fibre texture at the highest bias voltages. This result appears to be consistent with the observations of <10.0> fibre texture under conditions of very intense energetic particle bombardment [184]. The Series 2 coatings were less affected by increasing bias voltage because the relative ion flux was an order of magnitude lower than that of Series 1. This also explains why Arnell and Bates [98] found a <0001> fibre texture in their Mg coatings produced at a bias of -200V. It seems that the *i/a* flux ratio experienced with their sputtering process was probably intermediate between that of Series 1 and Series 2 in the present work.

The development of a <10.0> fibre texture in Mg coatings as a consequence of very intense energetic particle bombardment is a perplexing result. It is commonly accepted that the minimisation of surface energy is the driving force for strong fibre textures [180]. This is consistent with the observation of <0001> fibre texture at low bias voltages, since the close-packed basal planes possess the lowest surface energy. The presence of energetic particle bombardment during coating growth would usually favour the growth of such textures, as was found for the Zn and Al coatings (Chap.5 and Chap.6). This was not the case for the Mg coatings.

One possible explanation for the usual texture in Mg coatings can be gleaned from the textures produced in wires of cph structured metals. It is generally found that drawing or rolling of Mg wire causes the basal planes to rotate so that the <10.0>

direction coincides with the wire axis, and the basal planes are therefore parallel to the fibre axis [328]. A similar mechanism may have occurred in the Series 1 Mg coatings in response to exceptionally high compressive stresses induced by energetic ion bombardment. This would result in plastic flow of the <0001> fibre textured grains [123,129], perhaps contributing to the <10.0> fibre texture. The consequent relaxation of elastic stress also explains the lower compressive stress observed in the Series 1 coatings compared with Series 2 (Fig.7.3a). The latter coatings are unlikely to have developed sufficient residual stress to induce plastic flow and hence the strong <0001> fibre texture was retained in these coatings at all bias voltages.

Another possible explanation for the observed change in fibre texture relates to differences in resputtering yield relative to crystallographic orientation. Resputtering was particularly relevant to the deposition conditions of the Series 1 coatings. At a bias voltage of -200V, only 60% of the coating mass was deposited relative to that obtained at self bias (Table 7.1). It seems possible that preferential resputtering of the <0001> textured grains in favour of the <10.0> grains may have led to the modification in growth texture. The differential sputtering yields of single crystalline Mg targets have been reported in [329]. Atoms from the face of {0001} planes have a higher yield than those from the {10.0} and {11.0} planes. Therefore, very energetic Ar^+ ion bombardment of a polycrystalline Mg coating would possibly favour the growth a <10.0> fibre texture due to the preferred resputtering from {0001} surfaces. This would suggest that there is a competing mechanism for the development of fibre texture in Mg coatings. The driving force for minimisation of surface energy dominates under conditions of light to moderate bombardment, but preferential resputtering effects cause a change in texture when bombardment is excessively heavy.

7.3.2 Argon Burial and Residual Stress

It was apparent from the experimental results that the buried Ar content of the coatings was closely related to the residual compressive macrostress that existed in the Mg coatings. Both the Ar content and {0002} *d*-spacing followed similar trends with increasing bias voltage for both sets of coatings. This was examined further by plotting the {0002} *d*-spacing as a function of Ar content (Fig.7.5). An increase in *d*-spacing relative to that of strain free powder was interpreted as being due to residual compressive macrostress, since it was established that the strain-free lattice parameter of the Mg coatings was not subject to entrapment of Ar in solid solution (Table 7.4). The results for Series 2 were found to fit closely to a non-linear curve, such that the compressive strain in the coatings (*d*-spacing) increased parabolically with Ar content. The results for the Series 1 coatings were generally shifted to slightly lower Ar content. It is believed

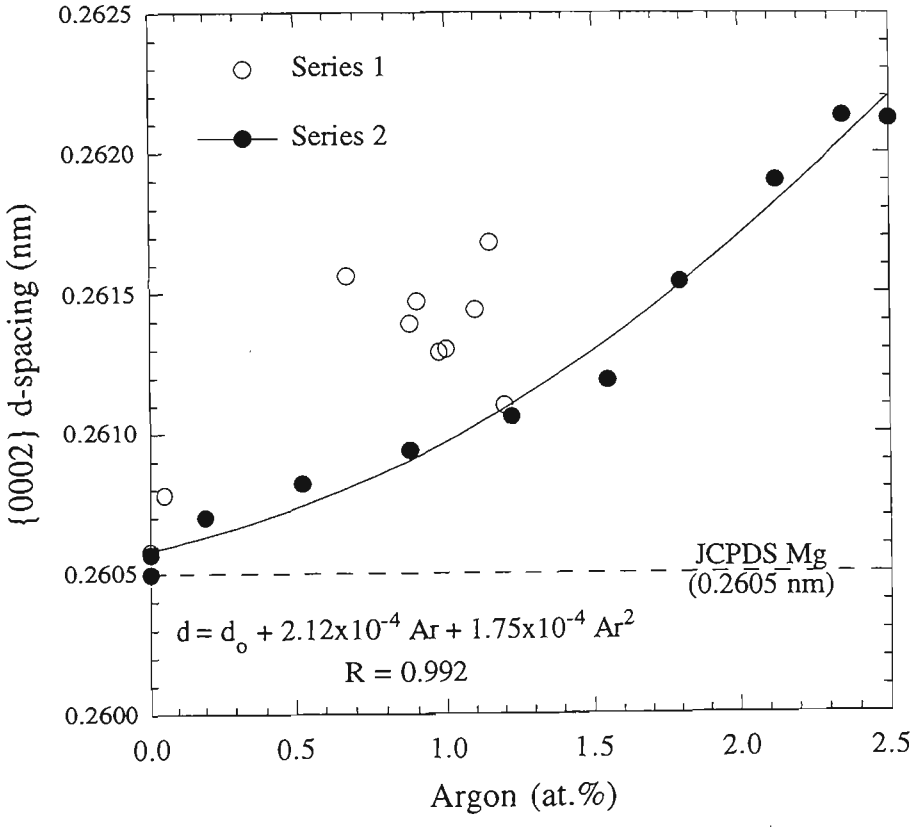

Fig.7.5 *Relationship between {0002} d-spacing of Mg coatings and the buried Ar content.*

that this is due to resputtering or diffusion of Ar from the coatings. The relationship between Ar content and residual macrostress therefore appears to have been somewhat dependent on the deposition parameters. In both cases, however, higher Ar content in the coatings signified the presence of compressive residual stress.

Following the same arguments presented in Chap.5, it is believed that the Ar in the coatings was not causative of the residual stress, but was merely an indicator of the factors that controlled the stress. In contrast to the Zn coatings which developed tensile stress in response to energetic ion bombardment, the present Mg coatings behaved in a more conventional manner by evolving compressive residual stress. Recrystallisation of the Mg coatings would have been more difficult owing to its higher melting point relative to Zn. Therefore, it is expected that the constrained shrinkage model that was applied to the Zn coatings is not applicable to the Mg coatings. The development of intrinsic stress in the Mg coatings would thus have been driven by similar mechanisms to those experienced with more refractory metal coatings.

The compressive stress in the Mg coatings is considered to have been caused by the "atomic-peening" mechanism whereby ion bombardment induces a high concentration of vacancies and other crystallographic defects [323]. Increasing the ion energy results in a greater proportion of radiation damage trapped below the surface of the coating as it grows [327]. These defects would be ideal sites for the trapping of larger Ar atoms [250]. The strain fields associated with the implanted Ar would be large, and it is presumed that the Ar atoms must be able to redistribute themselves to form bubbles, such that the lattice parameter of the Mg phase is unaffected. The presence of these bubbles in the final coating would probably contribute to broadening of the {0002} diffraction peaks (Fig.7.3c), although the effects of crystallite size cannot be ignored. Thus, the Ar in the coatings does not appear to directly contribute to the residual macrostress, but merely acts as an indicator of the lattice damage that is responsible for the compressive macrostress. The "effectiveness" of this indicator appears to decay at high *i/a* ratios (Series 1), as the fraction of the implanted Ar that is lost from the coating becomes significant.

7.4 Summary

Sputtered Mg coatings tended to form very strong <0001> fibre textures with low bombardment conditions, but transformed to <10.0> fibre texture at very energetic bombardment. Such changes in preferred orientation are thought to be caused by either plastic flow or preferential resputtering of <0001> oriented grains. The Mg coatings were much more susceptible to breakdown of the close-packed fibre texture than was the case for Zn and Al coatings. Mg coatings were also subject to a moderate degree of Ar burial, particularly with the less severe *i/a* conditions. The compressive residual stress in the coatings was correlated to the Ar content, but was considered to be an indicator of the factors responsible for stress generation rather than being causative.

Chapter 8

Aluminium-Zinc Alloy Coatings

8.1 Deposition Parameters

Four of the Al-Zn alloy targets described in Sect.4.2.1 were used to deposit sputtered coatings on Si wafers, with a range of ion assisted deposition conditions. All six Al-Zn alloy targets were used for the preparation of sputtered coatings for corrosion testing (Chap.13). The targets selected for preparation of ion assisted sputtered coatings were Al-24%Zn, Al-50%Zn, Al-73%Zn and Al-90%Zn. Three of these targets were chosen because they represented compositions that are very similar to commercial hot-dip galvanised coatings (Sect.1.2): Al-24%Zn is almost identical to Zincalume except that Si was not included; Al-50%Zn represents Lavegal but without the Mg additions; and Al-90%Zn is the same composition as Galfan/Superzinc except for the mischmetal or Mg additions. In this way, the three compositions (and one other) could be compared on equal ground without the potentially complicating factor of other alloy additions, as is the case with the hot-dipped coatings. It must be stressed however, that it was not the purpose of this thesis to directly compare the sputtered coatings with hot-dipped coatings, and generally no such comparison is made.

The important parameters for each series are listed in Tables 8.1 to 8.4. The same M3 magnet was used for all coatings, but for the Al-24%Zn and Al-50%Zn series it was slightly demagnetised (refer Sect.5.2.1). The thickness of each coating was estimated from the coating mass, assuming zero porosity and density given by a weighted average of the constituent elements. The coatings deposited at self bias from Al-24%Zn and Al-50%Zn targets were only about 0.5 μm thick. The self biased coatings from the Al-73%Zn and Al-90%Zn targets were within ±0.1 μm of the nominal 1 μm thickness.

Table 8.1 Deposition parameters for coatings prepared from Al-24%Zn target. Other process variables: base pressure 270 μPa; magnetron power ~80 W (low voltage supply); probe current 0.26 mA; deposition time 7 minutes per sample.

Magnetron Conditions		Substrate	Coating Mass
Voltage (V)	Current (A)	Bias (V)	(μg)
475	0.16	self (-21)	33 *
474	0.16	-30	118 *
473	0.16	-40	142
472	0.17	-50	131
471	0.17	-60	116
470	0.17	-70	111
470	0.17	-80	109
469	0.17	-90	109
469	0.17	-100	105
468	0.17	-110	84 *
466	0.17	earth	148

* coating mass in error due to substrate breakage

Table 8.2 Deposition parameters for coatings prepared from Al-50%Zn target. Other process variables: base pressure 53 μPa; magnetron power ~75 W (low voltage supply); probe current 0.22 mA; deposition time 5 minutes per sample.

Magnetron Conditions		Substrate	Coating Mass
Voltage (V)	Current (A)	Bias (V)	(μg)
569	0.13	self (-22)	200
568	0.13	-40	193
567	0.13	-60	193
565	0.13	-80	170
564	0.13	-100	129
563	0.13	-120	120
562	0.13	-140	116
562	0.13	-160	102
561	0.13	-180	101
561	0.13	-200	98
560	0.13	earth	191

Table 8.3 Deposition parameters for coatings prepared from Al-73%Zn target. Other process variables: base pressure 77 μPa; magnetron power 100 W (high voltage supply); probe current 0.389 mA at start, 0.393 mA at end; deposition time 5 minutes per sample.

Magnetron Conditions		Substrate	Coating Mass
Voltage (V)	Current (A)	Bias (V)	(μg)
497	0.20	self (-25)	427
496	0.20	-40	423
497	0.20	-60	406
498	0.20	-80	407
498	0.20	-100	327
497	0.20	-120	290
497	0.20	-140	245
496	0.20	-160	191
497	0.20	-180	112 *
499	0.19	self (-25)	395
495	0.20	earth	410

* coating mass in error due to substrate breakage

Table 8.4 Deposition parameters for coatings prepared from Al-90%Zn target. Other process variables: base pressure 65 μPa; magnetron power 100 W (high voltage supply); probe current 0.360 mA at start, 0.367 mA at end; deposition time 5 minutes per sample.

Magnetron Conditions		Substrate	Coating Mass
Voltage (V)	Current (A)	Bias (V)	(μg)
537	0.18	self (-25)	605
534	0.18	-40	591
533	0.18	-60	560
532	0.18	-80	522
532	0.18	-100	483
532	0.18	-120	458
531	0.18	-140	427
530	0.18	-160	400
530	0.18	-180	366
532	0.18	self (-25)	577
531	0.18	earth	591

8.2 Results and Discussion

8.2.1 Ion/Atom Flux Ratio

The calculated *i/a* ratios for the four Al-Zn targets are shown in Fig.8.1. The results for Al and Zn targets are also shown for comparison. Error bars of ±15% are indicated, and represent a conservative estimate of the expected error in the measurement. Furthermore, breakage of the Al-24%Zn coating at self bias created uncertainty in the mass measurement, and this was overcome by estimating the coating mass to be about 150 μg. The *i/a* ratio was found to be parabolically related to the Zn content of the target, and divided into two groups depending on the magnetic field strength. The ion current, when normalised by the magnetron current, was constant (within an error of ±5%) for all coatings in each M3 condition. Therefore, the parabolic decrease in *i/a* ratio with increasing Zn content was due to the concurrent increase in net sputtering rate of the target.

These results reveal an inherent problem with using unbalanced magnetron sputtering for the study of ion assisted deposition of alloys: the *i/a* ratio experienced by the coating is influenced by both the sputtering yield of the target material, and the magnetic field strength. The use of permanent magnets for providing the magnetic field means that the ion flux is essentially fixed for any given magnet assembly. Heating the magnets can be used to reduce the *i/a* ratio somewhat (Fig.8.1), but this variable is both difficult to predict and cannot be reversed without remagnetising. Consequently, the *i/a* ratio will be a function of the target composition due to its influence on the sputtering yield (Sect.8.2.2). The results of coatings prepared from targets of different composition are difficult to compare since they are likely to have experienced different *i/a* ratio. This is apparent for the present Al-Zn coatings which had a range of *i/a* ratios, depending on target composition and magnetic field strength. It is then fortuitous that the *i/a* ratios for the Al-50%Zn and Al-73%Zn targets were almost identical, which permits equal comparison of their results. The *i/a* ratios for the Al-90%Zn and pure Zn targets were also very similar.

8.2.2 Mass Deposition Rate

The mass deposition rates for each of the Al-Zn alloy coating series are shown as a function of the substrate bias voltage in Fig.8.2. The results for Al and Zn coatings are included for comparison. The deposition rates for the alloys were intermediate between those of pure Al and Zn. Increasing the Zn content of the alloy target resulted in an increase in the deposition rate. This is consistent with the higher density and greater

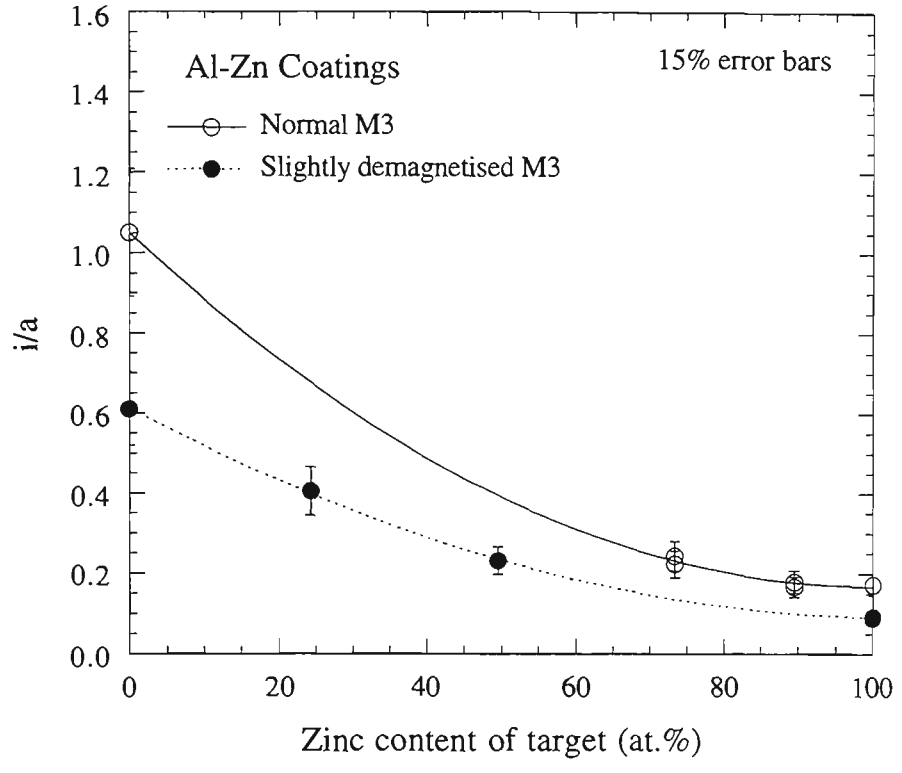

Fig.8.1 *Ion/atom arrival rate ratio as a function of Al-Zn target composition.*

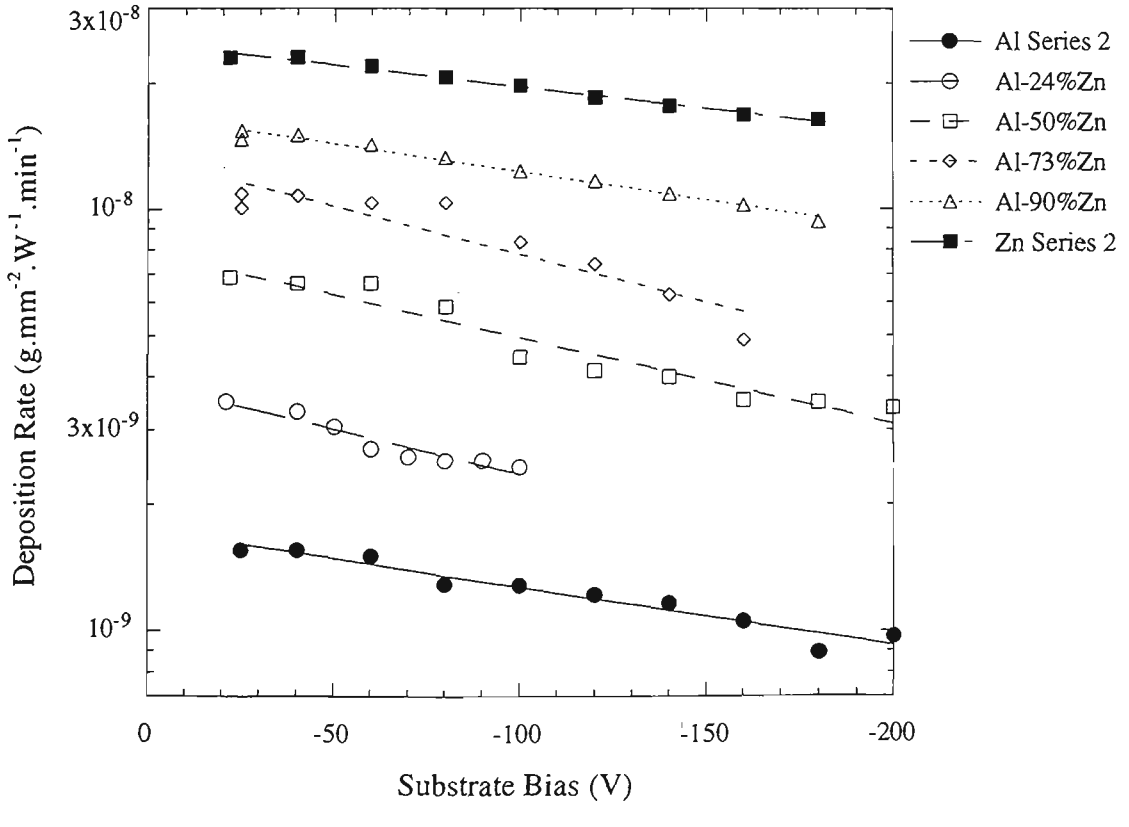

Fig.8.2 *Mass deposition rate for sputtered Al-Zn coatings. Note the ordinate axis is semi-logarithmic.*

sputter yield of Zn relative to Al. The earth bias results are not shown in Fig.8.2 but were almost identical to those of self biased coatings (-20 to -25V). Previous work [160,214] indicated that heating due to the large electron current experienced with earthed substrates could result in partial or complete reevaporation of Zn from Al-Zn coatings. Thus, it would appear that the substrate clamping measures adopted in the present work (Sect.4.1), were affective in minimising substrate heating.

The substrate bias had a significant effect on the coating mass, resulting in a general exponential decrease in deposition rate. Since the possibility of Zn reevaporation was minimised by effective substrate clamping, the reduction in coating mass with increasing bias voltage was most likely caused by resputtering as a result of ion bombardment during deposition. However, from these results alone it is not possible to ascertain whether or not there was any preferential resputtering of one of the alloy components. The answer to this question required EDS analysis of coating composition. The results for Al-24%Zn, Al-50%Zn and Al-73%Zn targets, also showed a sharp decrease in the mass deposition rate at bias voltages of -60V, -100V and -100V respectively. The EDS analysis described in the following section revealed that this was due to compositional effects.

8.2.3 Chemical Composition

Measurement of the coating composition by EDS not only indicated that preferential resputtering occurred in coatings from most of the targets, but also a considerable amount of buried Ar was detected in coatings deposited with the highest bias voltages. The Zn content of the deposited coatings are shown in Fig.8.3, relative only to the total amount of Al and Zn. Figure 8.4 indicates the measured Ar content of the sputtered alloy coatings. Series 4 Zn coatings are included in Fig.8.4 for comparison. The composition of coatings at self bias and earth bias were all within about ±2 at.% of the target composition. This range is slightly larger than the expected variability of ±1 at.% and could possibly be due to compositional inhomogeneity in the targets.

With small increases in the bias voltage above self bias, the Zn content of the alloy coatings remained relatively constant or decreased only slightly (Fig.8.3). This suggests that under such conditions Al and Zn are resputtered from the coating at approximately equal rates. The proportion of resputtered material also appears to have been minor, judging from the relatively minor changes in mass deposition rate (Fig.8.2). However, at a particular bias voltage the Zn content was found to decrease abruptly, coincident with an abrupt decrease in the mass deposition rate. These changes occurred at -60V for the Al-24%Zn target, and -100V for both the Al-50%Zn and Al-73%Zn targets. A second

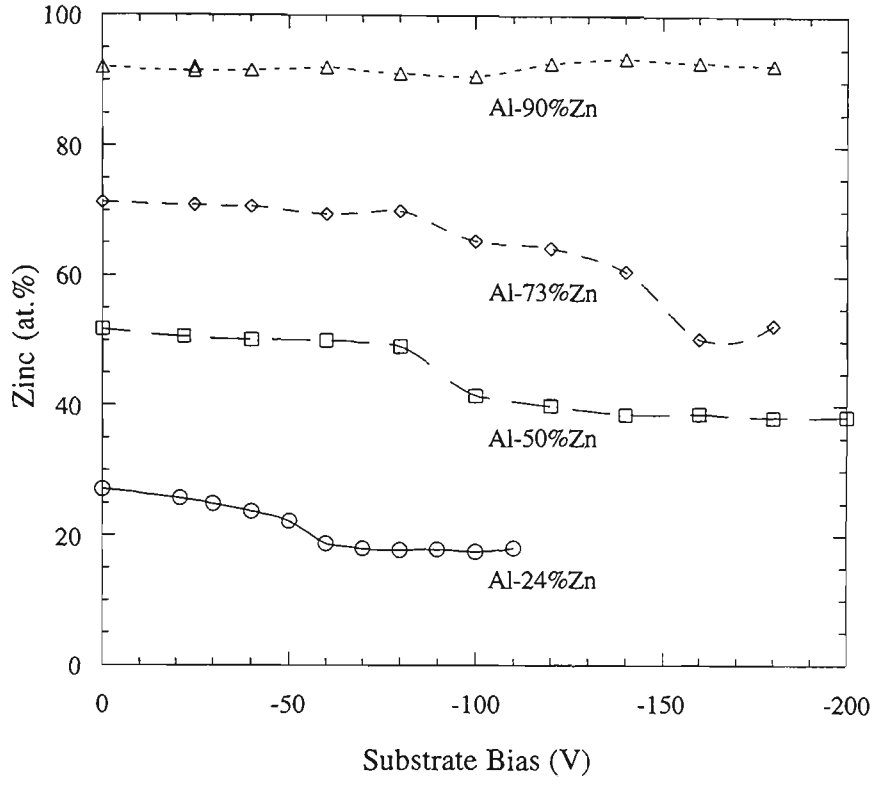

Fig.8.3 *Zn content of sputtered Al-Zn coatings, relative to the total amount of Al and Zn.*

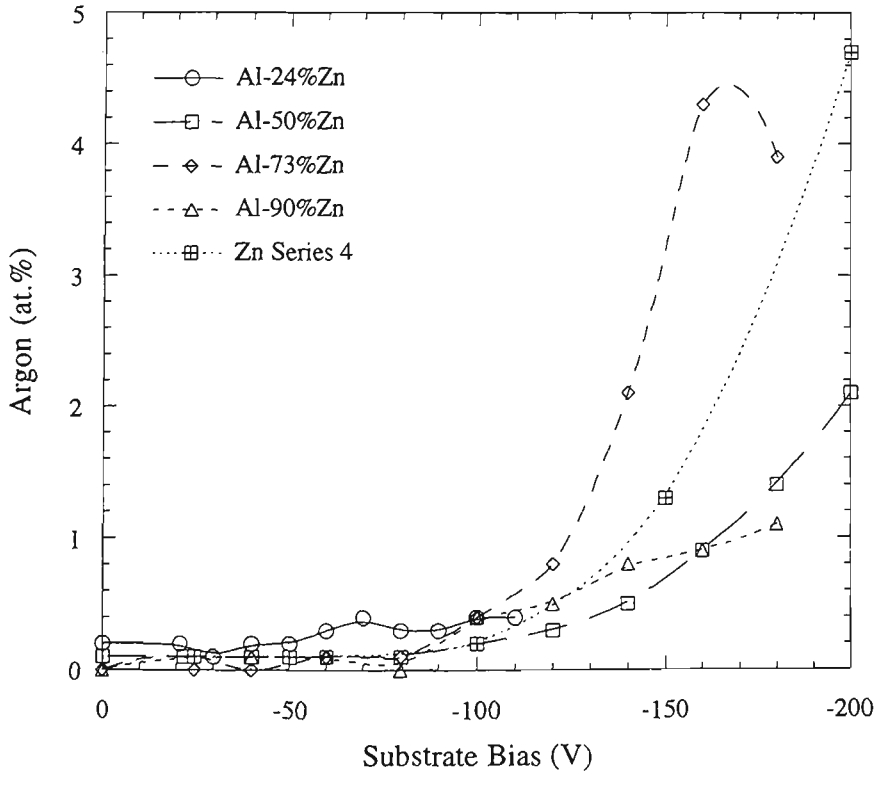

Fig.8.4 *Ar content of sputtered Al-Zn coatings.*

transition for the Al-73%Zn coatings occurred at -160V, perhaps in response to the large amount of buried Ar (Fig.8.4). The Al-90%Zn series coatings retained a constant Zn content within a range of ±1.5 at.% for all bias conditions.

Considering the differences in *i/a* ratio for each of the different targets, the transition in Zn content occurred at a normalised bias of about -23 $V.atom^{-1}$ (or ~30 $eV.atom^{-1}$ assuming plasma potential of ~7 eV). It would therefore appear that preferential resputtering of Zn from the Al-Zn coatings was activated above a critical normalised ion energy. The ensuing modification of the coating composition dominated the mass deposition rate trends due to the much greater density of Zn in comparison with Al. The Al-90%Zn series coatings were apparently unaffected by preferential resputtering. It is feasible that this was due to the low sensitivity of the EDS technique.

Most of the Al-Zn alloy coatings were susceptible to the retention of Ar at sufficiently high bias voltages. Generally, the buried Ar content increased continuously with bias voltage (Fig.8.4). The highest Ar content was found to be 4.3% for coatings deposited from the Al-73%Zn target at a bias of -160V. At slightly higher bias for this set of coatings, a reduction in Ar content was observed, which suggested a peak in Ar content akin to that observed in the Zn Series 4 coatings (Chap.5). The coatings from the Al-50%Zn target showed a continuous but much slower increase in Ar than was observed for the Al-73%Zn target. The *i/a* ratio for these two sets of coatings were similar (0.23), so they can be directly compared. Similarly, the Ar content of the Zn Series 4 coatings increased more rapidly than that of the Al-90%Zn coatings, while both shared an *i/a* ratio of 0.17. These observations suggest that coatings with a greater proportion of Zn were possibly more susceptible to inert gas burial, which is consistent with the results for pure Al and Zn coatings.

A very slight increase in Ar content is apparent for the Al-24%Zn coatings in Fig.8.4. This trend may simply be an artefact of the EDS measurement, owing to measurement of the Al K_α sum peak which overlaps the Ar K_α. An alternative test method would be necessary to establish the Ar content of these coatings.

8.2.4 Visual and SEM Examination

The surface appearance of all of the Al-Zn coatings is shown in Fig.8.5. Generally the coatings from the low Zn content targets produced lustrous coatings, while those from the Zn-rich targets were matt and dark blue-grey in colour. All coatings from the Al-24%Zn and Al-50%Zn targets were highly lustrous with a surface that closely replicated the polished silicon wafer substrate. They were also slightly bluish-white in

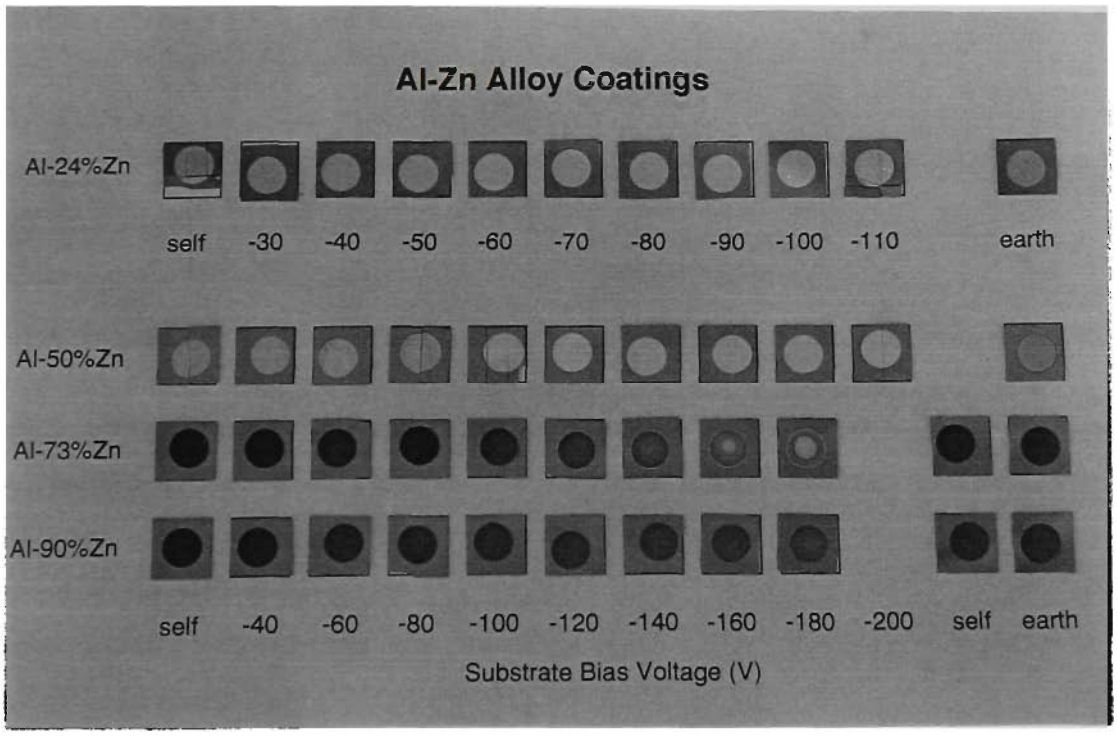

Fig.8.5 *Photograph of Al-Zn coatings taken about three years after deposition.*

colour. Hence, these alloy coatings were essentially identical in appearance to the pure Al coatings (Chap.6). Subsequent to about two years of ambient aging, the coatings from the Al-50%Zn target deposited with up to -80V bias developed a slight yellow tinge, which is presumably due to mild surface oxidation. Increasing the bias to -100V or greater appeared to prevent this discolouration. It is relevant that increasing the bias from -80V to -100V also resulted in a sharp change in the coating composition from 49 to 42%Zn (Fig.8.3). Thus, it seems that Al-Zn coatings with more than 45±4%Zn were susceptible to surface discolouration following ambient aging.

The coatings from the Al-73%Zn and Al-90%Zn targets generally had a non-reflective dark-blue-grey appearance. A similar, but lighter colour was noted for the pure Zn coatings (Chap.5). This appearance was attributed to the light-scattering effects of a population of relatively large protruding grains on the surface of the coatings. Increasing the bias voltage for the Zn coatings tended to reduce the number of these protruding grains, and hence the milky appearance was reduced. A similar but less dramatic trend was observed for the Al-Zn coatings, for which the blue-grey colour seemed to become less dark with increasing bias. Indeed the coatings deposited at a bias of -160V or higher with the Al-73%Zn target developed a bluish-white lustrous spot at the centre of the coated area (Fig.8.5). The coating in this region was found to contain about 52%Zn (Fig.8.3), while the outer matt blue-grey region contained about 60%Zn. This profile in Zn content across the coated area of the sample was probably caused by a similar profile in the ion current [60,65]. Thus, it appears that ion assisted deposition significantly affected the macroscopic appearance of the Al-Zn coatings, through its influence on their chemical composition. The moderately sharp boundary between a matt and a lustrous coating appearance can be located at about 56±4%Zn.

The morphological structure of a limited number of Al-Zn alloy coatings was examined on a field emission SEM. This was not pursued thoroughly due to limited access to the equipment, and only the Al-50%Zn and Al-24%Zn series were studied. SEM micrographs of the Al-24%Zn coatings deposited on self bias and -100V bias substrates are shown in Fig.8.6. Attempts were also made to examine the -60V bias sample, but a satisfactory image could not be obtained. The grains in the Al-24%Zn series coatings seemed to have a faceted shape, with the distribution of grain sizes on the surface of the coating affected by the bias voltage. At self bias, the grain size varied from about 20 nm up to 150 nm, but was typically about 50 nm (Fig.8.6a). The larger grains were not present on the surface of the -100V bias sample, although the average size was still in the order of 50 nm (Fig.8.6c). Fracture sections of the coatings did not seem to be very successful, because they showed signs of plastic deformation. This made it difficult to observe any inherent microstructural features (Fig.8.6b).

(a)

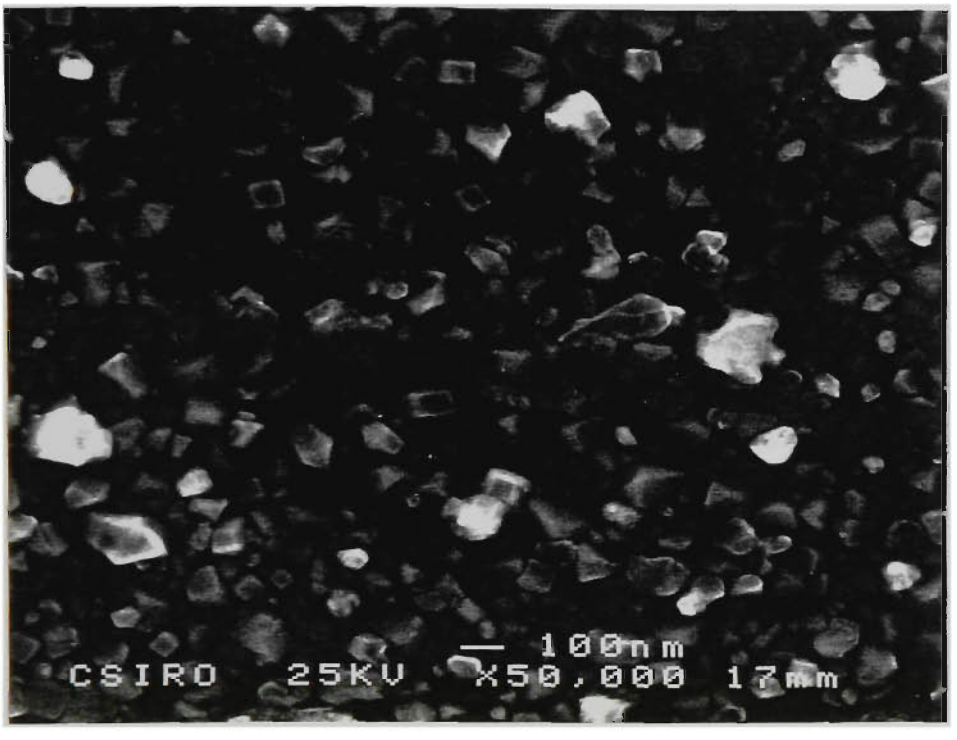

(b)

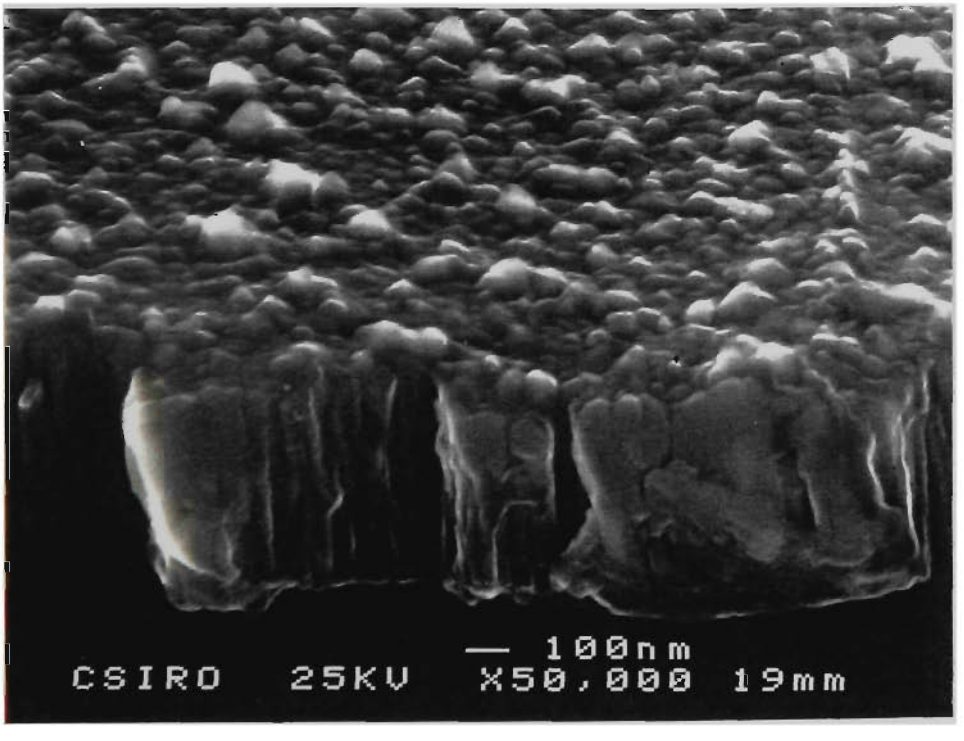

Fig.8.6 Surface and fracture-section SEM micrographs of the self bias (a,b), and -100V bias (c) coatings deposited from the Al-24%Zn target. *(see next page)*

(c)

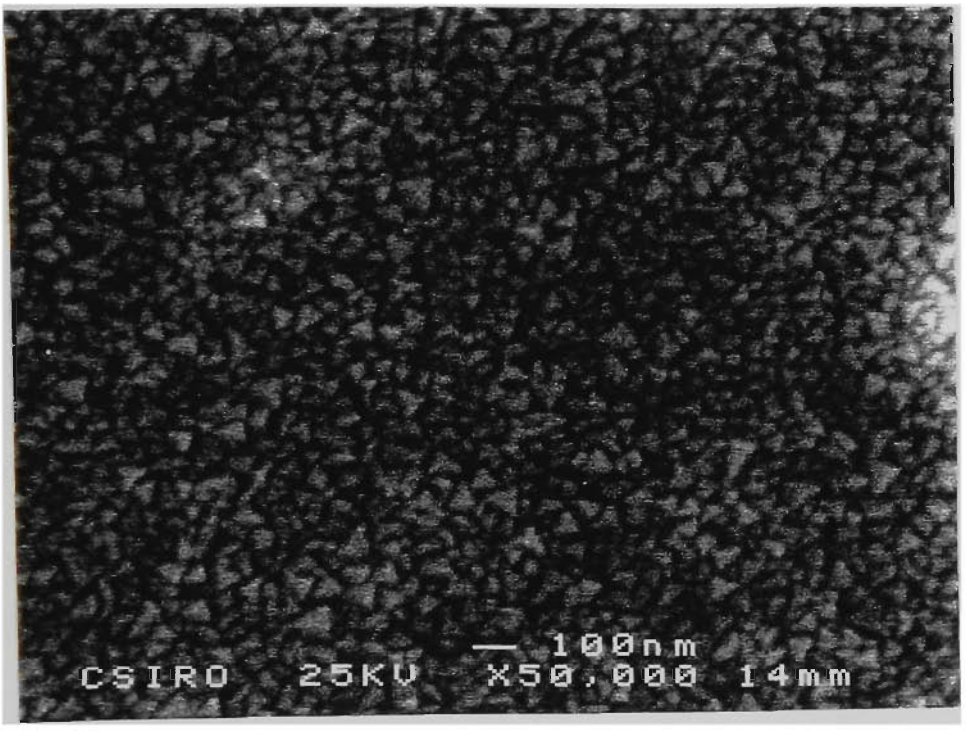

Field emission SEM micrographs of the Al-50%Zn series coatings prepared with self, -80V, -100V and -200V bias are shown in Fig.8.7. These suggest that the discolouration of the low bias coatings may have been related to their surface morphology. The coatings deposited with self bias (Fig.8.7a,b) and -80V bias (Fig.8.7c,d), displayed a surface consisting of a collection of small grains of about 100-200 nm diameter. The fracture section did not reveal any specific grain features and the morphology can best be described as an agglomerated structure. Increasing the bias voltage to -100V (Fig.8.7e,f), resulted in an obvious change in the coating morphology which was retained up to -200V bias (Fig.8.7g,h). The surface of the coatings consisted of very fine grains of 20-50 nm diameter. Some bright regions on the surface were still present, and are thought to indicate the presence of small clumps of outcropped grains. The fracture sections of the high bias coatings appeared to show a fine columnar structure. The high bias coatings were therefore much smoother than the low bias coatings, and this may have influenced surface oxidation due to the corresponding differences in available surface area.

The coating thicknesses of most of the above coatings were measured from the SEM micrographs, and the results are summarised in Table 8.5. For the Al-50%Zn series, the coating thickness decreased with increasing bias. A particularly large change in thickness was noted between -80 and -100V. The coating thickness calculated from the mass measurements, assuming bulk density, is also shown in the table. These values were similar to the actual cross-section thicknesses, which suggests that the coatings had very little porosity.

Table 8.5 Coating thicknesses measured from SEM sections and by calculation from coating mass assuming bulk density. The error for the SEM measurement is about ±0.05 μm

Al-Zn Series	Substrate Bias (V)	Coating Thickness (μm)	
		SEM Section	Coating Mass
Al-24%Zn	self bias	0.55	0.50
Al-50%Zn	self bias	0.50	0.52
	-80V	0.45	0.44
	-100V	0.35	0.36
	-200V	0.30	0.29

(a)

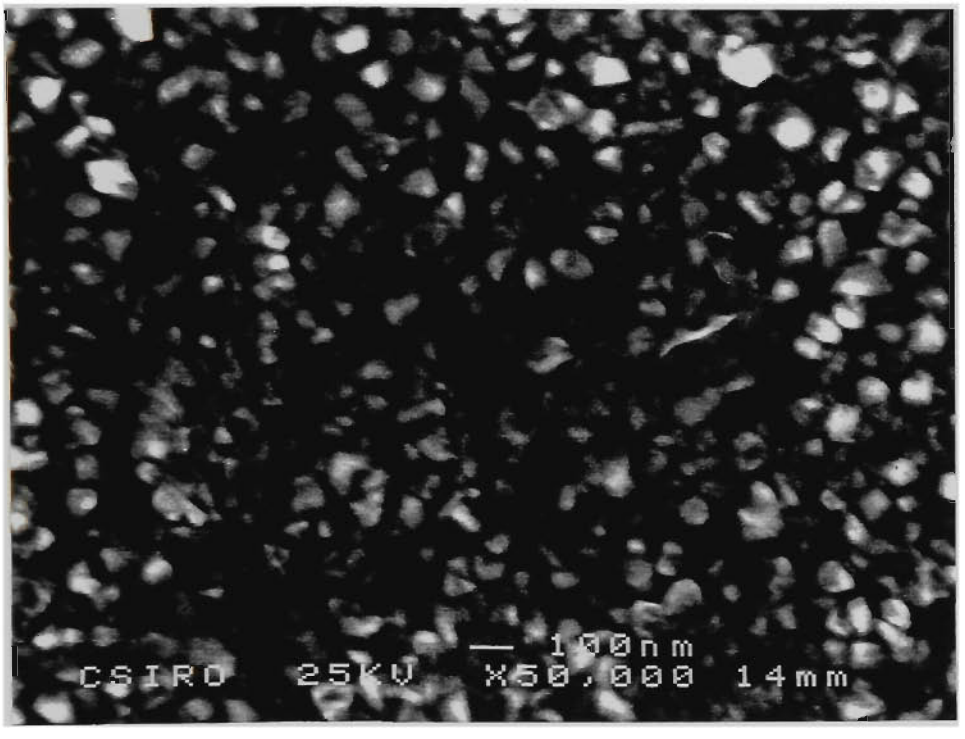

(b)

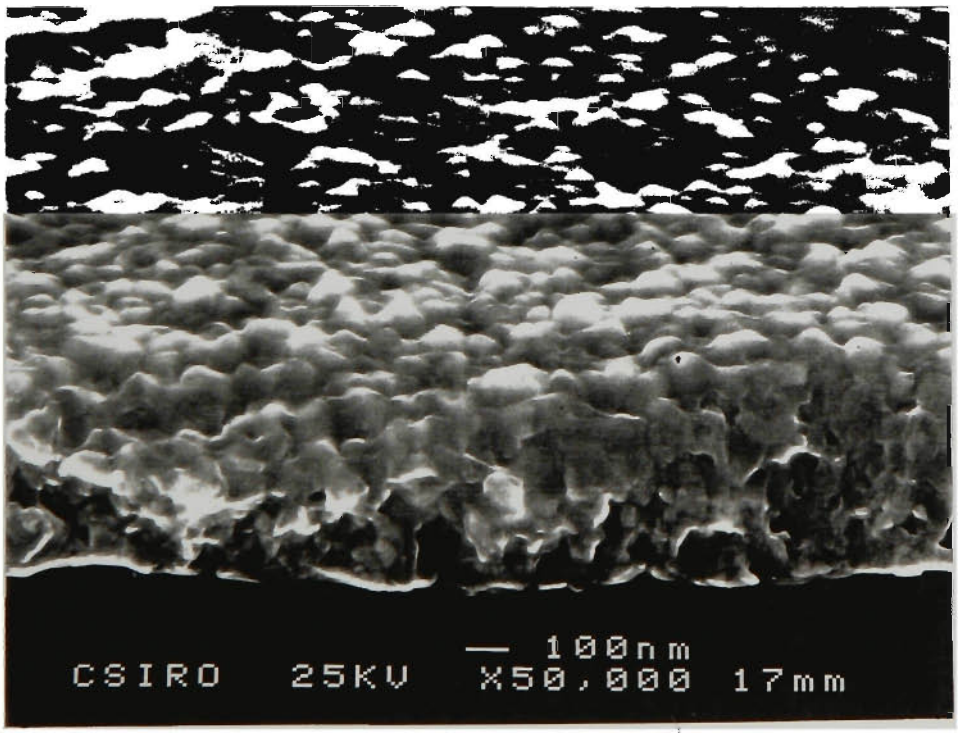

Fig.8.7 Surface and fracture-section SEM micrographs of the self (a,b), -80V (c,d), -100V (e,f), and -200V (g,h) bias coatings deposited from the Al-50%Zn target.

(see following pages)

(c)

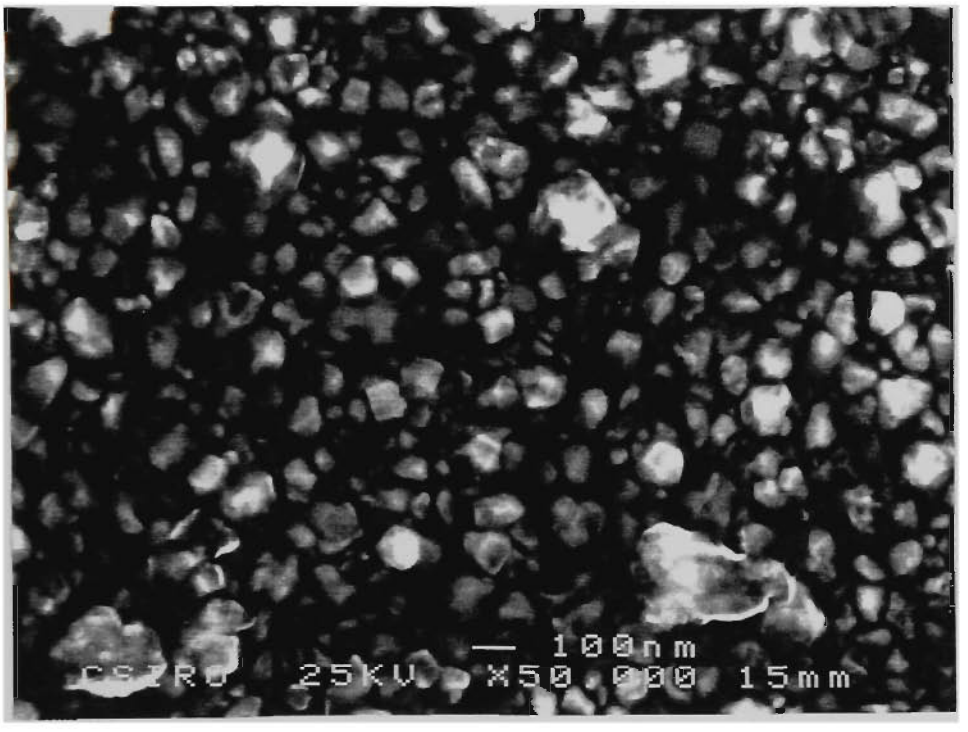

(d)

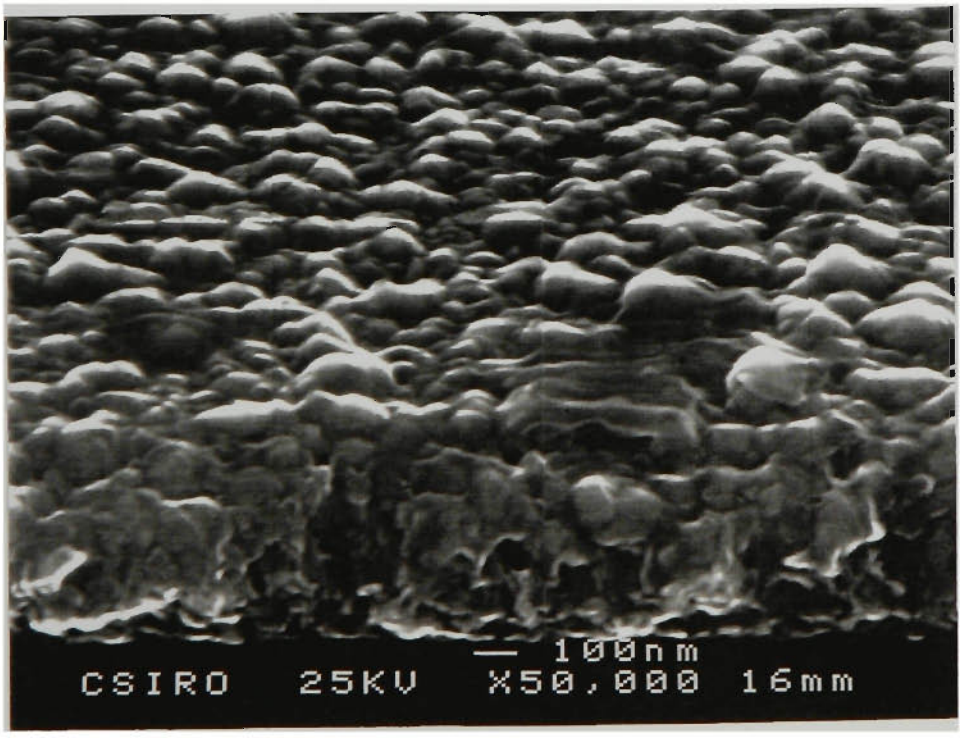

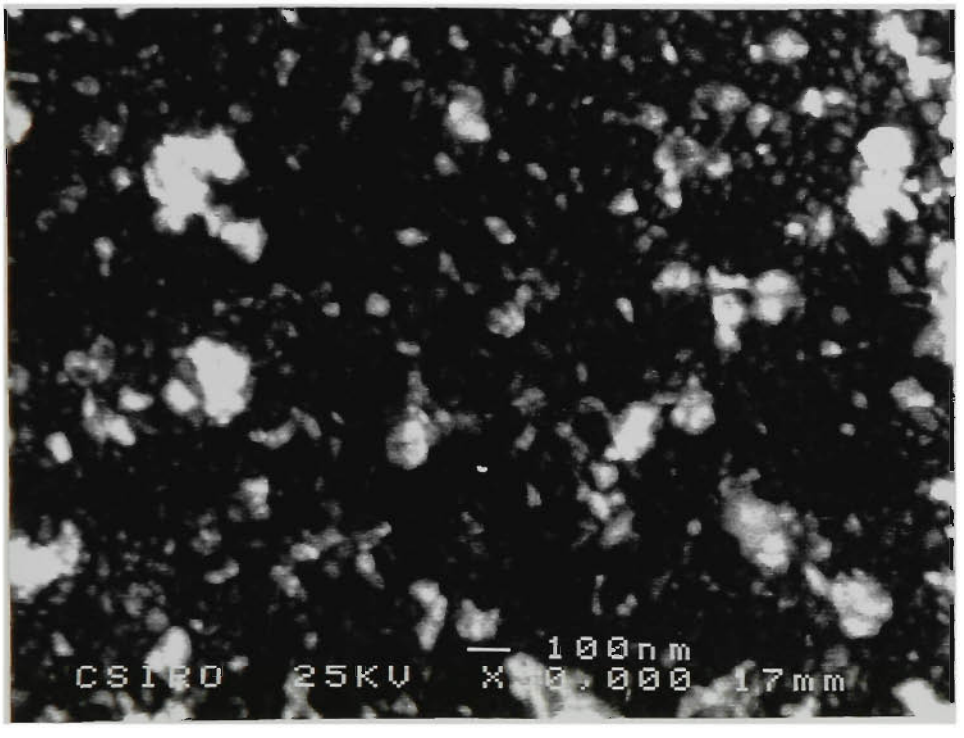

(e)

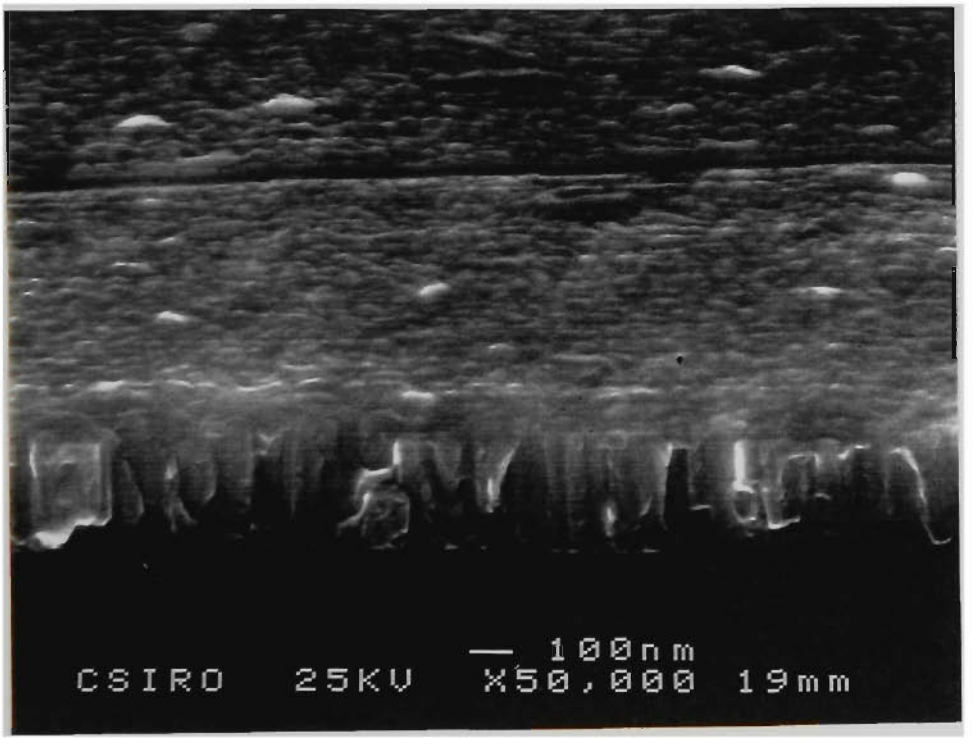

(f)

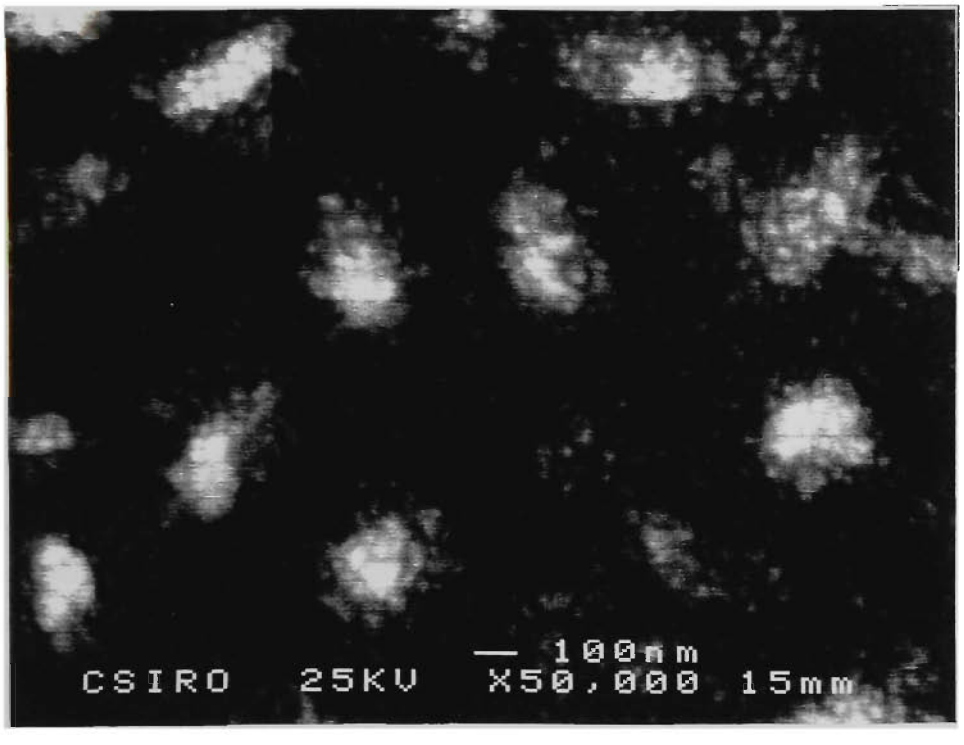

(g)

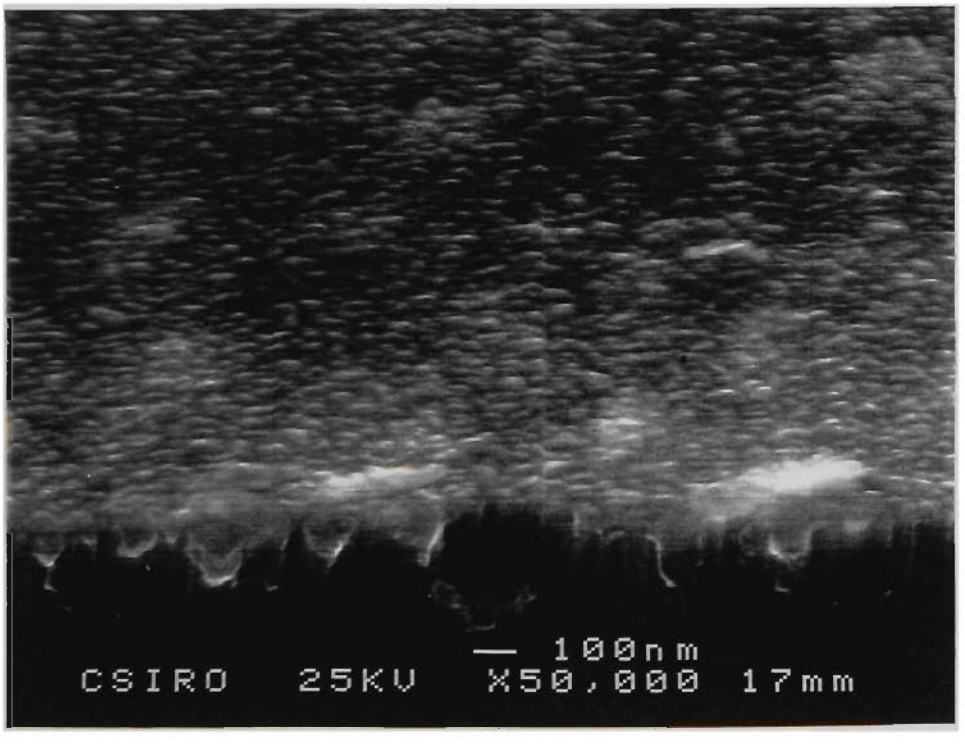

(h)

8.2.5 Bragg-Brentano X-Ray Diffraction

The Bragg-Brentano XRD spectra for the various coatings from the four different Al-Zn alloy targets are shown in Figs.8.8-8.11. The region between 2θ of 39.8° and 42.3° was not scanned for the Al-24%Zn and Al-50%Zn series in order to minimise the total scan time while maintaining a small step size to optimise the peak resolution. Early investigations indicated that no diffraction peaks were present within this 2θ region, and therefore scans of this range were unnecessary. The background signal was generally very low (~1.6 cps), due to the use of Si wafer substrates. An exception was found in the region from 32.6° to 37.6° 2θ which developed a higher background intensity due to anomalous diffraction from the silicon wafer (Sect.4.4.1).

The diffraction results indicated that α-(Al) and β-(Zn) phases were present in virtually all of the Al-Zn coatings produced. The only exception was for the Al-90%Zn series at bias voltages of -140V or higher, for which diffraction from the (Al) phase was too weak to detect reliably. An intense diffraction peak was observed for the Al-50%Zn series (Fig.8.9b) located midway between the expected positions for Al {111} and the Zn {10.0} planes. CGM analysis (Sect.8.2.6) confirmed that this peak corresponded to {111} fcc planes, and therefore it was attributed to the (Al) phase. No evidence for the formation of metastable intermetallic or amorphous phases was observed. It is suspected, however, that some degree of supersaturation of Zn in (Al) and Al in (Zn) occurred, and this is the subject of the CGM study. The most important aspects of the Bragg-Brentano XRD results for the (Al) and (Zn) phases are summarised in Figs.8.12 and 8.13 respectively.

(Al) Phase

The extent of preferred orientation in the (Al) phase of the Al-Zn coatings is shown in Fig.8.12a in terms of the ratio of {111} and {200} diffracted intensities. In many coatings the {200} peak was not detected, and was arbitrarily assigned a value of 1 cps. No results for the Al-90%Zn target are shown because the (Al) diffraction peaks were too weak to measure accurately. The ratio corresponding to random orientation is indicated by the horizontal dashed line at a value of 2.1 (100/47 [197]). Data points above this value indicate a <111> preferred orientation. Generally, the (Al) phase in the coatings exhibited a sharp transition from a random orientation at low bias voltages, to a strong <111> fibre texture at higher bias. The minimum bias voltage required to form the strong fibre texture was defined as V_t. The value of V_t was -50V, -100V and -160V for Al-24%Zn, Al-50%Zn, and Al-73%Zn targets respectively. A direct comparison of the latter two series suggests that increasing the Zn content of the target caused V_t to shift

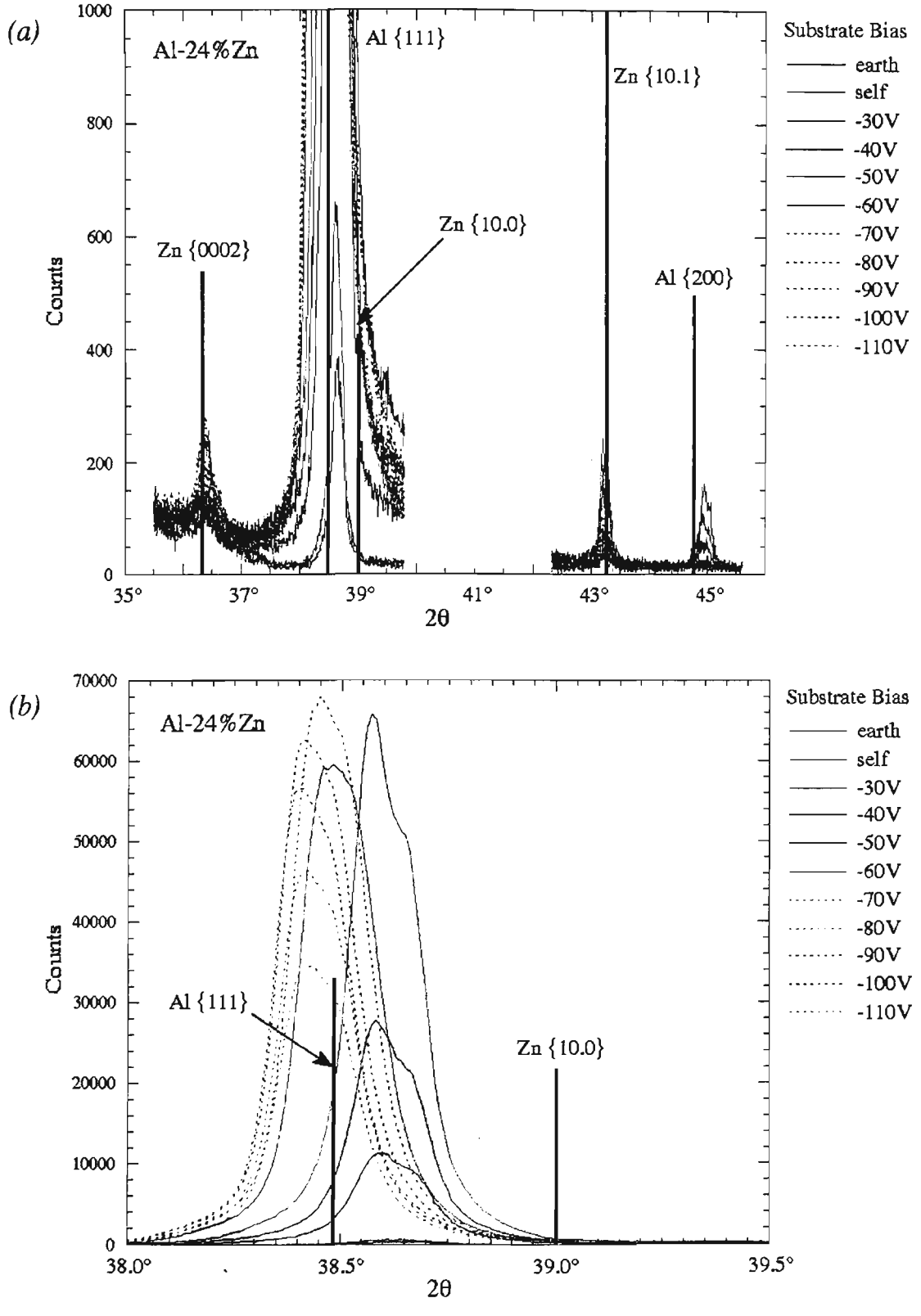

Fig.8.8 *Bragg-Brentano X-ray diffraction spectra for Al-24%Zn Series coatings*
(a) low intensity peaks
(b) high intensity Al {111} diffraction peak

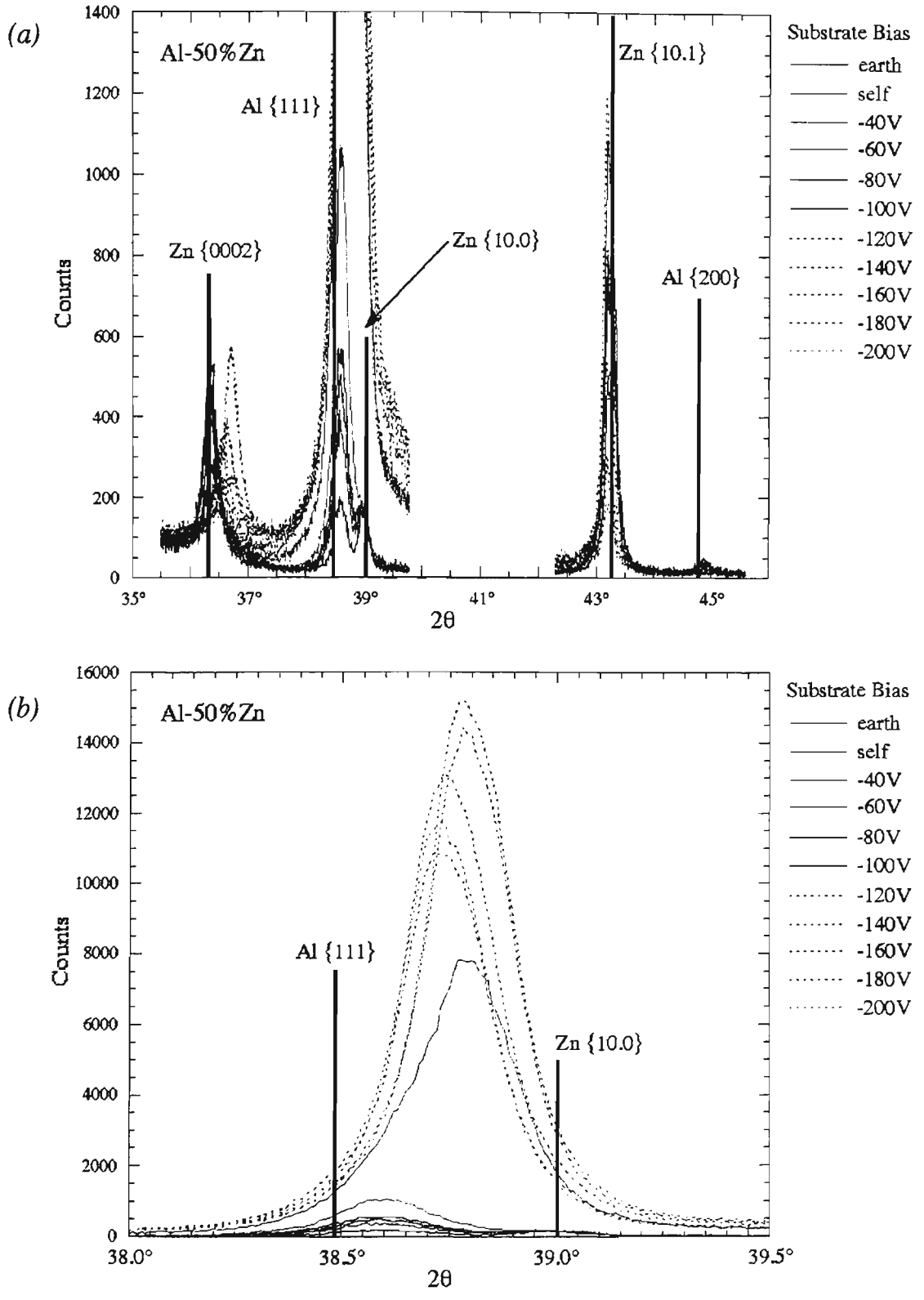

Fig.8.9 *Bragg-Brentano X-ray diffraction spectra for Al-50%Zn Series coatings*
(a) low intensity peaks
(b) high intensity Al {111} diffraction peak

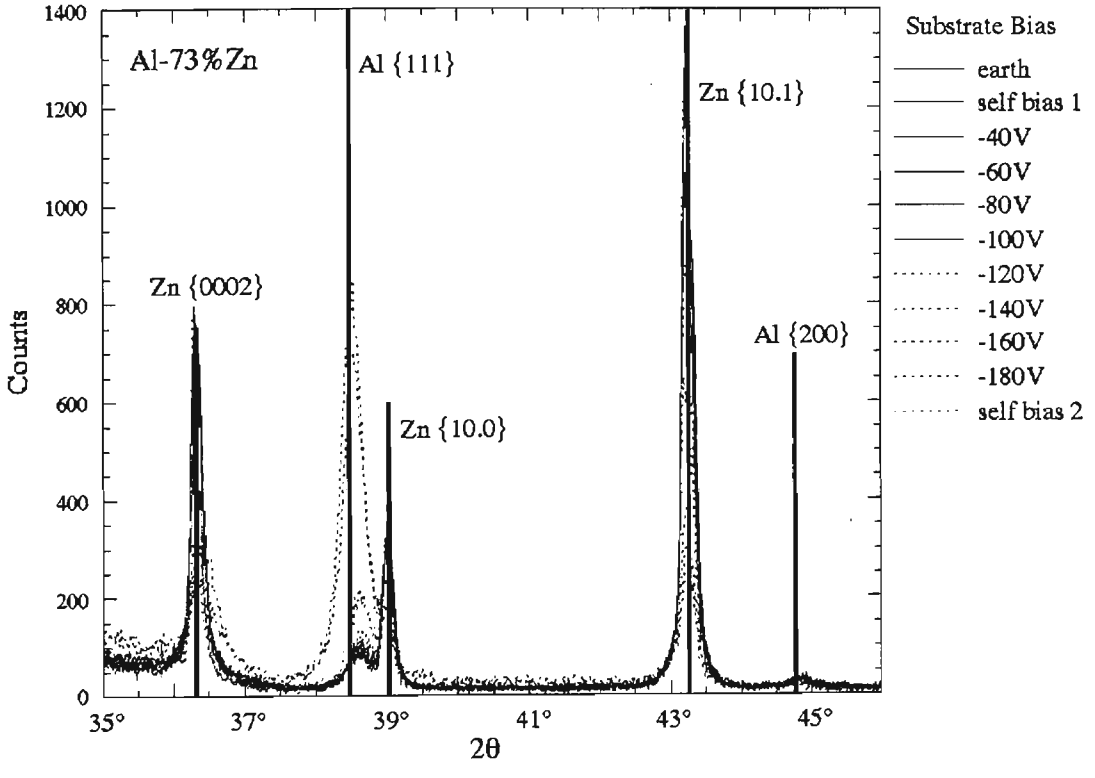

Fig.8.10 Bragg-Brentano X-ray diffraction spectra for Al-73%Zn Series coatings

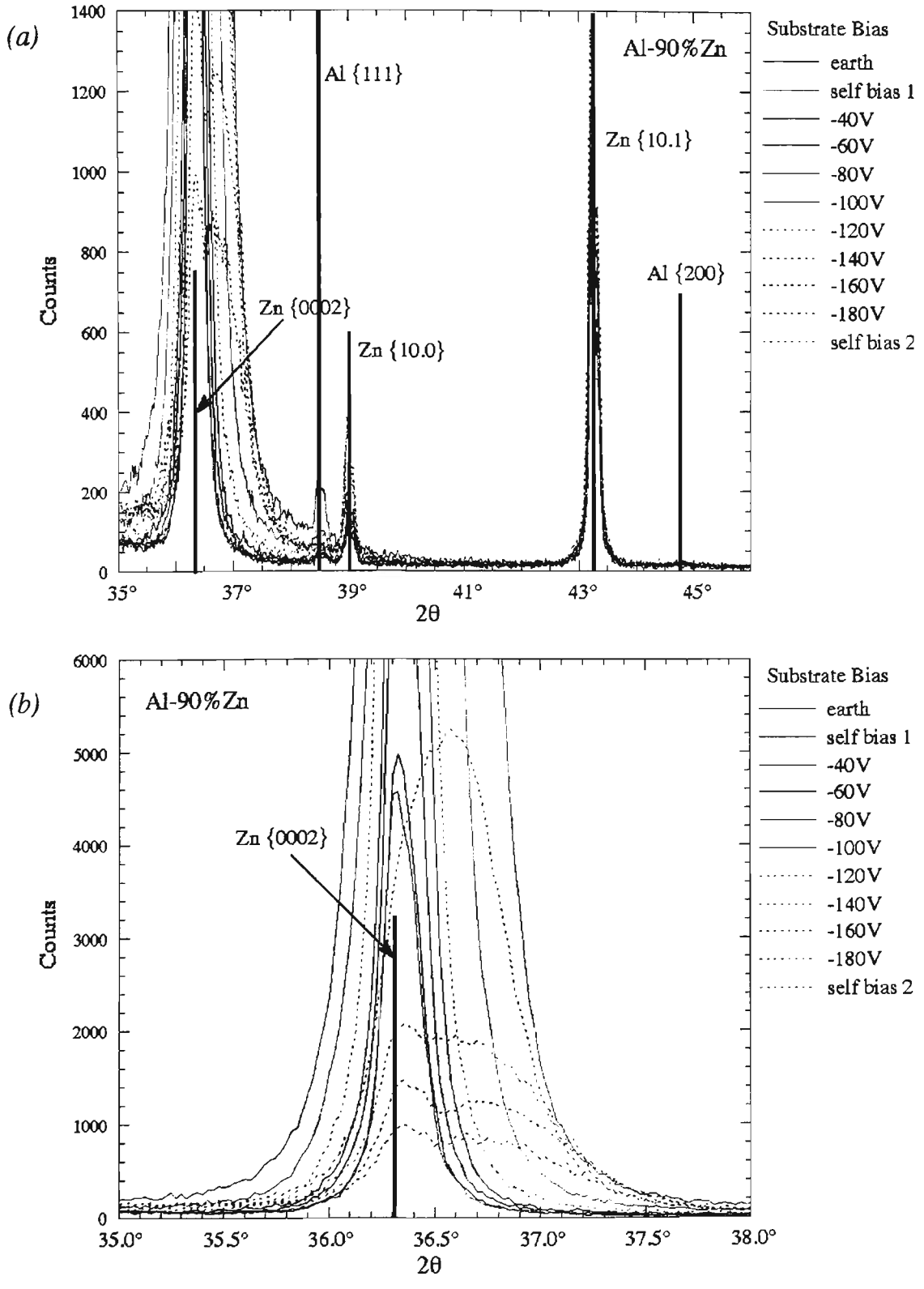

Fig.8.11 *Bragg-Brentano X-ray diffraction spectra for Al-90%Zn Series coatings*
(a) low intensity peaks
(b) medium intensity Zn {0002} diffraction peak showing peak splitting

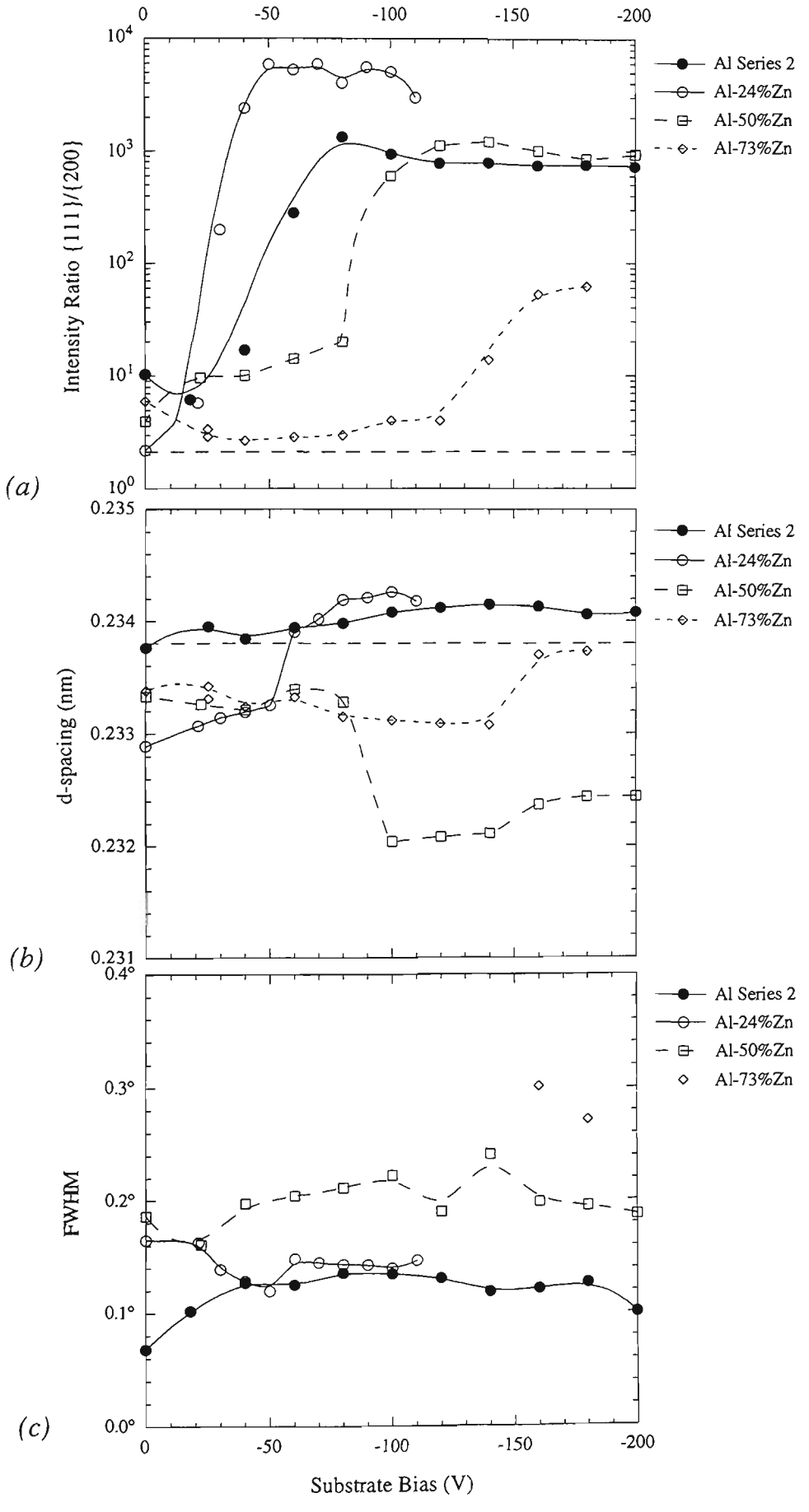

Fig.8.12 XRD results for the (Al) phase in Al Series 2 and Al-Zn coatings: (a) {111}/{200} peak intensity ratio, (b) d-spacing of {111} planes, and (c) FWHM of {111} peaks.

towards higher bias voltages. However, this trend appears to have been reversed as the Zn content was reduced. The value of V_t for the Al Series 2 coatings was -80V which is significantly higher than that of the Al-24%Zn series. Therefore, the presence of a relatively small proportion of Zn appeared to favour the development of the strong <111> fibre texture.

It is interesting to note that the value V_t corresponded very closely to the bias at which an abrupt depletion of Zn was observed (Fig.8.3). This suggests that the formation of the strong <111> fibre texture in the (Al) phase was somehow related to the onset of preferential resputtering of Zn. The interaction between (Al) preferred orientation and Zn content is discussed further in Sect.8.3.3.

The *d*-spacings of Al {111} planes in the various coatings are shown in Fig.8.12b. The *d*-spacing corresponding to a pure Al powder is indicated by the horizontal dashed line at 0.2338 nm [197]. Alloy coatings deposited at a bias voltage less than V_t appeared to share a very similar *d*-spacing of about 0.2332 nm, regardless of the Zn content of the target or the bias voltage. The *d*-spacing changed abruptly once the bias was increased to V_t or greater. For the coatings deposited with the Al-24%Zn and Al-73%Zn targets, the *d*-spacing increased sharply above V_t. However, the opposite trend was observed for the coatings from the Al-50%Zn target. These changes in *d*-spacing are most probably related to solid solution lattice parameter effects, although the impact of residual macrostress cannot be ignored. It should be noted that the {111} *d*-spacing for the Al Series 2 coatings increased slightly with bias voltage, and this was attributed entirely to the presence of a residual compressive macrostress (Chap.6). Therefore, it is likely that compressive stresses were also present in the (Al) phase of the alloy coatings. This was pursued further by CGM analysis (Sect.8.2.6).

The width of the Al {111} diffraction peaks for the alloy and Al coatings are shown in Fig.8.12c. The FWHM could not be determined for the Al-90%Zn series or most of the Al-73%Zn series because of the very low diffraction intensity (Figs.8.10 and 8.11). As a general observation from Fig.8.12c, the diffraction peak tended to broaden with increasing Zn content of the target. However, an increased bias voltage also had a significant effect on the peak width. This is demonstrated by comparing the results for the -160 and -180V bias samples from the Al-73%Zn target, with those from the Al-50%Zn series at bias voltages less than -80V. In both cases, the Zn content of the coating was very similar at about 50% (Fig.8.3). However, the coatings produced at the higher bias voltages showed a greater broadening of the Al {111} diffraction peaks. This could be related to the entrapped Ar in the Al-73%Zn series coatings (Fig.8.4), a grain refining

effect, or ion bombardment damage of the (Al) phase. It is not possible to assign a specific explanation without further work.

(Zn) Phase

The preferred orientation of the (Zn) phase in the various coatings is shown in Fig.8.13a, in terms of the ratio of {0002} and {10.1} peak intensities. For a randomly oriented powder, the value of this ratio is 0.53 (53/100 [197]), as indicated by the horizontal dashed line. Intensity ratios greater than this value indicate the presence of a <0001> fibre texture. Generally, the (Zn) phase in the Al-Zn coatings was found to be randomly oriented at low bias voltages and developed a moderate <0001> fibre texture at high bias. Between these two regimes, it appeared that there was a minima in the intensity ratio. The bias voltage corresponding to this minima was very similar to V_t. Increasing the bias voltage beyond V_t resulted in a rapid increase in the (Zn) intensity ratio, indicating the favoured growth of <0001> fibre texture. Thus it appears that the development of a <0001> fibre texture in the (Zn) phase possibly occurred in response to the transition in the (Al) phase from random orientation to a strong <111> fibre texture (Fig.8.12a).

The above observations do not seem to apply to the coatings from the Al-90%Zn target. This can be understood in light of the fact that the diffracted intensities for the (Al) phase in these coatings were very low (Fig.8.11), indicating that (Al) was present in only trace amounts. In contrast, the (Zn) phase in the Al-90%Zn series coatings seemed to have behaved in a similar fashion to the Zn Series 4 coatings. The (Zn) phase in both cases possessed a strong <0001> fibre texture even at low bias voltages (eg. self bias). The intensities of {10.0} and {10.1} diffraction peaks for all Al-90%Zn series coatings were relatively weak (Fig.8.11), indicating that the randomly oriented component was very minor in comparison to the <0001> fibre texture. Increasing the bias voltage resulted in a dramatic increase in the {0002} peak intensity, reaching a maximum at about -80V bias. Continued increase in bias caused the <0001> fibre texture to decrease in strength, such that at -180V bias the fibre texture component was similar in magnitude to the random orientation. Furthermore, the {0002} peak was observed to split into two distinct peaks above a bias of -120V (Fig.8.11). It is thought that the broader of these peaks was due to the <0001> fibre textured grains, while the relatively sharp peak at lower 2θ was attributed to the randomly oriented component of the coatings.

The {10.1} peaks for all of the Al-Zn coatings possessed a d-spacing that was very similar to that of a pure Zn powder (0.2901 nm [197]), as indicated in Figs.8.8 to 8.11. A similar observation was made for the pure Zn coatings, and it was concluded that

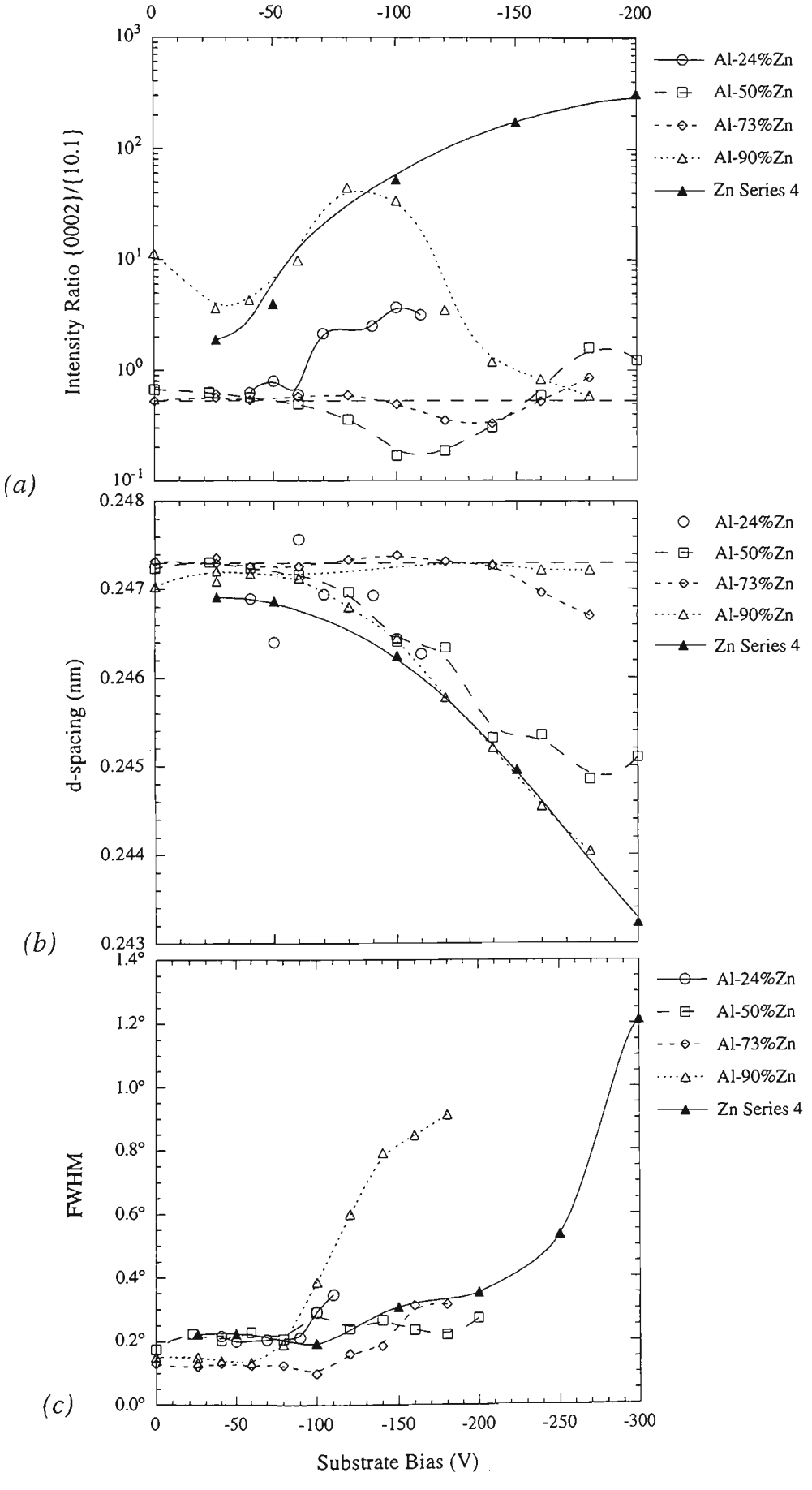

Fig.8.13 XRD results for the (Zn) phase in Zn Series 4 and Al-Zn coatings: (a) {0002}/{10.1} peak intensity ratio, (b) d-spacing of {0002} planes, and (c) FWHM of {0002} peaks.

those grains were essentially free of residual stress and solid solution effects. In the alloy coatings, the possibility of Al solid solubility and residual stresses cannot be immediately ignored. Judging from the relatively constant nature of the {10.1} *d*-spacing with changes in bias voltage and Zn content of the target, it is suspected that these effects were negligible for this group of grains. Similarly the {10.0} diffraction peaks were unaffected by bias or Zn content of the targets (Figs.8.8 to 8.11). Thus it seems reasonable to assume that the randomly oriented (Zn) grains in the alloy coatings were essentially free of residual stress and solid solubility. Unfortunately, the {10.0} and {10.1} peaks in each of the Al-Zn coatings were not of sufficient intensity to permit the application of CGM to provide an unequivocal resolution of this issue.

In contrast to the observations for the {10.0} and {10.1} diffraction peaks, the {0002} *d*-spacing was generally found to have a strong dependence on substrate bias. This is thought to be because the {0002} *d*-spacing reflected effects that were specific to the <0001> fibre textured grains, and not the randomly oriented component of the coatings. The trends in *d*-spacing of the {0002} diffraction peak for the Al-Zn coatings are summarised in Fig.8.13b, with a comparison to the pure Zn coatings. For all Al-Zn coatings except those from the Al-73%Zn target, this dependence was almost identical to that observed for the pure Zn coatings. The large scatter in the data for Al-24%Zn and Al-50%Zn series was due to the low peak intensity. The *d*-spacings of both {0002} peaks for the Al-90%Zn series (Fig.8.11), are shown in Fig.8.13b, the lower values corresponding to the fibre textured grains. The *d*-spacings for the fibre textured component in these coatings were strongly dependent on bias, while those of the randomly oriented grains were identical to that of pure Zn powder (0.2473 nm [197]).

Considering the similarity in the {0002} *d*-spacing trends with bias (Fig.8.13b), it is reasonable to assume that the mechanisms responsible for the *d*-spacing modification in the Zn coatings also applied to the (Zn) phase of the Al-Zn coatings. Thus it is probable that most of the Al-Zn coatings were subject to increasingly large tensile residual macrostress in the <0001> fibre textured (Zn) phase, as bias voltage was increased. This interpretation does not account for the possible compounding effect of lattice parameter modification due to Al solid solubility. Indeed, diffraction peaks for the (Al) phase were generally absent for several of the Al-90%Zn series coatings, which suggests that much of the Al in these coatings may have been dissolved in (Zn) solid solution. However, it was decided that this issue would not be pursued by CGM, following the problems experienced with examination of the (Al) phase (refer Sect.8.2.6).

The coatings produced with the Al-73%Zn target were generally found to have a random orientation under most bias conditions. Hence the {0002} *d*-spacing trends for

these coatings (Fig.8.13b) did not show the strong dependence on bias that was observed for all other Al-Zn coatings. Instead the {0002} *d*-spacing was essentially constant for most bias voltages, in parallel with the observations of the {10.1} peaks. Increasing the bias to V_t or greater was noted to correspond to an increase in the <0001> fibre texture, and it is not surprising that this bias also signaled the onset of a reduction in {0002} *d*-spacing. This interpretation supports the argument that modification of *d*-spacing in (Zn) grains only occurred in grains with a <0001> fibre texture.

The broadening of the (Zn) diffraction peaks was generally minimal, with FWHM values typically less than 0.3° for all peaks. This can be seen from the sharp nature of most of the (Zn) diffraction peaks in Figs.8.8 to 8.11. An exception to this trend was noted for the {0002} peaks corresponding to the <0001> fibre textured grains in the Al-90%Zn series coatings. In these coatings, the {0002} peaks broadened considerably with increasing bias above -80V (Fig.8.13c). This effect correlated with the increase in the proportion of inert gas trapped in these coatings (Fig.8.4). A similar correlation was found for the Zn coatings and was explained in terms of microstrain and/or crystallite size effects due to the possible existence of Ar bubbles in the <0001> fibre textured grains. In direct contrast to this correlation, the Al-73%Zn series coatings were found to retain a much higher proportion of entrapped Ar, but this did not seem to affect the FWHM of {0002} peaks to any great extent. This is probably because the <0001> fibre textured grains were not present to any great extent in the Al-73%Zn series coatings, and therefore the abovementioned Ar bubble mechanism did not seem to apply. Hence it appears that the entrapment of Ar in the Al-73%Zn series coatings may have been due to an alternative mechanism.

8.2.6 Crystallite Group Method

The <111> fibre textured group of (Al) grains in the Al-24%Zn and Al-50%Zn series were targeted for the determination of residual macrostress and strain-free lattice parameters via CGM. This method was not pursued for the <0001> fibre textured group of (Zn) grains, primarily because the peak intensity was insufficient to permit the analysis, and secondly because of certain problems experienced with the (Al) phase examination.

It appears that the solid solubility of the (Al) phase in the coatings changed somewhat in the elapsed time between Bragg-Brentano and asymmetric CGM experiments. In Fig.8.14, a comparison is made between the {111} *d*-spacing measured by Bragg-Brentano XRD two months after coating preparation, and the {222} *d*-spacing

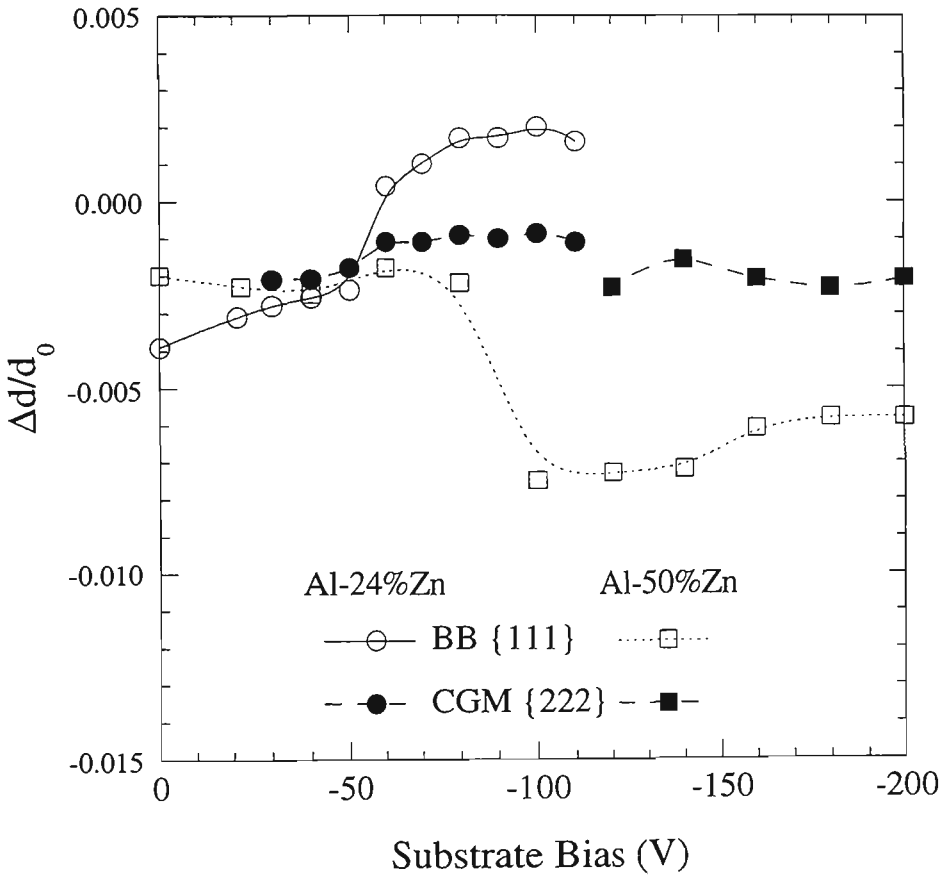

Fig.8.14 Comparison between the {111} d-spacing of (Al) phase measured by Bragg-Brentano XRD and the {222} d-spacing measured by CGM.

from the CGM scans performed two years later. A direct comparison is possible by plotting the d-spacing in terms of the strain parameter $\Delta d/d_o$. It would be expected that both sets of results should be identical since they represent diffraction from the same set of planes in the <111> crystallite family. Unfortunately, the d-spacing measurement for the CGM analysis was found to be markedly different from that conducted two years earlier by Bragg-Brentano scans. This effect is believed to be due to aging of the coating microstructure, with resultant changes in the proportion of Zn in (Al) solid solution, and possibly also the residual macrostress in the <111> fibre textured (Al) phase. It is also interesting to note that these effects seem to have only occurred in the coatings with the strongest <111> fibre textures (refer Fig.8.12a).

Regardless of the expected changes in the coatings due to aging, the CGM analysis was continued for the (Al) phase. It must be emphasised, however, that the following results do not necessarily reflect the state of solid solubility and residual macrostress that existed in the coatings at the time of Bragg-Brentano examination. Rather they are believed to indicate the state of the coating following a considerable aging period, and are therefore more "stable" than immediately after deposition. Aging effects are an important factor in the evaluation of metastable coatings, and are discussed further in Sect.8.3.2.

Data obtained from asymmetric diffraction scans are plotted in terms of the a lattice parameter of (Al) as a function of $\sin^2\psi$ in Fig.8.15. Linear regressions were fitted to the data, although the quality of fit was relatively poor. This was because of the relatively small changes in d-spacing that were experienced. The error bars shown for one set of data in Fig.8.15b indicate the expected range of error as determined from a standard quartz sample (±0.06%), and it is apparent that the linear regressions fall within the error range of each data point. The linear regression coefficients were used to calculate the strain free lattice parameter a_0 and the residual macrostress σ, using equations appropriate for the {111} texture observed in these coatings (Sect.4.4.4). The results of these calculations are graphed as a function of the bias voltage in Fig.8.16, along with the results for Al Series 2 coatings (Chap.6) for comparison.

The strain-free lattice parameter of the (Al) phase in the Al-Zn coatings was much lower than that of the Al Series 2 coatings. The a_o for Al coatings was virtually identical to that of pure Al powder indicated on Fig.8.16a by the dashed horizontal line at 0.40494 nm [197]. In comparison, the value of a_o for both sets of Al-Zn coatings was significantly less than that of the pure powder. A reduction in lattice parameter is expected with Zn in solid solution (Sect.3.4). Similarly, the lattice parameter for the Al-24%Zn series coatings was observed to increase sharply at a bias voltage

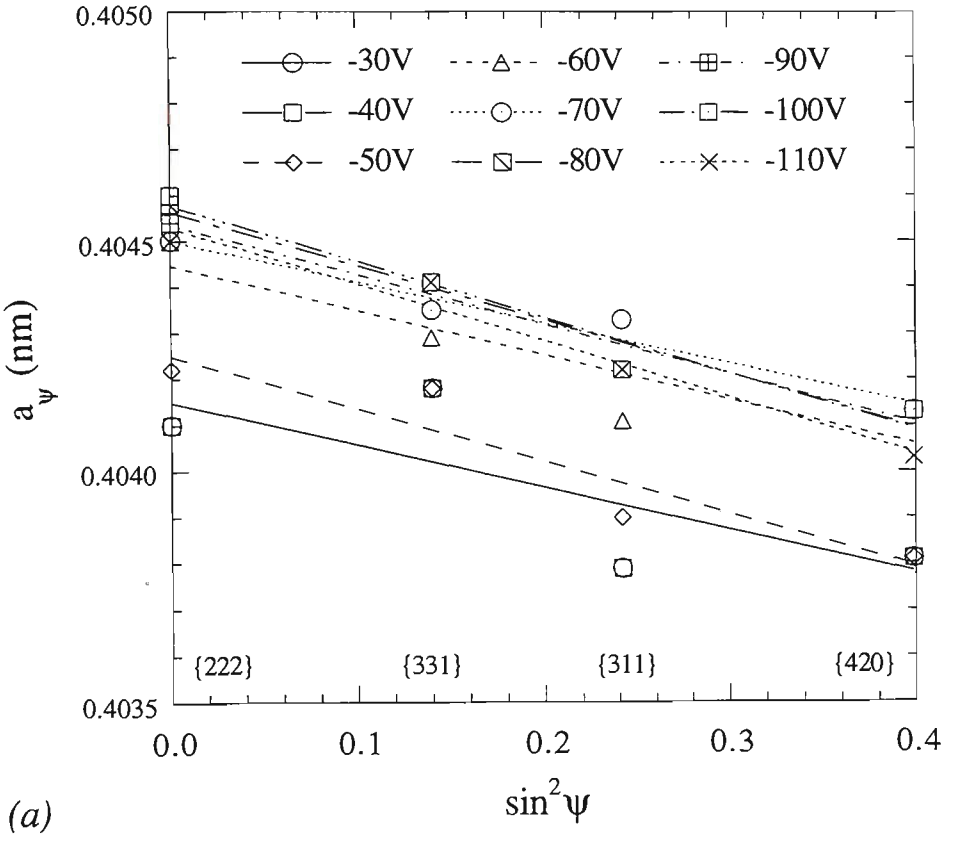

(a)

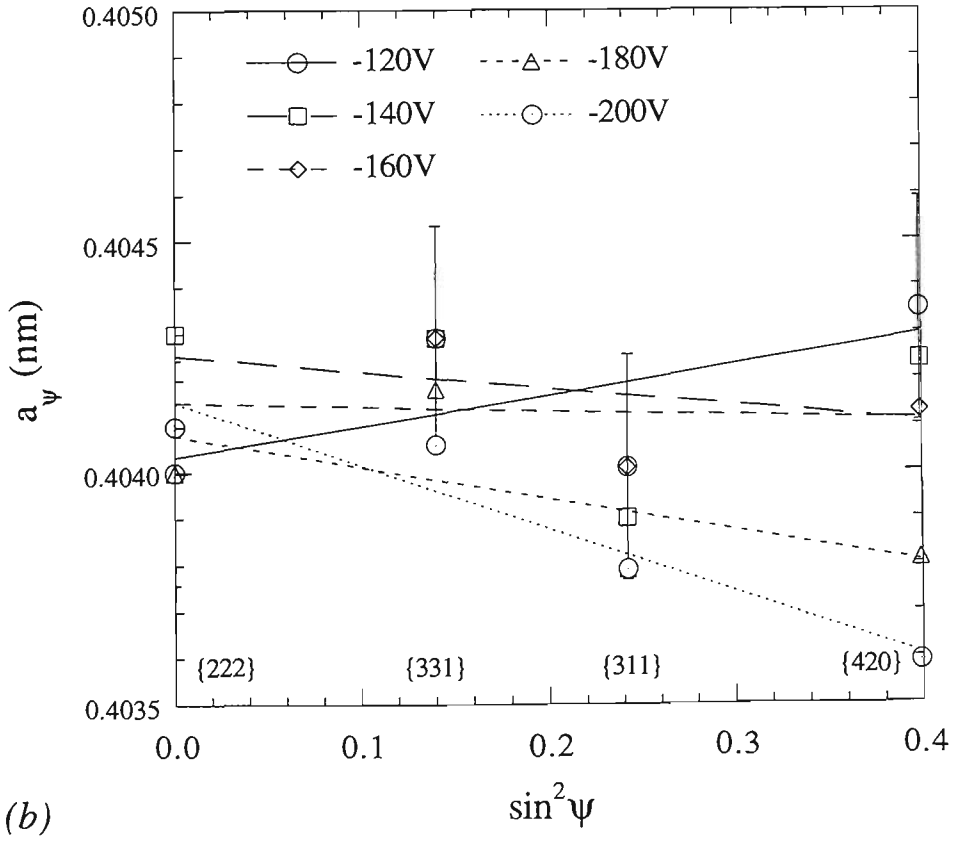

(b)

Fig.8.15 *$Sin^2\psi$ plots of CGM data for the <111> fibre textured (Al) grains in coatings from the Al-24%Zn (a) and Al-50%Zn (b) targets.*

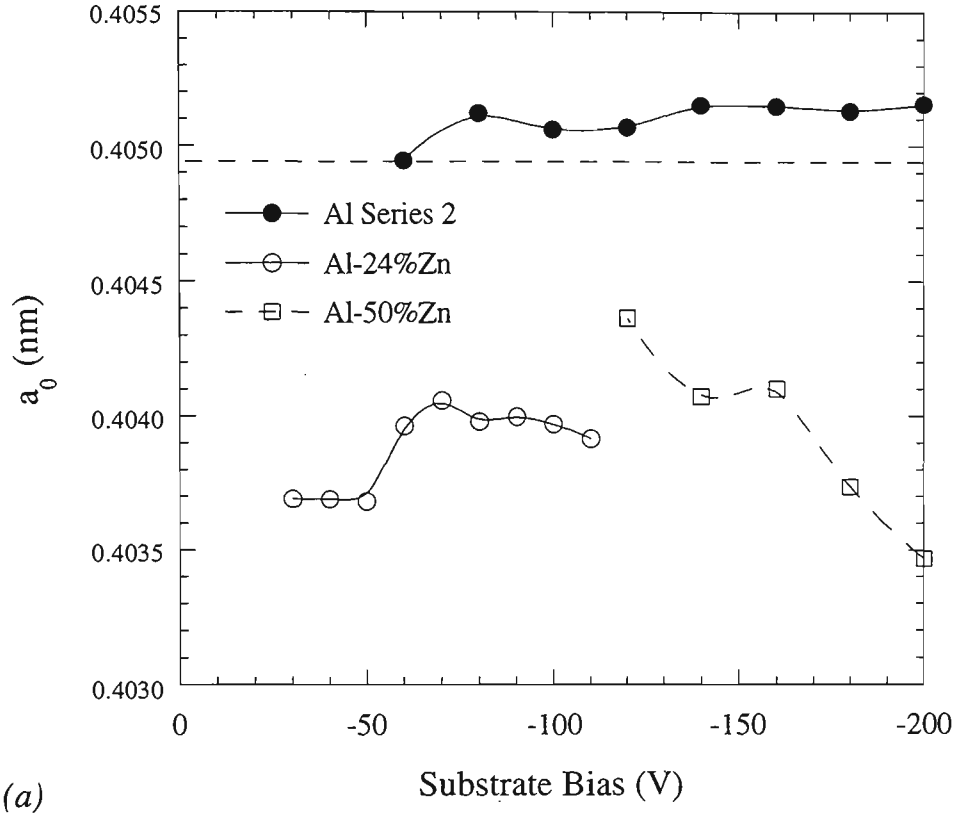

(a)

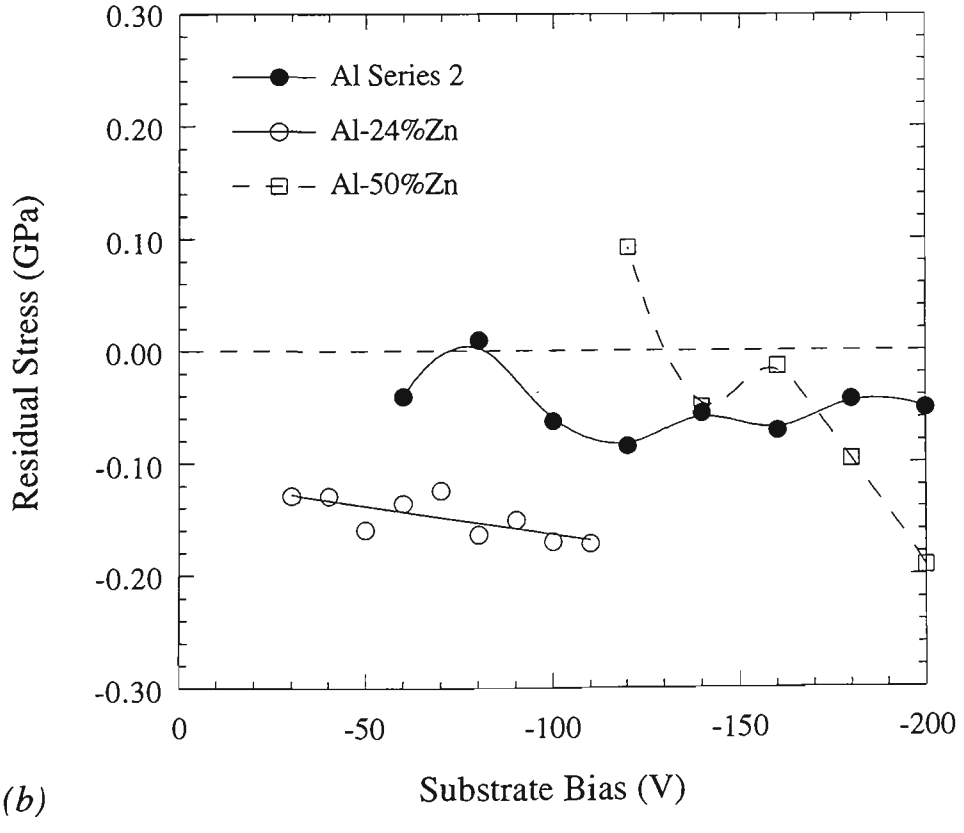

(b)

Fig.8.16 Strain-free lattice parameter (a) and residual macrostress (b) of the <111> fibre textured (Al) grains in coatings from the Al-24%Zn and Al-50%Zn targets. Results for the Al Series 2 coatings are shown for reference.

corresponding to V_t, in direct response to the sharp decrease in the Zn content of the coatings (Fig.8.12a). However, the coatings from the Al-50%Zn target were found to have a lattice parameter similar to that of the Al-24%Zn series coatings, in spite of their higher total Zn content. This suggests a limiting of the metastable solid solubility, and is discussed in greater detail in Sect.8.3.2.

The residual macrostress in the <111> fibre textured (Al) phase of the Al-Zn coatings was generally found to be compressive. For the Al-24%Zn series coatings, the compressive stress was about 150 MPa and tended to slightly increase with bias voltage, although this trend was within the expected range of error. The stress in the Al-50%Zn series coatings was slightly tensile at -120V bias, and decreased to a compressive stress of about 200 MPa at -200V bias. These stress levels are much greater than those of the Al Series 2 coatings, and possibly relate to the strengthening effect of Zn in (Al) solid solution. The accuracy of the stress measurements is questionable, however, in light of the range of error experienced in Fig.8.15b.

8.3 General Discussion

8.3.1 Comparison with Previous Work

There appear to have been only two previous studies of Al-Zn alloy PVD coatings that deliberately examined the influence of ion assistance on their composition and microstructure [143,160,212,214], and one of these studies was conducted by the present author [160,214]. Neither of the earlier investigations paid particular attention to ensuring accurate temperature control of the substrates. A comparison of these results with the present findings reveals that moderate increases in the substrate temperature play an important role in determining the coating microstructure, residual stress and surface appearance.

Li and Nowak [143,212] found that the substrate bias had a dramatic effect on the Zn content of coatings sputtered from an Al-25%Zn target. Coatings completely free of Zn could be deposited from this target by increasing the substrate bias to a sufficiently high level. However, it was also reported that the increased bias caused the substrate temperature to raise to at least 90°C, and hence reevaporation of Zn may have occurred. Shedden *et al* [160] reported similar effects for coatings deposited from an Al-20%Zn target by unbalanced magnetron sputtering. The high *i/a* ratio afforded by the unbalanced magnetron design resulted in the complete elimination of Zn from coatings deposited with a substrate bias of about -70V or greater. In this case, the high ion flux heated the substrates to a temperature of up to 130°C when negatively biased, or 180°C when earthed [214]. Overheating of the substrates was avoided in the present work, and the substrate temperature was about 50°C for all coatings. Preferential loss of Zn from the coatings was still encountered but nowhere near the extent experienced with the earlier studies [143,160,212,214]. Thus, it appears that substrate temperature plays a critical role in determining the composition of sputtered Al-Zn coatings, particularly in combination with elevated substrate bias.

The macroscopic appearance of the Al-Zn coatings seems to have been affected by both Zn content and the substrate temperature. Li and Nowak [143,212] reported that coatings with more than 30%Zn had a non-reflective surface appearance, while those with less than 12%Zn were smooth and lustrous. The Al-20%Zn coatings examined by Shedden *et al* [160] were found to have a matt appearance, and this was associated with a loosely packed porous structure. The transition from lustrous to matt coatings was somewhere between 12 and 20%Zn, for conditions where the substrates were permitted to heat to elevated temperatures. The much lower substrate temperature experienced in the present study caused the transition in surface appearance to shift to about 56±4%Zn.

Hence a greater proportion of Zn could be retained in the coating without disrupting the smooth surface appearance. The comparison of coating mass and cross-sectional thickness suggested that the lustrous coatings were also fully dense. Therefore, it appears advisable that the substrate temperature should be minimised for Al-Zn coatings if fully dense, smooth coatings are desired. This advice is opposite to conventional wisdom for elemental coatings, and probably relates to the dual phase nature of the Al-Zn coatings.

It is often assumed that ion assistance is a desirable variable for alloy coatings. This is reasonable on the basis of established knowledge for elemental coatings (Chap.2.4). However, it appears that the effects of ion assistance for alloy coatings have rarely been examined independent of the influence on composition. A valuable lesson can therefore be gained from comparison of coatings with a similar coating composition, but deposited with different ion assistance conditions. This is possible for the present study by comparing the low bias coatings from the Al-50%Zn series with those produced at -160V bias or higher from the Al-73%Zn target. In both cases, the coatings were found to contain about 50%Zn. The coatings deposited from the Al-50%Zn target with low bias voltages consisted of randomly oriented (Al) and (Zn) grains. There was perhaps a slight tendency towards <111> fibre texture in the (Al) phase. In contrast, the <111> fibre texture for the (Al) phase was highly developed in the Al-73%Zn series coatings at a bias of -160V or higher. The (Zn) phase had a tendency towards <0001> fibre texture. It can therefore be concluded that ion assistance modifies the microstructure of Al-Zn coatings by favouring the development of textured growth in both (Al) and (Zn) phases.

The microstructural modification afforded by ion assistance appears to be countered by a rise in residual tensile macrostress in the textured grains of the (Zn) phase, and perhaps some compressive macrostress in the (Al) grains. The burial of inert gas in the coatings was also observed to become prominent with energetic bombardment, and this is viewed as a deleterious effect. Consequently, it is considered that the automatic application of substrate bias for deposition of Al-Zn coatings is a practice that requires some caution. It is anticipated that thermal and ion flux gradients on substrates, would result in non-uniform distributions of both coating composition and residual stress. Variation in coating composition is particularly undesirable for corrosion protective coatings since it would provide a ready supply of anodic and cathodic areas on the coatings surface, leading to accelerated degradation. Thus, it appears that the perceived advantages of ion assisted deposition do not necessarily apply to alloy Al-Zn coatings. The use of bias voltages less than V_t is acceptable from the standpoint of preferential resputtering, but has only a minor affect on the coating microstructure.

8.3.2 Solid Solubility and Aging Effects

It is reasonable to assume that the lattice parameters measured by CGM for the Al-24%Zn and Al-50%Zn series coatings represent those of metastable (Al) solid solutions. They were determined after room temperature aging for approximately two years, and further changes are unlikely considering the kinetics involved. It would therefore be of interest to quantify the actual Zn content of these (Al) solid solutions. This is possible by applying equation 3.1 which was derived from published data for Al-Zn alloys (Sect.3.4.1). It is assumed that any buried Ar present in the coatings was not located in solid solution and therefore had no affect on the strain free lattice parameter. The results for Zn and Al coatings (Chaps.5 and 6) indicated that this was true for the elemental coatings, and it seems justified to extend this to the Al-Zn coatings.

The Zn content of the bulk coatings and the (Al) phase for the Al-24%Zn and Al-50%Zn series are shown in Fig.8.17 as a function of the substrate bias voltage. The error bars for the (Al) phase data points denote ±3%Zn, which is equivalent to the expected error in lattice parameter of ±0.06%. This large error marks the inherent problem with this form of analysis, since large changes in Zn content of the (Al) phase result in only small changes in lattice parameter (Sect.3.4.1). Regardless, some general trends can be noted. For the Al-24%Zn series, the (Al) phase contained about 15%Zn at low bias and about 11%Zn at high bias. In comparison, the (Al) phase in the Al-50%Zn series had a range of Zn content from about 7% at -120V up to 18% at -200V bias. In all cases the proportion of Zn in (Al) solid solution was notably less than the total Zn content of the coatings. This result is consistent with the observation of (Zn) phase in addition to the (Al) solid solution.

The proportion of Zn dissolved in (Al) solid solution immediately after deposition was potentially quite different to that reported in Fig.8.17. This was demonstrated in Fig.8.14, indicating that large changes in *d*-spacing were found to have occurred for the <111> fibre textured (Al) phase subsequent to a long aging period. A reasonable approximation of the initial solute content can be made in some cases. Considering the results for the Al-50%Zn series, the {111} *d*-spacing at bias greater than -80V soon after deposition was much lower than after a two year aging period (Fig.8.14). The initial *d*-spacing could possibly be accounted for by the presence of a very large tensile macrostress of about 800 MPa. However, this is considered highly unlikely due to the relatively low yield strength of Al-alloys. Alternatively, the initial *d*-spacing can be explained by the presence of about 35%Zn in (Al) solid solution. This seems to be the most likely explanation judging by the total Zn content in these coatings of about 38 to 42%. The remainder of the Zn content would be expected to form (Zn) phase. The

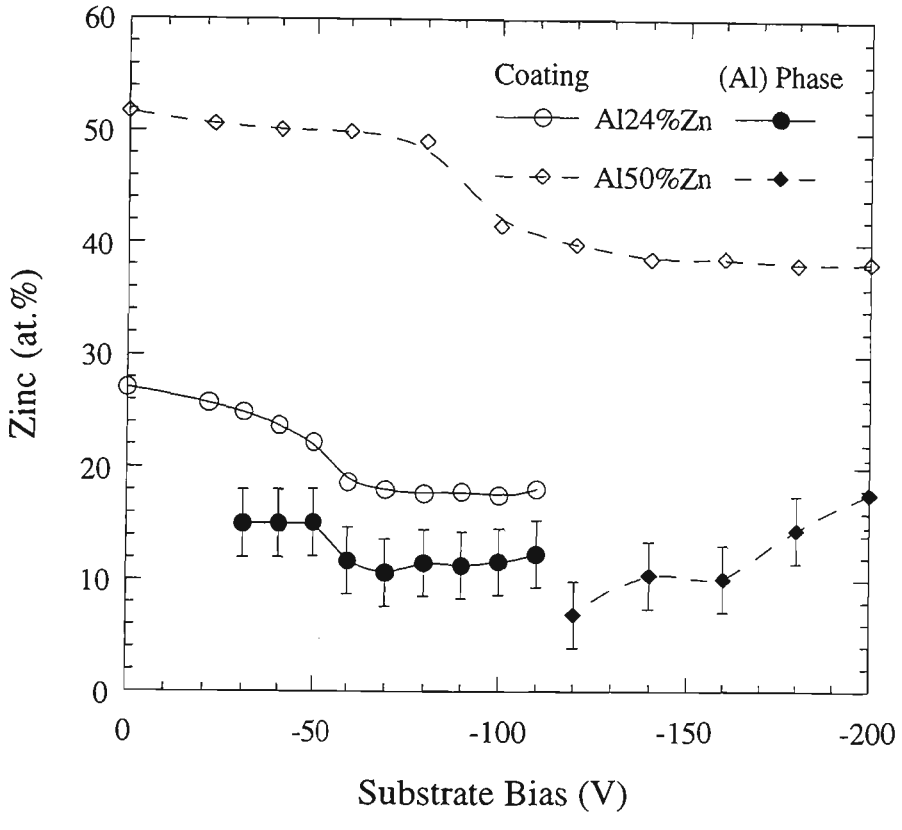

Fig.8.17 *Comparison between the bulk chemical composition and the Zn solute content of <111> fibre textured (Al) grains in coatings from the Al-24%Zn and Al-50%Zn targets.*

presence of a small residual macrostress is considered likely, but it appears that these coatings were primarily influenced by Zn solid solubility in (Al) phase. Spinodal decomposition of the supersaturated (Al) phase is believed to have eventually led to a reduction in the Zn solubility, and the growth of (Zn) phase. The CGM results corresponded to this late stage of the coating life, and consequently gave a different picture of solid solubility than was expected from the Bragg-Brentano examination.

The *d*-spacing results for the Al-24%Zn series coatings at bias voltages of -60V or greater were quite peculiar (Fig.8.14). The *d*-spacing soon after deposition was greater than that of a pure Al coating, which suggests that little or no Zn was present in solid solution. However, after two years aging the CGM analysis revealed that these coatings contained about 11%Zn in (Al) solid solution. This would seem to indicate that the (Al) phase absorbed Zn into solid solution during the aging period, which is thermodynamically impossible at room temperature. A similar effect occurred for the Al-73%Zn series coatings at substrate bias in excess of -160V. A possible explanation is that the *d*-spacing for the (Al) phase soon after deposition was influenced by a relatively large compressive macrostress, and that this stress relaxed with aging. Hence the proportion of Zn in (Al) solid solution for these coatings is not expected to have changed considerably over time, and the measured value of 11%Zn may have applied immediately after deposition. A rough estimation of the biaxial compressive macrostress required to explain the initial *d*-spacing suggested a value of about 300 MPa. Such compressive stresses would certainly appear possible in an (Al) phase subject to the strengthening effect of Zn in solid solution.

The above interpretation of the XRD results leads to a strange situation where the Al-24%Zn series coatings seem to have been more susceptible to decomposition of (Al) solid solution *during* deposition, than was suggested for the Al-50%Zn series. This is inconsistent with published work on the decomposition of bulk Al-Zn alloys which indicates that precipitation of (Zn) from the solid solution occurs much more rapidly with increasing Zn solubility (Sect.3.4). It can only be concluded that the kinetic development of Al-Zn coating microstructure needs further work.

The majority of the coatings examined in this study possessed a Zn content less than the eutectic composition (refer Sect.3.4.1). It is therefore not surprising that the coating microstructure was largely influenced by the formation of (Al) solid solution and subsequent decomposition. However, the coatings deposited from the Al-90%Zn target possessed a Zn content greater than the eutectic composition. Solidification from liquids of such compositions proceeds via the initial formation of proeutectic (Zn) phase followed by the eutectic. The Al-90%Zn series sputtered coatings might therefore have been

anticipated to be dominated by the growth of (Zn) phase. This was confirmed by the microstructural characterization. Indeed, it is suspected that extended solid solubility of Al in (Zn) phase may have been obtained. However, this issue was not pursued due to the abovementioned experiences with aging effects.

In summary, it is likely that the coatings sputtered from Al-Zn targets were probably influenced to varying degrees by both solid solubility and residual macrostress effects. However, changes that occurred with age appear to have influenced the coating microstructure and this complicated the interpretation of results. It is considered that a more complete understanding of sputtered Al-Zn coatings would be provided by a more thorough evaluation of solid solubility and residual stress as a function of time after deposition.

8.3.3 Preferential Resputtering

Preferential resputtering of Zn from the Al-Zn alloy coatings appears to have had a significant influence on their microstructural development. This is demonstrated by the trends in preferred orientation of the (Al) phase with respect to substrate bias (Fig.8.12a). It was noted that the onset of a very strong <111> fibre texture in the (Al) phase occurred at a sharply defined substrate bias, denoted V_t. Coincident with the development of this strong fibre texture, was a dramatic decrease in the Zn content of the coatings (Fig.8.3), due to preferential resputtering of Zn. When the value V_t was normalised by the *i/a* ratio in each case, it appeared that the transition was relatively independent of the Zn content, but it was generally much lower than for the Al coatings. Consequently, the <111> fibre texture seems to have developed in the alloy coatings with much less ion assistance than was required for the elemental Al coatings.

The development of the fibre texture in the alloy coatings can be understood from the effect of Zn in (Al) solid solution. In Chap.6, the <111> fibre texture in Al coatings was explained by the enhancement of surface mobility that occurs with ion assistance. A threshold ion energy was required before the Al atoms could relocate to their lowest surface energy condition which corresponded to the <111> orientation. It is expected that the same mechanism for fibre texture also occurred in the (Al) phase of the Al-Zn alloy coatings. However, in this case there was probably a large proportion of Zn dissolved in (Al) solid solution, and this would have an impact on the resputtering mechanism. Zn is a much heavier atom than Al, and would lead to a sputter yield amplification effect [145]. The partial resputter yield for Al would have increased with respect to the bulk Al yield, due to the concentration of collision cascades near the surface. Consequently, the surface mobility of Al atoms would be much greater on the Al-Zn alloy coatings than for

elemental Al coatings with the same ion assisted conditions. It follows that the growth of the strong <111> fibre texture in the alloy coatings should require significantly less ion assistance than is the case of elemental Al coatings.

The effect of the inherent energy of the sputtered atoms and back-reflected neutralised ions should also be considered. A quick simulation of the sputtering of pure bulk targets with 500 eV Ar^+ ions using TRIM [56], indicated that the average energy of sputtered Zn atoms is about 50 eV, in comparison with about 3 eV for Al atoms. Furthermore, owing to the low atomic mass of Ar in comparison with Zn, about 10% of the ions that bombard a pure Zn target are reflected and can bombard the coatings during growth. Each of these effects indicate that sputter deposition of Zn is a much more energetic process than that of Al, even without the presence of ion assistance. Therefore, it is anticipated that the energy delivered to the coating surface by sputtered and reflected species would increase in proportion with the Zn content of an alloy target. Such effects may also have contributed to the development of strong <111> fibre texture in the (Al) phase of the coatings at lower bias voltages, since less ion energy would be required.

It was also found that the development of a strong <111> fibre texture in the (Al) phase supported the growth of a <0001> fibre texture in the (Zn) phase. The sputter yield amplification effect may also have been the key to this phenomena. Although the presence of Zn in (Al) phase would have increased the partial yield of Al, it is expected to have had the opposite effect on the partial yield of Zn. Consequently, the partial yield of Zn from the (Al) solid solution may have been noticeably less than from the (Zn) phase. Thus, as the substrate bias was increased, it is anticipated that a condition was reached whereby much of the loosely bound Zn on the coating surface was resputtered, leaving an essentially monophase (Al) solid solution with a strong <111> fibre texture. This explains the sharp decrease in the Zn content at a specific substrate bias. The (Zn) phase subsequently detected in these coatings may have been produced by precipitation or spinodal decomposition from the supersaturated (Al) phase. This must have occurred very soon after initial deposition in order for ion bombardment to have caused sufficient damage to induce the tensile stresses thought to exist in the (Zn) phase (Fig.8.13b).

The above arguments are considered to apply to all of the coatings examined except the Al-90%Zn series. As already mentioned, these coatings are thought to have formed a (Zn) solid solution first, which possibly decomposed soon after deposition to form a small fraction of (Al) phase. A tensile stress was believed to have developed in the <0001> fibre textured (Zn) grains which increased with substrate bias in a fashion similar to that observed for the elemental Zn coatings. Consequently, it appears reasonable to assume that the same constrained shrinkage mechanism was responsible for this coating

stress (Sect.5.3.4). However, it was also noted that the <0001> fibre texture in the (Zn) phase of the alloy coatings tended to degrade at a much lower substrate bias than was the case for the Zn coatings. A similar effect was noted for the microstrain and/or crystallite size for the <0001> textured grains (Fig.8.13c). The cause of these effects could not be determined, although it is suspected to be related to the presence of Al in (Zn) solid solution.

8.4 Summary

All Al-Zn alloy coatings contained both (Al) and (Zn) solid solutions, without any intermetallic or amorphous phases. Most coatings were dominated by the formation of (Al) phase, which is consistent with the equilibrium phase diagram. A modest degree of supersaturation was found for (Al), with a maximum measured solute content of 18%Zn. In all cases the proportion of Zn in (Al) solid solution was notably less than the total Zn content of the coatings, which accounts for the detection of the (Zn) phase. It was argued that the Zn solute content was possibly as high as 35% immediately following coating deposition, but after ambient ageing the solute was rejected by spinodal decomposition. Coatings that possessed a Zn content in excess of the eutectic composition (89%Zn), tended to be dominated by the (Zn) solid solution. It is suspected that supersaturation of Al in (Zn) phase may have been obtained, although the (Al) phase was also present. The (Zn) phase behaved in a similar fashion to that described for pure Zn coatings.

Ion assisted deposition of Al-Zn coatings led to the preferential resputtering of Zn from the coatings. Generally, the substrate bias (ion energy) could be increased slightly without overly influencing the coating composition. However, at a critical value, defined as V_t, the Zn content abruptly decreased, and continued to reduce at higher bias. This compositional change was marked by the development of a strong <111> fibre texture in the (Al) phase. The fibre texture developed in the alloy coatings with much less ion assistance than was required for the elemental Al coatings. This was thought to be due to sputter yield amplification that followed from the presence of Zn atoms in (Al) solid solution. It was also recognised that the increased energetic neutral bombardment expected for Al-Zn alloy targets may have played a role.

A direct comparison was made of Al-Zn coatings having identical composition but produced with different ion bombardment conditions. From this it was determined that ion assistance modified the microstructure of Al-Zn coatings by favouring the development of textured growth in both (Al) and (Zn) phases. These effects were countered by a deleterious rise in residual tensile macrostress in the textured grains of the

(Zn) phase, and a moderate degree of compressive macrostress in the (Al) grains. The burial of inert gas in the coatings was also observed to become prominent with energetic bombardment, and this is viewed as a deleterious effect. Burial of inert gas was considered to be associated with the (Zn) phase.

The visual appearance of Al-Zn coatings was very much dependent on composition, substrate temperature and ion bombardment. Coatings deposited at a substrate temperature of 50°C retained a highly specular surface finish provided the Zn content was less than about 56%Zn. Coatings with higher Zn content had a non-reflective blue-grey appearance typical of pure Zn coatings prepared with minimal bombardment. Increasing the energy of ion bombardment led to preferential resputtering of Zn from the coatings such that the surface appearance could be altered from matt to specular according to the compositional changes. Combination of this work with previous studies [143,160,212] suggested that the transition from matt to specular coatings occurs at lower Zn contents if the substrate temperature is raised. Coatings deposited at elevated temperatures were also much more susceptible to preferential resputtering of Zn.

Chapter 9

Aluminium-Magnesium Alloy Coatings

9.1 Deposition Parameters

The five Al/Mg composite targets described in Sect.4.2 were used to prepare a range of Al-Mg alloy coatings on Si wafers, with substrate bias voltages from earth to -200V. The important parameters for each series are listed in Tables 9.1 to 9.5. The same M3 magnet was used for each series and was fully magnetised. The high voltage power supply was also used for all coatings and was operated at a nominal level of 100 W. It should be noted that the actual magnetron power for the Al90/Mg30 series of coatings was 105 W rather than 100 W.

The magnetron conditions were generally stable throughout each coating run, such that the magnetron voltage remained constant within ±6V, with only one exception. The discharge for the Al60/Mg60 target was highly unstable during the first hour of operation (Table 9.4), with some sudden large jumps in magnetron voltage (~15 V) followed by gradual drift. Very careful ramping of the magnetron power during the running-in period prior to coating was found necessary for this target. The discharge also briefly failed due to arcing for two of the samples from the Al60/Mg60 target. However, it is felt that the difficulties experienced in the operation of this target did not significantly influence the coatings produced (Sect.4.2.4). As a result of the development of a stepped erosion profile on the composite targets, it was anticipated that there may have been a slight change in the composition of the sputtered flux throughout the coating run. Self biased coatings were prepared at the beginning and end of each coating run in order to evaluate this effect.

Table 9.1 Deposition parameters for coatings prepared from Al115/Mg5 target. Other process variables: base pressure 54 μPa; magnetron power 100 W (high voltage supply); probe current 0.507 mA at start, 0.524 mA at end; deposition time 15 minutes per sample.

Magnetron Conditions		Substrate	Coating Mass
Voltage (V)	Current (A)	Bias (V)	(μg)
394	0.25	self (-25)	213
391	0.25	-40	202
389	0.25	-60	197
388	0.25	-80	192
387	0.25	-100	188
387	0.25	-120	183
388	0.25	-140	179
388	0.25	-160	161
389	0.25	-180	165
391	0.25	self (-26)	221
387	0.25	earth	230

Table 9.2 Deposition parameters for coatings prepared from Al105/Mg15 target. Other process variables: base pressure 82 μPa; magnetron power 100 W (high voltage supply); probe current 0.522 mA at start, 0.533 mA at end; deposition time 15 minutes per sample.

Magnetron Conditions		Substrate	Coating Mass
Voltage (V)	Current (A)	Bias (V)	(μg)
398	0.24	self (-25)	244
395	0.25	-40	232
393	0.25	-60	204
392	0.25	-80	196
391	0.25	-100	189
392	0.25	-120	183
392	0.25	-140	84 *
393	0.25	-160	165
395	0.24	-180	156
396	0.24	-200	151
394	0.25	earth	252

* coating mass in error due to substrate breakage

Table 9.3 Deposition parameters for coatings prepared from Al90/Mg30 target. Other process variables: base pressure 94 μPa; magnetron power 100 W (high voltage supply); probe current 0.645 mA at start, 0.675 mA at end; deposition time 15 minutes per sample.

Magnetron Conditions		Substrate	Coating Mass
Voltage (V)	Current (A)	Bias (V)	(μg)
383	0.27	self (-25)	300
378	0.28	-40	90 *
375	0.28	-60	322
373	0.28	-80	326
372	0.28	-100	280
371	0.28	-120	243
371	0.28	-140	221
371	0.28	-160	200
371	0.28	-180	193
371	0.28	-200	178
371	0.28	earth	338

* coating mass in error due to substrate breakage

Table 9.4 Deposition parameters for coatings prepared from Al60/Mg60 target. Other process variables: base pressure 96 μPa; magnetron power 100 W (high voltage supply); probe current 0.602 mA at start, 0.632 mA at end; deposition time 10 minutes per sample.

Magnetron Conditions		Substrate	Coating Mass
Voltage (V)	Current (A)	Bias (V)	(μg)
366	0.26	self (-26)	247
364-367	0.27	-40	240
361-375	0.27-0.26	-60	235 *
362-370	0.27-0.26	-80	233 *
359-364	0.27	-100	236
361-364	0.27	-120	242
358-361	0.27	-140	248
357	0.27	-160	226
357	0.27	-180	195
359	0.27	self (-26)	239
355	0.27	earth	250

* discharge failed during coating run and re-established after a few seconds

Table 9.5 Deposition parameters for coatings prepared from Al30/Mg90 target. Other process variables: base pressure 79 μPa; magnetron power 100 W (high voltage supply); probe current 0.647 mA at start, 0.664 mA at end; deposition time 10 minutes per sample.

Magnetron Conditions		Substrate	Coating Mass
Voltage (V)	Current (A)	Bias (V)	(μg)
353	0.28	self (-25)	334
350	0.28	-40	324
349	0.28	-60	313
347	0.28	-80	313
347	0.28	-100	303
347	0.28	-120	299
346	0.28	-140	292
346	0.28	-160	279
347	0.28	-180	262
350	0.28	self (-25)	324
345	0.28	earth	338

9.2 Results and Discussion

9.2.1 Ion/Atom Flux Ratio

The *i/a* ratios for the five Al/Mg targets are shown in Fig.9.1 as a function of the radial fraction of Mg on the target surface, f_{Mg}. The results for monolithic Al and Mg targets are also shown for comparison. Error bars of ±15% are indicated, and represent a conservative estimate of the expected error in the measurement. The *i/a* ratio tended to decrease with increasing f_{Mg}. This is due to the concurrent increase in net sputtering rate of the target. The ion current when normalized by the magnetron current was constant (within an error of ±6%) for all coatings. This is to be expected since all of these coatings were produced using the same M3 magnet assembly. It should also be noted that only the Al105/Mg15 and Al90/Mg30 series can be directly compared on the basis of equal *i/a* ratio (both ~0.75).

9.2.2 Mass Deposition Rate

The mass deposition rate for each of the Al-Mg coating series is shown as a function of the substrate bias voltage in Fig.9.2. The results for Al and Mg coatings are also included for comparison. The deposition rates for almost all of the composite targets were intermediate between those of Al and Mg. The only exception was for the coatings from the Al30/Mg90 target, for which the deposition rate increased above that of pure Mg as the bias voltage was increased. Judging by the higher *i/a* ratio of this composite target, it might be expected that the opposite result should have been observed. Furthermore, increasing the Mg radial fraction of the composite targets resulted in an increase in the deposition rate, consistent with the higher sputtering rate of Mg compared with Al.

The substrate bias had a significant effect on the coating mass, resulting in an exponential decrease in deposition rate for the Al115/Mg5, Al105/Mg15 and Al30/Mg90 series, similar to that of the Al and Mg series. This trend is due to resputtering induced by ion bombardment during deposition. The deposition rate trends for the Al90/Mg30 and Al60/Mg60 series were unusual in that they actually increased slightly, before showing a sharp decrease at higher bias voltages. The reason for this effect is discussed in Sect.9.2.4.

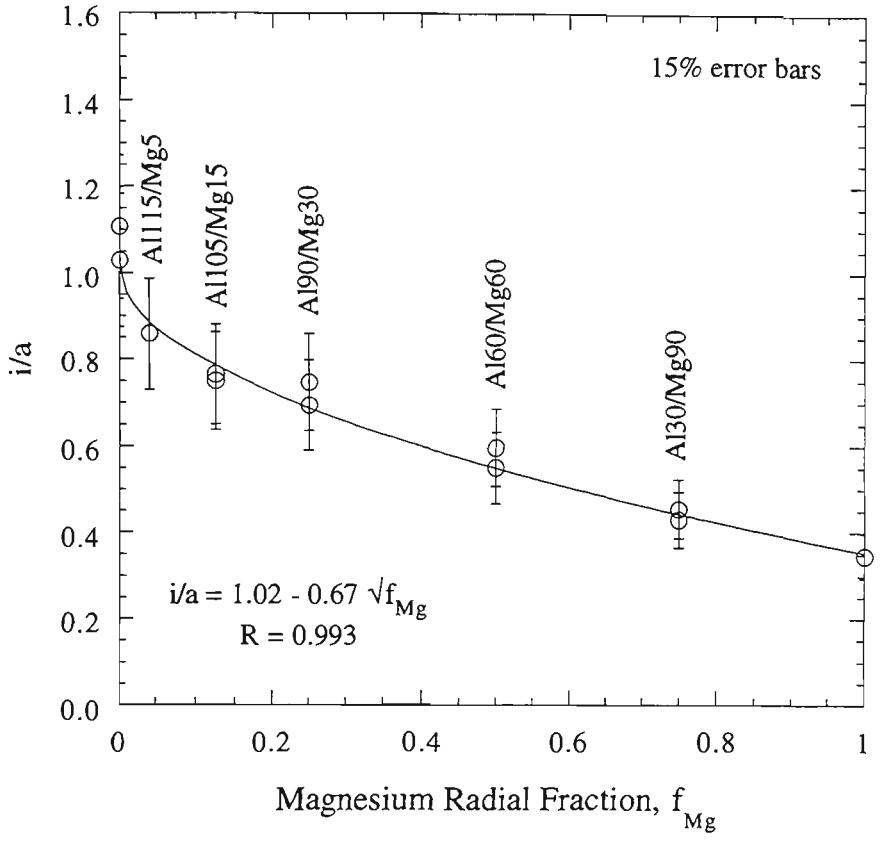

Fig.9.1 *Ion/atom arrival rate ratio as a function of the Mg radial fraction in Al/Mg composite targets.*

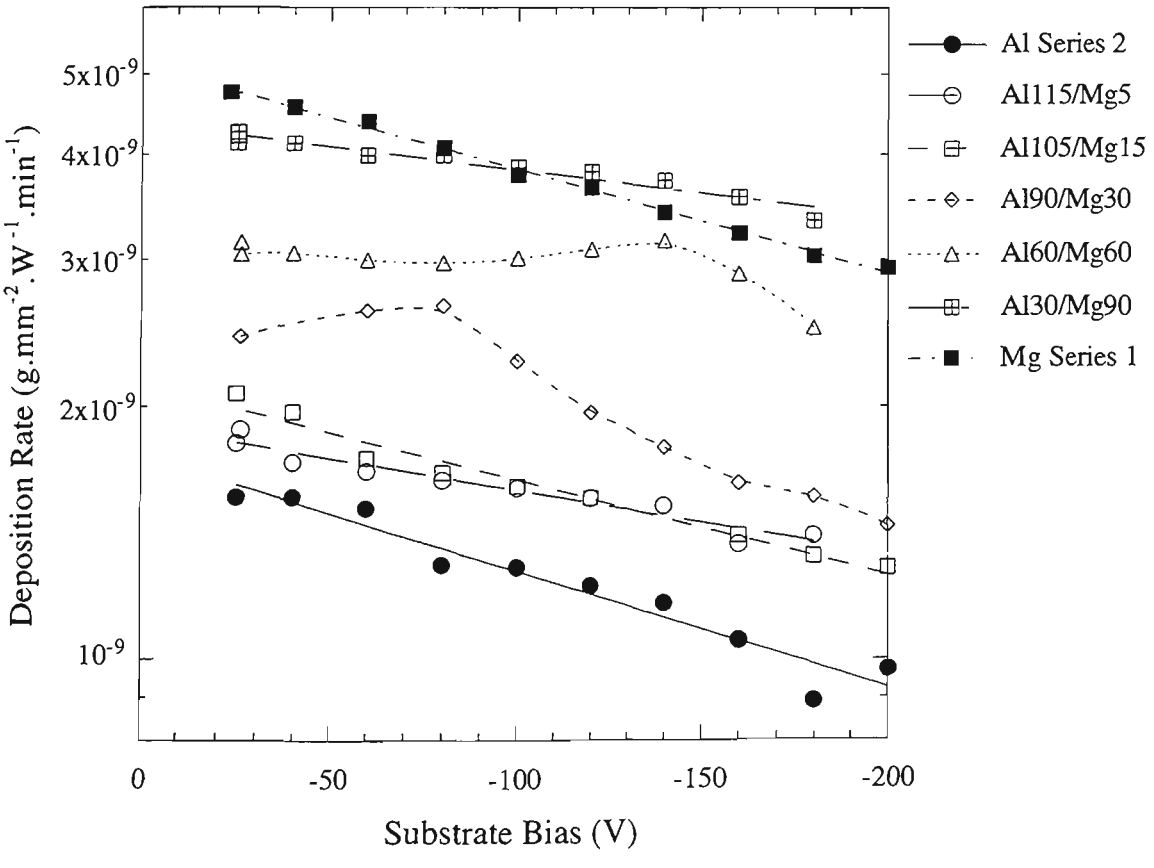

Fig.9.2 *Mass deposition rate for sputtered Al-Mg coatings. Note the ordinate axis is semi-logarithmic.*

9.2.3 Visual Examination

All of the Al-Mg alloy coatings prepared with the composite targets are shown in Fig.9.3a. This photograph was taken approximately two years after deposition. Throughout this period, each sample was stored individually in a sealed polyethylene bag and only removed for SEM, EDS, and XRD analysis. Despite the careful treatment given the samples, some showed signs of surface oxidation and staining as described below. It should be noted that immediately after deposition, all coatings had a highly lustrous appearance.

Both the Al115/Mg5 and Al105/Mg15 series of coatings retained their as-deposited surface appearance after two years of sample ageing. There were no observable differences in the appearance of coatings for all bias conditions. They all possessed the same highly lustrous appearance which replicated the surface finish of the silicon wafer substrate, but was distinguished from it by a metallic white colour (Fig.9.3a). In contrast, the appearance of the Al60/Mg60 and Al30/Mg90 series coatings were markedly influenced by the substrate bias voltage. Generally, coatings from these targets deposited with low bias voltages (earth to about -80V) were highly lustrous but developed some matt-white surface staining after several months ageing. At high bias voltages (above about -80V), the coatings were similarly lustrous immediately after their removal from the sputtering chamber. Subject to only a short period of exposure to atmospheric conditions, they developed blackened regions typically in the shape of a central spot or ring. Unfortunately, the kinetics of the surface blackening was not studied closely as it was unexpected phenomena. The blackened regions on these coatings are apparent in Fig.9.3a. This blackened material was friable and tended to flake away leaving the substrate exposed. Chemical analysis by EDS (Sect.9.2.4) indicated that the blackened region was heavily oxidized.

The coatings deposited from the Al90/Mg30 target at low bias voltages were similar to those from the Al60/Mg60 target. However, at bias voltages of -100V and greater, the coatings were quite different to all others. Immediately after deposition, they were highly lustrous like the Al105/Mg15 series coatings. After a few weeks of ageing, regions of delaminated blisters developed in the coatings. The blistered regions tended to originate in rings located at the outer portion of the coated area, and then radiated across the surface. A micrograph of the blisters on the sample deposited with -200V bias using the Al90/Mg30 target is shown in Fig.9.3b (p.3-029). This type of blister formation is widely recognized to be caused by residual biaxial compressive stress in the coatings.

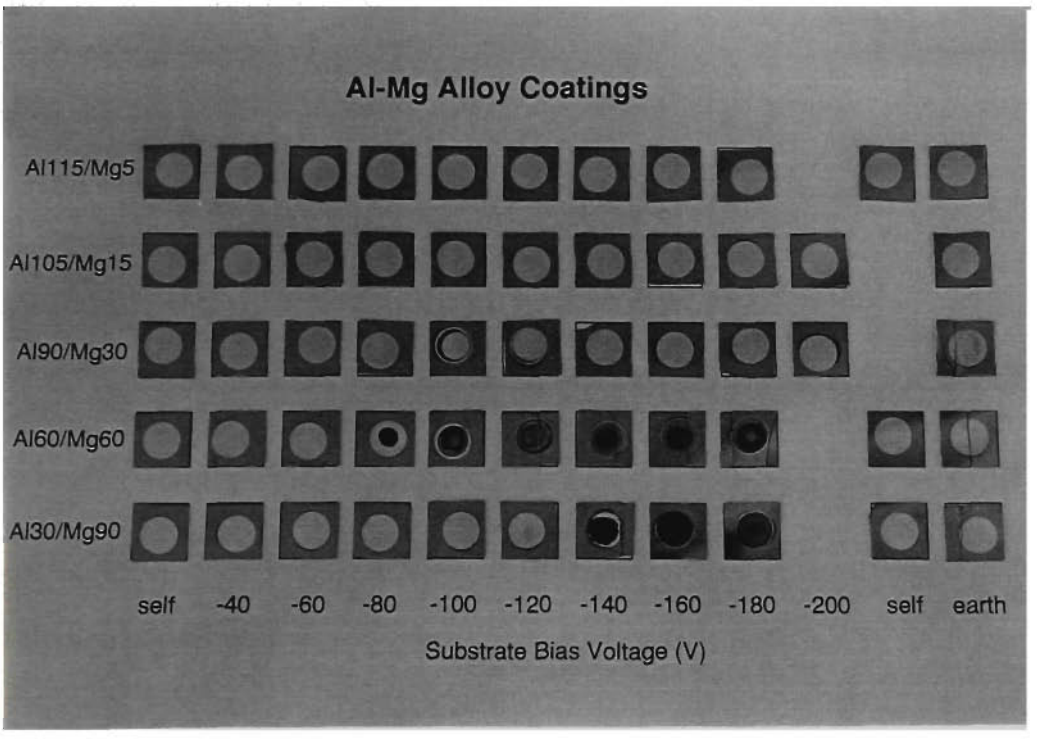

(a)

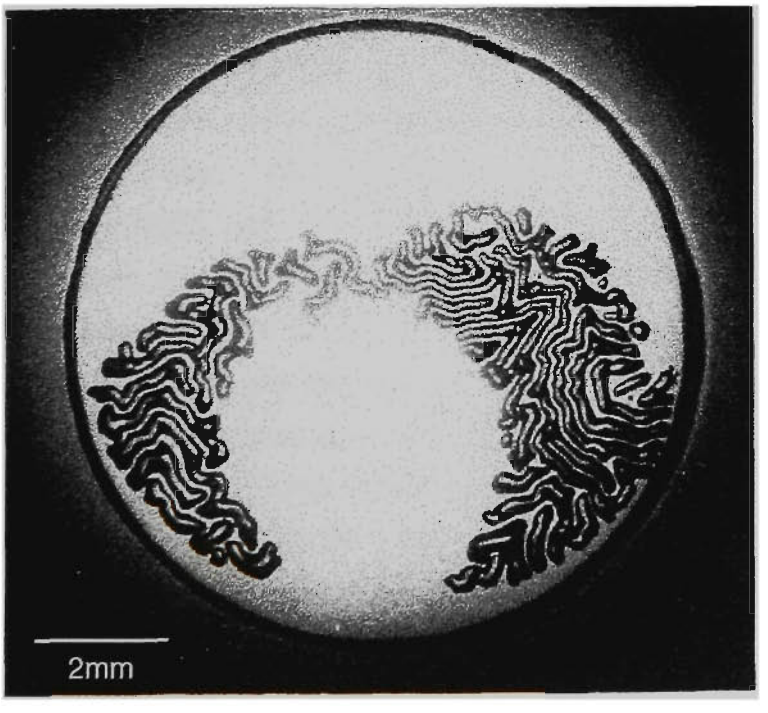

(b)

Fig.9.3 Photographs of Al-Mg coatings: (a) overview of all samples, taken about two years after deposition, (b) macro-scale view of the -200V bias sample from the Al90/Mg30 series showing rippled blisters, taken about two weeks after deposition.

9.2.4 Chemical Composition

The chemical compositions of the various coatings are presented in Figs.9.4 and 9.5. The Mg content of the deposited coatings are shown in Fig.9.4, relative only to the total amount of Al and Mg. Figure 9.5 indicates the measured Ar content of the sputtered coatings, relative to Al, Mg and Ar (ie. ignoring oxygen). These Ar values are extremely high especially for the coatings with 40-90% Mg (Al60/Mg60, Al30/Mg90 and some Al90/Mg30 coatings). The level of variability in the Mg content of the sputtered flux throughout each coating run is indicated by the duplicate results for some of the self bias (-25V) coatings in Fig.9.4. Generally, only the Al115/Mg5 and Al105/Mg15 targets were significantly affected by changes in the composition of the sputtered flux during the coating run. This was due to the stepped erosion profile on the target surface (Sect.6.2.4), but fortunately, the scale of the compositional change was overshadowed by the much greater impact of substrate bias.

The EDS analysis revealed that all of the coatings were susceptible to preferential resputtering of Mg resulting from energetic ion bombardment during deposition. The coatings with the lowest Mg content were the most sensitive to increases in bias voltage (Fig.9.4). The Mg content of the coatings decreased rapidly with increasing bias, for the Al115/Mg5, Al105/Mg15 and Al90/Mg30 targets. However, the Mg content of these coatings passed through a point of inflection, beyond which the Mg decreased only slightly with further increase in bias. This inflection point occurred at about -40V for Al115/Mg5, -50V for Al105/Mg15, and -90V for Al90/Mg30. A similar although less obvious change also occurred for the Al60/Mg60 series at a substrate bias of -140V. Comparison of the Mg content results for the Al105/Mg15 and Al90/Mg30, which shared similar *i/a* ratios (Fig.9.1), suggested that this inflection point was shifted to higher bias voltage as the Mg content of the sputtered flux was increased. The Mg composition of coatings prepared from the Al60/Mg60 and Al30/Mg90 targets decreased continuously with increases in substrate bias, although the voltage at which these changes became prominent tended to increase with Mg content of the target. This indicates that the alloy composition of the Mg-rich coatings were much less sensitive to increased substrate bias than were the Al-rich coatings.

The amount of Ar buried in the Al-Mg alloy coatings was found to be highly dependent on the coating composition, in addition to the bias voltage. A very small, relatively constant amount of Ar for all of the Al115/Mg5 and Al105/Mg15 series coatings is indicated in Fig.9.5. However, this is believed to be an artefact of the EDS measurement (refer Sect.4.3.4), and the actual Ar content is considered to be less than 1% for all bias voltages. In comparison, for the coatings prepared from the Al30/Mg90 and

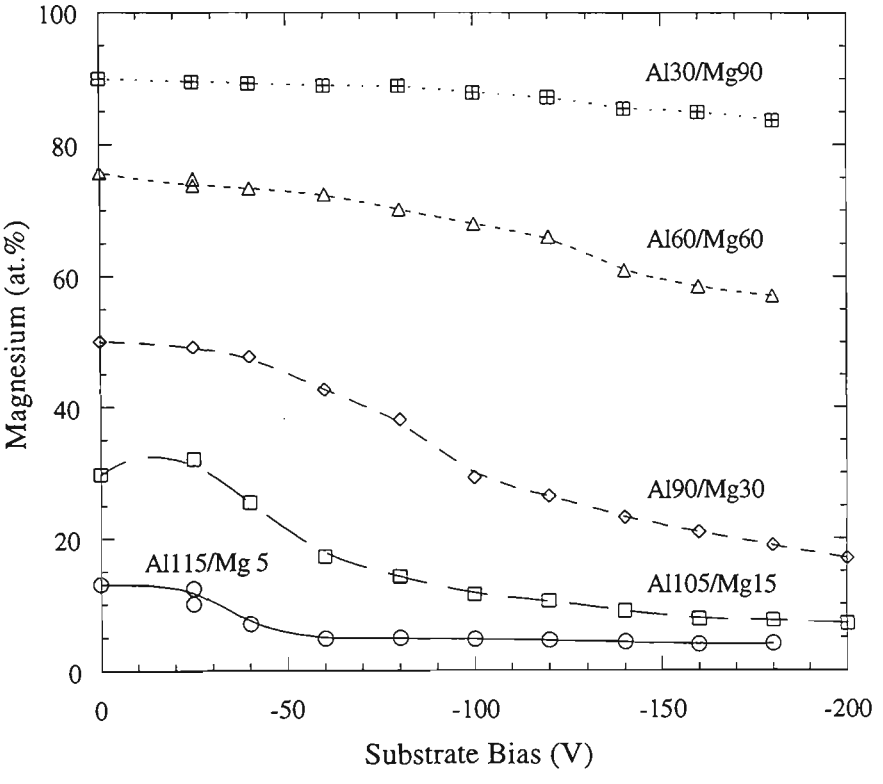

Fig.9.4 *Mg content of sputtered Al-Mg coatings, relative to the total amount of Al and Mg.*

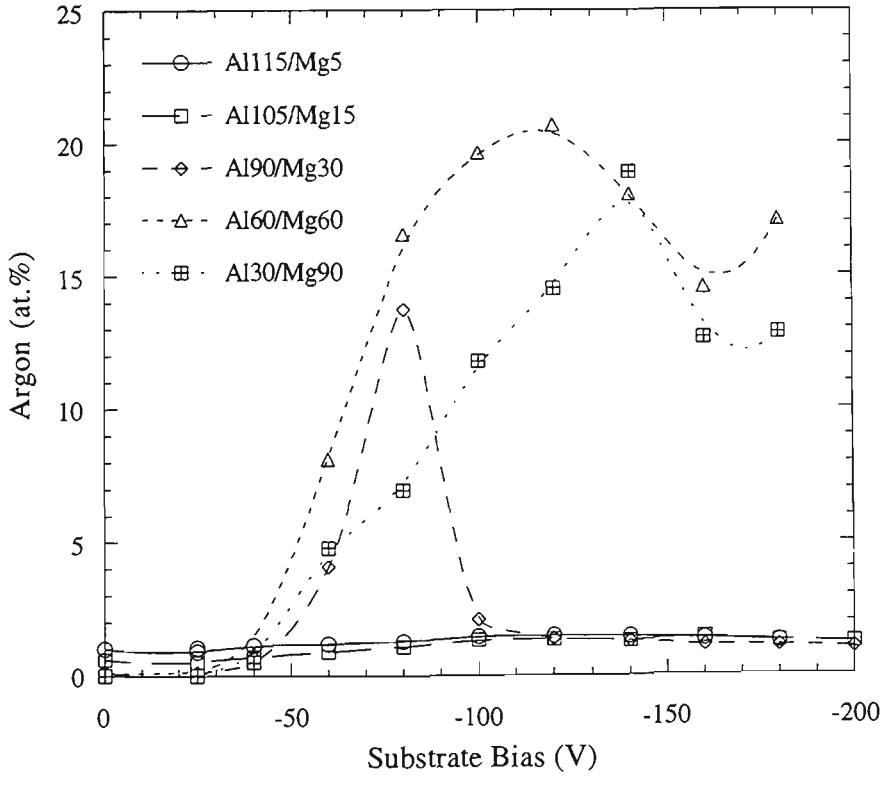

Fig.9.5 *Ar content of sputtered Al-Mg coatings, relative to the total amount of Al, Mg and Ar.*

Al60/Mg60 targets, the Ar content increased dramatically as the bias was increased beyond -40V, and tended to reach a maximum of about 20% Ar. Even higher amounts of buried Ar could be achieved, but short term ageing resulted in desorption of Ar from the coating and rapid oxidation. This point is discussed further in the following section. Of particular interest is the behaviour of the coatings prepared with the Al90/Mg30 target. As the bias voltage was increased to -80V, the Ar content of the coatings climbed dramatically. Further increases in bias voltage resulted in very little burial of Ar, and this corresponded with the Mg content of the coating dropping below about 35%. Therefore, strong evidence exists in Figs.9.4 and 9.5 that suggests the coatings with more than about 35%Mg were particularly susceptible to the retention of Ar, while those below this limit were not.

The entrapment of such high amounts of Ar in the coatings is believed to be responsible for the unusual behaviour of the mass deposition rate for many of the Al-Mg coatings (Fig.9.2). The atomic mass of Ar is about 50% greater than that of Al and Mg. Only relatively minor proportions of Ar in the coatings would therefore have a dramatic effect on the coating mass. Resputtering at increased substrate bias also caused a reduction in the proportion of metallic atoms in the coating. However, the increase in mass due to Ar burial generally outweighed the reduction in mass caused by resputtering. The deposited coating mass was observed to decrease at higher substrate bias when the contribution of resputtering became more prominent, and Ar burial reached a limiting level (Fig.9.5).

9.2.5 Chemical Composition Profiles

Many of the Al-Mg coatings that were found to contain high amounts of Ar were noted to be susceptible to rapid blackening within only a few weeks of ambient ageing (Figs.9.3 and 9.5). The blackening was usually restricted to a central spot, but in some cases, discontinuous rings of blackening were noted on the surfaces of some samples. This prompted cause for concern over the uniformity of the coating composition. Consequently, EDS compositional line profiles were conducted on the surfaces of a limited number of the Al-Mg alloy coatings.

The line profile for the -80V sample from the Al90/Mg30 series is shown in Fig.9.6. This sample is typical of coatings that contained less than about 15%Ar, and were free of the aforementioned surface blackening. A slight deviation in composition is notable near the outer edge of the coated region, which is thought to be related to the shielding effect of the cover mask. Otherwise, the chemical composition was relatively uniform over the entire coated region. In contrast, the line profile for the -100V sample

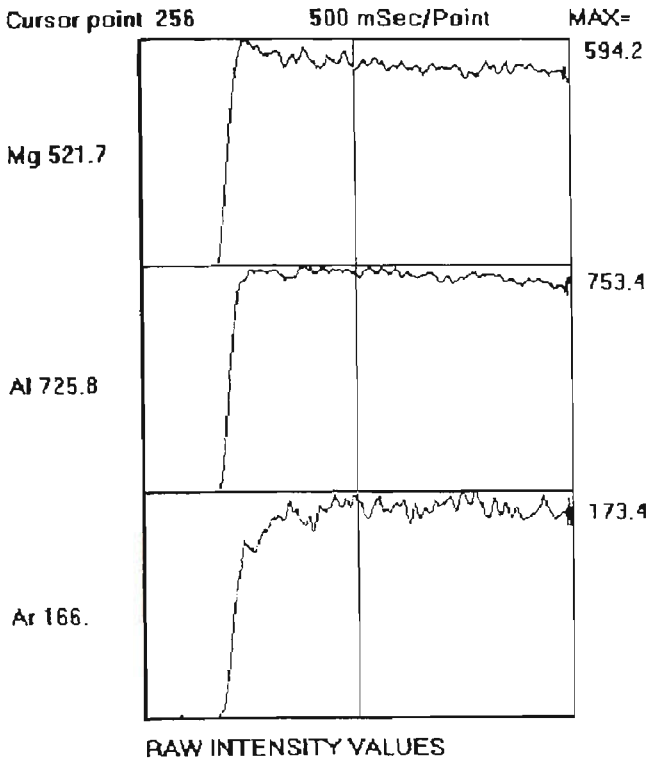

Fig.9.6 Chemical composition line profiles for Al90/Mg30 -80V bias coating. The profile extends from the outer edge of the coated area (left) to the centre (right).

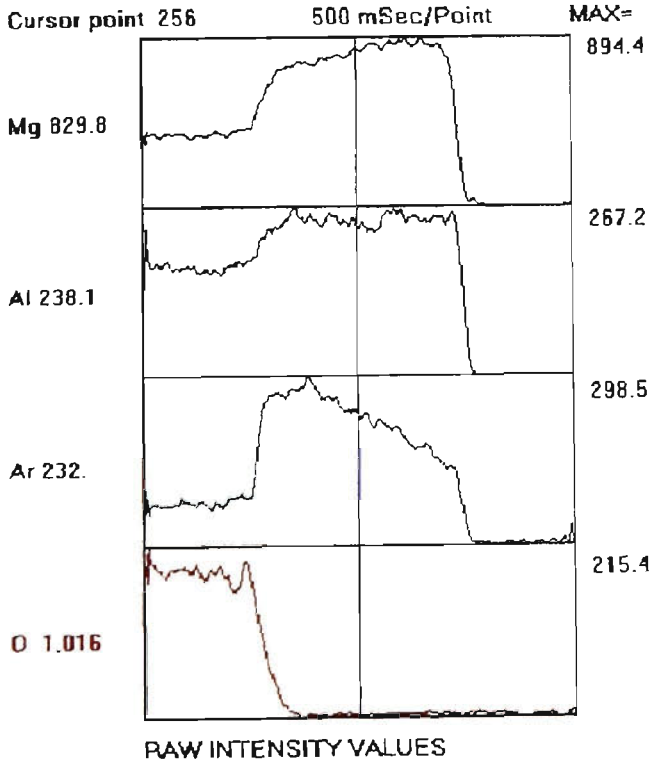

Fig.9.7 Chemical composition line profiles for Al60/Mg60 -100V bias coating. The profile extends from the centre of the coated area (left) to the outer edge (right).

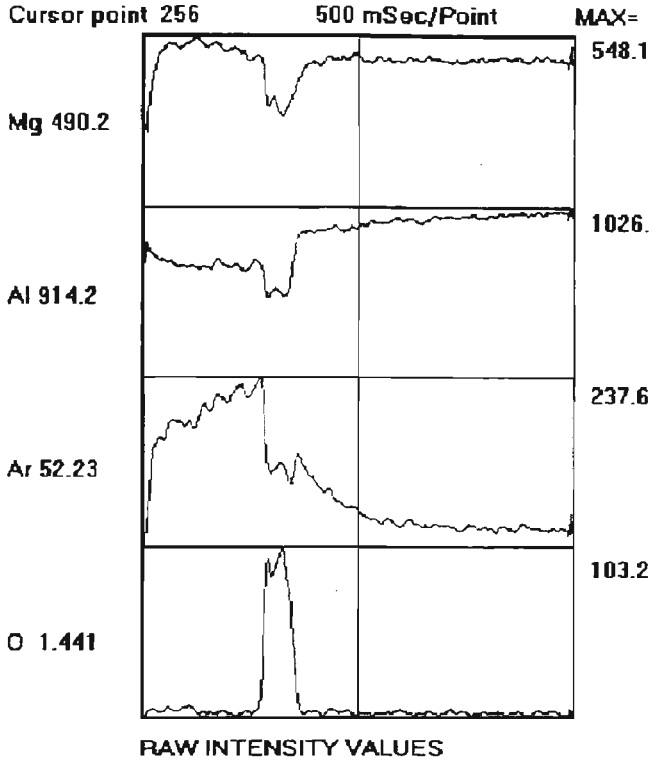

Fig.9.8 Chemical composition line profiles for Al90/Mg30 -100V bias coating. The profile extends from the outer edge of the coated area (left) to the centre (right).

from the Al60/Mg60 series is shown in Fig.9.7. The SEM micrograph accompanying this profile shows a blackened spot in the centre of the sample, that is correlated with a very high amount of oxygen, and a dramatically reduced Ar content. In the non-blackened region, the Ar content was noted to increase with distance from the coated edge, to a maximum of about 30%, immediately adjacent to the blackened spot. Based on this evidence, it is considered likely that the Ar content at the centre of the coating was actually much greater than 30% immediately after it was deposited. Upon removal of the sample from the vacuum chamber it released much of the entrapped Ar and the porous structure remaining was rapidly oxidized.

Similar trends were noted for samples that had a blackened ring, as opposed to a central spot. The line profile for the -100V sample from the Al90/Mg30 series is shown in Fig.9.8. At the time of examination (2 months after deposition), a blackened ring, approximately 1 mm wide was present on the coating surface, a few millimetres in from the outer edge of the coated area. The line profile across this ring indicated that the ring itself was heavily oxidized and had a reduced Ar content. Extrapolation of the Ar content either side of the blackened region suggests that the Ar content prior to oxidation was about 30%. Furthermore, the coated region on the outer side of the ring, was found to have a higher Mg and Ar content than the coating in the centre of the sample. It is anticipated that the actual ion current experienced during the growth of the coating would have been at maximum near the centre of the sample, and decreased slightly towards the outer edges, in agreement with previous experiments [60,65]. Therefore, the lower Mg content in the centre of the coating area is consistent with the higher ion flux and hence a greater proportion of preferential resputtering of Mg. Following a similar line of thought, it would be expected that the Ar content would adopt an opposite trend, being highest in the centre where the greater ion flux was experienced – completely opposite to the observed behaviour. This finding points to an additional mechanism for the retention of Ar in the alloy coatings, which is apparently related to the Mg content.

9.2.6 Bragg-Brentano X-Ray Diffraction

The Bragg-Brentano XRD scans for all of the coatings prepared from the Al/Mg composite targets are shown in Figs.9.9 to 9.13. The sharp diffraction peaks between 33° and 34° are due to the substrate and can be ignored. Most of the coatings were found to contain crystalline phases. Generally, only one diffraction peak was observed for each coating, indicating that the corresponding crystalline phase was extremely textured with the fibre axis perpendicular to the substrate surface. Unequivocal identification of the phase contributing to this peak was not possible because additional lower symmetry peaks were not detected. However, rapidly solidified Al-Mg melts have been shown to produce

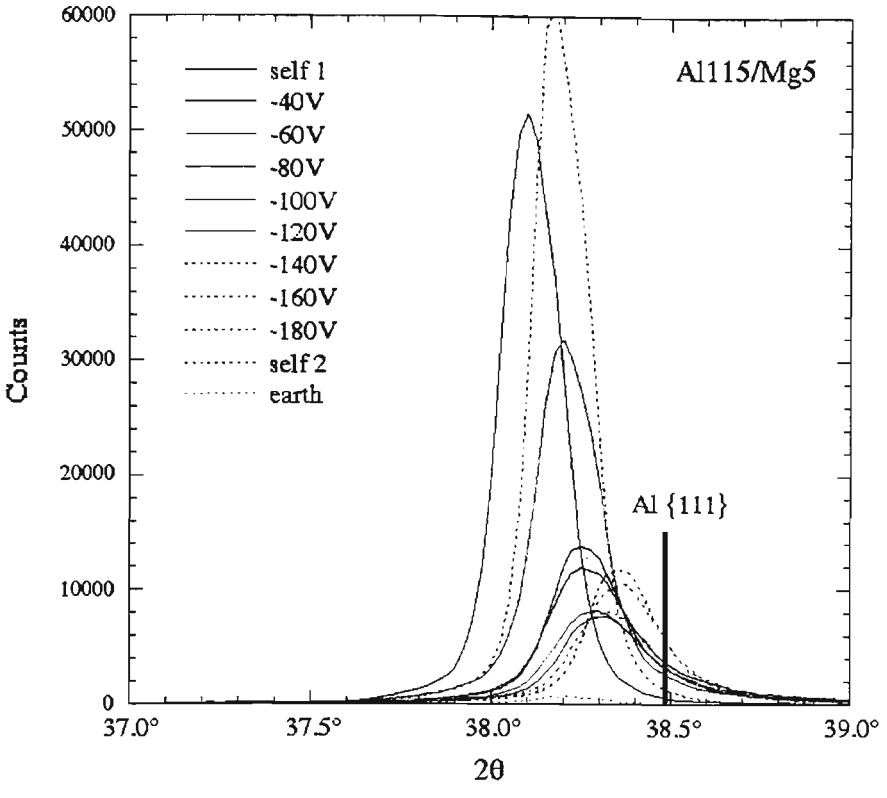

Fig.9.9 *Bragg-Brentano X-ray diffraction spectra for Al115/Mg5 Series coatings*

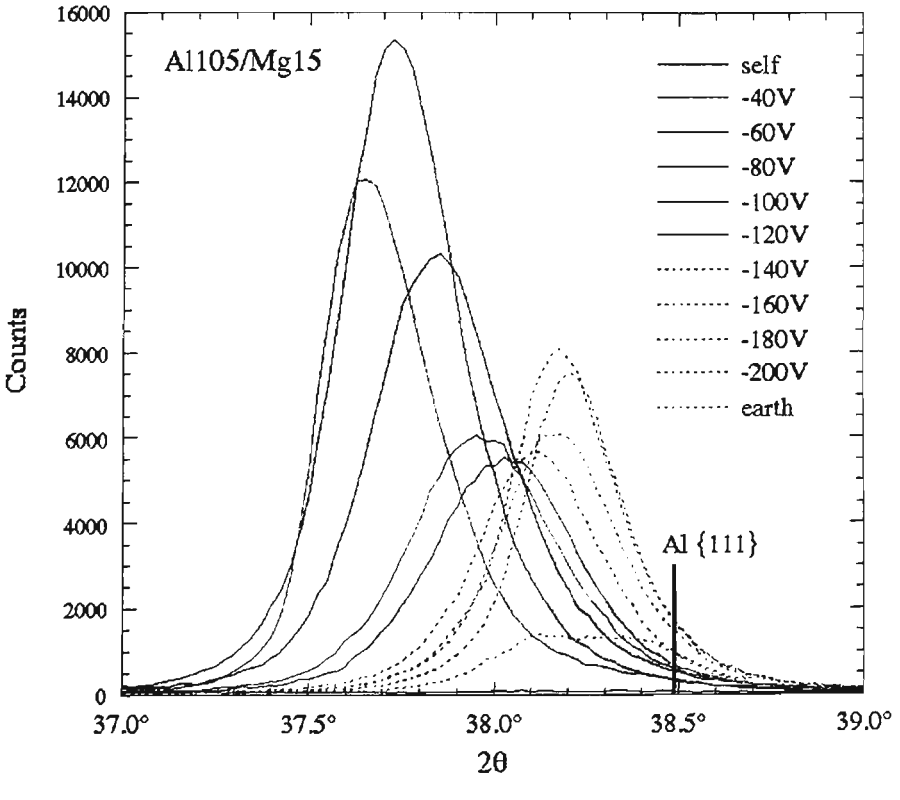

Fig.9.10 *Bragg-Brentano X-ray diffraction spectra for Al105/Mg15 Series coatings*

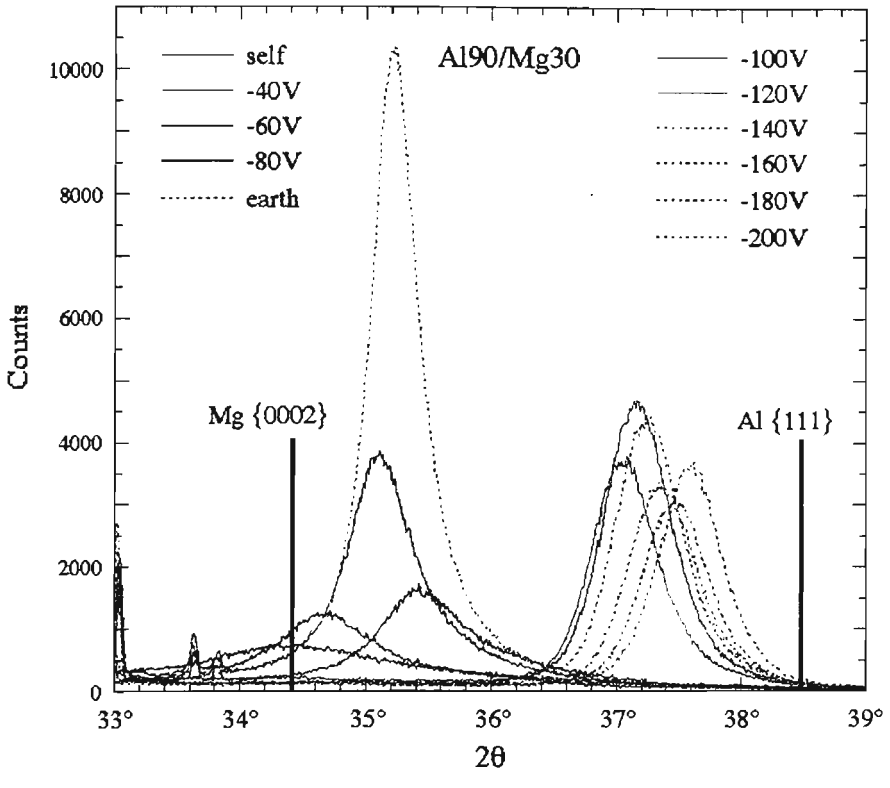

Fig.9.11 Bragg-Brentano X-ray diffraction spectra for Al90/Mg30 Series coatings

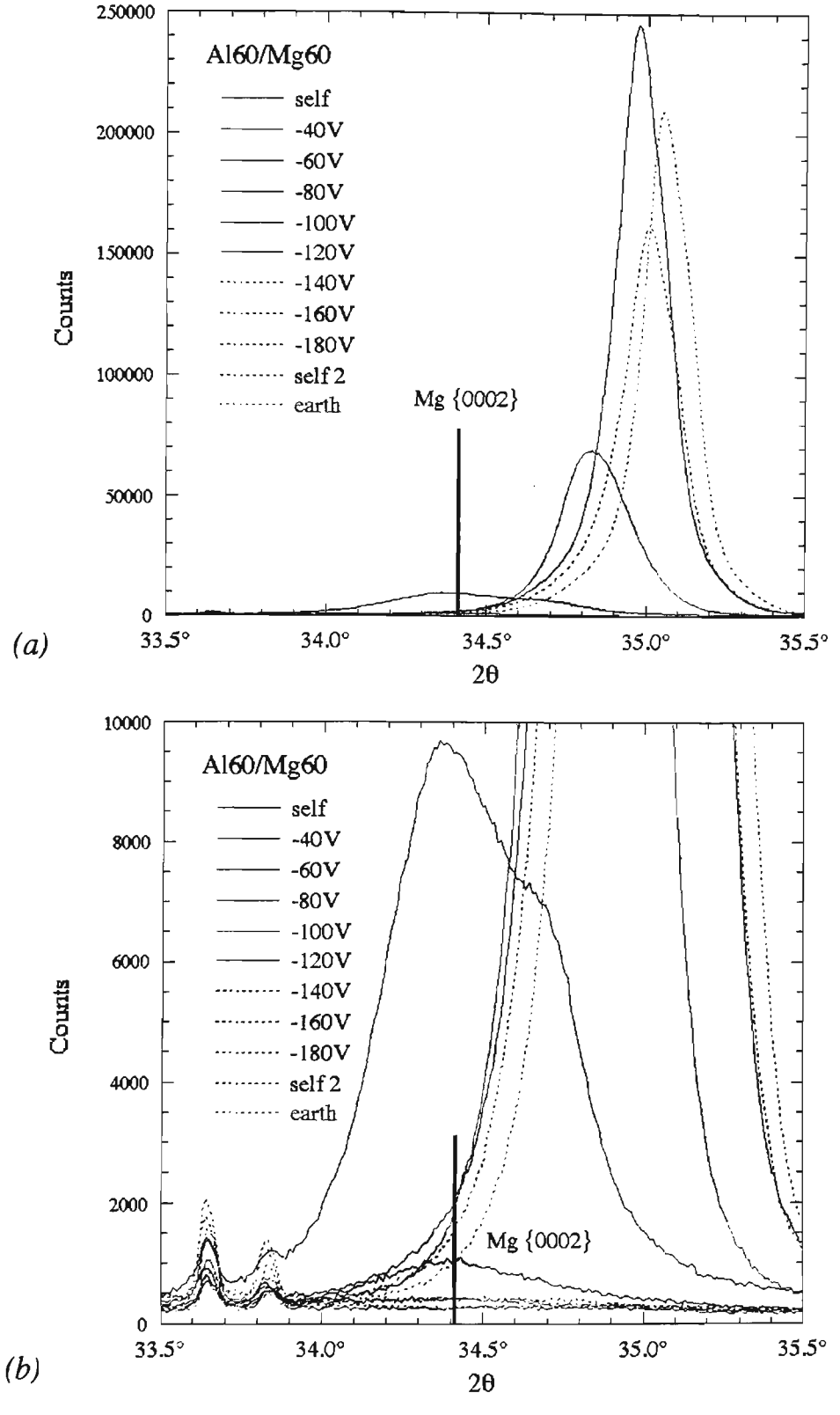

Fig.9.12 *Bragg-Brentano X-ray diffraction spectra for Al60/Mg60 Series coatings*
(a) high intensity Mg {0002} diffraction peaks
(b) low intensity Mg {0002} and amorphous diffraction peaks

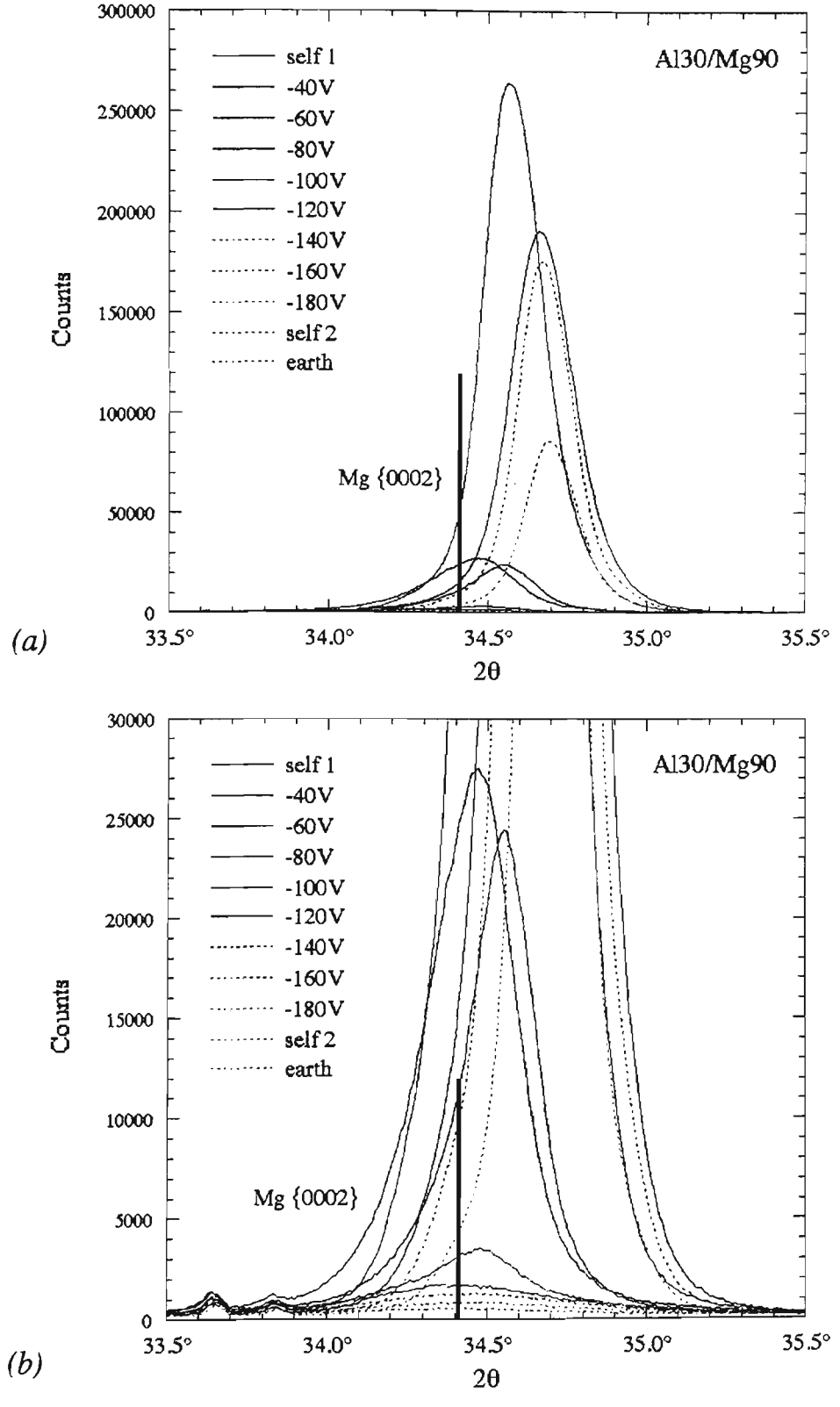

Fig.9.13 Bragg-Brentano X-ray diffraction spectra for Al30/Mg90 Series coatings
(a) high intensity Mg {0002} diffraction peaks
(b) low intensity Mg {0002} and amorphous diffraction peaks

metastable α-(Al) solid solutions with up to 38 at.% Mg, and similar observations have been made for δ-(Mg) phase (Sect.3.5.2). It is therefore assumed that *d*-spacings greater than 0.253 nm correspond to {0002} planes from δ-(Mg) phase, and those below 0.243 nm are attributed to {111} planes from α-(Al) phase. No diffraction peaks were observed in the range from 0.243 to 0.253 nm. The *d*-spacing, intensity and FWHM parameters for the α-(Al) and δ-(Mg) phases in each of the coatings are summarized in Figs.9.14 and 9.15 respectively. Only one of these crystalline phases was observed in each of the coatings, and the two phases did not coexist.

Very narrow and weak diffraction peaks with d-spacings of 0.265 and 0.266 nm were also observed in many of these Al-Mg alloy coatings (33.64° and 33.83° in Figs.9.9 to 13). It was previously speculated that these peaks may have been due to the presence of a distorted β-Al_3Mg_2 phase with lattice parameter of 2.85 nm [330]. However, these same peaks were also observed in Bragg-Brentano diffraction scans of an uncoated Si [100] wafer (Sect.4.4.1), and are totally unrelated to the coating. Therefore, it can be concluded that each Al-Mg coating contained no more than one crystalline phase. This does not rule out the possibility of an amorphous phase in the coatings which would have been undetectable by XRD. Indeed, some of the coatings appeared to contain only a small fraction of crystalline phase, and it can only be assumed that the bulk of the remaining coating was amorphous.

(Al) Phase

An α-(Al) solid solution with a very strong <111> fibre texture was found to be present in all of the Al115/Mg5 and Al105/Mg15 series coatings. The (Al) phase was also found to develop in the Al90/Mg30 series coatings, but only at a bias voltage of -100V or greater. The *d*-spacing, intensity and FWHM of the {111} peak is shown as a function of substrate bias in Fig.9.14 for these three sets of coatings. The results for the Al Series 2 coatings (Chap.5) are also shown for comparison. In each case, the Mg content of the alloy coatings was less than 35% (Fig.9.4), and the presence of (Al) phase is consistent with the reported maximum solid solubility of 38.4% (Sect.3.5.2).

For the Al115/Mg5 and Al105/Mg15 series coatings, the {111} diffraction peak was very weak at either earth or self bias voltages, and increased very sharply with only a slight increase in bias (Fig.9.14b). It is suspected that a nanocrystalline or amorphous phase was present at these low bias voltages, in preference to a crystalline α-(Al) phase, although this is speculative. A similar abrupt increase in {111} intensity for the (Al) phase was noted to occur in both pure Al (Fig.9.14b) and Al-Zn alloy coatings (Fig.8.12a). The Al115/Mg5 series developed the strong fibre texture at self bias,

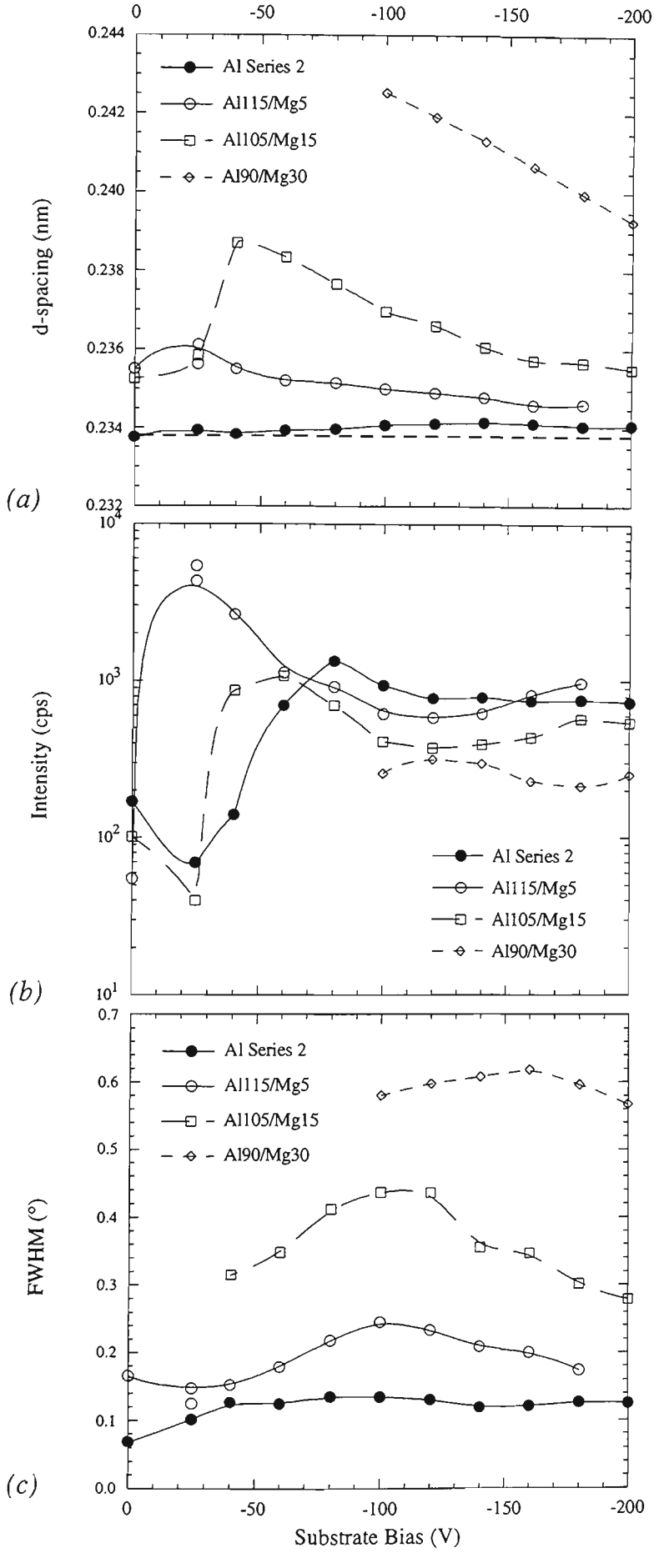

Fig.9.14 *XRD results for the (Al) {111} peak in Al Series 2 and Al-Mg coatings: (a) d-spacing, (b) peak intensity, and (c) FWHM.*

whereas a bias of -60V was necessary for the Al Series 2 coatings. Such effects could possibly be due to differences in *i/a* ratio, although in this case, the Al coatings experienced the highest *i/a*. It would therefore appear that the presence of Mg in the (Al) phase favoured development of the strong {111} fibre texture at comparatively lower substrate bias levels. Continued increase in the substrate bias resulted in a reduction of the {111} peak intensity, consistent with the concurrent reduction in the deposited coating mass (Fig.9.2).

The {111} *d*-spacing for the Al115/Mg5 and Al105/Mg15 series coatings was found to increase to a maximum (Fig.9.14a) when the fibre texture was at its strongest (Fig.9.14b). Further increase in bias resulted in a gradual reduction in the {111} *d*-spacing, in a similar fashion to the reduction in the fibre texture. This reduction in *d*-spacing for the (Al) was observed for all three sets of alloy coatings in Fig.9.14. However, the *d*-spacing was always found to be significantly greater than that of pure Al. It is highly likely that these peak shifts were caused by changes in the amount of Mg dissolved in solid solution, although the effect of residual stress should also be considered. Some slight differences in *d*-spacing were noted for the self bias sample from the Al115/Mg5 series deposited at the end of the coating run (self 2 in Fig.9.9), compared to the first self bias sample. This result is consistent with the observed differences in Mg content for these two coatings (Fig.9.4).

Increasing the substrate bias also tended to cause the (Al) diffraction peaks to broaden slightly, reaching a maximum FWHM at about -100V, and then decreasing again at higher bias (Fig.9.14c). This trend was similar to that of sputtered Al coatings, in spite of the slight differences in the *i/a* ratio. However, the diffraction peaks of the coatings tended to broaden as the Mg content of the targets was increased. The maximum width of the {111} peak was 0.18°, 0.25°, 0.44° and 0.62° for the Al Series 2, Al115/Mg5, Al105/Mg15, and Al90/Mg30 coatings, respectively. This increase in peak broadening reflected the increasing Mg content of the coatings (Fig.9.4). The broadening of the diffraction peaks may therefore be due to either a refinement of the grain size [85], or residual microstrain, both of which appear to result from the presence of Mg in solid solution.

(Mg) Phase

A δ-(Mg) solid solution with a very strong <0001> fibre texture was found to be present in all of the Al60/Mg60 and Al30/Mg90 series coatings. The (Mg) phase was also detected in the Al90/Mg30 series coatings, but only at a bias voltage of -80V or less. The *d*-spacing, intensity and FWHM of the {0001} peak is shown as a function of substrate

bias in Fig.9.15 for these three sets of coatings. The results for the Mg Series 1 coatings (Chap.7) are also shown for comparison.

Although no non-basal (Mg) peaks were detected in the alloy coatings, it appears that the {0001} diffraction intensity was highly dependent on the substrate bias (Fig.9.15b). Generally, this peak intensity reached a maximum at bias voltages of between earth and -40V. Further increase in the bias resulted in a dramatic reduction in the peak intensity. Similar behaviour was observed for the Mg Series 1 coatings, although some non-basal peaks were also detected. This was interpreted as a change from a strong <0001> fibre texture to a more randomly oriented texture. However, in the alloy coatings it would appear that no randomly oriented grains were detected. For bias voltages above about -80V, the very weak diffraction peaks suggest that the grain size of the (Mg) solid solution was severely reduced or that the coating had become predominantly amorphous.

The {0001} peak was found to be shifted to lower *d*-spacing than that of pure Mg (Fig.9.15a), and it is considered that some Al was dissolved in δ-(Mg) solid solution. At earth bias, the diffraction peak was similar to that observed at self bias. Increasing the bias voltage above self bias resulted in an increase in the {0001} *d*-spacing, combined with a rapid reduction in diffracted intensity and an increase in the FWHM (Fig.9.15). This trend in *d*-spacing implies that the amount of Al dissolved in solid solution was reduced by increasing the bias voltage, although the possible influence of residual stress on the peak position cannot be ignored. The diffraction peaks for the Al90/Mg30 series coatings were particularly broadened (Fig.9.15c), and thus it appears that these coatings were primarily amorphous with only a small fraction of crystalline grains. It is notable that the coatings found to have weak (Mg) {0001} peaks also had very large proportions of entrapped Ar (Fig.9.5). Thus, it seems that there is a relationship between the Ar content of the coatings and the possible amorphisation of the fibre textured (Mg) phase.

As a final point, it is worth emphasising that the crystal structure of the coatings deposited from the Al90/Mg30 target were strongly affected by the substrate bias. Those coatings produced with a bias of -80V or less were found to develop a <0001> textured (Mg) phase, that was somewhat amorphised at the upper bias range. However, increasing the bias to -100V or more saw the formation of <111> textured (Al) phase in the coatings. Concurrent with this structural change between -80V and -100V bias was a dramatic reduction in the Mg content from 38 to 29% (Fig.9.4). It appears that the modification to the crystal structure was therefore related to the chemical composition of the coating, rather than an inherent result of ion bombardment.

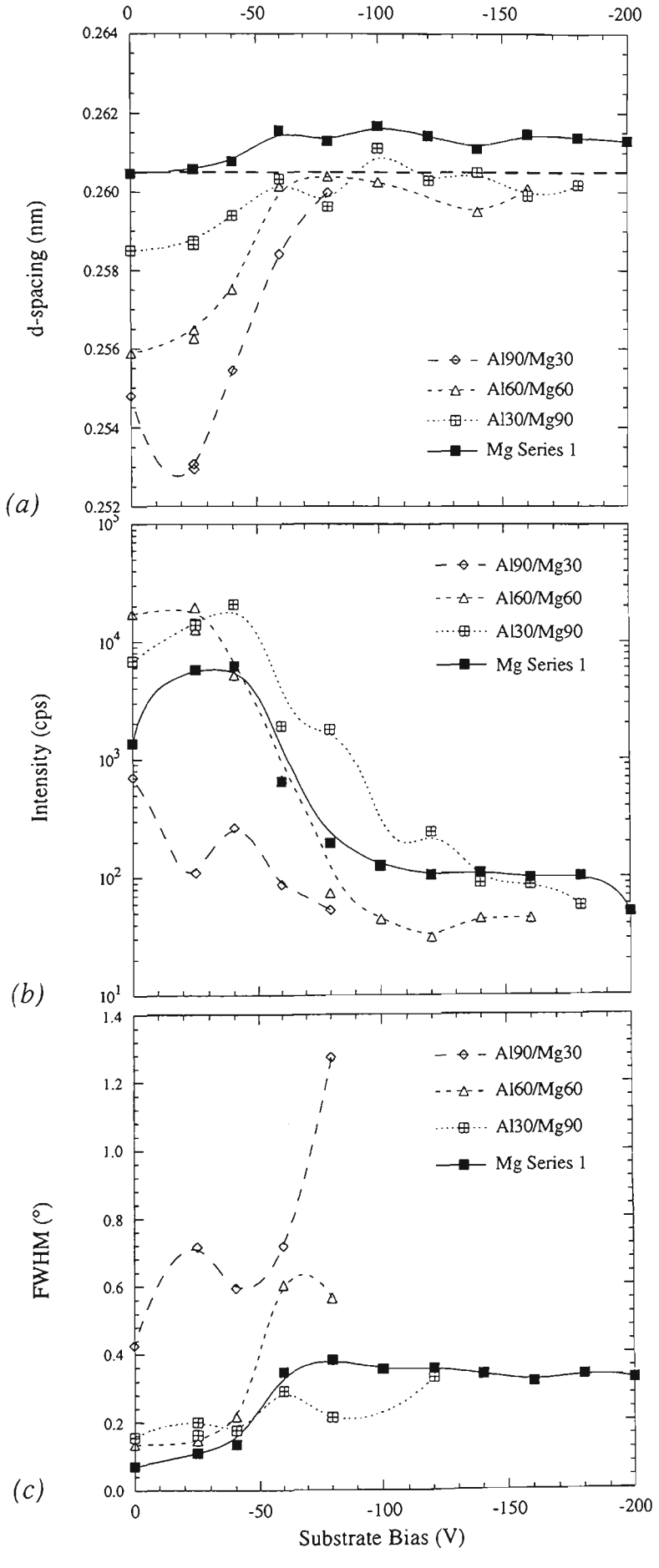

Fig.9.15 XRD results for the (Mg) {0002} peak in Mg Series 1 and Al-Mg coatings: (a) d-spacing, (b) peak intensity, and (c) FWHM.

9.2.7 Crystallite Group Method

The Bragg-Brentano diffraction scans for the various Al-Mg coatings revealed that the (Al) and (Mg) phases were present in each coating, but not simultaneously. The *d*-spacing for the detected plane in each of these phases was affected by bias voltage and coating composition. CGM was used to determine the residual macrostress and strain-free lattice parameters for the <111> fibre textured group of the α-(Al) phase, and the <0001> fibre textured group of the δ-(Mg) phase. The analysis was limited to coatings that displayed a diffraction peak intensity of more than ~500 cps in Figs.9.14 and 9.15. This restricted the CGM analysis to the following coatings: Al115/Mg5 with self bias or greater, Al105/Mg15 with -40V bias or greater, Al60/Mg60 with up to -60V bias, and Al30/Mg90 with up to -80V bias. Few of the Al90/Mg30 series coatings were suitable for CGM analysis because of the relatively weak diffraction peaks.

(Al) Phase

Asymmetric diffraction scans of the Al115/Mg5 and Al105/Mg15 series coatings provided diffraction peaks at the predicted positions, which confirmed that the crystalline phase in these coatings was fcc α-(Al). The lattice parameters calculated for the {222} peak from the asymmetric scans were virtually identical to those of the {111} peak in the Bragg-Brentano scans. This is despite the fact that Bragg-Brentano diffraction was conducted about three months after deposition, whereas the CGM analysis was conducted about twelve months after deposition. This result suggests that there were no changes in the α-(Al) phase with ageing of the Al-Mg coatings under atmospheric conditions, unlike that observed for the Al-Zn coatings (Chap.8).

The equivalent lattice parameters measured for the various peaks by asymmetric diffraction scans were plotted as a function of $\sin^2\psi$, as shown in Fig.9.16. Linear regressions were fitted to the data, and high correlation coefficients indicated an excellent fit to the data. The linear coefficients were used to calculate the strain free lattice parameter a_0 and the residual macrostress σ, using equations appropriate for the <111> texture in these coatings (Sect.4.4.4). The results of these calculations are graphed as a function of the bias voltage in Fig.9.17, along with the results for Al Series 2 coatings (Chap.6) for comparison.

The strain-free lattice parameters of α-(Al) phase in Al115/Mg5 and Al105/Mg15 series coatings all indicated the presence of Mg in solid solution (Fig.9.17a). At low bias voltages, a_o was significantly greater than that of sputtered Al coatings, which was in turn almost identical to that of pure Al powder. The maximum a_o was obtained at self bias for Al115/Mg5 and -40V bias for Al105/Mg15. This increased a_o is consistent with the

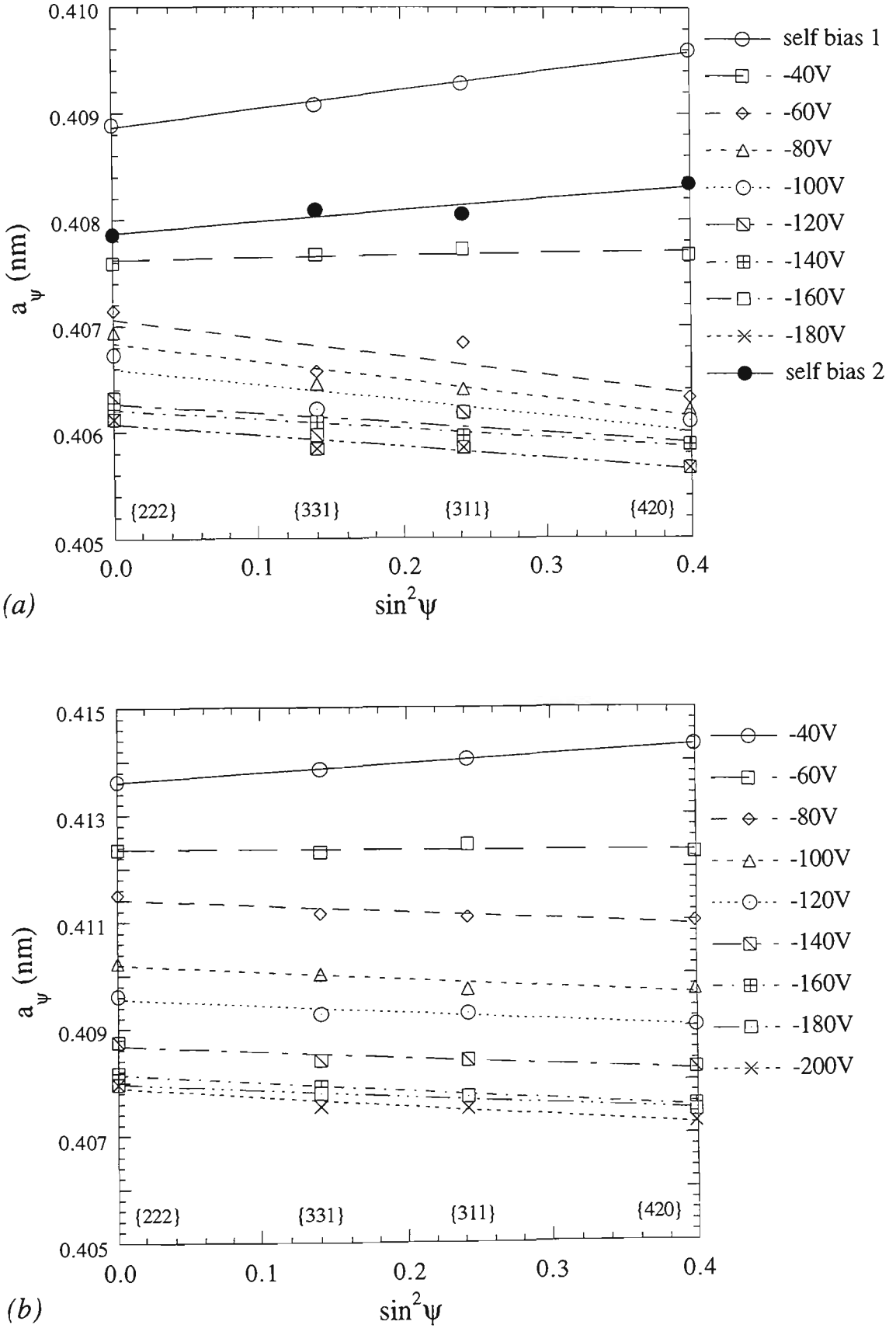

Fig.9.16 $Sin^2\psi$ plots of CGM data for the <111> fibre textured (Al) grains in coatings from the Al115/Mg5 (a) and Al105/Mg15 (b) composite targets.

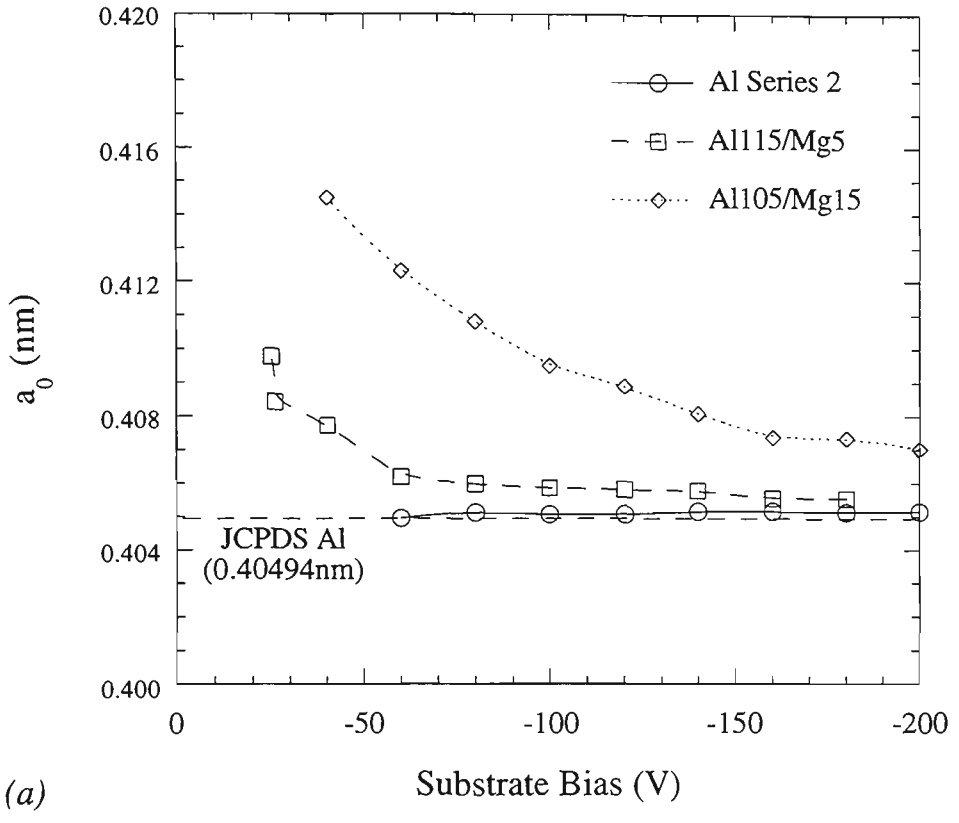

(a)

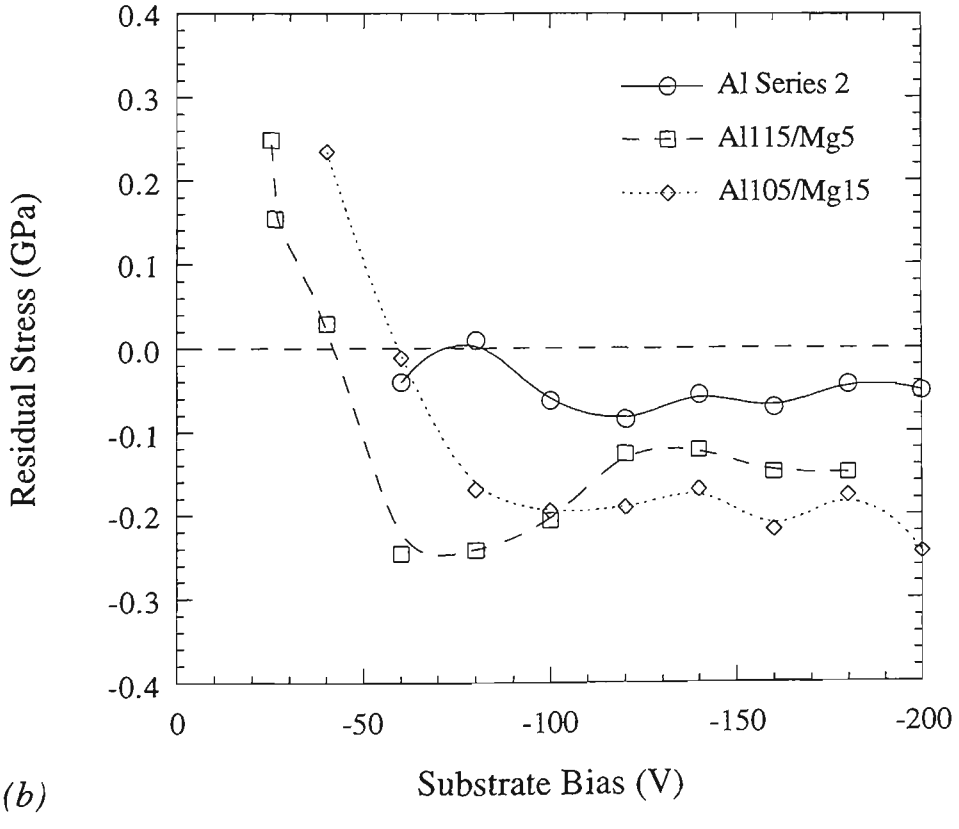

(b)

Fig.9.17 Strain-free lattice parameter (a) and residual macrostress (b) of the <111> fibre textured (Al) grains in coatings from the Al115/Mg5 and Al105/Mg15 composite targets. Results for the Al Series 2 coatings are shown for reference.

presence of Mg in α-(Al) solid solution. The coatings in the Al105/Mg15 series had much higher a_o than those of the Al115/Mg5 series, due to the greater proportion of Mg in the sputtered flux. Increasing the substrate bias caused a_o to decrease significantly. This result suggests that energetic ion bombardment of the alloy coatings during deposition caused Mg to be removed from the α-(Al) solid solution.

It must be reminded at this point, that the Mg content of the sputtered flux decreased slightly during each coating run, due to the changes occurring on the surface of the composite targets (Sect.4.2.4). This effect is reflected in the lattice parameters for the two self bias coatings for the Al115/Mg5 series (-25V); the higher lattice parameter is for the coating prepared at the start of the run (12.4%Mg), and the lower lattice parameter is for the coating at the end of the run (10.0%Mg). Therefore, it seems likely that the slight decrease in lattice parameter for the Al115/Mg5 series above -60V was primarily the result of this reduction in Mg content of the sputtered flux during the coating run. There is no doubt that the dramatic changes in lattice parameter noted at low bias for Al115/Mg5 and for all Al105/Mg15 series coatings are caused by real effects of bias voltage. Furthermore, it is worth noting that the overall trends in a_o are identical to those found for {111} d-spacing by Bragg-Brentano diffraction. The only notable difference is that bias-induced changes in Bragg-Brentano d-spacings were masked slightly by small variation in residual stress. It is therefore reasonable to assume, as a first approximation, that changes in d-spacing of the scale reported in Fig.9.14 are primarily caused by solid solution effects.

The residual macrostress in the α-(Al) phase of the Al115/Mg5 and Al105/Mg15 series coatings followed similar trends to each other (Fig.9.17b). The alloy coatings were subject to tensile stress at low bias voltages. With small increases in the bias, the stress reduced rapidly such that above about -50V, the residual stress became compressive. As the bias was increased further, the compressive stress increased to a maximum and then either decreased slightly (Al115/Mg5), or remained at about the same level (Al105/Mg15). These trends were similar to those observed for the Al Series 2 coatings, except that they were much greater in magnitude. This is consistent with the solid solution strengthening effect, which would enable the retention of a greater amount of residual elastic stress before the onset of plastic flow. However, the presence of such high tensile stresses in the low bias coatings is quite unexpected in light of their very smooth reflective surface finish, which is more typical of compressive stress. The constrained shrinkage model used to explain the tensile stresses in Zn coatings (Sect.5.3.4), is unlikely to have been active for the Al-alloy coatings due to their comparatively slower diffusivity. It seems

reasonable to conclude that the tensile stresses in these coatings were possibly caused by adsorbed impurities originating from the epoxy resin in the composite targets.

The α-(Al) phase in the high bias Al90/Mg30 series coatings was not examined by CGM due to low peak intensity. However, on the basis of the Al115/Mg5 and Al105/Mg15 series, it was anticipated that these coatings were also subject to compressive residual stress. The delaminated rippled surface noted for these coatings (Sect.9.2.3), supports the argument that compressive stresses were indeed present in these coatings. Furthermore, the *d*-spacings for the {111} planes were slightly greater than would be expected for an α-(Al) phase extrapolated from the actual coating compositions measured by EDS. This suggests that a moderate compressive stress was present in the coatings, and that the high bias Al90/Mg30 coatings consisted of a single-phase α-(Al) solid solution.

(Mg) Phase

The <0001> fibre textured δ-(Mg) crystallites in the Al30/Mg90 and Al60/Mg60 series coatings were also examined by CGM. Unfortunately, only a few of the coatings could be evaluated by CGM. The detection of diffraction peaks at the predicted positions confirmed that the crystalline phase in these coatings was cph δ-(Mg). As was observed for the α-(Al) phase in the Al-Mg coatings, no evidence for ageing of the δ-(Mg) phase was found in the asymmetric scans.

The *c* lattice parameter for each diffracted peak of the asymmetric scans was plotted as a function of $\sin^2\psi$ in Fig.9.18. Linear regressions were fitted to the data, and used to calculate the strain free lattice parameter c_0 and the residual macrostress σ, via equations appropriate for the <0001> fibre texture (Sect.4.4.4). The results of these calculations are summarized in Table 9.6.

The *c* lattice parameter for the δ-(Mg) phase in Al30/Mg30 and Al60/Mg60 series coatings all indicated the presence of Al in solid solution (Table 9.6). The lattice parameter was generally lower than that of pure Mg powder (0.52112 nm), consistent with a significant proportion of Al dissolved in solid solution. The one coating that was examined from the Al60/Mg60 series had a much lower lattice parameter than those of the Al30/Mg90 series, in accordance with the greater proportion of Al in the sputtered flux. It was not possible to determine with any certainty, the influence of substrate bias voltage on the strain-free lattice parameter of these Mg-rich coatings. However, the data presented in Table 9.6 suggests that increasing the bias caused the *c* lattice parameter to increase towards that of pure Mg. This is to be expected on the basis of the {0001} *d*-spacings measured by Bragg-Brentano XRD (Fig.9.15).

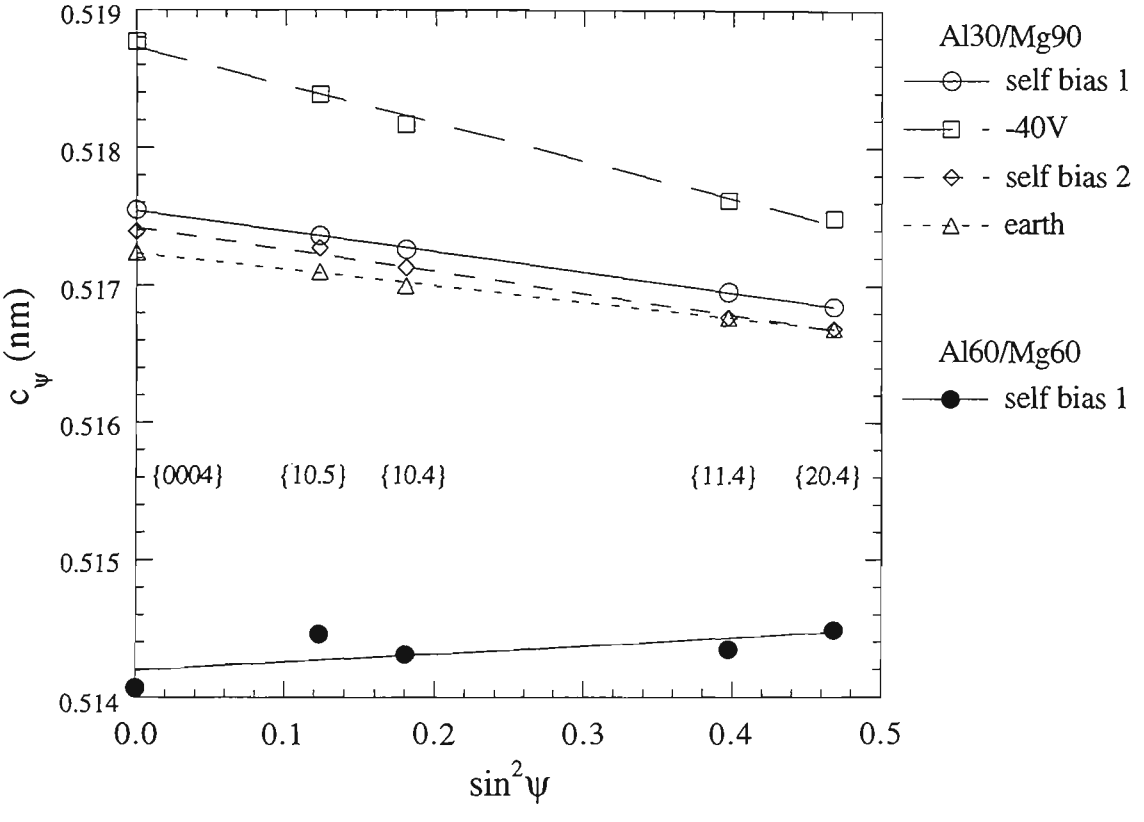

Fig.9.18 *$Sin^2\psi$ plots of CGM data for the <0001> fibre textured (Mg) grains in coatings from the Al30/Mg90 and Al60/Mg60 composite targets.*

Table 9.6 Strain-free lattice parameter and residual macrostress for the <0001> fibre textured crystallite group of the δ-(Mg) phase in Al-Mg coatings.

Substrate Bias (V)	strain-free *c* lattice parameter (nm)	residual macrostress (GPa)
Al30/Mg90 Series		
0 (earth)	0.51671	-0.08
-25 (self 1)	0.51688	-0.10
-25 (self 2)	0.51671	-0.11
-40	0.51749	-0.18
Al60/Mg60 Series		
self bias 1	0.51446	0.40

The residual macrostress in the δ-(Mg) phase of the Al30/Mg90 series coatings was compressive for all three of the low bias samples examined by CGM (Table 9.6). The magnitude of the compressive stress was similar to that obtained for the (Al) phase in the Al115/Mg5 and Al105/Mg15 series. The one coating examined from the Al60/Mg60 series was found to have a modest tensile stress. The entrapment of impurities sourced from the exposed epoxy resin on the composite target surface may have contributed to the generation of tensile stress, as was proposed for the (Al) phase.

9.3 General Discussion

9.3.1 Comparison with Previous Work

Supersaturation of the (Al) and (Mg) phases would certainly be expected to occur in Al-Mg coatings deposited by PVD, on the strength of experiences with rapidly solidified alloys (Sect.3.5.2). Several authors have made claims of supersaturated solid solutions in Al-Mg coatings, but it would appear that few of these claims were adequately substantiated. This is due to the inherent problems with conventional Bragg-Brentano XRD, whereby the measured *d*-spacings are influenced by both solid solution effects and residual macrostress. Consequently, residual stresses were ignored and any shifts in *d*-spacing have been attributed to solid solution effects [87,91,98,240-242].

The interpretation by most authors of the extent of solid solubility in the Al-Mg coatings is also flawed. For example, Arnell and Bates [98] claimed extended Mg solid solubility for the α-(Al) phase in their coatings. However, referencing their data to the established relationships between lattice parameter and Mg solute content (Sect.3.5.2), reveals that less than 2.7%Mg was present in (Al) solid solution for all of their coatings with up to 40%Mg. The α-(Al) phase reported in [98] was therefore not supersaturated since the calculated Mg content is similar to that experienced at room temperature under equilibrium conditions. Extended solid solubility of (Al) was also reported in [87,91], although no evidence for lattice parameter variations were presented to support these claims. The observations were based solely on the noted absence of second phase peaks in XRD scans. However, the absence of second phase diffraction peaks could be caused by the minimal volume fraction of a second phase, and does not rule out the possibility of its presence. Arnell and Bates [98] also claimed supersaturation of δ-(Mg). It appears that this could be valid, since the reported variations in lattice parameter (Fig.3.22), were similar in magnitude to those reported for rapidly solidified alloys of comparable composition (Fig.3.18). However, these arguments ignore the impact of any residual stresses that may be present in the coatings.

All previous work on Al-Mg coatings incorporated some degree of ion assistance in the preparation of the coatings. Only one of these studies [241,242] gave details of the conditions of ion bombardment, particularly with respect to the *i/a* ratio. Both the ion energy and *i/a* ratio are critical parameters for ion assisted deposition, and it is difficult to compare the previous work with the present investigation without such information. However, it is interesting to note that several of these earlier studies used an elevated substrate temperature. Arnell and Bates [87,91,98] did not measure the substrate temperature but indicated that the substrates were "too hot to touch" [244], suggesting a

temperature of at least 50°C and most likely in the order of 100°C. The ion plated coatings produced by Lee *et al* [240] were deposited with a substrate temperature of 130-170°C. Neither of these studies reported the presence of Ar entrapped in the coatings. In comparison, many of the coatings from the present investigation were found to have very high proportions of buried Ar (Fig.9.5), but only in those that contained the δ-(Mg) phase. The substrate temperature in the present case was only 50°C, and therefore it is felt that this may have contributed to the high Ar content.

Increasing the substrate temperature is expected to enable more rapid diffusion of Ar from the coatings. Hence, very little Ar would be retained in the coatings deposited at elevated temperatures. The use of low substrate temperatures may reduce the diffusional loss of Ar from the coatings during deposition, and contribute to high proportions of retained Ar. This is possibly a useful means of controlling the inert gas content of sputtered coatings and is recommended for further study.

9.3.2 Solid Solubility

Based on measurements of chemical composition and Bragg-Brentano XRD, it was established with reasonable reliability that coatings with up to about 32%Mg contained the α-(Al) solid solution. Coatings with more than about 38%Mg were found to include the δ-(Mg) solid solution. The strain-free lattice parameter measurements proved to be useful indicators of the proportion of solute present in these solid solutions. Empirical relationships between the lattice parameters of these phases and solute additions were presented in Sect.3.5.2. These equations were applied to the strain-free lattice parameter data for the α-(Al) and δ-(Mg) phases in the Al-Mg alloy coatings (Sect.9.2.7). Since the residual macrostress was found to be very small in most cases, the Bragg-Brentano *d*-spacing measurements were also converted to solute proportions in order to gain an appreciation for the solute content in coatings for which the CGM analysis could not be applied. The residual stress was assumed to be zero for this latter calculation.

The Mg solute content of the α-(Al) phase in the various Al-Mg coatings is shown as a function of substrate bias in Fig.9.19. The composition determined by EDS is also included for comparison. The solute level calculated from the Bragg-Brentano *d*-spacings was slightly greater than the EDS measurement (Fig.9.19b). When the compressive stress in the coatings was accounted for (Fig.9.19a), the α-(Al) solute content was slightly lower than the EDS measurement. However, the small difference between the EDS and CGM values is considered to be within experimental errors. These results suggest that the coatings from the Al115/Mg5 and Al105/Mg15 targets consisted of single-phase supersaturated α-(Al). CGM analysis was not possible for the Al90/Mg30

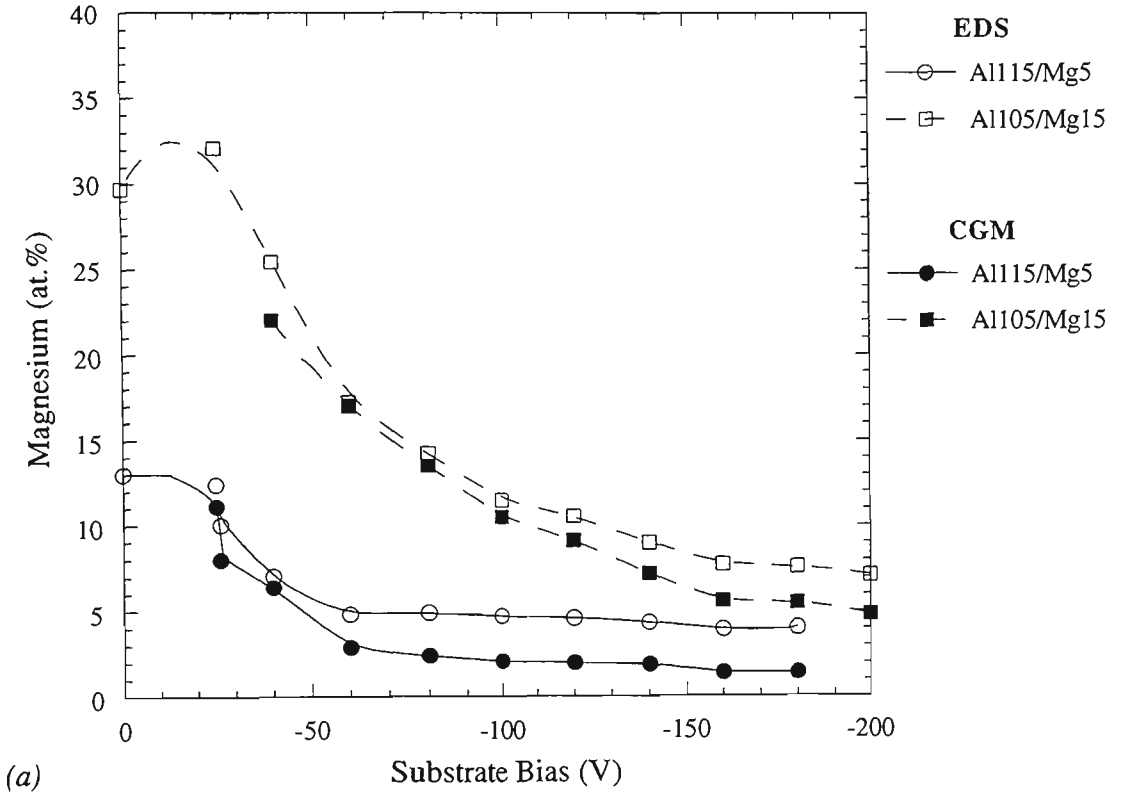

(a)

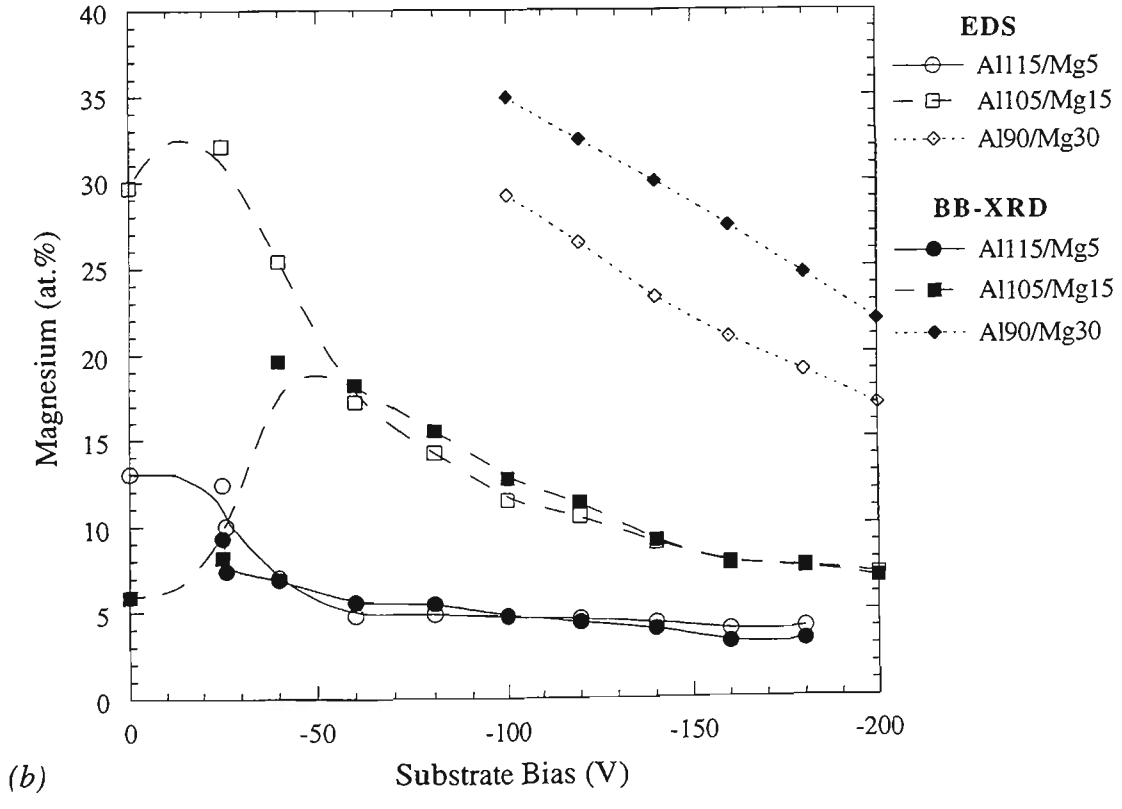

(b)

Fig.9.19 Comparison between the bulk chemical composition (EDS) and the Mg solute content of <111> fibre textured (Al) grains in coatings from the Al115/Mg5, Al105/Mg15, and Al90/Mg30 composite targets: (a) solute content calculated from strain-free lattice parameters derived using CGM, (b) solute content estimated from {111} d-spacing measured in Bragg-Brentano XRD scans.

series coatings, although the Bragg-Brentano results (Fig.9.19b) imply that relatively high proportions of Mg were dissolved in α-(Al) solid solution at a bias of -100V or greater. The calculated solute level was considerably greater than the bulk composition of the coating, and this is possibly caused by a comparatively large compressive stress in the α-(Al) phase. A rough estimate of the stress required to account for these differences in composition, suggested a compressive biaxial stress of about 700 MPa. It is not surprising that this stress level was apparently sufficient to cause delamination of the coatings (Fig.9.3b).

The solid solution results suggest the minor fraction of α-(Al) phase that existed in the low bias coatings (Fig.9.14b), contained only a small proportion of Mg in solid solution. Increasing the bias somewhat, led to the onset of a very strong <111> fibre texture in the α-(Al) phase, concurrent with a sharp increase in the solute content (Fig.9.19b). Thus it appears that the coatings with the strongest <111> fibre texture were able to retain the greatest proportion of Mg solute. Continued increase in the substrate bias caused a reduction in the Mg solute level, and this is thought to be caused by preferential resputtering of Mg (refer Sect.9.3.4). It is interesting to note that the upper limit of Mg solubility in the α-(Al) phase of the sputtered coatings may have been as high as 30% (Fig.9.19b). These findings are consistent with previous work on rapidly solidified Al-Mg alloys (Sect.3.5.2), which established that the α-(Al) solid solution can be extended up to about 38%Mg. It is likely that a similar boundary existed for the sputtered coatings, although the limited number of compositions examined did not permit confirmation.

The solid solubility of the δ-(Mg) phase could not be studied to the extent possible for the α-(Al) phase, since fewer samples were available for CGM analysis. The Al solute content of the δ-(Mg) phase in the Al-Mg coatings is shown as a function of substrate bias in Fig.9.20. The composition determined by EDS is also included for comparison. The relatively minor residual stresses found to exist in the δ-(Mg) phase (Table 9.6), seemed to have little effect on the solute level calculated from the Bragg-Brentano *d*-spacings. This is revealed by the minor differences between the solute content calculated from the CGM data (Fig.9.20a) compared with the Bragg-Brentano data (Fig.9.20b). Hence it seems reasonable to assume that the trends in Fig.9.20b approximate the Al solute level of the δ-(Mg) phase, even though they ignore the effect of residual stress.

The maximum Al solubility in the δ-(Mg) phase of the alloy coatings was found to be in the order of 30%, corresponding to the self bias coating from the Al90/Mg30 series (Fig.9.20b). Previous experiments on the rapid solidification of Al-Mg alloys indicated

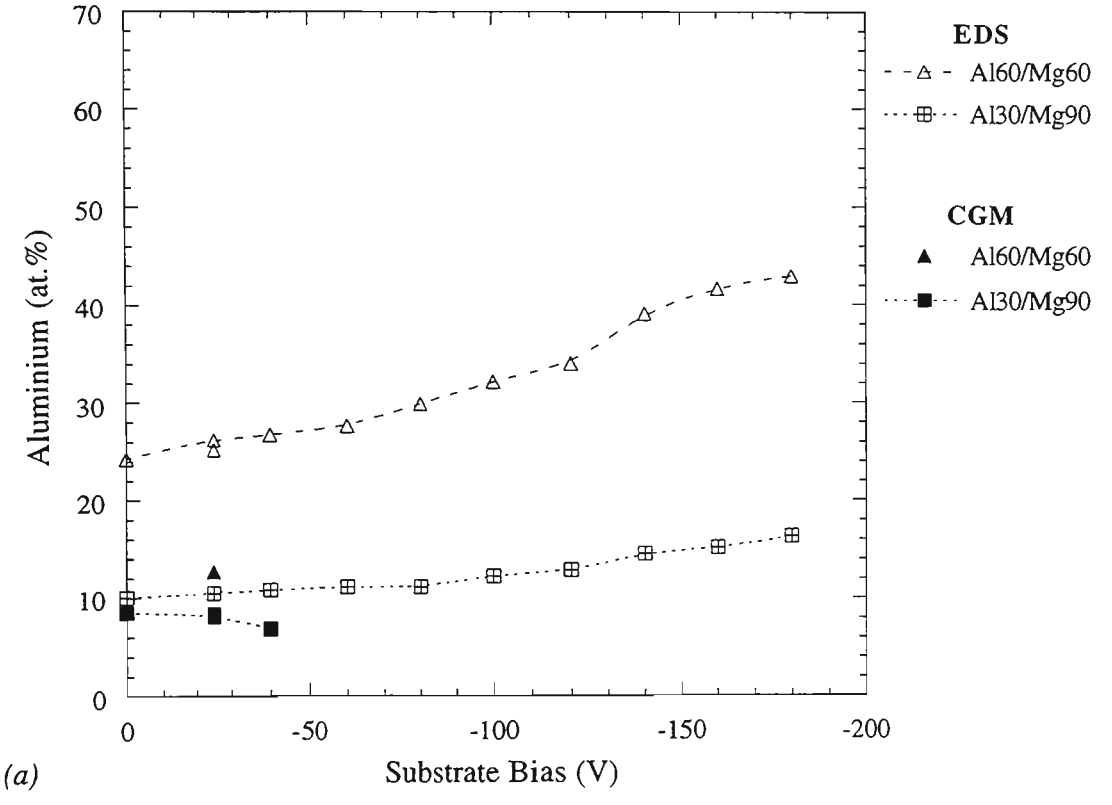

(a)

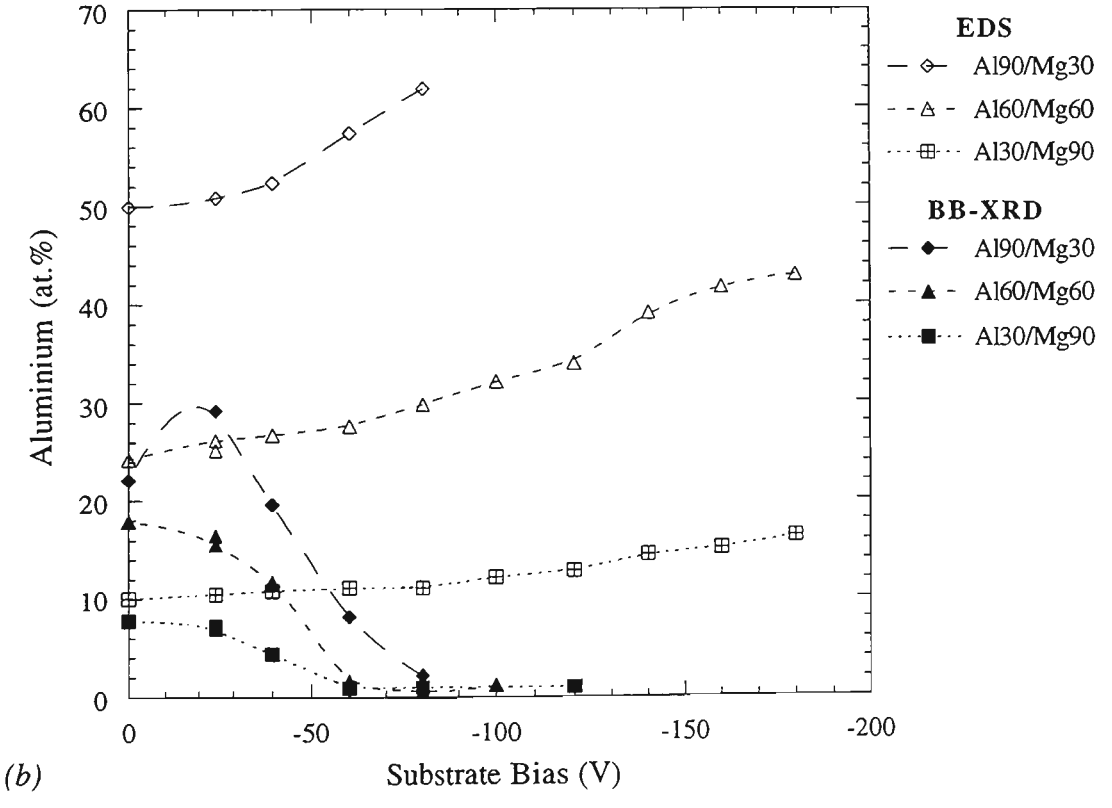

(b)

Fig.9.20 *Comparison between the bulk chemical composition (EDS) and the Al solute content of <0001> fibre textured (Mg) grains in coatings from the Al90/Mg30, Al60/Mg60, and Al30/Mg90 composite targets: (a) solute content calculated from strain-free lattice parameters derived using CGM, (b) solute content estimated from {0002} d-spacing measured in Bragg-Brentano XRD scans.*

that the limit of δ-(Mg) supersaturation was between 23 and 28%Al, and theoretical consideration suggested a limit of about 27%Al (Sect.3.5.2). The present results for this phase are therefore consistent with rapidly solidified alloys, provided that the slight over-estimate of Al solute content in the coatings can be explained by a moderate compressive macrostress.

It should also be noted that the solute content of the δ-(Mg) phase in the coatings was consistently much lower than that of the bulk coating (Fig.9.20). This suggests that a second undetected phase containing a greater proportion of Al was probably present in these coatings. Increasing the substrate bias resulted in a sharp decrease in both the Al content of δ-(Mg) solid solution, and the strength of the <0001> fibre texture (Fig.9.15b). In contrast, the net Al content of the coating was found to increase with bias. Thus, it seems that energetic bombardment inhibited the growth of the textured structure, in favour of an amorphous phase. Furthermore ion bombardment of the δ-(Mg) phase resulted in the rejection of Al from solid solution. The observed reduction in the total Mg content of these coatings can be explained by the preferential growth of an Al-rich amorphous phase at the expense of the textured δ-(Mg) phase.

9.3.3 Amorphous Phase

The work by Arnell and Bates [87,91,98] established that an amorphous phase could be produced in sputtered Al-Mg coatings. This was found to be the only phase present in coatings of between 45 and 50%Mg. The arguments presented above support the assertion that coatings with a Mg content in excess of about 38%, consisted of a supersaturated δ-(Mg) phase in addition to an undetected amorphous phase. The amorphous phase was found to be necessary to account for the observed differences between the Mg content of the δ-(Mg) phase calculated from the strain-free lattice parameter, and the actual Mg content of the entire coating as determined by EDS which was significantly lower.

An attempt was made to estimate the proportion of amorphous phase that was thought to be present in the coatings with the δ-(Mg) phase. The lever rule was used to calculate the proportion of amorphous phase A, for a coating consisting of δ-(Mg) solid solution and amorphous phase:

$$A = \frac{C_{Mg} - C}{C_{Mg} - C_A} \tag{9.1}$$

where C is the Mg content of the bulk coating measured by EDS, C_{Mg} is the proportion of Mg calculated to be present in δ-(Mg) solid solution, and C_A is the Mg content of the amorphous phase. It is immediately apparent that there are two unknown variables in this equation: A and C_A. However, the dramatic change in crystallographic structure for the Al90/Mg30 coatings between -80V and -100V bias, suggests that the composition of the amorphous phase may be very similar to that of the β-Al_3Mg_2 intermetallic phase (Sect.3.5.1). Therefore, the composition of the amorphous phase was assumed to be Al-39% Mg. The composition of Al-50%Mg determined by Arnell and Bates [98] was not used because the δ-(Mg) phase was detected to be present in such coatings.

Table 9.7 Composition of Mg-rich Al-Mg coatings

Target	Bias Voltage	Mg Content (at.%)		% Amorphous
		Coating	δ-(Mg) phase	
Al30/Mg90	earth	90	92	3
	self	90	92	4
	-40V	89	93	7
Al60/Mg60	self 1	74	87	28
	earth	76	82 *	15
	self 1	74	84 *	23
	self 2	75	83 *	19
Al90/Mg30	earth	50	78 *	71
	self	49	71 *	68
	-40V	48	80 *	79

* calculated from d-spacing of Mg {0002} peak in Bragg-Brentano scans, ignoring the influence of residual stress

The percentage of amorphous phase calculated for several Al-Mg coatings are listed in Table 9.7. No data for high bias samples are reported because they were also subject to high amounts of buried Ar, which appears to have influenced the stability of the amorphous phase (Sect.9.3.5). The amount of amorphous phase calculated for the Al30/Mg90 series is considered to be within the expected range of error, such that virtually no amorphous phase was actually present in those coatings. However, as the amount of Mg in the sputter target was increased to Al60/Mg60 and then Al90/Mg30, the proportion of amorphous phase in the coating increased markedly. Approximately two thirds of the material in the coatings deposited at low bias with the Al90/Mg30 are predicted to be amorphous. These values are likely to be inaccurate since they were calculated from Bragg-Brentano diffraction data and hence d-spacing measurements were

not necessarily strain-free. Thus, coatings with between about 40 and 90% Mg are believed to have contained a mixture of both δ-(Mg) and an amorphous phase, with the amorphous fraction decreasing with increases in the Mg content. The amorphous phase was possibly the only phase present in coatings of about Al-39%Mg.

It is fully appreciated that the evidence of amorphous phase in the Mg-rich Al-Mg alloy coatings is circumstantial. Confirmation would necessitate a much more thorough examination of the coating microstructure by transmission electron microscopy and thermal analysis by differential scanning calorimetry. This was considered beyond the scope of this thesis, but is recommended as a potential area for further research.

9.3.4 Stoichiometry and Preferential Resputtering

The stoichiometry of the deposited coatings was influenced by two factors: the sputtered flux composition and energetic particle bombardment. The composition of the sputtered flux from the target controlled the amount of each element initially available to the coating. The flux composition was determined by the relative areas of Al and Mg on the surface of the composite target, and the sputter yield for each metal. However, the final coating composition was affected by the energy and *i/a* ratio of the concurrent ion bombardment. As the bias voltage was increased, and hence the energies of the bombarding argon ions increased, Mg was preferentially resputtered from the alloy coating in greater proportions (Fig.9.4). It is tempting to attribute this effect to the much higher elemental sputter yield for Mg compared to Al [327]. However, this represents an overly simplistic view of the sputtering of alloys, and it is necessary to consider other factors.

The Al and Mg atoms in the alloy coatings were found to exist in close proximity as either supersaturated solid solutions, or possibly an amorphous phase. The collision cascades resulting from ion bombardment of the coatings would therefore interact with intermixed Al and Mg atoms, rather than distinct regions of essentially pure elements. Sputter yield amplification effects [145,146] are possible in cases where the atomic masses of the alloy constituents are very different, although Al and Mg are very similar in mass and no such effects are anticipated. Sputtering of the two different elements would then have been controlled by the surface binding energy. This is often estimated by the latent heat of sublimation corrected to a temperature of 0 K, for which the value of Al is about double that of Mg [250,331]. No data on the latent heat of sublimation for Al-Mg alloys could be found in the literature, and it is presumed that the elemental values are reasonable estimates. Thus, Mg would be preferentially resputtered from Al-Mg coatings due to the lower surface binding energy of Mg atoms.

It might be expected that the changes in the stoichiometry due to preferential resputtering could lead to a modification of the structure of coatings. This was indeed observed to occur for the Al90/Mg30 series coatings. At self bias, the coatings contained approximately equal amounts of Al and Mg , and the coatings were found to have a supersaturated δ-(Mg) solid solution in addition to a possible amorphous phase. With small increases in the bias voltage, Mg was preferentially resputtered from the coatings and the Al solute content of the δ-(Mg) phase was reduced. However, a dramatic decrease in *d*-spacing occurred at -100V bias corresponding to a change from a mixture of δ-(Mg) and amorphous phase to monophase supersaturated α-(Al) solid solution. This change in structure was concurrent with a reduction in Mg content from 38 to 29% (Fig.9.4). It is believed that the modification of alloy composition resulting from ion assisted deposition was the reason for the change in structure.

Another effect of ion bombardment was the modification of solid solubility. It was firmly established that increasing the substrate bias led to a reduction in the solute level of both α-(Al) and δ-(Mg) supersaturated solid solutions (Figs.9.19 and 9.20). This can be understood by considering the kinetics of metastable phase formation. The retention of supersaturated proportions of solute represents a high energy metastable state, and a strong driving force exists for a return to a lower energy state corresponding to reduced solubility. Under minimal ion assistance conditions, it appears that the kinetics required for such transformation were sufficiently sluggish to be completely avoided. Thus, coatings deposited with a low degree of ion assistance were generally the most supersaturated. An exception was noted for the α-(Al) phase for which a modest increase in the substrate bias was necessary to stabilise the strongly fibre textured and supersaturated structure. However, continued increase in substrate bias would have enhanced the adatom mobility, enabling solute atoms to migrate to lower energy states. It also seems feasible that the lattice damage induced by ion bombardment, may have led to enhanced diffusion via the vacancy mechanism. In both cases, it would be expected that increased ion energy would lead to a reduction in the solute level. This finding is opposite to the work of Enders *et al* [241,242] who claimed that increasing the energy of ion bombardment increased the solubility of Mg in the α-(Al) phase. However, these latter conclusions seem to have been based on misinterpretation of glancing angle XRD results.

9.3.5 Argon Burial

Extreme differences were found between the amount of Ar burial in coatings that contained more than about 38%Mg compared with those below this limit. Coatings prepared from the Al115/Mg5 and Al105/Mg15 targets, all consisted of single phase α-(Al) supersaturated solid solution, and contained less than 1%Ar for all bias voltages. In comparison, for the coatings prepared from the Al30/Mg90 and Al60/Mg60 targets, the Ar content increased dramatically as the bias was increased beyond -40V, and tended to reach a maximum of about 20% Ar. Even higher amounts of buried Ar could be achieved, but short term ageing resulted in desorption of Ar from the coating and rapid oxidation. Of particular interest is the behaviour of the coatings prepared with the Al90/Mg30 target. As the bias voltage was increased to -80V, the Ar content of coatings climbed dramatically. Further increases in bias voltage resulted in very little burial of Ar due to the transformation to an α-(Al) phase below 38%Mg.

These results are perplexing since previous studies generally indicated that the concentration of buried Ar increased parabolically with increasing bias voltage (Sect.2.4.3). It has been commonly assumed that Ar burial is caused by the entrapment of implanted energetic ions. In the Al-Mg alloy coatings, the δ-(Mg) phase appears to have a much greater affinity for retention of Ar than the α-(Al) phase deposited under identical conditions of ion assistance. There must obviously be an alternative mechanism for the retention of Ar in Al-Mg alloy coatings. The Ar may possibly be *alloyed* with the δ-(Mg) phase. There are no published experimental investigations regarding the solid solubility of Ar in (Mg) phase [332], although an analysis of the stability of a hypothetical MgAr compound has been made [333]. However, it was established for coatings deposited from both pure Al and pure Mg targets (Chaps.6 and 7), that the buried Ar was not significantly distributed in solid solution. It would seem highly unlikely that the buried Ar would then be retained in δ-(Mg) solid solution. Instead, it appears that the Ar contributed to amorphisation of the δ-(Mg) phase, and was probably retained in the amorphous phase. Such a model has precedent in work on other alloy systems [97,263]. An alternative explanation is that the diffusion of Ar in the δ-(Mg) phase was much slower than in the α-(Al) phase, resulting in the observed differences in Ar retention. Some evidence in favour of this explanation was found in the published diffusivity data for Ar in Mg [334], which was several orders of magnitude slower than Mg self-diffusion. Without further work, a more satisfactory explanation cannot be offered.

9.4 Summary

Each Al-Mg coating contained no more than one crystalline phase. Coatings with up to about 35%Mg possessed only minor amounts of (Al) crystallinity when deposited with minimal ion assistance. It is presumed that an amorphous phase existed as the major component in these coatings, perhaps as a result of trace amounts of contamination. Increasing the energy of ion assistance resulted in preferential resputtering of Mg, and produced coatings consisting entirely of (Al) solid solution with a very strong <111> fibre texture. The strongest (Al) fibre textures retained the greatest proportion of Mg solute (<30%Mg). The solute content of (Al) phase was reduced as the substrate bias was increased further. The residual biaxial stress in the (Al) phase was tensile at low bias voltages and became compressive above a bias of about -50V. The presence of tensile stresses at low bias supported the suggestion that trace amounts of contaminants were present in those coatings, and that they were removed by ion bombardment as bias was increased. These impurities were thought to derive from epoxy resin exposed at the joints of the composite targets.

Coatings with more than about 38%Mg consisted of the (Mg) solid solution with some Al supersaturation (<30%Al), plus an amorphous phase. It was assumed that the amorphous phase had a composition of about 38%Mg, which is equivalent to that of β-Al_3Mg_2. The (Mg) phase in coatings prepared with minimal ion assistance had a very strong <0001> fibre texture, which rapidly decayed as substrate bias was increased. Ion bombardment caused the rejection of Al from (Mg) solid solution, even though the coating was subject to preferential resputtering of Mg. It was also shown that the microstructure of Al-Mg coatings could be altered from a mixture of (Mg) and amorphous phase to single-phase (Al), in response to the compositional changes afforded by ion bombardment.

Burial of Ar in Al-Mg coatings was a serious concern. Coatings with more than about 20%Ar tended to blacken after ambient ageing, due to desorption of entrapped Ar and severe oxidation of the remnant porous structure. The Ar content increased sharply with bias, for coatings with more than 38%Mg, whereas virtually no Ar was present in coatings containing less than about 35%Mg. Entrapment of Ar was associated with the (Mg) phase which eventually led to its amorphization. It was suggested that the diffusion of Ar in (Mg) may have been much slower than in (Al), leading to accumulation of very large amounts of inert gas in the coatings. Apart from the coatings affected by Ar burial, the visual appearance of all Al-Mg coatings was highly lustrous, and similar to that of Al and Mg coatings.

Chapter 10

Zinc-Magnesium Alloy Coatings

10.1 Deposition Parameters

The five Zn/Mg composite targets described in Sect.4.2.2 were used to prepare a range of Zn-Mg alloy coatings on Si wafers, with substrate bias voltages from earth to -180V. Each coating series utilised the same fully magnetised M3 magnet, and the high voltage power supply operated at 100 W. The important parameters for each series are listed in Tables 10.1 to 10.5.

The magnetron conditions were generally very stable throughout each coating run, with the magnetron voltage remaining constant within ±4V. There were three notable exceptions to this observation. Firstly, a large drop in magnetron voltage was observed for the first sample in the Zn60/Mg60 series. This was actually an instrumental effect due to interference by rf leakage from a nearby rf-power magnetron sputtering system. During the deposition of this first sample, it was noted that when the rf discharge was switched on, the magnetron voltage for the Zn60/Mg60 target dropped abruptly. The rf leakage was later found to be the result of a poorly earthed component on the rf sputtering chamber. Secondly, the discharge for the Zn20/Mg100 target was highly unstable during the first hour of operation (Table 10.4), with some sudden large jumps in magnetron voltage (~5 V) followed by gradual drift. This problem was similarly encountered with one of the Al/Mg composite targets (Chap.9), although the changes in voltage were less severe in the present case. The discharge also briefly failed due to arcing for the first sample in this series. This behaviour was discussed in Sect.4.2.4. As a check on the possible variation in sputtered flux composition, self biased coatings were prepared at the beginning and end of each coating run for all of the composite targets.

Table 10.1 Deposition parameters for coatings prepared from Zn90/Mg30 target. Other process variables: base pressure 80 μPa; magnetron power 100 W (high voltage supply); probe current 0.377 mA at start, 0.384 mA at end; deposition time 4 minutes per sample.

Magnetron Conditions		Substrate	Coating Mass
Voltage (V)	Current (A)	Bias (V)	(μg)
517	0.19	self (-25)	613
516	0.19	-40	589
515	0.19	-60	540
514	0.19	-80	506
514	0.19	-100	470
514	0.19	-120	453
514	0.19	-140	431
513	0.19	-160	415
513	0.19	-180	392
514	0.19	self (-25)	594
509	0.19	earth	598

Table 10.2 Deposition parameters for coatings prepared from Zn60/Mg60 target. Other process variables: base pressure 73 μPa; magnetron power 100 W (high voltage supply); probe current 0.508 mA at start, 0.515 mA at end; deposition time 4 minutes per sample.

Magnetron Conditions		Substrate	Coating Mass
Voltage (V)	Current (A)	Bias (V)	(μg)
439-422	0.22-0.23	self (-25)	471
422	0.23	-40	419
422	0.23	-60	433
420	0.23	-80	463 *
421	0.23	-100	381
421	0.23	-120	351
421	0.23	-140	351
422	0.23	-160	328
424	0.23	-180	325
426	0.23	self (-25)	457
422	0.23	earth	458

* coating deposited for 4 min 15 sec

Table 10.3 Deposition parameters for coatings prepared from Zn40/Mg80 target. Other process variables: base pressure 290 μPa; magnetron power 100 W (high voltage supply); probe current 0.532 mA at start, 0.537 mA at end; deposition time 4 minutes per sample.

Magnetron Conditions		Substrate	Coating Mass
Voltage (V)	Current (A)	Bias (V)	(μg)
386	0.25	self (-25)	382
384	0.25	-40	335 *
383	0.25	-60	366
383	0.25	-80	351
382	0.25	-100	340
381	0.25	-120	325
381	0.25	-140	321
381	0.25	-160	304
382	0.25	-180	297
384	0.25	self (-26)	373
379	0.25	earth	393

* coating mass in error due to substrate breakage

Table 10.4 Deposition parameters for coatings prepared from Zn20/Mg100 target. Other process variables: base pressure 96 μPa; magnetron power 100 W (high voltage supply); probe current 0.626 mA at start, 0.648 mA at end; deposition time 5 minutes per sample.

Magnetron Conditions		Substrate	Coating Mass
Voltage (V)	Current (A)	Bias (V)	(μg)
359	0.27	self (-25)	365 #
356-359	0.27	-40	371 *
356-362	0.27	-60	354
356-360	0.27	-80	355
354-356	0.27	-100	360
359-360	0.27	-120	343
355-362	0.27	-140	336
357-359	0.27	-160	324
356-359	0.27	-180	308
359-360	0.27	self (-25)	355
354	0.27	earth	370

discharge extinguished via an arc for approximately 2 seconds during this deposition

* coating deposited for 5 min 10 sec

Table 10.5 Deposition parameters for coatings prepared from Zn10/Mg110 target. Other process variables: base pressure 74 μPa; magnetron power 100 W (high voltage supply); probe current 0.650 mA at start, 0.669 mA at end; deposition time 5 minutes per sample.

Magnetron Conditions		Substrate	Coating Mass
Voltage (V)	Current (A)	Bias (V)	(μg)
352	0.27	self (-26)	272
350	0.27	-40	264
349	0.28	-60	262
348	0.28	-80	263
347	0.28	-100	271
346	0.28	-120	276
346	0.28	-140	277
346	0.28	-160	261 *
345	0.28	-180	274
346	0.28	self (-26)	266
341	0.28	earth	280

* coating mass in error due to substrate breakage

10.2 Results and Discussion

10.2.1 Ion/Atom Flux Ratio

The *i/a* ratios for the five Zn/Mg composite targets are shown in Fig.10.1 as a function of the radial fraction of Mg on the target surface, f_{Mg}. The results for monolithic Zn and Mg targets are also included for comparison. Error bars of ±15% are indicated, and represent a conservative estimate of the expected error in the measurement. Targets with a higher proportion of Mg provided a higher *i/a* ratio. The ion current when normalized by the magnetron current was constant (within an error of ±12%) for all coatings. This is to be expected since all of these coatings were produced using the same M3 magnet assembly. The increase in *i/a* ratio with Mg content was therefore due to changes in the net sputtering rate of the target.

10.2.2 Mass Deposition Rate

The mass deposition rate for each of the Zn-Mg coatings is shown as a function of the substrate bias voltage in Fig.10.2. The results for Zn and Mg coatings are also included for comparison. The deposition rates for all of the composite targets were intermediate between those of Zn and Mg. Increasing the Mg radial fraction of the composite targets resulted in a decrease in the mass deposition rate, consistent with the slower deposition rate for Mg compared with Zn. Substrate bias of between earth and about -40V tended to have little affect on deposition rate. Results for earth bias samples are not shown, as the deposition rates were almost identical to those of self bias coatings.

Generally the mass deposition rate showed an exponential dependence on substrate bias, as indicated in Fig.10.2 by the linear curve fit for the semi-logarithmic axes. The slope of this line was not always negative, however, which suggested that some coatings actually increased in mass as bias was raised. Those targets that provided a Zn-rich sputtered flux (Zn90/Mg30, Zn60/Mg60, Zn40/Mg80) all showed an exponential decrease in deposition rate as the bias was increased above about -40V. This trend is due to resputtering induced by ion bombardment during deposition. In contrast, the mass deposition rate for coatings deposited with an Mg-rich sputtered flux (Zn20/Mg100, Zn10/Mg110), was relatively constant and perhaps increased slightly with increasing bias voltage. Similar slightly positive departures in the deposition rate were noted in the results for Zn60/Mg60 series coatings. This result is counterintuitive since elevated substrate bias voltages invariably cause resputtering of the coating, and therefore a reduction in mass. The reason for this effect is discussed in Sect.10.2.4.

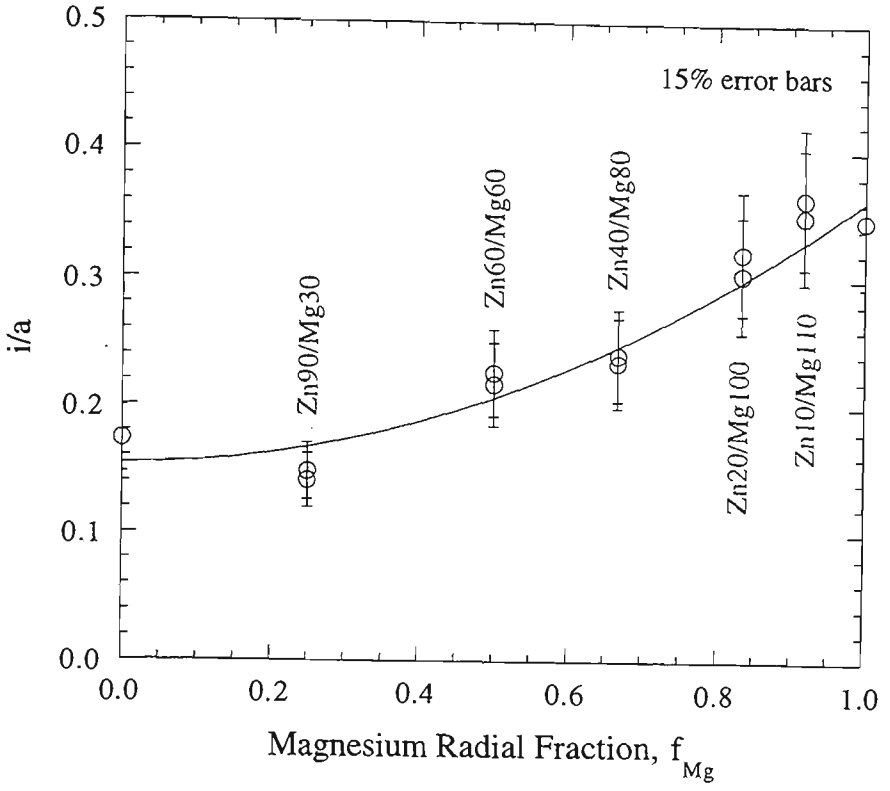

Fig.10.1 *Ion/atom arrival rate ratio as a function of the Mg radial fraction in Zn/Mg composite targets.*

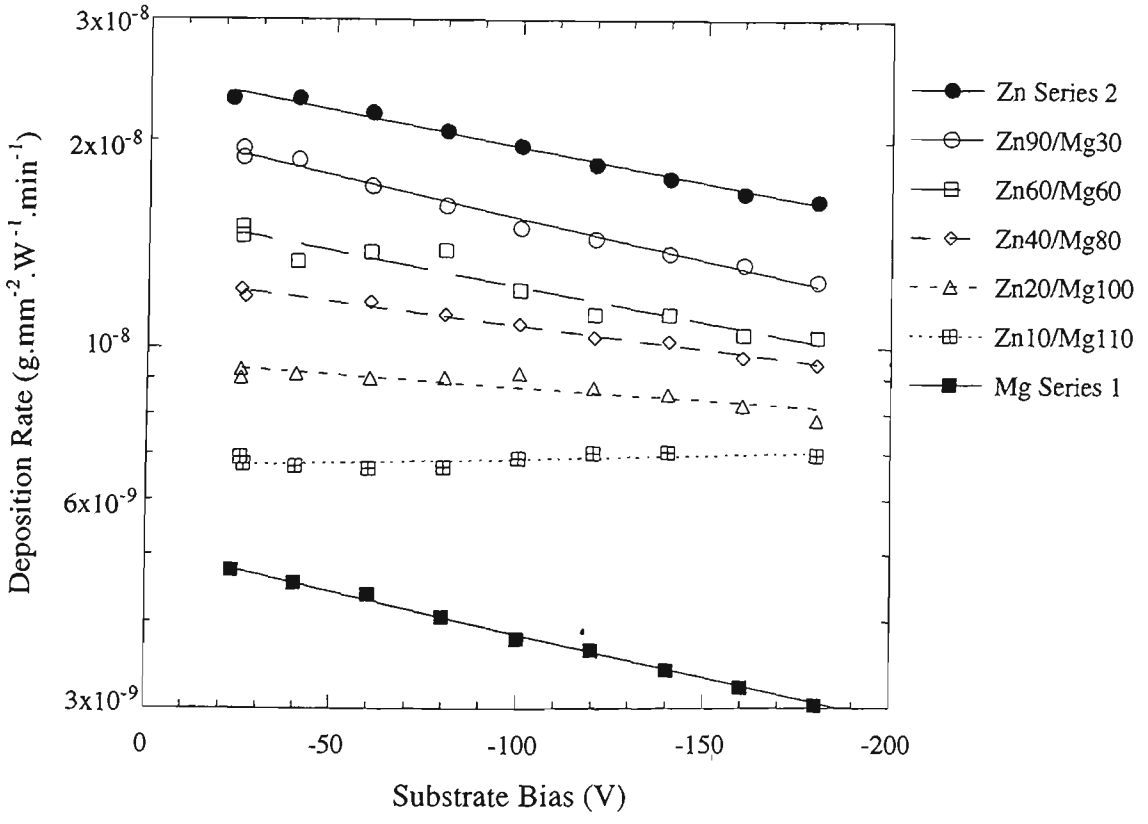

Fig.10.2 *Mass deposition rate for sputtered Zn-Mg coatings. Note the ordinate axis is semi-logarithmic.*

10.2.3 Visual Examination

With only a few exceptions, immediately after removal from the sputtering chamber, all of the Zn-Mg coatings were highly lustrous and metallic white in colour. The surface appearance replicated the highly polished finish of the Si wafer substrates. The noted exceptions were for the Zn90/Mg30 series coatings produced with earth, self and -40V bias. The surface of these coatings were very similar to those of pure Zn coatings (Chap.5), with a blue-grey colour and matt appearance. However, increasing the substrate bias to -60V and higher resulted in the elimination of this surface condition in favour of the lustrous finish characteristic of all other Zn-Mg coatings. Additionally, some of the Zn20/Mg100 coatings were found to have a slightly frosted surface appearance, particularly for the -100V sample.

Between the time of coating preparation and evaluation of chemical composition by EDS (a period of between one and four weeks), the -180V samples from the Zn40/Mg80 and Zn10/Mg110 series were noted to have developed blackened regions in the centre of each coated area. This blackened region was observed with the Mg-rich Al-Mg alloy coatings (Chap.9) and corresponded to regions of heavy oxidation. Approximately fourteen months after deposition of the coatings, this blackened oxide was observed to have developed on many more of the Zn-Mg samples from the composite target series. The coated surfaces of all the Zn-Mg samples prepared with the composite targets are shown in Fig.10.3. This photograph was taken approximately two years after deposition, and the coatings were unchanged from the observations made after fourteen months ageing. Throughout this ageing period, each sample was stored individually in a sealed polyethylene bag and only removed for SEM, EDS, and XRD analysis.

The coatings most severely affected by the surface blackening were those from the Zn90/Mg30, Zn20/Mg100 and Zn10/Mg110 targets, deposited with -100V bias or more. The coatings produced with the remaining two targets were affected at higher bias voltages. The reasons for these differences in behaviour are not entirely clear, but seem to be related to the burial of inert gas (Sect.10.2.4). Most of the Mg-rich Zn-Mg coatings produced at low substrate bias also showed signs of surface oxidation and staining, presumably due to handling over this ageing period.

Finally, the coatings deposited from the Zn10/Mg110 composite target at low bias voltages (self and -40V bias), were found to develop regions of delaminated blisters, after an ageing period of about a year. The blistered regions tended to initiate at small defects in the coating, such as pinholes induced by physical damage. From these locations, the blistered regions appeared to have grown outwards, eventually covering the entire surface

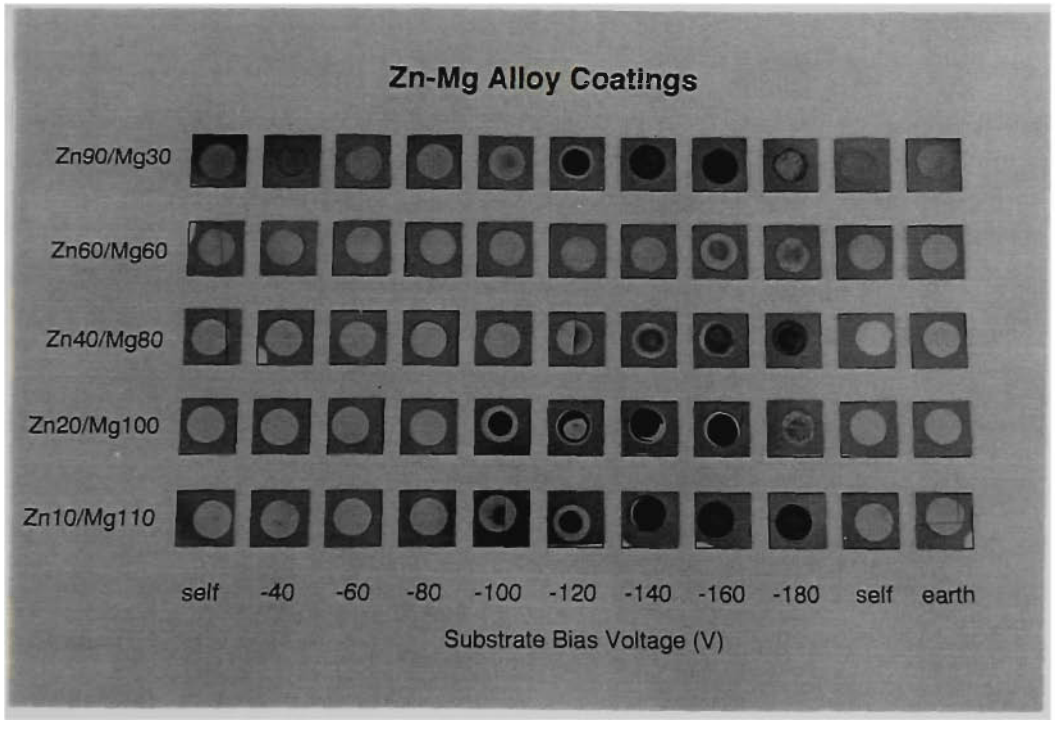

Fig.10.3 *Photographs of Zn-Mg coatings, taken about two years after deposition.*

in the case of the -40V bias sample. Similar blistering was reported for some of the Al-Mg coatings (Chap.9), and is thought to indicate the presence of residual biaxial compressive stress in the coatings. Subsequent CGM analysis of these coatings (Sect.10.2.7) confirmed the presence of compressive stresses in these Zn-Mg coatings.

10.2.4 Chemical Composition

The chemical compositions of the various coatings are presented in Figs.10.4 and 10.5. The Mg content of the deposited coatings are shown in Fig.10.4, relative only to the total amount of Zn and Mg. Figure 5 indicates the measured Ar content of the sputtered coatings. These buried Ar content of the Zn-Mg coatings were very high in comparison to common experience for sputtered coatings, but are comparable to the results obtained for some of the Al-Mg coating compositions (Chap.9). The Mg-rich coatings produced from the Zn20/Mg100 and Zn10/Mg110 targets seemed to be particularly susceptible to the retention of Ar.

The composition of the sputtered flux from each of the composite targets appeared to be relatively stable throughout the deposition runs. The composition of the self bias coatings differed by no more than ±1 at.% from the beginning to the end of each coating run (Fig.10.4). This result is counter to expectations, since minor compositional variations were anticipated due to differential etching rates of the two metals on the target surface (Sect.4.2.4). It is thought that the large differences between the sputter yields of Zn and Mg were largely compensated by the greater density of Zn, such that the volumetric erosion rate of each metal was quite similar. Hence a stepped erosion profile was not prominent on the Zn/Mg composite targets, and the composition of the target did not drift significantly with target usage. It should be recognised, however, that the Zn/Mg targets were only operated for a total time of less than two hours each, and compositional variations may develop with greater usage.

The EDS analysis revealed that all of the coatings were susceptible to preferential resputtering of Mg resulting from energetic ion bombardment during deposition (Fig.10.4). This result is perhaps counterintuitive when one considers the much higher elemental sputter yield of Zn in comparison with Mg. However, it must again be emphasised that the sputtering behaviour of alloys is much different to that of the component metals in their elemental form (Sect.2.4.4). The coatings from the Zn40/Mg80 and Zn20/Mg100 targets showed the greatest reduction in Mg content with increasing bias. In comparison, the more dilute coatings produced from the Zn60/Mg60 and Zn10/Mg110 targets were only slightly affected by preferential resputtering of Mg. Thus, the susceptibility to preferential resputtering appeared to be related to the coating

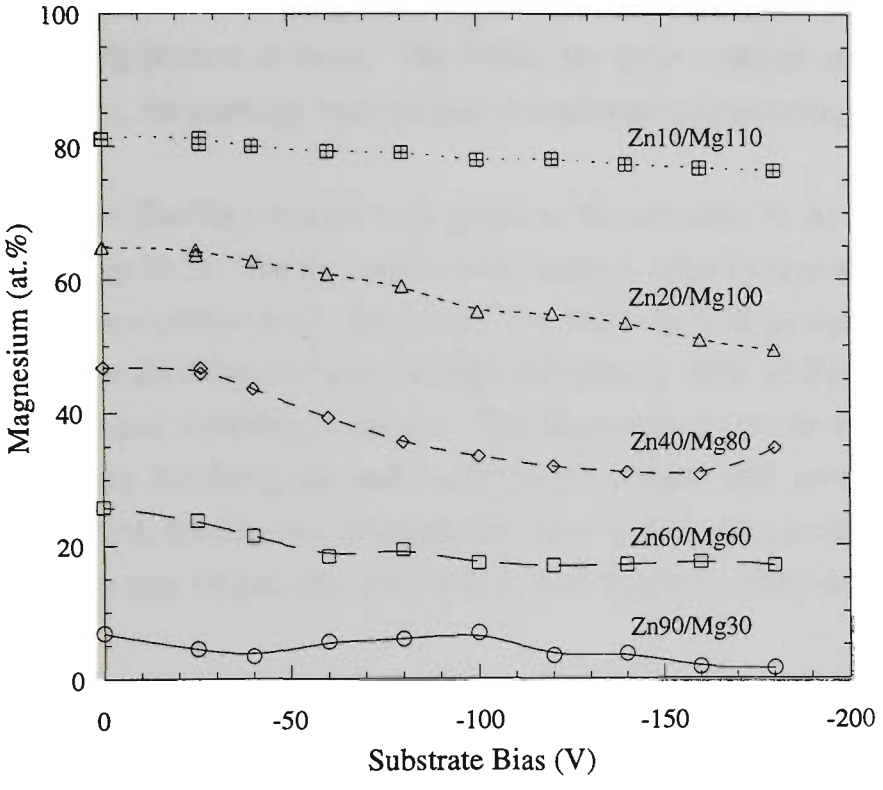

Fig.10.4 *Mg content of sputtered Zn-Mg coatings, relative to the total amount of Zn and Mg.*

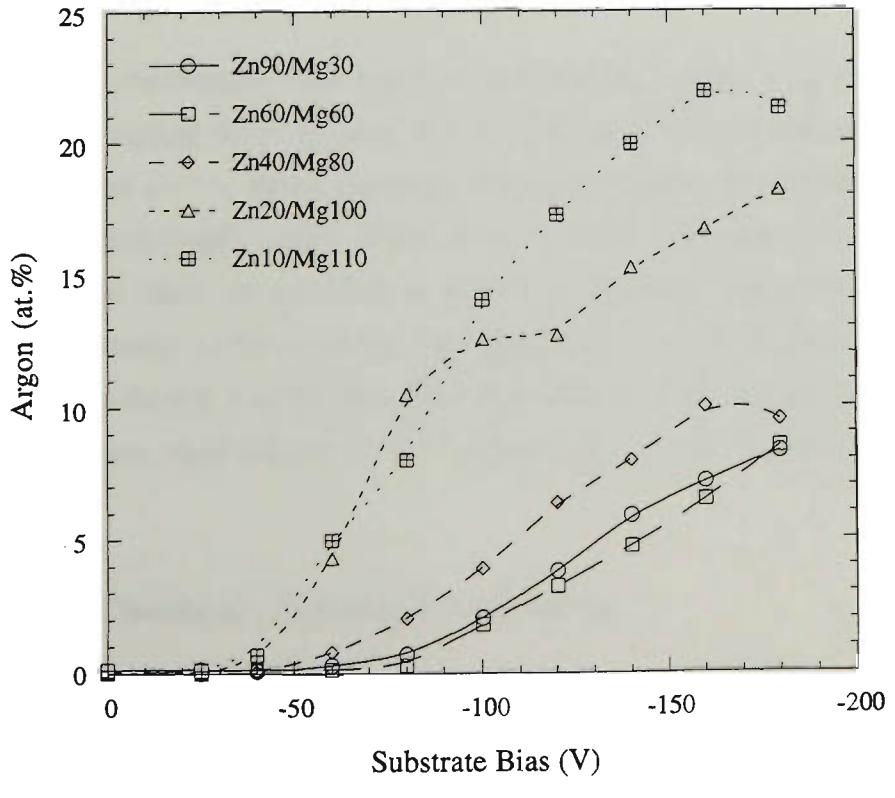

Fig.10.5 *Ar content of sputtered Zn-Mg coatings, relative to the total amount of Zn, Mg and Ar.*

composition rather than to any small differences in *i/a* ratio (Fig.10.1). The Mg content of the Zn90/Mg30 series coatings was difficult to measure accurately due to the small proportion of Mg present in them. The results for these coatings suggested that above about -100V bias, the coatings were subject to preferential resputtering of Mg.

All of the Zn-Mg coatings were prone to the retention of Ar at sufficiently high bias voltages (Fig.10.5). The Ar content of all coating series increased as the bias voltage was raised above a critical level. Buried Ar was first detectable in significant proportions at about -40V for Zn10/Mg110 and Zn20/Mg100 targets, -60V for Zn40/Mg80, and -80V for Zn60/Mg60 and Zn90/Mg30 targets. The highest levels of Ar were detected in the coatings from the Zn10/Mg110 and Zn20/Mg100 targets, with proportions as high as 22%Ar. Therefore, the Mg-rich coatings seemed to be the most susceptible to retention of Ar, although this may be partially attributed to their higher *i/a* ratios during deposition.

The presence of buried Ar in the coatings is thought to have been responsible for the unusual variation in the mass deposition rates for the Mg-rich coatings (Fig.10.2). It was noted above that increasing the substrate bias led to the preferential loss of Mg from the coatings, in addition to the entrapment of an increasing proportion of Ar. Thus, the Mg atoms in the coating were partially replaced by Ar atoms, which have a considerably greater atomic mass. The entrapped Ar therefore had the effect of simply adding extra mass to the deposited coating, without serving any functional purpose.

A good correlation was apparent between the amount of Ar detected in each coating and the ageing time required for the formation of the blackened oxide on their surface. In each series, those coatings with the highest Ar content were the first to blacken. The Zn60/Mg60 series which was the least susceptible to the retention of Ar was also the least likely to succumb to surface blackening. However, the amount of Ar required to be present in the coatings for blackening to occur tended to be higher for the Mg-rich coatings than it was for the Zn-rich coatings. This suggests that the blackening and Ar burial were each related to the coating composition rather than directly to each other.

10.2.5 Chemical Composition Profiles

The variation in chemical composition across the diameter of the coated area of a limited number of samples was evaluated by EDS compositional line profiles. The line profiles for the -120V and -180V samples in the Zn10/Mg110 series are shown in Fig.10.6, and are representative of the general observations for all other coatings. For the -120V sample (Fig.10.6a), the Zn and Mg content across the diameter of the coated area

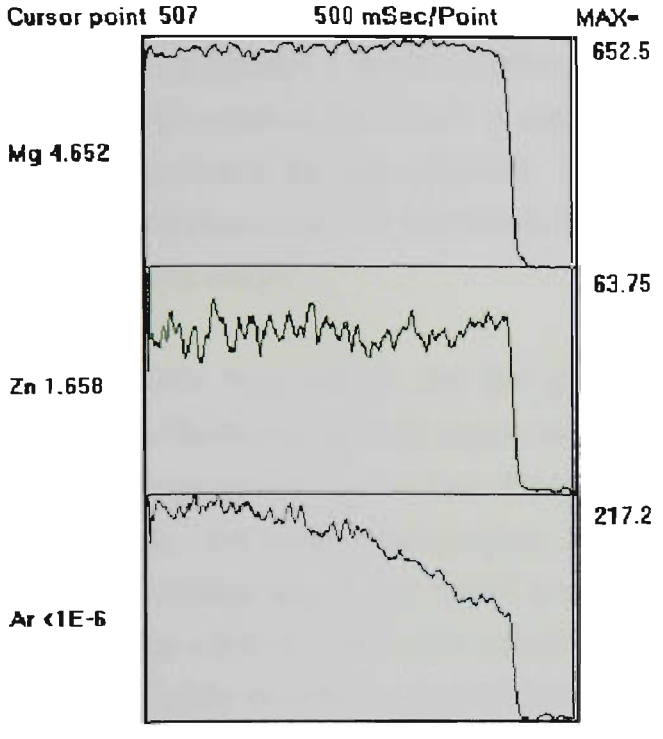

(a)

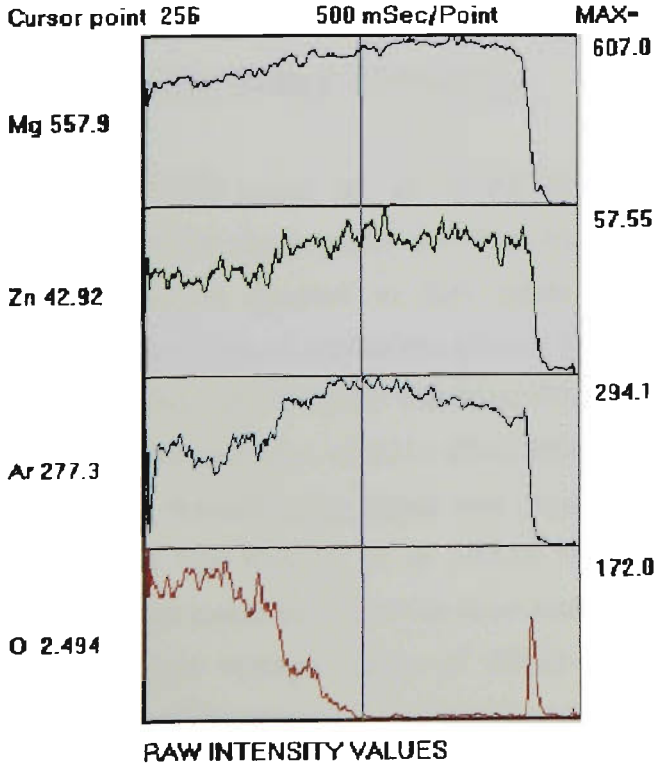

(b)

Fig.10.6 Chemical composition line profiles for Zn10/Mg110 Series coatings: (a) -120V bias; and (b) -180V bias. The profile extends from the centre of the coated area (left) to the outer edge (right).

was very uniform. The Ar content tended to decrease over the outer one or two millimetres diameter. This is possibly due to the inherent concentration of the ion current at a central spot (Sect.2.2.4), or perhaps a shielding effect of the cover mask. In either case, the higher Ar content at the centre of the sample is expected to correlate with a local *i/a* ratio which is slightly higher than at the outer diameter. Following this observation, it is important to note that the compositional data reported in Sect.10.2.4 corresponds to the composition at the centre of each sample.

In contrast to the -120V bias sample, the line profile for the -180V sample (Fig.10.6b) includes part of a blackened oxidised region at the centre of the coated area. In the SEM micrograph, this area appears darker than the surrounding coating due to the lower atomic mass of the oxide. For some other samples, this area appeared very bright due to charging effects. The affected region was found to contain very high amounts of oxygen, and the Ar content was relatively lower than outside this region. The Zn and Mg contents were also reduced slightly in order to account for the high amount of oxygen. Following the arguments presented in Chap.9, it is believed that oxidation of the coating was coincident with the release of entrapped Ar.

10.2.6 Bragg-Brentano X-Ray Diffraction

The Bragg-Brentano XRD scans for all of the Zn-Mg coatings are shown in Figs.10.7 to 10.11. Many of the sharp peaks and high background between 32.5° and 37.5° (eg. Fig.10.8), should be ignored as they relate to the Si wafer substrate (Sect.4.4.1). Significant proportions of crystalline phases were detected only in coatings deposited from the Zn90/Mg30, Zn20/Mg100 and Zn10/Mg110 targets. The latter two series of coatings were found to include a <0001> fibre textured (Mg) phase (Figs.10.10 and 10.11). A <0001> fibre textured (Zn) phase was present in the Zn90/Mg30 series coatings, in addition to what was thought to be <111> fibre textured Mg_2Zn_{11} phase (Fig.10.7). A range of different intermetallics were also detected in the Zn90/Mg30 series coatings deposited with low bias voltages, some of which could not be identified. The coatings prepared from the Zn60/Mg60 and Zn40/Mg80 targets provided diffraction scans with only a single broad, low intensity peak (Figs.10.8 and 10.9), that is characteristic of an amorphous phase. The individual phases of the coatings are described at greater length in the following text.

(Zn) and Mg_2Zn_{11} Phases

The XRD scans of the Zn90/Mg30 series coatings were dominated by a single very intense diffraction peak that was observed to split into two separate peaks as the bias

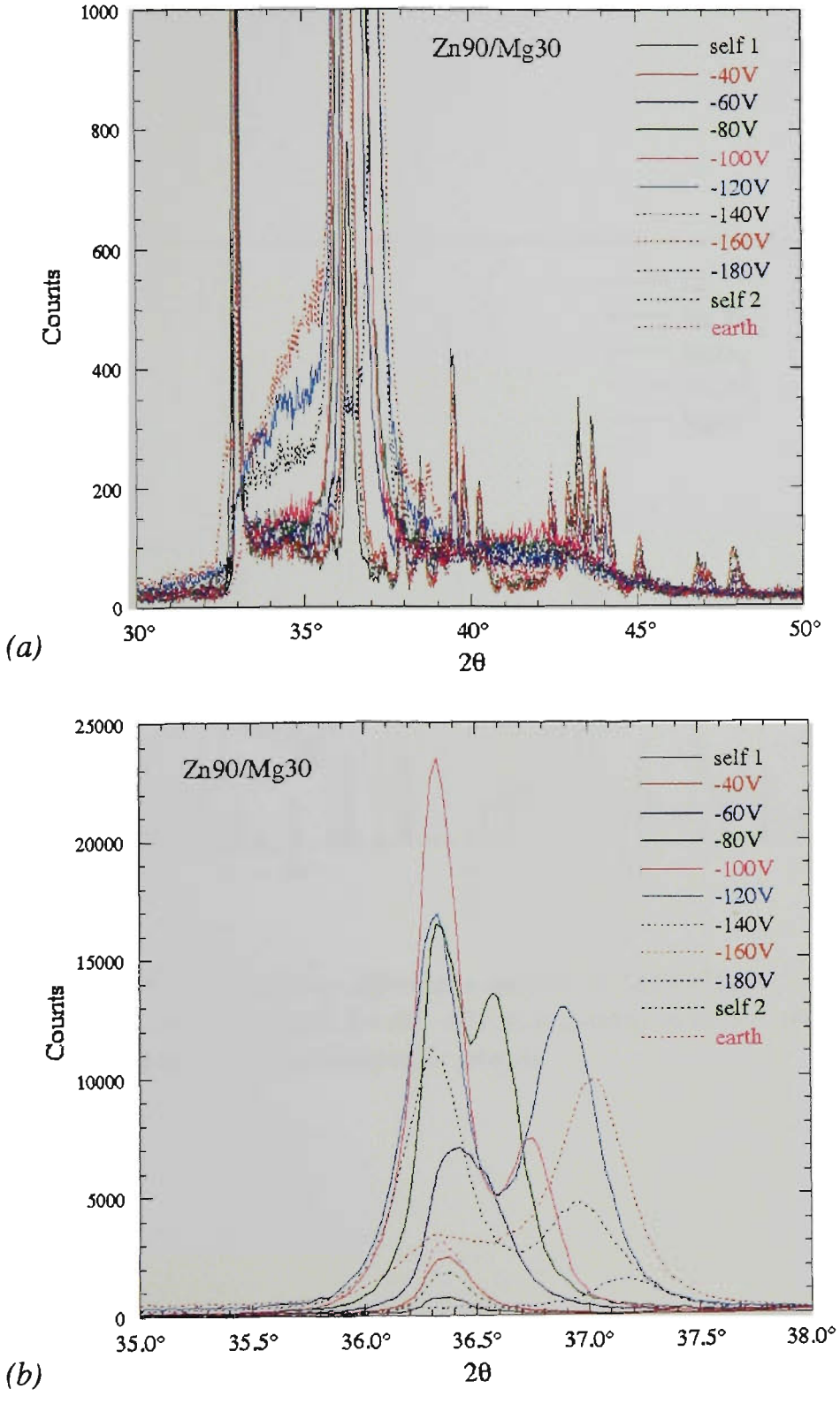

Fig.10.7 *Bragg-Brentano X-ray diffraction spectra for Zn90/Mg30 Series coatings*
(a) low intensity peaks
(b) high intensity Zn {0002} and Mg_2Zn_{11} {222} diffraction peaks

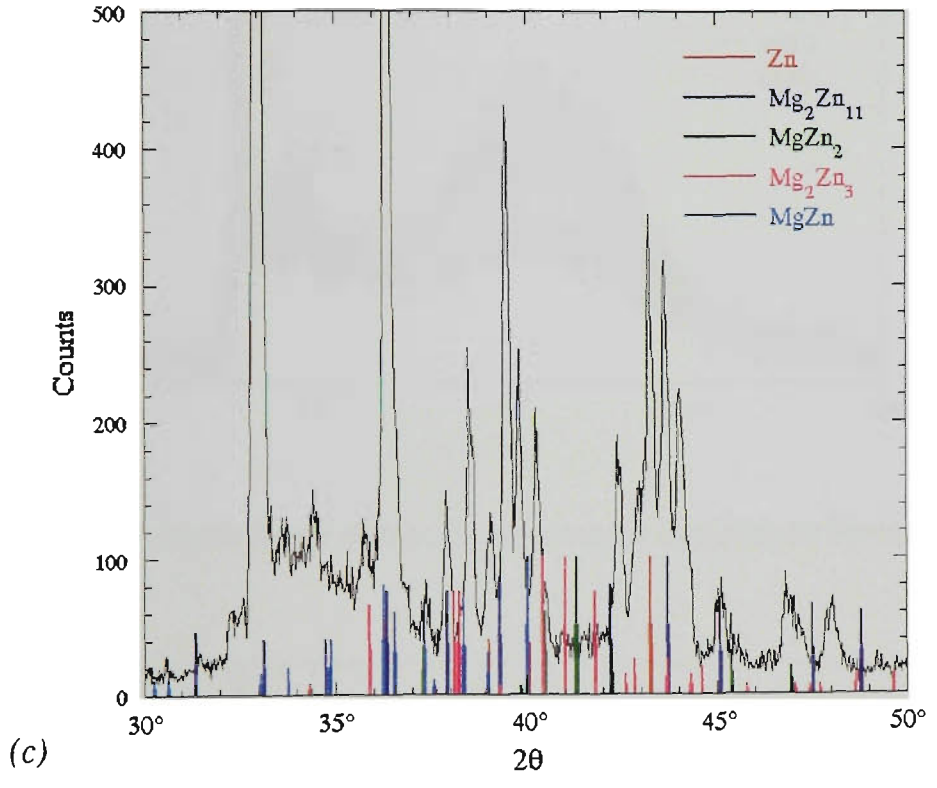

Fig.10.7 *Bragg-Brentano X-ray diffraction spectra for Zn90/Mg30 Series coatings (c) low intensity peaks for the -40V bias coating matched against various Mg-Zn intermetallic phases*

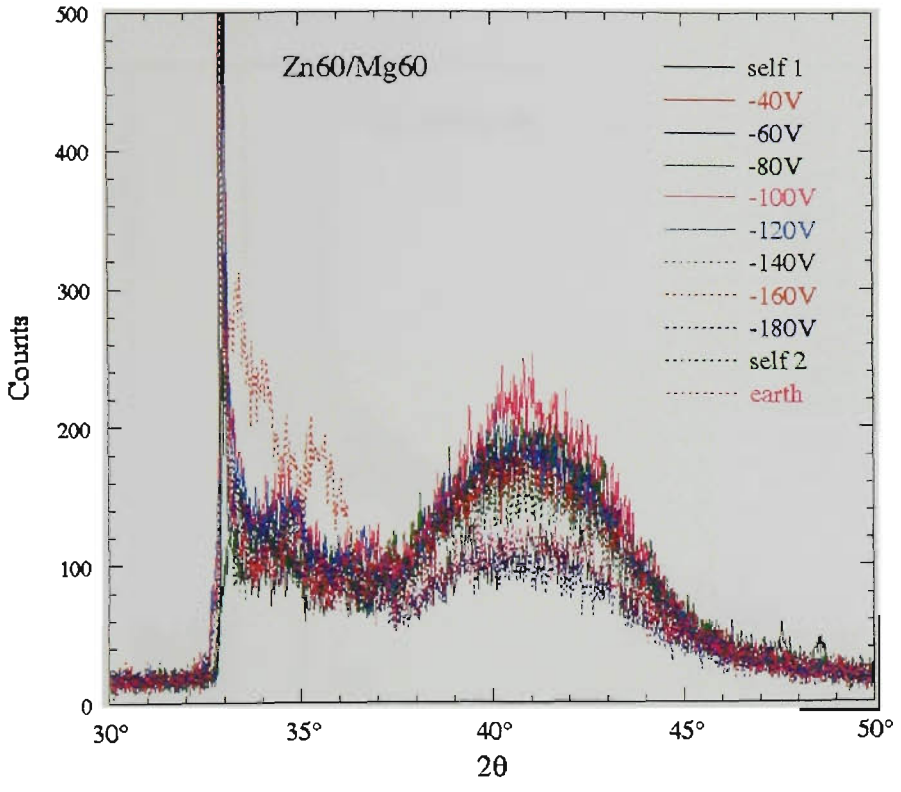

Fig.10.8 *Bragg-Brentano X-ray diffraction spectra for Zn60/Mg60 Series coatings*

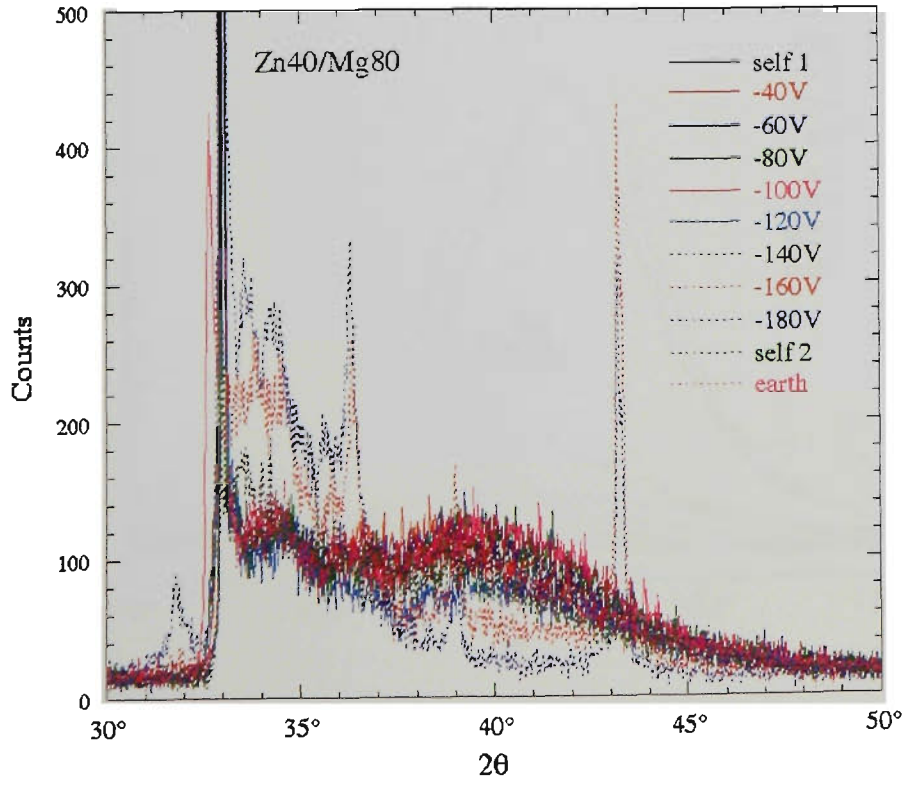

Fig.10.9 *Bragg-Brentano X-ray diffraction spectra for Zn40/Mg80 Series coatings*

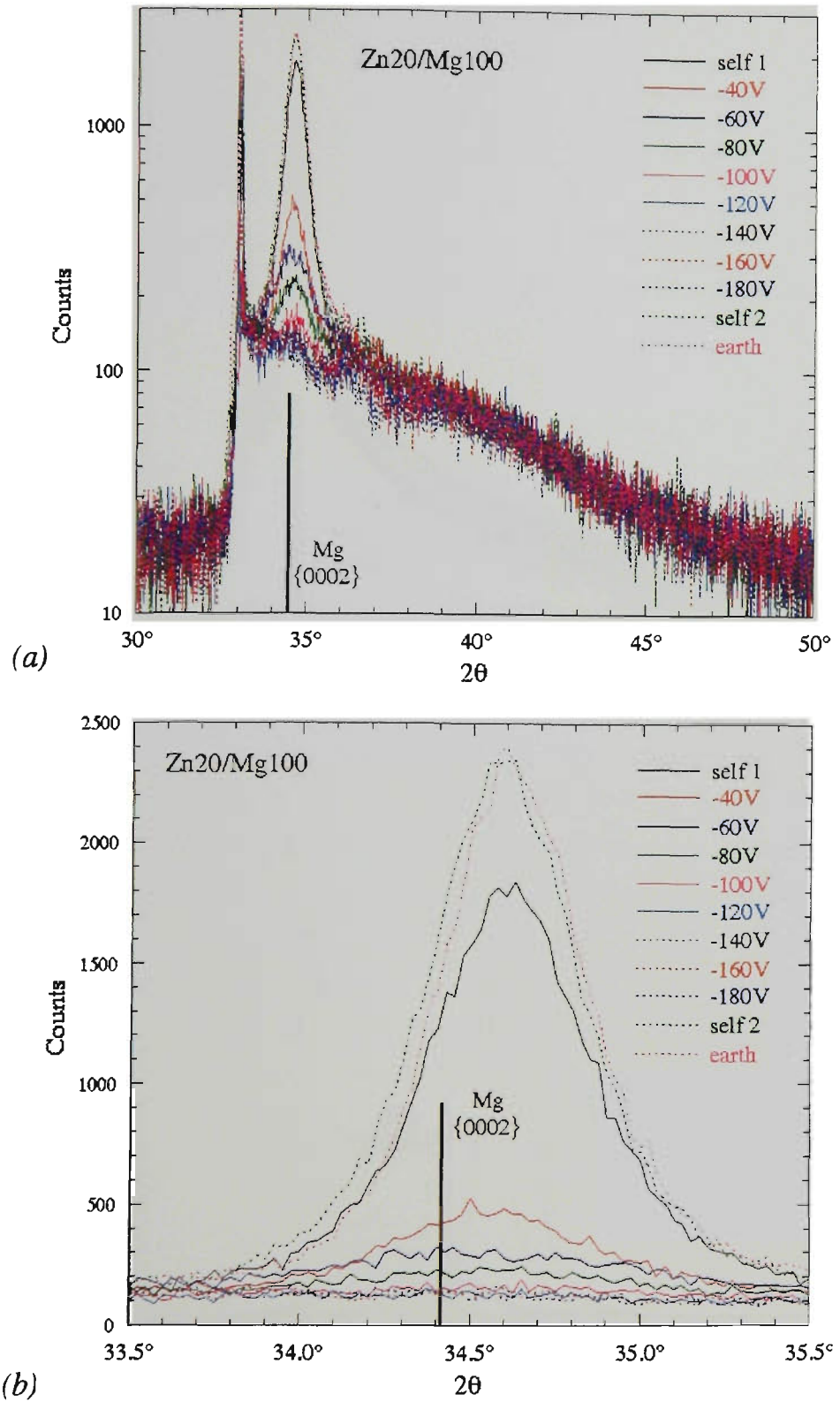

Fig.10.10 Bragg-Brentano X-ray diffraction spectra for Zn20/Mg100 Series coatings (a) semi-logarithmic scale showing amorphous background at about 40° (b) high intensity Mg {0002} diffraction peak

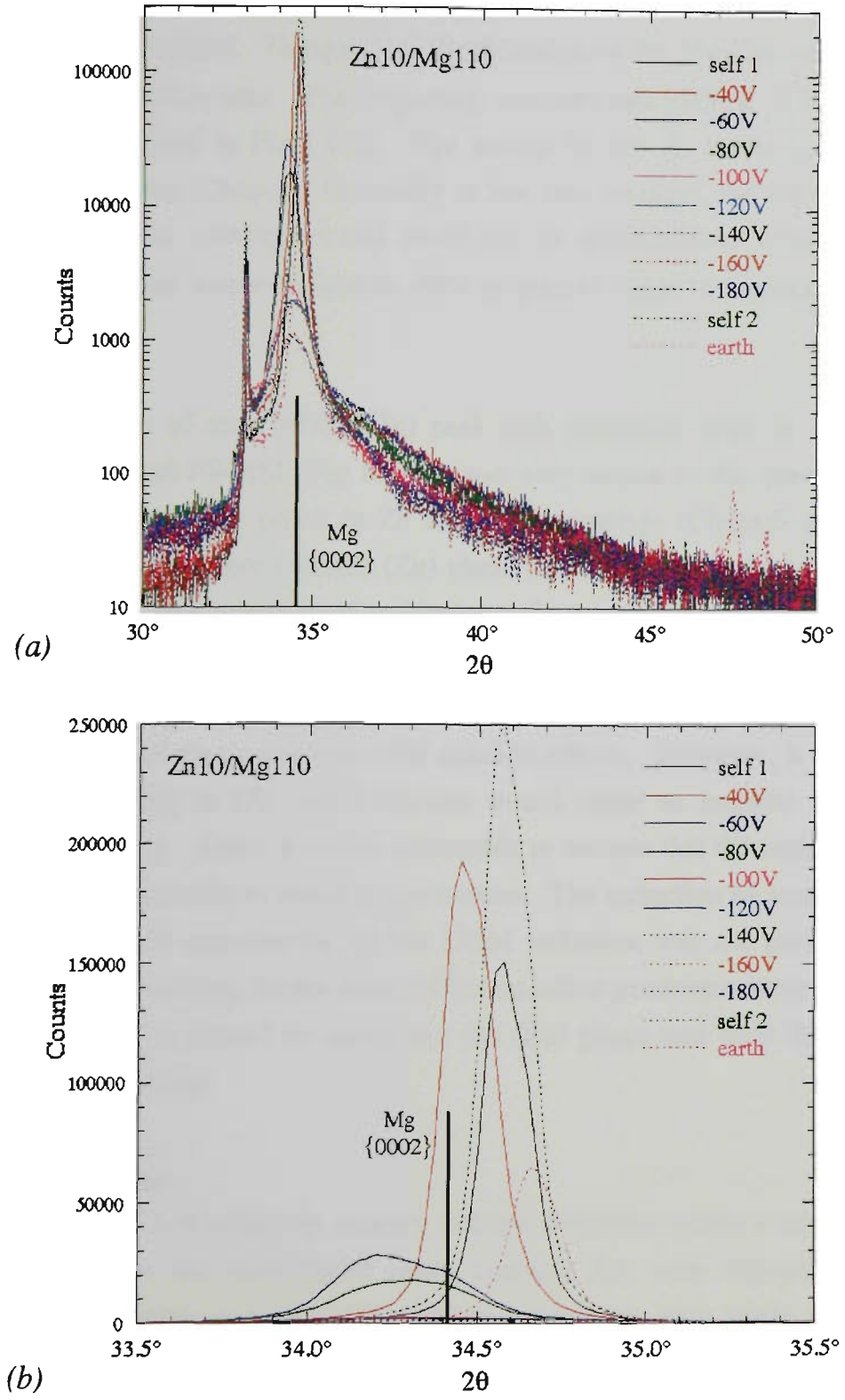

Fig.10.11 Bragg-Brentano X-ray diffraction spectra for Zn10/Mg110 Series coatings (a) semi-logarithmic scale showing amorphous background at about 40° (b) high intensity Mg {0002} diffraction peak

was increased (Fig.10.7). One of these peaks was attributed to <0001> fibre textured (Zn) solid solution and the other was thought to be due to a <111> fibre textured Mg_2Zn_{11} intermetallic phase. Unequivocal identification of the Mg_2Zn_{11} phase was not possible from the available data. The *d*-spacing, intensity and FWHM of these two sets of peaks are summarised in Fig.10.12. The results for the Zn Series 4 coatings are included for comparison (Chap.5). Generally at low bias voltages, the {0002} (Zn) and {222} Mg_2Zn_{11} peaks overlapped and could not be distinguished from each other. However, once the bias was increased to -80V or greater, these two peaks were clearly resolved (Fig.10.7b).

The behaviour of the {0002} (Zn) peak with increasing bias, in terms of the intensity, *d*-spacing and FWHM (Fig.10.12), was very similar to that previously noted for the <0001> textured (Zn) phase in Zn and Al-Zn coatings (Chaps.5 and 8). This suggests that the <0001> fibre textured (Zn) phase present in the Zn-Mg alloy coatings was subject to increasing amounts of residual tensile macrostress as bias voltage was increased. The {0002} *d*-spacing appeared to be more severely affected by increasing bias than was noted for the pure Zn coatings (Fig.10.12a). This shift in *d*-spacing could be due to either residual macrostress or solid solution effects. However, it is anticipated that the presence of Mg in (Zn) solid solution would cause an increase in the lattice parameters (Sect.3.6.1). Thus, it seems reasonable to assume that the trends in {0002} *d*-spacing were due primarily to residual macrostress. The extraction of strain free lattice parameters and residual macrostress via the CGM technique was not pursued for this phase, since no published data for the solute effect on lattice parameters were available for comparison. Finally, it should be noted that the (Zn) phase was only detected in the Zn90/Mg30 series coatings.

Intermetallic Phases

A multitude of low intensity, sharply defined diffraction peaks were also present in the XRD scans for the Zn90/Mg30 series coatings that were deposited with bias voltages of between earth and -60V (Fig.10.7a). Attempts were made to match the observed diffraction peaks with those of known Zn-Mg intermetallic phases (Fig.10.7c), but with only limited success. Table 10.6 lists the observed *d*-spacing and relative intensity for each diffraction peak from the -40V bias sample, matched with various possible phases. The peak intensities were normalised with respect to the diffraction peak at 0.228 nm, which was the second-most intense peak. This data indicates that (Zn) phase was also present with a randomly-oriented texture. There was some indication that randomly oriented Mg_2Zn_{11} was present, which is probable considering the relatively low Mg content of these coatings (Fig.10.4). However, many Mg_2Zn_{11} lines were absent including {400} which is one of the most intense lines [197]. Much of the remaining data

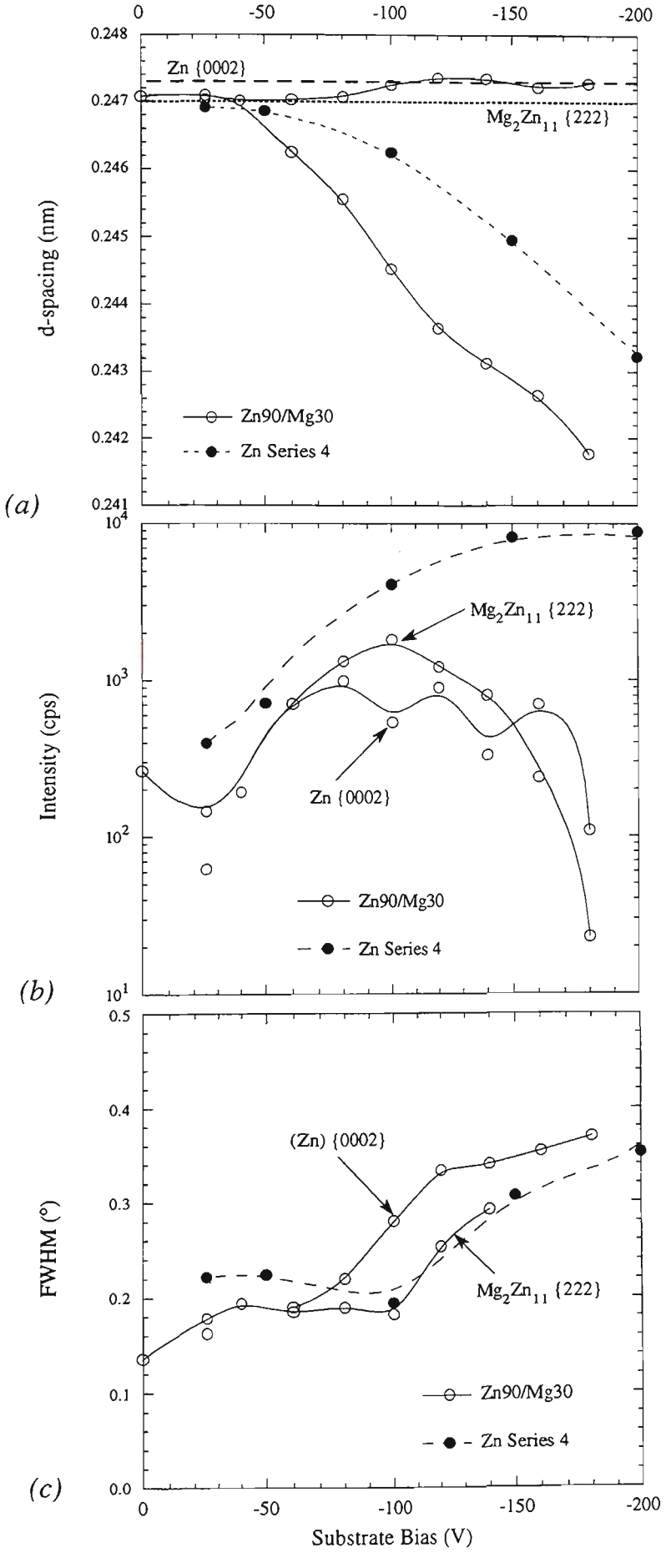

Fig.10.12 XRD results for the (Zn) {111} peak and Mg_2Zn_{11} {222} peaks in Zn90/Mg30 series coatings. Results for Zn Series 4 are shown for reference: (a) d-spacing, (b) peak intensity, and (c) FWHM.

could be matched to lines from $MgZn_2$, Mg_2Zn_3 and MgZn, although many lines from these phases were missing and the matches in relative intensity were very poor. Furthermore, several diffraction peaks were detected in the coatings which could not be matched to any known Zn-Mg phase. From this it can be surmised that there were one or more intermetallic phases present in these coatings that have not previously been reported in the literature.

Table 10.6 *d*-spacing and relative intensity data for the -40V bias sample from the Zn90/Mg30 series matched with various possible phases. All detected diffraction peaks in the range from 10° to 60° 2θ are listed (Cu K_α radiation). Data corrected for $K_{\alpha 2}$ diffraction. Relative intensities are normalised with respect to the peak at 0.228 nm. Data shown in bold-type could not be satisfactorily matched to any known Zn-Mg phase.

d-spacing measured (nm)	Relative Intensity	*d*-spacing from tables (nm)	Phase	*d*-spacing measured (nm)	Relative Intensity	*d*-spacing from tables (nm)	Phase
0.62	4	0.63	Mg2Zn3	0.238	63	0.237	Mg2Zn11
0.59	10	0.603	Mg2Zn11	0.235	17	0.23458	MgZn
		0.6062	MgZn	**0.234**	**37**		
0.55	22	0.54	Mg2Zn3	0.231	23	0.23096	MgZn
0.50	27	0.495	Mg2Zn11			0.2308	Zn
		0.5043	MgZn	**0.228**	**100**		
0.475	35	0.473	Mg2Zn3	0.226	64	0.22526	MgZn
0.456	77	0.451	MgZn2			0.2260	MgZn2
0.411	43	0.409	Mg2Zn3	0.224	47	0.22378	MgZn
0.402	47	0.399	Mg2Zn3			0.2227	MgZn2
		0.399	MgZn2	**0.221**	**9**		
0.389	5	0.3881	MgZn	**0.213**	**41**		
0.377	3	0.3789	MgZn	**0.211**	**53**		
0.351	<1	0.350	Mg2Zn11	0.209	52	0.2091	Zn
0.345	8	0.34376	MgZn	0.207	70	0.207	Mg2Zn11
0.336	**9**			**0.206**	**58**		
0.317	**18**			0.201	27	0.201	Mg2Zn11
0.311	2	0.3105	MgZn2	0.1998	7	0.1997	MgZn2
0.307	**3**			0.1939	14	0.1934	MgZn2
0.296	1	0.29495	MgZn	**0.1926**	**10**		
0.292	<1	0.29149	MgZn	**0.1900**	**23**		
0.287	**<1**			0.1828	<1	0.1865	Mg2Zn11
0.285	3	0.285	Mg2Zn11	**0.1785**	**1**		
0.280	**3**			**0.1706**	**6**		
0.247	690	0.2473	Zn	0.1686	9	0.1687	Zn
		0.247	Mg2Zn11	0.1584	2	0.1586	Mg2Zn11
		0.24572	MgZn	**0.1576**	**1**		
0.241	23	0.24078	MgZn	0.1557	<1	0.1556	MgZn2
		0.2411	MgZn2				

It was interesting to note that the numerous intermetallic phases detected in the low bias coatings of the Zn90/Mg30 series were completely absent after the bias was increased to -80V or greater (Fig.10.7). They appeared to be replaced by the very intense diffraction peaks which were attributed to strongly fibre textured (Zn) and Mg_2Zn_{11}

phases. The bias of -80V was also noted to signal an increase in the proportion of Ar buried in the coatings (Fig.10.5). It seems feasible that the burial of Ar in the coatings may have contributed to disruption of the growth of the intermetallic phases. Alternatively, the increase in Ar content was merely symptomatic of the primary phenomena responsible for the development of the strong fibre texture in the crystalline phases.

Amorphous Phase

The Bragg-Brentano XRD scans for the majority of coatings deposited from the Zn60/Mg60 and Zn40/Mg80 targets were characterised by a single broad low intensity peak (Figs.10.8 and 10.9). This broad peak was typically located at a 2θ angle of about 40-41°, and had a FWHM of about 5°. Such peaks have been reported for rapidly solidified Zn-Mg alloys [256], and are typical of the amorphous phase which can be formed in these alloys. Therefore, it can be concluded that the coatings with between about 17 and 46%Mg (Fig.10.4), were usually entirely amorphous.

A few of the coatings that were found to possess an amorphous structure were also observed to produce some very weak crystalline diffraction peaks. Such peaks were noted for the first of the self bias samples in the Zn60/Mg60 series, for which a series of very weak diffraction peaks were overlaid on the amorphous peak (Fig.10.8). Some of these peaks could be attributed to Mg_2Zn_{11}, Zn and perhaps $MgZn_2$, but the indexing was not satisfactory due to the very low peak intensities and absence of many lines. This coating contained 24%Mg (Fig.10.4), and the equilibrium phases in a conventionally solidified alloy of this composition are Mg_2Zn_{11} and $MgZn_2$ (Sect.3.6.1). It would therefore appear that the self bias coating was partially crystallized, presumably as a result of decomposition of the as-deposited amorphous structure. Similar peaks were also detected for the earth bias sample of the Zn10/Mg110 series (Fig.10.11b). A series of sharp peaks observed for the -160V and -180V bias samples of the Zn40/Mg80 series (Fig.10.9) were possibly related to the oxidised surface of these coatings (Sect.10.2.4).

(Mg) Phase

The most notable feature of the XRD scans for the Zn20/Mg100 and Zn10/Mg110 series coatings was a single diffraction peak at about 34.5° for the low bias samples (Figs.10.10 and 10.11). This peak can be attributed to the existence of (Mg) phase with a strong <0001> fibre texture. A strong texture was surmised because none of the non-basal peaks were detected. The *d*-spacing, intensity and FWHM of this peak are graphed as a function of substrate bias voltage in Fig.10.13. The results for the Mg Series 1 coatings are included for comparison (Chap.7).

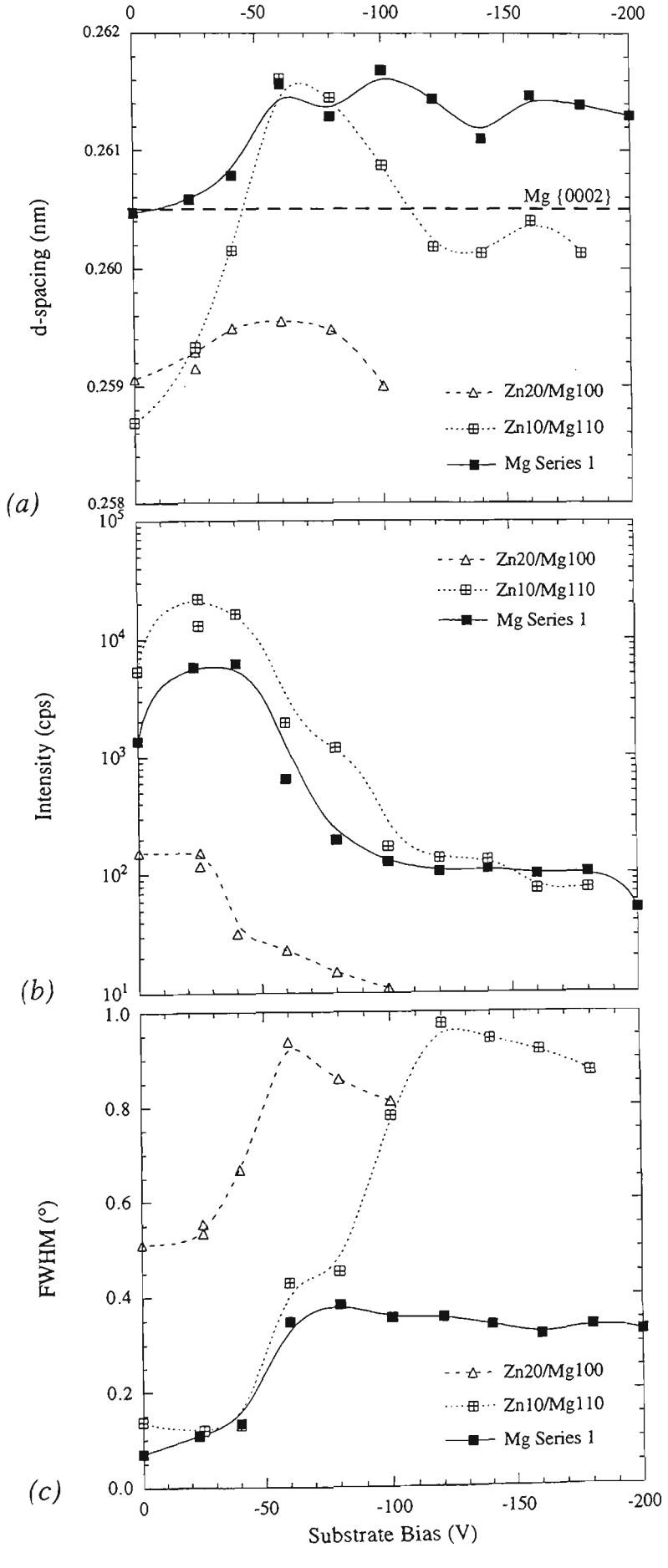

Fig.10.13 XRD results for the (Mg) {0002} peak in Mg Series 1 and Zn-Mg coatings: (a) d-spacing, (b) peak intensity, and (c) FWHM.

The intensity of the {0002} peak for the (Mg) phase was generally at a maximum for the self bias coatings, and decreased dramatically as the bias voltage was increased (Fig.10.13b). The Zn10/Mg110 series and the pure Mg coatings can be directly compared because they shared a similar *i/a* ratio (Fig.10.1). The trends in {0002} intensity for these alloy coatings were very similar to those of the pure Mg coatings, suggesting that the same mechanism was responsible in both cases for the breakdown of fibre texture at high bias. Weak diffraction from non-basal planes was detected for the pure Mg coatings, which suggested that small increases in bias favoured the random orientation of (Mg). However, non-basal (Mg) peaks were not detected for any of the Zn-Mg alloy coatings, and hence it appears that the (Mg) solid solution was amorphised as the bias was increased. The same conclusions were drawn for the (Mg) phase in Al-Mg coatings which indicates a common feature for the (Mg) phase independent of the solute element.

The {0002} *d*-spacing of the (Mg) phase was generally observed to increase as the bias was raised from earth to -60V (Fig.10.13a). This change in *d*-spacing was very sharp for the Zn10/Mg110 series and relatively minor for the Zn20/Mg100 series. At the low bias range, the *d*-spacings were less than those of pure Mg coatings, which suggested that some Zn may have been present in (Mg) solid solution, especially for the Zn20/Mg100 series. Increasing the bias beyond about -40V caused the *d*-spacing to shift to a value typical of a pure Mg coating, which implies that some of the Zn may have been rejected from solid solution in these coatings. However, the effect of macrostress on the Bragg-Brentano *d*-spacing measurement cannot be ignored and its relative impact was examined by CGM analysis in Sect.10.2.7.

The diffraction peak for the (Mg) phase was also observed to broaden to a much greater extent than was previously noted for the Mg Series 1 coatings (Fig.10.13c). For bias voltages of up to -80V, the FWHM of the {0002} peak in the Zn10/Mg110 series was indistinguishable from that of the Mg Series 1 coatings. However, increasing the bias beyond this level resulted in a dramatic increase in the FWHM of the peak for the alloy coatings. This supports the proposal that the (Mg) phase in the high bias coatings of the Zn10/Mg110 series was amorphised, or at least severely decreased in grain size. The (Mg) phase in the Zn20/Mg100 series coatings showed a similar increase in peak broadening. However, the FWHM at low bias was considerably greater than that of the Zn10/Mg110 series, possibly as a result of the higher Zn content of these coatings.

The diffraction scans for coatings that contained the (Mg) phase also seemed to indicate that an amorphous phase may have been present as a second phase. A very broad low intensity peak was observed in the diffraction data for the Zn20/Mg100 series

coatings (Fig.10.10a). The broad peak was partially obscured by the overlaying diffraction due to the Si wafer substrate, but above $2\theta \approx 37.5°$ the count rate was not affected by diffraction from the substrate. This peak was most likely due to an amorphous phase which coexisted with the (Mg) phase in the coatings. For bias voltages of -100V for greater, the amorphous peak was the only diffracted intensity that could be attributed to the coatings. Similarly, the Zn10/Mg110 series coatings deposited with a bias of -100V or greater, tended to show a {0002} peak that resembled the diffraction profile typical of an amorphous phase (Fig.10.11a). An asymmetric tail on the high 2θ side of the Mg {0002} peak was present in most of the diffraction scans, suggesting an amorphous phase in the coatings.

10.2.7 Crystallite Group Method

CGM was used to determine the strain-free lattice parameters and residual macrostress for the <0001> fibre textured crystallite group in the (Mg) phase of several coatings. Only the earth, self and -40V bias samples from the Zn10/Mg110 series possessed diffraction peaks of sufficient intensity to permit the analysis. Some of the {0002} peaks for the (Zn) phase in the Zn90/Mg30 series were sufficiently intense to enable CGM examination, but the simultaneous presence of a textured Mg_2Zn_{11} phase would have potentially complicated the interpretation. Furthermore, data relating the Mg solute content to the lattice parameters of (Zn) solid solutions was not available in the literature (Sect.3.6.1). Consequently, the fibre textured (Zn) phase was not examined by CGM.

The asymmetric diffraction scans conducted for the <0001> oriented crystallite family of the (Mg) phase, provided diffraction peaks at the predicted positions, confirming that the crystalline phase in these coatings was cph (Mg). The lattice parameters calculated for the {0004} peak from the CGM analysis were identical to those of the {0002} peak in the Bragg-Brentano scans, within the expected range of error. This is despite the delay between Bragg-Brentano diffraction (two months after deposition), and the CGM analysis (seven months after deposition). This result suggests that there were no changes in the (Mg) phase with ageing of the coating under atmospheric conditions. The c lattice parameter for each diffraction peak of the asymmetric scans was plotted as a function of $\sin^2\psi$ in Fig.10.14. Linear regressions were fitted to the data, and high correlation coefficients indicated an excellent fit to the data. The linear coefficients were used to calculate the strain free lattice parameter c_o and the residual macrostress σ, using equations appropriate for the <0001> texture in these coatings (Sect.4.4.4). The results of these calculations are summarized in Table 10.7.

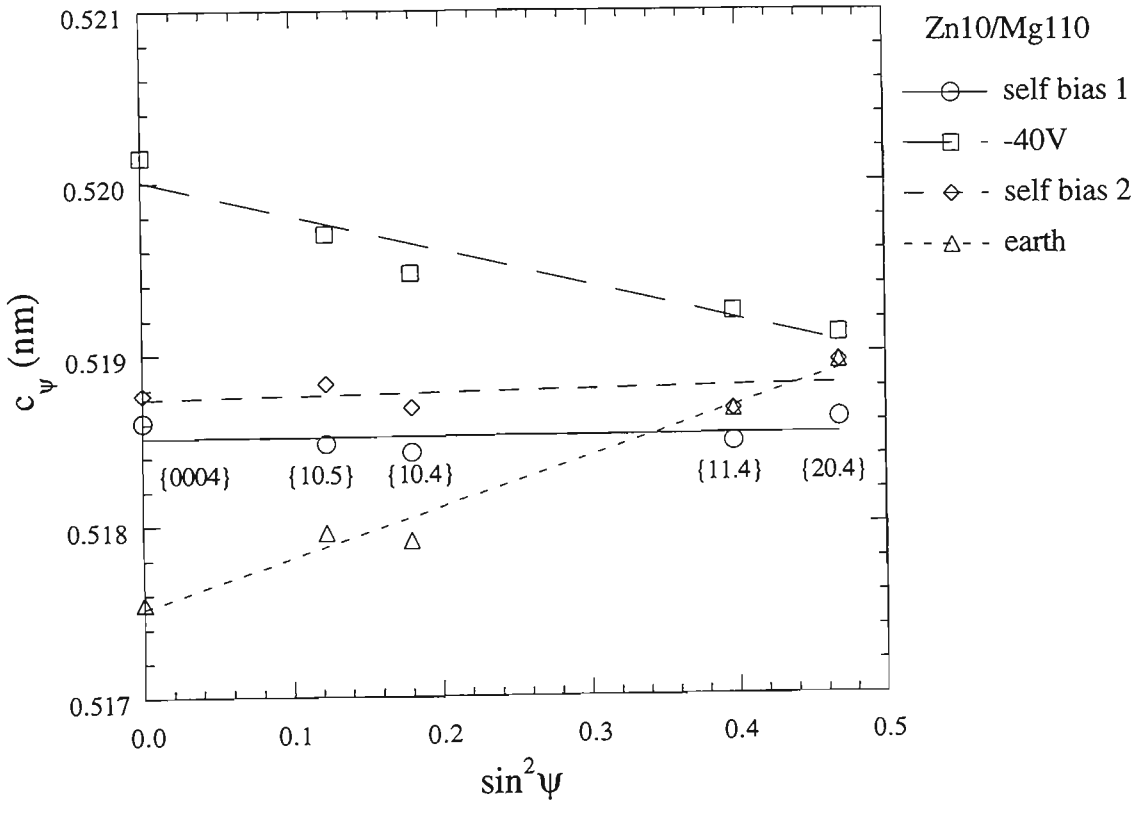

Fig.10.14 Sin²ψ plots of CGM data for the <0001> fibre textured (Mg) grains in coatings from the Zn10/Mg110 composite target.

Table 10.7 Strain-free lattice parameter c_o and residual macrostress σ for <0001> fibre textured (Mg) phase in Zn10/Mg110 series coatings.

Substrate Bias (V)	strain-free *c* lattice parameter (nm)	residual macrostress (GPa)
0 (earth)	0.51860	0.21
-26 (self 1)	0.51853	0.00
-26 (self 2)	0.51880	0.01
-40	0.51925	-0.15

The c_o lattice parameter for the (Mg) phase in Zn10/Mg110 coatings all indicated the presence of Zn in solid solution (Table 10.7). The lattice parameter was generally lower than that of pure Mg powder (0.52112 nm [197]), which is consistent with a significant proportion of Zn being dissolved in solid solution (Sect.3.6.1). It was not possible to determine with any certainty, the influence of substrate bias voltage on the strain-free lattice parameter of these Mg-rich coatings, because of the small range of samples examined. However, the data suggests that increasing the bias caused the *c* lattice parameter to increase slightly towards that of pure Mg. This result is consistent with the findings for the (Mg) phase in Al-Mg coatings (Chap.9).

The residual macrostress in the (Mg) phase of the coatings showed a continuous decrease from a small tensile stress at earth bias through to a small compressive stress at -40V bias. This change in residual stress accounted for the majority of the trends in *d*-spacing shown in Fig.10.13, while the small change in strain-free lattice parameter had little influence. Both the trends and the magnitude of residual stress were similar to those determined for the (Mg) phase in the Al-Mg coatings (Chap.9). It must be emphasized that the residual macrostress reported in Table 10.7 relates to the stress in the (Mg) phase, and not necessarily the entire coating. It does not account for the residual stress of the amorphous phase that is thought to have been present in these coatings in addition to the (Mg) phase. However, the compressive stress determined for the (Mg) phase in the -40V bias sample is consistent with the blistered delamination observed to occur in this coating (Sect.10.2.3). This suggests that for the -40V bias sample, the compressive stress in the (Mg) phase dominated the overall stress state of the entire coating.

10.3 General Discussion

10.3.1 Comparison with Previous Work

The limited amount of work on Zn-Mg PVD coatings has indicated that amorphous phases can form in coatings deposited on low temperature substrates (Sect.3.6.3). Amorphous coatings have been produced for alloys containing between 10 and 90%Mg, when deposited onto liquid nitrogen-cooled substrates [263]. However the thermal stability of this amorphous phase was poor, as it was found to crystallize by the formation of $Mg_{51}Zn_{20}$ at a temperature of only 80 to 90°C [262]. It is not surprising then that evaporated Zn-Mg coatings deposited at substrate temperatures of over 150°C have been reported to contain various intermetallic phases [23]. Amorphous phases have not been reported for Zn-Mg coatings deposited at such high substrate temperatures.

It appears that no previous studies have examined the structure of Zn-Mg alloy coatings deposited at substrate temperatures close to ambient. The present investigation utilised a substrate temperature of 50°C which is intermediate to those employed by other authors [23,262,263]. Only coatings with between about 15 and 50%Mg were found to be entirely amorphous under such conditions. The moderately low deposition temperature appears to have prevented the formation of intermetallic phases. Counter to expectations, the amorphous phase commonly observed in rapidly solidified alloys [256,257] was not detected in the present sputtered coatings. Admittedly, the critical composition range between 65 and 77.5%Mg was not examined, but alloy coatings with about 64 and 80%Mg were each found to contain (Mg) solid solution in addition to an amorphous phase. This suggests that all alloy coating compositions with more than about 64%Mg will probably contain at least some (Mg) phase, whereas rapidly solidified alloys of about 72%Mg are known to be entirely amorphous. The absence of the amorphous phase in sputtered coatings of such compositions may possibly be related to the structure of the rapidly solidified alloy. It has been established [252,260,261] that there is a strong similarity between the short range order of Zn-72%Mg liquids and the amorphous phase formed. Hence, the amorphous phase appears to be closely related to the liquid phase. The deposition of sputtered coatings completely avoids the liquid phase, and thus it might be anticipated that an amorphous phase of similar structure would also be avoided. The stable phases at ambient temperatures in a slow cooled Zn-72%Mg alloy are (Mg) and MgZn. If it is assumed that the formation of MgZn in the sputtered coatings was kinetically unfavourable (refer Sect.10.3.3), then the observation of (Mg) phase in addition to an amorphous phase is consistent with this model.

In contrast to the observations for Mg-rich coatings, the substrate temperature of 50°C was sufficiently high to enable the formation of various intermetallic phases in coatings with 3 to 7%Mg. Rapidly solidified alloys have been found to retain up to 7.2%Mg in (Zn) solid solution [254]. Thus it would appear that the moderate substrate temperature may have been responsible for the disruption of (Zn) solid solution and the growth of intermetallic phases in the alloy coatings. Another possible scenario is that the energetic neutral bombardment (backscattered ions and sputtered Zn atoms) of the sputtered coatings during deposition may have increased the adatom mobility and enabled precipitation of intermetallic phases. However, increased ion bombardment resulting from elevated bias voltages tended to suppress the formation of randomly oriented intermetallics, which seems to negate this argument. In either case, the limit of Mg solid solubility in the (Zn) phase of the sputtered coatings was apparently much less than can be achieved through rapid solidification.

As a final note, the long term stability of the Zn-Mg alloy coatings is open to some question. Evidence was found in some amorphous coatings for the presence of trace amounts of intermetallic phases (Sect.10.2.6). This is consistent with observations for rapidly solidified Zn-Mg alloys. It has been demonstrated that both amorphous phases [252,259] and supersaturated solid solutions [254] in Zn-Mg alloys are susceptible to transformation to more stable structures at modestly elevated temperatures (<200°C), or even after long term ambient ageing. Thus it is feasible that the structures of the sputtered Zn-Mg coatings relate to the time and temperature conditions experienced, and longer term ageing may lead to structural changes.

10.3.2 Solid Solubility

On the basis of chemical composition and Bragg-Brentano XRD, it was established that Zn-Mg coatings with between 1 and 7%Mg contained the (Zn) solid solution in addition to various intermetallic phases. Unfortunately, it was not possible to indisputably determine the extent of Mg solubility in the (Zn) phase for several reasons. Firstly, no reliable data could be found in the literature that related the (Zn) lattice parameters to the Mg solute content. Secondly, the complex mixture of intermetallic phases simultaneously present in these coatings would have considerably complicated the CGM analysis. Thirdly, the intensity of the Zn {0002} diffraction peak for most of the coatings was insufficient to permit the CGM analysis.

Confronted with these difficulties, an attempt was made to extract solid solubility data from the Bragg-Brentano XRD results. It has been established that rapidly solidified Zn-Mg alloys can retain as much as 7.2%Mg in (Zn) solid solution [254]. It would seem

reasonable to assume, based on data for pure Zn and Mg, that addition of Mg to (Zn) would cause the lattice parameters to increase. However, the observed {0002} *d*-spacings for the Zn90/Mg30 series coatings (Fig.10.12), were consistently lower than that of pure Zn powder. It would appear that there was minimal Mg solubility in the (Zn) phase of the coatings, and the *d*-spacings for the (Zn) phase were probably dominated by residual stress, as were the *d*-spacings for the Zn coatings. The (Zn) phase in the alloy coatings seemed to be more severely affected by increased bias voltages than that of the pure Zn coatings. The reason for this is not clear, but is perhaps related to the existence of intermetallic phases in the alloy coatings, rather than a solid solubility effect.

Alloy coatings with more than 64%Mg were found to contain <0001> fibre textured (Mg) phase and CGM analysis indicated that the strain-free lattice parameters were reduced relative to those of pure Mg. This suggests that some Zn was present in (Mg) solid solution. An empirical relationship between the (Mg) *c* lattice parameter and solute additions (Sect.3.6.1) was used to determine the proportion of Zn in solid solution. The Zn solute content in the four Zn-Mg coatings examined by CGM (Table 10.7), was found to range from 2.3 to 3.2% with an average of 2.8%. The estimated error in this calculation is ±0.4 at.%, based on a lattice parameter error of ±0.06% determined from a standard quartz sample. Therefore, the variation in solute content was within the range of error, and the average calculated value of 2.8% represents the maximum amount of Zn which can be dissolved in (Mg) solid solution by sputter deposition. This value is identical to the Zn solubility limit established for rapidly solidified [249,255] and solid quenched [225,247] Zn-Mg alloys. It would seem that supersaturated (Mg) solid solutions are impossible to achieve by either PVD or rapid solidification processes.

There is some suggestion from the lattice parameter data (Table 10.7), that the proportion of Zn in (Mg) solid solution decreased slightly as bias was increased from earth to -40V. As noted above, this variation was within the experimental error and cannot be relied upon. It is interesting to observe that the Bragg-Brentano *d*-spacing data (Fig.10.13) suggested the Zn solubility in the Zn10/Mg110 coatings ranged from 4.6% at earth bias, to 1.0% at -40V bias. However, this solubility trend is erroneous since CGM analysis indicated the Zn solubility was relatively constant at about 2.8%, and the residual macrostress was the main cause of the *d*-spacing trends. This is a good example of where Bragg-Brentano data can be complicated by concurrent solid solubility and residual macrostress effects.

10.3.3 Amorphous Phase

The XRD examination of Zn-Mg alloy coatings indicated that most contained an amorphous phase. In the case of the Zn40/Mg80 and Zn60/Mg60 series, the amorphous phase was generally the only phase present in the coatings. Considering the composition of the coatings produced from these targets, it would therefore appear that sputtered coatings with between about 15 and 50% Mg are likely to be single-phase amorphous. This corresponds to the composition range over which the various intermetallic Mg-Zn phases are located in the equilibrium phase diagram (except for $Mg_{51}Zn_{20}$), as shown in Fig.3.25. The crystal structures of these intermetallic phases are complex with large unit cells. This suggests that the formation of an amorphous phase in the sputtered coatings may have been attributable to the slow crystallization kinetics of the intermetallic phases. Unfortunately, no rapid solidification studies at such compositions were available for comparison.

The determination of Zn solubility in the (Mg) phase provided further evidence for the existence of an amorphous phase in the Zn-Mg alloy coatings. The (Mg) phase contained no more than about 2.8%Zn in each coating, compared with a bulk composition of at least 19%Zn and 35%Zn for the Zn10/Mg110 and Zn20/Mg100 series respectively. Therefore, an amorphous phase with much higher Zn content must have been present in these coatings in order to account for the discrepancy. The lever rule was used to estimate the proportion of this amorphous phase (equation 9.1). For the purpose of this calculation, the amorphous phase was assumed have a composition of Zn-50%Mg. The coatings produced from the Zn10/Mg110 target were found to be about 35% amorphous, whereas the amorphous phase accounted for about 70% of each coating from the Zn20/Mg100 series. These calculations apply to the coatings produced at bias voltages of between earth and -40V.

The high bias samples were not considered in the above analysis because they were also subject to large proportions of buried Ar, which influenced the stability of the (Mg) phase. Increasing the substrate bias voltage resulted in the retention of very high amounts of Ar in the coatings (Fig.10.5). Simultaneously, the XRD intensity for the Mg {0002} peak was found to reduce drastically (Fig.10.13). Trends similar to this were found for the Mg-rich Al-Mg alloy coatings (Chap.9). For the Al-Mg coatings, it was concluded that the buried Ar caused the amorphization of the (Mg) phase. It is likely that the results for the Mg-rich Zn-Mg alloy coatings can be explained in the same fashion. Therefore, it is apparent that the (Mg) phase is particularly susceptible to amorphization by the burial of Ar, irrespective of the presence of Al or Zn as a solute.

10.3.4 Preferential Resputtering

Increasing the substrate bias voltage had a significant impact on the chemical composition of the Zn-Mg coatings. Not only did high bias voltages result in the burial of large amounts of inert Ar in the coatings, but it also reduced the Mg content relative to that produced at lower bias voltages. The latter observation indicates that Mg was preferentially resputtered due to the enhanced energy of ion bombardment associated with increased bias voltages. This finding is perhaps counterintuitive in light of the elemental sputtering yields of pure Zn and Mg. Simulations using TRIM software [56], indicate that Zn and Mg, when bombarded with 500 eV Ar^+ ions, have a sputter yield of 4.4 and 0.51 respectively. From this it might be expected that ion bombardment of a Zn-Mg alloy coating would result in preferential resputtering of Zn, since it has the higher elemental sputtering yield. The results obtained are completely opposite to this expectation. This is primarily because the sputtering behaviour of an alloy material is distinctly different from that of an elemental target, as has been discussed at greater depth in Sect.2.4.4.

In an attempt to better understand the preferential resputtering behaviour of the Zn-Mg alloy coatings, a series of Monte Carlo simulations of the ion assisted deposition process were conducted using the T-DYN software [148]. The composition of the atomic flux for the simulation was arbitrarily selected as Zn-46%Mg, matching the coating composition obtained at self bias with the Zn40/Mg80 target. The simulation incorporated a flux of energetic Ar^+ ions that bombarded the Zn-Mg coating as it deposited. The *i/a* ratios used in the simulations were 1.33, 1.00, 0.50 and 0.25. Results of the simulations are summarised in Fig.10.15, compared with the experimental results for the Zn40/Mg80 series (assuming plasma potential $\approx +10$V). Data points from the $i/a=1.33$ series are not shown for ion energies of 180 and 200 eV because the erosion rate was found to exceed that of deposition.

The T-DYN simulations confirmed that Mg was preferentially resputtered from the coatings as the ion energy was increased (Fig.10.15a). This effect can be understood in terms of the sputter yield amplification effect [145,146]. Ions interacting with an amorphous mixture of Zn and Mg experience a series of collision cascades. The atomic mass of Zn atoms is much greater than that of Mg atoms. This is particularly relevant for Mg resputtering, since the close proximity of Zn atoms leads to a concentration of collision cascades, and thus the partial sputter yield of Mg is amplified with respect to the elemental yield. The opposite effect is observed for Zn atoms in the alloy coating. This has the overall outcome of reversing the relative differences between the elemental yields of Zn and Mg, such that for the alloy coating the partial yield of Mg exceeds that of Zn. Consequently, as the ion energy (Fig.10.15a) and/or *i/a* ratio (Fig.10.15b) is increased,

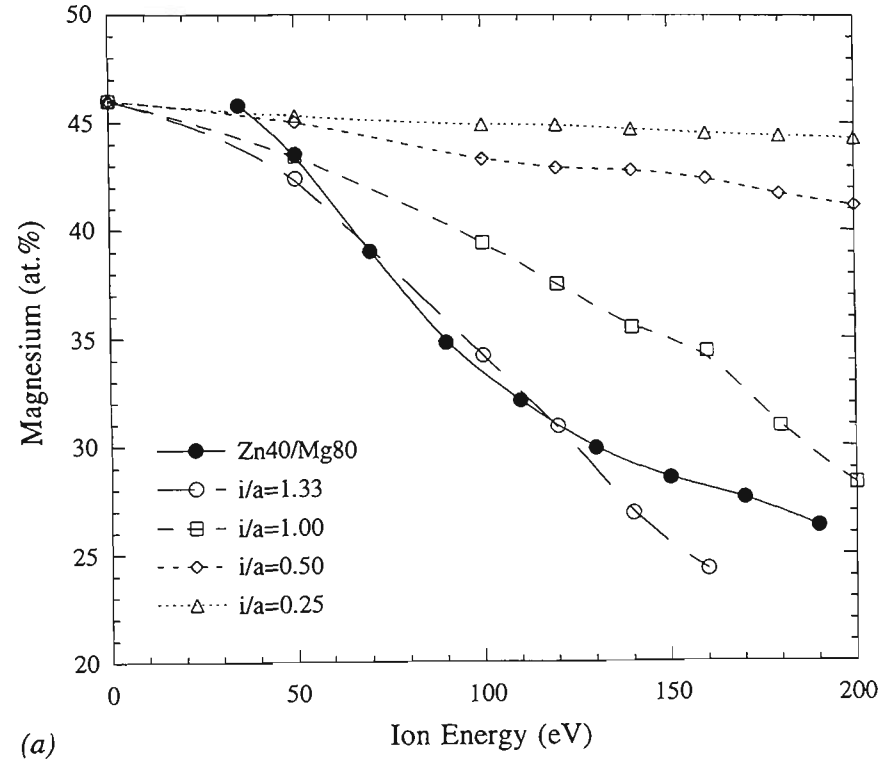

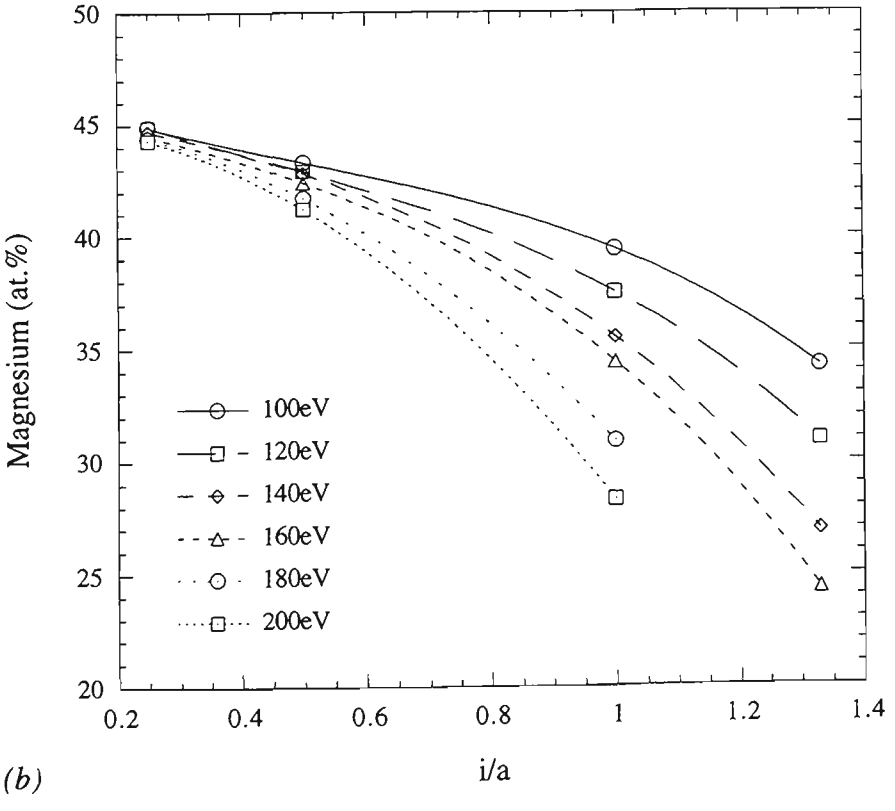

Fig.10.15 Results of ion assisted deposition simulations using T-DYN. The composition of the atomic flux was Zn-46%Mg, and the coatings were simultaneously bombarded with Ar^+ ions at normal incidence. The Mg content of the deposited coatings are shown as a function of ion energy (a), and ion/atom arrival rate ratio (b). Experimetnal data for the Zn40/Mg80 series are shown for reference.

the proportion of Mg retained in the coatings decreases due to preferential resputtering of Mg.

In spite of the qualitative replication of the experimental results, the quantitative comparison with the simulations was unsatisfactory. An *i/a* ratio of between 1.00 and 1.33 was required to obtain a composition-energy relationship similar to the experimental results achieved at *i/a* of 0.24. Thus, the experimental results were subject to a much greater degree of preferential resputtering of Mg than in the simulations. Such differences may simply be due to the inherent inaccuracies of simulating low energy sputtering processes with the binary collision model inherent to T-DYN (Sect.2.4.4). It is also feasible that thermal effects may have induced segregation of Mg to the surface which would contribute to enhanced preferential resputtering of Mg. Thermal effects cannot be simulated with the T-DYN software, but have been previously used to explain the preferential resputtering of Si from metal silicides at elevated temperatures [142,150]. Although the deposition temperature in the present investigation was only 50°C, this equates to a fairly high homologous temperature T/T_m of about 0.39 (or 0.47 if the peritectic temperature is used for T_m). Thus, thermal effects such as diffusion may have influenced the surface composition of the coatings, and in turn, enhanced the preferential resputtering of Mg.

Finally, it is interesting to note that preferential resputtering of the lighter component atoms was observed for the Zn-Mg alloy coatings, but not for the Al-Zn alloy coatings (Chap.8). This seems surprising since the atomic masses of Al and Mg are very similar and one might expect a sputter yield amplification effect in both alloy systems. The answer to this puzzle lies in the surface binding energies of these three elements, estimated from the cohesive energy or latent heat of sublimation at absolute zero. The cohesive energy of Al, Mg and Zn atoms are 3.39, 1.51 and 1.35 $eV.atom^{-1}$, respectively [331]. Thus, Zn and Mg atoms share a similar surface binding energy, and the effects of sputter yield amplification can override these small differences. However, the surface binding energy of Al is much greater than that of Zn. This means that the preferential resputtering behaviour will be driven by thermodynamic differences between Al and Zn, and the effect of sputter yield amplification will be largely concealed. Some preliminary T-DYN simulations confirmed the preferential resputtering of Zn from Al-Zn coatings, although very high *i/a* ratios were required to see the effect ($i/a \approx 2$).

10.4 Summary

Unbalanced magnetron sputtered Zn-Mg coatings were subject to preferential resputtering of Mg. This observation was counter to the trend anticipated from surface binding energy. Computer simulations using T-DYN [148] indicated that a sputter yield amplification effect was active, whereby the partial yield of Mg was enhanced by the close proximity of the heavier Zn atoms. The modification to the partial yields was sufficient to override the differences in elemental sputter yields. These simulations did not completely explain the preferential loss of Mg from the coatings, implying that thermal effects may have influenced the surface composition during deposition.

A range of crystalline and amorphous phases were detected in the Zn-Mg coatings. Various intermetallic phases were present in coatings with between 3 and 7%Mg, including some unidentified phases. Increasing the bias disrupted formation of the randomly oriented mixture of intermetallic phases in favour of fibre textured Mg_2Zn_{11}. These intermetallics were in addition to (Zn) solid solution which developed a strong <0001> fibre texture as bias was increased. The limit of Mg solubility in the (Zn) phase was consequently much less than is achievable via rapid solidification. It was speculated that this may have been due to energetic neutral bombardment of the coatings during deposition, which enabled nucleation of the complex structured intermetallics. The (Zn) solid solution was subject to the development of large tensile stresses as substrate bias was increased, similar to that observed for the pure Zn coatings.

Coatings with between about 15 and 50%Mg, were usually entirely amorphous when deposited at 50°C. The fast quench rate of sputter deposition is thought to have prevented formation of the complex structured intermetallic phases. The amorphous phase that is often reported for rapidly solidified Zn-Mg alloys was not found in the sputtered coatings. It was suggested that this may have been caused by the absence of the liquid phase, that imparts short range structural order in rapidly solidified alloys.

Alloy coatings with more than 50%Mg consisted of a mixture of <0001> fibre textured (Mg) phase and an amorphous phase assumed to have a composition of Zn-50%Mg. The maximum Zn solubility in the (Mg) phase was 2.8%, and is identical to that of rapidly solidified and solid quenched Zn-Mg alloys. The (Mg) solid solution was amorphised as the bias was increased, due to retention of very large proportions of Ar. Zn-rich alloy coatings were also susceptible to the retention of Ar, but to a lesser extent than for the Mg-rich compositions. The presence of such high proportions of buried Ar resulted in a similar form of oxidation to that observed for the Al-Mg coatings.

Chapter 11

Aluminium-Magnesium-Zinc Alloy Coatings

11.1 Deposition Parameters

Two Al/Mg/Zn composite targets (Sect.4.2.2) were used to prepare a range of Al-Mg-Zn alloy coatings on Si wafers with substrate bias voltages ranging from earth to -180V. The important parameters for each series are listed in Tables 11.1 and 11.2. All coatings were prepared with the same fully magnetised M3 magnet, and the high voltage power supply operated at 100 W. Based on experience with the Al/Mg and Zn/Mg composite targets, it was fully expected that a stepped erosion profile would develop on these targets. Consequently, coatings were prepared at the start and near the end of each series with nominally identical conditions (self bias), in order to examine changes in the coating composition. The magnetron conditions were very stable throughout each coating run, with the magnetron voltage remaining constant within ±5V. This observation suggested that the sputtered flux from the target was also reasonably stable. Furthermore, the operation time with each target was kept to a minimum in order to spare the targets from excessive sputter erosion.

Table 11.1 Deposition parameters for coatings prepared from Al85/Mg25/Zn10 target. Other process variables: base pressure 72 μPa; magnetron power 100 W (high voltage supply); probe current 0.623 mA at start, 0.627 mA at end; deposition time 10 minutes per sample.

Magnetron Conditions		Substrate	Coating Mass
Voltage (V)	Current (A)	Bias (V)	(μg)
388	0.25	self (-26)	339
387	0.25	-40	331
386	0.25	-60	319
387	0.25	-80	318
387	0.25	-100	248
386	0.25	-120	234
385	0.25	-140	199
386	0.25	-160	182
386	0.25	-180	170
388	0.25	self (-26)	335
384	0.25	earth	340

Table 11.2 Deposition parameters for coatings prepared from Al105/Mg10/Zn5 target. Other process variables: base pressure 72 μPa; magnetron power 100 W (high voltage supply); probe current 0.603 mA at start, 0.595 mA at end; deposition time 15 minutes per sample.

Magnetron Conditions		Substrate	Coating Mass
Voltage (V)	Current (A)	Bias (V)	(μg)
401	0.24	self (-26)	378
399	0.24	-40	340
398	0.24	-60	300
398	0.24	-80	260
399	0.24	-100	240
400	0.24	-120	229
400	0.24	-140	217
401	0.24	-160	207
403	0.24	-180	200
407	0.24	self (-26)	352
405	0.24	earth	366

11.2 Results and Discussion

11.2.1 Ion/Atom Flux Ratio

The calculated *i/a* ratios and the deposition rates at self bias for the two Al-Mg-Zn coating series are shown in Table 11.3. The duplicate results correspond to coatings produced at the start and end of each series. The results for one of each series of Al, Mg and Zn coatings (Chaps.5 to 7), are included for the purpose of comparison. The ion flux when normalized by the magnetron current was constant for each of the two ternary target coating runs. Furthermore, it was within the range experienced for the Al, Mg and Zn targets. The mass deposition rate at self bias was much more variable between the elemental targets, which was reflected in the *i/a* ratio. The deposition rate results are covered in more detail in the following section. The *i/a* ratio for both ternary targets was within the range observed for the elemental targets. Reducing the Al content of the composite target caused a small reduction in the *i/a* ratio, due mainly to the concomitant increase in deposition rate.

Table 11.3 Characteristic deposition conditions for Al-Mg-Zn coatings at self bias, in comparison with elemental coatings.

Series	*i/a* ratio	Deposition Rate ($g.mm^{-2}.W^{-1}.min^{-1}$)	Normalized Ion Flux *i/I* ($ion.C^{-1}.mm^{-2}$)
Al85/Mg25/Zn10	0.627	$4.32x10^{-9}$	$2.88x10^{14}$
	0.627	$4.27x10^{-9}$	$2.89x10^{14}$
Al105/Mg10/Zn5	0.762	$3.21x10^{-9}$	$2.90x10^{14}$
	0.790	$2.99x10^{-9}$	$2.86x10^{14}$
Al Series 2	1.051	$1.56x10^{-9}$	$2.46x10^{14}$
Mg Series 1	0.347	$4.75x10^{-9}$	$2.60x10^{14}$
Zn Series 4	0.173	$2.39x10^{-8}$	$3.02x10^{14}$

The *i/a* data obtained for the binary alloy coatings of Al-Zn, Al-Mg and Zn-Mg, described in previous chapters, were combined with the data in Table 11.3 to construct a ternary map for the variation of *i/a* ratio in the Al-Mg-Zn system (Fig.11.1). The axes are shown in terms of the composition of the sputtered flux produced from each target (at.%), and the *i/a* increment is 0.1. It must be noted that this map applies to deposition using the configuration described in Sect.3.1, and with a fully magnetised M3 magnet assembly. Minor addition of Al and/or Mg to a Zn sputtered flux has only a small influence on the *i/a* ratio. However, intermediate to large additions of Al cause a rapid increase in *i/a*, and a moderate increase for Mg additions. This trend reflects the relative differences in the

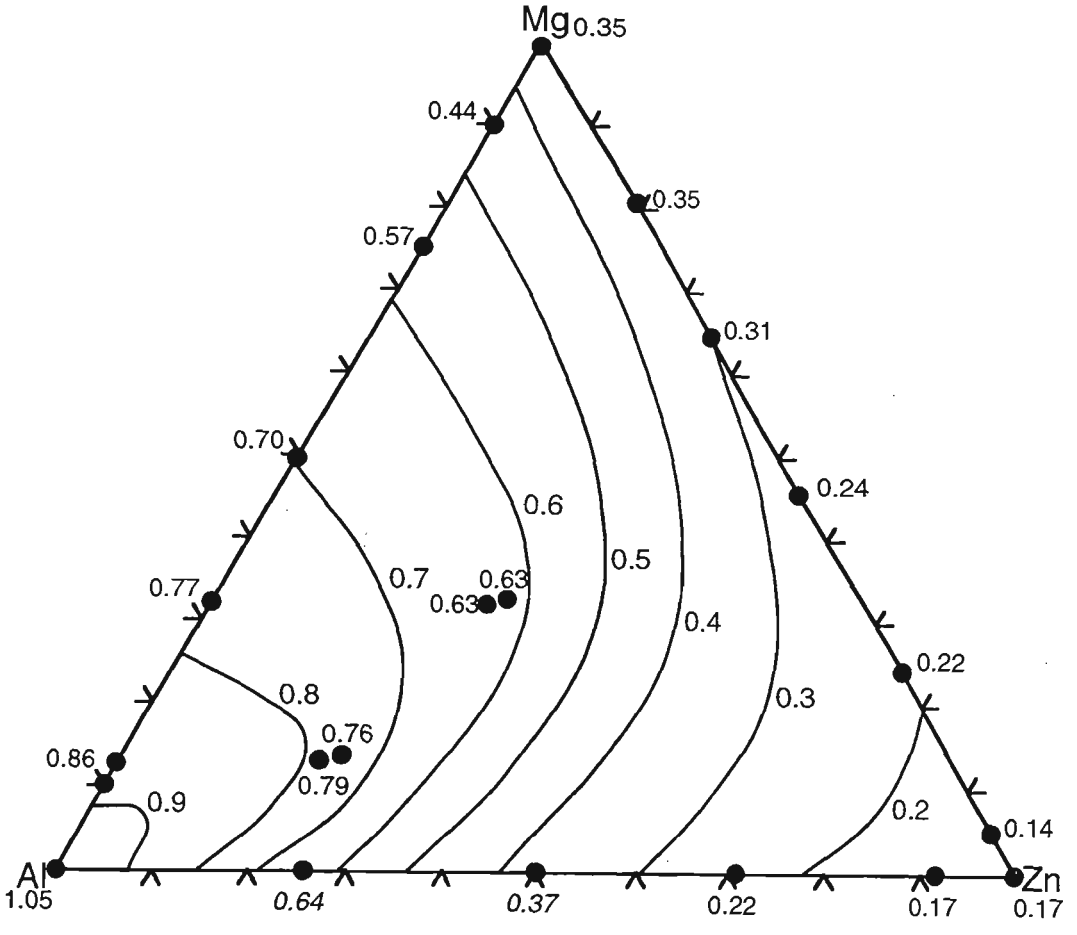

Fig.11.1 *Extrapolated i/a ratio contour diagram for the ternary Al-Mg-Zn system, derived from data for elemental, binary, and ternary coatings. The interval of i/a is 0.1.*

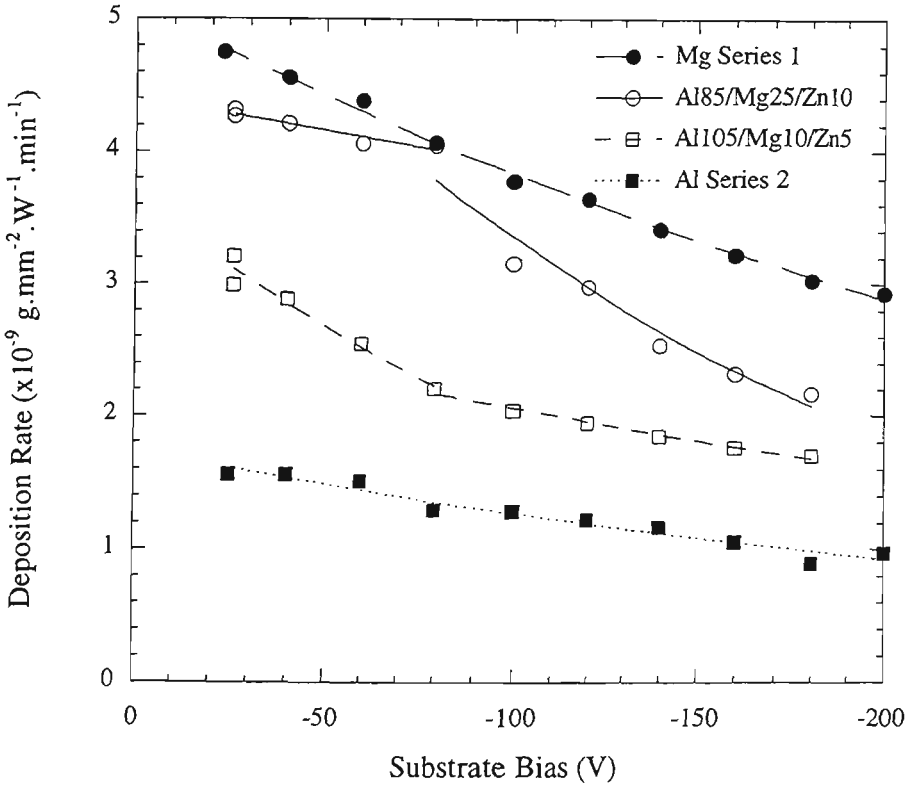

Fig.11.2 *Mass deposition rate for sputtered Al-Mg-Zn coatings. Note the ordinate axis is linear, and the curve fits are expontential.*

sputtering rate of these metals. Given that the normalized ion flux is relatively independent of the type of material in the target (refer Table 11.3), Fig.11.1 essentially represents the inverse of mass deposition rate.

11.2.2 Mass Deposition Rate

The mass deposition rates for the two ternary composite targets are shown as a function of the substrate bias voltage in Fig.11.2. The rates were found to be intermediate between those of the Al and Mg targets, which are also shown for the purpose of comparison. Increasing the substrate bias voltage above self bias, caused a reduction in the deposition rate. At about -80V, bias there appeared to be a change in the slope of the best fit curves shown in this graph. For bias below this limit, the Al105/Mg10/Zn5 series was strongly affected by small changes in bias, whereas the Al85/Mg25/Zn10 series deposition rate changed only slightly. For bias voltages above -80V, this situation was reversed, as the Al85/Mg25/Zn10 series was more dramatically influenced by small bias increases than was the Al105/Mg10/Zn5 series. In each of these regions, the data could be represented by an exponential curve fit which is consistent with the established trends in sputter yield at such low ion energies [327]. The cause of this dramatic change in deposition rate at about -80V bias, was subsequently found to be related to the chemical composition of the coatings, as discussed in Sec.11.2.4. The deposition rates for the earth bias coatings are not shown in Fig.11.2, since they are unrelated to the observed trends with bias voltage. Earthing the substrate platform had very little effect on the mass deposition rate, and it was very similar to that obtained at self bias.

The deposition rate measurements in Fig.11.2 were subject to a large error in comparison with the results from other coating series, particularly for the Al85/Mg25/Zn10 series. This variability was due to the small deposited mass, which increased the relative error of the deposition rate measurement. The maximum relative error was about ±6%. These error bars are not shown for reasons of clarity, but the curves fits each fell within the range of error.

11.2.3 Visual Examination

Immediately after removal from the sputtering chamber, all of the Al-Mg-Zn coatings were highly lustrous and metallic white in colour. The surface finish replicated the highly polished finish of the Si wafer substrates. No distinguishing features could be observed between the coatings produced at different bias voltages. Photographs of the

samples are not presented since they are identical in appearance to coatings in the Al115/Mg5 and Al105/Mg15 targets, for which photographs are presented in Fig.9.3a.

This surface appearance was unchanged throughout the time period between coating preparation and the last set of experimental measurements, about one year after initial coating preparation. However, after a further six months of storage, some of the coatings were found to have developed a slightly frosted, brown-coloured appearance. The affected coatings were mostly those produced from the Al85/Mg25/Zn10 target. It is thought that this appearance was the result of handling of the samples and consequent staining due to oxidation. The long term stability of these coatings under controlled conditions is still unknown, and is recommended as an area for further work.

11.2.4 Chemical Composition

The Al, Mg and Zn content of each of the ternary coatings are graphed as a function of the substrate bias voltage in Fig.11.3. This data is also represented on a ternary phase diagram in Fig.11.4, in relation to the room temperature isothermal section of the equilibrium ternary phase diagram (Sect.3.7.1). Significant proportions of Ar were also detected in the coatings, particularly for the Al85/Mg25/Zn10 series. The percentage of Ar in the coatings is graphed as a function of bias voltage in Fig.11.5. It must be emphasised that the Ar content of the coatings was neglected for the presentation of Figs.3 and 4.

The substrate bias voltage had a very substantial influence on the ternary composition of the coatings. For the Al85/Mg25/Zn10 series coatings, increasing the bias voltage up to -80V, caused substantial preferential resputtering of Mg, and a corresponding enrichment in Al and Zn (Fig.11.3a). Construction of a tie-line between 100%Mg and the Al-Zn axis in Fig.11.4 indicates that the Zn content relative to Al decreased only very slightly over this bias voltage regime, such that the Zn/Al ratio was fairly constant at about 0.82. In effect, the composition shifted away from the (Mg) phase, towards the Al-Zn boundary. Increasing the bias voltage from -80V to -100V caused a dramatic shift in the coating composition. Both the Mg and Zn content decreased significantly, resulting in a large increase in the Al content. The overall shift in composition is best represented in the ternary diagram (Fig.11.4). Simultaneous with this dramatic change in composition was a rapid increase in the amount of Ar buried in the coating (Fig.11.5). With further increase in bias voltage, the Mg and Zn content decreased at a similar rate, causing the proportion of Al to increase. It would appear that under these conditions, both Zn and Mg were preferentially resputtered from the coatings.

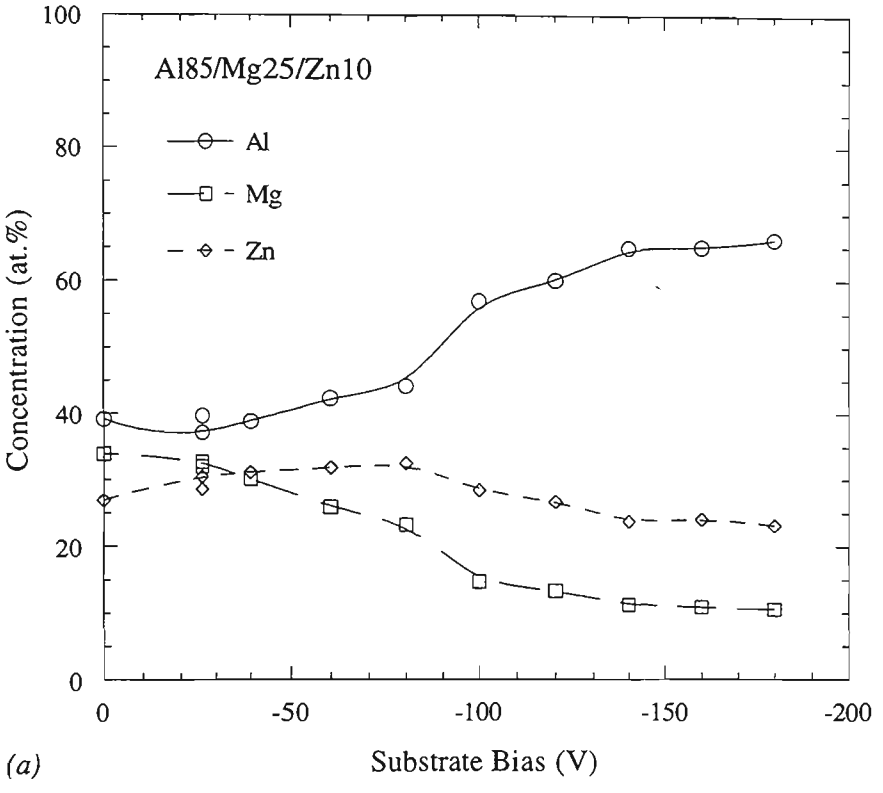

(a)

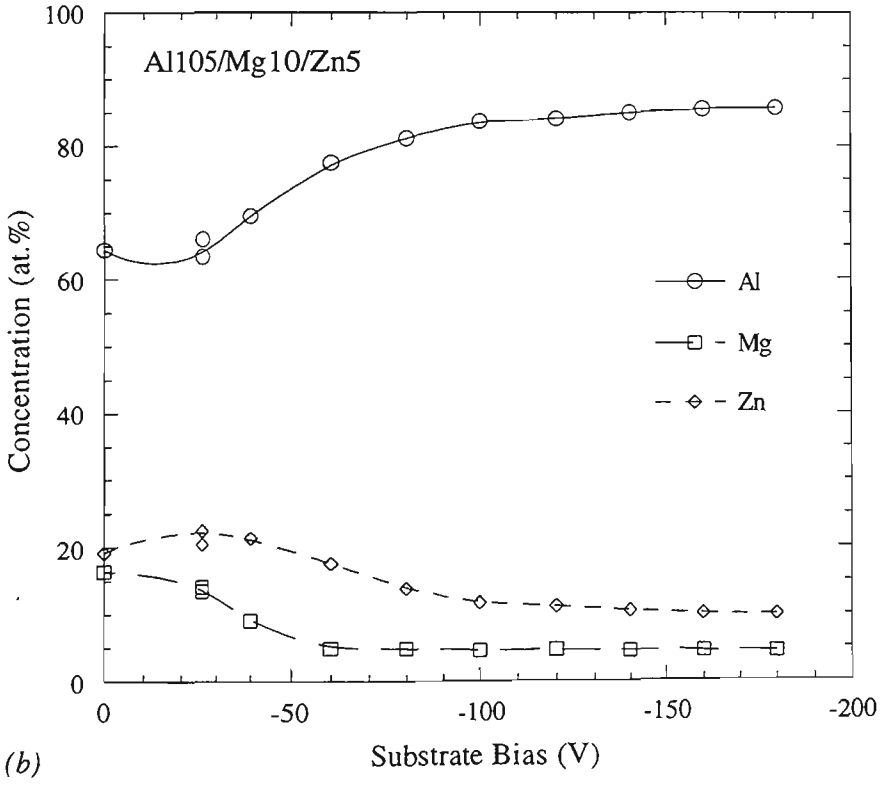

(b)

Fig.11.3 Chemical composition of sputtered Al-Mg-Zn coatings, relative to the total amount of Al, Mg, and Zn: (a) Al85/Mg25/Zn10 target, (b) Al105/Mg10/Zn5 target.

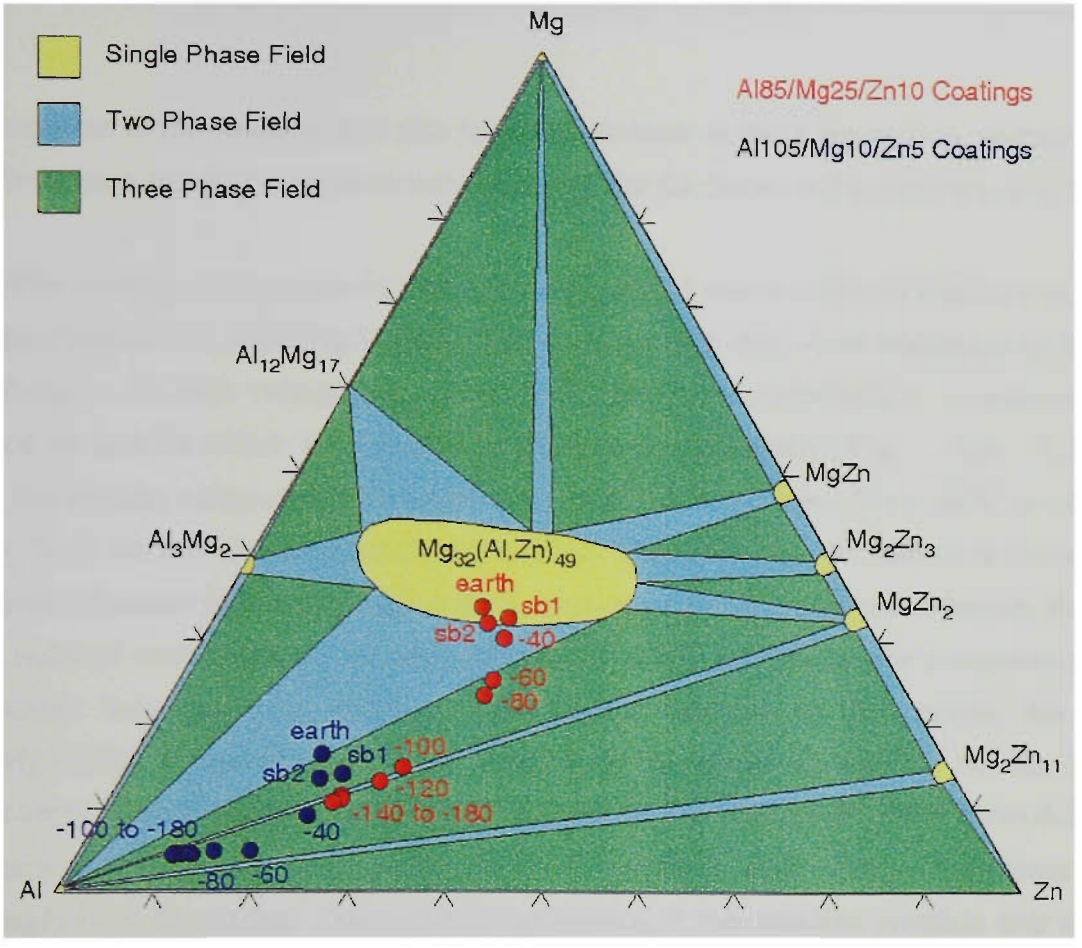

Fig.11.4 Chemical composition of Al85/Mg25/Zn10 and Al105/Mg10/Zn5 series coatings represented on the Al-Mg-Zn isothermal section at room temperature. The phases indicated refer to equilibrium conditions and do not necessarily reflect the coating structure. Note compositions are atomic %.

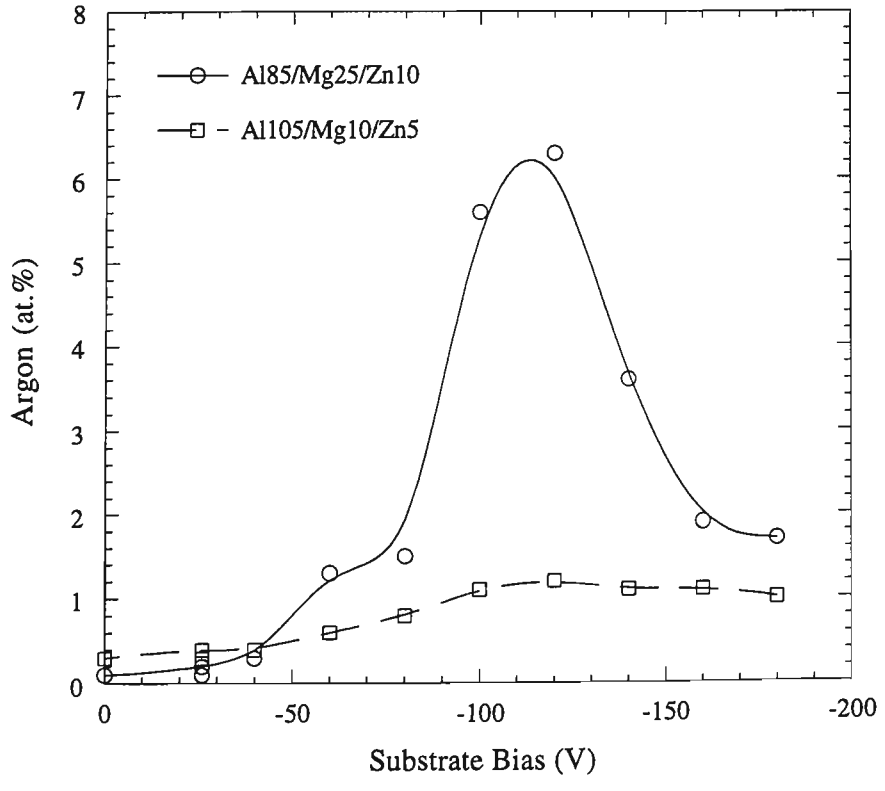

Fig.11.5 Ar content of sputtered Al-Mg-Zn coatings, relative to the total amount of Al, Mg, Zn, and Ar.

The Ar content of the coatings was also found to decrease at these higher bias voltages, in a similar fashion to what was previously observed for the Series 4 Zn coatings (Fig.5.2).

The coating composition for the Al105/Mg10/Zn5 series followed similar trends to those observed for the Al85/Mg25/Zn10 series, except that they were translated to lower bias voltages. At bias voltages less than -40V, Mg was preferentially resputtered in favour of Al and Zn which both tended to increase proportionally (Fig.11.3b). A large shift in the coating composition occurred when the bias was raised from -40V to -60V, whereby both the Mg and Zn content were reduced, causing the Al content to increase. With further increase in bias, the Mg content remained relatively constant whereas the Zn content reduced continuously. At bias voltages of -100V or greater, the composition of the coatings was relatively stable. The modest increase in Ar content for the Al105/Mg10/Zn5 series (Fig.11.5), is thought to be mainly an artefact of the EDS measurement. Due to the overlap of the Ar K_α and Al K_α "sum peak" (refer Sect.4.3.4), the apparent increase in Ar content for these coatings most likely represents the increasingly high Al content. Granted this explanation, it still remains possible that some Ar was buried in the Al105/Mg10/Zn5 series coatings, although it was probably about an order of magnitude lower than the indicated levels.

These results indicate that there is a difference between the two series of ternary coatings in terms of the bias voltage at which resputtering of Zn became prominent. One possible explanation for this lies in the observation that the *i/a* ratio for the Al105/Mg10/Zn5 series was about 25% higher than that of the Al85/Mg25/Zn10 series (Table 11.3). It might therefore be expected that the higher *i/a* ratio for the Al105/Mg10/Zn5 series would have meant the coatings would be more sensitive to small increases in bias, as was observed. However, it is also likely that the composition of the coatings would have had a significant impact on the partial resputtering yields of the individual components. A thorough understanding of the effects of *i/a* ratio on composition would necessitate additional work which is beyond the scope of this thesis.

The duplicate coatings deposited on self biased substrates provide an indication of the variation in composition that occurred during each coating run. Generally, the self bias coating produced at the end of each coating run contained slightly less Zn and Mg than those produced at the beginning of the run (Fig.11.4). This is to be expected from the higher erosion rate of these metals in comparison with Al, which caused the development of a stepped erosion track on the target surface. The consequences of this stepped profile were discussed at greater length in Sect.4.2.

Lastly, it is noteworthy that the behaviour of the Zn content of the ternary coatings with respect to substrate bias, is reflected by the mass deposition rate trends (Fig.11.2). This is because the atomic mass of Zn is markedly greater than that of Al and Mg. Relatively small amounts of Zn consequently had a strong effect on the coating mass, and hence the mass deposition rate trends were driven largely by the Zn content of the coatings, in combination with the reduction in mass due to resputtering.

11.2.5 Bragg-Brentano X-Ray Diffraction

The Bragg-Brentano XRD scans for each set of ternary alloy coatings are shown in Figs.11.6 and 11.7. These scans were conducted about three months after the coatings were deposited. Only one typically very intense diffraction peak from the coatings was detected in the 2θ range examined (30°-50°). The *d*-spacing, intensity and FWHM parameters measured for this peak are summarized in Fig.11.8. Several of the coatings prepared at low bias voltages, provided diffraction scans with only a single broad, low intensity peak, which is characteristic of an amorphous phase. The features of the diffraction scans are described at greater length in the following text.

(Al) Phase

The single intense diffraction peak observed for many of the ternary alloy coatings (Figs.11.6 and 11.7), is interpreted to indicate the presence of a crystalline phase with a strong preferred orientation. The *d*-spacing of this peak was slightly greater than that of the {111} plane in pure (Al) phase, and tended to decrease towards it with increasing bias voltage (Fig.11.8a). It has been firmly established in preceding chapters that energetic ion bombardment at elevated bias voltages resulted in the rejection of solute from the terminal solid solutions in Al-Zn, Al-Mg and Zn-Mg coatings. Therefore, it seems reasonable to assume that the strong crystalline peak detected in the XRD scans is attributable to an (Al) solid solution with a strong <111> fibre texture. This was subsequently verified for several samples by the use of CGM (Sect.11.2.6).

The diffracted intensity for the Al {111} planes behaved very differently for the two series of coatings (Fig.11.8b). The peak was generally very weak for the coatings produced at low bias voltages. For the Al85/Mg25/Zn10 series, the peak intensity increased exponentially with bias voltage (Fig.11.8b), reaching a maximum for the -180V bias sample, still without the development of any other crystalline peaks (Fig.11.6). However, in the Al105/Mg10/Zn5 series, the peak intensity increased by about three orders of magnitude as the bias was raised from -60V to -80V. Simultaneously, only a small change in the coating composition occurred. With further increase in bias, the peak intensity decreased before reaching a relatively constant level. Similar dramatic changes

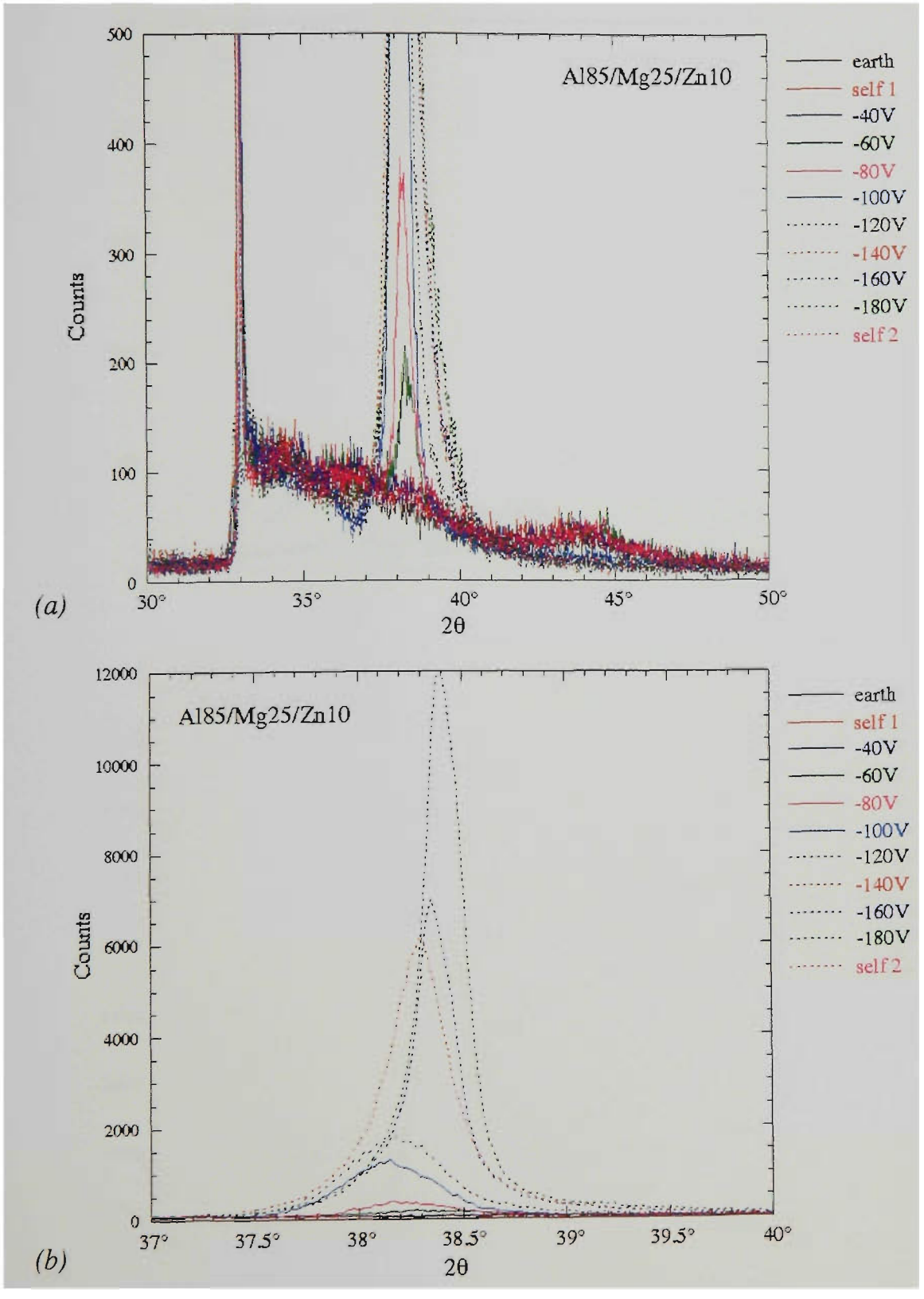

Fig.11.6 *Bragg-Brentano X-ray diffraction spectra for Al85/Mg25/Zn10 Series*
(a) low intensity profile showing amorphous peak at about 44°
(b) high intensity Al {111} diffraction peak

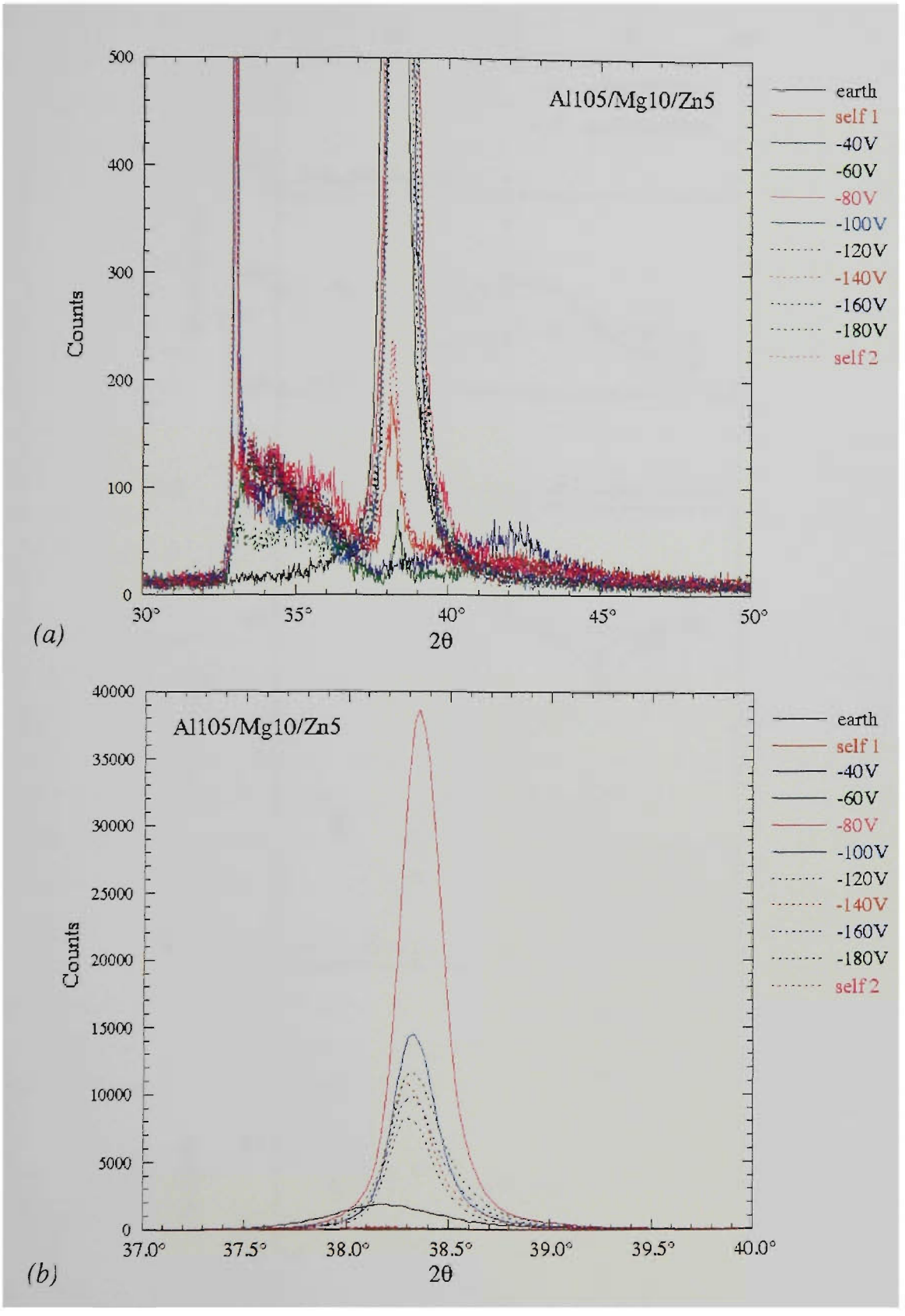

Fig.11.7 *Bragg-Brentano X-ray diffraction spectra for Al105/Mg10/Zn5 Series*
(a) low intensity profile showing amorphous peak at about 42°
(b) high intensity Al {111} diffraction peak

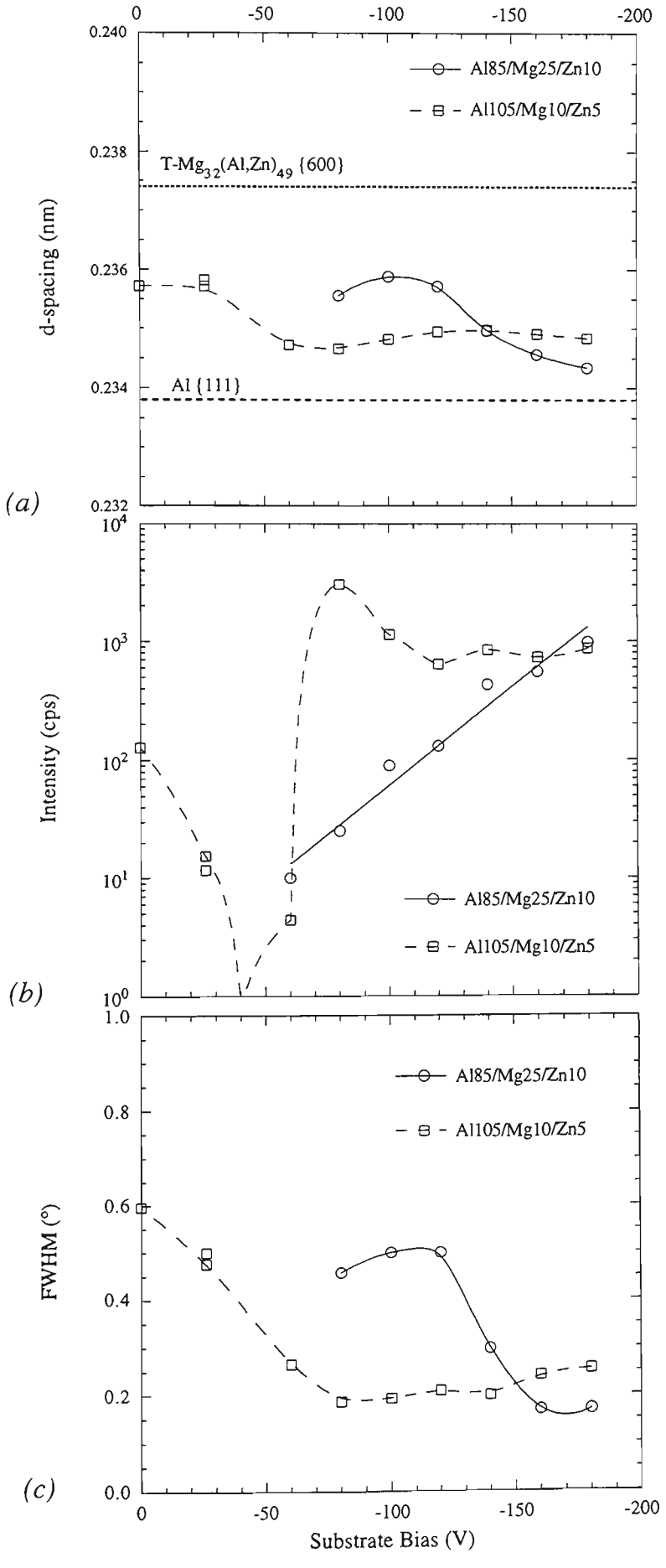

Fig.11.8 XRD results for the (Al) {111} peak in Al-Mg-Zn coatings: (a) d-spacing, (b) peak intensity, and (c) FWHM. The {111} and {600} d-spacings for strain-free powders of Al and T-$Mg_{32}(Al,Zn)_{49}$, respectively, are shown in (a) for reference.

in the crystallinity of the coating were observed for the Al115/Mg5 and Al105/Mg15 series coatings described in Chap.9. It would appear that the moderate energy ion bombardment associated with these bias conditions enabled the growth of (Al) phase with a very strong <111> fibre texture. The same cannot be said for the Al85/Mg25/Zn10 series for which the development of a strong <111> fibre texture was much more gradual.

The intensity of the <111> (Al) peak in the Al105/Mg10/Zn5 series increased by about an order of magnitude when the bias voltage was reduced from self to earth bias (Fig.11.8b). Earthing the substrates during deposition results in a reduction in the kinetic energy of the bombarding ions, but also substantially increases the electron current which passes through the sample. This high electron flux constitutes an additional source of surface heating for the sample. It is feasible that the electron bombardment may have aided in the growth of the textured (Al) phase, by providing additional thermal energy to the surface of the coating.

It appeared that the *d*-spacing of the Al {111} peaks in both sets of coatings tended towards a relatively constant value as bias was increased. This effect could possibly be caused by solid solubility effects. It was observed that the coatings at low bias were subject to preferential resputtering of Mg. This would tend to cause a reduction in the (Al) lattice parameter due to the larger atomic radii of Mg [250]. Beyond a bias of -80V for Al85/Mg25/Zn10 and -40V for Al105/Mg10/Zn5, the coatings were affected by preferential resputtering of both Mg and Zn. The reduction in lattice parameter due to the loss of Mg would be partially overcome by the expected increase in lattice parameter as a result of the smaller atomic radius of Zn. This may explain why the *d*-spacing is relatively constant at high bias voltages. However the effect of residual macrostress on Bragg-Brentano *d*-spacing cannot be ignored. A better understanding of the relative impact of these two variables was gained by CGM analysis.

It is interesting to note that the Al {111} peak was reasonably broad at the lower bias voltages, and became sharper as the bias was increased (Fig.11.8c). This trend appears to correlate with the observed Ar content of the Al85/Mg25/Zn10 coatings (Fig.11.5), in a fashion similar to that observed for the Series 4 Zn coatings (Chap.5). The crystalline peak for the Al105/Mg10/Zn5 series was also observed to decrease in FWHM, but this trend was probably artificial due to the very low diffracted intensity for self bias coatings. The source of the peak broadening is probably residual microstrain, but it is also possible that a crystallite size effect was present. From the data available it is not possible to ascertain which source of peak broadening was dominant.

Amorphous Phase

Coatings in the Al85/Mg25/Zn10 series with bias voltages of between earth and -40V did not have any crystalline peaks in their XRD scans, apart from those attributed to the substrate (Fig.11.6a). A single broad, low intensity peak was present at about $2\theta \approx 44°$, that signals the existence of an amorphous phase in the coatings. Considering the absence of any crystalline peaks, it is reasonable to conclude that these coatings were entirely amorphous with no second phase. The amorphous peak was still present in the diffraction scans for the -60V and -80V bias coatings, for which the crystalline peak was very weak. However, the amorphous peak was absent for all other coatings produced at higher bias voltages. This suggests that the -60V and -80V bias samples contained a combination of amorphous and crystalline phases whereas all others consisted only of amorphous or crystalline phases.

The coating deposited from the Al105/Mg10/Zn5 target with a bias voltage of -40V also did not provide any crystalline diffraction peaks. A broad low intensity peak located at $2\theta \approx 42°$ was observed, which indicates the presence of an amorphous phase. The broad peak was also present in the self bias and -60V bias coatings, in addition to the weak crystalline peak attributed to trace proportions of (Al) phase. Therefore, it seems that these low bias coatings primarily consisted of an amorphous phase, with a small fraction of a <111> textured (Al) solid solution.

11.2.6 Crystallite Group Method

CGM analysis was restricted to the following coatings: Al85/Mg25/Zn10 with -160V and -180V bias, and Al105/Mg10/Zn5 with -80V bias or greater. None of the remaining coatings could be analysed because crystalline diffraction peaks where either not present in the Bragg-Brentano scans, or they were of insufficient intensity to permit CGM examination.

Asymmetric diffraction scans were conducted for the <111> oriented crystallite family of the (Al) phase in the coatings. The detection of diffraction peaks at the predicted positions confirmed that the crystalline phase in these coatings was fcc (Al) phase. The {111} *d*-spacings measured by Bragg-Brentano XRD are compared with the {222} *d*-spacings determined from the CGM scans in Fig.11.9. The CGM lattice parameters were consistently lower than those from the Bragg-Brentano analyses. Since the {222} planes are simply a higher order reflection of {111} planes, there should be no difference between these two measurements. The Bragg-Brentano work was conducted about three months after deposition, whereas the CGM analysis was performed about nine months later. It is feasible that the observed differences were due to relaxation of the residual

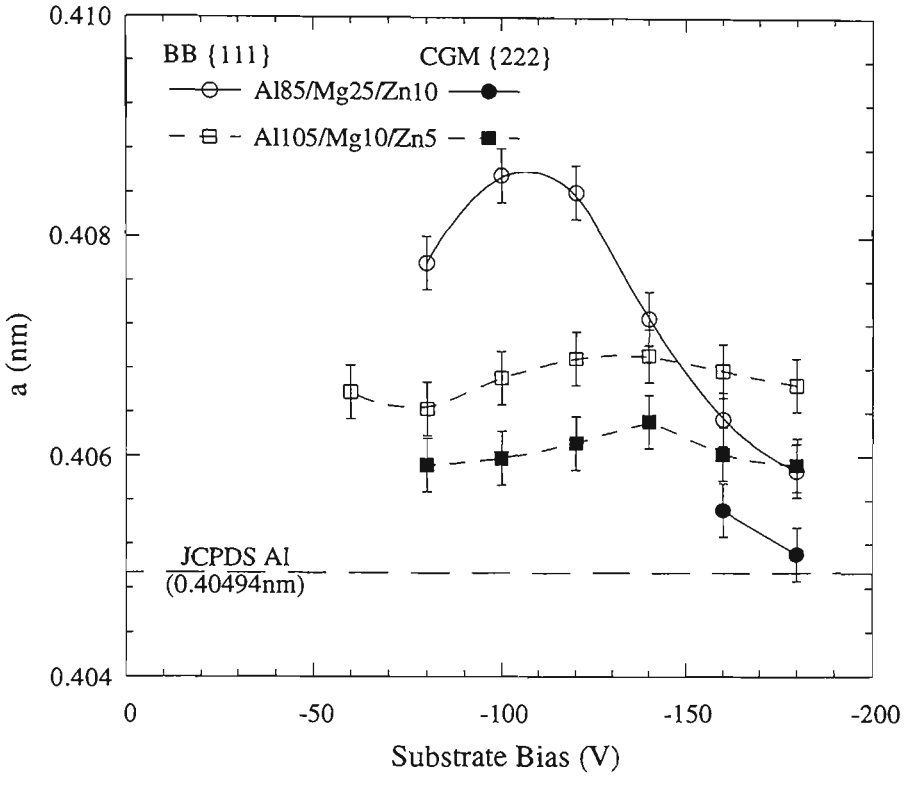

Fig.11.9 Comparison between the {111} d-spacing of (Al) phase measured by Bragg-Brentano XRD and the {222} d-spacing measured by CGM.

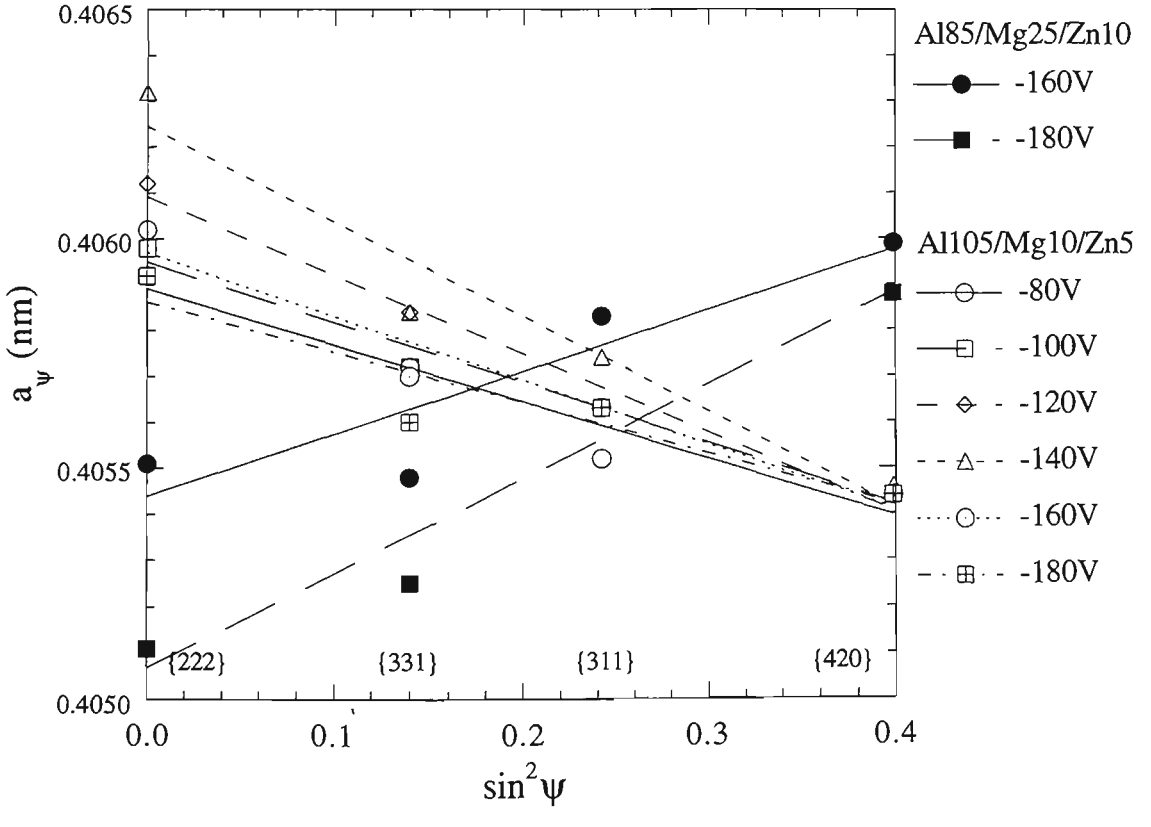

Fig.11.10 $Sin^2\psi$ plots of CGM data for the <111> fibre textured (Al) grains in coatings from the Al/Mg/Zn composite targets.

macrostress or degradation of supersaturated (Al) phase resulting from prolonged ageing. It should be realised that these results relate to coatings as they existed after about one year of ageing.

The lattice parameters measured for the various peaks by asymmetric diffraction scans were plotted as a function of $\sin^2\psi$, as shown in Fig.11.10. Linear regressions were fitted to the data, and the high correlation coefficients obtained indicated an excellent fit to the data. The linear coefficients were used to calculate the strain free lattice parameter a_0 and the residual macrostress σ, using equations appropriate for the <111> texture in these coatings (Sect.4.4.4). The results of these calculations are graphed as a function of the bias voltage in Fig.11.11, along with the results for Al Series 2 coatings (Chap.6) for the purpose of comparison.

The strain-free lattice parameters of (Al) in the Al105/Mg10/Zn5 series were found to be generally slightly greater than those of the pure Al coatings (Fig.11.11a). However, the magnitude of this difference was less than the range of error. It can then be concluded that a_o of the (Al) phase in these alloy coatings was essentially the same as that of pure Al. In contrast, a_o of the coatings from the Al85/Mg25/Zn10 series was significantly greater than that of pure Al. Unfortunately, only two of these coatings could be examined by CGM and therefore no trend in lattice parameter with respect to substrate bias could be determined.

The coatings produced with the two ternary targets provided coatings with opposite magnitudes of residual macrostress (Fig.11.11b). The stress in the Al105/Mg10/Zn5 series was compressive in every case, and its magnitude was typically two to four times greater than that reported for the Al Series 2 coatings. The compressive stress increased to a maximum at -140V bias, and then decreased with further increase in bias. In comparison, the limited results available for the Al85/Mg25/Zn10 series coatings indicated that the residual macrostress was tensile but similar in magnitude to the compressive stress in the Al105/Mg10/Zn5 series coatings. The presence of residual tensile stress in highly reflective coatings such as these is highly unusual, since tensile stresses are usually associated with loosely-packed porous coatings (Sect.2.4.2). It is unlikely that either the contrained shrinkage model or the impurity model would apply to these coatings produced under conditions of high bias. However, it should be recalled that the (Al) phase in the Al85/Mg25/Zn10 coatings is probably only a minor second phase, and the bulk of the coating is thought to be amorphous (Sect.11.2.5). The tensile stress in the (Al) phase might be in response to a larger compressive stress in the amorphous phase.

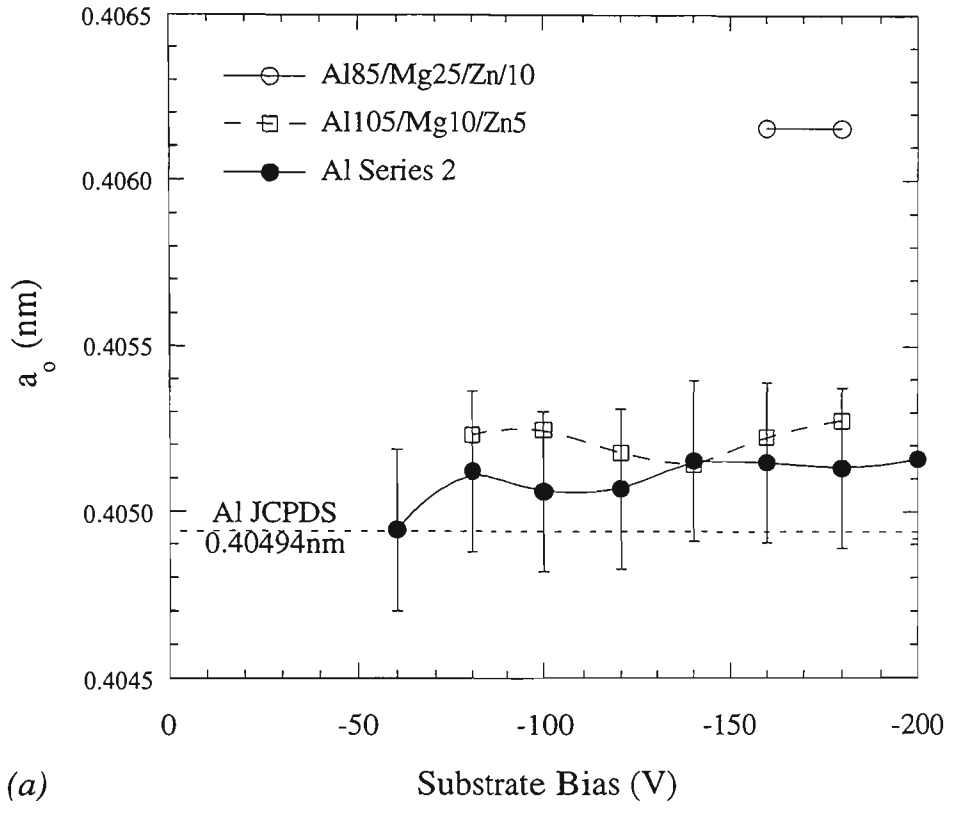

(a)

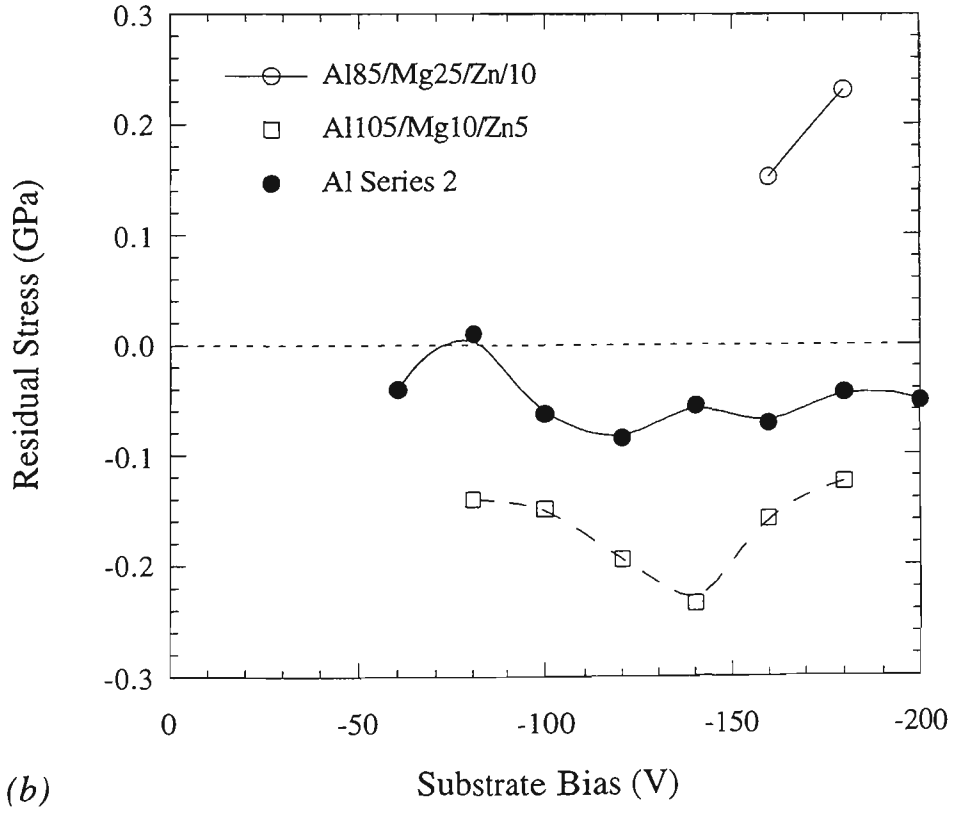

(b)

Fig.11.11 Strain-free lattice parameter (a) and residual macrostress (b) of the <111> fibre textured (Al) grains in coatings from the Al/Mg/Zn composite targets. Results for the Al Series 2 coatings are shown for reference.

11.3 General Discussion

11.3.1 Comparison with Previous Work

Many of the ternary coatings prepared for this work were found to contain (Al) solid solution with a strong <111> fibre texture. No other crystalline phases in the coatings could be detected by XRD. This is despite the chemical composition measured for the coatings which located them in regions on the ternary phase diagram which indicated (Al) in equilibrium with a variety of intermetallic phases (Fig.11.4). For example, under slow-cooled solidification an alloy of the composition corresponding to that of the earth and self bias Al85/Mg25/Zn10 coatings, would be expected to form only *T*-$Mg_{32}(Al,Zn)_{49}$. The compositions corresponding to the remaining coatings from this series, and all coatings from the Al105/Mg10/Zn5 series, would form a combination of (Al) solid solution with *T*, $MgZn_2$ and Mg_2Zn_{11} phases in various proportions, when slowly solidified. This (Al) solid solution has only minimal solid solubility under equilibrium conditions at room temperature. However, in the case of the sputtered coatings, it is feasible that the (Al) phase possessed some degree of supersaturation. With this in mind, an attempt was made to evaluate the extent of supersaturation of the (Al) phase in the ternary coatings (Sect.11.3.2).

It appears highly unlikely that either the ternary *T* phase or icosahedral phase observed in rapidly solidified $Mg_{32}(Al,Zn)_{49}$ alloys [234,237,238,272], were present in any of the sputtered coatings. The *d*-spacing of the {600} line in *T* phase is shown in Fig.11.8a for reference. This line from the *T* phase was the closest match to the measured *d*-spacings. However, considering the complex crystal structure of the *T* phase, and the relatively poor match with the observed *d*-spacing, it is doubtful that it was present in any of the coatings examined. Similarly, the closest *d*-spacings for the icosahedral phase at such compositions were 0.2423 and 0.2292 [197], and both of these are well beyond the scale in Fig.11.8a.

Instead of forming such complex crystalline phases, it looks likely that the sputtered coatings developed an amorphous phase. This amorphous phase was exclusive in several coatings, but usually occurred in addition to the <111> fibre textured (Al) solid solution (Sect.11.2.5). It is worth noting that the complex structured intermetallic phases were also avoided in the Zn-Mg coatings, in favour of an amorphous phase (Chap.10). Thus, the formation of *T* and icosahedral phases may possibly be related to short range order in the liquid phase, as was thought to be the case for the rapidly solidified amorphous phase in Zn-72%Mg alloys (Sect.10.3.1). The formation of an amorphous phase in the ternary alloy coatings may then be understood, since the liquid phase is not

involved in the deposition process. Furthermore, the complex crystal structures of the Mg-Zn intermetallics are not expected to readily form due to their very slow kinetics. It cannot be stressed too strongly, however, that this is a speculative suggestion.

11.3.2 Solid Solubility

The lattice parameter is usually a good indicator of solid solubility, and this was put to effective use in previous chapters to determine the extent of solid solubility in binary alloy coatings. However, the lattice parameter possesses two degrees of freedom in ternary alloy systems, which creates difficulties with the interpretation of solid solubility. It is possible to gain some insight into the extent of supersaturation, but the interpretation is not conclusive.

It is well established that the addition of Zn to (Al) solid solution causes the lattice parameter to decrease (Sect.3.4), while additions of Mg to (Al) have the opposite effect but with a much greater impact (Sect.3.5). Empirically derived relationships for Zn and Mg solute additions to (Al) phase (equations 3.1 and 3.3), can be combined to give the following equation for the ternary system:

$$a\ (\text{nm}) = 0.40494 - 8.3306\text{x}10^{-5}\ \text{Zn (at.\%)} + 4.3387\text{x}10^{-4}\ \text{Mg (at.\%)} \qquad (11.1)$$

This relationship does not account for any synergistic or antagonistic alloying effects that may occur with the mutual presence of both solutes. However, considering the accuracy with which Vegard's Law applies to Al-Zn and Al-Mg binary alloys, it seems reasonably valid to ignore these effects. From equation 11.1, it can be shown that when the ratio of Zn to Mg in the ternary alloy is equal to 5.21, the lattice parameter of the (Al) solid solution will be identical to that of pure Al. This demonstrates that it is not possible to derive a specific ternary composition from a known lattice parameter using this equation. Furthermore, any given lattice parameter for (Al) can be represented by a line on the ternary isothermal diagram rather than a single point.

Lines which represent the average strain-free lattice parameter for each coating series were derived from equation 11.1, and graphed in relation to the composition of the coatings in Fig.11.12. The only coating shown in this diagram are those for which CGM analysis was conducted. The line representing the lattice parameter for the Al105/Mg10/Zn5 series coatings passed very close to the measured chemical composition, and was within the range of error. Consequently, these coatings probably consisted mainly of (Al) phase, such that the majority of Mg and Zn was located in solid solution. The particular combination of Mg and Zn present in the (Al) phase, appears to

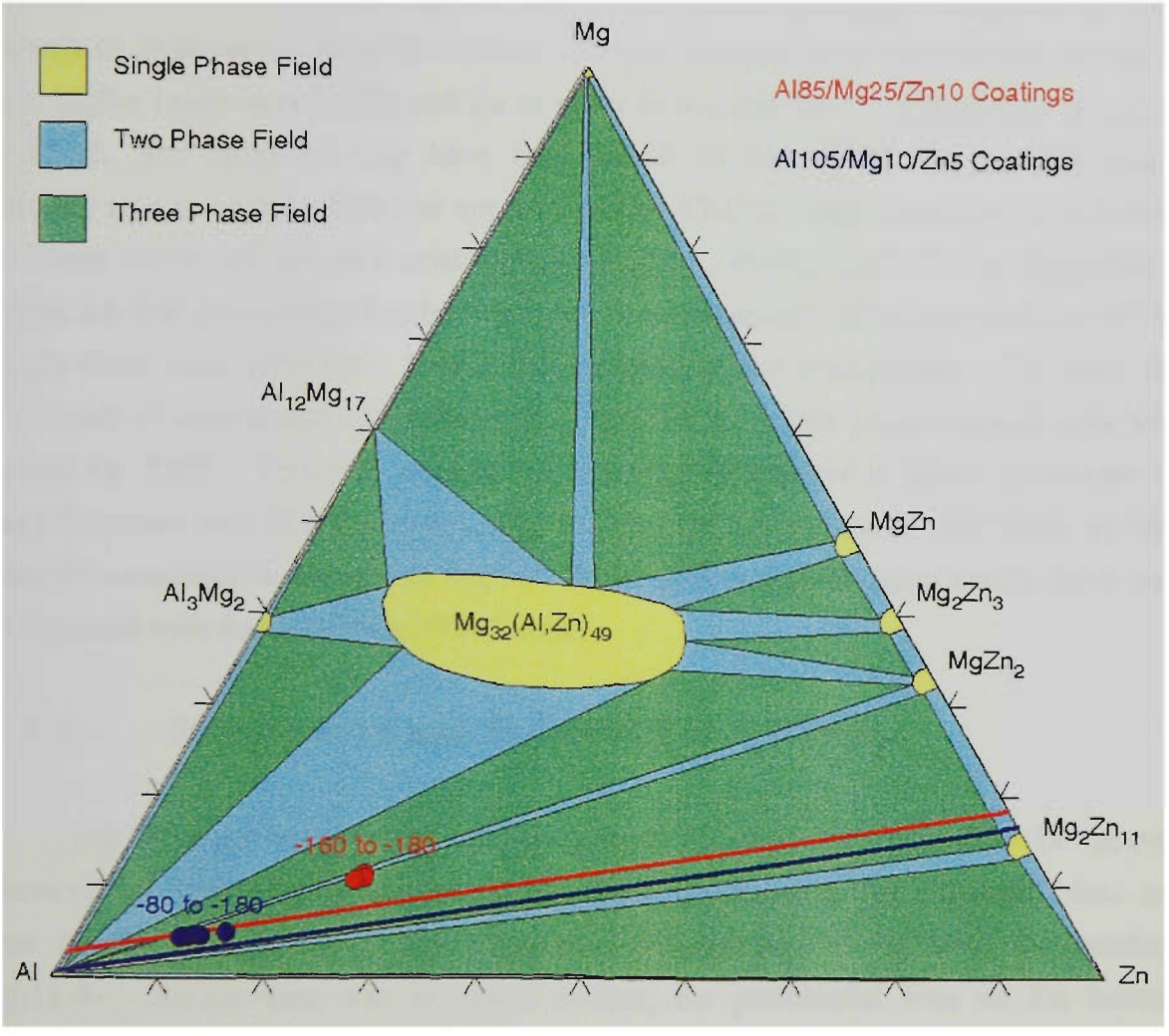

Fig.11.12 Chemical composition (at.%) of some of the Al85/Mg25/Zn10 and Al105/Mg10/Zn5 series coatings represented on the Al-Mg-Zn isothermal section at room temperature. The red and blue lines represent the lattice parameter of (Al) phase measured for the coatings shown, as calculated from equation 11.1.

have had the effect of maintaining a lattice parameter which was very similar to that of pure Al.

A much greater separation between the measured composition and the line predicted from the lattice parameter was found for the Al85/Mg25/Zn10 series coatings (Fig.11.12). This confirms that an amorphous phase probably coexisted in these coatings, in addition to (Al) solid solution. The amorphous phase must have contained a much higher proportion of Mg and Zn in order to account for the differences shown in Fig.11.12, and therefore may have been based on an Mg-Zn intermetallic phase. Although an amorphous phase was not detected by XRD for these coatings, it is feasible that it was undetected due to a small volume fraction. Furthermore, it was suggested in Sect.11.2.6 that the coatings had been subject to some ageing with consequent loss of Mg and Zn from solid solution. If this had resulted in the precipitation of a very fine distribution of intermetallic precipitates, it is unlikely that these phases would have been detected by XRD. This may explain the observed differences in lattice parameter for Bragg-Brentano and CGM analyses (Fig.11.9). The (Al) phase is still likely to have retained a considerable amount of Mg and Zn in solid solution; significantly more than that obtained with the Al105/Mg10/Zn5 series.

11.3.3 Stoichiometry and Preferential Resputtering

The chemical composition of the ternary coatings was found to be heavily influenced by energetic ion bombardment. Small increases in the substrate bias, and hence the ion energy, caused the preferential resputtering of Mg from the coatings (Fig.11.4). As the bias was increased further, the preferential loss of Zn became prominent, such that both Mg and Zn were reduced. It was noted that once the bias reached a sufficiently high level (-140V for Al85/Mg25/Zn10 and -100V for Al105/Mg10/Zn5), the composition of the coatings was relatively stable, suggesting some form of steady-state condition.

The preferential loss of Mg from the ternary coatings at very low bias voltages was consistent with the observations made for the Al-Mg binary coatings (Chap.9). Mg possesses a very low surface binding energy and has the lowest atomic mass of the three metals in the ternary coatings. The presence of Zn in the coatings is expected to have contributed a significant sputter yield amplification effect for the Mg phase, similar to that observed for the Zn-Mg coatings (Chap.10). Consequently, it is not surprising that Mg was preferentially resputtered at such low bias voltages in light of its thermal and elastic collision properties.

The activation of preferential resputtering of Zn at a higher bias condition is also consistent with the results discussed for Al-Zn coatings (Chap.8). It was apparent for the binary alloys that the preferential loss of Zn from the coatings was initiated by the onset of a strong <111> fibre texture in the (Al) phase. However, in the ternary alloy coatings, it appears that the onset of Zn preferential resputtering occurred at a substantially lower bias than was necessary for the development of the fibre texture in (Al) phase. This seems to suggest that the development of texture in the (Al) phase and the rejection of Zn from the coatings were not necessarily dependent parameters, as was proposed for the Al-Zn coatings. However, it does appear likely that both factors were strongly influenced by the specific effects of ion bombardment in combination with the coating composition. The textured growth in the (Al) phase required sufficient adatom mobility for it to develop, and this was afforded by energetic ion bombardment. Hence the coating composition influenced the texture due to the sputter yield amplification effect. Similarly, the preferential resputtering of Zn was dependent on composition via the surface binding energy and sputter yield amplification. It would be valuable to conduct an extensive simulation study for ternary alloy deposition with concurrent ion bombardment in order to help clarify some of these effects.

It is noteworthy that the self and -40V bias coatings from the Al105/Mg10/Zn5 series were of essentially the same chemical composition as the high bias coatings produced with the Al85/Mg25/Zn10 target (Fig.11.4). The only significant difference in composition was that some of the latter coatings also contained a high proportion of buried Ar (Fig.11.5). The microstructures of these two sets of coatings were decidedly different. The Al85/Mg25/Zn10 coatings were found to contain (Al) phase with a very strong <111> fibre texture, compared with the almost completely amorphous structure of the Al105/Mg10/Zn5 coatings. It would therefore appear that the formation of textured (Al) phase in coatings of this particular composition was favoured when energetic ion bombardment was present, whereas they were primarily amorphous in cases where the ion bombardment was of much lower energy. This finding is in agreement with the development of fibre texture in pure Al coatings (Chap.6), and therefore suggests that the presence of Mg and Zn in solid solution did not interrupt the textured growth.

Finally, mention should also be made of the buried Ar content of the coatings (Fig.11.5). Similar behaviour was observed for the Zn, Mg, and some Al-Zn coatings described in previous chapters. It is considered that such peaks in the Ar content may possibly have been due to a dynamic balance between the implantation of Ar^+ ions into the coating as it was deposited, opposed by the reduction in deposition rate that resulted from resputtering (Fig.11.2). The reduction in Ar content at high bias voltages therefore occurred because the deposition rate was reduced to a sufficient level to enable much of

the Ar to diffuse or resputter out before being trapped in the coating. The existence of Ar in these coatings apparently did not cause amorphization of the crystalline phase as it seemed to do for (Mg) in Al-Mg and Zn-Mg coatings (Chaps.9 and 10). This is possibly because the buried Ar was associated with the amorphous phase rather then the (Al) solid solution.

11.4 Summary

Ternary Al-Mg-Zn alloy coatings were highly susceptible to compositional modification by ion bombardment. With small increases in the substrate bias, the coatings were rapidly depleted of Mg while maintaining an essentially constant Al/Zn ratio. Beyond a critical substrate bias, preferential resputtering of Zn became active such that the composition of the coatings shifted towards pure Al. The coating composition tended to approach a steady state condition as bias was increased further. Therefore, it appears that stoichiometric control of ternary Al-Mg-Zn coatings is particularly difficult when ion assistance is incorporated.

The microstructure of the ternary coatings was characterised by either crystalline or amorphous phases depending on the chemical composition and ion assistance conditions. No ternary or binary intermetallic phases were present. Coatings produced with a minimum of ion assistance were generally dominated by an amorphous phase. It is feasible that this phase was stabilised by the presence of impurities derived from the epoxy resin in the composite targets. Increasing the substrate bias led to development of (Al) solid solution with a strong <111> fibre texture. The degree of supersaturation could not be specified, although there was some indication that single-phase (Al) coatings were produced at the highest bias conditions, with about 10-12%Zn and 5%Mg in solution. Elevated substrate bias also resulted in the entrapment of Ar in the coatings that had a large proportion of amorphous phase. The buried Ar did not seem to interrupt formation of the fibre textured (Al) phase.

Chapter 12

Electrochemical Performance

12.1 Deposition Parameters

In light of the extensive effort devoted to the microstructural characterization of the sputtered coatings described in the previous chapters, only a limited effort was given to the evaluation of their electrochemical behaviour. The substrate bias voltage was eliminated as a variable, principally because of the associated problems encountered with excessive Ar burial and preferential resputtering. Only self biased coatings were prepared for electrochemical evaluation. Each of the sputtering targets described in Sect.4.2 were used to deposit coatings for evaluation. Generally, five coatings were prepared for each specific coating composition, and the electrochemical behaviour of most of these was examined in order to gain an appreciation for the variability of the tests. Pure Mg coatings were not included in this study because it was anticipated that the corrosion rate would be excessive for a sacrificial coating (Sect.3.3).

The coatings prepared for electrochemical evaluation were deposited onto low-carbon steel substrates. Steel substrates were necessary for the corrosion tests because the coatings were very thin in comparison with commercial hot-dipped coatings. The sputtered coatings were nominally 1 μm compared with about 20 μm typically for galvanised steel sheet products. It was anticipated that the coverage of the thin coating on the substrate would not be complete and galvanic coupling between the coating and substrate would invariably occur. The measured potentials are those of a galvanic couple of the thin coating and steel, and not of the coating alone. This would tend to increase the corrosion potential and corrosion current density for coatings that were more active than steel, due to the increased cathodic area supplied by the exposed steel.

Thicker coatings would improve the coverage of the steel surface, and it is certainly possible to produce thicker coatings by sputtering. This path was not pursued for several reasons. The coating thickness of sputtered coatings is directly governed by the deposition time and magnetron power. It was undesirable to operate the magnetron targets at a power greater than 100 W because it was feared that the attendant target

heating may have caused failure of the epoxy adhesive used in their construction. This left the deposition time as a possible variant. However, the deposition of 20 μm coatings would have required an excessive coating preparation time, and the number of different coating compositions examined would have been extremely limited. The composite targets were also unsuited to long periods of operation, since the development of stepped erosion profiles resulted in a gradual drift in the sputtered flux composition.

A summary of the generic deposition conditions common to all of the coatings prepared for electrochemical evaluation is given in Table 12.1. The individual coating parameters specific to each series of coatings are summarised in Table 12.2. The deposition times for each target were selected so that they provided nominally 1 μm thick coatings, calculated from the mass deposition rates reported in previous chapters. Prior to corrosion testing, the chemical compositions of the coatings were checked by EDS analysis. The average coating composition measured for each target is also listed in Table 12.2. It should be noted that the composition of the alloy coatings from each target did not necessarily match the composition determined for the corresponding ion assisted coatings (Chaps.8 to 11). This is because the targets were quite heavily eroded by the time they were used for deposition of the coatings for corrosion evaluation, and this influenced the sputtered flux composition, particularly for the composite targets. Generally, the observed difference in composition between these two sets of coatings was within ±5 at.%. The individual coatings are referred to throughout the remainder of this chapter in terms of their actual composition, in preference to the target descriptor. For general reference, the composition of all coatings is summarised on a ternary diagram in Fig.12.1.

Table 12.1 Generic deposition parameters common to all sputtered coatings (unless noted otherwise).

Substrates	low-carbon steel discs; 22 mm diameter, 0.8 mm thickness
Exposed area of substrates	18 mm diameter (via cover mask)
Target to substrate distance	60 mm
Substrate temperature	50°C
Ar flow rate	18 sccm
Operating pressure	0.20 Pa
Magnetron power	100 W high voltage supply
Magnet configuration	M3 (fully magnetised)
Coating thickness	1 μm nominal
Number of coatings prepared	5

Table 12.2 Specific deposition parameters and chemical composition of coatings prepared for electrochemical evaluation.

Target	Base Pressure (μPa)	Magnetron		Self Bias (V)	Deposition Time (min)	Composition (at.%)		
		Voltage (V)	Current (A)			Al	Mg	Zn
Al [1]	84	410	0.48	-24	9	100	–	–
Zn	67	459	0.21	-26	3	–	–	100
Al-11%Zn	88	378	0.26	-26	14	91.1	–	8.9
Al-24%Zn	68	415	0.24	-27	10	74.8	–	25.2
Al-39%Zn	106	483	0.20	-26	9	59.5	–	40.5
Al-50%Zn	72	458	0.21	-26	8.5	45.1	–	54.9
Al-73%Zn	120	494	0.20	-26	6	26.4	–	73.6
Al-90%Zn	94	527	0.19	-26	4.5	8.4	–	91.6
Al115/Mg5	80	399	0.25	-26	14	91.5	8.5	–
Al105/Mg15	63	411	0.24	-26	12	74.9	25.1	–
Al90/Mg30	96	385	0.25	-26	8.5	59.1	40.9	–
Al60/Mg60	89	359	0.28	-26	6.5	28.0	72.0	–
Al30/Mg90	69	353	0.28	-26	4.5	13.8	86.2	–
Zn90/Mg30	97	514	0.19	-25	3.5	–	3.4	96.6
Zn60/Mg60	72	438	0.22	-26	4.5	–	20.4	79.6
Zn40/Mg80	96	388	0.25	-26	5	–	43.0	57.0
Zn20/Mg100 [2]	57	363	0.27	-27	6	–	65.0	35.0
Zn10/Mg110 [2]	81	345	0.28	-27	6	–	81.5	18.5
Al85/Mg25/Zn10	60	390	0.25	-26	11	39.8	30.4	29.8
Al105/Mg10/Zn5	72	412	0.24	-26	14	66.8	13.1	19.9

(1) The Al coatings were deposited with a magnetron power of 200W

(2) Only three coatings were prepared from the Zn20/Mg100 and Zn10/Mg110 targets

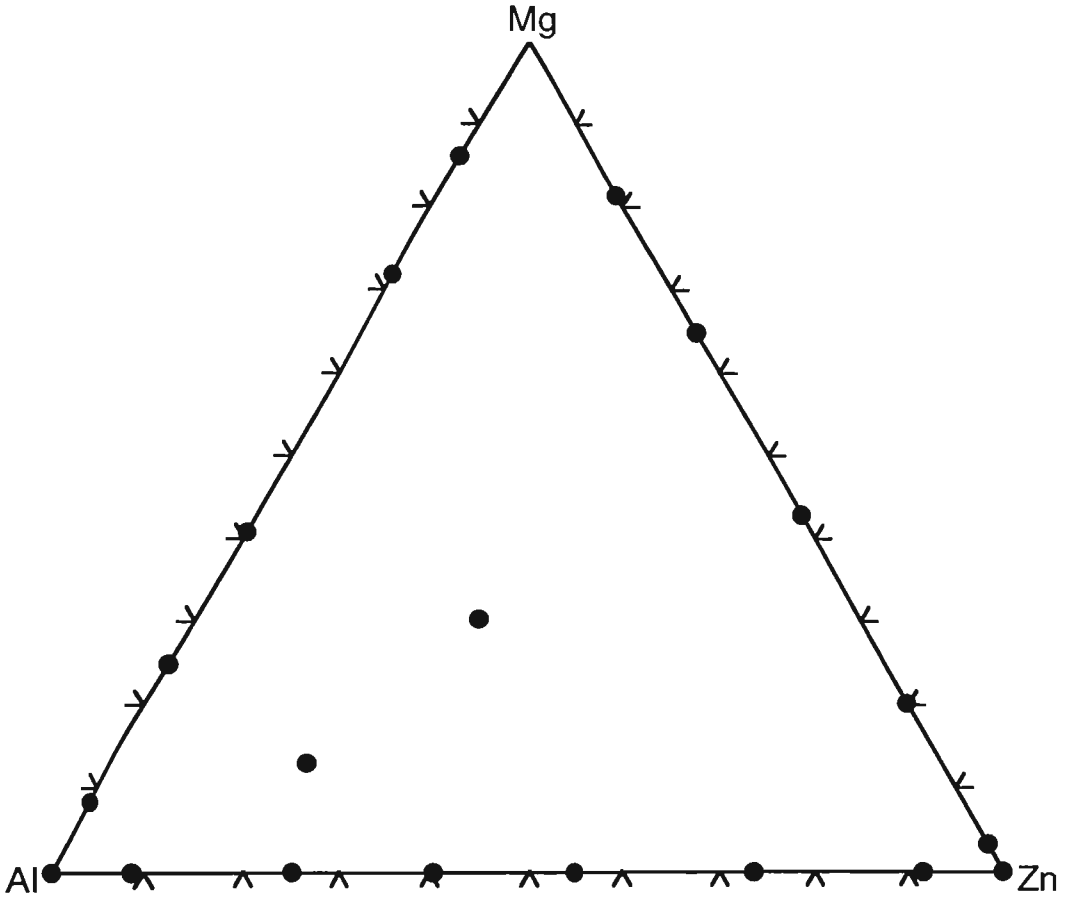

Fig.12.1 Summary of the chemical compositions of coatings used for electrochemical tests.

12.2 Results and Discussion

The results of the corrosion potential monitoring and anodic potentiodynamic polarisation scans are presented in the following sections for the coatings: elemental metallic, Al-Zn binary alloy, Al-Mg binary alloy, Zn-Mg binary alloy, and Al-Mg-Zn ternary alloy. A description of the polarization behaviour of the steel substrate is also presented. The results for the coatings are discussed individually within each of these sections, and a broad overview is given in Sect.12.3.

12.2.1 Steel Substrate

Before commencing the evaluation of the electrochemical behaviour of the coatings, it was salient to examine the steel substrate material. A potentiodynamic polarisation scan of the low carbon steel substrate is presented in Fig.12.2. This scan was conducted after the sample had begun to develop red rust, and was therefore in an activated state. The corrosion potential was found to be about -650 mV (SCE), which is similar to other reported values, eg. -670 mV in 3.5 wt.% $NaCl_{(aq)}$ (equivalent to 21 $g.L^{-1}$ Cl^-) [239]. The anodic scan was commenced below the corrosion potential, and the initial rapid reduction in current density was probably related to the consumption of available oxygen in solution near the sample. Hence, the diffusion limited cathodic reaction was not observed, even though it is expected to have been present. By projecting the portion of the cathodic curve between potentials of -740 to -640 mV (Fig.12.2), it was possible to estimate a diffusion limited current density of about $4x10^{-6}$ $A.cm^{-2}$. In air-saturated non-agitated aqueous solutions, the limiting current density for oxygen reduction is typically about 10^{-4} $A.cm^{-2}$ [2]. In the present case, the solubility of oxygen would have been considerably reduced by nitrogen bubbling. Thus, the limiting current density for oxygen reduction was perhaps an order of magnitude lower than in a saturated solution. This gives a theoretical value of about 10^{-5} $A.cm^{-2}$, which agrees reasonably well with the limiting current density estimated from the experimental results.

The anodic portion of the polarisation scan for the steel sample was marred by instrumental artefacts between -600 and -560 mV (SCE), and again at about -460 mV. This was caused by instability in the current ranges of the potentiostat (Sect.4.5.3). However, the general behaviour can be surmised by extrapolation, ignoring the noisy current signals. The Tafel slope at low overpotentials (less than +100 mV) was about 60 mV (Fig.12.2), which is typical of such steels in the present electrolyte [3]. At higher potentials, the Tafel slope increased to about 200 mV, consistent with slight passivity or perhaps diffusion limited anodic polarisation. These very high anodic currents are not particularly relevant, since sheet steels are rarely polarised to such levels in practical

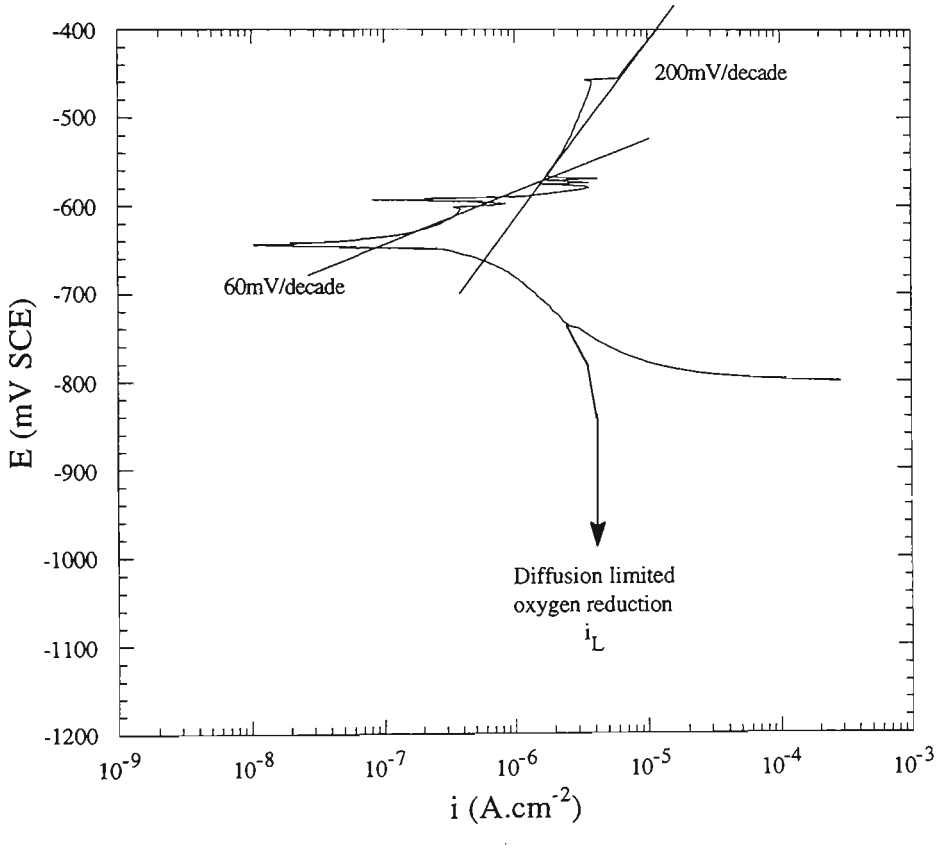

Fig.12.2 Potentiodynamic polarisation scan for sheet steel substrate material.

application. Of much greater significance in the present situation is the cathodic behaviour, since the aim of sacrificial protection is to couple the steel with a more active material.

12.2.2 Elemental Metallic Coatings

The corrosion potential and potentiodynamic polarisation scans for the Zn and Al coatings are shown in Figs.12.3 and 12.4 respectively. The corrosion potentials for both Zn and Al coatings dropped sharply during the first few minutes of immersion before reaching a relatively constant value after 10-15 minutes. The corrosion potential of the Zn coatings was considerably more noble than is usually reported for bulk Zn. This could quite possibly have been caused by galvanic coupling effects with the poorly covered steel substrate. The Zn coatings were still considerably more active than the Al coatings, and this difference matches well with common experience on bulk materials.

The potentiodynamic polarisation scans indicated that the corrosion behaviour of the sputtered coatings was similar to that of the bulk materials. The Zn coatings showed no sign of a passive region (Fig.12.3b), and the active region followed a straight line represented by a Tafel slope of about 60 mV. The corrosion potential measured during the anodic scan, indicated by the cusp between -900 and -1000 mV (SCE), was very similar to those recorded before the scan was commenced. The slight variability in this "dynamic" corrosion potential was conceivably caused by small differences in the relative proportion of steel substrate exposed through each coating. In comparison to the Zn coatings, the polarisation scans for the Al coatings showed a large passive region (Fig.12.4b). For bulk Al in chloride solutions, there is usually a very sharply defined pitting potential followed by a rapid increase in current density [3]. Instead, a very gradual change from passive to transpassive behaviour was observed for the Al coatings. The reason for this behaviour is possibly related to a contribution of anodic currents from the steel substrate at potentials greater than -650 mV.

12.2.3 Aluminium-Zinc Alloy Coatings

The corrosion potential and polarisation scans for the six different compositions of Al-Zn alloy coatings are shown in Figs.12.5 to 12.10. Four samples of each coating composition were examined. The important parameters extracted from the potentiodynamic polarisation curves are summarised in Fig.12.11. These graphs show the impact of Zn content on the corrosion potential E_{corr} and pitting potential E_{pit} , polarization resistance R_p, and passive current density i_p. Data for the Al-Mg-Zn coatings are also shown in Fig.12.11 and are discussed in Sect.12.2.6. It should be noted that the

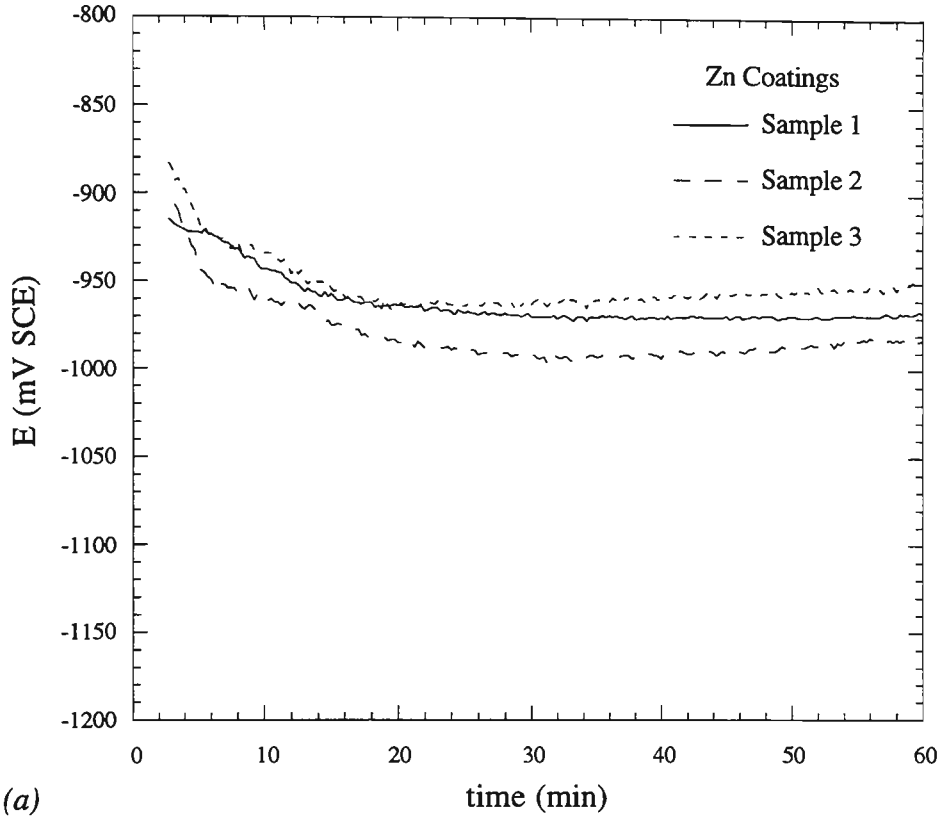

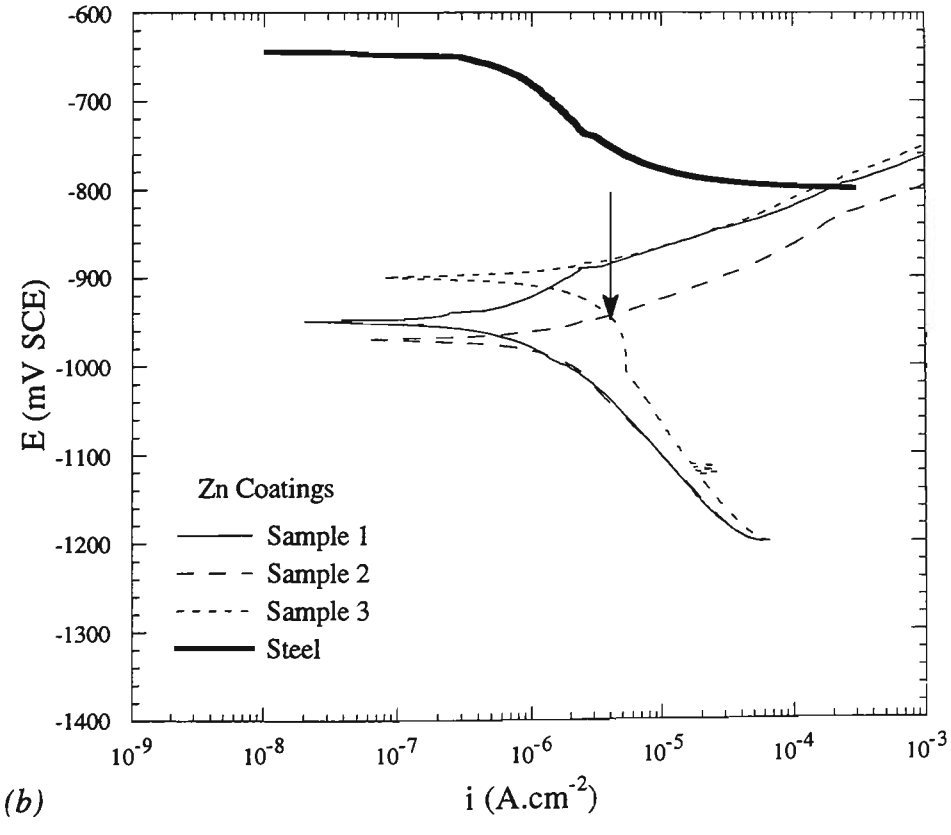

Fig.12.3 Electrochemical results for Zn coatings: (a) corrosion potential as a function of time after immersion, (b) potentiodynamic polarisation scans. The cathodic portion of the scan of steel is shown for reference. The diffusion limited current density for oxygen reduction on steel is indicated by the arrow.

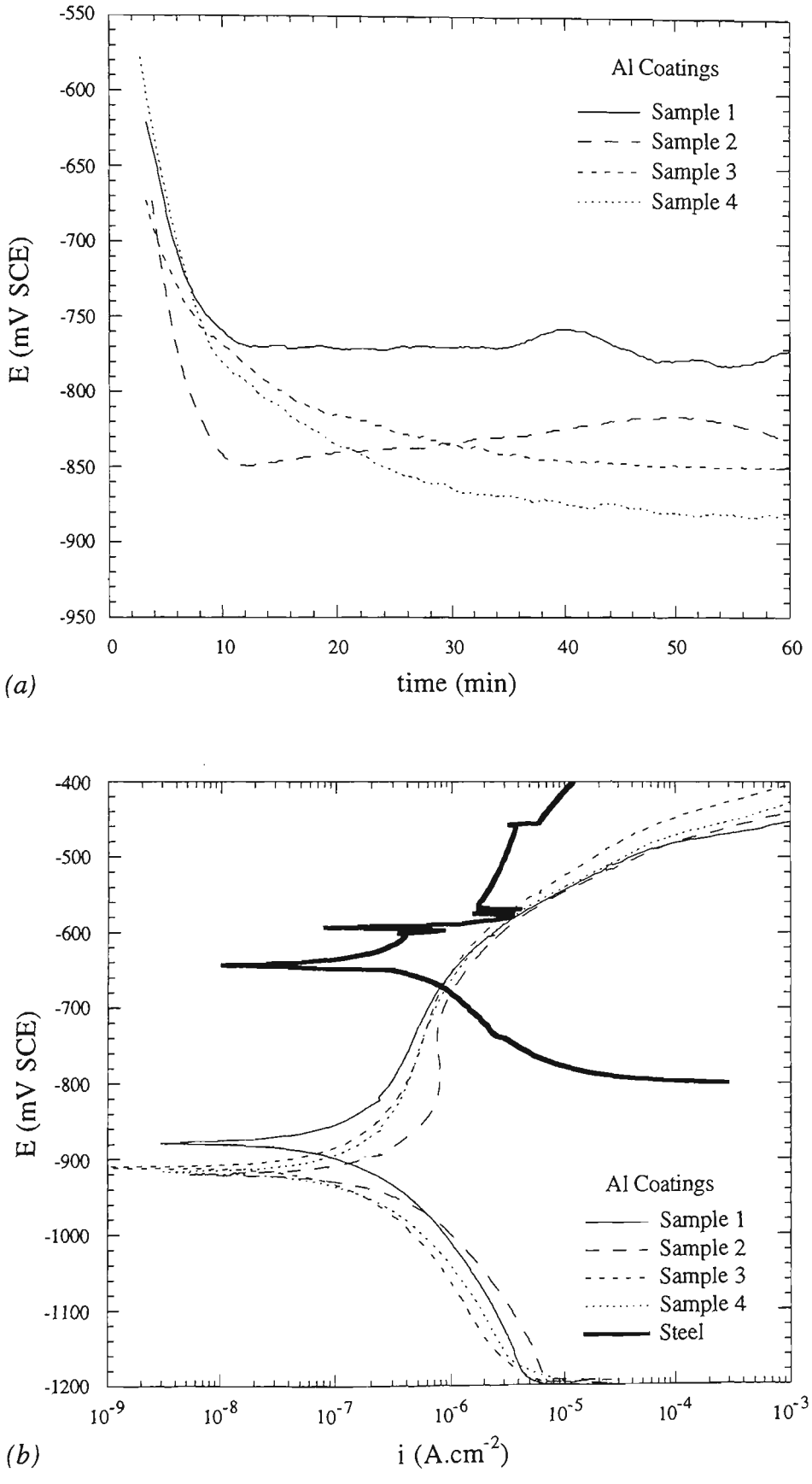

Fig.12.4 Electrochemical results for Al coatings: (a) corrosion potential as a function of time after immersion, (b) potentiodynamic polarisation scans. The polarisation scan of steel is shown for reference. The diffusion limited current density for oxygen reduction on steel is indicated by the arrow.

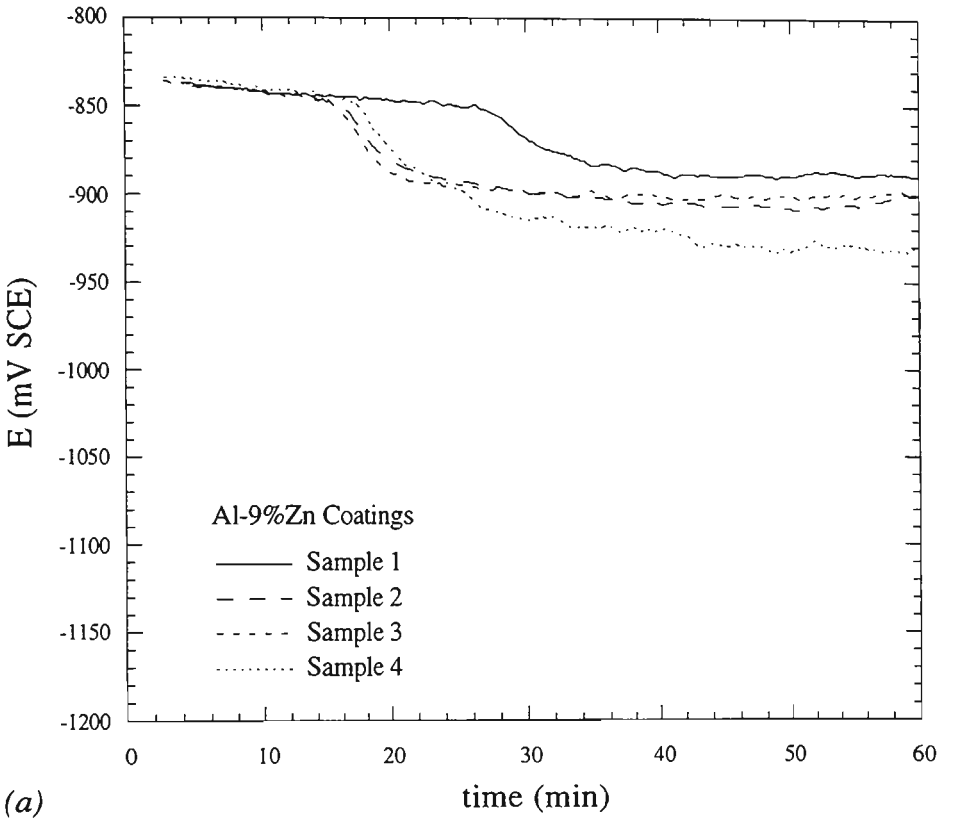

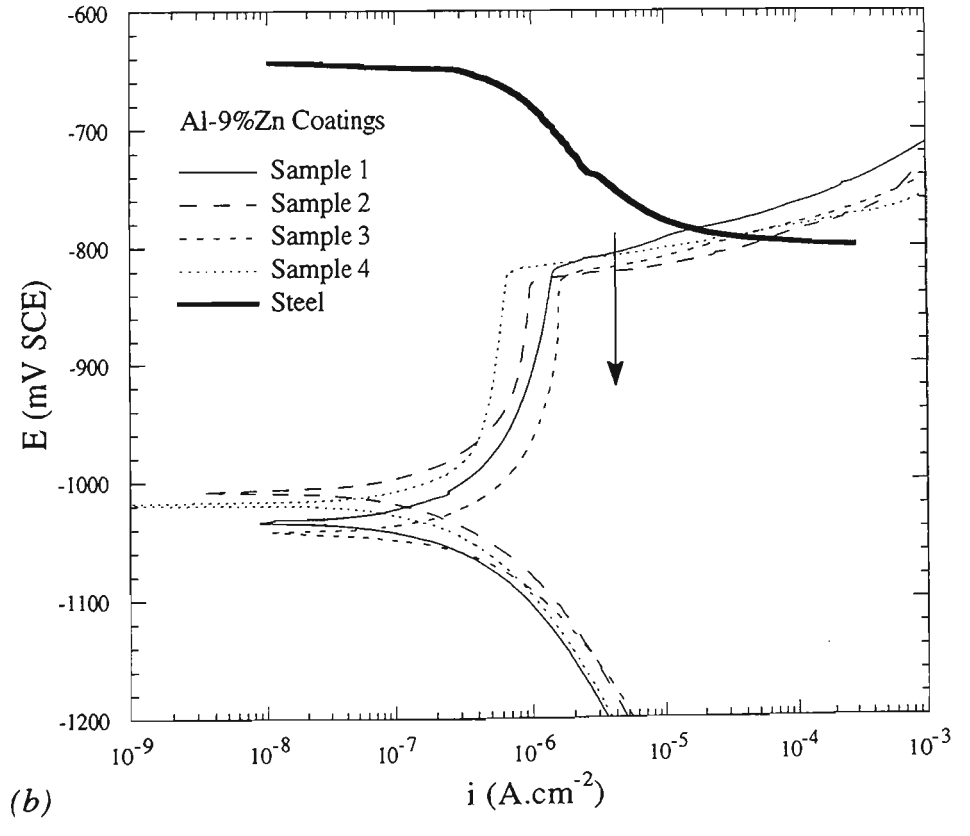

Fig.12.5 Electrochemical results for Al-9%Zn coatings: (a) corrosion potential as a function of time after immersion, (b) potentiodynamic polarisation scans. The cathodic portion of the scan of steel is shown for reference. The diffusion limited current density for oxygen reduction on steel is indicated by the arrow.

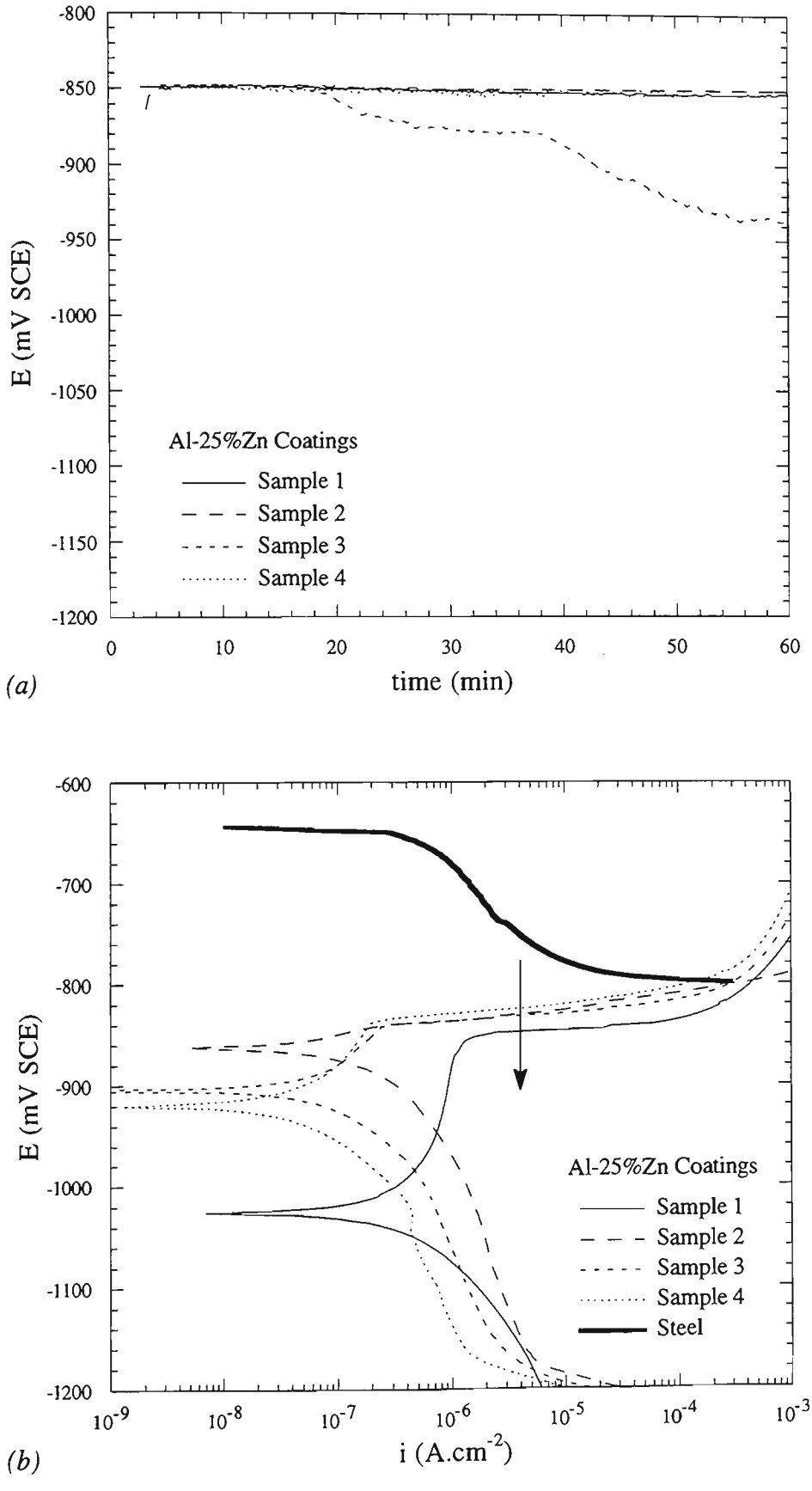

Fig.12.6 Electrochemical results for Al-25%Zn coatings: (a) corrosion potential as a function of time after immersion, (b) potentiodynamic polarisation scans. The cathodic portion of the scan of steel is shown for reference. The diffusion limited current density for oxygen reduction on steel is indicated by the arrow.

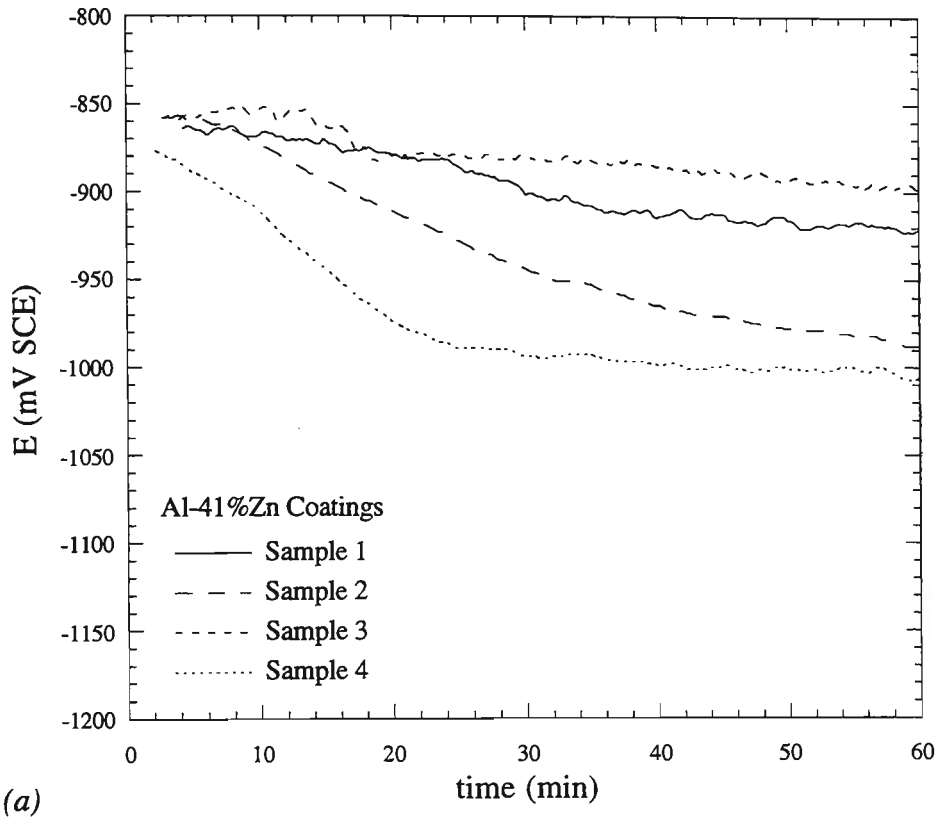

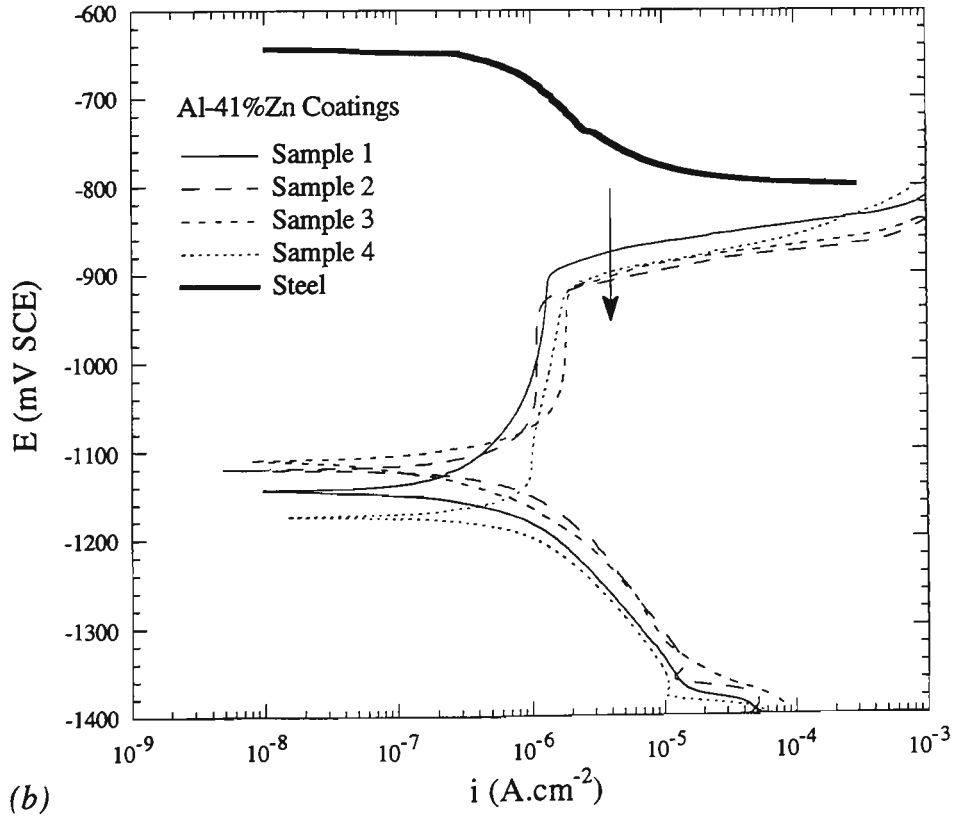

Fig.12.7 Electrochemical results for Al-41%Zn coatings: (a) corrosion potential as a function of time after immersion, (b) potentiodynamic polarisation scans. The cathodic portion of the scan of steel is shown for reference. The diffusion limited current density for oxygen reduction on steel is indicated by the arrow.

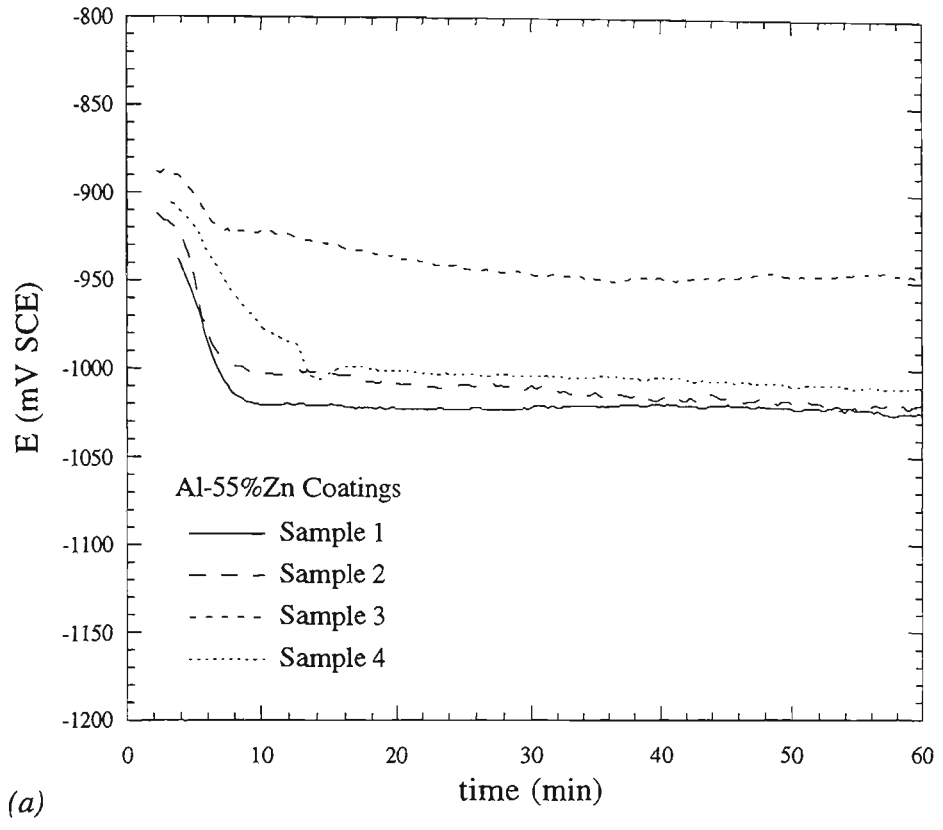

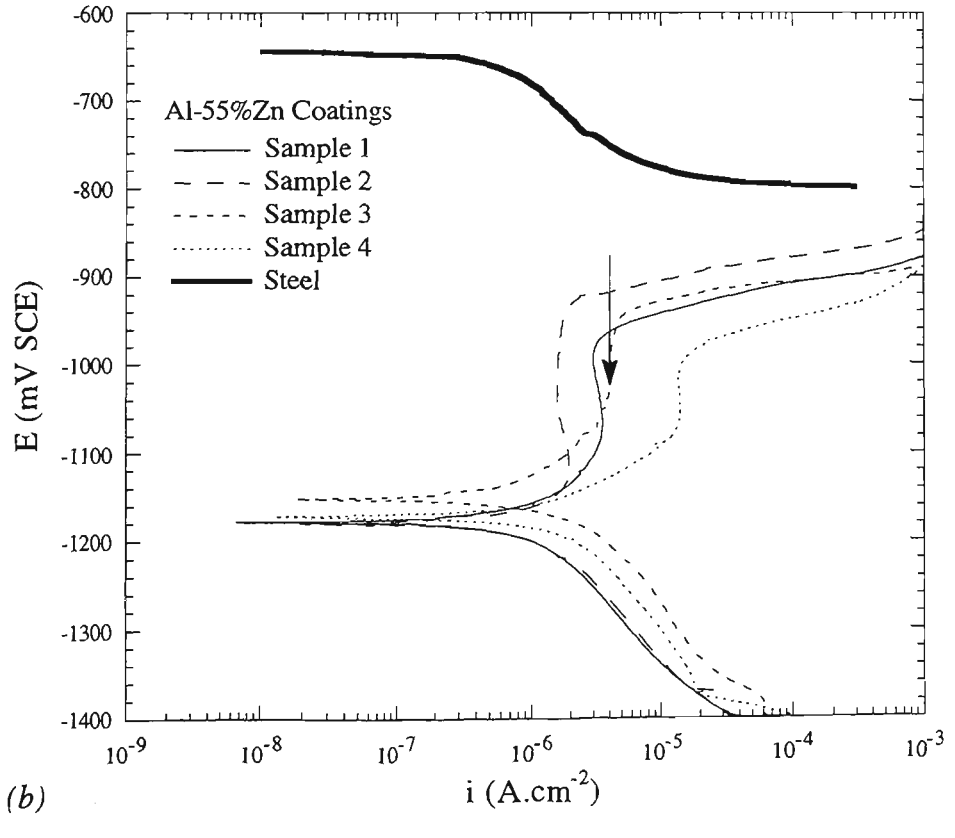

Fig.12.8 Electrochemical results for Al-55%Zn coatings: (a) corrosion potential as a function of time after immersion, (b) potentiodynamic polarisation scans. The cathodic portion of the scan of steel is shown for reference. The diffusion limited current density for oxygen reduction on steel is indicated by the arrow.

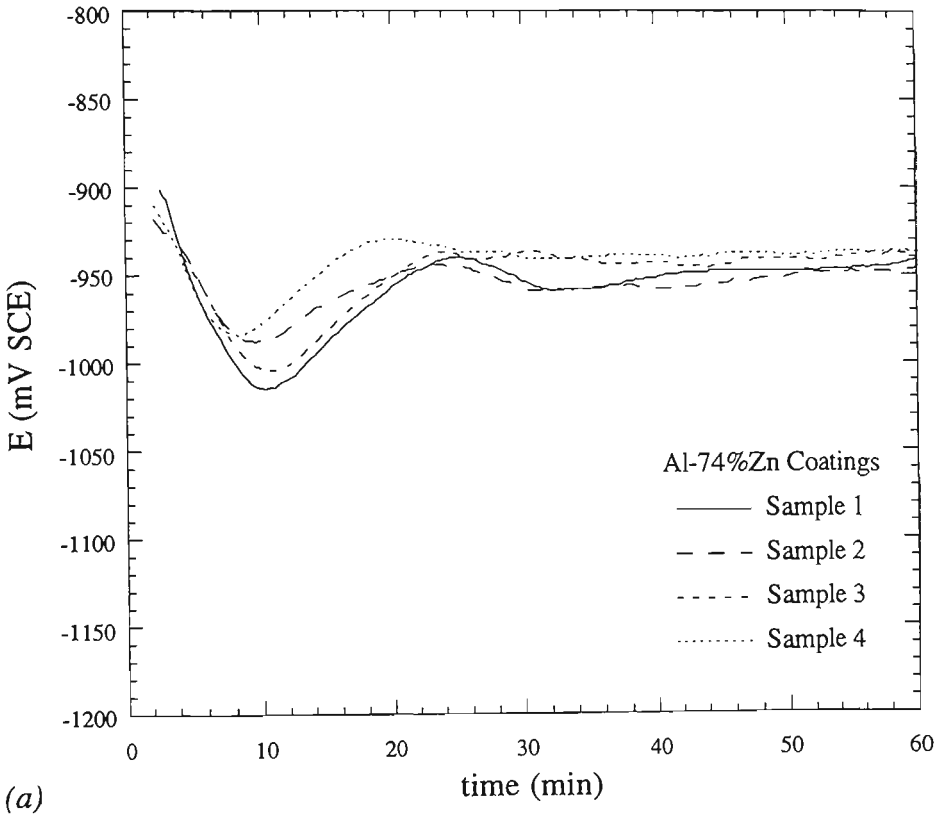

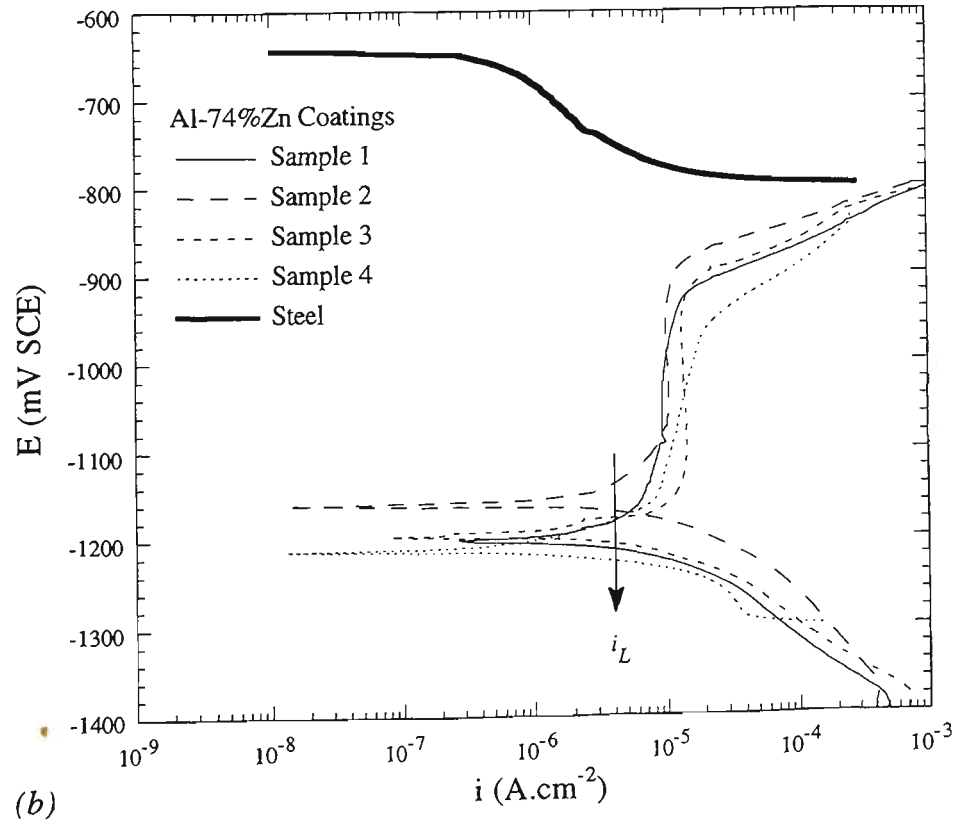

Fig.12.9 Electrochemical results for Al-74%Zn coatings: (a) corrosion potential as a function of time after immersion, (b) potentiodynamic polarisation scans. The cathodic portion of the scan of steel is shown for reference. The diffusion limited current density for oxygen reduction on steel is indicated by the arrow.

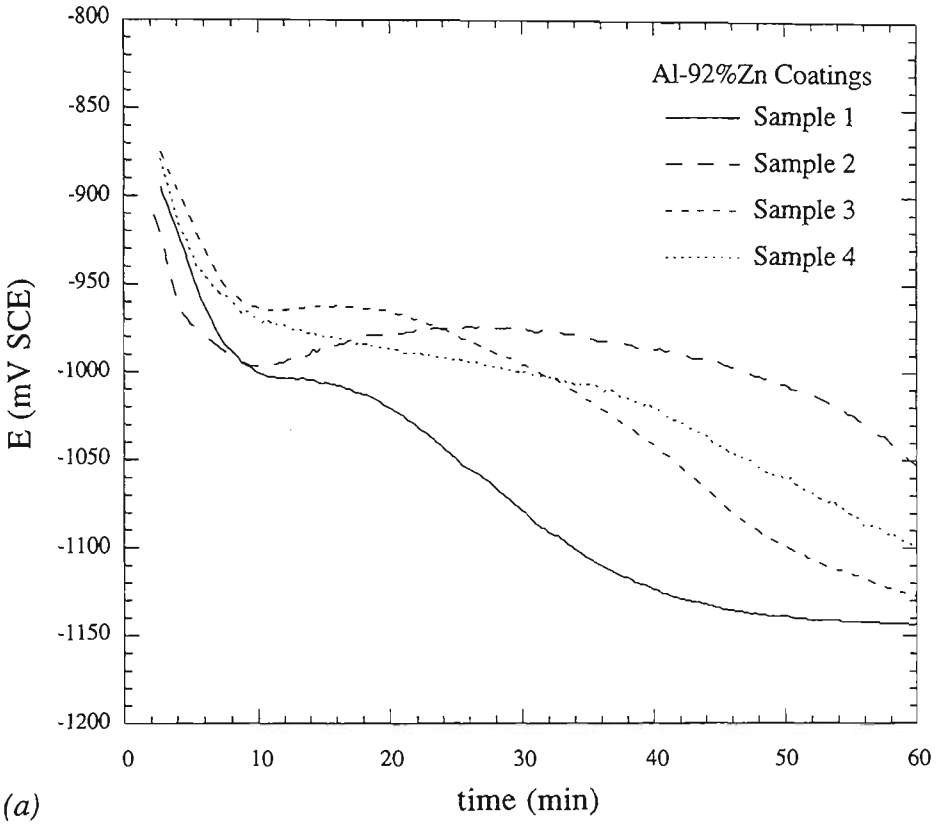

(a)

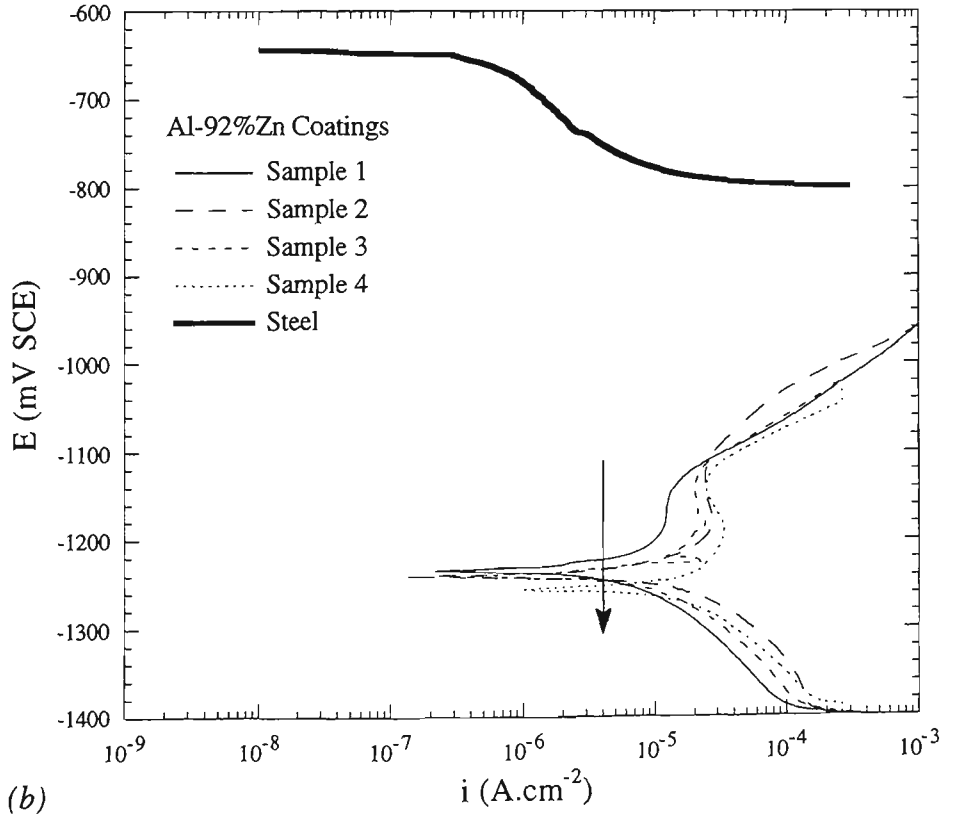

(b)

Fig.12.10 Electrochemical results for Al-92%Zn coatings: (a) corrosion potential as a function of time after immersion, (b) potentiodynamic polarisation scans. The cathodic portion of the scan of steel is shown for reference. The diffusion limited current density for oxygen reduction on steel is indicated by the arrow.

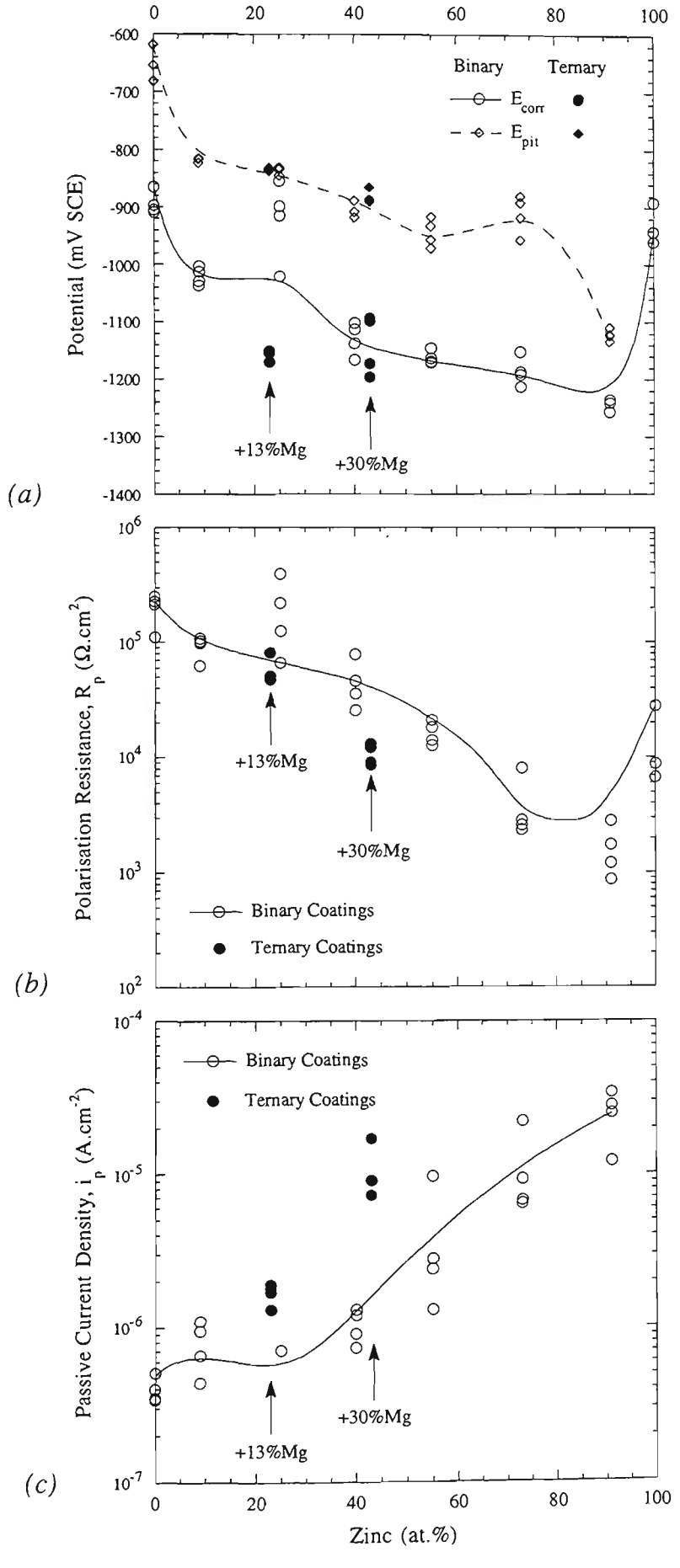

Fig.12.11 Summary of data extracted from polarisation scans for Al-Zn coatings: (a) corrosion potential E_{corr} and pitting potential E_{pit}, (b) polarisation resistance R_p, and (c) passive current density, i_p. The data for ternary Al-Mg-Zn coatings are also shown for comparison.

E_{corr} shown in Fig.12.11a was measured from the potentiodynamic polarisation scans and is denoted in the following text as a "dynamic" E_{corr}.

The E_{corr} for all of the samples was generally about -850 mV (SCE) immediately after immersion in the test solution (Figs.12.5a to 12.10a). Coatings with less than about 55%Zn remained at this potential for anywhere between a few minutes and over an hour. After this period, the E_{corr} of the low Zn coatings dropped sharply and then stabilised at a second relatively constant value of between -900 and -1020 mV (SCE). The potential corresponding to this second plateau region tended to decrease as the Zn content of the alloy was raised. This potential was similar to the corrosion potential measured for the pure Zn coatings, and suggests that the dominant degradation mechanism in the Al-Zn alloys was Zn corrosion. This result is to be expected, based on the lower corrosion potential of Zn compared with Al (Figs.12.3 and 12.4), and the dual phase microstructure of the coatings (Chap.8). The Al-74%Zn coatings displayed an unusual oscillation in their E_{corr} (Fig.12.9a), before stabilising at about -940 mV (SCE). Comparable behaviour in the E_{corr} of the Al-92%Zn coatings was observed, although a much greater time was required before stable conditions were attained. The minimum E_{corr} of the Al-92%Zn coatings was about 200 mV more active than that of pure Zn coatings.

In general, the Al-Zn coatings were found to contain an active-passive transition with a reasonably large passive region. A "nose" on the polarisation curve, which indicates the critical current density for passivation, was only observed to be present for the Al-55%Zn and Al-92%Zn coatings. This was probably because the cathodic current due to oxygen reduction could not be sufficiently reduced to observe the true active region for the coatings [322]. The value of the critical current density in these coatings was only slightly greater than the passive current density. The onset of transpassive behaviour in most cases was marked by a very sharp increase in the current density at a well defined pitting potential. The pitting potential for the high Zn coatings was more gradually distributed. The current density in the passive region for the Al-74%Zn and Al-92%Zn coatings was comparatively high, and it is therefore possible that the anodic reaction became diffusion limited, and did not truly exhibit passivation. Further work using much slower scan rate and thicker coatings would be necessary to provide a more conclusive indication of the electrochemical behaviour of these Zn-rich sputtered coatings.

The polarisation scans for each Al-Zn composition were very reproducible, except for the Al-25%Zn coatings (Fig.12.6b). The main source of variability in the multiple samples of this composition was in the "dynamic" E_{corr}, which influenced the size of the passive region. Sample 1 in this series showed a very large passive range, sample 2 followed entirely active behaviour (possibly transpassive), and the remaining two samples

had a very short passive region. The scan on sample 1 was commenced at -1400 mV (SCE), whereas the other three samples were commenced at -1200 mV (SCE). Furthermore, the comparatively long delay before the corrosion potential began to decrease (Fig.12.6a), infers that the passive layer on these coatings was very stable. A large range in R_p was also found for these coatings, indicating a large variability in the corrosion rate (Fig.12.11b). Combination of these results suggests that only the first sample was fully activated before reaching the anodic portion of the polarisation scan. This is an interesting finding since it suggests that the passive layer on the surface of Al-25%Zn alloy coatings is particularly resilient to breakdown. However, the Al-25%Zn coatings would also be susceptible to localised corrosion due to irregular breakdown of the passive film.

Increasing the Zn content of the Al-Zn alloy coatings tended to shift E_{corr} and E_{pit} to more active potentials (Fig.12.11a). The separation between E_{corr} and E_{pit} was relatively independent of Zn content. This trend was continuous for all of the alloy Al-Zn coatings. However, the E_{corr} of the pure Zn coatings was much greater than that of the Al-92%Zn coatings. The corrosion potential of the alloy coatings was sufficiently active to suggest that the (Al) phase corroded in an active fashion. It is feasible that the activation of Al corrosion was aided by supersaturation of Zn in the (Al) phase (Chap.8). Furthermore, the relatively high E_{corr} of the Zn coatings may have been due to excessive cathodic currents resulting from the exposure of steel through the thin coating.

The Zn content had a definite impact on the corrosion rate of the coatings, as indicated by the trends in R_p (Fig.12.11b). The addition of up to 40%Zn had only a small effect on R_p, causing it to reduce by a factor of about two. Raising the Zn content above 40% saw an exponential decrease in R_p, indicating a similar rate of increase in the corrosion rate of the coatings. The result is consistent with the observed order of magnitude difference in R_p between pure Al and Zn coatings. However, the magnitude of R_p for the Zn-rich alloy coatings (Al-74%Zn and Al-92%Zn), were unusual in that they were considerably lower than the R_p for pure Zn coatings. This means that the Zn-rich Al-Zn alloy coatings corroded at a faster rate than the pure Zn coatings. A possible reason for this is that the Zn-rich alloy coatings were more porous and loosely packed than the pure Zn coatings, as suggested by the slightly darker appearance (Sect.8.2.4). Activation of the (Al) phase, as mentioned above, may also have contributed to the very low R_p values.

The addition of more than 40% Zn to Al-Zn alloy coatings had the effect of sharply increasing i_p (Fig.12.11c). The presence of a reasonably large fraction of (Zn) grains in the alloy coating would intuitively be expected to raise i_p, since the Zn coatings

behaved in an entirely active manner (Fig.12.4b). However, the observed trends in E_{corr} suggested that the (Al) phase also behaved in an active fashion, possibly due to the presence of Zn in solid solution. Combination of the E_{corr} and i_p results suggest that the increase in i_p with Zn content may have been related to reduced passivation efficiency of the (Al) phase.

12.2.4 Aluminium-Magnesium Alloy Coatings

The corrosion potential and polarisation scans for the five different compositions of Al-Mg alloy coatings are shown in Figs.12.12 to 12.16. In the graphs of corrosion potential, data points are not shown for those samples which were monitored continuously. Four samples of each coating composition were examined, except for the Al-72%Mg and Al-86%Mg for which only three samples were tested. Fig.12.17 summarises the polarisation curves in terms of the effect of Mg content on the corrosion potential E_{corr}, pitting potential E_{pit}, polarization resistance R_p, and passive current density i_p. Data for the Al-Mg-Zn coatings are also shown in Fig.12.17 and are discussed in Sect.12.2.6.

The corrosion potential behaviour for the Al-Mg alloy coatings during the initial one hour immersion period seemed to fall into two different groupings. For coatings with up to 41%Mg, E_{corr} tended to gradually increase with immersion time, before reaching a relatively constant value after 10 to 20 minutes (Figs.12.12a to 12.14a). This slow shift in E_{corr} is probably related to the development of a passive layer on the surface of the coatings. The E_{corr} after one hour immersion in the nitrogen-bubbled solution tended to decrease as Mg content was increased. In comparison, the E_{corr} of coatings with 72% and 86%Mg was very active during the initial stages of immersion; typically -1300 mV (SCE) or less (Figs.12.15a and 12.16a). After a period of between 1 and 10 minutes, depending on Mg content, the corrosion potential for the Mg-rich coatings increased sharply until it reached a relatively constant value of about -900 mV (SCE). This latter corrosion potential was very similar to that of the pure Al coatings. It was also observed that numerous gas bubbles were generated on the surface of these coatings, and the bubbling was particularly strong on the highest Mg content coating. For this reason, the Al-86%Mg coating was immersed for only 40 minutes before commencing the polarisation scan. Even after the polarisation scans were completed and the samples were cleaned and dried, it was observed that small bubbles continued to be evolved from some residual moisture trapped in pits in the coating.

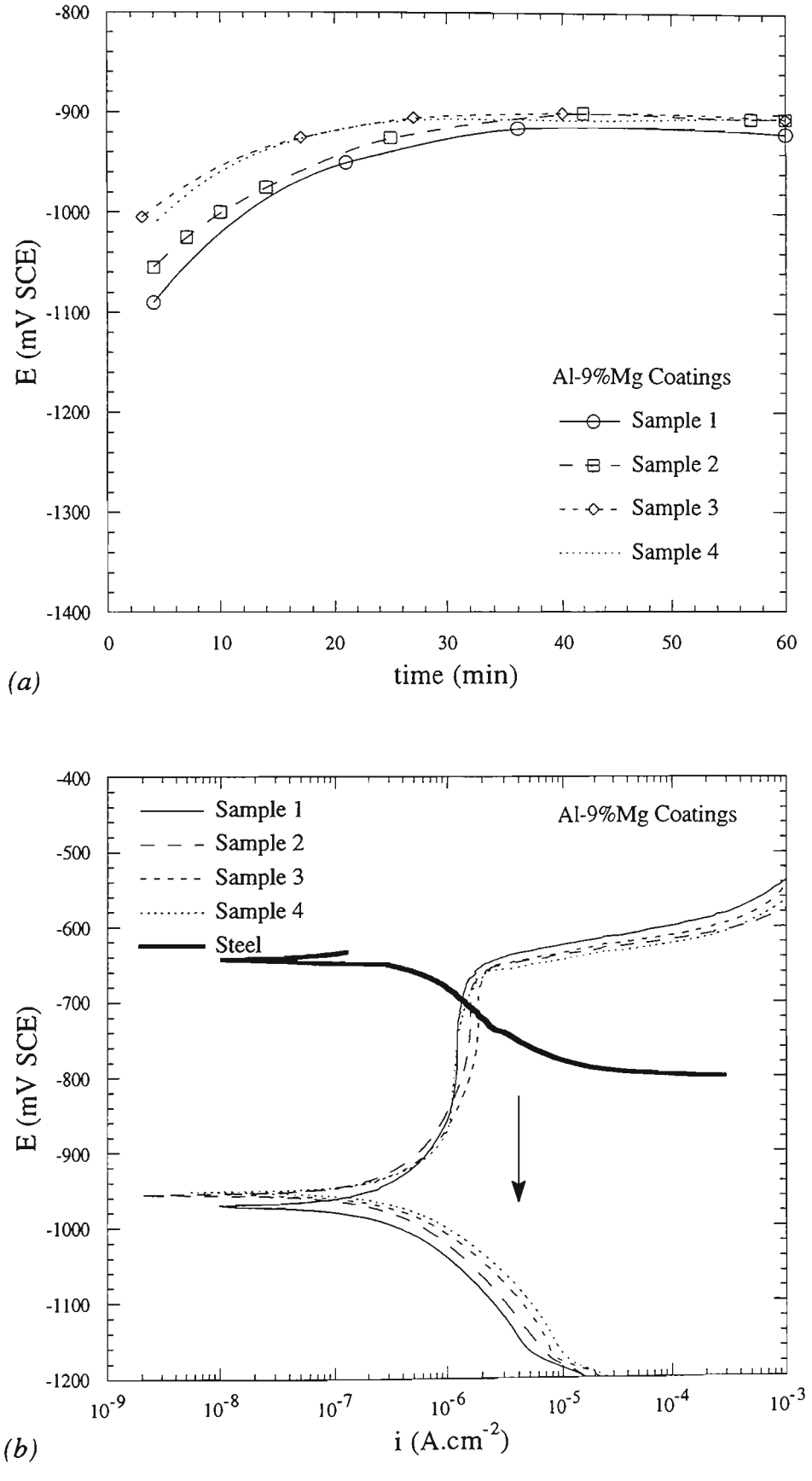

Fig.12.12 Electrochemical results for Al-9%Mg coatings: (a) corrosion potential as a function of time after immersion, (b) potentiodynamic polarisation scans. The cathodic portion of the scan of steel is shown for reference. The diffusion limited current density for oxygen reduction on steel is indicated by the arrow.

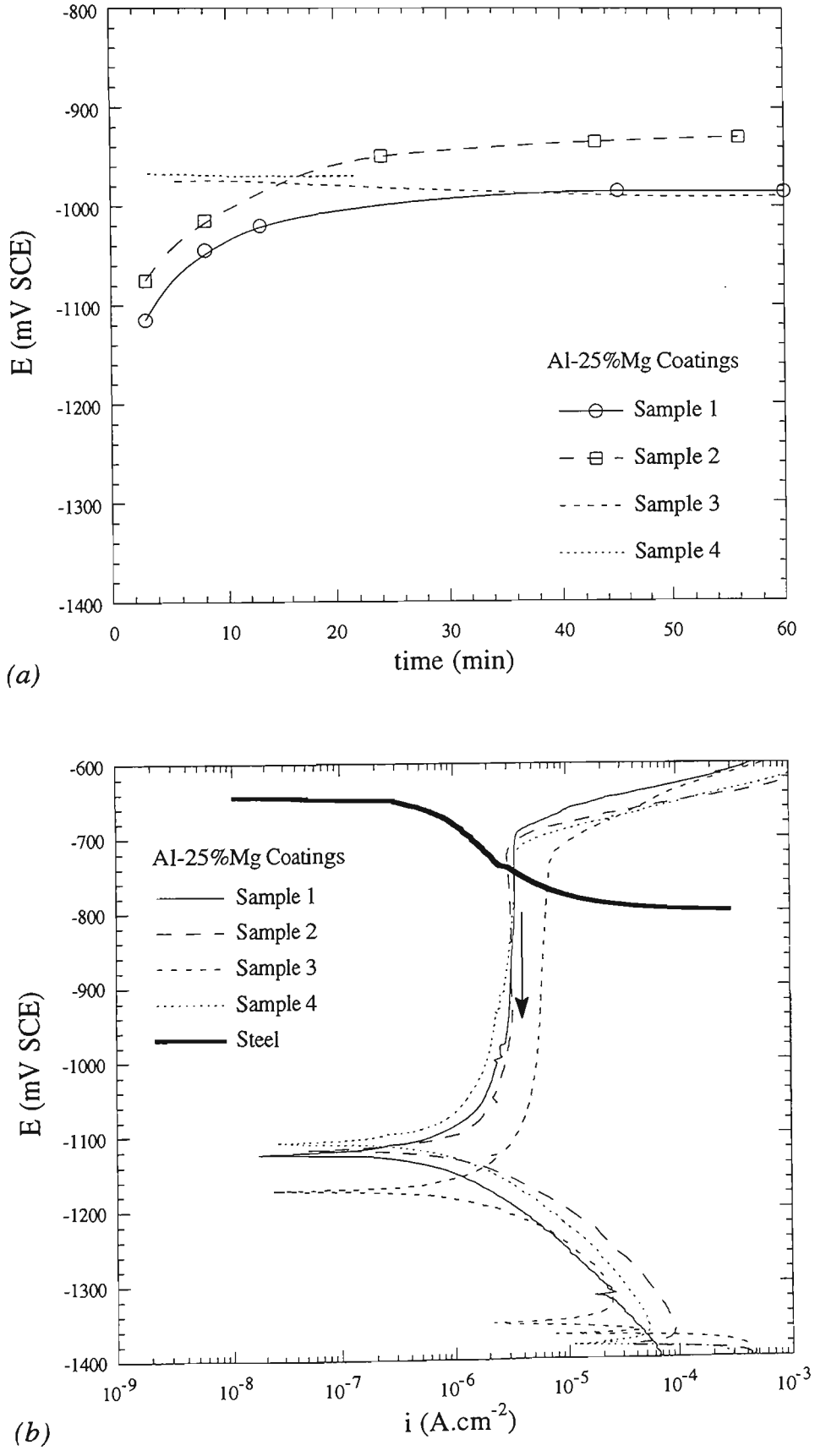

Fig.12.13 Electrochemical results for Al-25%Mg coatings: (a) corrosion potential as a function of time after immersion, (b) potentiodynamic polarisation scans. The cathodic portion of the scan of steel is shown for reference. The diffusion limited current density for oxygen reduction on steel is indicated by the arrow.

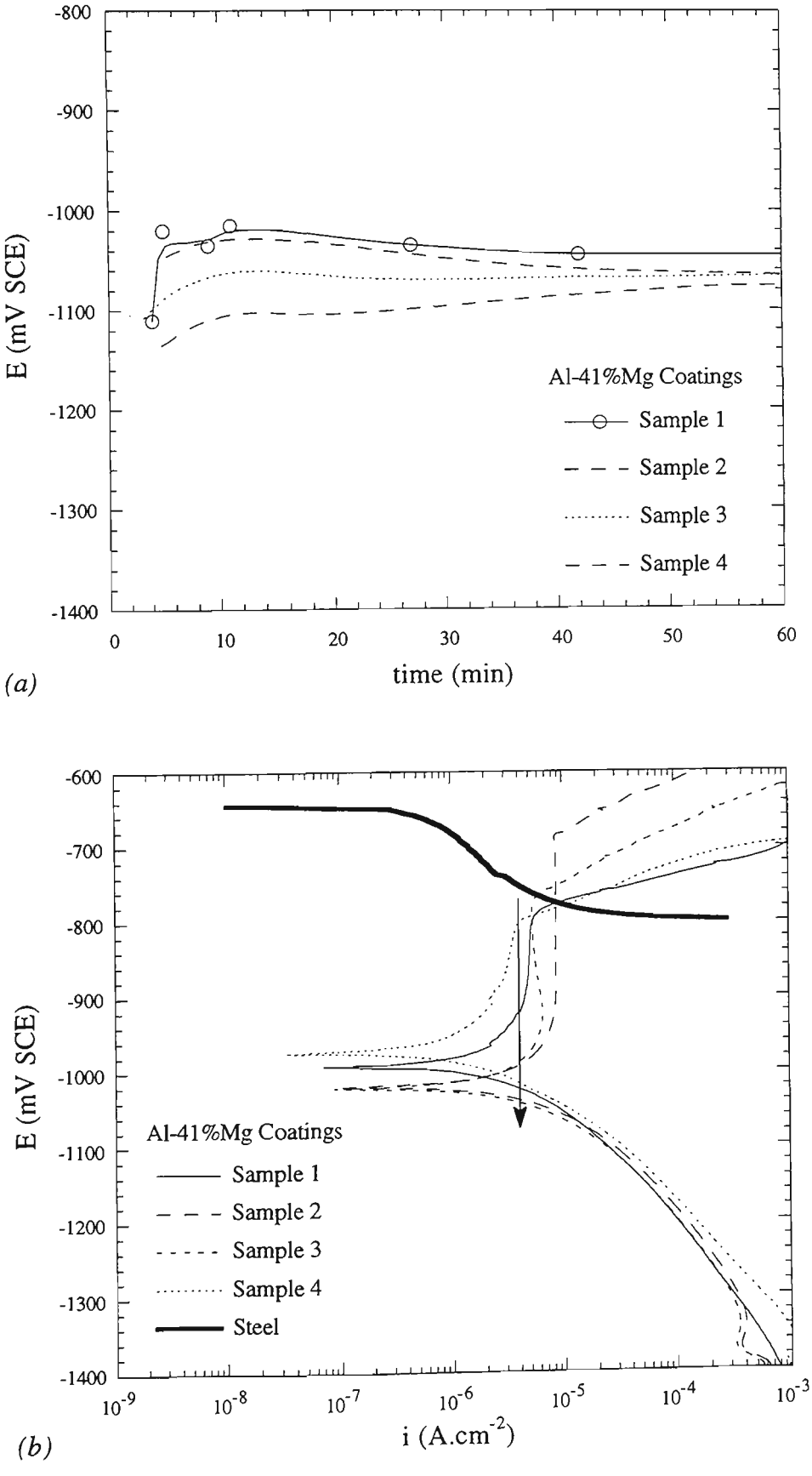

Fig.12.14 Electrochemical results for Al-41%Mg coatings: (a) corrosion potential as a function of time after immersion, (b) potentiodynamic polarisation scans. The cathodic portion of the scan of steel is shown for reference. The diffusion limited current density for oxygen reduction on steel is indicated by the arrow.

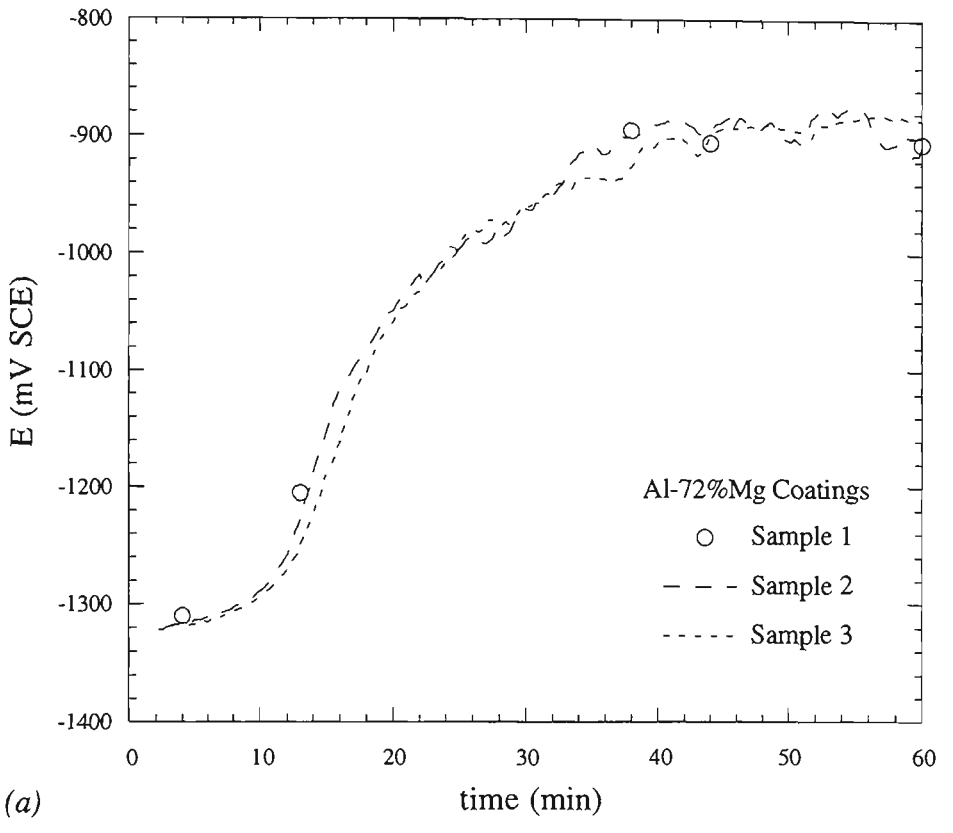

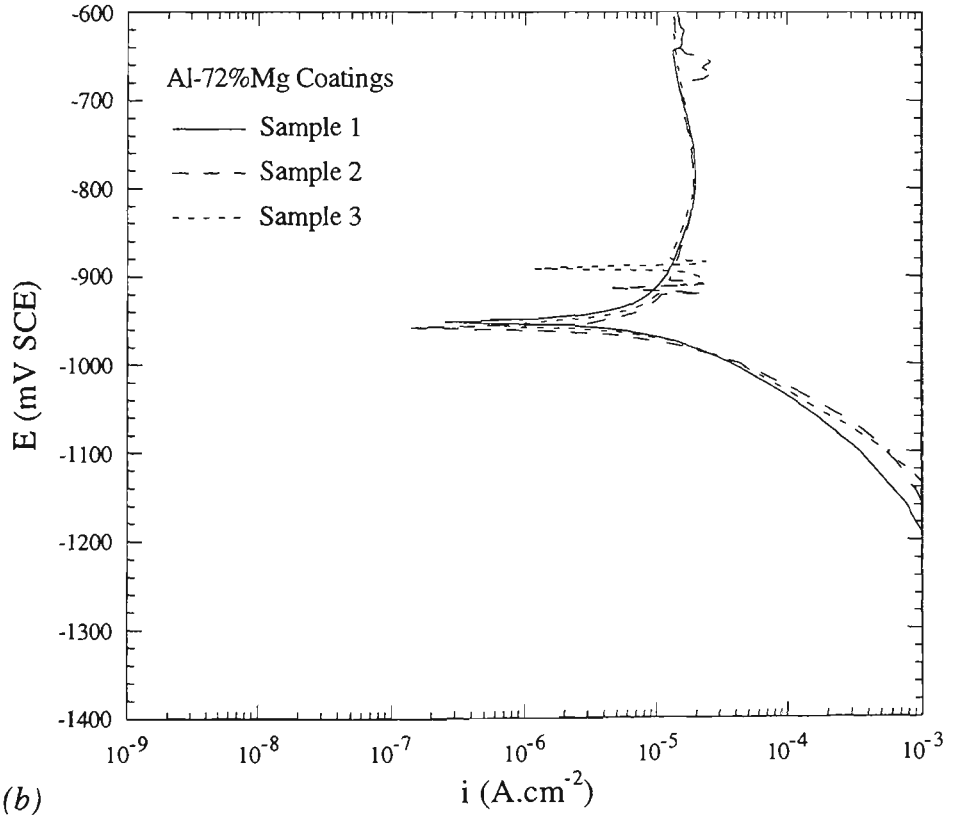

Fig.12.15 Electrochemical results for Al-72%Mg coatings: (a) corrosion potential as a function of time after immersion, (b) potentiodynamic polarisation scans. The cathodic portion of the scan of steel is shown for reference. The diffusion limited current density for oxygen reduction on steel is indicated by the arrow.

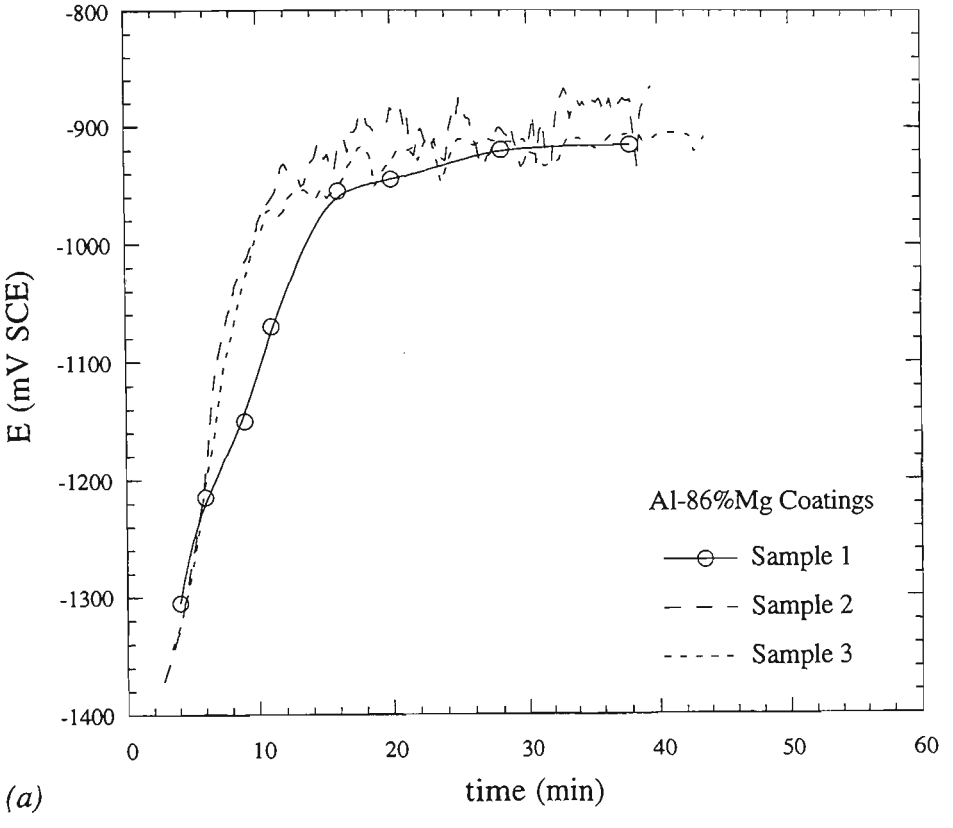

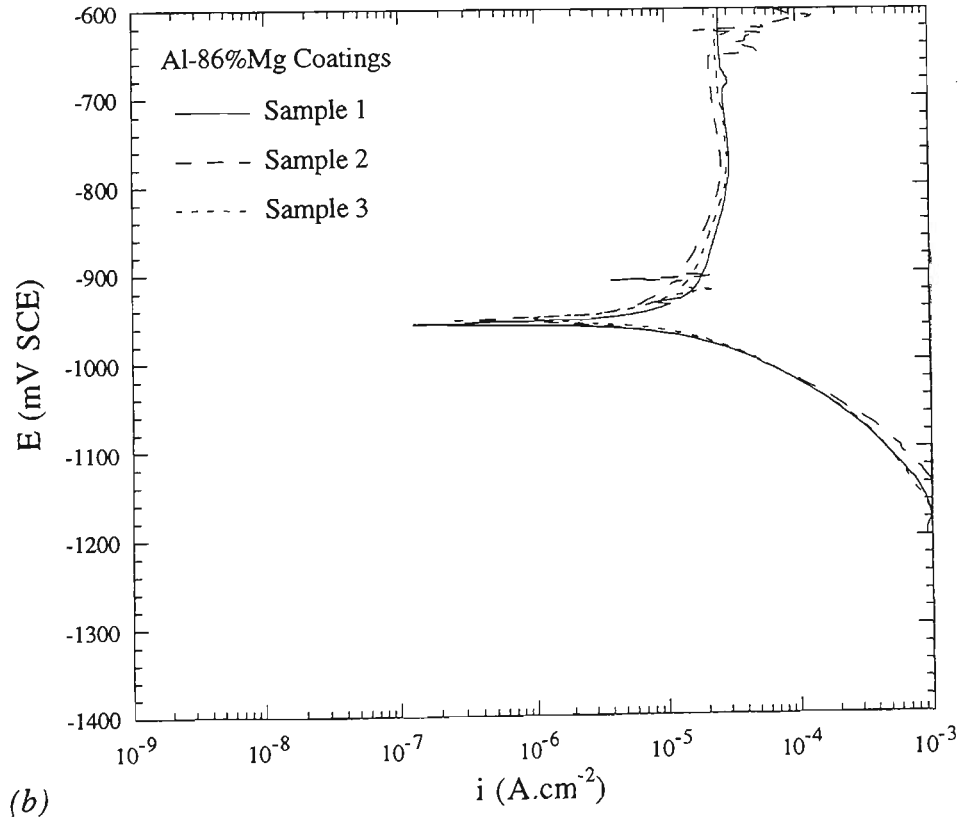

Fig.12.16 Electrochemical results for Al-86%Mg coatings: (a) corrosion potential as a function of time after immersion, (b) potentiodynamic polarisation scans. The cathodic portion of the scan of steel is shown for reference. The diffusion limited current density for oxygen reduction on steel is indicated by the arrow.

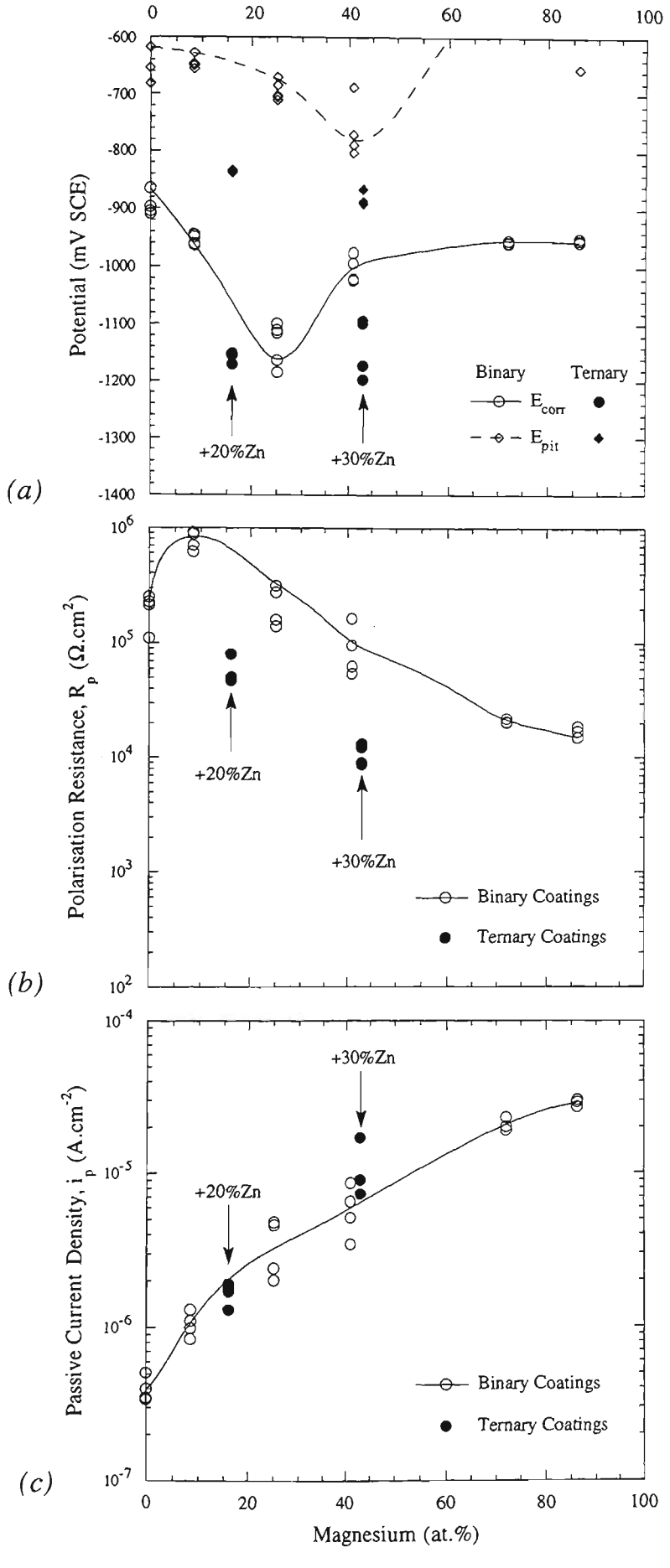

Fig.12.17 Summary of data extracted from polarisation scans for Al-Mg coatings: (a) corrosion potential E_{corr} and pitting potential E_{pit}, (b) polarisation resistance R_p, and (c) passive current density, i_p. The data for ternary Al-Mg-Zn coatings are also shown for comparison.

The gas evolved from the Al-72%Mg and Al-86%Mg coatings was most likely hydrogen. The corrosion potential would have been sufficiently low to enable the reduction of water according to the following cathodic reaction [192]:

$$2H_2O + 2e^- \rightarrow H_2 + 2OH^- \qquad (12.1)$$

It is thought that the overall behaviour of the high Mg content coatings was typical of rapid dealloying whereby the Mg was preferentially corroded, leaving an Al-enriched alloy. This confirms the findings of Baldwin *et al* [239], who found that Mg content of 55% or greater resulted in selective dissolution of Mg leaving a surface enriched in the more noble Al. The possibility of non-Faradaic spallation of Mg also cannot be ruled out, since Mg is recognised to have low sacrificial protection efficiency [2]. Such compositions therefore appear to be completely unsatisfactory for use as sacrificial coatings on sheet steel, since the corrosive attack in only mild conditions was excessively aggressive.

The polarisation scans for each of the low Mg content coatings were generally very similar in form (Figs.12.12b to 12.14b). They all showed the same gradual transition from active to passive behaviour at overpotentials of less than 100 mV, without displaying a noticeable critical current density. As for the Al-Zn coatings, a "nose" on the polarization curves for the Al-Mg coatings was absent, probably because the cathodic currents could not be sufficiently reduced to enable the coatings to corrode in a true active state [322]. The passive current density remained at an essentially constant value up to the pitting potential, which was sharply defined. The polarisation scan rate was accidentally set to 2 $mV.s^{-1}$ for one of the Al-25%Mg and two of the Al-41%Mg coatings, although it did not appear to affect the results. In fact, the polarisation scans for all of the Al-Mg compositions were the most reproducible of all the sputtered coatings examined.

Polarisation scans were conducted on the Al-72%Mg and Al-86%Mg coatings, despite the apparent loss of much of the Mg from the coating during the immersion period (Figs.12.15b and 12.16b). The anodic portion of the scans for each composition reached a relatively constant current density of about 10^{-5} $A.cm^{-2}$. It is believed that this behaviour is related to diffusion limited anodic corrosion rather than a true passive state. The current density did not change noticably when pitting was observed to commence, providing further evidence that a passive state had not been achieved with these compositions. Furthermore, if the cathodic reaction represented by equation 12.1 had indeed been operative during the early stages of immersion, then it is also likely that the pH would have increased as a result. This would have had dire consequences for the

corrosion of Al, since the passive layer on Al breaks down under alkaline conditions [3]. Unfortunately, solution pH was not measured and this corrosion mechanism cannot be confirmed.

The Mg content of the coatings had a significant impact on the various electrochemical parameters extracted from the polarisation curves (Fig.12.17). In the Al-rich coatings, the addition of Mg caused the dynamic E_{corr} to decrease in proportion with Mg content (Fig.12.17a). The E_{corr} of the Al-41%Mg coating broke this trend as it increased to a value of about -1000 mV (SCE). Higher Mg content did not appear to affect the E_{corr} measured from the polarisation scans, and it remained at about the same level. This difference in behaviour exhibited by low- and high-Mg content Al-Mg alloy coatings is believed to be related to the differences in microstructure. It was found in Chap.9 that coatings with less than about 35%Mg consisted of a single-phase supersaturated (Al) solid solution. Coatings with more than about 35%Mg were either completely amorphous, or consisted of an (Mg) solid solution plus an amorphous phase for the very high Mg content coatings. Thus, increasing the Mg content of the (Al) solid solution caused a reduction in E_{corr} due to the very active E_{corr} of pure Mg. This trend continued until about 35%Mg, when the solubility limit was reached and the (Al) phase did not form. The amorphous phase which developed at these compositions had a significantly higher E_{corr}. The dynamic E_{corr} of the Al-72%Mg and Al-86%Mg coatings probably relates mainly to the amorphous phase, since it would appear that much of the (Mg) phase was dissolved during the first few minutes of immersion (Figs.12.15a and 12.16a). This would account for the relatively constant value of the dynamic E_{corr} at Mg content of 41% and higher.

The pitting potential of Al-Mg coatings with up to 25%Mg was generally unaffected by the Mg content. It remained at a value typical of the pure Al coatings (about -650 to -700 mV SCE), such that the range of potentials covered by the passive region (ie. E_{pit} to E_{corr}) increased with Mg content. The passive region in the Al-41%Mg coatings returned to values typical of the Al coatings, but with a lower E_{pit}. Coatings with higher Mg content did not appear to display true passive behaviour, as has been already discussed.

Coatings which consisted of supersaturated (Al) solid solution (Al-9%Mg and Al-25%Mg), were found to have an R_p which was similar to or greater than that of pure Al coatings (Fig.12.17b). This suggests that the presence of Mg in (Al) solid solution has a stabilising effect on the passive layer, causing a slight improvement in the corrosion rate. This behaviour seems to run opposite to the sharp increase in i_p observed to occur with increasing Mg content (Fig.12.17c). It would appear that, relative to pure Al

coatings, the formation of the passive layer requires higher anodic currents when Mg is present in the coatings, but offers a greater degree of protection once it has formed.

12.2.5 Zinc-Magnesium Alloy Coatings

The corrosion potential and polarisation scans for the five different compositions of Zn-Mg alloy coatings are shown in Figs.12.18 to 12.22. The corrosion potential was not continuously monitored during the immersion period for any of these samples. The data points in the graphs correspond to irregular manual readings from the potentiostat. Three or four samples of each coating composition were examined, and the results for each are shown. Fig.12.23 summarises the polarisation curves in terms of the effect of Mg content on the corrosion potential E_{corr}, pitting potential E_{pit}, polarization resistance R_p, and passive current density i_p.

During the initial immersion period, the E_{corr} for coatings with up to 43%Mg tended to decrease with immersion time (Figs.12.18a to 12.20a). A relatively constant E_{corr} of about -1100 mV (SCE) was attained after one hour immersion, independent of the amount of Mg in the coating. However, the higher Mg content coatings reached this stable potential much more rapidly than coatings with less Mg. The E_{corr} for coatings with 65% and 82%Mg were found to be very constant throughout the one hour immersion period (Figs.12.21a and 12.22a). The E_{corr} of the alloy coatings was influenced by the Mg content. An Mg content of more than 43% tended to cause the stable E_{corr} to reduce significantly, reaching a minimum value of about -1300 mV (SCE) for Zn-82%Mg. Gas bubbles were observed to develop on the surface of these Mg-rich coatings, after only a few minutes immersion. The very active corrosion potential suggests that water reduction via equation 12.1, may have been the principal cathodic reaction, leading to the evolution of hydrogen gas. It is interesting to note that the sharp increase in corrosion potential observed for the Mg-rich Al-Mg alloy coatings (Figs.12.15a and 12.16a), did not occur for any of the Zn-Mg coatings. Furthermore, the corrosion potential of the Zn-rich Zn-Mg alloy coatings after the completion of the polarisation scan was typically very similar to that before the scan. This suggests that Mg dealloying did not occur in the Zn-Mg coatings, consistent with previous findings [37,38].

The polarisation scans for the Zn-Mg alloys provided some surprising results. Both Zn and Mg bulk metals do not usually show active-passive behaviour with the type of test solution used in the present investigation. This was confirmed for the pure Zn coatings (Fig.12.3b). Pure Mg coatings were not examined, but are expected to behave in a similar fashion [192]. The polarisation scans of the alloy coatings (Figs.12.16b to

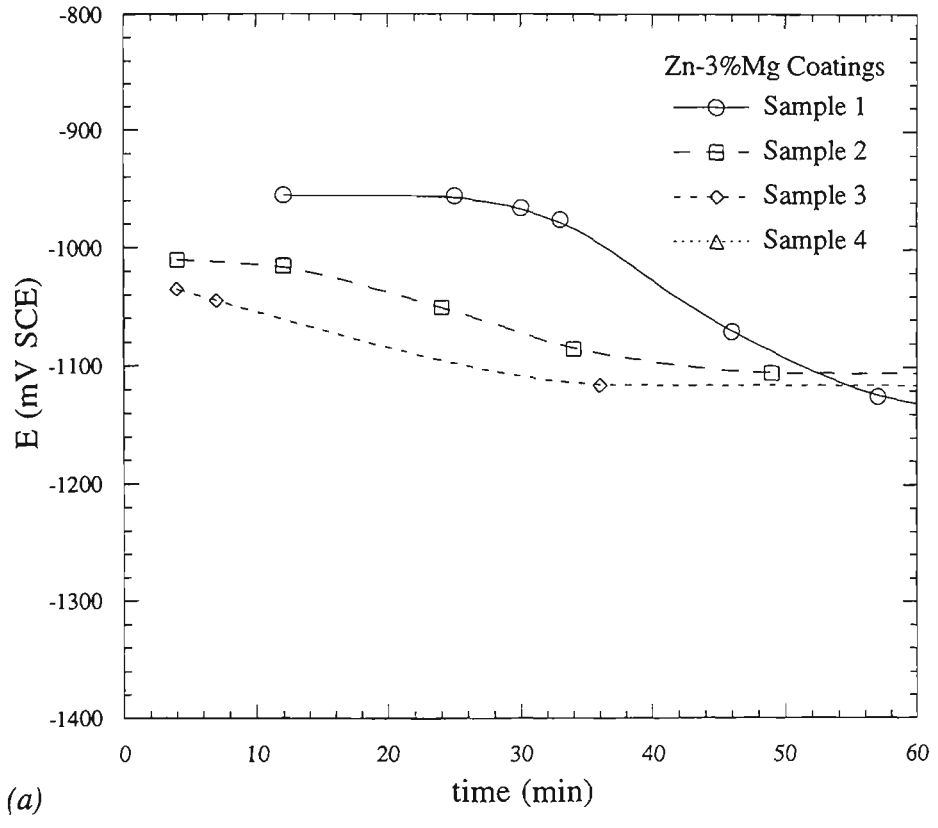

(a)

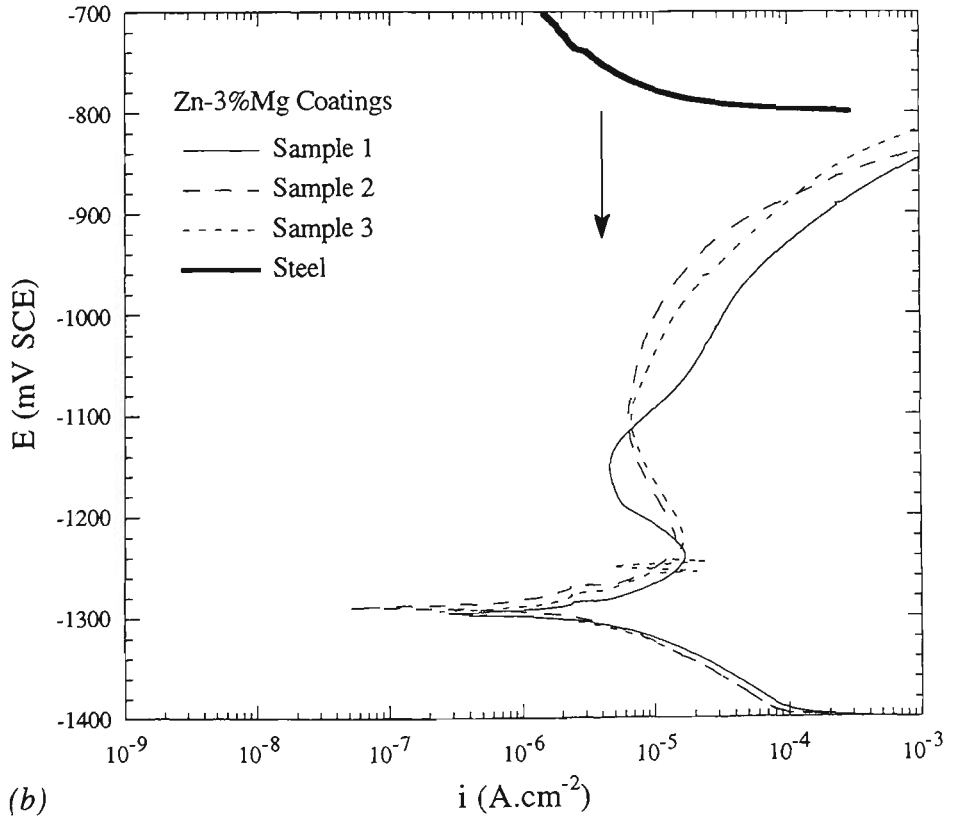

(b)

Fig.12.18 Electrochemical results for Zn-3%Mg coatings: (a) corrosion potential as a function of time after immersion, (b) potentiodynamic polarisation scans. The cathodic portion of the scan of steel is shown for reference. The diffusion limited current density for oxygen reduction on steel is indicated by the arrow.

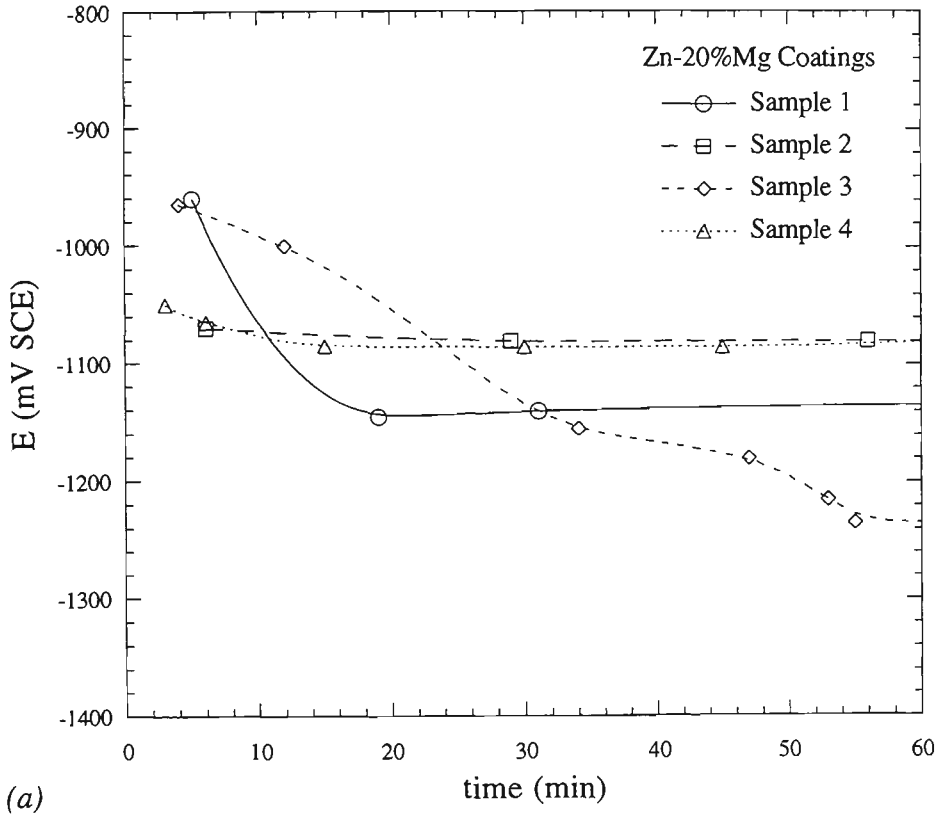

(a)

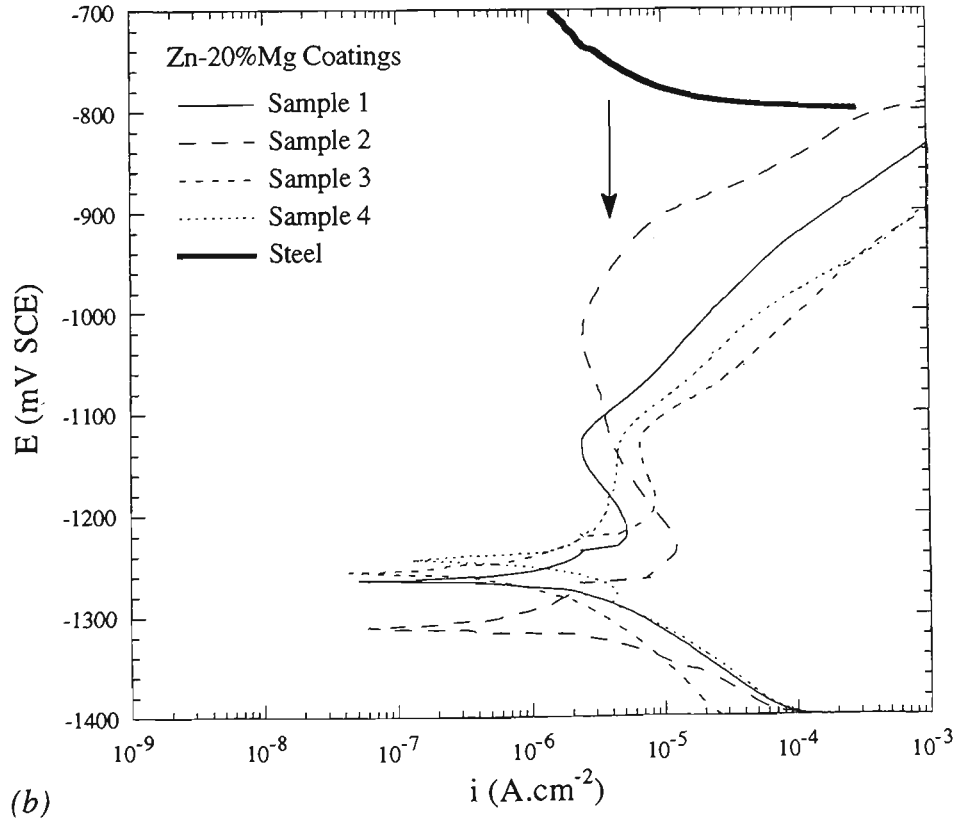

(b)

Fig.12.19 Electrochemical results for Zn-20%Mg coatings: (a) corrosion potential as a function of time after immersion, (b) potentiodynamic polarisation scans. The cathodic portion of the scan of steel is shown for reference. The diffusion limited current density for oxygen reduction on steel is indicated by the arrow.

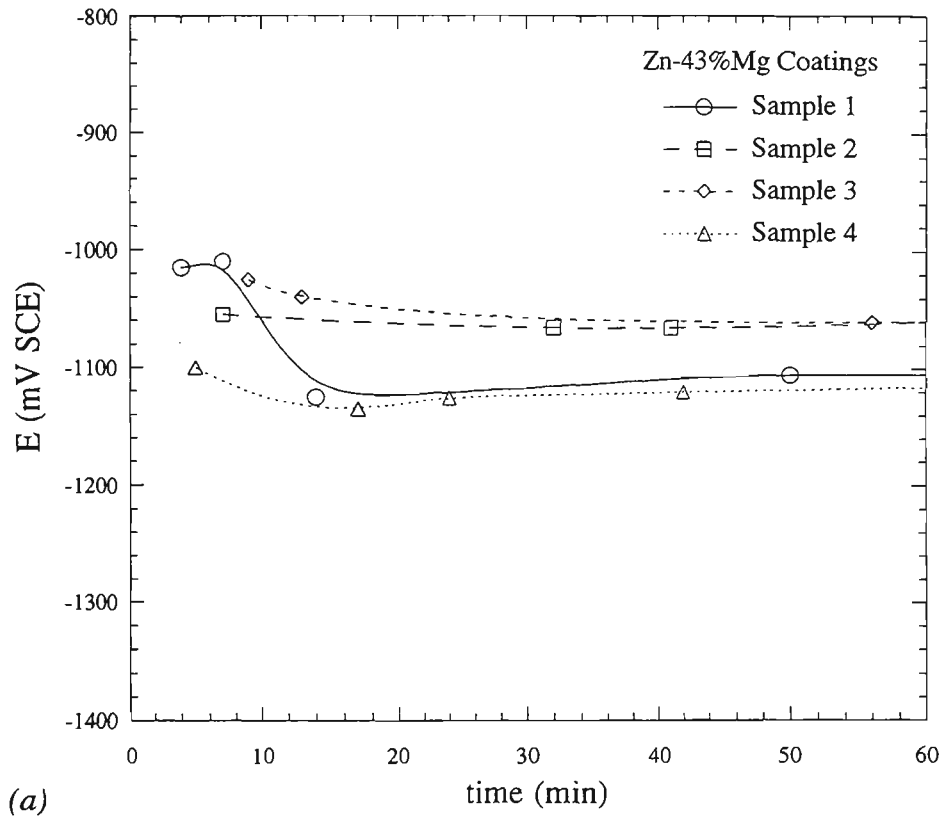

(a)

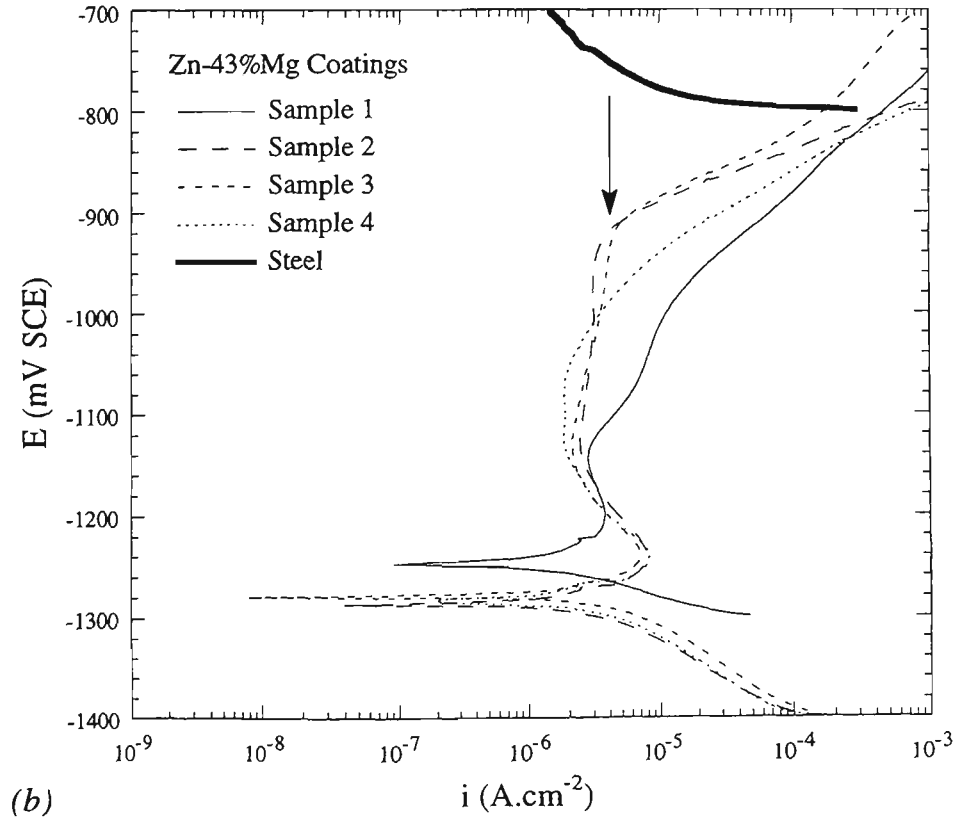

(b)

Fig.12.20 Electrochemical results for Zn-43%Mg coatings: (a) corrosion potential as a function of time after immersion, (b) potentiodynamic polarisation scans. The cathodic portion of the scan of steel is shown for reference. The diffusion limited current density for oxygen reduction on steel is indicated by the arrow.

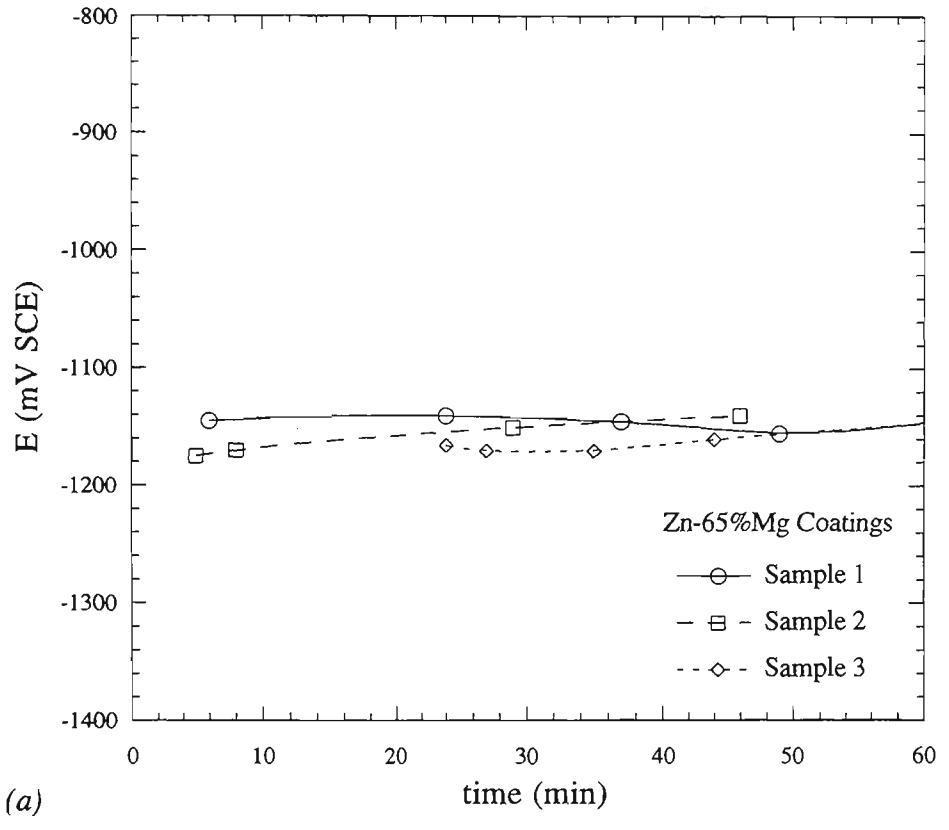

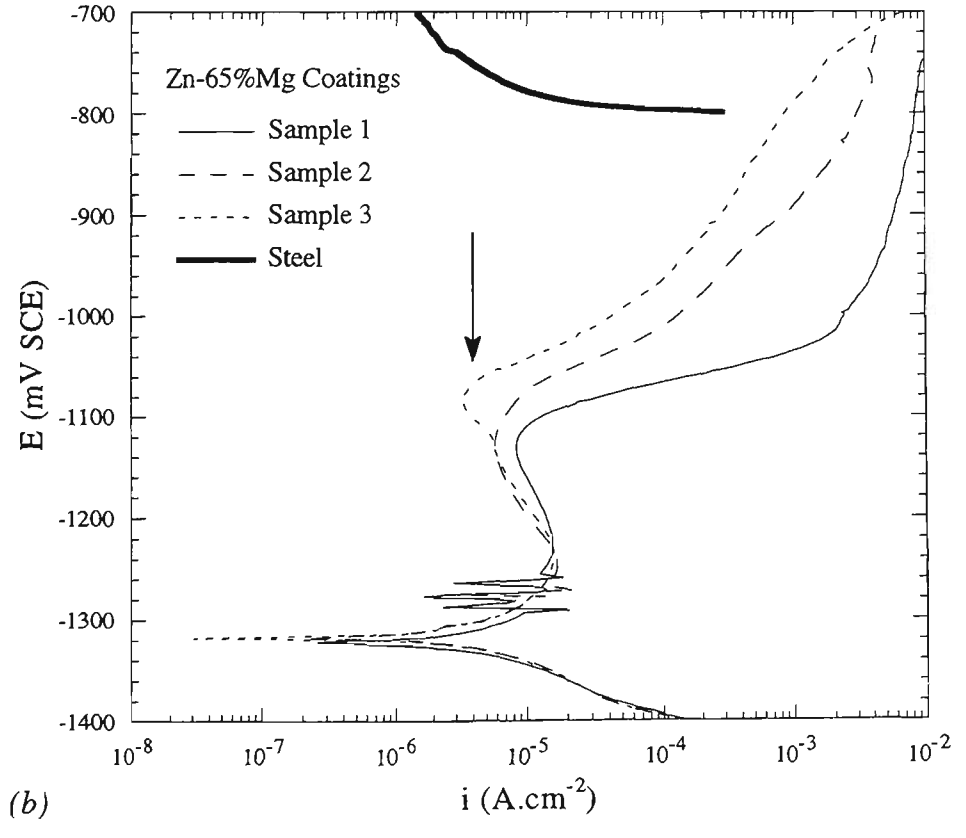

Fig.12.21 Electrochemical results for Zn-65%Mg coatings: (a) corrosion potential as a function of time after immersion, (b) potentiodynamic polarisation scans. The cathodic portion of the scan of steel is shown for reference. The diffusion limited current density for oxygen reduction on steel is indicated by the arrow.

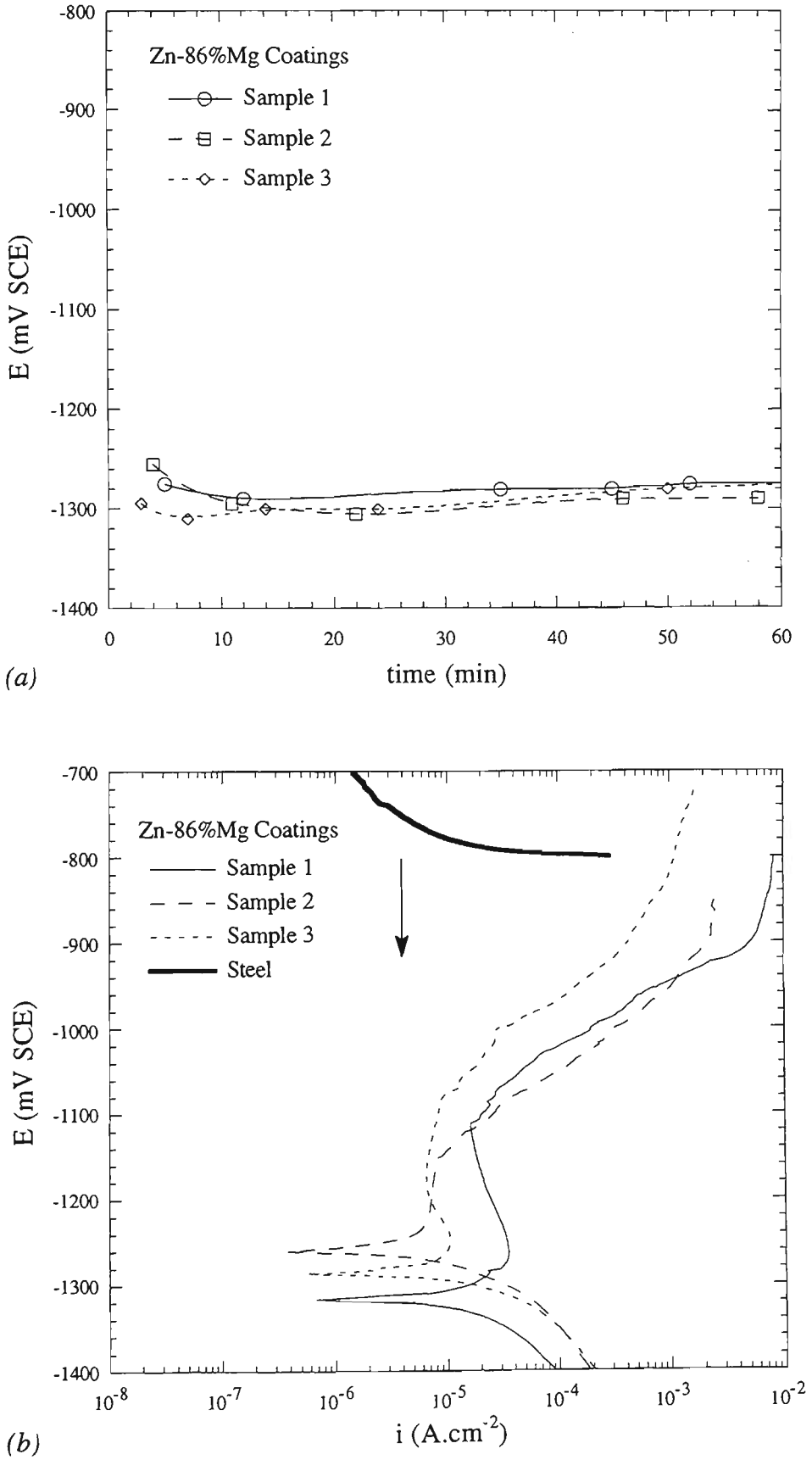

Fig.12.22 Electrochemical results for Zn-86%Mg coatings: (a) corrosion potential as a function of time after immersion, (b) potentiodynamic polarisation scans. The cathodic portion of the scan of steel is shown for reference. The diffusion limited current density for oxygen reduction on steel is indicated by the arrow.

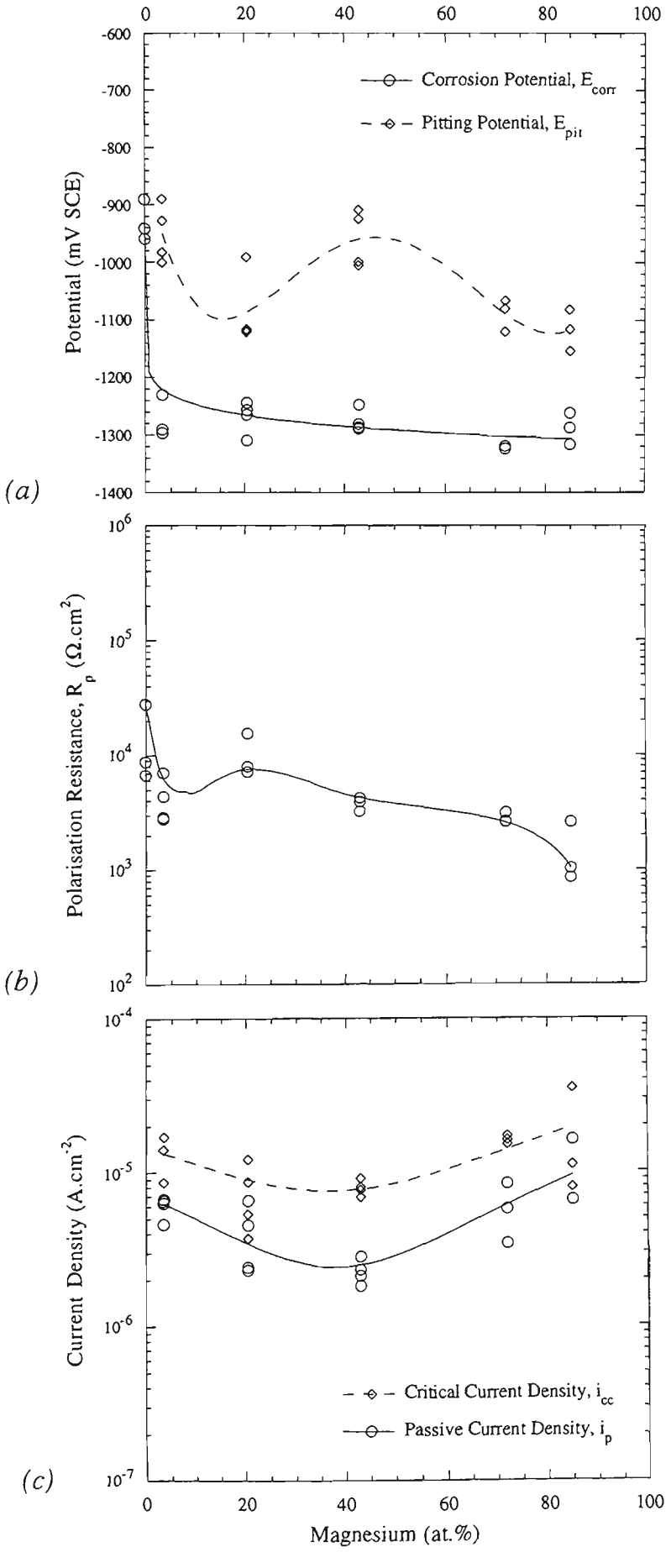

Fig.12.23 Summary of data extracted from polarisation scans for Zn-Mg coatings: (a) corrosion potential E_{corr} and pitting potential E_{pit}, (b) polarisation resistance R_p, and (c) critical current density, i_{cc}, and passive current density, i_p.

12.20b) appeared to show the typical S-shaped curve that is characteristic of an active-passive transition. The results were reasonably reproducible, which suggests that it was not an isolated effect. The polarisation scans of the Zn-20%Mg coatings were the least reproducible, mainly due to variation in E_{pit}. The development of passivity in these alloy coatings is most probably related to the amorphous phase formed in most these sputtered coatings (Chap.10). It is often reported [3] that amorphous alloys have unexpectedly good corrosion performance, and it is generally thought that this relates to the absence of grain boundaries, second phases, compositional segregation, and crystalline defects.

The E_{corr} for the Zn-Mg alloy coatings measured from the potentiodynamic polarization scans was relatively constant and independent of the Mg content (Fig.12.23a). For the Zn-82%Mg coatings, this dynamic E_{corr} was similar to that measured in the nitrogen bubbled solution prior to commencing the polarization scan. However, higher E_{corr} was measured before the scans for all other coating compositions. This suggests that the passive layer formed on the surface of the Zn-Mg alloy coatings was stable during immersion, but could be broken down by reasonably large cathodic polarization.

A sharply defined pitting potential was only encountered in a few of the coatings, and its absence in the other scans was possibly caused by diffusion limited anodic reaction due to the high current density. For the Zn-3%Mg and Zn-43%Mg alloy coatings, E_{pit} was similar in magnitude to E_{corr} of the pure Zn coatings (Figs.12.23a). The E_{pit} for Zn-20%Mg and Mg-rich coatings was generally lower, providing a reduced passive protection region. As a result, the transpassive region of the polarisation curves for the Zn-rich alloy coatings (Figs.12.18b to 12.20b), was almost identical to the position of the anodic region in the Zn anodic scans (Fig.12.3b). This suggests that corrosion behaviour of the Zn-rich Zn-Mg alloy coatings is similar to that of pure Zn coatings at these high overpotentials. However, under appropriate conditions, there is the possibility of reduced corrosion rates due to passivation of the Zn-Mg alloy coatings.

The corrosion rate of the Zn-20%Mg coatings, indicated by R_p measurements (Fig.12.23b), was similar to that of pure Zn coatings. The corrosion rate of all other Zn-Mg coatings was at least double that of the Zn coatings. On the basis of the highly active nature of Mg, a much greater increase in corrosion rate might have been expected. It would therefore appear that the microstructures and phases formed in the sputtered Zn-Mg coatings were able to afford some degree of protection via passivation. All of these alloy coatings required a critical current density to be passed before the passive region was encountered. The i_{cc} was typically between two and five times greater than the minimum passive current density i_p (Fig.12.23c). A minimum in both current

densities was found for the Zn-43%Mg composition, which suggests that the passive layer formed on the alloy coatings was in the most stable condition at this composition. This is possibly because the 43%Mg composition was likely to have been entirely amorphous with no second phases (Chap.10).

12.2.6 Aluminium-Magnesium-Zinc Alloy Coatings

The corrosion potential and polarisation scans for the two different compositions of Al-Mg-Zn ternary alloy coatings are shown in Figs.12.24 and 12.25. Four samples of each coating composition were examined, and the results for each are shown. The corrosion potential during the immersion period was monitored automatically, and recorded at 15 second intervals. The polarisation curves were summarised in terms of the corrosion potential E_{corr}, polarization resistance R_p, passive current density i_p, and pitting potential E_{pit}. These results were compared with those for binary Al-Zn and Al-Mg coatings in Figs.12.11 and 12.17 respectively, in order to appreciate the impact of ternary additions.

The E_{corr} of both sets of ternary coatings behaved in a similar fashion during the one hour immersion period (Figs.12.24a and 12.25a). The potential was very active immediately after immersion, and increased to a relatively constant value within about 20 minutes. In this respect, the behaviour of the ternary coatings was very similar to the Al-rich Al-Mg coatings. The E_{corr} after one hour immersion was about -960 mV (SCE) for the Al-13%Mg-20%Zn coatings, and -1090 mV (SCE) for the Al-30%Mg-30%Zn coatings. Comparing these values with those for the Al-Mg coatings with similar Al/Mg ratio, suggests that the presence of Zn in the ternary coatings has very little influence on E_{corr} during the one hour immersion period.

The polarisation curves of the two ternary alloy compositions were similar to each other in general form. In both cases, the anodic current increased very slowly in a fashion typical of passive behaviour. The Al-13%Mg-20%Zn coatings had a very sharply defined pitting potential of about -835 mV (SCE). The Al-30%Mg-30%Zn coatings experienced a much more gradual transition into the transpassive region, with a pitting potential of between -860 and -890 mV (SCE). The current density in the passive region for the Al-30%Mg-30%Zn was about an order of magnitude higher than that in the more dilute alloy coatings.

The impact of ternary Mg additions to Al-Zn compositions is shown in Fig.12.11. Generally, the addition of Mg caused a reduction in E_{corr} and R_p, increased i_p, while having very little impact on E_{pit}, relative to the behaviour of Al-Zn coatings with

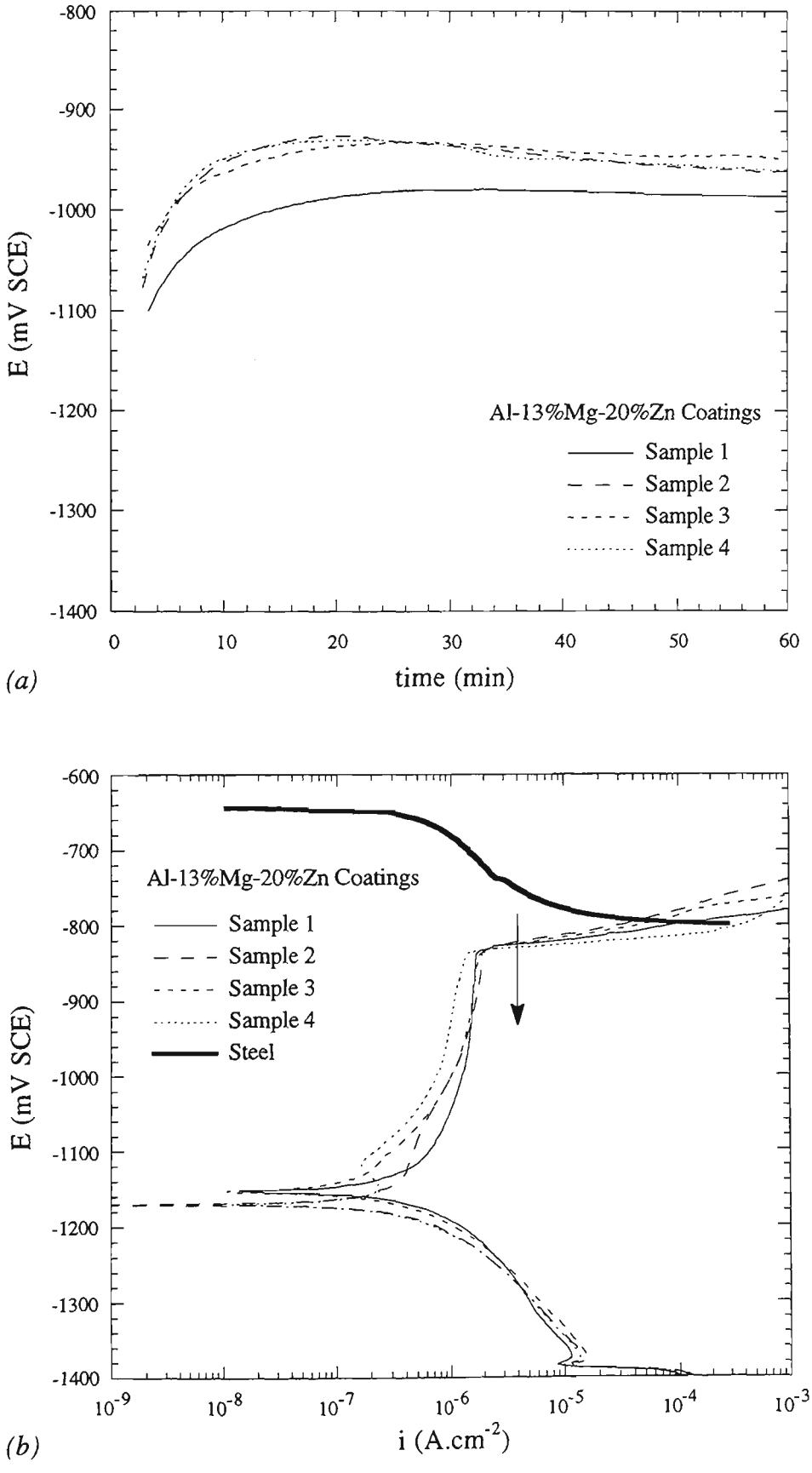

Fig.12.24 Electrochemical results for Al-13%Mg-20%Zn coatings: (a) corrosion potential as a function of time after immersion, (b) potentiodynamic polarisation scans. The cathodic portion of the scan of steel is shown for reference. The diffusion limited current density for oxygen reduction on steel is indicated by the arrow.

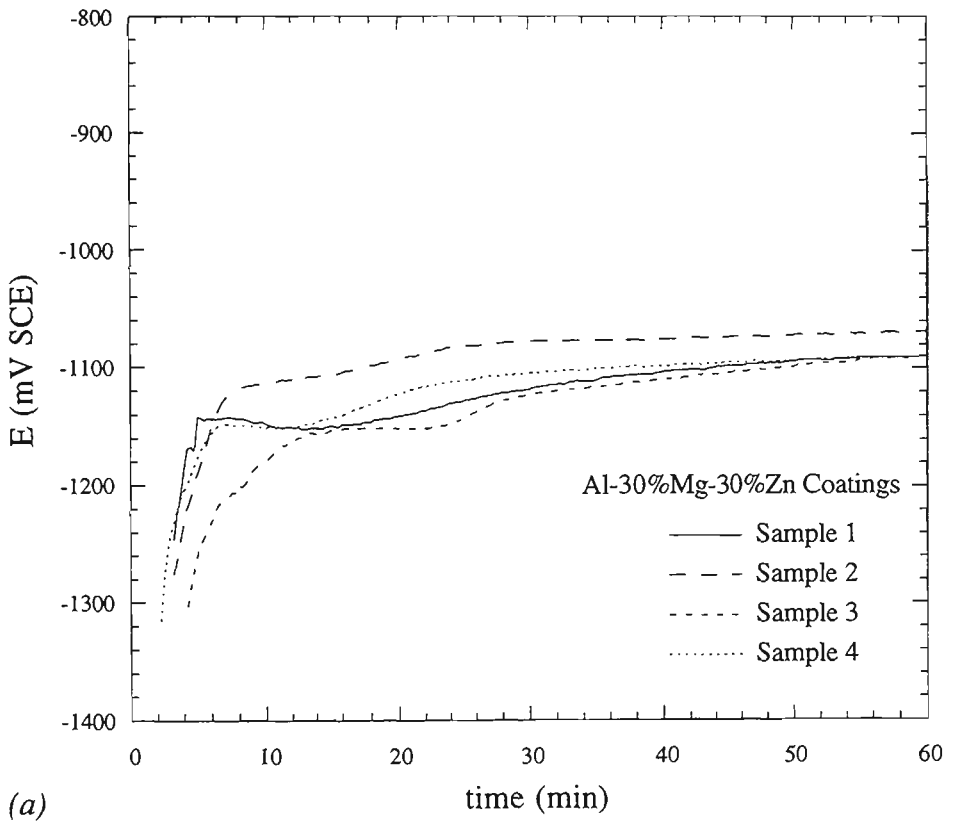

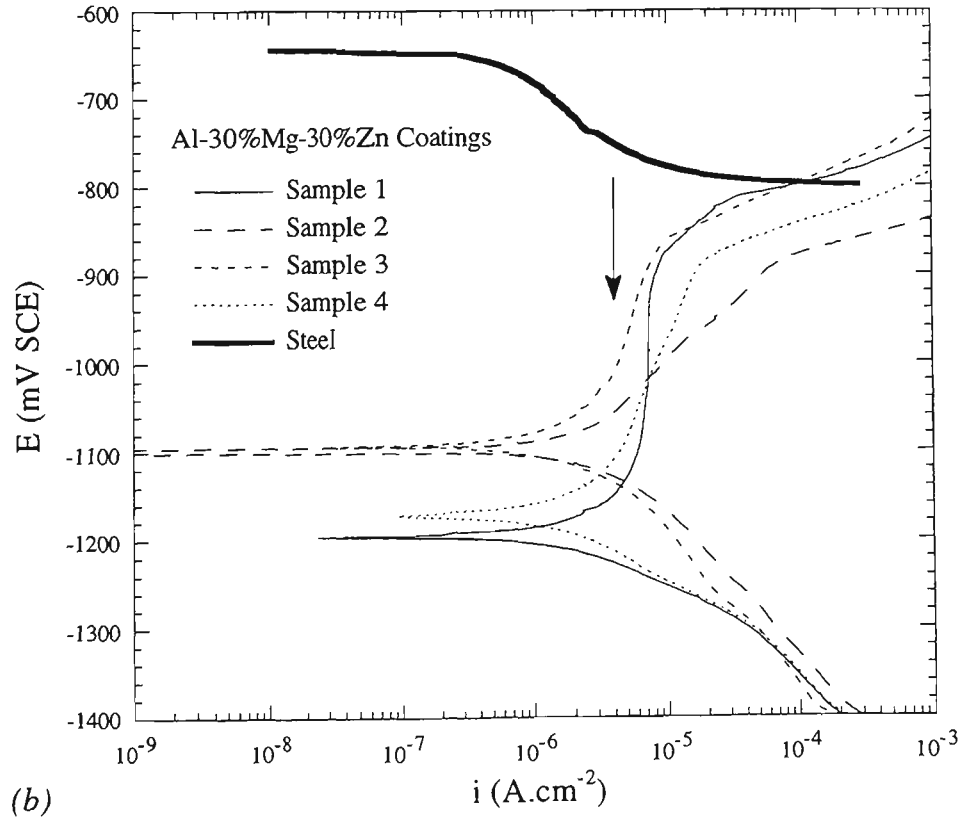

Fig.12.25 Electrochemical results for Al-30%Mg-30%Zn coatings: (a) corrosion potential as a function of time after immersion, (b) potentiodynamic polarisation scans. The cathodic portion of the scan of steel is shown for reference. The diffusion limited current density for oxygen reduction on steel is indicated by the arrow.

equivalent Al/Zn ratios. In effect, the Al-13%Mg-20%Zn coatings behaved similarly to the Al-40%Zn coatings, and the Al-30%Mg-30%Zn coatings were similar to the Al-73%Zn coatings. It would therefore appear that Mg additions to Al-Zn compositions have an effect akin to increased Zn content. This is to be expected from the point of view of both Mg and Zn being active metals. However, the microstructure of the ternary coatings differed considerably from that of the binary Al-Zn coatings. The microstructural characterisation described in Chap.11 indicated that these ternary coatings were either entirely amorphous (Al-30%Mg-30%Zn) or mostly amorphous with a small amount of (Al) solid solution (Al-13%Mg-20%Zn). In comparison, the Al-Zn coatings did not contain an amorphous phase, and were found to segregate into (Al) and (Zn) phases (Chap.8). Thus, in this particular case, the formation of an amorphous phase does not appear to offer any advantage in corrosion performance to the crystalline dual phase structure.

A comparison between the electrochemical parameters for the two ternary compositions and the binary Al-Mg coatings is provided in Fig.12.17. The addition of Zn caused a large reduction in E_{corr}, E_{pit} and R_p, while having little effect on i_p, compared with binary Al-Mg coatings with similar Al/Mg ratio. This suggests that Mg has a much greater influence than Zn on the stability of the passive layer. It is possible that this behaviour relates to the way in which the ternary element impacts on the microstructure of the coating. Additions of Mg appear to be absorbed into (Al) solid solution or promote the formation of an amorphous phase. In comparison, Zn additions have little effect on the (Al) solid solution, and favour the formation of either an amorphous phase or crystalline (Zn) phase. The passive layer on the Al-Zn and Al-Mg binary coatings was shown to be related primarily to the (Al) phase. Therefore, the significance of Mg additions can be understood in terms of the impact they have on the passivation behaviour of (Al) phase.

12.3 General Discussion

12.3.1 Ideal Behaviour of a Protective Coating for Sheet Steel

An ideal protective coating for sheet steel must possess a unique combination of excellent barrier protection and sufficient sacrificial protection over a wide range of service conditions. Barrier protection shields the steel from general surface corrosion by the application of a material that corrodes much slower than steel. This results in a low corrosion rate to provide long term protection to the steel surface. However, metallic barrier coatings are often more noble than steel, and complete coverage of the substrate is required to prevent accelerated galvanic corrosion of the steel. In the vast majority of sheet steel applications, the exposure of sheared edges to the environment is unavoidable, and the possibility of scratches through the coating, exposing the steel substrate, must also be accounted for. Hence there is a need for some sacrificial protection ability for the coating. By the very nature of a sacrificial coating, it must corrode at a faster rate than the steel substrate when both are exposed to the environment. Optimum sacrificial protection of steel is achieved when its E_{corr} is reduced by about 200 mV, and therefore requires the use of active metals. It is obvious that the ideal protective coating for steel sheet must possess a balance of barrier and sacrificial properties, in order to extend the service life of the sheet steel to a maximum level.

The electrochemical tests described in the previous sections were conducted with the aim of trying to identify potential coating compositions which afforded a combination of good barrier and sacrificial protection. The measurement of various corrosion parameters from polarisation curves is a relatively easy process. However, the interpretation of their significance is another matter entirely. It is not immediately obvious what should be the optimum values for E_{corr}, i_p and E_{pit}. With this in mind, several criteria for optimum protective coatings for sheet steel were developed. In the first case (Sect.12.3.2), where i_p (coating) is greater than i_L (steel), the passive region of the polarization scan for the coatings does not influence the galvanic couple with steel. The E_{corr} of the coating should be as low as possible to provide good sacrificial protection, but not at the expense of an excessively low R_p. In the second case (Sect.12.3.3), i_p (coating) is less than i_L (steel) and the passive region plays an important role in determining the sacrificial properties of the coating. The important variable in this situations is E_{pit}. It will be shown that E_{pit} of the coatings should ideally be at least 200 mV more negative than E_{corr} of the steel in order to provide sufficient sacrificial protection. Throughout this discussion, the criteria relating to i_p and i_L assume equal anodic and cathodic areas. Obviously it is the anodic and cathodic currents that are important, and hence the ratio of cathode to anode areas is also considered. Finally, these

criteria were used to evaluate the expected performance of the sputtered coatings (Sect.12.3.4).

As a general simplification, it has been assumed in this work that the service conditions can be simulated by dilute chloride solutions. This is a reasonably valid assumption for most applications of sheet steel for roofing and walling in the Australian market. However, many locations in North America, South East Asia, and Europe are also susceptible to polluted acid rain conditions typified by high sulphate levels and low pH. The performance of sputtered coatings in such environments was considered beyond the scope of this thesis.

12.3.2 Galvanic Corrosion of Active Coatings

It is commonly assumed that the E_{corr} of the coating is the principal variable controlling the sacrificial protection ability of a coating. The E_{corr} does impact on the sacrificial performance, but generally it is only important in cases where the coating does not show a large passive region. In these circumstances, the diffusion limited cathodic reaction on steel intersects the Tafel region of the anodic curve, and the resulting galvanic potential E_g is determined largely by E_{corr} of the coating. An example of this type of behaviour is shown in Fig.12.26a, where curve A represents the anodic behaviour of an active metal coating. The intersection between the diffusion limited cathodic curve for steel and the anodic curve for the coating defines the galvanic potential and current density. As the value of E_g is reduced by lowering the E_{corr} of the coating, the rate of anodic reaction on the steel is reduced exponentially. Thus, large differences between E_{corr} of the coating and the steel ensure adequate reduction in the corrosion rate of the steel. It is considered that a reduction of about 200 mV in E_{corr} will provide adequate sacrificial protection for steel. Assuming a Tafel slope of about 60 mV (Sect.12.2.1), this corresponds to about 30 times reduction in the rate of anodic dissolution of steel.

The E_{corr} is also important for determining the sacrificial properties of coatings that display an active-passive transition. It is generally only significant, however, in cases where the i_p is greater than the diffusion limited current density i_L for oxygen reduction on steel. Under these circumstances, the coating is likely to corrode in an active state at a current density less than i_p. This situation is demonstrated in Fig.12.26a by curve B which represents an active-passive metal with a high passive current density. It should be noted that the diffusion limited cathodic curve for steel intersects the active anodic region of the coating. Consequently, the E_{corr} of the coating effectively determines the E_g. This condition is demonstrated for the Al-74%Zn coatings in Fig.12.9b. This is an ideal situation since the E_{corr} of the coating would dominate the polarisation of the steel

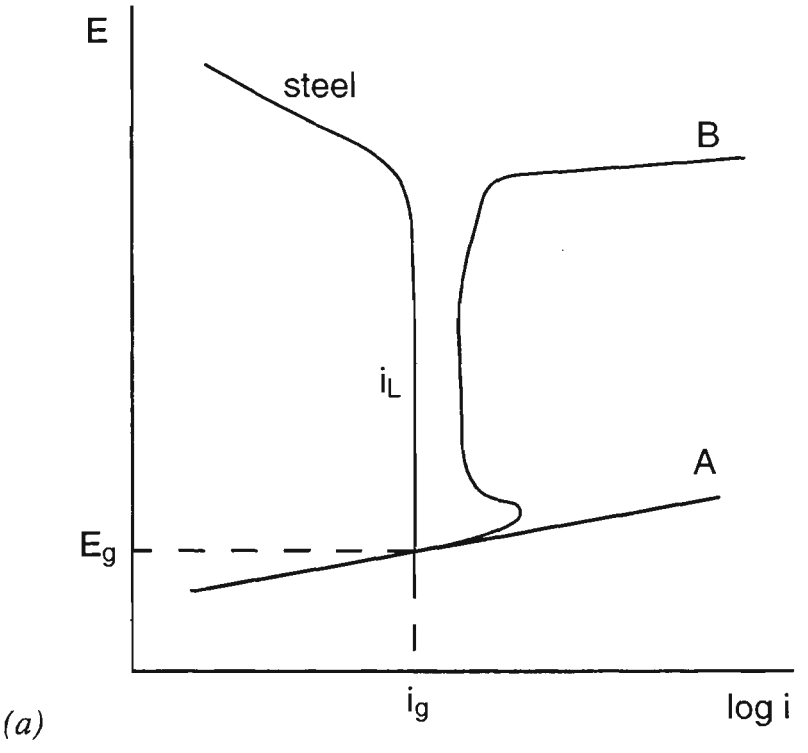

(a)

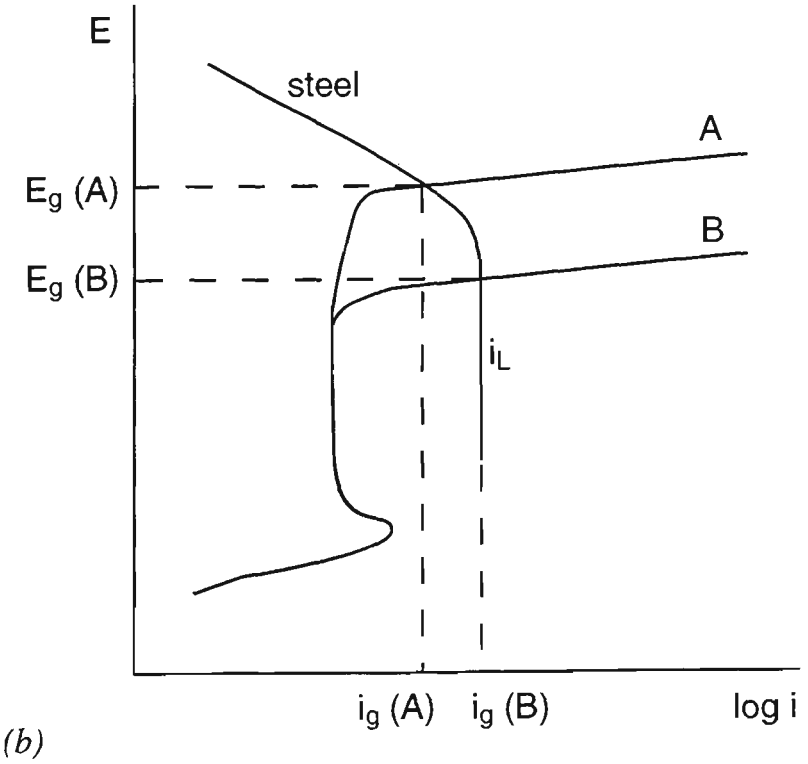

(b)

Fig.12.26 Schematic Evans diagrams illustrating the effects of a galvanic couple between steel and coating: (a) coating corrosion in the active state, (b) coating corrosion affected by a large passive region. Refer to the text for explanation.

and therefore afford excellent sacrificial protection. However, it is also possible that the very low E_g developed in the coating/steel galvanic couple would be sufficiently active to produce hydrogen evolution by direct reduction of water (equation 12.1). This would cause an increase in the cathodic current, such that the E_g could be within the passive region of the coating, thus reducing the sacrificial protection but without excessively raising the corrosion rate of the coating.

Baldwin *et al* [239] concluded that sputtered Al-Mg alloy coatings would become progressively more sacrificial with increasing Mg content. This conclusion was based on the observation that increased Mg content caused a reduction in E_{corr}. Similar behaviour was noted in the present investigation for Mg content of up to about 35% (Fig.12.17). It is certainly possible that such low E_{corr} could improve sacrificial protection. However, it is felt that the interpretation by Baldwin *et al* [239] was somewhat premature considering that they did not examine the anodic behaviour of the coatings. As it will be shown (Sect.12.3.3), the anodic behaviour has a significant impact on the sacrificial protection ability, particularly for coatings that display an active-passive transition.

12.3.3 Galvanic Corrosion of Passive Coatings

The most obvious advantage of an active-passive coating for steel is that the low corrosion rates typical of the passive state would be expected to afford good barrier protection. Indeed, most of the Al-Zn and Al-Mg coatings were in a passive state when commencing the anodic portion of the polarization scans, in spite of the precautions taken to minimise cathodic currents (ie. deaeration, quiescent conditions, scanning from cathodic potentials), perhaps due to partial exposure of steel through the thin coatings. This can be demonstrated by plotting the R_p as a function of i_p for all of these coatings, as shown in Fig.12.27. An approximately inverse relationship between R_p and i_p was established for each set of coatings, extending over about two decades of current density. This could only occur if the coatings were in a passive state at the corrosion potential. The relationship between R_p and i_p differs between alloy systems, such that a given i_p does not necessarily provide the same R_p for both systems. In this respect, it is interesting to note that the results for ternary Al-Mg-Zn coatings appear to lie midway between those for Al-Zn and Al-Mg coatings. It can therefore be concluded that the best barrier protection would be provided by a coating with the lowest possible passive current density. Furthermore, it seems that the presence of Mg in the coatings enables the development of a much more protective passive layer.

For a coating that displays active-passive behaviour, E_{corr} does not necessarily govern the degree of sacrificial protection for a steel substrate. It is necessary to consider

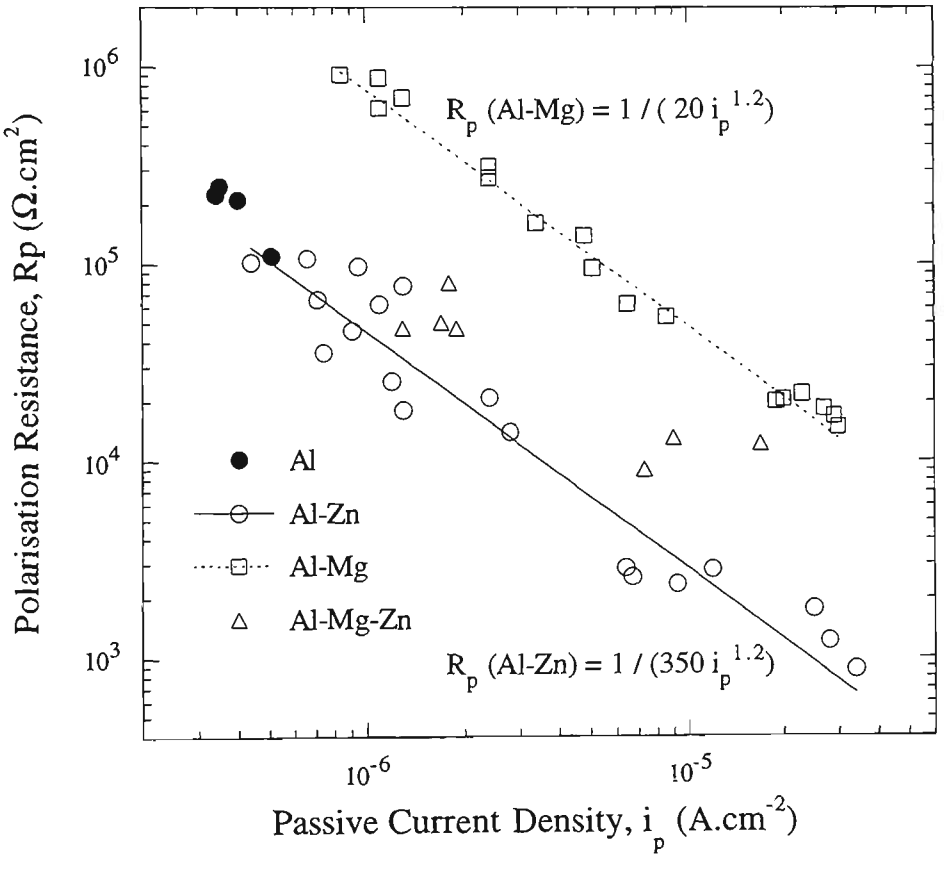

Fig.12.27 Relationship between polarisation resistance and passive current density for sputtered coatings.

the total anodic polarization behaviour with respect to the kinetics of the cathodic reaction on the steel. This is particularly relevant when i_p of the coating is less than i_L of steel, such that the coating is able to spontaneously passivate when galvanically coupled with steel. A schematic diagram is presented in Fig.12.26b to demonstrate the significance of the passive region. Curves A and B represent coatings with relatively high and low E_{pit}, respectively. The reduction of dissolved oxygen is assumed to be the rate limiting step of the cathodic reaction on steel, and direct reduction of water is not considered. In both cases, i_p of the coating is less than i_L of steel. For coating A, the E_g is much higher than would be expected for an entirely active coating. The intersection between the anodic curve A and the cathodic curve for the steel couple occurs within the transpassive region of the coating. The relatively high values for E_g are due to the close proximity of E_{pit} for these coatings to E_{corr} for the steel. In comparison, curve B possesses a much lower E_{pit}, which results in a lower E_g, and hence better sacrificial protection of the steel. It can be concluded from this analysis that E_{pit} is much more important than E_{corr} in determining the sacrificial protection ability of passive coatings. Ideally, E_{pit} should be about 200 mV lower than the E_{corr} of steel in order to ensure adequate protection.

The above interpretation applies to equal areas of steel and coating. In actual applications the exposed steel area can be considerably larger than the coating area. The cathodic and anodic polarization curves must then be compared on the basis of current, and not current density. Steel/coating area ratios greater than one effectively shift the cathodic curve to higher currents. The E_g of the steel/coating couple will then be greater than that predicted for equal areas, and hence the coating will provide much less sacrificial protection to the steel. Similar arguments apply under aerated or agitated conditions, which both would cause the i_L for oxygen reduction to be shifted to higher current density [2,3]. Consequently, active-passive coatings would be more likely to passivate under such conditions, and the pitting behaviour would become very important for evaluating sacrificial protection.

It is important to recognise at this point that E_{pit} is affected considerably by the concentration of chloride ions in solution. High chloride concentrations tend to aid the breakdown of passive films, causing a reduction in E_{pit} [2,3]. Therefore it is feasible that coatings not expected to provide sufficient sacrificial protection in the present chloride solution, may be adequate for aggressive, high chloride conditions. This may explain the results obtained by Baldwin *et al* [239] for Al-Mg coated steel tested in a salt spray cabinet. They obtained the longest coating life with an Al-22%Mg composition. Based on the present work, such a coating would be expected to exhibit an E_{pit} of about -650 mV (SCE) in 100mg.L^{-1} Cl^- [NaCl] aqueous solution (Fig.12.17a). This coating would consequently afford very little sacrificial protection for the steel substrate under

such dilute chloride conditions. The chloride levels in salt spray testing are considerably higher (5 wt.% NaCl [239]), and it is expected that E_{pit} for the coating under such conditions, would have been considerably more active. Thus, the successes reported for the Al-22%Mg composition probably relate only to high chloride conditions and excellent barrier protection. By corollary, it would seem that the salt spray test is not suited to evaluating the performance of protective coatings which exhibit active-passive behaviour, particularly when the expected applications do not involve such high levels of chloride ions.

12.3.4 Evaluation of Sputtered Coatings

Following the criteria developed in the previous sections, the electrochemical results for the various sputtered coatings were evaluated by a process of elimination to predict an optimum composition for corrosion protection of sheet steel.

Aluminium-Magnesium Coatings

The pure Al, Al-9%Mg and Al-25%Mg coatings were found to have excellent barrier protection properties. The corrosion rates for these coatings, revealed by the inverse of R_p (Fig.12.17b), were the lowest of all coatings examined in this thesis. Unfortunately, they also possessed an E_{pit} that was similar to, or only slightly more active than the E_{corr} of steel (Fig.12.17a). Such coatings would therefore not provide any significant sacrificial protection for sheet steel in dilute chloride aqueous solutions. It is conceivable that higher chloride levels might assist in reducing the E_{pit} of these coatings to a level that would enable modest sacrificial protection.

Increasing the Mg content to 41% had the effect of reducing the E_{pit} somewhat, such that the sacrificial protection ability of the coating was improved. However, the criteria of an E_{pit} that is 200 mV more active than E_{corr} of steel was not met for any Al-Mg alloy coating. It would therefore appear that binary Al-Mg coatings are unsuitable for the corrosion protection of sheet steel. The noted good performance of some Al-Mg coatings in salt spray cabinet testing [239] is not expected to translate to general atmospheric exposure conditions. As already noted, this is possibly due to the aggressive conditions encountered with the high chloride environment in salt spray testing, which are not representative of typical service conditions.

Coatings with an Mg content of more than about 50% were found to be unsuitable as protective coatings for steel. The Al-Mg alloy coatings in this category (Al-72%Mg and Al-86%Mg) displayed signs of rapid dealloying during the initial one hour immersion

period, with the evolution of hydrogen bubbles. The production of hydrogen gas was possible via direct reduction of water because of the very active E_{corr} (Fig.12.15a and 12.16a). The presence of (Mg) solid solution in the coatings is thought to be responsible for the poor corrosion resistance, as a result of the limited protection afforded by the thin film of magnesium hydroxide $Mg(OH)_2$ that forms on this phase [239].

Aluminium-Zinc Coatings

Sputtered coatings of Al-92%Zn possessed only a very small passive region, in accordance with the low Al content (Fig.2.11). The E_{corr} and E_{pit} for this composition were considerably more active than E_{corr} for pure Zn coatings. This suggests that such coatings would provide a high degree of sacrificial protection for sheet steel, but at the expense of very high corrosion rate. This was confirmed by the very low R_p and high i_p determined for this composition. Hence the barrier protection properties of the Al-92%Zn sputtered coating were very poor. The barrier protection afforded by the passive layer was improved somewhat by decreasing the Zn content to 74%. This resulted in a substantial increase in E_{pit} and a large reduction in i_p. The corrosion rate of the Al-74%Zn coating was improved with respect to Al-92%Zn, but was still higher than that of pure Zn coatings. These findings are somewhat surprising in light of the reported improvement in corrosion performance of commercial Galfan coatings (approximately Al-90%Zn), relative to commercial galvanised coatings. The poor performance of the sputtered Zn-rich Al-Zn coatings possibly relates to the loosely-packed porous structure that was indicated by their dark, non-reflective surface appearance (Fig.8.5). This would cause an increase in the surface area exposed to the corrosive media, thereby increasing the corrosion rate relative to pure Zn.

Moving to the Al-rich Al-Zn compositions, the Al-9%Zn coatings were found to retain much of the excellent barrier protection properties of the pure Al coatings. This was indicated by a very high R_p and low i_p, that were similar or slightly inferior to those of the Al coatings (Fig.12.11). Unfortunately, the sacrificial protection provided by this coating is suspected to be relatively poor under aerated conditions or modestly large steel/coating area ratios. This finding is based on the measured E_{pit} which was only about 160 mV more active than the E_{corr} of steel. A marginal improvement in sacrificial protection was suggested by the slight decrease in E_{pit} when Zn content was raised to 25%. The passive layer on the Al-25%Zn coating appeared to offer good barrier protection, but was susceptible to irregular breakdown as evidenced by the large spread in E_{corr} and R_p results. The Al-25%Zn composition is almost identical to that of commercial Zincalume/Galvalume, except for the absence of Si and other minor elements. The

predicted good barrier protection and moderate sacrificial protection for sputtered coatings with this composition agrees well with in-service performance of the hot-dipped coatings.

The criteria for a 200 mV separation between E_{pit} for the coating and E_{corr} for steel, was achieved for both the Al-41%Zn and Al-55%Zn compositions (Fig.12.11). It follows that both of these coating compositions are expected to provide a sufficient degree of sacrificial protection for a steel substrate, over a wide range of aeration conditions and steel/coating area ratios. The sacrificial protection ability is predicted to be noticeably better than that for the Al-25%Zn coatings, in both deaerated and aerated conditions. This is because the higher Zn content contributed to a reduction in both E_{corr} and E_{pit}. Unfortunately, the improvement in sacrificial protection is likely to come at a price of reduced coating life. The corrosion rate of the Al-55%Zn coatings was much greater than that of the Al-25%Zn coatings, according to the lower R_p and higher i_p. It would therefore appear that the optimum coating in terms of providing good barrier and sacrificial protection for a sheet steel substrate, corresponds to the Al-41%Zn composition.

Aluminium-Magnesium-Zinc Coatings

The performance of the ternary Al-Mg-Zn coatings appeared to be most closely replicated by the Al-Zn alloys. The Al-13%Mg-20%Zn coatings were found to display a very reproducible E_{pit} that was similar to that of the Al-25%Zn coatings (Fig.12.11). However, the E_{corr} of the ternary composition was dramatically lower than that of this binary coating. These effects were consistent with observed trends for the Al-Mg coatings (Fig.12.17a), which showed a decrease in E_{pit} with increasing Mg content and a comparatively small change in E_{pit}. This suggests that the Al-13%Mg-20%Zn coatings would provide similar sacrificial protection to Al-25%Mg coatings under aerated conditions and with large steel/coating area ratios. More importantly, in cases where the coating could corrode in the active state, such as in deaerated solution or with a small steel/coating area ratio, the sacrificial protection afforded by the ternary coating would be substantially improved relative to Al-25%Zn coatings. Such improvement would possibly be compromised by a small increase in corrosion rate, as suggested by the slight reduction in R_p and increase in i_p. In this respect, the Al-13%Mg-20%Zn coatings are expected to perform in a similar fashion to Al-41%Zn coatings. Thus it would appear that the Zn in a binary Al-Zn alloy coating can be partially replaced by Mg additions, at the expense of a small increase in E_{pit}. This effect may be advantageous to offset the excessive reduction in E_{pit} observed with increasing Zn content.

The Al-30%Mg-30%Zn coatings contained a similar Al/Zn ratio as the Al-41%Zn coatings. The presence of 30%Mg in the coatings had the effect of shifting most of the electrochemical parameters towards values typical of an Al-Zn alloy with increased Zn content, except for the E_{pit} which was increased. The value of E_{pit} for these ternary coatings was still acceptable with respect to a 200 mV separation from E_{corr} for steel. However, the high Mg content caused i_p to increase excessively, such that the corrosion rate of this ternary composition is expected to be similar to that of an Al-73%Zn coating. It would therefore appear that the optimum level of Mg in a ternary Al-Mg-Zn coating is between 13% and 30%.

Zinc-Magnesium Coatings

The sputtered Zn-Mg coatings provided some unexpected results since they all tended to show active-passive behaviour. It is feasible that this is related to the metastable amorphous phase in the sputtered coatings. A modestly protective passive layer was apparently formed on the surface of the coatings, which aided in minimising the detrimental effects of adding Mg. The Zn-65%Mg and Zn-82%Mg coatings were not adequately protected and the corrosion rates of these coatings were excessive. The very active E_{corr} for these coatings also meant that direct reduction of water was possible, providing an alternate cathodic reaction. As for the Al-Mg coatings, this poor corrosion performance is thought to be related to the presence of (Mg) solid solution in the coatings. The Zn-rich Zn-Mg coatings had similar E_{corr} measured during the potentiodynamic scan. However, the E_{corr} measured before the test, with agitated conditions was notably higher. It appears that a passive layer formed on these coatings, although the i_p was relatively high compared with the Al-alloy coatings.

The Zn-20%Mg coating provided a similar R_p to the pure Zn coating, while displaying a dramatically reduced E_{corr}. Hence Zn-20%Mg coatings are expected to offer improvements in sacrificial protection relative to pure Zn coatings, while maintaining similar barrier protection due to the formation of a passive layer. It is feasible that this passive layer, may actually aid in improving the long term performance of the coating, as suggested by the reduction in i_p with increasing Mg content (Fig.12.23). This conclusion goes some way towards understanding the interest shown in Zn-Mg alloy coatings by some Japanese coated-steel producers [23,24,39,264,265,266]. It must be added, however, that the service life of a Zn-Mg alloy coating is not expected to exceed that of the best Al-Zn or Al-Mg-Zn coatings, primarily because of the comparatively high corrosion rate, and thus poorer barrier protection properties.

Chapter 13

Conclusions

13.1 Methodology

The preparation and microstructural evaluation of the sputtered alloy coatings described in this thesis incorporated several conventional techniques in addition to some rather novel ones. The use of composite sputter targets for coating deposition, and the Crystallite Group Method for characterisation of the strain-free lattice parameters and residual biaxial stress, represent two such unusual approaches that proved extremely valuable.

13.1.1 Composite Sputter Targets

A novel design of composite target was developed for this work that enabled preparation of alloy coatings. The targets consisted of segments of different metals attached sequentially to the surface of a circular copper backing plate, which permitted direct water-cooling. A conventional epoxy resin adhesive was used in the construction of the targets. Each target was capable of providing a reasonably stable sputtered flux composition over a period of up to several hours operation. Some drift in sputtered flux composition was noted to occur for Al/Mg targets especially, due to the markedly different volumetric etch rates of the constituent metals. Exposure of the epoxy resin between the joints on the target surface possibly contributed some impurities to the coatings. No contaminants were detected by chemical analysis, but residual tensile stresses in the (Al) phase of several coatings, and the stabilisation of an amorphous phase in Al-rich alloys, hint at their presence.

13.1.2 Crystallite Group Method

The Crystallite Group Method (CGM) was used extensively throughout this work for the simultaneous measurement of both residual biaxial macrostress and strain-free lattice parameters of crystalline phases in sputtered coatings. This powerful XRD

technique targets specific crystallite groups, such that the strongly fibre textured structures typical of PVD coatings can be examined independent of elastic anisotropy. All previous studies have considered only materials with a cubic crystal structure, and CGM was used for the first time to evaluate coatings with a hexagonal crystal structure. For this purpose, appropriate equations were developed specifically for <0001> fibre textured hexagonal coatings. The principal assumption necessary for these calculations was that the *c/a* ratio is unaffected by any solid solubility. The CGM approach also assumes that the single crystal elastic compliances are not affected by the presence of solute in solid solution, which is also a common assumption for all other XRD-based stress analysis.

13.2 Coating Stoichiometry

Bombardment of the coating with energetic ions during deposition alters the chemical composition by preferential resputtering. This leads to non-stoichiometric coatings or gradients in alloy composition over large coated areas, which are difficult to predict or simulate. Therefore, ion assisted deposition is not recommended for preparation of alloy coatings.

For Al-Zn, Al-Mg, and Al-Mg-Zn coatings, the element with the lowest surface binding energy was depleted by preferential resputtering. Composition of Al-Zn coatings was stable for low energy ion bombardment, but Zn was preferentially resputtered above a critical bias voltage. The Mg content of Al-Mg coatings was sharply depleted with only small bias voltage increases. Ternary Al-Mg-Zn coatings were highly susceptible to compositional changes by preferential resputtering of Mg at low bias, and both Mg and Zn at high bias. For each series, increasing substrate bias led to enrichment of Al in the coatings.

Surface binding energy was not the only parameter controlling preferential resputtering. The Zn-Mg coatings were susceptible to preferential resputtering of Mg, which has a higher surface binding energy than Zn. Large differences in atomic mass of Zn and Mg caused a sputter yield amplification effect, whereby the partial yield of Mg was enhanced by the close proximity of heavier Zn atoms. The modification to the partial yields was sufficient to override the small differences in elemental sputter yields.

Ion bombardment led to the burial of large proportions of Ar in the sputtered coatings. Entrapped Ar was insoluble in the crystalline phases, and was thought to segregate into bubbles. Susceptibility to Ar burial was phase dependent, whereby the (Mg) phase retained the highest Ar content (<30 at.%), followed by the amorphous and (Zn) phases. The (Al) phase did not retain detectable amounts of Ar. Ar content climbed

parabolically with increasing substrate bias. In many cases, Ar content reached a maximum and decreased with continued increase in bias. This effect was caused by a balance between entrapment by ion implantation, and loss of Ar by vacancy diffusion and perhaps resputtering. The presence of such high proportions of inert gas in the coatings had several effects. In coatings with more than about 20 at.%Ar, the buried inert gas escaped after ambient ageing and the remnant porous structure was rapidly oxidised. The (Mg) phase was amorphized by buried Ar, while the bubbles of Ar in (Zn) phase caused residual microstrain.

13.3 Metastable Phases

13.3.1 Crystalline Phases

The terminal solid solutions were the dominant crystalline phases in coatings prepared from the Al-Mg-Zn ternary system. The crystalline phases often possessed strong fibre textures, usually with the close-packed planes oriented parallel to the coating surface. Up to 30 at.%Mg was retained in (Al) solution for Al-Mg coatings, and increasing the bias voltage caused rejection of the solute. It was suspected that as much as 35 at.%Zn was present in the (Al) phase of Al-Zn coatings immediately after deposition, but the solute was reduced to less than 18 at.% following short term ageing. The combined solubility of Mg and Zn in ternary (Al) could not be determined. Increasing substrate bias enabled the development of a strong <111> fibre texture in (Al) phase. Formation of fibre textured (Al) required less ion assistance when Mg or Zn was present in solid solution, due to sputter yield amplification.

The solubility of Al and Mg in (Zn) phase was not measured, but all indications suggested it was in the order of less than 1 at.%. The (Zn) phase existed in two distinct crystallite groups of randomly oriented and <0001> fibre textured grains. This behaviour was independent of any Al or Mg in the coating, due to their minimal solubility. The randomly oriented grains were situated on the extreme surface, and were responsible for the matt appearance of all Zn-rich coatings. Raising the substrate bias produced smooth specular coatings by favouring growth of the strongly fibre textured grains. The fibre textured grains were associated with high proportions of buried Ar.

The (Mg) phase was able to retain as much as 30 at.%Al in supersaturated solid solution, although ion assistance caused a reduction in solubility. The solubility of Zn in (Mg) was limited to 2.8 at.%. When deposited with low bombardment conditions, the (Mg) phase had a strong <0001> fibre texture, which was degraded as substrate bias was increased. At the most energetic bombardment conditions there was a tendency for

growth of <10.1> fibre textured (Mg) phase, possibly because of plastic flow or preferential resputtering of <0001> oriented grains.

Intermetallic phases were only detected in Zn-Mg coatings. Those with between 3 and 7 at.%Mg, deposited at low bias voltages, contained a range of intermetallics. At least one phase could not be identified, and thus represents a new metastable phase. Increasing substrate bias led to growth of Mg_2Zn_{11} with a strong <111> fibre texture. Traces of intermetallics were detected in some other Zn-Mg coatings, and were thought to be formed after ambient ageing.

13.3.2 Amorphous Phases

There was strong indication that amorphous phases were present in many of the sputtered coatings. These "amorphous" phases may be nanocrystalline, as the XRD evidence is insensitive to very fine crystallites. The Al/Mg and Al/Mg/Zn composite targets provided amorphous Al-rich alloy coatings at low bias conditions. It is thought that impurities derived from the epoxy resin in the target destabilised the crystalline structure. In the case of the (Mg) phase, burial of Ar appears to have caused amorphization, independent of the presence of Al or Zn in solid solution.

Zn-Mg coatings containing between 15 and 50 at.%Mg were entirely amorphous. This may have occurred because the growth of complex intermetallic equilibrium phases was kinetically unfavourable. Similarly, the β-Al_3Mg_2 phase in Al-Mg coatings was avoided by the formation of an amorphous phase. However, the amorphous Zn-72 at.%Mg phase reported for rapidly solidified alloys, was not observed in the coatings. This was possibly because the liquid phase, which has similar structural units to the rapidly solidified amorphous phase, was avoided in the coating deposition process.

13.4 Residual Stress

The (Al) and (Mg) phases in coatings sputtered from monolithic targets were subject to zero or small residual compressive macrostresses when deposited with minimal ion bombardment conditions. Increasing the substrate bias caused an increase in the compressive stress, due to the atomic peening mechanism. The same phases in coatings deposited from composite targets were in a state of tensile stress at low bias, and abruptly transferred to a compressive stress as the bias was increased. The tensile stresses were explained by the impurity model, whereby epoxy resin sputtered from the joints in the composite targets caused trace contamination of the coatings.

Residual stress in the (Zn) phase was restricted to the <0001> fibre textured grains. The stress was consistently tensile and increased continuously with bias (above about -100V). This is highly unusual for coatings with a very dense columnar structure. Tensile stress development was attributed to a constrained shrinkage model, involving recrystallization of the bombardment-damaged coating.

13.5 Electrochemical Performance

All coatings examined are expected to provide a degree of sacrificial protection to low-carbon sheet steel, as a result of their active corrosion potentials. However, the majority of the coatings also exhibited passive regions in their anodic polarization curves. It was demonstrated for these active-passive coatings that passive current density and pitting potential are critical in determining corrosion behaviour of the coating. Optimum barrier protection of the substrate would be ensured by maximising polarization resistance of the coating, which is equivalent to minimising passive current density.

Following these criteria, sputtered Al-Mg coatings with up to 41 at.%Mg were shown to be incapable of providing sufficient sacrificial protection for steel substrates. Large passive regions which dominated the polarization curves, indicate that the coating would corrode sacrificially, but with only a small cathodic overvoltage on the steel. Other Al-Mg coatings with higher Mg content were also unsuitable because they were subject to very rapid corrosion rates, presumably by dissolution of (Mg) phase.

Sputtered Al-Zn coatings should supply an optimum combination of good barrier and sacrificial properties. The electrochemical behaviour of these alloy coatings was intermediate between pure Al and pure Zn coatings. As the Zn content of the coatings was increased, the corrosion potential, pitting potential, and polarization resistance tended to decrease continuously. The best combination of properties was thought to exist for the Al-41 at.%Zn coating composition. Similar corrosion behaviour was observed for coatings of Al-13 at.%Mg-20 at.%Zn suggesting that Zn in binary Al-Zn coatings can be partially replaced by Mg, at the expense of a small increase in pitting potential. The optimum level of Mg in such ternary coatings was thought to be between 13 and 30 at.%.

The modest passive regions noted for Zn-Mg coatings can be attributed to either the amorphous or intermetallic phases. Zn-20 at.%Mg coatings should offer improvements in sacrificial protection relative to pure Zn coatings. It is also feasible that the formation of a passive layer, not found with pure Zn or Mg coatings, may improve the barrier protection of the alloy coating.

13.6 Suggestions for Further Work

Several aspects of the present investigation highlighted a need for further research which can be summarised as follows:

1) Development of composite targets with the aim of avoiding contamination of coatings by sputtered epoxy adhesive. A design that avoids exposure of the resin on the sputtering surface is an obvious solution.

2) Use of elevated substrate temperatures for the control of inert gas burial in sputtered coatings. Some work on the diffusivity of Ar in Al, Mg and Zn would also prove valuable for understanding the susceptibility to entrapment of Ar during deposition.

3) The effect of ambient and elevated temperature ageing on the stability of metastable phases in sputtered alloy coatings, particularly Al-Zn.

4) Examination of the various types of "amorphous" phases reported here, using transmission electron microscopy and appropriate calorimetry techniques, in order to determine if they are nanocrystalline rather than amorphous.

5) Testing the constrained shrinkage model for explaining tensile stresses in Zn coatings by studying unbalanced magnetron sputtered Sn or Pb coatings. Other candidate metals would be Cd, In or Tl, but would require extreme safety precautions.

6) Controlled tests of the Crystallite Group Method using samples of known solid solubility and residual stress, in order to thoroughly evaluate the reliability of the technique.

7) A vastly extended corrosion testing programme would be highly beneficial. Such a study should incorporate a range of laboratory tests in addition to outdoor exposure. It would be valuable to conduct a comparative study of conventional hot-dipped coatings such as Zincalume and Galfan, with PVD coatings of the same chemical composition but with the characteristic fine grained microstructure.

Chapter 14

References

1 F.Porter, *Zinc Handbook*, Marcel Dekker, New York, 1991.

2 M.G.Fontana, *Corrosion Engineering*, Third Edition, McGraw-Hill, New York, 1986.

3 D.A.Jones, *Principles and Prevention of Corrosion*, MacMillan, New York, 1992.

4 I.Suzuki, *Corrosion-Resistant Coatings Technology*, Marcel Dekker, New York, 1989.

5 J.Stavros, "Continuous Hot Dip Coatings"; in *Metals Handbook*, Ninth Edition, Vol.13, ASM, Metals Park OH, 1987, pp.432-436.

6 H.E.Townsend, A.R.Borzillo, *Galvatech '95*, ISS, Warrendale PA, pp.171-177, 1995, Proc. Use and Manufacture of Zinc and Zinc Alloy Coated Sheet Steel Products into the 21st Century, Chicago IL, 17-21 Sep 1995.

7 C.Ayoub, A.Davin, F.E.Goodwin, D.Coutsouradis, *Zinc Coated Steel Sheet*, ZDA, London, pp.SA2/1-31, 1989, 2nd Int. Conf. on Zinc-Coated Steel Sheet, Rome, 9-10 June 1988

8 A.Bonaretti, A.Capoccia, G.Giardetti, U.Mucchino, *Zinc Coated Steel Sheet*, ZDA, London, pp.SC6/1-13, 1989, 2nd Int. Conf. on Zinc-Coated Steel Sheet, Rome, 9-10 June 1988.

9 M.Memmi, U.Mucchino, G.Giardetti, *Zinc Coated Steel Sheet*, ZDA, London, pp.SC7/1-11, 1989, 2nd Int. Conf. on Zinc-Coated Steel Sheet, Rome, 9-10 June 1988.

10 M.Lamberigts, V.Leroy, M.Kuhn, L.Renard, *Galvatech '92*, Verlag Stahleisen, Düsseldorf, pp.412-416, 1992, 2nd Int. Conf. Zinc and Zinc Alloy Coated Sheet Steel Amsterdam, Netherlands, 8-10 September 1992.

11 K.M.Frommann, V.A.Paramonov, B.L.Birger, *Galvatech '95*, ISS, Warrendale PA, pp.189-192, 1995, Proc. Use and Manufacture of Zinc and Zinc Alloy Coated Sheet Steel Products into the 21st Century, Chicago IL, 17-21 Sep 1995.

12 D.A.Finlayson, John Lysaght (Australia) Ltd., C.T. Rep. No.3027, 1970.

13 D.Finlayson, John Lysaght (Australia) Ltd., C.T. Rep. No.3033, 1970.

14 D.Finlayson, John Lysaght (Australia) Ltd., C.T. Rep. No.3034, 1970.

15 K.C.Taylor, US Patent 3,326,177, 1967.

16 L.E.Helwig, M.V.Murray, British Patent 1,187,802, 1970.

17 L.E.Helwig, M.V.Murray, US Patent 3,594,214, 1971.

18 W.E.Vincent, J.Davies, I.S.Rees, British Patent 1,252,882, 1971.

19 L.E.Helwig, M.V.Murray, *Metal Finishing*, Nov, 37-40; Dec, 31-37, 1975.

20 K.Scribner, John Lysaght (Australia) Ltd., C.T. Rep. No.2866, 1966.

21 D.A.Finlayson, John Lysaght (Australia) Ltd., C.T. Rep. No.3105, 1971.

22 T.W.Smythe, John Lysaght (Australia) Ltd., C.T. Rep. No.3139, 1971.

23 K.Shimogori, H.Satoh, M.Toyama, H.Nishimoto, K.Ikeda, J.Kawafuku, S.Miyake, S.Nomura, H.Sakai, US Patent 5,135,817, 1992.

24 Y.Fukui, M.Matsuno, H.Tanaka, T.Miono, K.Sakamoto, Y.Ariyoshi, M.Saito, US Patent 5,648,177, 1997.

25 S.Schiller, G.Jäsch, *Thin Solid Films*, **54**, 9-21, 1978.

26 H.Lämmermann, K.Frommann, *Metallurgical Plant and Technology Int.*, **15** (1) 78-87, 1992.

27 S.Schiller, G.Beister, M.Neumann, G.Jaesch, *Thin Solid Films*, **96**, 199-216, 1982.

28 S.Schiller, U.Heisig, M.Neumann, G.Beister, *Vakuum-Technik*, 1986, 8th Int. Conf. Vacuum Metallurgy, 30 Sep. - 4 Oct. 1985, Linz, Austria.

29 S.Schiller, H.Förster, G.Hötzsch, G.Jäsch, *Steel Times*, **213** (9) 437-438, 1985.

30 M.Maeda, A.Morita, H.Furukawa, K.Wake, Y.Shimozato, K.Yanagi, M.Kato, T.Wada, *Mitsubishi Heavy Industries Technical Review*, **22** (2) 185-191, 1985.

31 S.Kamura, T.Aiko, K.Nakamura, Proc. JRCM Symposium, 19 September 1990, Paper 3, 1990.

32 M.Maeda, K.Nakamura, T.Ito, T.Aiko, S.Furuya, K.Hashimoto, K.Yanagi, H.Furukawa, T.Taguchi, *Mitsubishi Heavy Industries Technical Review*, **24** (3) 185-191, 1987.

33 A.Morita, K.Chohata, Y.Hirose, *Zinc Coated Steel Sheet*, SD1/1-5, 1988, 2nd Int. Conf. Zinc Coated Steel Sheet, Rome, 9-10 June 1988, ZDA, London.

34 K.Chohata, M.Saito, Y.Hirose, A.Morita, *Galvatech '89*, ISS (Japan), 37-44, 1989, Int. Conf. Zinc and Zinc Alloy Coated Steel Sheet, Tokyo, 1989.

35 H.Taketsu, M.Suzuki, Y.Nakagawa, T.Deguchi, *Nisshin Steel Tech. Rep.*, **58**, 74-84, 1988.

36 Y.Uchida, Y.Hirose, Y.Kusanagi, A.Morita; in *Corrosion-Resistant Automotive Sheet Steels*, ASM International, Metals Park, OH, 155-163, 1988, Chicago, Illinois, 24-30 September 1988.

37 J.Kawafuku, J.Katoh, M.Toyama, K.Ikeda, H.Nishimoto, H.Satoh; in *Proc. 5th Automotive Corrosion & Prevention Conf.*, SAE P-250, p.43-50, 1991, Dearborn MI, 21-23 Oct 1991.

38 J.Katoh, J.Kawafuku; in K.Yamakawa, H.Fujikawa (ed.), *Recent Advances in Coated Steels Used for Automobile*, Elsevier Science, Japan, 125-143, 1996.

39 K.Shimogori, H.Satoh, M.Toyama, H.Nishimoto, K.Ikeda, J.Kawafuku, S.Miyake, S.Nomura, H.Sakai, US Patent 5,002,837, 1991.

40 M.Hashimoto, S.Miyajima, W.Ito, S.Ito, T.Urata, T.Komori, I.Ito, M.Onoyama, Surf. Coat. Technol., **36**, 837-845, 1988.

41 I.Itoh, T.Komori, Y.Oikawa, M.Onoyama, M.Hashimoto, S.Itoh, S.Saita, T.Murata, *Nippon Steel Tech. Rep.*, **43** (10) 8-15, 1989.

42 T.Hyodo, H.Kagechika, H.Kibe, Y.Yasue, N.Okude, *J. Vac. Sci. Technol. A*, **10** (4) 1662-1668, 1992.

43 J.C.Shin, Y.P.Lee, K.D.Choi, J.H.Jun, *Galvatech '92*, Verlag Stahleisen, Düsseldorf, 1992, 2nd Int. Conf. Zinc and Zinc Alloy Coated Sheet Steel, Amsterdam, Netherlands, 8-10 September 1992.

44 J.H.Jun, K.D.Choi, Y.P.Yee, J.C.Shin, *Galvatech '92*, Verlag Stahleisen, Düsseldorf, 346-350, 1992, 2nd Int. Conf. Zinc and Zinc Alloy Coated Sheet Steel Amsterdam, Netherlands, 8-10 September 1992.

45 J.H.Jun, B.M.Lim, J.C.Shin, *Zinc Coated Steel Sheet*, SF2/1-8, 1994, 4th Int. Conf. Zinc Coated Steel Sheet, Paris, June 1994, EGGA, London.

46 D.M.Mattox, *J. Vac. Sci. Technol. A*, **7** (3) 1105-1114, 1989.

47 B.Chapman, *Glow Discharge Processes*, John Wiley & Sons, Toronto, Canada, 1980.

48 R.Behrisch (ed.), *Sputtering by Particle Bombardment I: Physical Sputtering of Single-Element Solids*, Springer-Verlag, Berlin, 1981.

49 F.A.Smidt, *Int. Materials Reviews*, **35** (2) 61-128, 1990.

50 W.Gissler, H.A.Jehn (ed.), *Advanced Techniques for Surface Engineering*, Kluwer Academic, Dordrecht, The Netherlands, 1992.

51 W.D.Sproul, K.O.Legg (ed.), *Advances in Surface Engineering*, Technomic, Lancaster PA, c.1994.

52 R.F.Bunshah, "Evaporation"; in R.F.Bunshah (ed.), *Handbook of Deposition Technologies for Films and Coatings*, Second Edition, Chap.4, Noyes, Park Ridge NJ, 1994.

53 D.A.Glockner, S.I.Shah (ed.), *Handbook of Thin Film Process Technology*, IOP, UK, 1995.

54 J.A.Thornton, J.E.Greene, "Sputter Deposition Processes"; in R.F.Bunshah (ed.), *Handbook of Deposition Technologies for Films and Coatings*, Second Edition, Chap.5, Noyes, Park Ridge NJ, 1994.

55 M.T.Robinson, A.L.Southern, *J. Appl. Phys.*, **39** (7) 3463, 1968.

56 P.Ziegler, J.J.Cuomo, *TRIM version 95.4 software and documentation*, March 8, 1995.

57 B.Window, *J. Vac. Sci. Technol. A*, **11** (4) 1522-1527, 1993.

58 D.W.Hoffman, J.-S.Park, T.S.Morley, *J. Vac. Sci. Technol. A*, **12** (4) 1451-1456, 1994.

59 B.A.Shedden, F.N.Kaul, M.Samandi, B.Window, *Surf. Coat. Technol.* (in press), 5th Int. Conf. Plasma Surface Engineering, Garmisch-Partenkirchen, Germany, 9-13 Sept 1996.

60 B.Window, N.Savvides, *J. Vac. Sci. Technol. A*, **4** (2) 196-202, 1986.

61 B.Window, G.L.Harding, *Proc. 1st Int. Symp. Sputtering and Plasma Processes*, Tokyo, 1991.

62 S.Kadlec, J.Musil, *J. Vac. Sci. Technol. A*, **13** (2) 389-393, 1995.

63 B.Window, N.Savvides, *J. Vac. Sci. Technol. A*, **4** (3) 453-456, 1986.

64 B.Window, G.L.Harding, *J. Vac. Sci. Technol. A*, **10** (5) 3300-3304, 1992.

65 B.Window, G.L.Harding, *J. Vac. Sci. Technol. A*, **8** (3) 1277-1282, 1990.

66 H.-C.W.Huang, C.M.Serrano, *J. Vac. Sci. Technol. A*, **1** (3) 1409-1415 1983.

67 A.G.Dirks, J.J.van den Broek, *Thin Solid Films*, **96**, 257-263, 1982.

68 A.G.Dirks, J.J.van den Broek, P.E.Wierenga, *J. Appl. Phys.*, **55** (12) 4248-4256, 1984.

69 A.G.Dirks, J.J.van den Broek, *J. Vac. Sci. Technol. A*, **3** (6) 2618-2622, 1985.

70 J.J.van den Broek, A.G.Dirks, P.E.Wierenga, *Thin Solid Films*, **130**, 95-101, 1985.

71 J.Kim, D.S.Yee, *Thin Solid Films*, **128**, 67-78, 1985.

72 D.McIntyre, J.-E.Sundgren, J.E.Greene, *J. Vac. Sci. Technol. A*, **6** (3) 1708-1709, 1988.

73 E.B.Graper; in D.A.Glockner, S.I.Shah (ed.), *Handbook of Thin Film Process Technology*, Chap.1, IOP, UK, 1995.

74 M.L.Tarng, G.K.Wehner, *J. Appl. Phys.*, **42** (6) 2449-2452, 1971.

75 D.Popov, P.Mashkov, D.Tzaneva, *Vacuum*, **45** (9) 967-971, 1994.

76 C.Eisenmenger-Sittner, A.Bergauer, A.Wagendristel, W.Gärtner, *J. Vac. Sci. Technol. A*, **10** (5) 3260-3265, 1992.

77 Y.Nagai, C.Nishimura, T.Toshima, *J. Vac. Sci. Technol. A*, **3** (6) 2147-2151, 1985.

78 A.van der Jagt, W.Chen, *J. Vac. Sci. Technol. A*, **4** (2) 203-209, 1986.

79 Y.H.Shing, Y.Chang, A.Mirshafii, L.Hayashi, S.S.Roberts, J.Y.Josefowicz, N.Tran, *J. Vac. Sci. Technol. A*, **1** (2) 503-506, 1983.

80 A.Bourjot, M.Foos, C.Frantz, *Surf. Coat. Technol.*, **43/44** (1-3) 533-542, 1990.

81 J.J.Cuomo, R.J.Gambino, *J. Vac. Sci. Technol.*, **12** (1) 79-83, 1975.

82 F.Sanchette, T.-H.Loi, C.Frantz, *Surf. Coat. Technol.*, **57** (2-3) 179-182, 1993.

83 J.L.Vossen, *J. Vac. Sci. Technol.*, **8** (5) S12-30, 1971.

84 A.Belkind, E.Ezell, W.Gerristead, Z.Orban, P.Rafalko, D.Dow, J.Felts, R.Laird, *J. Vac. Sci. Technol. A*, **9** (3) 530-536, 1991.

85 A.M.Kazakos, D.E.Fahnline, R.Messier, L.J.Pilione, *J. Vac. Sci. Technol. A*, **10** (6) 3445-3450, 1992.

86 A.M.Kazakos, D.E.Fahnline, R.Messier, L.J.Pilione, *J. Vac. Sci. Technol. A*, **10** (6) 3439-3444, 1992.

87 R.D.Arnell, R.I.Bates, *Le Vide, les Couches Minces*, Supplément au No.261 Mar-Apr, 309-311, 1992.

88 D.P.Monaghan, D.G.Teer, P.A.Logan, K.C.Laing, R.I.Bates, R.D.Arnell, *Surf. Coat. Technol.*, **60**, 592-596, 1993.

89 R.I.Bates, R.D.Arnell, *Surf. Coat. Technol.*, **89** (3) 204-212, 1997.

90 R.I.Bates, R.D.Arnell, 5th Int. Conf. Plasma Surface Engineering, Garmisch-Partenkirchen, Germany, 9-13 Sept 1996.

91 R.I.Bates, R.D.Arnell, *Surf. Coat. Technol.*, **68/69**, 686, 1994.

92 C.Bowden, A.Matthews, *Surf. Coat. Technol.*, **76/77**, 508-515, 1995.

93 S.Ashida, T.Yoshida, K.Akashi, *J. Vac. Sci. Technol. A*, **4** (5) 2388-2390, 1986.

94 Y.Taga, *J. Vac. Sci. Technol. A*, **13** (3) 991-995, 1995.

95 C.M.Gilmore, C.Quinn, E.F.Skelton, C.R.Gossett, S.B.Qadri, *J. Vac. Sci. Technol. A*, **4** (6) 2598-2600, 1986.

96 M.R.Lake, G.L.Harding, *J. Vac. Sci. Technol. A*, **2** (3) 1391-1393, 1984.

97 R.W.Knoll, E.D.McClanahan, *J. Vac. Sci. Technol. A*, **1** (2) 271-274, 1983.

98 R.D.Arnell, R.I.Bates, *Vacuum*, **43** (1/2) 105-109, 1992.

99 F.Sanchette, T.-H.Loi, A.Billard, C.Frantz, *Surf. Coat. Technol.*, **74/75**, 903-909, 1995.

100 S.Rohde, S.A.Barnett, C.-H.Choi, *J. Vac. Sci. Technol. A*, **7** (3) 2273-2279, 1989.

101 S.B.Qadri, W.W.Fuller, K.E.Kihlstrom, R.W.Simon, E.F.Skelton, D.Van Vechten, S.A.Wolf, *J. Vac. Sci. Technol. A*, **3** (3) 664-666, 1985.

102 M.Wright, T.Beardow, *J. Vac. Sci. Technol. A*, **4** (3) 388-392, 1986.

103 A.Belkind, Z.Orban, S.Berg, P.Carlsson, *J. Vac. Sci. Technol. A*, **11** (2) 314-318, 1993.

104 A.Belkind, *J. Vac. Sci. Technol. A*, **11** (4) 1501-1509, 1993.

105 J.A.Thornton, *J. Vac. Sci. Technol.*, **11** (4) 666-670, 1974.

106 B.A.Movchan, A.V.Demchishin, *Phys. Met. Metallography*, **28** (4) 653-660, 1969.

107 J.A.Thornton, *J. Vac. Sci. Technol.*, **12** (4) 830-835, 1975.

108 J.A.Thornton, *J. Vac. Sci. Technol. A*, **4** (6) 3059-3065, 1986.

109 R.Messier, A.P.Giri, R.A.Roy, *J. Vac. Sci. Technol. A*, **2** (2) 500-503, 1984.

110 C.Fountzoulas, W.B.Nowak, *J. Vac. Sci. Technol. A*, **9** (4) 2128-2137, 1991.

111 R.Messier, *J. Vac. Sci. Technol. A*, **4** (3) 490-495, 1986.

112 R.Hübler, L.Alberts, G.K.Wolf, *Surf. Coat. Technol.*, **60**, 549-555, 1993.

113 V.Dietz, P.Ehrhart, D.Guggi, H.-G.Haubold, W.Jäger, M.Prieler, W.Schilling, *Surf. Coat. Technol.*, **43/44**, 963-974, 1990.

114 K.-H.Müller, *J. Vac. Sci. Technol. A*, **4** (2) 184-188, 1986.

115 K.-H.Müller, *J. Appl. Phys.*, **62** (5) 1795-1799, 1987.

116 F.R.Weber, H.Oechsner, *Surf. Coat. Technol.*, **59**, 234-238, 1993.

117 G.Knuyt, C.Quaeyhaegens, J.D'Haen, L.M.Stals, *Surf. Coat. Technol.*, **74/75**, 604-608, 1995.

118 G.Knuyt, C.Quaeyhaegens, J.D'Haen, L.M.Stals, *Surf. Coat. Technol.*, **76/77**, 311-315, 1995.

119 D.R.Askeland, *The Science and Engineering of Materials*, S.I. Edition, Chapman & Hall, London, 1991.

120 J.W.Patten, E.D.McClanahan, J.W.Johnston, *J. Appl. Phys.*, **42** (11) 4371-4377, 1971.

121 S.D.Dahlgren, J. Vac. Sci. Technol., **11** (4) 832-836, 1974.

122 S.D.Dahlgren, W.L.Nicholson, M.D.Merz, W.Bollmann, J.F.Devlin, R.Wang, *Thin Solid Films*, **40**, 345-353, 1977.

123 B.Window, F.Sharples, N.Savvides, *J. Vac. Sci. Technol. A*, 6 (4) 2333-2340, 1988.

124 F.M.d'Heurle, *Int. Materials Reviews*, **34** (2) 53-68, 1989.

125 H.Windischmann, *J. Vac. Sci. Technol. A*, **9** (4) 2431-2436, 1991.

126 H.Windischmann, *Crit. Rev. Solid State and Mater. Sci.*, **17** (6) 547-596, 1992.

127 D.W.Hoffman, *J. Vac. Sci. Technol. A*, **12** (4) 953-961, 1994.

128 D.W.Hoffman, J.A.Thornton, *Thin Solid Films*, **40**, 355-363, 1977.

129 B.Window, *J. Vac. Sci. Technol. A*, **7** (5) 3036-3042, 1989.

130 B.Window, G.L.Harding, C.Horrigan, T.Bell, *J. Vac. Sci. Technol. A*, **10** (5) 3278-3282, 1992.

131 C.Fang, *Modelling of Stresses in Sputter-Deposited Thin Films*, PhD thesis, Columbia University, USA, 1993.

132 I.Petrov, L.Hultman, J.-E.Sundgren, J.E.Greene, *J. Vac. Sci. Technol. A*, **10** (2) 265-272, 1992.

133 M.F.Ashby, D.R.H.Jones, *Engineering Materials*, Vol.1, Pergamon, Oxford, 1980.

134 P.J.Rudeck, J.M.E.Harper, P.M.Fryer, *J. Vac. Sci. Technol. A*, **7** (3) 2289-2293, 1989.

135 A.Terrasi, S.Ravesi, C.Marcellino, C.Spinella, S.Pannitteri, *J. Vac. Sci. Technol. A*, **13** (6) 2827-2831, 1995.

136 J.Musil, J.Matous, V.Valvoda, *Vacuum*, **46** (2) 203-210, 1995.

137 R.Kuzel, Jr., V.Valvoda, M.Chládlek, J.Musil, J.Matous, *Thin Solid Films*, **263**, 150-158, 1995.

138 K.R.Bijkerk, A.Van Veen, G.J.Van Der Kolk, T.Minemura, *J. Less-Common Metals*, **145** (1-2) 189-195, 1988.

139 H.F.Winters, E.Kay, *J.Appl. Phys.*, **38**, 3928, 1967.

140 B.Window, G.L.Harding, *J. Vac. Sci. Technol. A*, **11** (4) 1447-1450, 1993.

141 H.F.Winters, D.L.Raimondi, D.E.Horne, *J. Appl. Phys.*, **40** (7) 2996-3006, 1969.

142 J.M.E.Harper, S.Berg, C.Nender, I.V.Katardjiev, S.Motakef, *J. Vac. Sci. Technol. A*, **10** (4) 1765-1771, 1992.

143 L.Li, W.B.Nowak, *J. Vac. Sci. Technol. A*, **12** (4) 1587-1594, 1994.

144 J.M.E.Harper, R.J.Gambino, *J. Vac. Sci. Technol.*, **16**, 1901, 1979.

145 S.Berg, A.M.Barklund, B.Gelin, C.Nender, I.Katardjiev, *J. Vac. Sci. Technol. A*, **10** (4) 1592-1596, 1992.

146 S.Berg, A.M.Barklund, C.Nender, I.Katardjiev, H.Barankova, *Surf. Coat. Technol.*, **54/55**, 131-135, 1992.

147 S.Berg, I.V.Katardjiev, *Surf. Coat. Technol.*, **68/69**, 325-331, 1994.

148 J.P.Biersack, S.Berg, C.Nender, *Nucl. Instrum. Methods Phys. Res. B*, **59/60**, 21, 1991.

149 J.P.Biersack, L.G.Haggmark, *Nucl. Instrum. Methods*, **174**, 257, 1980.

150 C.Hedland, P.Carlsson, H.-O.Blom, S.Berg, I.V.Katardjiev, *J. Vac. Sci. Technol. A*, **12** (4) 1542-1546, 1994.

151 K.Hashimoto, N.Kumagai, H.Yoshioka, J.H.Kim, E.Akiyama, H.Habazaki, S.Mrowec, A.Kawashima, K.Asami, *Corr. Sci.*, **35** (1-4) 363-370, 1993.

152 F.Sanchette, A.Billard, C.Frantz, 5th Int. Conf. Plasma Surface Engineering, Garmisch-Partenkirchen, Germany, 9-13 Sept 1996.

153 D.A.Finlayson, *Vacuum*, **21** (1/2) 35-39, 1971.

154 J.L.Robertson, B.A.Unvala, *Phil. Mag.*, **24** (2) 1253-1256, 1971.

155 M.Neirynck, W.Samaey, L.Van Poucke, *J. Vac. Sci. Technol.*, **11** (4) 647-652, 1974.

156 Z.Wang, R.Harris, Mater. Characterization, **30** 155-173, 1993.

157 P.Gimondo, F.Arezzo, B.Grifoni, G.Jäsch, *Proc. Computer Methods and Experimental Measurements for Surface Treatment Effects*, Computational Mechanics Pub., 379-388, 1993, Southampton, UK, 20-22 April 1993.

158 F.Arezzo, P.Gimondo, V.Ferrari, *Galvatech '95*, ISS, Warrendale PA, pp.235-241, 1995, The Use and Manufacture of Zinc and Zinc Alloy Coated Sheet Steel Products into the 21st Century, Chicago IL, 17-21 Sep 1995.

159 J.G.Na, *J. Vac. Sci. Technol. A*, **13** (6) 2739-2741, 1995.

160 B.A.Shedden, M.Samandi, B.Window, *Surf. Coat. Technol.*, **68/69**, 332-338, 1994.

161 C.G.Fountzoulas, *Plasma-Assisted Deposition of Films*, PhD thesis, Northeastern University, USA, 1989.

162 R.J.Schmitt, *Mechanical Working and Steel Processing*, Vol.31, Iron and Steel Society, Warrendale, Pennsylvania, 125-129, 1994, 35th Mechanical Working and Steel Processing Conf. Pittsburgh, Pennsylvania, 24-27 October 1993.

163 F.K.Urban III, S.W.Feng, J.J.Nainaparampil, *J. Vac. Sci. Technol. B*, **11** (5) 1916-1920, 1993.

164 S.W.Feng, J.J.Nainaparampil, M.F.Tabet, F.K.Urban III, *Thin Solid Films*, **253**, 402-406, 1994.

165 G.Musa, H.Ehrich, M.Mausbach, *J. Vac. Sci. Technol. A*, **12** (5) 2887-2895, 1994.

166 W.J.James, P.-L.Tseng, *J. Vac. Sci. Technol. A*, **3** (6) 2634-2638, 1985.

167 P.-L.Tseng, *Electrochemical Behaviour of Zinc and Plasma-Deposited Zinc in Sulphate Electrolytes*, PhD thesis, University of Missouri, 1987.

168 M.Gong, Y.Wang, G.Zhou, *Materials Protection (China)*, **24** (2) 10-14, 1991.

169 N.Parkansky, R.L.Boxman, S.Goldsmith, Yu.Rosenberg, *Surf. Coat. Technol.*, **76/77**, 352-357, 1995.

170 B.D.Cullity, *Elements of X-Ray Diffraction*, Second Edition, Addison Wesley, Reading MA, 1978.

171 I.C.Noyan, J.B.Cohen, *Residual Stresses*, Springer, New York, 1987.

172 K.S.Fancey, C.A.Porter, A.Matthews, *J. Vac. Sci. Technol. A*, **13** (2) 428-435, 1995.

173 C.M.Cotell, J.K.Hirvonen, *Surf. Coat. Technol.*, **81**, 118-125, 1996.

174 McDonnell Douglas Corporation, McDonnell Douglas Ivadizer System, PO Box 576, St Louis, MO 63166, USA.

175 R.D.Bland, G.J.Kominiak, D.M.Mattox, *J. Vac. Sci. Technol.*, **11** (4) 671-674, 1974.

176 C.M.Egert, D.G.Scott, *J. Vac. Sci. Technol. A*, **5** (4) 2724-2727, 1987.

177 M.A.Korhonen, C.A.Paszkiet, *Scr. Metall.*, **23** (8) 1449-1454, 1989.

178 S.Masaki, H.Kobayashi, H.Morisaki, *Nucl. Instrum. Methods Phys. Res. B*, **59/60**, 292-296, 1991.

179 C.Y.Chang, R.W.Vook, *J. Vac. Sci. Technol. A*, **9** (3) 559-562, 1991.

180 Y.W.Kim, I.Petrov, J.E.Greene, S.M.Rossnagel, *J. Vac. Sci. Technol. A*, **14** (2) 346-351, 1996.

181 T.J.Ruden, *Mater. Aust.*, **22** (9) 22-24, 1990.

182 T.G.Nieh, J.Wadsworth, *Thin Solid Films*, **152**, 525-534, 1987.

183 T.G.Nieh, J.Wadsworth, *J. Mater. Sci. Lett.*, **6**, 1150-1152, 1987.

184 E.I.Tochitsky, R.N.Gritskevich, V.E.Obukhov, *Thin Solid Films*, **131**, 289-295, 1985.

185 O.F.Hagena, G.Knop, R.Fromknecht, G.Linker, *J. Vac. Sci. Technol. A*, **12** (2) 282-288, 1994.

186 W.B.Nowak, J.Seyyedi, *Fundamental Aspects of Corrosion Protection by Surface Modification*, Corrosion Division Proceedings, Vol. 84-3, The Electrochemical Society, Pennington, NJ, 89-96, 1984.

187 F.Chang, M.Levy, B.Jackman, W.B.Nowak, *Surf. Coat. Technol.*, **39/40**, 721-731, 1989.

188 T.Z.Kattamis, F.Chang, M.Levy, *Surf. Coat. Technol.*, **43/44**, 390-401, 1990.

189 F.Chang, M.Levy, B.Jackman, W.B.Nowak, *Surf. Coat. Technol.*, **48**, 31-39, 1991.

190 K.R.Baldwin, D.J.Bray, G.D.Howard, R.W.Gardiner, *Mater. Sci. Technol.*, **12** (11) 937-943, 1996.

191 G.L.Makar, J.Kruger, *Int. Materials Reviews*, **38** (3) 138-153, 1993.

192 G.Song, A.Atrens, D.St John, J.Nairn, Y.Li, *Corr. Sci.*, **39** (5) 855-875, 1997.

193 M.Hansen, *Constitution of Binary Alloys*, Second Edition, McGraw-Hill, New York, 1958.

194 J.L.Murray, *Bull. Alloy Phase Diagrams*, **4** (1) 55-73, 1983.

195 *ASM Handbook*, Tenth Edition, Vol.3, ASM, Materials Park, OH, 1992.

196 E.C.Ellwood, *J. Inst. Metals*, **80**, 217-224, 1951.

197 Joint Committee on Powder Diffraction Standards (JCPDS), International Center for Diffraction Data, Swarthmore, PA; CD ROM Database.

198 E.Schmid, G.Wassermann, *Z. Metallkde.*, **26**, 145-150, 1934.

199 H.J.Axon, W.Hume-Rothery, *Proc. Roy. Soc. (London)*, **A193**, 1-24, 1948.

200 J.E.Dorn, P.Pietrokowsky, T.E.Tietz, *Trans. AIME*, **188**, 933-943, 1950.

201 W.J.Helfrich, R.A.Dodd, *Trans. AIME*, **224**, 757-762, 1962.

202 G.R.Goldak, J.G.Parr, *J. Inst. Metals*, **92**, 230-233, 1963.

203 K.G.Satyanarayana, *J. Mater. Sci.*, **16**, 1233-1248, 1981.

204 L.Vegard, *Z.Kristallogr.*, **67**, 239, 1928.

205 M.L.Fuller, R.L.Wilcox, *Trans. AIME*, **122**, 231-243, 1936.

206 A.A.Presnyakov, Y.A.Gorban, V.V.Chervyakova, *Russ. J. Phys. Chem.*, **35** (6) 632-633, 1961.

207 R.P.Elliot, *Constitution of Binary Alloys*, First Supplement, McGraw-Hill, New York, 1965.

208 S. an Mey, *Z. Metallkde.*, **84** (7) 451-455, 1993.

209 S.Agarwal, H.Herman, *Scr. Metall.*, **7**, 503-508, 1973.

210 P.G.Boswell, G.A.Chadwick, *Acta Metall.*, **25**, 779-792, 1977.

211 W.B.Nowak, L.E.Burns, V.G.Harris, *J. Vac. Sci. Technol. A*, **7** (3) 2350-2354, 1989.

212 L.Li, PhD thesis, Northeastern University, USA, 1993.

213 F.Abd El-Salam, A.M.Ibraheim, A.H.Ammar, A.Y.Morsy, *Vacuum*, **46** (11) 1299-1303, 1995.

214 B.A.Shedden, unpublished work, University of Wollongong, Australia, 1994.

215 D.G.Teer, O.A.Abu Zeid, *Thin Solid Films*, **72**, 291-296, 1980.

216 F.C.Chang, M.Levy, R.Huie, M.Kane, P.Buckley, T.Z.Kattamis, G.R.Lakshminarayan, *Surf. Coat. Technol.*, **49**, 87-96, 1991.

217 U.Koch, M.Meyer, *Government Research Announcements and Index*, N92-12108/6/XAB, pp.23, 1991.

218 J.C.S.Fernandes, M.G.S.Ferreira, *Surf. Coat. Technol.*, **53** (1) 99-100, 1992.

219 J.L.Murray, *Bull. Alloy Phase Diagrams*, **3** (1) 60-74, 1982.

220 D.M.Poole, H.J.Axon, *J. Inst. Metals*, **80**, 599-604, 1951.

221 E.C.Ellwood, *J. Inst. Metals*, **80**, 605-608, 1951.

222 R.B.Hill, H.J.Axon, *J. Inst. Metals*, **83**, 354-356, 1954.

223 W.Hume-Rothery, G.V.Raynor, *Proc. Roy. Soc. (London)*, **177A**, 27, 1940.

224 G.V.Raynor, *Proc. Roy. Soc. (London)*, **180A**, 107-121, 1942.

225 R.S.Busk, *J. Metals*, **2**, 1460-1464, 1950.

226 D.Akhtar, R.Gopalan, T.P.Rajasekharan, *Z. Metallkde.*, **78** (3) 201-203, 1987.

227 H.L.Luo, C.C.Chao, P.Duwez, *Trans. Metall. Soc. AIME*, **230**, 1488-1490, 1964.

228 B.Predel, K.Hülse, *Z. Metallkde.*, **69** (11) 690, 1978.

229 K.F.Kobayashi, T.Awazu, P.H.Shingu, *Trans. Jpn. Inst. Met.*, **28** (11) 934-944, 1987.

230 J.L.Murray, *Mat. Res. Soc. Symp. Proc.*, Vol.19, 249-262, Materials Research Society, 1983.

231 F.Hehmann, *Acta Metall. Mater.*, **38** (6) 979-992, 1990.

232 P.Van Mourik, N.M.Maaswinkel, Th.H.de Keijser, E.J.Mittemeijer, *J. Mater. Sci.*, **24** (10) 3779-3786, 1989.

233 C.Suryanarayana, S.K.Tiwari, T.R.Anantharaman, *Z. Metallkde.*, **69** (3) 155-156, 1978.

234 T.Rajasekharan, D.Akhtar, R.Gopalan, K.Muraleedharan, *Nature*, **322** (6079) 528-530, 1986.

235 K.F.Kobayashi, T.Awazu, P.H.Shingu, *Z. Metallkde.*, **79** (3) 194-201, 1988.

236 U.D.Kulkarni, G.K.Dey, R.T.Savalia, S.Banerjee, *Phil. Mag. Lett.*, **64** (3) 169-174, 1991.

237 R.Banerjee, R.T.Savalia, E.G.Baburaj, G.K.Dey, U.D.Kulkarni, *Mater. Sci. Eng.*, **A165** (2) 149-156, 1993.

238 R.Banerjee, R.T.Savalia, N.Prabhu, D.Prakash, U.D.Kulkarni, G.K.Dey, *Scr. Metall. Mater.*, **31** (5) 583-588, 1994.

239 K.R.Baldwin, R.I.Bates, R.D.Arnell, C.J.E.Smith, *Corr. Sci.*, **38** (1) 155-170, 1996.

240 M.-H.Lee, R.Ichino, M.Okido, T.Oki; in H.Henein, T.Oki (ed.) *Proc. First Int. Conf. Processing Materials for Properties*, TMS, 1.141-1.144, 1993.

241 B.Enders, H.Martin, G.K.Wolf, *Surf. Coat. Technol.*, **60**, 556-560, 1993.

242 B.Enders, S.Krauss, K.Baba, G.K.Wolf, *Surf. Coat. Technol.*, **74/75**, 959-965, 1995.

243 C.Eisenmenger-Sittner, A.Bergauer, H.Bangert, W.Bauer, *J. Vac. Sci. Technol. A*, **12** (2) 536-541, 1994.

244 R.I.Bates, University of Salford, Personal Communication, 1996.

245 W.G.Moffat, *Binary Phase Diagrams Handbook*, Vols.I-V, General Electric, Schenectady, NY, 1976.

246 J.B.Clark, L.Zabdyr, Z.Moser, "Magnesium-Zinc"; in *Phase Diagrams of Binary Magnesium Alloys*, ASM, Metals Park, OH, 1988.

247 D.Hardie, R.N.Parkins, *Phil. Mag.*, **4**, 815-825, 1959.

248 E.Schmid, H.Seliger, *Metallwirtschaft*, **11**,409-411, 1932.

249 D.Themines, W.Riehemann, W.Henning, B.L.Mordike, *Mat. Res. Soc. Symp. Proc.*, Vol.58, 275-280, MRS, 1986.

250 E.A.Brandes, G.B.Brook (ed.), *Smithells Metals Reference Book*, Seventh Edition, Butterworth-Heinemann, Oxford, 1992.

251 I.Higashi, N.Shiotani, M.Uda, T.Mizoguchi, H.Katoh, *J. Solid State Chem.*, **36**, 225-233, 1981.

252 Y.Khan, *J. Mater. Sci.*, **24**, 963-973, 1989.

253 C.Barrett, T.B.Massalski, *Structure of Metals*, Third Edition, Pergamon, Oxford, 1980.

254 H.Y.Liu, Y.Li, H.Jones, *Int. J. Rapid Solidification*, **7** (2) 151-166, 1992.

255 I.Stulikova, B.L.Mordike, W.Riehemann, *Int. J. Rapid Solidification*, **3**, 95-107, 1987.

256 A.Calka, M.Madhava, D.E.Polk,, B.C.Giessen, H.Matyja, J.Vander Sande, *Scr. Metall.*, **11**, 65-70, 1977.

257 T.Matsuda, U.Mizutani; in T.Matsumoto, K.Suzuki (ed.), *Proc. 4th Int. Conf. Rapidly Quenched Metals*, Japan Institute of Metals, Sendai, p.1315, 1982.

258 M.Ito, H.Narumi, T.Mizoguchi, T.Kawamura, H.Iwasaki, N.Shiotani, *J. Physical Society of Japan*, **54** (5) 1843-1854, 1985.

259 A.Calka, *J. Phys. F: Met. Phys.*, **16**, 1577-1582, 1986.

260 P.Andonov, P.Chieux, *J. Non-Cryst. Solids*, **108**, 58-74, 1989.

261 P.Andonov, P.Chieux, *J. Non-Cryst. Solids*, **93**, 331-349, 1987.

262 M.-L. Thèye, V. Nguyen-Van, S.Fisson, *Nucl. Instrum. Methods Phys. Res. B*, **31** (10) 6447-6455, 1985.

263 J.J.Hauser, J.Tauc, *Nucl. Instrum. Methods Phys. Res. B*, **17** (8) 3371-3380, 1978.

264 J.Kawafuku, *CAMP-ISIJ*, **2**, 1634-1635, 1989.

265 J.Kawafuku, J.Katoh, M.Toyama, H.Nishimoto, K.Ikeda, H.Satoh, *Tetsu-to-Hagane (J. Iron and Steel Inst. Japan)*, **77** (7) 995-1002, 1991.

266 J.Kawafuku, J.Katoh, M.Toyama, K.Ikeda, H.Satoh, *Kobe Steel Eng. Rep.*, **43** (3) 19-22, 1993.

267 W.Guertler, M.Guertler, E.Anastasiadias, *A Compendium of Constitutional Ternary Diagrams of Metallic Systems*, WADC Tech. Rep. 58-615, Israel Program for Scientific Translations, Jerusalem, 1969.

268 W.Köster, W.Dullenkopf, *Z. Metallkde.*, **28**, 363-367, 1936.

269 G.V.Raynor, W.Hume-Rothery, *Trans. Faraday Soc.*, **44**, 29, 1948.

270 D.R.Nelson, *Sci. Am.*, **255** (2) 43-51, 1986.

271 T.Rajasekharan, R.Gopalan, D.Akhtar, *Key Eng. Mater.*, **13-15** (I) 249-256, 1987.

272 S.Chandra, C.Suryanarayana, *Phil. Mag. B*, **58** (2) 185-202, 1988.

273 D.W.Hoffman, J.A.Thornton, *Thin Solid Films*, **45**, 387-396, 1977.

274 A.Verma, K.L.Chopra, *Key Eng. Mater.*, **13-15** (I) 275-278, 1987.

275 J.Reyes-Gasga, M.Jose-Yacaman, *J. Vac. Sci. Technol. A*, **8** (4) 3455-3459, 1990.

276 D.Mukherjee, K.Ravichandran, N.U.Nayak, *Tool and Alloy Steels*, **25** (9) 355-359, 1991.

277 G.Goldschmied, W.Karner, *Proc. New and Alternative Materials for the Automotive Industry*, Automotive Industry Ltd., Croydon, UK, 267-273, 1992, Florence, Italy, 1-5 June 1992.

278 G.Goldschmied, W.Karner, G.Jäsch, *Galvatech '92*, Verlag Stahleisen, Düsseldorf, 396-401, 1992, 2nd Int. Conf. Zinc and Zinc Alloy Coated Sheet Steel Amsterdam, Netherlands, 8-10 September 1992.

279 K.Steinfelder, G.Jäsch, H.Förster, *Proc. Electron Beam Melting and Refining*, Bakish Materials Corp., Englewood, NJ, 101-105, 1992, Reno, NV.

280 J.M.Bordes, Pôle Universitaire, France, Personal Communication, 1997.

281 T.W.Smythe, BHP Coated Steel Australia, Personal Communication, 1997.

282 S.A.Nicholson, BHP Steel, SCPD, RTC Rep. No.1165, 1993.

283 B.Window, F.Sharples, *J. Mater. Res.*, **3** (5) 856-861, 1988.

284 Target Materials Inc., 1145, Chesapeake Ave, Columbus, OH, USA.

285 D.E.Leyden, "X-Ray Spectrometry"; in *ASM Handbook*, Ninth Edition, Vol.10, ASM, Metals Park, OH, pp.82-101, 1986.

286 *Residual Stress Measurement by X-Ray Diffraction*, SAE J784a, Society of Automotive Engineers, Warrendale, PA, 1980.

287 J.A.Sue, G.S.Schajer, "Stress determination for coatings"; in *ASM Handbook*, Tenth Edition, Vol.5, ASM, Materials Park, OH, pp.647-653, 1994.

288 V.Valvoda, R.Kuzel, Jr., R.Cerny, D.Rafaja, J.Musil, S.Kadlec, A.J.Perry, *Thin Solid Films*, **193/194**, 401-408, 1990.

289 A.J.Perry, B.D.Sartwell, V.Valvoda, D.Rafaja, D.L.Williamson, A.J.Nelson, *J. Vac. Sci. Technol. A*, **10** (4) 1446-1452, 1992.

290 A.J.Perry, V.Valvoda, D.Rafaja, *Thin Solid Films*, **214**, 169-174, 1992.

291 A.J.Perry, J.R.Treglio, D.G.Bhat, S.P.Boppana, T.Z.Kattamis, K.Schlichting, G.Dearnaley, D.E.Geist, *Surf. Coat. Technol.*, **68/69**, 294-300, 1994.

292 A.J.Perry, J.R.Treglio, J.P.Schaffer, J.Brunner, V.Valvoda, D.Rafaja, *Surf. Coat. Technol.*, **66**, 377-383, 1994.

293 D.E.Geist, A.J.Perry, J.R.Treglio, V.Valvoda, D.Rafaja, *The Rigaku Journal*, **11** (2) 9-14, 1994.

294 A.J.Perry, J.R.Treglio, V.Valvoda, D.Rafaja, *J. Vac. Sci. Technol. A*, **13** (3) 1067-1072, 1995.

295 C.J.Shute, J.B.Cohen, *J. Appl. Phys.*, **70** (4) 2104-2110, 1991.

296 R.Kuzel, Jr., R.Cerny, V.Valvoda, M.Blomberg, M.Merisalo, *Thin Solid Films*, **247**, 64-78, 1994.

297 A.J.Perry, *J. Vac. Sci. Technol. A*, **8** (3) 1351-1358, 1990.

298 P.Van Houtte, L.De Buyser, *Acta Metall. Mater.*, **41** (2) 323-336, 1993.

299 T.J.Vink, M.A.J.Somers, J.L.C.Daams, A.G.Dirks, *J. Appl. Phys.*, **70** (8) 4301-4308, 1991.

300 T.J.Vink, W.Walrave, J.L.C.Daams, A.G.Dirks, M.A.J.Somers, K.J.A.van den Aker, *J. Appl. Phys.*, **74** (2) 988-995, 1993.

301 H.U.Baron, V.Hauk, *Z. Metallkde.*, **79** (2) 127-131, 1988.

302 H.Behnken, V.Hauk, *Thin Solid Films*, **193/194**, 333-341, 1990.

303 B.M.Clemens, J.A.Bain, *MRS Bulletin*, **17** (7) 46-51, 1992.

304 R.Kuzel, Jr., R.Cerny, V.Valvoda, M.Blomberg, M.Merisalo, S.Kadlec, *Thin Solid Films*, 268 (1-2) 72-82, 1995.

305 Y.-W.Kim, J.Moser, I.Petrov, J.E.Greene, S.M.Rossnagel, *J. Vac. Sci. Technol. A*, **12** (6) 3169-3175, 1994.

306 C.Quaeyhaegens, G.Knuyt, L.M.Stals, *Surf. Coat. Technol.*, **74/75**, 104-109, 1995.

307 F.N.Kaul, University of Wollongong, Australia, Honours Thesis, 1995.

308 B.A.Shedden, F.N.Kaul, *Int. Schools and Conf. on X-Ray Analytical Methods*, Sydney, Australia, 18-25 January 1996, Australian X-Ray Analytical Assoc., p.C-28 (abstract only), 1996.

309 P.F.Willemse, B.P.Naughton, C.A.Verbraak, *Mater. Sci. Eng.*, **56**, 25-37, 1982.

310 P.F.Willemse, B.P.Naughton, *Mater. Sci. Technol.*, **1**, 41-44, 1985.

311 V.Hauk, H.-J.Nikolin, *Textures Microstruct.*, **8-9**, 693-716, 1988.

312 L.Pintschovius, V.Hauk, W.K.Krug, *Mater. Sci. Eng. A*, **92**, 1-12, 1987.

313 C.Quaeyhaegens, L.M.Stals, M.Van Stappen, *Mater. Sci. Eng. A*, **139**, 242-248, 1991.

314 Grazing incidence attachment, Siemans AG, Germany, Order No. C79000-M3476-C136-03, 1988.

315 V.Hauk, G.Vaessen, *Z. Metallkde.*, **76**, 102-107, 1985.

316 R.Thokala, J.Chaudhuri, *Thin Solid Films*, **266**, 189-191, 1995.

317 ASTM Standard G5-87, "Standard References Test Method for Making Potentiostatic and Potentiodynamic Anodic Polarization Measurements", *Annual Book of ASTM Standards*, Vol.03.02, ASTM, 1991, pp.73-79.

318 B.A.Shedden, University of Wollongong, Australia, Honours Thesis, 1992.

319 G.W.Walter, *Corr. Sci.*, **35** (5-8) 1391-1404, 1993.

320 M.Samandi, B.A.Shedden, D.I.Smith, G.A.Collins, R.Hutchings, J.Tendys, *Surf. Coat. Technol.*, **59**, 261-266, 1993.

321 ASTM Standard G3-89, "Standard Practice for Conventions Applicable to Electrochemical Measurements in Corrosion Testing", *Annual Book of ASTM Standards*, Vol.03.02, ASTM, 1991, pp.56-63.

322 E.L.Liening, "Electrochemical corrosion testing techniques"; in *Process Industries Corrosion: The Theory and Practice*, NACE, Houston, TX, pp.85-122, 1986.

323 M.V.Swain, B.Window, *Residual Stresses III, Science and Technology*, H.Fujiwara, T.Abe, K.Tanake (ed.), Elsevier, London, p.744, 1992, 3rd Int. Conf. Residual Stresses, Tokushima, Tokyo, July 1991.

324 E.Klokholm, B.S.Berry, *J. Electrochem. Soc.*, **115**, 823, 1968.

325 E.Klokholm, *J. Vac. Sci. Technol.*, **6**, 138, 1969.

326 H.E.Schiott, *Rad. Effects*, **6**, 107, 1970.

327 H.H.Andersen, H.L.Bay, "Sputtering yield measurements"; in R.Behrisch (ed.), *Sputtering by Particle Bombardment*, Chap.4, Springer-Verlag, Berlin, 1981.

328 G.E.Dieter, *Mechanical Metallurgy*, McGraw-Hill, London, 1988.

329 H.E.Roosendaal, "Sputtering yields of single crystalline targets"; in R.Behrisch (ed.), *Sputtering by Particle Bombardment*, Chap.5, Springer-Verlag, Berlin, 1981.

330 B.A.Shedden, M.Samandi, B.Window, *Surf. Coat. Technol.* (in press); 5th Int. Conf. Plasma Surface Engineering, Garmisch-Partenkirchen, Germany, 9-13 Sept 1996.

331 R.Hultgren, P.D.Desai, D.T.Hawkins, M.Gleiser, K.K.Kelly, D.D.Wagman, *Selected values of the thermodynamic properties of the elements*, ASM, Metals Park, OH, 1973.

332 A.A.Nayeb-Hashemi, J.B.Clark, "Argon-Magnesium"; in *Phase Diagrams of Binary Magnesium Alloys*, ASM, Metals Park, OH, 1988.

333 A.M.Altshuler, Yu.Kh.Vekilov, G.R.Umarov, *Phys. Lett.*, **73A** (3) 216-217, 1979.

334 H.R.Glyde, K.I.Mayne, *Phil. Mag.*, **12** (119) 919-937, 1965.